University of Liège
Department of Electrical Engineering & Computer Science

Uncovering the molecular and cellular mechanisms of reliable neuromodulation in highly heterogeneous neurons

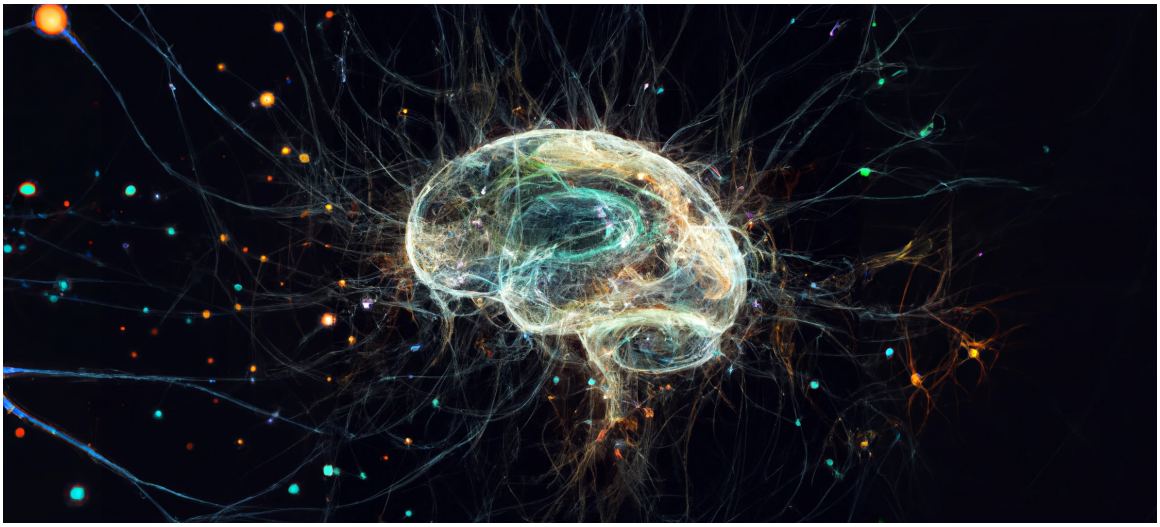

a PhD dissertation
by Arthur Fyon
Advisor: Prof. Guillaume Drion

Thesis submitted in partial fulfillment of
the requirements for the degree of Doctor
of Philosophy (PhD) in Engineering Science

December 2024

Jury members

Philippe Vanderbemden, Professor at the Université of Liège, Belgium (President);

Guillaume Drion, Professor at the Université of Liège, Belgium (Supervisor);

Pierre Sacré, Professor at the Université of Liège, Belgium;

Dominique Engel, Professor at the Université of Liège, Belgium;

Jean-Marc Goaillard, Institut de Neurosciences de la Timone, Centre national de la recherche scientifique (CNRS), Aix-Marseille Université, France;

Frédéric Crevecoeur, Professor at the Université Catholique de Louvain, Belgium;

Résumé

Cette thèse explore les mécanismes qui permettent une neuromodulation fiable dans des neurones présentant une variabilité significative des propriétés des canaux ioniques. La neuromodulation influence dynamiquement l'activité neuronale et le comportement des réseaux en ciblant les canaux ioniques via des voies réceptrices métabotropiques. Ces cascades de signalisation complexes doivent surmonter l'hétérogénéité neuronale intrinsèque, posant des défis pour comprendre leurs effets. Ce travail combine neurosciences computationnelles, théorie des systèmes dynamiques et ingénierie de contrôle pour élucider comment la neuromodulation atteint une fiabilité dans des systèmes biologiquement variables. La recherche se divise en trois contributions majeures :

1. **Compréhension des mécanismes de dégénérescence neuronale** : À l'aide de techniques de réduction dimensionnelle appliquées à des modèles à conductance, deux mécanismes principaux de dégénérescence neuronale sont identifiés. Le premier implique des ajustements proportionnels uniformes des conductances des canaux ioniques, tandis que le second reflète une variabilité cryptique des ratios de conductances qui se manifeste lors de perturbations. Ces mécanismes, parfois concurrents ou alignés selon l'état neuromodulatoire, influencent les corrélations entre conductances. Cette analyse montre comment la neuromodulation suit des trajectoires spécifiques au type de neurone dans l'espace des conductances, garantissant des effets robustes malgré la variabilité.

2. **Développement d'un contrôleur neuromodulatoire basé sur les GPCR** : Un système de contrôle inspiré des voies de signalisation est introduit. Ce contrôleur traduit les signaux neuromodulateurs en ajustements en temps réel des densités de canaux ioniques. Ce système adaptatif modélise l'excitabilité neuronale comme une boucle de rétroaction, simplifiant ainsi la complexité de la neuromodulation. Les simulations montrent sa capacité à maintenir une activité neuronale constante au sein d'une population de neurones présentant une large variabilité des propriétés des canaux ioniques.

3. **Interaction entre neuromodulation et homéostasie** : La synergie entre la neuromodulation et les régulations homéostatiques est explorée. La neuromodulation ajuste sélectivement les corrélations spécifiques des canaux ioniques, tandis que l'homéostasie ajuste globalement toutes les conductances pour maintenir des niveaux intracellulaires de calcium. La modélisation de leur interaction révèle comment ces mécanismes complémentaires préservent une activité neuronale robuste. Cette approche combinée atténue les défaillances potentielles qui résulteraient de l'utilisation isolée de l'un ou l'autre mécanisme.

Ces principes de la neuromodulation sont appliqués à la robotique, où un réseau neuromodulateur est utilisé pour reconfigurer dynamiquement les motifs de locomotion d'un robot quadrupède. Ce système permet des transitions fluides entre différents rythmes. La robustesse et l'adaptabilité de cette approche offrent des applications potentielles en ingénierie neuromorphique. En intégrant des perspectives expérimentales et computationnelles avec la théorie du contrôle, cette thèse fournit une compréhension complète de la fiabilité de la neuromodulation face à la variabilité neuronale, faisant progresser les bases théoriques des neurosciences et de l'ingénierie bio-inspirée.

Mots clés – Neuromodulation, Variabilité neuronale, Modèle à conductance

Abstract

This dissertation explores the mechanisms behind reliable neuromodulation in neurons exhibiting significant variability in ion channel properties. Neuromodulation, driven by agents such as dopamine, serotonin, and histamine, dynamically influences neuronal activity and network behavior by targeting ion channels via metabotropic receptor pathways. These complex signaling cascades must overcome intrinsic neuronal heterogeneity, posing challenges to understanding their consistent effects. This work combines computational neuroscience, dynamical systems theory, and control engineering to uncover how neuromodulation achieves reliability in such variable systems. The research is divided into three major contributions:

1. **Understanding Neuronal Degeneracy Mechanisms**: Using dimensionality reduction techniques on conductance-based models, two primary mechanisms of neuronal degeneracy are identified. The first, homogeneous scaling, involves uniform proportional adjustments in ion channel conductances, while the second, variability in conductance ratios, reflects cryptic variability in dynamic properties that manifest under perturbations. These mechanisms often compete or align depending on the neuromodulatory state, affecting conductance correlations. This analysis highlights how neuromodulation follows indirect but neuron-type-specific trajectories in conductance space, ensuring robust effects despite variability.

2. **Development of a GPCR-Based Neuromodulation Controller**: A novel control system inspired by G-protein coupled receptor signaling pathways is introduced. The controller translates neuromodulatory signals into real-time adjustments of ion channel densities using dynamic input conductances as control variables. This adaptive system models neuronal excitability as a feedback control loop, simplifying the complexity of neuromodulation. Simulations demonstrate its ability to maintain consistent neuronal activity patterns across a population of neurons with widely varying ion channel properties.

3. **Interaction Between Neuromodulation and Homeostasis**: The synergy between neuromodulation and homeostatic regulation is explored. Neuromodulation selectively adjusts specific ion channel correlations, while homeostasis broadly scales all conductances to maintain intracellular calcium levels. Modeling their interaction reveals how these complementary mechanisms maintain robust neuronal activity. The combined approach mitigates potential failures that would arise from either mechanism in isolation.

Additionally, the principles of neuromodulation are extended to robotics, where a neuromodulatory network is used to dynamically reconfigure locomotion patterns in a quadruped robot. This system enables seamless transitions between rhythmic gaits, such as trotting and galloping, by modulating specific neuromodulatory neurons. The robustness and adaptability of this approach offer potential applications in neuromorphic engineering and neural network control. By integrating experimental and computational insights with control theory, this dissertation provides a comprehensive framework for understanding how neuromodulation achieves reliability in the face of neuronal variability. It advances the theoretical foundation for both neuroscience and bio-inspired engineering applications.

Keywords – Neuromodulation, Neuronal variability, Conductance-based model

Acknowledgements

I have always imagined that embarking on a PhD is like being pulled from the well-defined path of academic study and dropped into the middle of a vast ocean. The ocean represents the incredibly rich literature surrounding your subject, while the distant land symbolizes the unique piece of research you aim to contribute to the world. At first, you have no clear sense of direction, nor any means of transportation beyond your own arms and legs to keep afloat. Throughout the PhD journey, however, you gradually construct a rowing boat, then a motorized vessel, and eventually equip yourself with a map, a compass, and a spyglass to navigate the waters. These tools are forged not only through your own effort but, more importantly, through the invaluable guidance, motivation, and support of those around you. As I finally set foot on the land I have sought, I would like to take a moment to thank all the people who helped me assemble my marine adventurer equipment.

First and foremost, I would like to express my deepest gratitude to my (greatest) supervisor (of all time), Prof. Guillaume Drion. Working under his guidance has been an honor and a privilege. Guillaume is a passionate and exceptionally talented researcher in the field of computational neuroscience, whose expertise and vision have profoundly shaped this thesis. He not only provided me with the flexibility to explore and grow but also made himself readily available whenever I encountered obstacles, always bringing enthusiasm and insight to every brainstorming session. His ability to unlock solutions with a single meeting is nothing short of a superpower. I vividly remember our first discussion about my PhD journey. I described myself as a "problem solver" but admitted to lacking creativity. He responded with a reassuring smile, saying that this would complement his "dreamer" profile—full of great ideas needing practical implementation. Over time, Guillaume fostered an environment that allowed me to evolve. By the end of my PhD, he told me that I had become one of the most creative students he had ever supervised—a compliment I will always treasure. Guillaume, I cannot thank you enough for introducing me to the academic world, guiding me through its complexities, and helping me become the researcher I am today.

I would also like to extend my heartfelt gratitude to Prof. Alessio Franci and Prof. Pierre Sacré for their invaluable guidance and support throughout my PhD journey. While not officially co-supervisors of this thesis, they have certainly played a pivotal role, complementing Guillaume mentorship with their unique perspectives and expertise. Their constructive feedback and insightful advice were instrumental in shaping my manuscripts and, more broadly, my approach to research. I am deeply grateful for the time and energy they devoted to our brainstorming sessions and for the opportunity to collaborate on a publication together. Their dedication and encouragement have significantly contributed to the success of this thesis, and I cannot thank them enough for their unwavering support.

I would also like to express my gratitude to the other members of my jury: Prof. Philippe Vanderbemden, Prof. Dominique Engel, Prof. Jean-Marc Goaillard, and Prof. Frédéric Crevecoeur. Thank you for graciously accepting to be part of my jury and for dedicating your time and energy to reviewing my work and attending my defense. Your insights and

expertise have been invaluable.

I would like to express my gratitude to the F.R.S.-FNRS for funding my research and providing me with the opportunity to delve into the study of neuromodulation within computational neuroscience.

Within the academic world, I would like to extend my thanks to all the current and former members of the newly established Neuroengineering Laboratory at the University of Liège, led by the three distinguished professors mentioned earlier. My gratitude goes to Anaëlle, Antoine, Asad, Ben, Caroline D., Caroline M., Christian, Fatemeh, Florent, Jérôme, Kathleen, Loris, Pascal, Quentin, Rodrigo, Sergio, and Sven. Thank you for the time you spent listening to my presentations during lab meetings, offering valuable feedback and ideas, and for fostering such a collaborative and enjoyable atmosphere both during work and our outings. A special thanks goes to Kevin for introducing me to various specialized topics in experimental neuroscience, for proofreading some of my work, and for opening opportunities for collaboration during my time at the University after completing my PhD. Your support and generosity have been deeply appreciated.

Still within the academic world, though not for professional reasons, I would like to thank Prof. Philippe Vanderbemden and his team—Jean-François, Michel, Thor, Nicolas, and Thomas—for warmly welcoming me during their coffee breaks and lunches, which were always refreshing and filled with laughter. During every break, uniting Thor, Michel, and friends, outstanding unity flourished over understanding resolutions.

More specifically, I want to express my gratitude to Michel and Thor. Thor and I first became friends while working on some of our master's projects, and we later decided to share an office during our PhDs. That decision turned out to be one of the best we ever made, as our friendship grew stronger with each passing day. A few months later, Michel, a close colleague of Thor's whom I barely knew at the time, joined our office, 1.15. This, too, proved to be one of the best decisions of my life, as yet another true friendship blossomed. I will always treasure the countless hours we spent together in the office—working, laughing, and building the bonds of friendship. Sharing time and friendship, friends offered real dedication, growing and maintaining bonds, inspiring trust. These moments were not only a source of joy but also one of the greatest driving forces that carried me through my PhD journey.

I would also like to thank all of my friends—Mathieu, Nelson, Yannick, Antoine, Alexandre, Jean, Martin, Quentin, and Benjamin—for the wonderful moments we shared. These times provided much-needed breaks from the mental rumination that a PhD often brings, making the journey all the more enjoyable.

During my PhD, I spent a significant amount of time working from home, and I cannot thank my close family enough—my parents, my grandmothers, and my late grandfather—for providing me with a calm and supportive environment that allowed me to focus on my work without interruption. It truly felt like an all-inclusive plan, and their unwavering support made all the difference.

Finally, and by no means least, I would like to express my infinite gratitude to the incredible

woman with whom I share my life, Floriane. Her support has been the driving force that pushed me to surpass myself and create the body of work contained in this thesis. When I was feeling down, she was there to comfort me; when I was elated from achieving something or when one of my manuscripts was accepted, she was there to celebrate with me. During late nights and public holidays, when I had to work, she understood and allowed me to focus, always offering thoughtful gestures that I undoubtedly needed.

I am proud to say that this thesis is not only the result of the academic guidance I received, but also of the daily support and love I have been fortunate to receive from her and others. I am truly grateful to share my life with you and could not imagine my future without you. I love you.

You may think that three pages of acknowledgments is excessive for a PhD thesis, but I believe this section is the most personal, where I can express all my feelings apart from the professional content of the manuscript. I truly feel that this part should be as long as the PhD candidate feels necessary, because writing these feelings is, for me, one of the most sincere ways to express them.

I dedicate this work to my loved one.

University of Liège

Liège, December 2024

Arthur Fyon

Table of contents

The most that can be expected from any model is that it can supply a useful approximation to reality. All models are wrong, but some models are useful

George Box

Introduction

Research question

Brain activity is constantly shaped by the action of numerous neuromodulators and neuropeptides such as dopamine, serotonin, and histamine, to name a few (Bargmann and Marder, 2013; Marder et al., 2014). Neuromodulators dynamically influence single neuron activity and input/output properties as well as the strength and dynamics of synaptic connections, providing a mean to constantly adapt a neuronal network activity in response to ever changing needs, contexts and environments (Bargmann and Marder, 2013; Marder and Calabrese, 1996; Marder and Bucher, 2001; Marder et al., 2014; McCormick et al., 2020). To achieve this modulation, neuromodulators dynamically reshape the density, dynamics and kinetics of many single cell transmembrane proteins, making whole brain functional signaling strongly dependent on the robustness and reliability of neuromodulation mechanisms at the molecular and cellular levels.

Although neuromodulation has been shown to be ubiquitous in the nervous system for several decades, the mechanisms underlying their reliable action are still elusive to date for two main reasons. First, neuromodulators affect neuronal signaling through the activation of metabotropic receptors. These receptors do not directly influence membrane ion channels but involve second messengers that trigger complex signaling cascades. These signaling cascades eventually target ion channels in a neuron specific manner, resulting in a wide range of effects in different neuron types, most of which are very difficult to identify experimentally. Likewise, many different neuromodulators can target the same ion channels, or subset of ion channels, leading to possibly interfering effects (Marder and Bucher, 2007). Secondly, past research has convincingly highlighted that ion channel densities and other properties, which are the end targets of neuromodulators, can be highly variable in neurons of the same types, sometimes varying up to 5 folds (Schulz et al., 2006b). This raises the question of how neuromodulators can possibly have reliable effects at the whole brain level while indirectly targeting such variable properties at the molecular and cellular levels.

Attempting to provide answers to this question is the core goal of this thesis. We propose to study the molecular and cellular mechanisms underlying reliable neuromodulation in highly variable neurons by combining approaches from experimental and computational neuroscience, dynamical systems and feedback control. Our innovative strategy is to analyze cellular neuromodulation from a feedback systems perspective as a direct, feedforward neuromodulator action on ion channel density cannot lead to reliable effects on highly variable neurons. We have explored and quantified how various sets of ion channel properties can lead to similar firing activities, a property called degeneracy (Prinz et al., 2004; Drion et al., 2015c), by working with high dimensional conductance based models. The goal is to extract functional variables that uniquely determine neuronal activity and can be related to the degenerate physiological variables such as ion channel density.

In the core of thesis, we exploit the qualitative physiological structure of metabotropic receptor signaling to construct a feedback control system capable of providing reliable neuromodulation

in highly variable cells. The goal is to relate the newly defined functional variables to the intermediate signaling pathway by decomposing the neuromodulation process into three main steps: (i) the neuromodulator activates a metabotropic receptor, (ii) the receptor modifies the neuron activity target by acting on a second messenger (such as cyclic AMP), and (iii) the second messenger involves a feedback control loop to reach the novel activity target by tuning the properties of a predefined ion channel subset.

Outline and structure

This thesis sits at the intersection of two research fields: neuroscience and computational neuroscience. While these areas might seem similar due to their names, the former is rooted in the biological sciences, whereas the latter belongs to the realms of engineering and computer science. Chapter 1 covers the essential neuroscience concepts necessary for understanding this thesis, including an overview of the central nervous system (Section 1), an exploration of neurons and neuronal excitability (Section 2), the role of reliable neuromodulation (Section 3), and discussions on degeneracy, ion channel correlations, and homeostasis (Section 4). It also provides a practical example integrating these concepts through the gastric system of crabs (Section 5). By the end of this chapter, readers should have a comprehensive understanding of how neuromodulation occurs in biological systems and how it interacts with mechanisms such as degeneracy and homeostasis, setting the stage for modeling these processes (Section 6).

Chapter 2 shifts to computational neuroscience, outlining the key concepts necessary for understanding the thesis modeling work. This includes how to model neuronal excitability using conductance-based models and networks (Section 7), an introduction to neurodynamics (Section 8), an introduction to control theory (Section 9), a review of a published model for homeostatic control (Section 10), a state-of-the-art approach to modeling neuromodulation (Section 11), a strategy for addressing degeneracy and the high dimensionality of conductance-based models by viewing neurons as feedback systems (Section 12), and a detailed description of the specific models used in this thesis (Section 13). By the end of this chapter, readers should be equipped with the necessary background to engage with the thesis contributions.

Chapter 3 outlines the scientific contributions of this thesis. Section 14 delves into the mechanistic understanding of neuronal degeneracy. Through dimensionality reduction, we identified two interacting physiological mechanisms that fully explain ion channel correlations. This insight led to the development of an efficient algorithm for generating degenerate neuronal populations, which surpasses current random search techniques. The algorithm was further refined to enable reliable neuromodulation of these degenerate populations, allowing us to explore how ion channel correlations change under neuromodulation.

Section 15 focuses on the core contribution of this thesis: the development of a reliable neuromodulation adaptive control model for ion channel conductances. Building on the mechanistic understanding of neuronal degeneracy, an adaptive controller was designed to equip any conductance-based model with the ability to achieve reliable neuromodulation in diverse conditions.

In Section 16, the analysis of this adaptive controller is extended by combining it with a previously published homeostatic controller. Since both controllers influence the same actuators (ion channels), it is not immediately clear how their combined actions ensure robust neural function. The combined neuromodulation-homeostatic ion channel controller was also tested on small neuronal networks, such as central pattern generators (CPGs).

Finally, Section 17 explores potential applications of this combined controller in neuromorphic engineering. Specifically, it introduces a new architecture for incorporating reliable neuromodulation into CPGs, allowing these circuits to switch from one rhythmic pattern to another without altering the connectome, thereby eliminating the need for synaptic plasticity.

Chapter 4 highlights the key methodological contribution of this thesis (Section 18): a Julia package that automates the computational processes developed throughout the research. This package serves as an accessible tool for both computational and experimental neuroscientists, enabling them to explore the adaptive neuromodulation controller with minimal programming knowledge. Users can simulate any conductance-based model equipped with this adaptive neuromodulation control with only a few lines of code, without needing in-depth mathematical expertise. This tool facilitates broader dissemination and practical application of the thesis results.

Finally, chapter 5 summarizes the key findings of this thesis, discusses its limitations, and proposes future research directions. It reflects on the scope and impact of the results, while acknowledging areas where improvements or further investigation are necessary (Section 19). Additionally, it offers perspectives on how the methodologies and concepts introduced in this work can be extended or refined in future studies (Section 20). This last chapter is followed by a series of appendices, which provide supplementary materials and detailed explanations that support the main content of the thesis.

Contributions

The contributions of this thesis can be found in articles, posters in conference and oral presentations in conference, available at our institutional repository.

- **Published journal article:**
  - Fyon Arthur, Franci Alessio, Sacré Pierre and Drion Guillaume (2024). Dimensionality reduction of neuronal degeneracy reveals two interfering physiological mechanisms. *PNAS Nexus*
    https://doi.org/10.1093/pnasnexus/pgae415
- **Published conference article:**
  - Fyon Arthur, Sacré Pierre, Franci Alessio and Drion Guillaume (2023). Reliable neuromodulation from adaptive control of ion channel expression.
    IFAC-PapersOnLine and IFAC World Congress, July 2023, oral presentation (Yokohama, Japan).
    https://doi.org/10.1016/j.ifacol.2023.10.1610

- **Preprint under submission process:**
  - Fyon Arthur and Drion Guillaume (2024). Neuromodulation and homeostasis: complementary mechanisms for robust neural function.
    Arxiv preprint
    https://arxiv.org/abs/2412.04172
- **Conference oral presentations:**
  - Fyon Arthur and Drion Guillaume (2024). An adaptive controller of reliable neuromodulation on mixed feedback systems.
    Benelux Meeting on Systems and Control, March 2024, oral presentation (Blankenberge, Belgium).
    https://hdl.handle.net/2268/315706
  - Fyon Arthur and Drion Guillaume (2021). Apparent neuromodulation-dependent correlation levels in neuron ion channel expression result from a competition between passive and active membrane properties.
    SfN Annual Meeting, November 2021, oral presentation (online).
    https://hdl.handle.net/2268/267590
- **Conference posters:**
  - Fyon Arthur and Drion Guillaume (2024). Neuromodulation robustly tunes rhythmic patterns in a fixed connectome: application to gait control.
    FENS Forum, June 2024, poster (Vienna, Austria).
    https://hdl.handle.net/2268/321005
  - Fyon Arthur and Drion Guillaume (2023). Neuromodulation and homeostasis: complementary mechanisms in ion channel expression adaptation for robust neural function.
    Bernstein Conference, September 2023, poster (Berlin, Germany).
    https://hdl.handle.net/2268/307323

Part I

Background in Neuroscience

This chapter provides a comprehensive background in neuroscience essential for a complete understanding of this thesis. The primary focus is on biological neuroscience, while the subsequent chapter places emphasis on the background of computational neuroscience. The initial section delves into fundamental concepts in neuroscience, exploring both the macroscopic and microscopic realms. Special attention is given to the structure and functions of neurons in cognition and neuronal signal processing. Following this, there is a section dedicated to the unique characteristic that sets neurons apart from other cells: neuronal excitability. This excitability undergoes constant reshaping and modulation, a topic covered in section 3. Subsequently, the chapter delves into the state-of-the-art understanding of three crucial aspects of neurons central to this thesis: degeneracy, ion channel correlations, and homeostatic plasticity. The chapter concludes with a description of a well-known neuronal system that will be studied in the final stages of this thesis: the stomatogastric nervous system of the crab and of the lobster.

1 Central nervous system basics

Before delving into key findings in neuroscience relevant to this thesis, let us recap some fundamental concepts.

1.1 Macroscopic physiology

While this thesis predominantly focuses on the dynamics of single cells or small neuronal networks, it is essential to start with an overview of the brain at macroscopic level before describing its cellular components.

1.1.1 Anatomy of the whole central nervous system

The nervous system stands as the central processing unit in every creature within the animal kingdom, emitting, integrating, and sensing chemical and electrical signals throughout the entire body to construct cognitive functions, consciousness, memory, and more. This intricate system divides into the central nervous system (CNS), comprising the brain and spinal cord, and the peripheral nervous system (PNS), encompassing everything else (Thau et al., 2022).

The brain, housed within the skull, is a complex organ composed of nervous tissue, responsible for critical functions such as locomotion, sensation, communication, and memory. Nervous tissue consists of two main cell types: neurons and glial cells, each fulfilling distinct roles. Neurons are responsible for processing and transmitting information essential for neural activities, while glial cells, which outnumber neurons by a ratio of 10:1 or more (Von Bartheld et al., 2016),

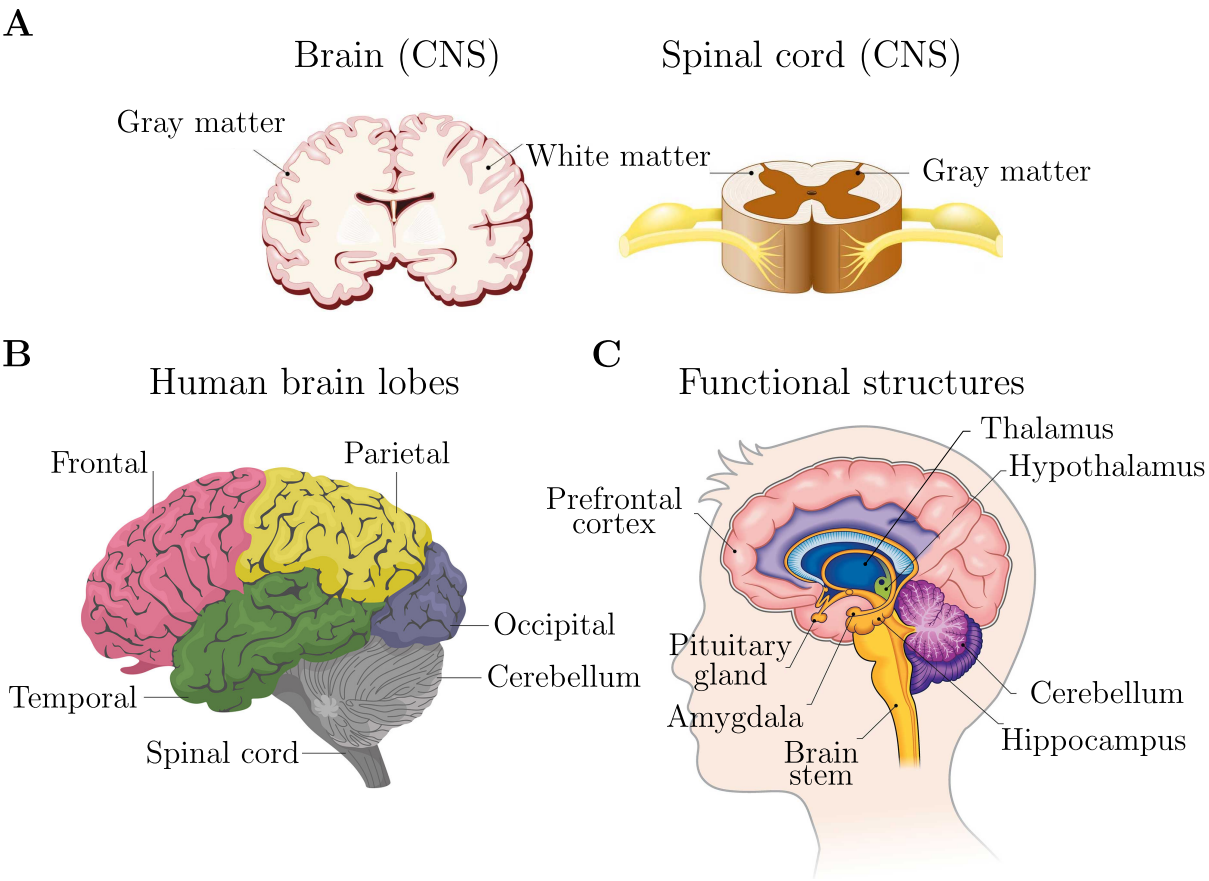

Figure 1.1: Macroscopic anatomy of the brain. A. The nervous system comprises two primary divisions: the central nervous system (CNS), encompassing the brain and spinal cord, and the peripheral nervous system (PNS), which includes all other neural structures. Within the CNS, neural tissue is characterized by its color, either gray or white. **B.** The brain is anatomically divided into distinct functional regions known as lobes. **C.** Below the lobes, specific functional structures can be identified within or outside the brain. Taken from Hopkins (2004).

provide structural support and perform various critical functions (Jessen, 2004). Across the brain, diverse types of neurons and glial cells exhibit remarkable variability in structure, molecular composition, function, and activity. Notably, neurons use electrical and chemical signals to process and transmit information.

The brain can be divided both anatomically and functionally. The most fundamental division is into the left and right hemispheres, often referred to as the left and right brain. These hemispheres are specialized for processing different types of information and governing distinct cognitive functions (Sperry, 1975).

Another common classification is based on the color of neural tissue. Gray matter, primarily composed of cell bodies, is located at the brain periphery and serves as the center for information processing. In contrast, white matter, predominantly made up of myelinated neuronal fibers, is situated at the brain core and functions as the relay center for information transmission. The distinct coloration of these tissues arises from the specific distribution of cellular parts (Figure 1.1A).

Functional zones in the brain, uncovered through functional imaging, reveal a high degree of

functional specificity in the information conveyed by neuronal systems (Gazzaniga, 1989). The cortex, the largest functional zone on the brain periphery, is organized into six layers and governs functions such as speech, movement control, and vision (Jawabri and Sharma, 2023). Further functional divisions include lobes—frontal, temporal, parietal, and occipital (Duvernoy, 2005) (Figure 1.1B). Each lobe, explained in the next section, handles specific neural functions, and depending on these functions, lobes can be subdivided into ultra-specific areas like the Broca area for word articulation or the Wernicke area for language audition (Embick et al., 2000).

The cortex is covering more complex regions, called subcortical. The thalamus, centrally located, serves as a critical relay for sensory and motor information, impacting alertness, sleep, and consciousness (Sherman and Guillery, 2006). Located under the thalamus, the hypothalamus plays a crucial role in regulating circadian rhythms and other physiological functions (Pop et al., 2018). Between the brain and spinal cord, the cerebellum and brain stem play crucial roles in motor control and spatial navigation. While regions like the amygdala, pituitary gland, brain stem, or hippocampus are vital for living organisms, they fall beyond the scope of this thesis (Figure 1.1C).

1.1.2 Functions

The central nervous system primarily functions as an integrative system (Bernstein, 1970). Essentially, every functional area of the brain receives input information, originating from other brain areas or sensory inputs. It then processes this information and generates signals directed either to other brain areas or motor parts. Each brain area specializes in specific functions at different hierarchical levels. The brain organization spans various spatial scales, exemplified by the occipital lobe, which serves as the visual center known as the visual cortex. In a hierarchical manner, the visual cortex receives stimuli from the eyes, processes it, and outputs signals to other brain areas to control eye movements (Gilbert, 1983) (see Figure 1.2A and B for an example on the macaque visual system).

Within the visual cortex, distinct areas like the primary visual cortex (V1) and V2 (a higher-order area) exist, operating on the same input-process-output principle. For example, V1 receives sensory information from the eyes and outputs information to V2. Additionally, V1 specializes in tasks such as encoding the orientation and spatial information of visual stimuli, while V2 analyzes more complex visual features, including motion, intricate shapes, and position (Olshausen and Field, 2005).

This underscores the notion that the brain resembles a puzzle, with each piece contributing harmoniously to a specific function and neuronal architecture, while these interconnected pieces complement one another. One example of this complexity is how visual information is processed from the retina to the visual cortex.

1.1.3 Measuring whole brain activity

In order to better understand the intricacies of brain functions, neuroscientists employ various techniques to measure brain activity, each differing in spatial and temporal resolutions, invasiveness, and complexity. Before the development of such measuring techniques, the only way

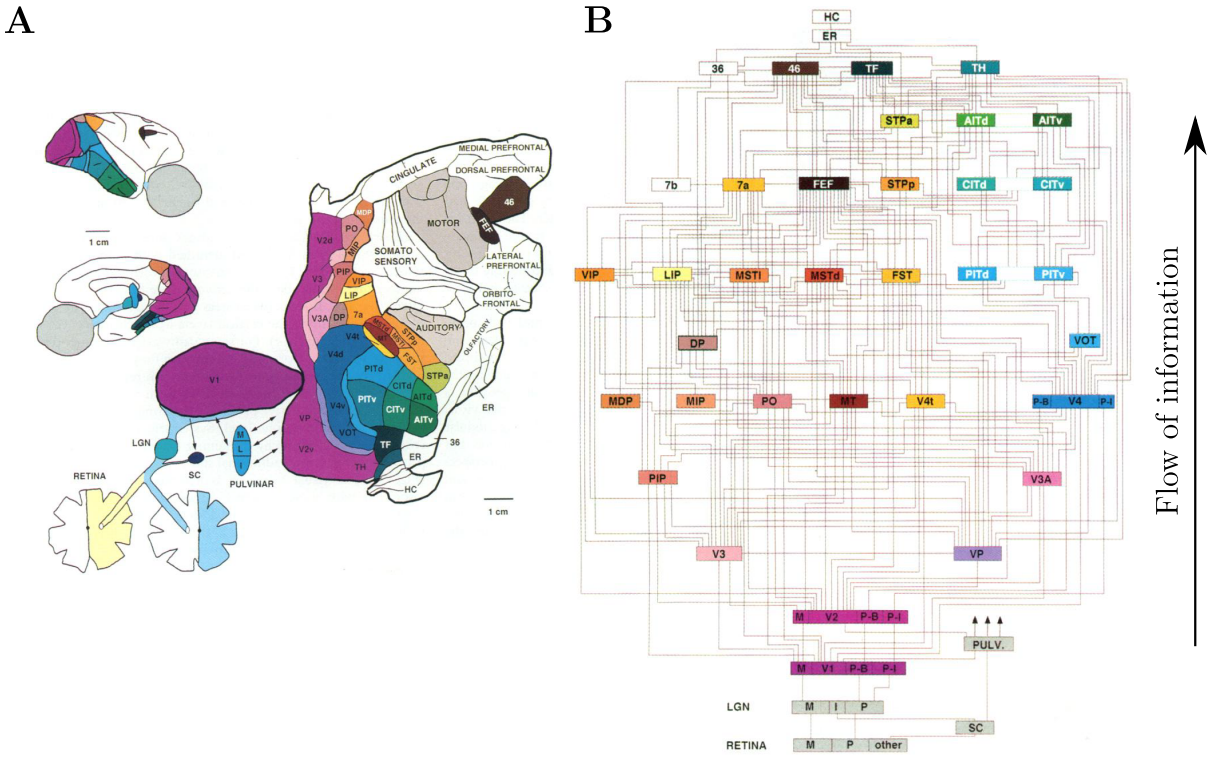

Figure 1.2: Visual information processing in a macaque brain. A. Anatomical depiction of the macaque visual system, illustrating lateral and medial views of the right hemisphere. All structures depicted are several millimeters thick. The abbreviations denote various visual cortex areas, and detailed descriptions are given in Van Essen et al. (1992). **B.** Hierarchical organization of visual areas in the macaque. Information processing proceeds from the retina to the visual areas, culminating in progressively higher levels of integration. Adapted from Van Essen et al. (1992), where the direction of the flow of information has been added.

for neuroscientists to understand the brain was through surgical practices on deceased patients, allowing them to glean insights into brain anatomy (Finger, 2001). However, functional mapping of the brain remained elusive during this period. Among the various methods used to study brain area functions, the following two are the most widely used today:

- **Functional Brain Imaging:**
  Brain imaging techniques such as magnetic resonance imaging (MRI), computer tomography scanner (CT scan) or positron emission tomography scan (PET scan) are commonplace in hospitals for observing the static anatomy of the brain (Figure 1.3A and B). Neuroscientists have adapted these techniques to obtain a functional 3D image of the brain by recording metabolic activity as an indirect measure of brain activity. Functional MRI (fMRI), for instance, records images of local cerebral hemodynamic variations, which increase when specific brain areas are stimulated. This is because stimulated neuronal cells process information and demand energy, which is supplied through the blood (Figure 1.3A). Although functional brain imaging techniques offer better temporal resolution, they generally have lower spatial resolution compared to classical brain imaging techniques (Heeger and Ress, 2002).

- **Electroencephalogram (EEG) and Magnetoencephalogram (MEG):**

Every active neuron in the brain produces electrical activity, generating transitory variations in electric and magnetic fields that propagate through the brain, skull, and skin. EEG and MEG involve externally recording the global activity of the brain by capturing either the electric or magnetic fields produced by different neuronal populations. This is accomplished using electrodes affixed to the scalp. EEG primarily measures the activity of cortical neurons (those located in the cortex) to study brain rhythms (Figure 1.3C), while MEG is employed to measure the activity of deeper structures such as the hypothalamus (da Silva, 2013) (Figure 1.3D).

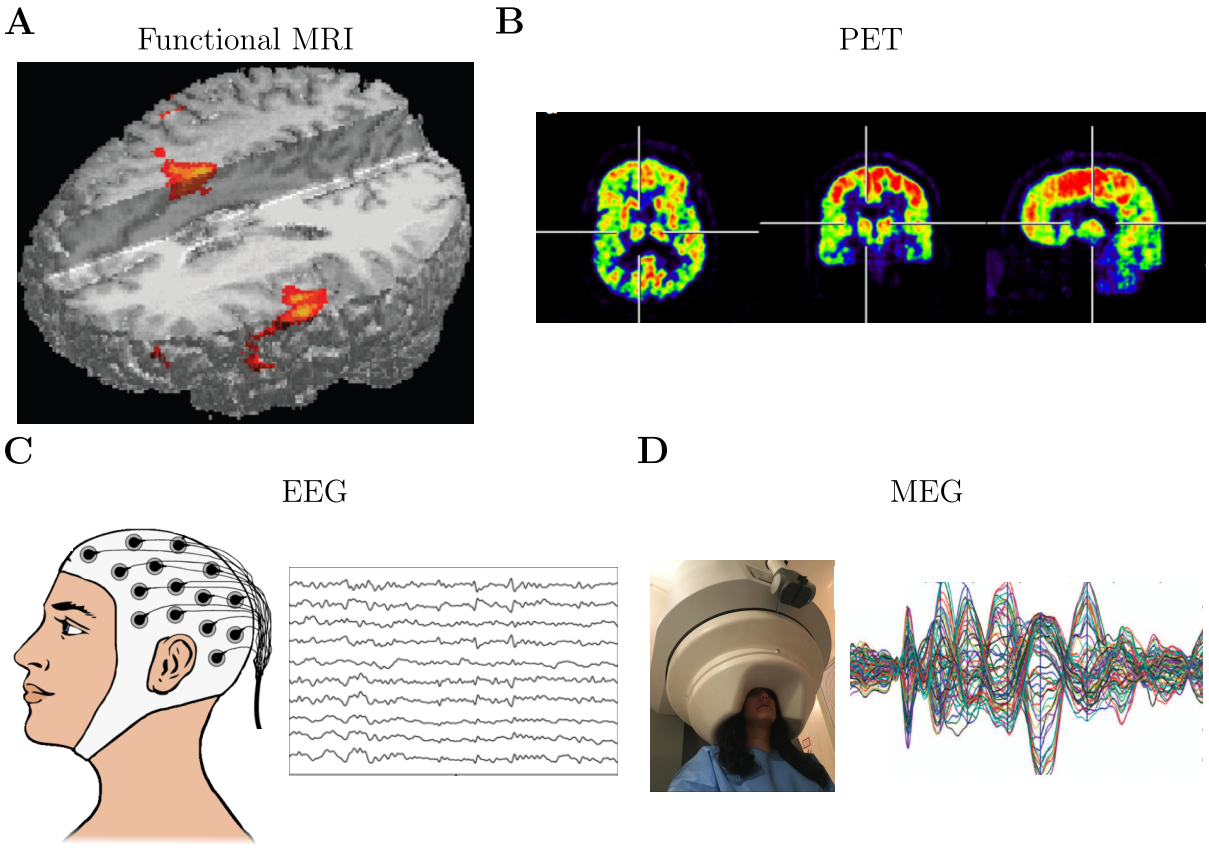

Figure 1.3: Different whole brain imaging techniques. **A.** Illustration of a 3D reconstruction derived from fMRI signals. Highlighted voxels indicate regions of heightened oxygen consumption. **B.** Representation of a 2D projection of PET signals. Highlighted areas correspond to regions exhibiting increased uptake of the administered radioactive molecule (often modified glucose). **C.** Diagram depicting an EEG setup and the corresponding signals. Each scalp electrode records the overall electrical activity of the brain. **D.** Photograph showing a MEG setup and the associated signals. Adapted from Smith (2004); Heiss (2009); Nagel (2019); Shafi et al. (2015), with titles added to each panel.

1.2 Microscopic physiology

As previously outlined, neuronal tissue primarily consists of glial cells and neurons. Given that neurons serve as the information processors while glial cells mainly provide support, this section will be entirely devoted to the study of neurons.

1.2.1 Anatomy of the neurons

Functionally, the brain constitutes a highly interconnected network of tens of billions of neurons, serving as elementary units for information processing (Herculano-Houzel, 2009). Neurons, as highly specialized cells capable of information processing, are divided into three main parts: numerous dendrites, responsible for receiving input signals from other neurons; the soma or cell body, which integrates signals from the dendrites; and a single axon, a potentially extensive channel used to transmit the output signal of the soma (Stevens, 1979). The output signal of a neuron is known as an action potential, a rapid and highly reproducible electrical event occurring at the neuronal membrane, which propagates through saltatory conduction along the axon. Functionally, the input-output relationship of a neuron follows an all-or-none law: if the input surpasses a certain threshold, the neuron fires an action potential; otherwise, it remains silent. These fundamental neuronal characteristics will be explored in greater detail in the subsequent sections.

While neurons share a common functional architecture, the spatial distribution of dendrites around the soma and the location of the axon can vary significantly depending on the neuron function or its location within the brain. For instance, cortical neurons are predominantly pyramidal neurons, characterized by distinct apical and basal dendritic trees and a pyramidal-shaped soma, with a vertical axon directed towards the external layer of the cortex (Spruston, 2008) (Figure 1.4A). Another example is that of Purkinje cells in the cerebellar cortex, which possess a unique morphology featuring a substantial, flat, and highly branched dendritic tree, along with a singular, elongated axon forming an inhibitory projection to the cerebellar nuclei. In this case, the plane of the dendritic trees is perpendicular to the folds of the cerebellar cortex in the external layer, while the cell bodies are located deeper (Paul and Limaiem, 2022) (Figure 1.4B). Finally, Chandelier cells are a specialized type of neuron (more precisely, interneurons) characterized by short axonal terminals that form vertically oriented rows of boutons resembling candlesticks, along with highly variable dendritic tree structures. These neurons, which are also found in the cortex, have a distinct function compared to pyramidal neurons (Hökfelt et al., 1998) (Figure 1.4C). Furthermore, a link has been identified between a reduction in their axonal terminals and schizophrenia (Pierri et al., 1999).

1.2.2 The neuronal membrane: the ion channels

Compared to other cells, neurons have a lot in common, such as the nuclei, the smooth/rough endoplasmic reticulum, the cytoskeleton, the cell membrane, etc. However, their uniqueness and excitability primarily arise from the specific combination of ion channels they possess. Ion channels are transmembrane proteins with a pore through which ion can flow through. Because the cell membrane is a bi-layer of phospholipids, it serves as a boundary between the intracellular and extracellular worlds (Yèagle, 1989). This membrane is permeable to water and small uncharged molecules, but completely impermeable to ions and large molecules such as proteins. So, ion channels are the only gateways through which ions can flow in or out. Moreover, specific types of ion channels are always specific to a given ion, such as potassium (K^+), sodium (Na^+), chloride (Cl^-), or calcium (Ca^{+2}); these being the most common ions encountered in the extracellular fluid and in the intracellular medium (Hille and Catterall, 2012). Ion channels

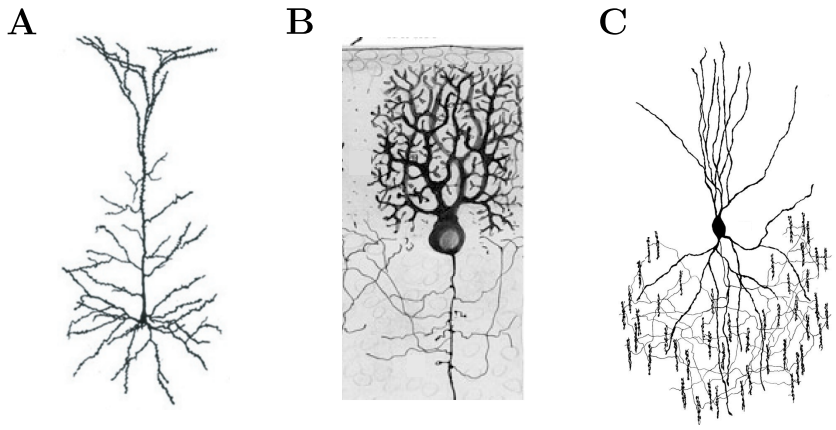

Figure 1.4: Different types of neuronal structure. A. Illustration depicting the structure of a layer V pyramidal cell. **B.** Example of the structure of a Purkinje cell found in the cerebellum. **C.** Example illustrating the structure of a Chandelier cell. Taken from Spruston (2008); Sotelo and Rossi (2021); DeFelipe (1999).

exhibit selective permeability to specific ions, and they are named after the ions to which they are permeable.

Ion channels are structurally complex molecules that function like tunnels with an opening-closing mechanism. When closed, they maintain the electrochemical gradient of the ions they regulate without specific roles. Once they open, ion channels become permeable to a specific ion, allowing ions to flow according to their electrochemical gradient (Catterall, 1995). For example, if there are many positive sodium ions outside the cell and few inside, and the membrane voltage is below the sodium ion reversal potential (around 40 mV (Begenisich and Cahalan, 1980)), opening sodium channels allows for inward flow of these ions into the cell. This flow creates ionic currents that, in turn, modify the membrane voltage (Figure 1.5A). Thus, ion channels are responsible for the electrical activity of neurons.

Ion channels are typically characterized by gates, including activation and inactivation gates, which are specific amino acid sequences within complex molecular subunits (Zhou and McCammon, 2010) (Figure 1.5C and D). The closing-opening mechanisms of ion channels might vary a lot in terms of dynamics (*i.e.* time constants and gating kinetics), but is often trigger by changes in the membrane voltage. This means that ion channels are voltage-dependent (sometimes calcium-dependent or other), highlighting already a feedback loop in the system, since ion channels alter voltage membrane through ionic currents. Furthermore, we will see that neurons are able to produce a high variety of electrical signaling thanks to the myriad of combinations of ion channels that can be built, given that a different type of ion channel produce a different ionic current, and so affect differently the membrane voltage dynamics (Dunlop et al., 2008). Note that ion channels are passive transporters and do not requires energy such as adenosine triphosphate (ATP).

In addition to ion channels, key actors on the cell membrane that participates to the membrane voltage are ionic pumps, especially the sodium–potassium pump (known as Na^+/K^+-ATPase). The latter is an active transporter that uses cell energy (ATP) to actively pump sodium and potassium ions in the opposite direction of the electrochemical gradients. Specifically, this pump

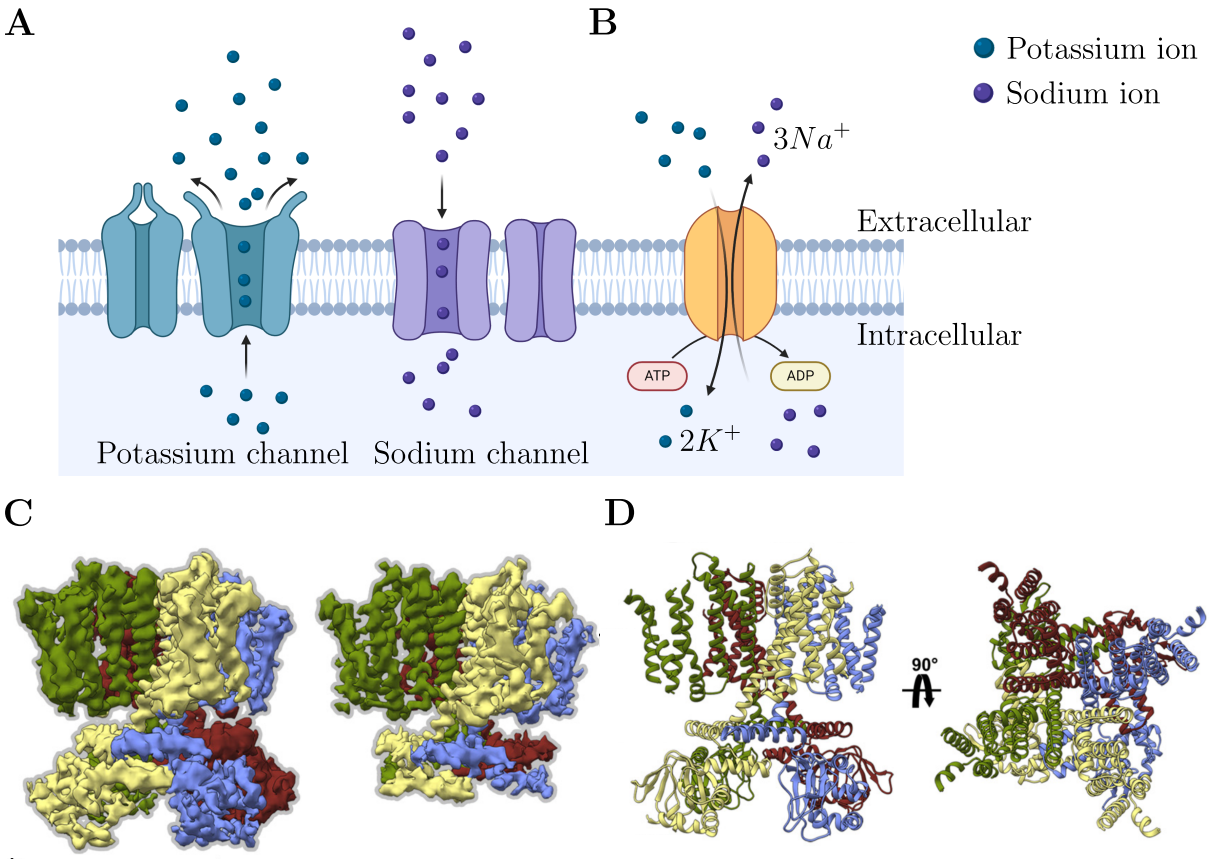

Figure 1.5: The neuronal membrane: ion channels and active pumps. A. Illustration demonstrating the opening and closing of potassium (blue) and sodium (violet) ion channels, facilitating the passage of respective ions across the membrane according to their electrochemical gradients. Typically, the potassium electrochemical gradient is outward-directed, while the sodium electrochemical gradient is inward-directed. **B.** Na^+/K^+-ATPase (yellow) functions as an active ionic pump. For each ATP molecule dephosphorylated to ADP, it expels 3 sodium ions and pumps in 2 potassium ions. The primary purpose of this mechanism is to uphold the electrochemical gradients of potassium and sodium ions. **C.** Three-dimensional reconstruction depicting a prokaryotic cyclic nucleotide-gated ion channel, with each subunit colored distinctly. **D.** Ribbon diagrams displaying two orthogonal perspectives of a prokaryotic cyclic nucleotide-gated ion channel, with each subunit distinguished by color. Created with BioRender and taken from James et al. (2017).

uses a molecule of ATP to pump out 3 sodium ions and pump in 2 potassium ions (Skou and Esmann, 1992) (Figure 1.5B). So, this kind of pumps is responsible in regenerating electrochemical gradients of ions once these had been reduced greatly due to the opening of ion channels, resulting in the neuron being able to produce again electrical activity.

It is interesting to observe that, at rest, the voltage across the neuronal membrane is non null, meaning that there is drastically different ion concentrations in the intra- and extracellular domains thanks to the ionic pumps. At rest, one can measure that the voltage inside neurons is 60 mV lower than the one of the extracellular domain, resulting in a membrane voltage of -60 mV in a majority of cases. Indeed, potassium ions and anions (commonly negatively charged proteins) are highly concentrated inside the cell, while sodium, calcium, and chloride ions are highly concentrated outside the cell, among other charged agents. This results in what is known

as the resting potential of the neuron (Jones, 1989). This resting potential can be computed using the Hodgkin-Huxley-Katz equation (Qaswal, 2020).

1.2.3 The neuronal event: the action potential, an all-or-none response

Each input that a neuron receives, whether it is an electrical signal from another neuron at its dendrites or a different type of stimulus such as pressure or a chemical signal, undergoes integration in the soma, slightly modifying the membrane potential. Subsequently, specific ion channels open, thereby further altering the membrane potential, and this process continues. If the input is substantial enough to raise the membrane potential beyond a certain threshold-still not fully understood-a temporally localized positive feedback loop is triggered, causing the membrane potential to sharply rise to approximately 40 mV—a phenomenon known as depolarization. Following depolarization, the membrane potential returns to its resting state, referred to as repolarization. In general, this event is highly reproducible and depends solely on whether the input surpasses the threshold, embodying the all-or-none response commonly referred to as the action potential or spike (Izhikevich, 2000). However, its shape can vary, affecting neurotransmitter release (Borst and Sakmann, 1999). In the subsequent discussion, an inward current refers to an ionic or externally applied current that causes the membrane potential to rise, which is generally true except for chloride ions due to their negative charge. Conversely, an outward current results in a decrease in membrane potential. This concept encapsulates what is termed neuronal excitability.

Generally, the action potential is a rapid (in the order of milliseconds) and spatially localized reversal in the polarity of the membrane potential (Barnett and Larkman, 2007). It is initiated at the axon initial segment and swiftly propagates along the axon, which may be myelinated, to reach the terminal arborization. This region is rich in synapses, the junctions between neurons, which will be examined in subsequent sections. The minimal combination of ion channels capable of generating spikes comprises sodium and potassium channels, and only these two will be considered in the following discussion.

At rest, ion channels are closed, and the membrane permeability to ions is close to zero. Additionally, the electrochemical gradient of sodium points toward the inside of the neuron, while the electrochemical gradient of potassium points in the opposite direction, maintained by the Na-K-ATPase, an active transporter (Sweadner and Goldin, 1980). If the input stimulus is weak and does not exceed the threshold, the membrane potential is brought back to its resting state. Once the membrane potential reaches the threshold for activation of sodium channels, these channels open, leading to an increase in membrane permeability to sodium ions. This allows a rapid inward flow of sodium ions, initiating the onset of the action potential (Figure 1.6A). This phase is the depolarization or the upstroke of the action potential. Once the membrane potential reaches its peak value, the inactivation gates of sodium ion channels activate, reducing the permeability of the membrane to sodium ions and halting the rise in potential (Kole et al., 2008). It is important to note that sodium inactivation gate dynamics occur on a slower timescale than the activation gate dynamics, roughly by a factor of 10.

Furthermore, as the membrane potential rises, potassium ion channels open via their activation

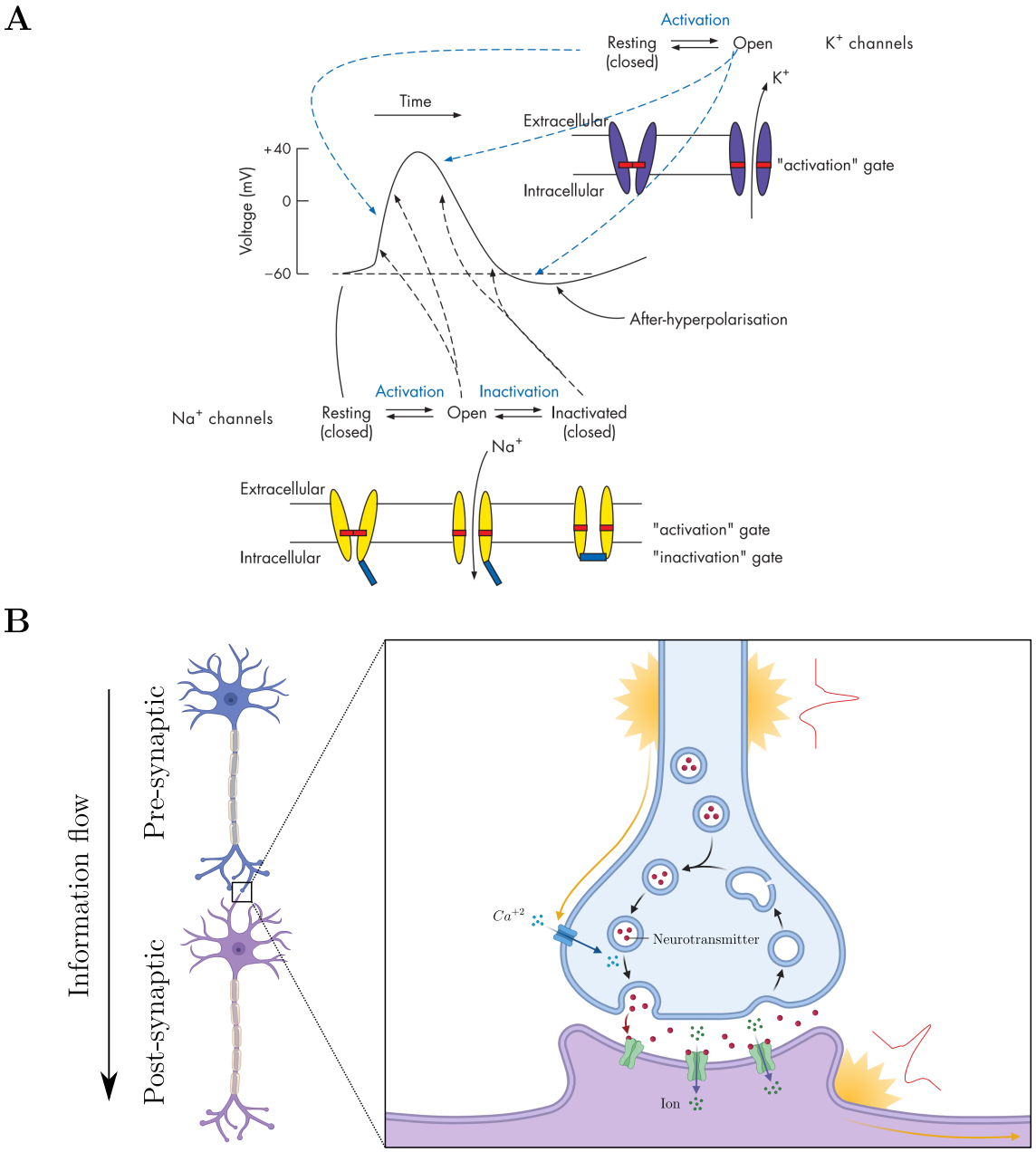

Figure 1.6: The action potential and the synapse. A. Diagram illustrating the action potential and associated models depicting the sequence of activation and inactivation of voltage-sensitive Na^+ and K^+ channels. Arrows indicate the states of the respective ion channels during different phases of the action potential. The dashed line on the action potential trace represents the resting membrane potential, emphasizing the rebound after-hyperpolarization. **B.** Synapses serve as the connection points between axons of pre-synaptic neurons and dendrites of post-synaptic neurons. Upon arrival of the action potential at the pre-synaptic terminal, voltage-gated calcium channels open, allowing calcium ions to enter. These ions facilitate vesicle docking and neurotransmitter release. The released neurotransmitters bind to receptors on the post-synaptic dendrites, leading to the opening or closing of channels, thereby inducing excitatory or inhibitory post-synaptic potentials. Created with BioRender and taken from Barnett and Larkman (2007).

gate, increasing potassium membrane permeability. However, this process occurs on a slower timescale because these channels are activated more slowly. This leads to an outward flow

of potassium ions, generating an outward current that causes the membrane potential to decrease—the downstroke of the action potential or repolarization. Unlike sodium ion channels, potassium ion channels do not have inactivation gates, causing the membrane potential to go lower than the resting potential, around −90 mV. This is known as hyperpolarization (Mitterdorfer and Bean, 2002) (Figure 1.6A). During this state, potassium activation gates close, and sodium inactivation gates reopen. Subsequently, the membrane potential rises to the resting potential, and the neuron is ready to fire another spike.

Due to the inactivated state of sodium channels, the neuron is less capable or even incapable of firing another spike, as fewer sodium channels are available for recruitment in generating an action potential. This period is referred to as the refractory period, which can be divided into the absolute and relative refractory periods. The absolute refractory period occurs at the beginning of hyperpolarization and denotes a period during which a neuron is unable to fire another spike, regardless of the input amplitude. The remaining hyperpolarization constitutes the relative refractory period, where a larger input is required to induce spike firing compared to when the neuron is at its resting potential (Farmer et al., 1960). Since the membrane potential is lower than the resting potential, a higher input is necessary to reach the threshold.

In the subsequent discussion, various other ion channels will be examined. While the main roles of channels like calcium channels do not affect the generation of action potentials, they influence the temporal distribution of spikes as well as the shape of the spike, thereby providing neurons with functional versatility. Now that the mechanisms underlying neuronal activity generation have been outlined, the next section delves into how neurons are connected one to each other.

1.2.4 Connection between neuronal cells: the synapse

As previously mentioned, the flow of information within a neuron occurs from dendrites to the axon, passing through the soma. Moreover, the brain is a highly interconnected network of neurons. Consequently, following the information flow, the axon of the first neuron must be connected to the dendrites of subsequent neurons. This connection point is called a synapse. The first neuron is referred to as the presynaptic neuron, while the subsequent one is called the postsynaptic neuron. The synapse comprises the very end of the presynaptic neuron axon, known as the presynaptic terminal, and the beginning of the dendrites of the postsynaptic neuron, called the postsynaptic element. The presynaptic terminal contains numerous vesicles containing specific molecules known as neurotransmitters. The membrane of the postsynaptic element is equipped with receptors for these neurotransmitters, and these receptors are special ion channels controlled by neurotransmitters. These two regions are separated by a thin extracellular gap known as the synaptic cleft, which is filled with extracellular fluid (Hall and Sanes, 1993) (Figure 1.6B).

Due to the synaptic cleft in chemical synapses, the electrical signal is halted, and synaptic transmission of neuronal information is accomplished through a chemical signal. When an action potential reaches the presynaptic terminal, the vesicles containing neurotransmitters move closer to the synaptic cleft, and the presynaptic neuron releases a bundle of neurotransmitters into the synaptic cleft. This release is the result of a complex signaling cascade initiated by the opening of calcium ion channels triggered by the action potential, leading to an increase

in intracellular calcium concentration. The neurotransmitters then bind to their postsynaptic receptors, and depending on the nature of the neurotransmitters, they either open or close the receptors, inducing depolarization or hyperpolarization of the postsynaptic membrane potential (Figure 1.6B). These changes further propagate to the soma of the postsynaptic neuron. This process is respectively referred to as excitatory postsynaptic potential (EPSP) or inhibitory postsynaptic potential (IPSP), defining either an excitatory or an inhibitory synapse (Choquet and Triller, 2013). Once the information is transmitted, neurotransmitters are taken back up inside the presynaptic terminal, making them ready for another action potential.

In summary, neuronal information transmission relies solely on an electrical signal within a single neuron, where the action potential gradually propagates from the soma (or dendrites) to the axon (or synaptic) terminals. In contrast, neuronal information transmission between neurons relies on a chemical signal—neurotransmitters—to propagate from one neuron to another. It is worth noting that there also exist purely electrical synapses, known as gap junctions. These consist of intercellular non-selective channels that allow the direct diffusion of ions and small molecules between adjacent cells (Goodenough and Paul, 2009). In this case, ions can flow directly from one neuron to another without the need for a chemical signal.

1.2.5 The fundamental function of neurons: event based encoding

Since action potentials are uniform for a specific type of neuron, neuronal activity is often represented as a sequence of discrete events—spikes—as a reasonable approximation. Graded transmission is known to occur in some neurons, and variations in subthreshold voltage can influence the shape of action potentials (Graubard et al., 1983). However, in this context, only the timing of these events, referred to as spike times, is typically considered significant. As a result, preserving the full voltage trace over time is unnecessary, as all the information processed by neurons is encoded in the decision to fire or not. Consequently, the way neurons process information differs significantly from analog (continuous value) or digital (storing numbers in a series of bits) systems. Neuronal information processing can be succinctly summarized as follows: "if neuronal input is sufficiently large, then the neuron will fire a spike." Thus, with a sufficiently intense and prolonged stimulus, neurons can generate a train of spikes at a specific frequency referred to as spike frequency or rate (Rabinovich et al., 2008).

Numerous studies have indicated that neurons coding for a specific stimulus are more likely to exhibit a high spike frequency when exposed to that stimulus. Conversely, these neurons are more likely to have a low spike frequency when stimulated with an unrelated stimulus. Consequently, various hypotheses have emerged regarding how information is represented and transmitted in the brain, collectively known as neural code (Guo et al., 2021). Here is a non-exhaustive list of current hypothesized coding schemes:

- **Rate Coding:**
  This scheme posits that the rate of neuron firing increases with the amplitude of the stimulus. Information is encoded in the firing frequency, often referred to as frequency coding. However, due to the stochastic nature of neurons, the rate might vary from trial to trial for a specific stimulus. Scientists use either spike-count rate, a time window

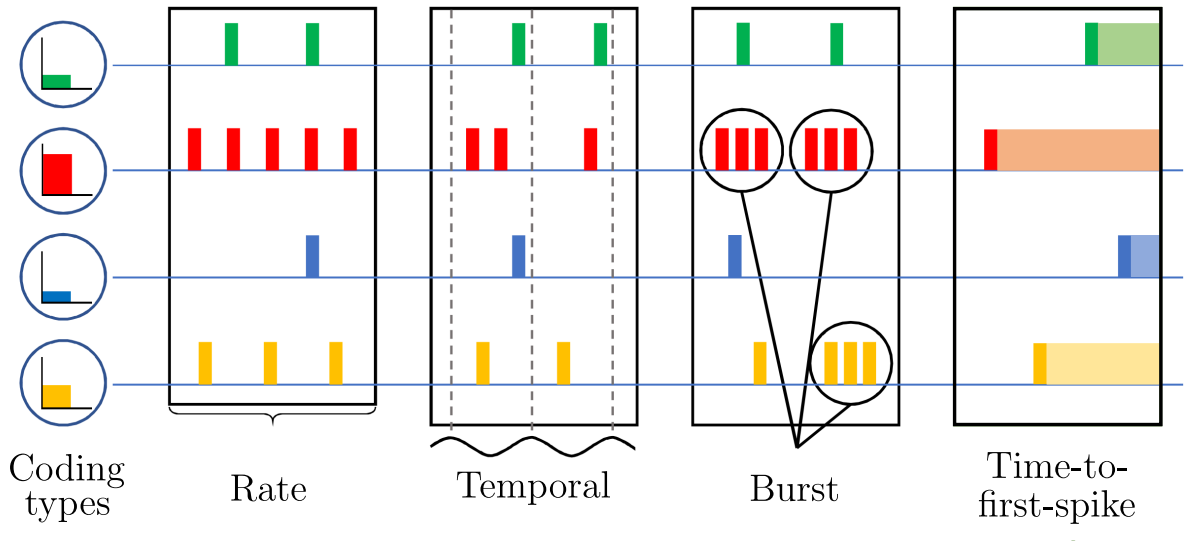

Figure 1.7: The different neural code. From left to right: rate coding, which encodes the stimulus in spike frequency; temporal coding, which encodes the stimulus in the phase of the firing pattern; burst coding, which encodes the stimulus in bursts; and time-to-first-spike coding, which encodes the stimulus in the neuron that first spikes. Note that in this illustrative example, red exhibits the highest response in every coding scheme, followed by yellow, green, and then blue. Adapted from Park et al. (2020b), with modifications made to the text at the bottom.

averaging technique, or time-dependent rate, an across-trial averaging technique (Gautrais and Thorpe, 1998) (Figure 1.7).

- **Temporal Coding:**
  Information is stored in precise spike timings or in high-frequency firing-rate fluctuations, embedded in temporal code. In some cases, information is stored at the millisecond timescale of spike times. One example include time-to-first-spike that states that neurons encode the stimulus in their latency to spike after that a specific stimulus that occurs. In such coding, the first neuron that spikes is the one with the highest response to that specific stimulus, followed by other firing neurons that have a larger latency (Figure 1.7). Another example is phase-of-firing, where information is stored in the statistical moments of interspike interval (ISI) probability distribution (Rucci et al., 2018) (Figure 1.7).

- **Population Coding:**
  Information is stored through the combined activities of numerous neurons, changing spike joint probability distributions rather than individual spike probability distributions. This suggests that information is processed and stored collectively by many neurons, influencing how they interact with each other. Neurons are considered too noisy to solely encode information. The mathematical framework varies, with information encoded in correlation values between spikes from different neurons or in the mean of neurons with the greatest response (Tkačik et al., 2010).

It is also worth mentioning the burst code outside of the bullet list. Neurons, up to now, have been observed to fire single spikes in what is termed tonic firing. However, neurons can also exhibit burst firing or burst code in neural code terms (Figure 1.7). Bursting is characterized

by high-frequency packets of spikes followed by relatively long periods of silence, periodically (Van Pottelbergh et al., 2018). Bursting is characterized by many mathematical features: the active period is the moment when the packet of spikes occur; the quiescent period is the moment when the neuron is at resting potential; the interburst period is the overall bursting period, the time between two bursts; the interburst frequency is the inverse of the interburst period; the intraburst period is the time span between two successive spikes inside of a burst; the intraburst frequency is the inverse of the intraburst period; the duty cycle is the ratio between the active period and the interburst period, the percentage of time in which the neurons is firing; the number of spikes per burst; the spike latency is the delay between the start of the depolarization and the first spike; the plateau potential is the low membrane potential that can be observed during the burst, which is often a more depolarized state than the resting potential; and the after depolarizing potential (ADP) is a depolarization that does not lead to an action potential occurring right after the burst (Drion et al., 2012).

In burst coding mode, information is stored in the bursting behavior of neurons, with a sufficiently high stimulus leading to bursting among several neurons, constituting a salient syllable of the neural code (Ávila-Åkerberg et al., 2010). Furthermore, information may be contained in the different characteristics of bursting, especially the duty cycle and various periods, as these characteristics rely only on spike times, not the entire voltage trace.

1.2.6 Measuring single cell activity: electrophysiology

Compared to whole brain recording, neuroscientists also rely on studying single neuron activities, one at a time or individual members of a whole population. This refers to electrophysiology, the branch of neuroscience that investigates the electrical activity of living neurons and the molecular and cellular processes that control their signaling (Engel, 2018). Electrophysiology relies on many different techniques that greatly varies through spatial scales and so complexity: from a single neuron recording using a single probe to recording hundreds of living neurons in a population thanks to an array of electrodes. These techniques allows to observe and study the electrical activity of neurons, and potentially to extract the spike times of a population to study its neural code. However, all of these techniques are very invasive and requires surgery, this is why most of the electrophysiological studies are conducted on animals. Here is a non-exhaustive list of electrophysiology measurement techniques and their utility scopes:

- **Single neuron recording:**
  Recording a single neuron electrical activity can be conducted in three different ways, depending on where the electrodes are placed.
  - Intracellular recording: A very sharp glass microelectrode is inserted inside the neuron (through the membrane) to measure its intracellular potential (Brette and Destexhe, 2012). This technique allows the measurement of membrane potential and observation of smooth curves of action potentials. This is the most invasive technique for a cell.
  - Extracellular recording: An electrode is placed in the extracellular fluid near the recorded neuronal membrane. This technique measures variations in electrical fields produced by ionic currents induced by neuronal activity (Lempka et al., 2011). It

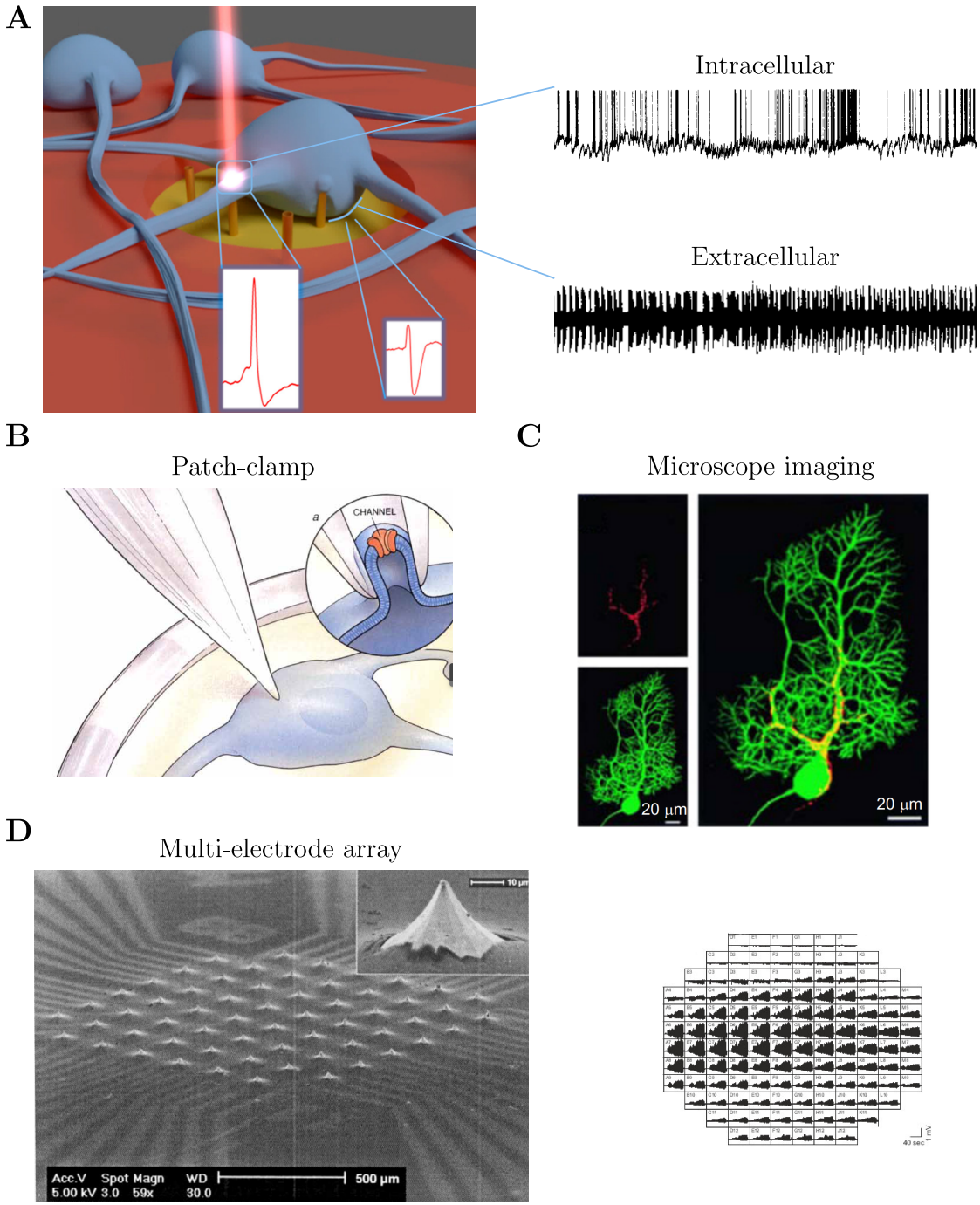

Figure 1.8: Single cell activity measurement techniques. **A.** Comparison between intracellular and extracellular recording methods. On the left, a 3D illustration shows an electrode positioned inside the neuron for intracellular recording and outside the neuron for extracellular recording. Associated measurements are depicted on the right. **B.** Illustration of the patch-clamp technique, which bridges intracellular and extracellular recording. A glass pipette adheres to the neuronal membrane and records intracellular activity-like signals. **C.** Microscopic image showing a neuron visualized using calcium fluorescence. **D.** Electron microscope image displaying a multi-electrode array composed of 60 electrodes (left), alongside an example of measurements obtained from epileptic patients (right). Adapted from Dipalo et al. (2017); Steriade and Contreras (1995); Neher and Sakmann (1992); Heuschkel et al. (2002); Dossi et al. (2014); Grienberger and Konnerth (2012), with titles added to each panel.

does not measure the membrane potential but can capture sharp variations during action potentials, enabling the extraction of spike times.

- Patch-clamp recording: A glass microelectrode is sealed to the neuronal membrane, creating a patch that isolates a specific zone in the membrane. This technique, commonly used today, allows the direct measurement of membrane potential or ionic current without stretching the neuronal membrane, without risking killing the cell (Hill and Stephens, 2021).

Note that all these electrical signals must be subsequently amplified to be observable on a monitor.

- **Multi-Electrode Array (MEA):**
  MEAs are electrical devices that contain up to thousands of extracellular electrodes, which can be inserted into neuronal tissue to record the activity of a whole population. This enables the simultaneous recording of thousands of neurons and allows the recovery of single neuron activity through spike sorting algorithms. The data produced can be used to study neural code of populations. (Chapin, 2004).

- **Calcium and voltage imaging:**
  Calcium and voltage imaging techniques allow the measurement of neuronal activity indirectly using signals resulting from electrical neuronal activity. They also enable the observation of the anatomical structure of neurons, such as dendritic trees, after surgery and dissection. These techniques can be divided in two categories, depending on what these are measuring (Sancataldo et al., 2019). First, there is optical calcium imaging. By injecting a fluorescent substance sensitive to calcium, its concentration can be monitored over time by measuring spatial fluorescence levels. Changes in calcium concentration can be correlated with neuronal electrical activity. Second, fluorescent dyes sensitive to voltage can be injected into neuronal tissue to monitor neuronal electrical activity directly by measuring spatial fluorescence levels.

2 Investigating neuronal excitability

Neurons exhibit excitability, characterized by a resting state that can transition to firing spikes in response to specific stimuli. The concept of neuronal excitability is encapsulated in a textbook definition: a "subthreshold" synaptic input results in a modest graded PSP, whereas a "suprathreshold" input triggers a substantial all-or-none action potential. The latter is notably of a magnitude significantly larger than the amplitude observed in subthreshold responses (Izhikevich, 2007). This chapter delves into the exploration of various types of neuronal excitability, as encountered in electrophysiology.

2.1 Different excitability types

As previously discussed, neurons showcase noteworthy diversity in their anatomical attributes. In addition to these structural differences, there are considerable variations in their electrophysiological activities. It is worth emphasizing that, despite these divergences, the common thread unifying this diversity lies in the inherent characteristic of neuronal excitability.

2.1.1 The first categorization of neurons: current frequency curves

Historically, the very first attempt at classifying neurons based on their dynamical behavior was pioneered by Hodgkin and Huxley in 1948 (Hodgkin, 1948). In this experiment, they applied constant external currents of various amplitudes to excitable membranes, analyzing the resulting membrane potential. The common point among all neurons, derived from the concept of neuronal excitability, is that, at low currents, neurons remain silent, while at high currents (above the threshold), neurons spike regularly at a certain frequency. The threshold current is referred to as the rheobase.

The first two dynamical categories of neurons that were discovered are evident when examining current-frequency (I-f) curves of different neuronal types, namely, Type I and Type II neurons. These curves indicate the frequency (ordinate) at which the neuron is firing at a given current (abscissa). A neuron that is silent is considered to have a null spike frequency.

- **Type I neuronal excitability:**
  This type of neuron has the remarkable ability to fire spikes at arbitrarily low frequencies, with respect to external current amplitudes above the threshold. This means that their I-f curves are continuous, starting at a null frequency and continuously increasing as the current surpasses the threshold. Physiologically, the firing frequency for such neurons can range from a few hertz to a few hundred hertz (Tateno et al., 2004). Thus, these neurons exhibit remarkable adaptation ability, as their firing frequency can change over three orders of magnitude. They can be conceptualized as analog systems, where the firing frequency is continuously tunable. Another perspective is that the external applied current is coded into the firing frequency of the neuron. A physiological example of such neurons could be layer 5 pyramidal neurons from the rat primary visual cortex (Nataraj et al., 2010) (Figure 2.1A).

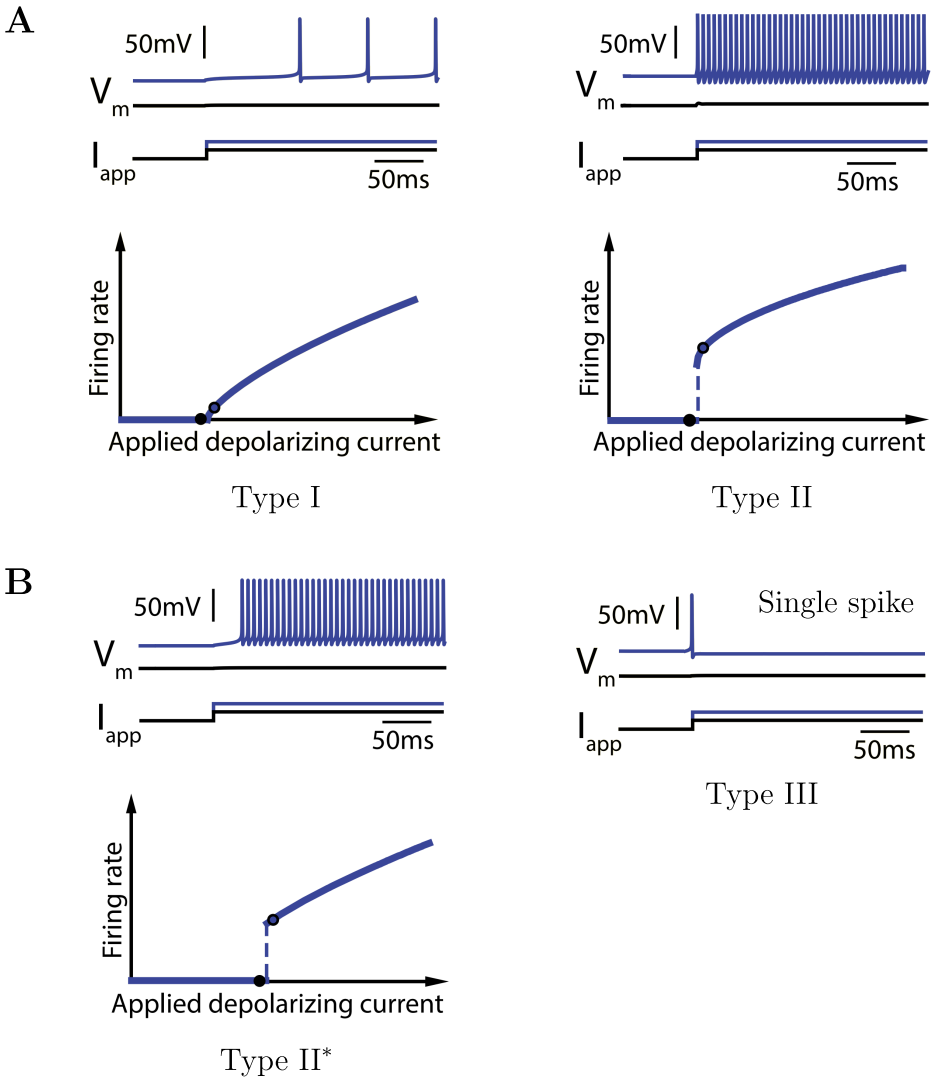

Figure 2.1: Different neuronal excitability types. A. Voltage traces and I-f curves for type I (left) and type II (right) neurons. These two types were historically the first discovered; the main distinction lies in the fact that type I neurons can fire at an arbitrarily slow rate, while type II neurons have a minimum firing frequency. **B.** Voltage traces for type II* (left) and type III (right) neurons, along with the I-f curve for type II* only. Type II* neurons share the exact same I-f curve as type II neurons but exhibit a specific latency before the first spike. Type III neurons fire only a single spike, which explains why an I-f curve is not applicable to such neurons. Adapted from Drion et al. (2015c), with the figure reorganized and type III added.

- **Type II neuronal excitability:**
  In contrast to Type I neurons, Type II neurons cannot fire spikes at very low frequencies. When the external current exceeds the threshold, such neurons instantly fire spikes at a frequency of around 100 Hz, increasing to a few hundred hertz as the current amplitude rises (Kawaguchi, 1995). Thus, the I-f curve for Type II neurons is discontinuous and has a vertical jump at the threshold current when the neuron starts to spike. Moreover, the spike frequency range of such neurons spans only one order of magnitude. These neurons can be conceptualized as binary systems, where they either stay silent or spike at a relatively high frequency. A physiological example of such neurons could be mesencephalic V neurons

from the rat brainstem (Seki et al., 2020) (Figure 2.1A).

Over time, and with additional research, especially in the computational world, other types of neurons have been discovered. In addition to Type I and Type II neurons, this chapter will also cover the characteristics of Type III and Type II* neurons to highlight the richness of neuronal excitability. However, this list is not exhaustive. The difference here will not lie in the I-f curve but rather in the temporal response of the membrane potential when subjected to an external current pulse.

- **Type II* neuronal excitability:**
  When examining the I-f curve for Type II* neurons, it is quasi to a Type II one. Indeed, Type II* neurons also have a discontinuous I-f curve with high-frequency tonic firing. However, they behave differently when looking at the time evolution of membrane potential subjected to a pulse of external current: there is an arbitrarily long latency between the start of the current pulse and the first spike. This behavior initially resembles Type I neurons, with a long period of silence and potentially an arbitrarily low frequency. However, as soon as it starts spiking, it closely resembles a Type II neuron, with a relatively high firing frequency. These neurons are not commonly encountered in physiology but rather arise from computational studies on Type I and Type II neurons (Drion et al., 2015c). Indeed, this behavior emerges when neurons can exhibit characteristics of both Type I and Type II. Type II* arises when neuronal parameters are pushed outside of physiological limits (Figure 2.1B).

- **Type III neuronal excitability:**
  This type of neuron cannot sustain tonic firing, even for currents one order of magnitude higher than the rheobase. When subjected to a suprathreshold external current pulse, Type III neurons will only fire a single spike (or maybe a few spikes) and then become silent at a high resting potential. The new resting potential is higher due to the constant current, and it is proportional to it (Prescott, 2014). Thus, for such neurons, the I-f curve is not well-defined. They can be conceptualized as event encoding systems, firing single spikes when the input varies significantly. A physiological example of such neurons could be lamina I neurons from the dorsal horn of the spinal cord (Grudt and Perl, 2002) (Figure 2.1B).

In summary, classification of neurons based on their dynamic behavior reveals a spectrum of excitability profiles ranging from the continuous adaptability of type I neurons to the binary nature of type II neurons. The exploration extends to type III and II* neurons, highlighting the diversity of neuronal responses. This classification framework highlights the adaptability and richness of functions inherent in the different types of neurons.

2.1.2 Further categorization of neurons

The preceding categorization of neuronal dynamics primarily applies to neurons in tonic firing mode, with the exception of type III neurons. These neurons produce trains of spikes at different frequencies depending on their input, whether it be an externally applied current in electrophysiology or dendritic input in biology. However, the biological landscape encompasses a multitude of firing patterns found in various organs, including the brain, spinal cord, and

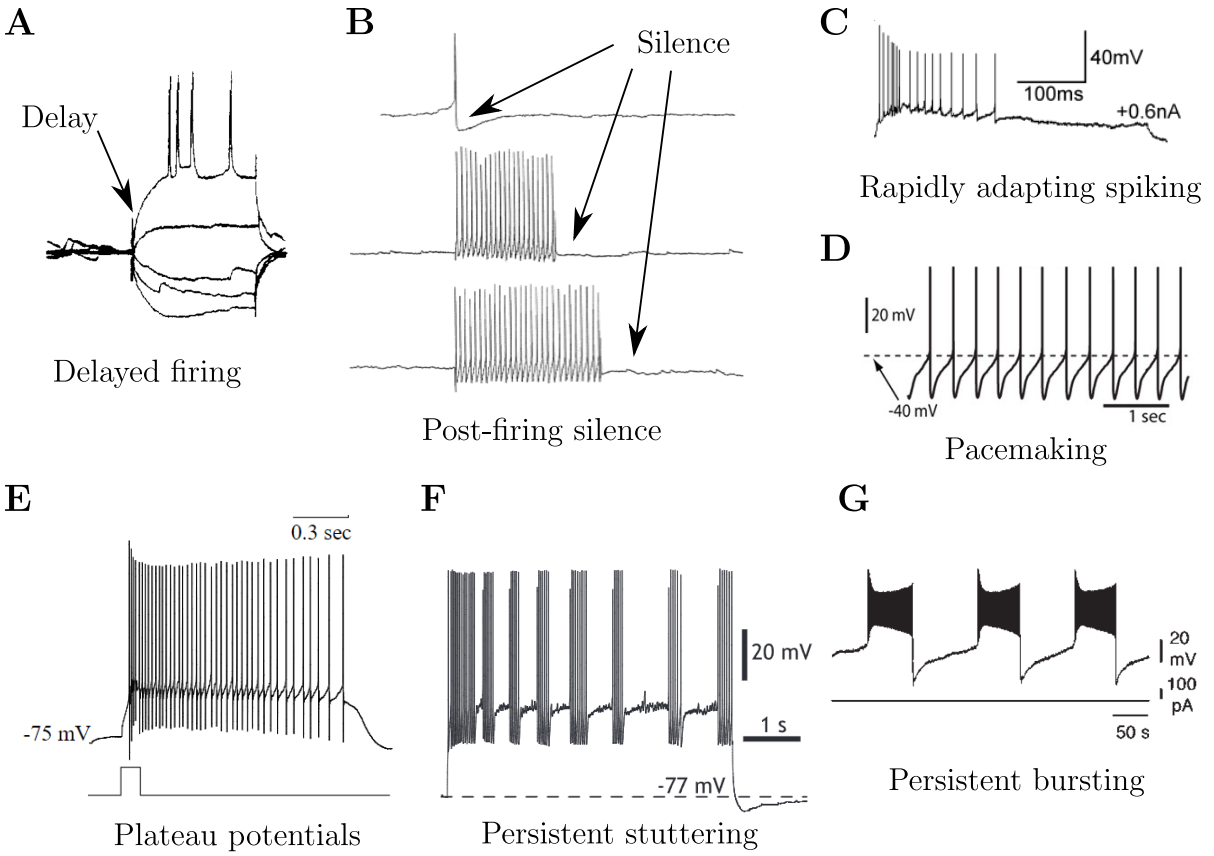

Figure 2.2: Other types of firing patterns. A. Delayed firing observed in cells of the rat fascia dentata. **B.** Post-firing silence observed in interneurons innervating both interneurons and pyramidal cells in the rat hippocampus. **C.** Rapidly adapting spiking observed in interneurons in CA1 of the adult rat hippocampus. **D.** Robust pacemaking observed in substantia nigra dopaminergic neurons. **E.** Plateau potentials observed in subthalamic neurons. **F.** Persistent stuttering observed in rat striatal fast-spiking neurons. **G.** Persistent bursting observed in deep dorsal horn neurons. Adapted from Scharfman and Schwartzkroin (1990); Cobb et al. (1997); Pawelzik et al. (2002); Guzman et al. (2009); Otsuka et al. (2004); Sciamanna and Wilson (2011); Marder (2003), with modifications made to the text at the bottom of each panel.

other organs like the heart of humans and animals. The following non-exhaustive list, based on Izhikevich and Hoppensteadt (2004) and Komendantov et al. (2019), outlines different firing patterns encountered in biology that do not conform to the tonic spiking case. Physiological examples are provided where commonly encountered in biology.

- **Silence:**
  Irrespective of the firing pattern, period of silence can be observed during the stimulation.
  - Delayed firing, as previously discussed in type II* neurons, involves a delayed onset of spiking activity compared to the initiation of external stimulation. In this scenario, when subjected to a current step, the neuron remains silent initially, only later initiating the firing of spikes. This phenomenon is observed in Mossy cells located in the hilar region of the rat fascia dentata (Lubke et al., 1998) (Figure 2.2A).
  - Post-firing silence, in contrast, entails a period of silence observed at the conclusion of

stimulation, following the occurrence of multiple spikes. At the extreme end of this pattern, characterized by a single spike followed by silence, it is associated with type III neurons. This behavior is encountered in specific types of interneurons located in the CA2 region of the hippocampus, particularly those linking stratum radiatum and stratum pyramidale (Mercer et al., 2012) (Figure 2.2B).

- Subthreshold oscillations occur when certain neurons display oscillations in their membrane potential that are insufficient to trigger spikes. This phenomenon, known as subthreshold oscillations, is observed in specific types of interneurons located in the CA1 region of the hippocampus, among other regions (V-Ghaffari et al., 2016). Such oscillations can correspond to calcium oscillations, as demonstrated in dopamine neurons when sodium channels are blocked (resulting in no spikes being produced) (Jehasse et al., 2021).

- **Other types of spiking:**
  A train of spikes can be observed, either with a varying frequency or without, making it not well-suited to the previous categorization of neurons.

  - Adapting spiking occurs when neurons are subjected to an external pulse of current, leading to an immediate initiation of spike firing. However, the frequency gradually decreases across subsequent spikes, resulting in an increase in the ISI. This firing pattern is observed in interneurons at the stratum radiatum-stratum lacunosum-moleculare border in the CA1 area of the rat hippocampus (Vida et al., 1998).

  - Rapidly adapting spiking is a firing pattern closely resembling adapting spiking, but with a significantly faster adaptation. The neuron transitions into tonic spiking in only a few spikes, indicating that the adaptation is a quick transient response at the beginning of external stimulation. This pattern is observed in individual parvalbumin-immunoreactive and cholecystokinin-immunoreactive interneurons in the CA1 area of the rat hippocampus (Pawelzik et al., 2002) (Figure 2.2C).

  - Pacemaking neurons are characterized by a consistently constant autonomous firing frequency, regardless of the external stimulation to which they are exposed. The primary function of these neurons is to maintain a consistent firing frequency. This behavior is observed in dopaminergic neurons (Drion et al., 2011) (Figure 2.2D).

  - The plateau potential represents a specific case of bistability in neurons. When stimulated, these neurons enter spiking mode with an increasing frequency while the stimulation is active. Once the stimulation ceases, the neuron remains in tonic spiking mode with a decreasing frequency until reaching a stable frequency. Described as bistable, these neurons can transition from silence to tonic firing with a short transient pulse, demonstrating a non-fading memory phenomenon. This behavior is observed in neurons from the dorsal horn of the spinal cord involved in the pain processing pathway (Marder, 2003) (Figure 2.2E).

  - Inhibition-induced spiking closely resembles tonic spiking neurons, with the distinction that the external stimulation is a negative pulse of current—an inhibitory stimulation.

In essence, these neurons are sensitive and excitable when subjected to inhibition inputs. It is noteworthy that a similar behavior can also be observed in bursting neurons. This phenomenon is observed in neurons from the thalamus (Kim et al., 2017).

- **Stuttering:**
  This is a specific neuronal behavior that lies between the bursting and tonic spiking modes, where both bursts and single spikes can be observed.
  - Transient stuttering is characterized by the observation of bursts of spikes at the very beginning of constant external stimulation, indicating that the neuron is in bursting mode. However, once this transient bursting behavior subsides, the neuron transitions into tonic spiking mode until the end of the stimulation. The term "stuttering" is aptly used to describe this firing pattern, as the neuron exhibits bursts resembling a stutter at the beginning of its activity. This pattern is encountered in lateral entorhinal area layer V neurons in the cortex (Hamam et al., 2002).
  - Persistent stuttering represents the prolonged manifestation of stuttering, characterized by a sequence of spike packets (the stutters) followed by a period of silence. Although closer to bursting, it cannot be strictly categorized as such due to the insufficient ratio between the ISI within two stutters and the ISI within two spikes in the same stutter. This firing pattern is observed in neurogliaform projecting neurons in the CA1 region of the rat hippocampus (Fuentealba et al., 2010) (Figure 2.2F).
- **Bursting:**
  The discussion will now pivot to the interaction of bursting neurons, with an emphasis on their coordination, rather than delving into a detailed description of individual bursts. It is important to note that the analysis will focus on intrinsic burst generation, as opposed to forced burst generation, which is a form of bursting observed in tonic spiking neurons subjected to a specific sequence of input, mimicking the effect of bursting.
  - Transient slow-wave bursting, when applied to bursting, can be associated with type III neurons. In this mode, neurons fire a single burst only at the beginning of the stimulation, followed by a period of silence. Additionally, the amplitude of the spikes in this burst often decreases, forming a typical trapezoid-shaped burst. This behavior is observed in CA2 pyramidal neurons (Chevaleyre and Siegelbaum, 2010).
  - Persistent bursting, also known as tonic bursting, is a firing pattern distinguished by similar bursts separated by a consistent period of silence. Both intra- and interburst frequencies remain constant over time. However, various variations of tonic bursting exist, contingent on the values of the bursting characteristics outlined earlier. This pattern is observed, among others, in CA1 pyramidal neurons (Golomb et al., 2006) (Figure 2.2G). To provide a comprehensive view, there are four different global shapes of bursting: parabolic, elliptic, square wave, and pseudo-plateau (Desroches et al., 2022). Parabolic bursting is characterized by a sinusoidal shape of the low state of the neuron, where the spikes occur at a much more depolarized state than the resting

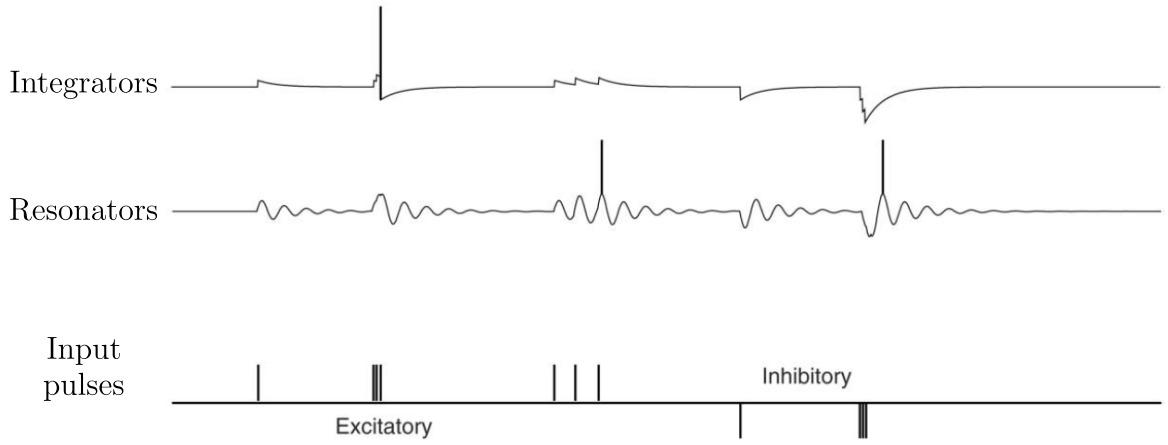

Figure 2.3: Integrators versus resonators. Integrators tend to favor high-frequency input, whereas resonators prefer pulse trains that share the resonant frequency (middle triplet). Only resonators exhibit post-inhibitory spiking. Adapted from Izhikevich (2001), with some text removed and added to the left of each trace.

period. This is observed in Aplysia R15 neurons (Adams, 1985). Elliptic bursting is characterized by a constant resting voltage, both in burst and silence periods, and is encountered in pancreatic beta-cells (Bertram et al., 2008). Square wave bursting resembles parabolic bursting, but the silence period has a much more squared shape. This is observed in dorsal-root-ganglia neurons of a rat (Jian et al., 2004). Finally, pseudo-plateau bursting is characterized by low amplitude spikes with a strong plateau potential, observed in pituitary cells of a rat (Tabak et al., 2011).

Furthermore, many neurons can exhibit multiple of these characteristics simultaneously or over time. Neurons should not be seen as fixed dynamical units fulfilling a single role, but rather as time-varying dynamical units capable of executing numerous functions and switching between modes over time.

To provide a more comprehensive view of neuronal excitability, it is noteworthy to mention the single spike trigger classification by Izhikevich (2001). This paper describes two different mechanisms of spike generation dynamically. Neurons can be seen either as integrators or as resonators.

- **Integrators:**
  These neurons integrate input stimulation (currents) to build up membrane potential and eventually reach the threshold to fire spikes. Consequently, when subjected to very short pulses of external currents, these neurons prefer high-frequency stimulation to fire as soon as possible. The closer the input pulses, the more the neuron integrates, reaching the threshold sooner and firing a spike (Figure 2.3 top trace).

- **Resonators:**
  In contrast, these neurons react differently to the second pulse they are subjected to: "The effect of the second pulse depends on its time relative to the period of oscillation", similar to physical resonators. If the two pulses are well-timed to make the neuron resonate, it will

fire a spike; otherwise, it will be more reticent to do so, as the pulses do not align with the resonance frequency of the neuron (Figure 2.3 middle trace).

2.2 Excitability type depends on ion channels distributions

The key players in neuronal excitability are ion channels. As previously discussed in the context of action potential generation, these channels are responsible for internal changes in membrane potential, ultimately leading to action potentials. Specifically, potassium (delayed) and sodium (fast) channels were highlighted as a minimal combination leading to excitability. Various types of ion channels exist, each exhibiting different degrees of ion selectivity. These channels play a vital role in the regulation of membrane potential and excitability by governing ion fluxes (Di Resta and Becchetti, 2010). Notably, there are several types of potassium ion channels (e.g., calcium-controlled "KCa", inward rectifier "KIR", A-type "A", etc.) and channels permeable to other ions, such as calcium ion channels (T-type "CaT", L-type "CaL", N-type "CaN", etc.), among others (Yu et al., 2016). The diverse types of neuronal excitabilities emerge from either distinct external stimulations (a train of current pulses can induce bursts in inherently tonic spiking neurons) or internal factors, such as different combinations and concentrations of ion channels on the neuronal membrane.

2.2.1 Different ion channels lead to different behavior

The dynamic interplay of ion channels is fundamental in shaping neuronal firing patterns. Fast sodium currents, responsible for the action potential upstroke, and delayed rectifier potassium currents, governing its downstroke, play specific roles in firing patterns. To illustrate the diverse impact of ion channels on neuronal behavior, three types of neurons found in sensory systems will be discussed: cerebellar granule cells, thalamocortical relay cells, and electrosensory lateral-line lobe pyramidal cells (Krahe and Gabbiani, 2004). It is important to note that fast sodium and delayed rectified potassium ion channels are omnipresent in these neurons and will not be discussed individually.

Cerebellar granule cells, the brain smallest and most numerous neurons located in the cerebellar cortex, exhibit unique characteristics. Despite having only a few short dendrites, they are the most electrotonically compact neurons. When subjected to an external current near the firing threshold, these cells display short, high-frequency bursts of spikes *in vitro*. This behavior suggests an association with subthreshold oscillations in the theta-frequency range (3-12 Hz) (Chadderton et al., 2004) (Figure 2.4A). The bursting pattern is characterized by an afterdepolarization following the last spike of the burst and a fast afterhyperpolarization after each spike. Cerebellar granule cells possess five types of ion channels contributing to their dynamic behavior:

- Calcium channels ("Ca"), involved in handling intracellular calcium ion concentration;
- Calcium-dependent potassium channels ("KCa"), responsible for controlling the fast afterhyperpolarization;
- Resurgent sodium channels ("NaR"), mediating the afterdepolarization;
- Persistent sodium channels ("NaP"), initiating the bursting behavior;

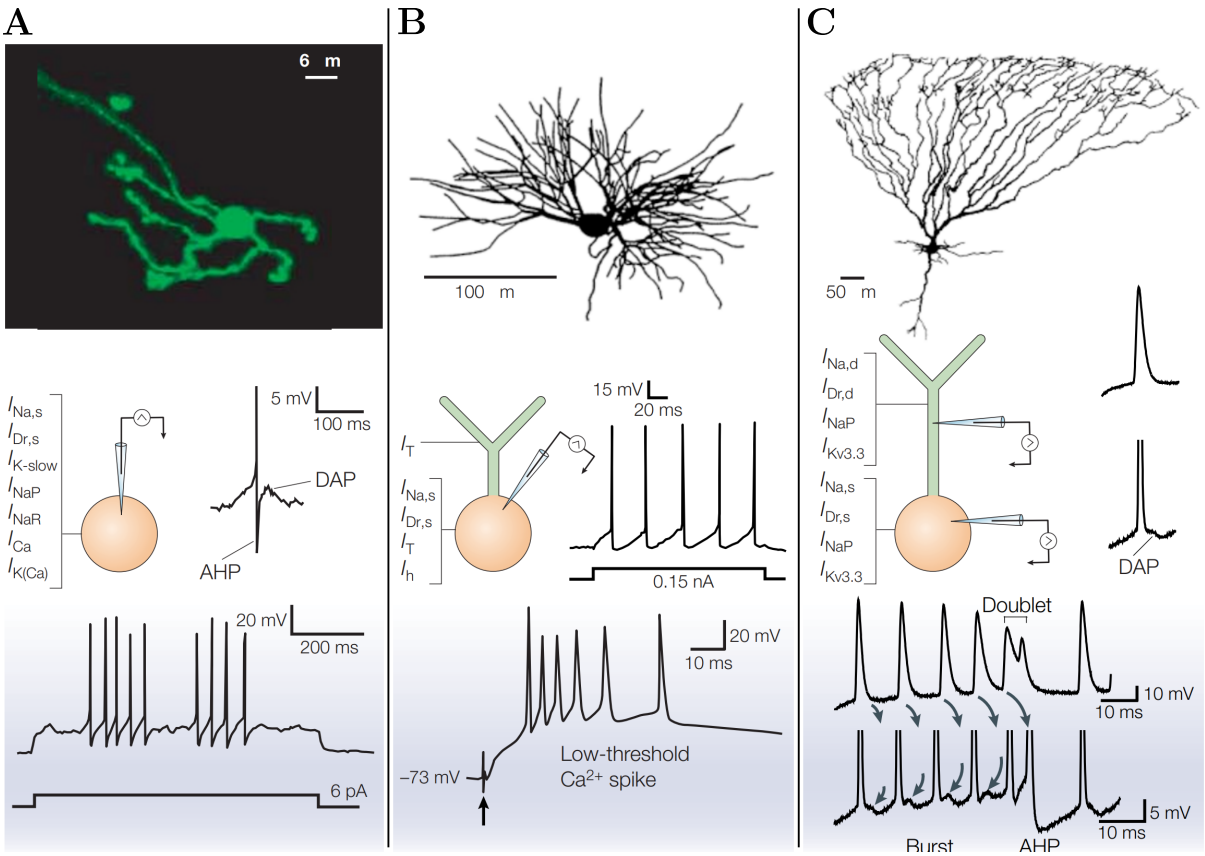

Figure 2.4: Different ion channels lead to different behavior. A. Microscopic imaging of a cerebellar granule cell (top), depiction of associated ion channels and spike shape (middle), and representation of two bursts elicited in response to a current pulse (bottom). **B.** Schematic of a thalamocortical relay cell (top), depiction of associated ion channels, and traces illustrating tonic mode with small depolarization (middle) and decreasing frequency hyperpolarized burst induced by strong depolarization (bottom). **C.** Schematic of an electrosensory lateral-line lobe pyramidal cell (top), depiction of associated ion channels and spike shapes in dendrites and soma (middle), and representation of somatic and dendritic spike bursts terminated by a doublet. Taken from Krahe and Gabbiani (2004).

- Slow potassium channels ("K-slow"), terminating the burst.

Thalamocortical relay cells, integral to the thalamus and actively involved in its relay function, play a crucial role in transmitting somatosensory information to the cortex for integration (Sherman, 2001). These cells universally exhibit two distinct response modes—tonic and burst—which depend on the status of voltage-dependent dendritic membrane channels (Figure 2.4B). The firing patterns vary based on dendritic input. Excitation by a constant current leading to a depolarized membrane results in regular tonic firing, facilitated by classical sodium and potassium channels. Conversely, under strong excitation following a prolonged period of inhibition, these cells display bursting behavior with delayed firing and a decreasing firing frequency during the burst. Thalamocortical relay cells are composed of two types of ion channels:

- Low-voltage-activated calcium channels ("T"), responsible for initiating and terminating bursts in response to inhibitory input by producing a long-lasting calcium spike;
- Hyperpolarization-activated cation channels ("H"), which can interact with T-type channels

to produce bursts in an oscillatory manner.

Electrosensory lateral-line lobe pyramidal cells, located in the lobe of the same name in weakly electric fish, are notable for their easily studiable nature and their coding of specific somatosensory receptive fields, featuring an antagonistic center–surround organization (Bastian et al., 2002). These cells exhibit autonomous and spontaneous firing activity in bursting mode (Mathieson and Maler, 1988). The bursts have a low intraburst frequency, and each spike, broader than usual, is followed by an afterdepolarization (Figure 2.4C). The burst is terminated by higher frequency doublets with a strong afterhyperpolarization. These cells are composed of four types of ion channels:

- Slow dendritic sodium channels ("Na,d"), which broaden the spikes;
- Slow delayed rectifier potassium channels ("Dr,d"), also contributing to spike broadening;
- Persistent sodium channels ("NaP"), initiating the bursting behavior;
- Specific potassium channels ("Kv3.3"), which are responsible for a fast afterhyperpolarization. Their inactivation leads to afterdepolarization by recruiting sodium channels. As the burst progresses, the afterdepolarization increases due to the inactivation of these potassium channels. Once the afterdepolarization surpasses the threshold, a second spike is triggered (doublets), terminating the burst.

These examples underscore the point that diverse neuronal activities can arise not only from different external inputs but also from various combinations of intrinsic ionic currents. The intricate interplay of ion channels and their specific roles contributes to the richness and variability observed in neuronal firing patterns.

2.2.2 Different ion channel concentrations lead to different excitability types

The capacity of a single type of neuron to display different dynamical behaviors when exposed to the same external stimulation has been observed in studies such as Savic et al. (2001). This variability arises from various biological phenomena through which neurons can modify their membrane composition. Specifically, neurons do not alter the types of ion channels present but rather adjust the densities of these channels on their membranes. For example, an increase in sodium channels leads to more sodium ions flowing, resulting in changes in ionic currents. This modulation of ion channel concentration on the neuronal membrane, in turn, influences ionic currents and tunes neuronal excitability.

In practice, quantifying the number of a specific type of ion channel to compute its concentration is nearly impossible. Instead, electrophysiologists measure what is referred to as ionic conductance. Ion channels act as electrical conductances, allowing ions to flow in or out and create a current when opened. However, these ionic conductances vary over time and voltage. When all channels are closed, the ionic conductance is nearly zero, producing no current. As channels open, the ionic conductance increases. To eliminate ambiguity related to time- and voltage-varying conductance, the ionic channel conductance of a specific ion channel is defined as the maximal conductance created by that type of ion channel when all channels are fully opened, providing a standardized

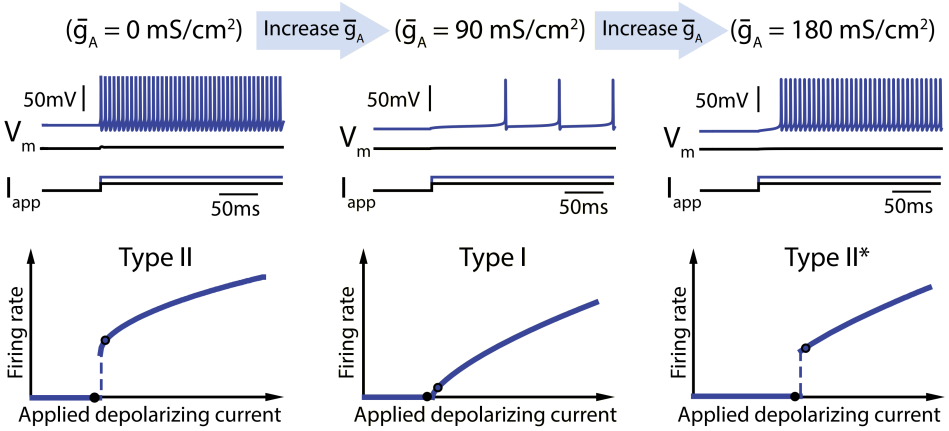

Figure 2.5: Different ion channel concentrations lead to different excitability types. Increasing the quantity of A-type potassium channels induces a transition in the neuron behavior from type II to type I. Further augmentation results in the emergence of a subtype denoted as type II*. Adapted from Drion et al. (2015c), with the yellow background in the middle removed.

measure (Hille, 2008).

The computational results presented in Drion et al. (2015c) offer insights into the impact of modifying the ionic conductance of specific ion channels on neuronal excitability (Figure 2.5). In this study, a model of a neuron from the squid giant axon is employed, featuring the fundamental ion channel components of fast sodium and delayed rectifier potassium currents. This neuron exhibits type II excitability in physiology. To explore the effects of ion channel modulation, a third type of current, the A-type potassium current, is introduced. When the conductance of this A-type potassium current is maintained below 60 $\mathrm{mS/cm^2}$, it does not alter the excitability type.

Upon increasing the A-type potassium current conductance to 90 $\mathrm{mS/cm^2}$, the neuron undergoes a transition from type II to type I excitability, characterized by a very low spiking frequency around the threshold current. Further elevating the conductance to 180 $\mathrm{mS/cm^2}$ leads to the observation of type II* excitability. These findings imply that depending on the conductance of the A-type potassium current, or its concentration on the neuronal membrane, the neuron can manifest three distinct types of neuronal excitability. Consequently, by modulating the A-type potassium current conductance, the neuron can be tuned to exhibit different firing patterns, allowing it to fulfill diverse functional roles.

3 Modulating the neuronal excitability: the role of reliable neuromodulation

Neurons possess the capability to exhibit various types of excitability and behavior, allowing them to fulfill diverse functions. Neuromodulation is a crucial biological process responsible for regulating neuronal activities within the brain. This modulation is facilitated by molecules known as neuromodulators or neuropeptides, including dopamine, noradrenaline, and serotonin. These molecules dynamically influence the activity of single neurons, affecting input/output properties and influencing the strength and dynamics of synaptic connections. Neuromodulation provides a means to adapt the activity of neuronal networks in response to ever-changing needs, contexts, and environments (Bargmann and Marder, 2013).

In this section, we will explore the macroscopic effects of neuromodulation, particularly its applications to brain states. Subsequently, we will delve into the molecular and cellular effects of neuromodulators. Finally, we will discuss the modulation of single neurons and the robustness of this intricate process.

3.1 Macroscopic effect of neuromodulation

3.1.1 What are brain states?

The daily life of biological beings is characterized by different states, with two prominent ones being waking and sleep states. These states involve distinct behaviors: in the waking state, organisms are active both cognitively and physically, while in the sleep state, there is a transition to physical inactivity, and cognitive processes exhibit a different pattern. Furthermore, the waking and sleep states can be further categorized into active/quiet waking and rapid eye movement (REM)/non-rapid eye movement (NREM) sleep, among potentially other subcategories. The transitions between and maintenance of these various brain states are orchestrated by the entire central nervous system, particularly the brain (Bradley et al., 2022).

The concept of a brain state, as defined by Zagha and McCormick (2014), refers to a recurrent set of stable neuronal conditions over a behaviorally significant period. This can manifest as distinct patterns of ongoing neural activity or in the responses of neurons to stimuli. Importantly, brain states can be defined across various spatial and temporal scales. At a small spatial scale, individual neurons may robustly switch between different firing patterns, such as from tonic firing to bursting (Figure 3.1A). The spatial and temporal scales are often proportional, with switches at smaller spatial scales occurring rapidly, while switches at larger spatial scales occur more slowly.

Zooming out to the scale of a neuronal circuit or brain region, certain areas may be activated based on the demands of a specific task (Figure 3.1B). For example, selective attention may activate specific regions in the parietal and frontal lobes, along with the temporal lobe, and these switches can occur over the course of minutes. Scaling up further to the entire brain, transitions between waking and sleep states represent a brain state switch that unfolds over the timescale of hours. On a larger scale, pathological conditions like epilepsy can lead to uncontrolled activity

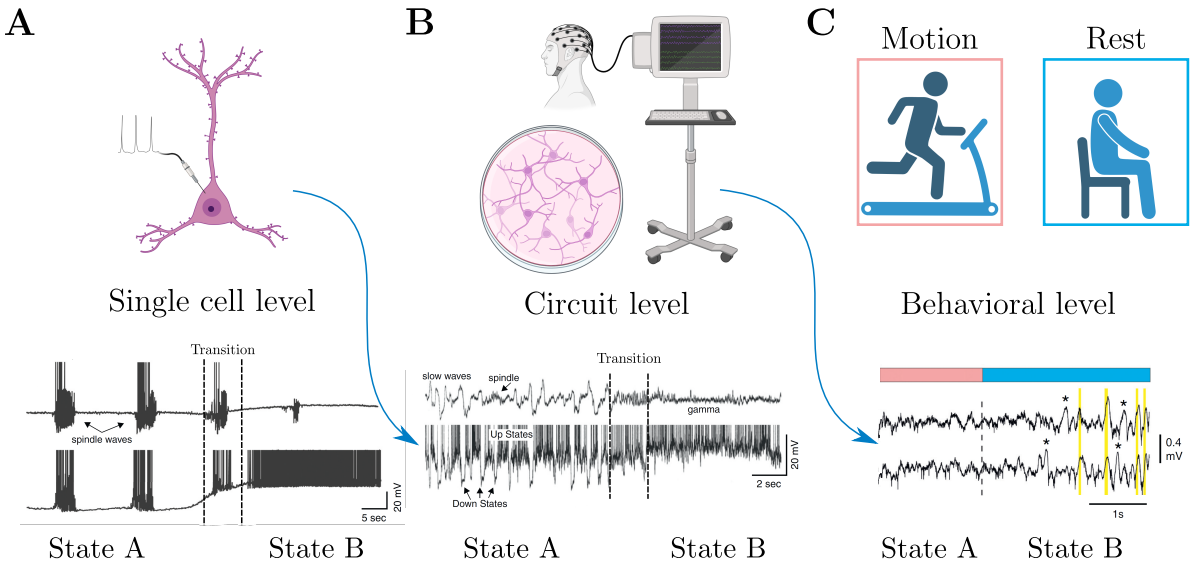

Figure 3.1: Brain states across scales. A. Brain states can be observed at the single-neuron level, where any change in activity can be perceived as a transition between states. Here, transitions from bursting to silence (top trace) and to tonic spiking (bottom trace) are depicted. **B.** Brain states can be observed at the neuronal circuit level, with different states of the EEG signal, for instance. Here, the EEG signal transitions from slow waves to gamma waves. Such transitions at the circuit level are caused by transitions at the single-cell level. **C.** Brain states can be observed at the behavioral level. Here, transitions in behavior can be externally observed and are caused by transitions at the circuit level, which are in turn influenced by transitions at the single-cell level. Created with BioRender and adapted from Zagha and McCormick (2014); Jacquerie (2023), with the figures reorganized and text and arrows added.

across the entire brain, resulting in seizures, and this can be observed on a timescale of minutes to hours.

At the most extreme ends of spatial and temporal scales, changes in behavior may be driven by long-term alterations in brain states, such as those associated with aging or the acquisition of motor skills in a specific sport (Figure 3.1C). Various recording techniques, from single-neuron recordings to broader measures like heart and respiratory rates, can be employed to observe brain states across different scales. These states are not only observable in neural activity but can also be inferred from changes in other physiological parameters, providing a comprehensive view of the brain dynamic states across various contexts and timescales.

Absolutely, our behaviors and activities are intricately governed by a multitude of brain states that manifest at different levels, from the individual neuron to broader neural circuits and entire brain regions. It is important to recognize that higher-level brain states are the culmination of the collective activity of numerous individual neurons in a given region. However, due to the sheer complexity and the vast number of neurons involved, recording every single neuronal activity is currently impractical. Understanding how the activities of individual neurons contribute to overall behaviors like memory, decision-making, or thinking remains a significant challenge.

High-level recording techniques, such as EEG, play a crucial role in identifying brain states, particularly those that occur across larger populations of neurons. EEG, for example, captures

the integrated electrical activity of a substantial number of neurons, providing insights into overall brain function at a macroscopic level. Each recording technique serves a specific purpose in identifying brain states across different spatial and temporal scales.

Furthermore, the brain is adept at transitioning between various brain states, and EEG, with its ability to measure whole-brain activity or brain waves, is instrumental in detecting these transitions. In the subsequent discussion, the focus will be on exploring the fluctuations in brain waves as a means of understanding the dynamic nature of brain states.

3.1.2 Brain state neuromodulation

The brain exhibits various states, as observed through EEG waves, categorized by their frequency and amplitude (Buzsáki, 2006). These states, from slowest to fastest waves, include:

- Delta oscillations at 0-4 Hz;
- Theta oscillations at 4-8 Hz;
- Alpha oscillations at 8-12 Hz;
- Beta oscillations at 12-30 Hz;
- Gamma oscillations at 30-120 Hz.

The brain wave amplitudes are inversely proportional to their frequencies, so characterizing them using only frequency is sufficient. Each wave category has been associated with a specific level of cognition and mental activity (Herting and Chu, 2017). The higher the brain wave frequency, the higher the cognition and mental processing. Delta oscillations are associated with deep sleep, where the brain is less active, while theta oscillations are linked to tired states or deep relaxation, such as yoga or NREM sleep. Alpha oscillations are associated with a quiet, relaxed, and calm waking state. Beta and gamma oscillations are connected to an active waking brain state, concentration, and high cognition, with engaged processing for the fastest brain waves. It is important to note that REM sleep EEG looks like active waking states but is characterized by null muscle tone (Figure 3.2). REM sleep is the period where dreams occur, indicating heightened brain activity similar to when awake.

All of these brain waves emerge from the amalgamation of individual neuron activities in the brain. This implies that, during periods of active cognition, neurons are notably active and desynchronized, while in deep sleep states, neurons tend to fire synchronously, generating large-amplitude waves with low frequency. This once again underscores the interconnectedness of brain states at various spatial and temporal scales, with each state being a consequence of another.

Throughout a typical day, individuals spend several hours in an active or quiet waking state before transitioning into sleep states. Specifically, during waking hours, the brain states fluctuate between alpha and beta oscillations for normal cognition and brain activity, and possibly gamma oscillations during mentally demanding tasks such as memorization or mental computations. Subsequently, during sleep, the brain cycles through NREM and REM sleep. In NREM sleep, the brain gradually transitions from theta oscillations to delta oscillations, while in REM sleep, the brain is in an active state, displaying either beta or theta oscillations (Hobson, 2005) (Figure 3.2).

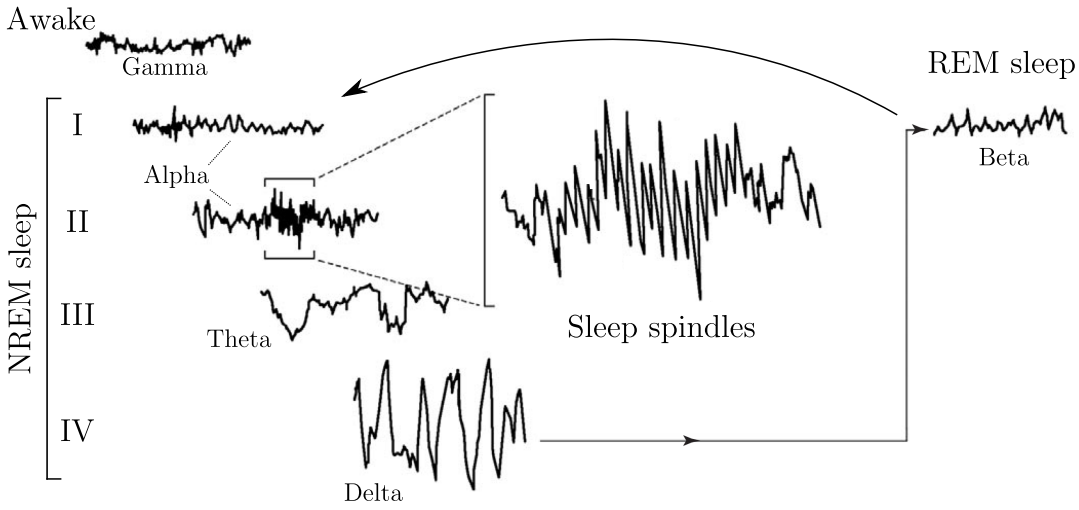

Figure 3.2: Different types of EEG waves. The awake state is characterized by high-frequency EEG waves, such as gamma waves. Sleep encompasses different states: REM sleep, where a mixture of beta and gamma waves can be recorded on EEG, and NREM sleep, which is divided into four stages. NREM sleep Stage 1 is characterized by slower waves known as alpha oscillations. Stage 2 is similar to Stage 1 but is distinguished by the presence of sleep spindles—transient high-frequency waves. Stage 3 is composed of slower waves called theta oscillations. The final stage is marked by the highest amplitude and the slowest waves, known as delta waves. Adapted from Muzur et al. (2002), with added text and arrows.

The alterations in brain states are induced by neuromodulation and neuromodulators. The brain is consistently exposed to a variety of chemical substances, including neuromodulators. Examining the concentrations of neuromodulators in the brain during different brain states reveals specific mixtures with varying concentrations for each state. For instance, during deep sleep, the concentration of neuromodulator A may be high, while those of B and C are low. Conversely, in an active processing state, the concentration of neuromodulator A is low, and the concentrations of B and C are high. Thus, distinct patterns of neuromodulator concentration characterize different brain states, facilitating transitions between states. To shift from one state to another, the brain adjusts the concentration of the neuromodulator mixture to match the pattern required for the target brain state. The action of neuromodulators then prompts the brain to switch states (Tyree and De Lecea, 2017).

3.2 The key molecules: the neuromodulators

3.2.1 What are neuromodulators

Neuromodulators and neurotransmitters are both distinct and similar molecules. Neurotransmitters, broadly defined, are chemicals released by a first neuron that reach target neurons, often released in the synaptic cleft. These neurotransmitters reach the target neuronal membrane and bind to ionotropic and metabotropic receptors, which directly create ionic currents when bound to their specific neurotransmitter. They play a crucial role in the synaptic transmission of neuronal information, transforming the electrical signal into a chemical one and back into electrical. There is a broad range of such molecules, including acetylcholine

(ACh), dopamine (DA), norepinephrine (NE), serotonin (5-HT), and histamine (HA) (Dicks, 2022).

Neuromodulators are a subset of neurotransmitters. In most cases, these molecules do not actively act in the synaptic cleft but rather have a more diffuse effect. Specific neurons, like dopaminergic neurons, are responsible for diffusing neuromodulators, such as DA, in the extracellular domain on a whole-brain scale, allowing an entire region to be subjected to the action of neuromodulators. Additionally, neuromodulators do not bind to ionotropic receptors but to metabotropic ones. These receptors do not allow ions to permeate like ionotropic ones but instead induce cellular changes in the neuron that, in turn, modify the electrical behavior of neurons. In general, they do not directly transmit information like neurotransmitters in the synaptic cleft, although some can act as neurotransmitters, such as ACh on nicotinic receptors. Instead, they influence behavioral changes in a potential neuronal population by modifying neuronal excitability (Bargmann, 2012).

Neuromodulators are ubiquitous in central nervous systems. However, due to their diffuse effects and their high number, identifying exactly their role might be challenging. Furthermore, neuromodulators may have overlapping functions, used for robustness, that further complexify the analysis (Gu, 2002). Here is a short and non-exhaustive list of neuromodulators, with emphasis on their pathway and suspected functions (Figure 3.3A). Note that neuropeptides can also produce a neuromodulatory function but will not be described here.

- **Acetylcholine:**
  ACh originates from both the basal forebrain and the mesopontine tegmentum. It can act either as a fast neurotransmitter at the neuromuscular junction or as a neuromodulator with more diffuse effects. ACh can influence neuronal excitability, synaptic transmission, and provoke synaptic plasticity. It tunes the state of neuronal networks and modifies their input-output properties. Thus, it plays a major role in brain state transitions (Picciotto et al., 2012).

- **Dopamine:**
  Dopaminergic neurons are located in the substantia nigra and the ventral tegmental area, projecting to the striatum, nucleus accumbens, amygdala, hypothalamus, olfactory bulb, and cortex. Dopamine, known as the reward and pleasure molecule, plays a major role in the reward system (Wise and Rompre, 1989).

- **Norepinephrine:**
  Norepinephrine, also known as noradrenaline, is released by noradrenergic neurons in the locus coeruleus. It projects to the cortex, cerebellum, hippocampus, thalamus, and other regions, playing a critical role in arousal and alertness (Berridge, 2008).

- **Serotonin:**
  Serotonergic neurons in the raphe nuclei of the brainstem project to the cortex, hypothalamus, and other areas. Serotonin plays a critical role in learning and memory, mood management, as well as environmental integration (Mohammad-Zadeh et al., 2008).

- **Histamine:**
  Histaminergic neurons in the hypothalamus project mainly to the cortex. Histamine

plays a critical role in vital functions such as the sleep-wake cycle, locomotion, memory consolidation, and retrieval (Nomura et al., 2021).

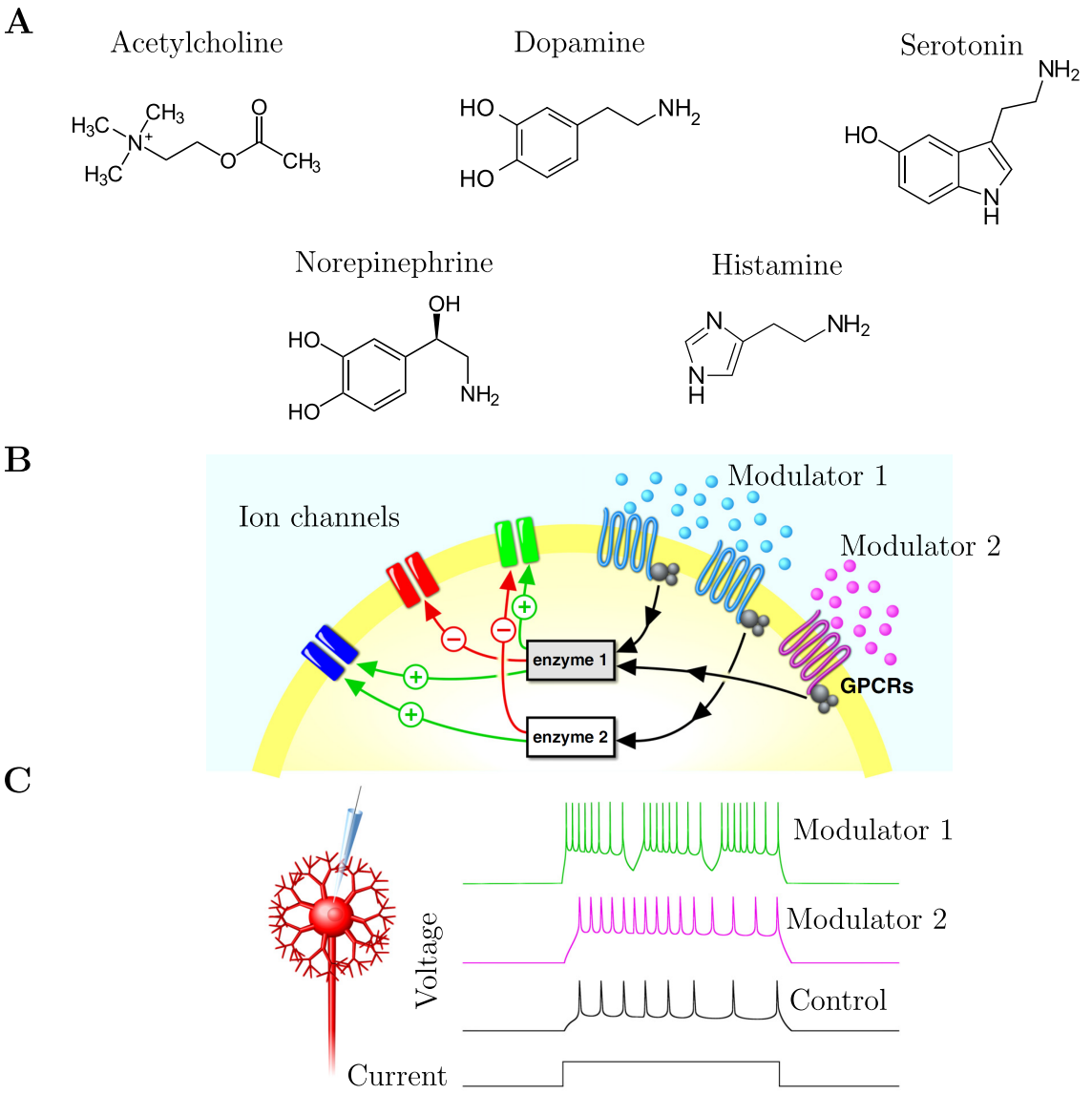

Figure 3.3: Neuromodulators and their action on neurons. **A.** Detailed molecular structures of neurotransmitters such as ACh, dopamine, norepinephrine, serotonin, and histamine. **B.** Schematic representation of the action of neuromodulators on neurons. Initially, neuromodulators bind to their receptors, which are often G protein-coupled receptors. This binding initiates a complex signaling cascade within the neuron, ultimately influencing the effective quantity of ion channels, *i.e.*, their conductance. **C.** Illustration demonstrating the effects of neuromodulators on single-cell electrophysiology. Taken from Nadim and Bucher (2014).

3.2.2 The effects of neuromodulators on neuronal properties

Neuromodulators bind to metabotropic receptors, which are often coupled to G-protein complexes, forming G-protein coupled receptors (GPCRs) (Marcus and Bruchas, 2023). When a neuromodulator binds to its specific GPCR, it activates the G-protein complex, initiating a complex and highly specific signaling cascade involving second messengers such as calcium

ions. Subsequently, there may be activation of kinases and phosphatases that phosphorylate or dephosphorylate target ion channel proteins, thereby modifying the effective conductance of these ion channels. Hence, neuromodulators play a crucial role in the regulation of ion channels. However, it is essential to note that ion channel regulation can be achieved through various other mechanisms, including direct gating by cyclic nucleotides (Podda and Grassi, 2014), as well as the direct and indirect effects of tyrosine kinases (Ahn et al., 2007). Consequently, this implies that every type of ion channel can be modulated, in part, by neuromodulation (Figure 3.3B).

In the same neuron, neuromodulators can influence multiple types of ion channels through the same signaling pathway. Furthermore, they can exert different effects on different channels, enhancing the conductance of one while decreasing the conductance of another (Nadim and Bucher, 2014). Additionally, a single neuromodulator molecule can impact a neuron through various signaling cascades, resulting in different modulations of neuronal excitability. Moreover, a particular type of ion channel can be modulated by numerous different neuromodulators, either in convergent or divergent actions (Santi et al., 2006) (Figure 3.3C).

For example, dopamine can adjust calcium channels in teleost retinal horizontal cells and also modulate sodium channels in prefrontal cortex neurons (Pfeiffer-Linn and Lasater, 1998). Different neuromodulators often target distinct subsets of ion channels in a neuron, enabling specific and diverse regulatory effects. However, there can also be convergence of modulatory effects onto the same ion channel (Swensen and Marder, 2000). This implies that a single ion channel may be influenced by multiple neuromodulators, and their combined effects can lead to a complex and integrated modulation of the channel activity. Such convergence adds a layer of sophistication to the regulation of neuronal excitability and function, allowing the nervous system to finely tune its responses to various inputs and conditions.

3.3 Electrophysiology of neuromodulation

The investigation of neuromodulation in electrophysiology has been a focus of intense research by electrophysiologists. Significant progress has been made over the past decades, particularly in the study of small circuits within invertebrate nervous systems, such as the stomatogastric ganglion of the crab or the leech heartbeat neural network, among others. Eve Marder, based at Brandeis University in Boston, USA, has been a key figure in experimental discoveries related to neuromodulation, as outlined in Nassim (2018) and associated references.

In practical terms, the electrophysiological study of neuromodulation involves recording specific types of neurons, either extracellularly or intracellularly. Initially, recordings are made in a saline bath containing a fluid that mimics extracellular fluid, representing the control activity. Subsequently, specific neuromodulators are added to the bath to observe the resulting switch in recorded neuronal activity. This process is often exemplified by examining transitions from tonic firing to bursting, and the following examples will provide insight into these phenomena before summarizing neuromodulation principles.

3.3.1 Measuring single cell neuromodulation

The application of neuromodulators can significantly influence neuronal electrical activity. In the context of isolated intracellular recordings from lateral pyloric (LP) and pyloric dilator (PD) neurons, as well as extracellular recordings from the lateral ventricular nerve (lvn) that carries axons of these neurons, notable findings emerge. These neurons are part of the stomatogastric systems in crabs and play a crucial role in pyloric rhythms. When these neurons are isolated from others, they are generally silent under control conditions. However, the application of various neuromodulatory substances induces rhythmic patterns (Marder and Weimann, 1992) (Figure 3.4A). An initial observation is that different neuromodulators can produce a similar overall effect, activating the network. This would illustrate the redundancy in the action of neuromodulators, where one substance may compensate for another when the priority is maintaining rhythmic activity rather than preserving the precise shape of the rhythm. This highlights the robustness of neuromodulation. However, each rhythm activated by different substances is distinct, indicating that the circuit can be reconfigured in numerous ways using different neuromodulators. For example, when exposed to dopamine, both neurons exhibit tonic firing mode and a fast rhythm, while exposure to pilocarpine results in a slower rhythm with both neurons in bursting mode. This example effectively illustrates the principles mentioned earlier, emphasizing that multiple neuromodulators can influence the same ion channels, and their actions can converge.

Another illustrative example involves the isolated anterior burster (AB) neuron, a component of the pyloric network that plays a pacemaking burster role. Under control conditions, this neuron exhibits a regular bursting pattern at a specific frequency, generating a characteristic burst shape. When exposed to proctoline, the AB neuron maintains its pacemaking rhythms, but there is an increase in oscillation amplitudes compared to the control. This effect is also observed with muscarinic agonists like pilocarpine or oxotremorine. However, when nicotine is applied, the low voltage of the oscillations undergoes a significant depolarization, eventually leading to a depolarization block where the neuron loses its pacemaking function (Hooper and Marder, 1984) (Figure 3.4B). This example emphasizes that certain neuromodulators may not visibly alter the electrical activity of the neuron while preserving its function, possibly contributing to increased resilience. On the other hand, neuromodulators targeting specific receptors, which activate other receptors and distinct signaling cascades (such as the conventional nicotinic receptor), can have completely different effects on ion channels. This, in turn, may lead to rhythm disruptions and loss of function. In the presented case, the current activated by proctoline and pilocarpine is voltage-dependent, possessing an integrated brake or adaptation mechanism that preserves the burst-generating mechanism in AB neurons.

The transition from tonic firing to bursting in single neurons is highly relevant for studying neuronal activity on a broader scale, especially considering its association with switches in brain waves. During high-frequency brain waves, recorded neuronal populations typically exhibit tonic firing with asynchronous activity. In contrast, during low-frequency brain waves, neurons tend to be in bursting mode with synchronous firing (Takahashi et al., 2006). This transition is crucial for understanding neuronal activity in a larger context and may occur due to various factors

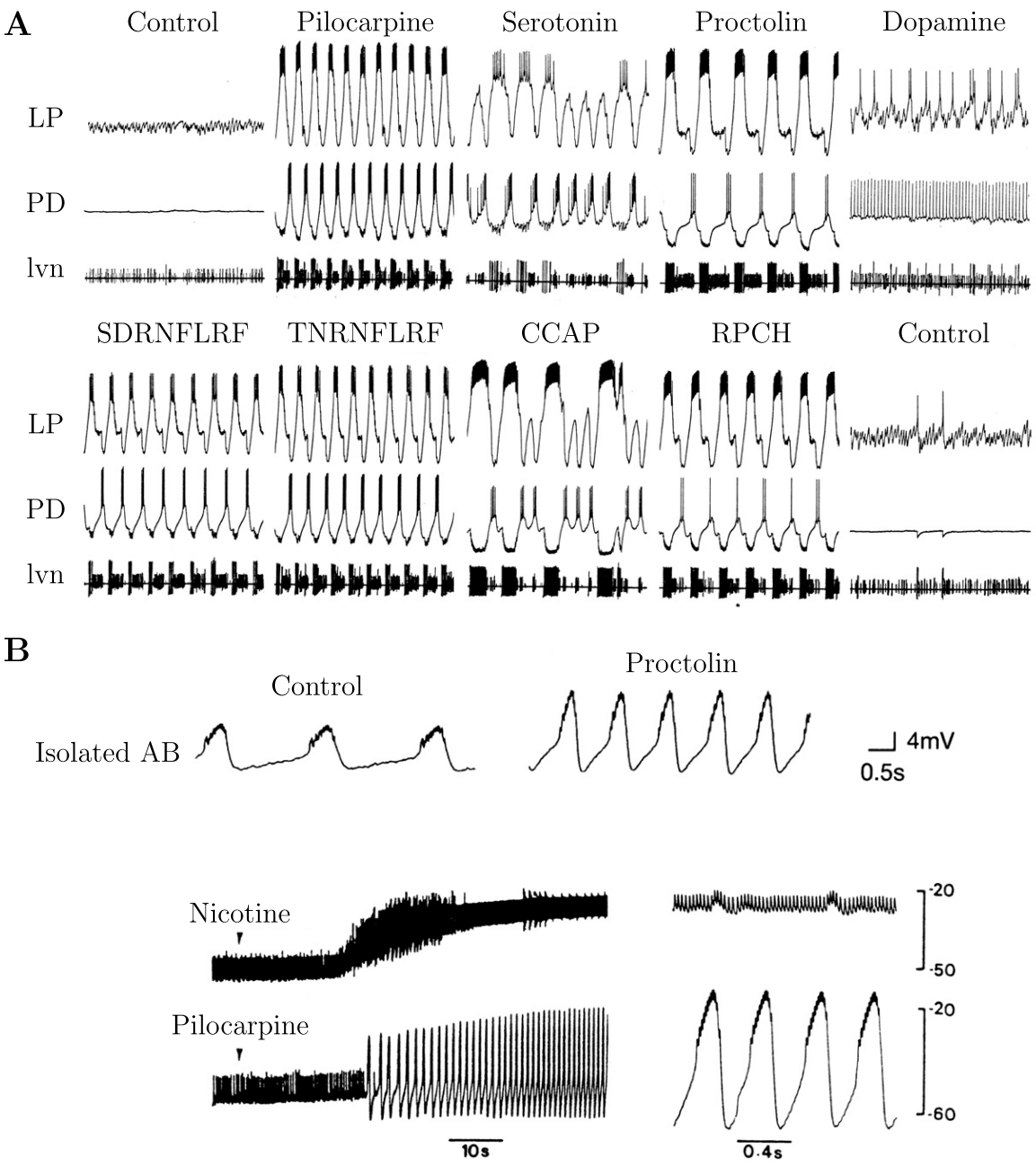

Figure 3.4: Electrophysiology of neuromodulation. A. Activity of LP and PD neurons as well as the lvn nerve under control conditions and after application of several neuromodulators. In control conditions, silent activity is observed. Various neuromodulators can activate the LP/PD rhythm in different ways. **B.** Under control conditions, isolated AB neurons burst. Upon application of proctolin or pilocarpine, the amplitude of the oscillations is significantly increased. However, the application of nicotine abolishes the pacemaking role of AB neurons. Taken from Marder and Weimann (1992); Hooper and Marder (1984).

such as synaptic inputs, environmental changes, or alterations in extracellular fluid. Here, the focus is on transitions induced by neuromodulation. Thalamic neurons, particularly thalamic reticular neurons, play a key role in the transmission of neuronal information. Thalamic reticular neurons switch from bursting (in sleep states) to high-frequency tonic firing (in wake states) under the influence of serotonin, norepinephrine, or glutamate—neuromodulators found in high concentrations during wakefulness (Crabtree, 2018). Thalamic relay neurons exhibit similar

switches when exposed to acetylcholine, norepinephrine, or histamine (McCormick and Bal, 1997). In a broader context, cortical neurons also transition from bursting activity to low-frequency tonic firing during the switch from sleep to wake states, influenced by acetylcholine or norepinephrine (Dahan et al., 2007). Pre-Botzinger neurons, central units in respiratory rate control, can switch from pacemaking tonic firing to bursting under the influence of norepinephrine (Ramirez, 2011). It is noteworthy that external drugs, like ketamine, can act as abnormal neuromodulators, leading to abnormal brain states. For example, in lateral habenula neurons in the epithalamus, exposure to such drugs drastically reduces bursting behavior, resulting in a non-physiological situation and disrupting the function of these neurons.

Thus, brain activity is continually shaped by the actions of various neuromodulators and neuropeptides. Neuromodulators dynamically influence the activity of single neurons, impacting input/output properties and the strength and dynamics of synaptic connections. This dynamic modulation allows neuronal networks to adapt to changing needs, contexts, and environments. To achieve this modulation, neuromodulators dynamically alter the density, dynamics, and kinetics of many transmembrane proteins within individual cells. The reliability and robustness of neuromodulation mechanisms at the molecular and cellular levels are crucial for the proper functioning of whole-brain signaling.

Neuromodulation regulates essential nervous system properties that cannot be achieved through synaptic plasticity alone. For example, it plays a critical role in selective attention (Noudoost and Moore, 2011) and is responsible for global switches in brain states, significantly impacting how the brain encodes and reacts to external information in different contexts (Zagha and McCormick, 2014). A recent noteworthy example is the crucial role of neuromodulation in the voluntary control of locomotion. Through a brain-spine interface, researchers have successfully alleviated walking deficits in rodents (Van den Brand et al., 2012) and primates (Capogrosso et al., 2016) suffering from paralyzing spinal cord injuries by specifically restoring neuromodulation below the lesion site. Another example demonstrates how neuromodulators can influence spike-timing dependent plasticity, thereby tuning this plasticity rule (Brzosko et al., 2019). While experimental studies have highlighted the ubiquity of neuromodulation in all nervous systems, the basic principles governing this mechanism have yet to be fully formulated.

3.3.2 State of the art on neuromodulation principles

Decades of research on experimental systems have revealed fundamental properties that have advanced our understanding of neuromodulation, as outlined in Marder (2012):

1. Even the simplest circuits are multiply modulated by a plethora of neuromodulators and neuropeptides (Marder and Bucher, 2007).
2. Neuromodulation can be state-dependent, meaning the effect of a neuromodulator can depend on the target neuron activity state (Marder et al., 2014).
3. Neuromodulators often target several ion channels in one neuron type, and both the channel types and their modulation differ from neuron to neuron (Marder and Bucher, 2007).
4. Many coexistent neuromodulators can target the same channel type, leading to possible

interferences between them (Bucher and Marder, 2013).

5. The same functional neuromodulatory state can be achieved through very different channel combinations, a property called degeneracy (Prinz et al., 2004).

6. Neuromodulation must coexist with homeostatic plasticity, a mechanism that slowly tunes neuron membrane properties to maintain a target activity level (Desai, 2003; Turrigiano, 2012).

In addition to these principles, it is crucial to acknowledge that neuromodulation can act on either the micro- or macroscale (Shine et al., 2021). While this thesis primarily focuses on the microscale, where neuromodulators directly act on ion channels and tune neuronal membrane excitability, it is important to note that on the macroscale, behavioral changes can be observed, such as alterations in the sleep-wake cycle. This raises the challenging question of how neuromodulators can reliably produce effects at the whole-brain level while indirectly targeting such variable properties at the molecular and cellular levels. Addressing this question constitutes the central goal of my thesis.

3.4 Robustness of neuromodulation

As mentioned, neuromodulators exert reliable and flexible actions on single neuron dynamics, influencing fundamental circuit function. However, the robustness and predictability of neuromodulator actions remain elusive due to the observed variability in intrinsic parameters across animals. Past research has compellingly demonstrated that ion channel densities and other properties, which constitute the end targets of neuromodulators, can exhibit high variability among neurons of the same types. For instance, Schulz et al. (2006b) illustrates that two LP neurons recorded from different crabs, under the same neuromodulator action, display nearly identical electrical activity, yet their intrinsic neuronal parameters (such as ion channel conductances) differ drastically, varying up to fivefold (Figure 3.5A-E). This discrepancy raises the challenging question of how neuromodulators can reliably produce effects at the whole-brain level while indirectly targeting such variable properties at the molecular and cellular levels.

Moreover, the impact of neuromodulators on neuronal signaling through the activation of metabotropic receptors significantly complicates the analysis. These receptors do not directly influence membrane ion channels but engage second messengers that initiate intricate signaling cascades. These cascades eventually target ion channels in a neuron-specific manner, producing a diverse array of effects in different neuron types, many of which are challenging to identify experimentally. Additionally, numerous neuromodulators can target the same ion channels or subsets of ion channels, potentially leading to interfering effects.

The focus of this thesis will be on exploring the dynamic effects of neuromodulation in reshaping neuronal signaling using engineering tools. Investigating the mechanisms of reliable neuromodulation in variable neurons has the potential to significantly impact traditional approaches to electrophysiological experimental research and drug development. Conventional strategies often involve studying or treating abnormal neuronal signaling by directly targeting ion channels with specific channel blockers. However, experimental data and computational studies

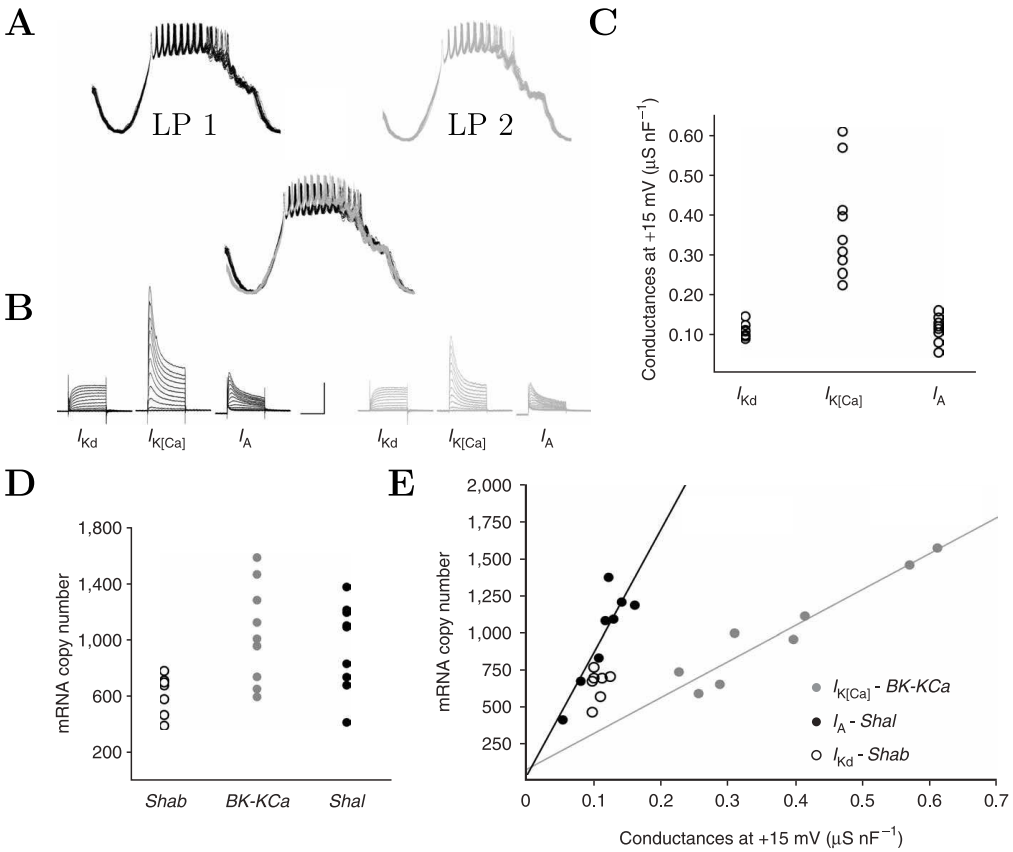

Figure 3.5: Neuromodulation is robust against intrinsic neuronal parameter variability. A. Rhythmic activity of two LP neurons from different crabs. When overlapped, the voltage traces exhibit remarkable similarity without any correction. **B.** Raw current measurements of three different potassium currents. **C.** Variability in conductance values of three potassium currents across different crabs, despite very similar activity. **D.** mRNA abundance for ion channels carrying potassium ions in LP neurons varies among crabs. *Shab* denotes Kd ion channels, *BK-KCa* denotes K[Ca] ion channels, and *Shal* denotes A ion channels. **E.** Correlation between ion channel mRNA abundance and measured membrane conductance in LP neurons, suggesting that mRNA abundance is a reliable indicator of ionic conductances. Taken from Schulz et al. (2006b).

suggest that such direct actions on ion channel properties may lead to unreliable outcomes due to interneuronal variability (Drion et al., 2011).

Understanding how neuromodulation addresses this reliability problem could pave the way for novel experimental and therapeutic strategies that yield more consistent observations and outcomes. This might involve targeting multiple channel types simultaneously in specific proportions (Goaillard and Dufour, 2014) or finding ways to manipulate the (potentially dysfunctional) physiological mechanism by intervening in the feedback control system itself. This could include modulating second messengers and specific components of intracellular signaling cascades.

4 Degeneracy, ion channel correlations and homeostatic plasticity

As mentioned earlier, neuromodulation is intrinsically linked to degeneracy, ion channel correlations, and homeostatic plasticity, which will sometimes be referred to as homeostasis in this thesis for simplicity. This section briefly recaps what is known about these phenomena and explores the interactions and challenges in studying the neuromodulation of these processes.

4.1 Degeneracy

4.1.1 State of the art

Biological systems exhibit significant variability in both cellular and system-wide properties. In the nervous system, properties such as ion channel conductances can vary widely, not only between neurons of the same type across different animals of the same species, but also within neurons of the same type in a given individual, all while maintaining proper electrical functioning (Prinz, 2017). This intrinsic parameter variation, allowing diverse configurations while preserving neuronal excitability, is referred to as degeneracy or non-uniqueness (Goaillard et al., 2009). This should not be confused with redundancy, which implies the existence of an exact replica of a given entity or mechanism. Degeneracy refers to the idea that the same problem can have multiple solutions, or that different combinations of ion channel conductances can produce the same voltage activity, in the case of neurons (Goaillard and Marder, 2021).

The concept of degeneracy extends to synaptic parameters such as voltage-gated ion channel conductances. Synaptic parameters naturally exhibit variation to support neuronal plasticity, a process that continuously remodels synaptic connections to facilitate learning and the formation, retention, and recall of memories. Degeneracy is now viewed as a biological robust feature, serving as a complementary mechanism to other natural phenomena involving parameter variation, such as neuromodulation or plasticity, rather than as a flaw in the system.

In a study examining variability in synaptic parameters in silico for hippocampal Schaffer collateral synapses, the authors employed the Monte Carlo method to generate randomly parameterized models (Mukunda and Narayanan, 2017). They retained valid model parameter sets that exhibited the desired electrical behavior. The results demonstrated that synaptic parameter sets of computational models, capable of producing biologically realistic properties, could vary over wide ranges—several-fold—from synapse to synapse while still maintaining proper functioning (Figure 4.1A). This underscores the concept of degeneracy.

Another noteworthy example is found in a study of the pyloric rhythm (Prinz et al., 2004). The researchers successfully replicated the same apparent rhythm using a completely different set of parameters, specifically ion channel conductances in the different neurons participating in this rhythm. This exemplifies how different sets of parameters can lead to similar functional outcomes, highlighting the robustness of degeneracy in neuronal systems (Figure 4.1B).

Coupled with degeneracy, Schulz et al. (2007) showed that these variable parameters may

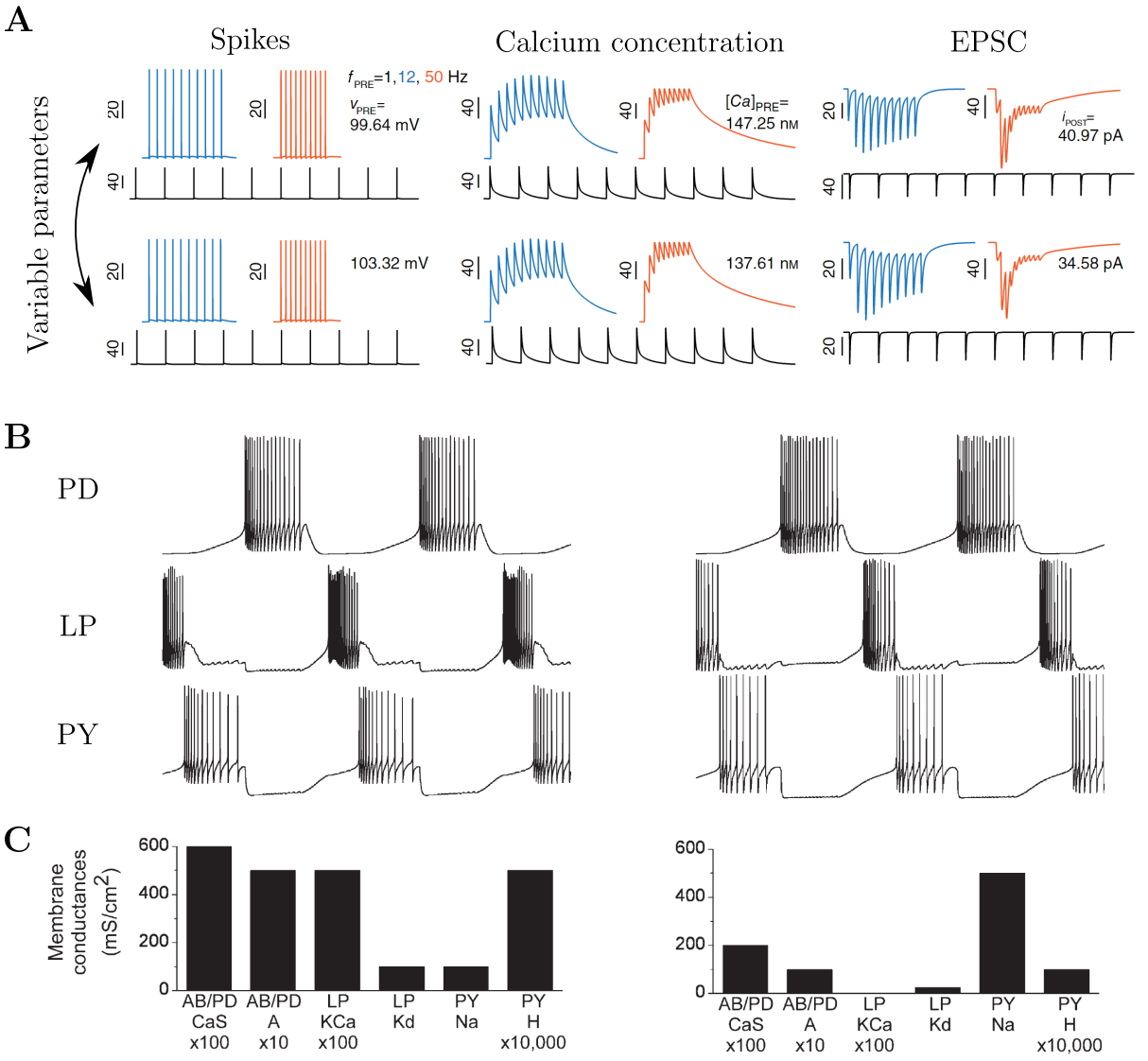

Figure 4.1: Degeneracy, the ability to have significant variability in neuronal parameters while preserving similar activity. A. Hippocampal Schaffer collateral synapses exhibit strikingly similar activity in terms of spike timing, calcium concentration, and excitatory postsynaptic current (EPSC). However, both models possess drastically different parameters. **B.** Two pyloric networks demonstrate highly similar activity. **C.** Despite their similar activity, both networks exhibit drastically different parameter distributions, particularly in terms of ionic conductances. Adapted from Mukunda and Narayanan (2017); Prinz et al. (2004), with added text on the left and top of panel A.

produce correlations between ion channel expressions, although some of these correlations are not necessarily required to maintain the desired activity pattern (Taylor et al., 2009). These parameter correlations can be seen as a robustness and resilience feature, where a dynamic neuronal system can counter external perturbations (such as ion channel blockade or other) on a subset of intrinsic parameters by adjusting other parameters following these correlations, to maintain proper physiological function (Tobin et al., 2009). Over the years, degeneracy has come to be seen more and more as a positive feature of biological systems (such as neuronal systems or genetic code), rather than as an unwanted side effect of the biological manufacturing process or noise. Thus, degeneracy may be a perfect candidate to be the keystone of neuronal system

robustness and versatility, what Prinz (2017) call "degeneracy rules!".

4.1.2 Interplay with neuromodulation and challenges

As degeneracy implies the potential for identical external behavior with different parameter sets, the space of possible firing patterns is inherently of lower dimension than the hyperspace of ion channel conductances. The segmentation of this potentially high-dimensional space into clusters of similar external behavior becomes essential for understanding degeneracy mechanisms (Golomb and Rinzel, 1994). In this perspective, neuromodulation emerges as a reliable process, allowing neurons to transition robustly from one cluster to another, adapting firing patterns with versatility. Neuromodulation, proven to modify ion channel conductances, enables neurons to navigate this complex high-dimensional parameter space. While degeneracy is vital for neuronal robustness, it complicates the dynamic analysis of neuromodulation, challenging the likelihood of a simple, linear rule, especially in the presence of complex cluster shapes (Swensen and Bean, 2005).

Given the ubiquity of degeneracy in both experimental and computational studies (Sobie, 2009; Tang et al., 2012), understanding its interaction with neuromodulation is crucial for comprehending how neuromodulators can reliably impact the entire brain while indirectly influencing variable molecular and cellular properties. According to Marder et al. (2014), these interactions prompt three fundamental questions:

1. Can neurons with degenerate parameter sets give robust and reliable responses to modulation (Szücs and Selverston, 2006)?
2. Given this robustness, can neurons with comparable external activity respond differently to neuromodulatory substances (Goldman et al., 2001)?
3. What kind of response to neuromodulation can be expected from neurons of a given type?

Answers to these questions remain elusive, and this thesis aims to contribute insights into the intricate interplay between neuromodulation and degeneracy. While the picture is not entirely clear, some computational studies have already identified key mechanisms in this interaction (LeMasson et al., 1993; Baines et al., 2001).

In Marder et al. (2014), the authors employed a model with seven types of ion channel conductances, including a T-type calcium channel "CaT" and a calcium-controlled potassium channel "KCa." Two parameter sets were generated, and 2D firing pattern heat maps (in CaT and KCa) were created for both sets to observe the neuron capability to generate different firing patterns based on varying conductances for the two ion channels of interest. The heat maps exhibited degeneracy, with various parameter combinations resulting in the exact same firing pattern. Despite similar color patterns in the two heat maps, increasing one channel conductance had globally the same effect on both models, yet they were distinct. Introducing a fixed neuromodulation rule affecting only one type of ion channel (CaT) revealed non-robust effects. For instance, with a low amount of KCa channels, a short decrease in CaT channel conductance either did not alter the firing pattern (remaining in tonic firing) or completely modified it, transitioning from bursting behavior to tonic spiking. Similar observations were made

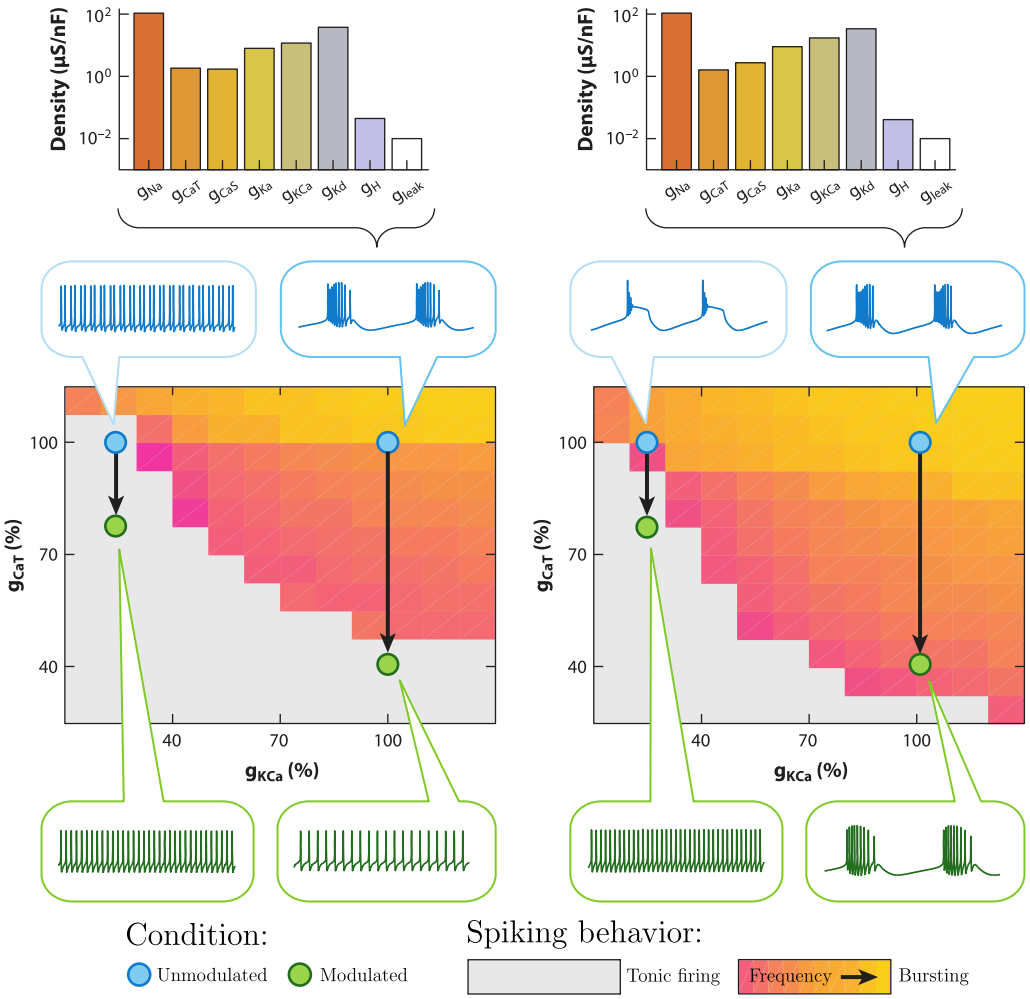

Figure 4.2: Rigid neuromodulation rule leads to unreliable effect due to degeneracy. Conductance density distributions for two different neurons (left and right) closely resemble each other (top). The phenotype heat maps in the same parameter regions exhibit qualitatively identical patterns for both models. However, slight modifications occur near the boundary from tonic spiking to bursting. Due to these slight modifications, a rigid neuromodulation rule on one ionic current (here KCa) results in unreliable effects, with variability in the neuromodulated phenotype. Taken from Marder et al. (2014).

with the second neuromodulation rule, where, for a high amount of KCa channels, a significant decrease in CaT channel conductances led to unreliable neuromodulatory effects (Figure 4.2). Thus, neuromodulatory rules, influencing one or more ion channel conductances, cannot be rigid and should adapt to their own strength and the values of other conductances in the neuron. In other words, neuromodulation should be state-dependent to produce reliable actions.

Another experimental study aimed to explore the impact of non-physiological perturbations on similar neuromodulatory actions (Harris-Warrick and Flamm, 1987). Dopamine, serotonin, and octopamine demonstrated analogous effects on the anterior burster neuron. Essentially, these neuromodulators, when applied to an isolated AB neuron, activated the neuron rhythm, inducing a bursting mode. Despite minor differences, the resulting bursting patterns under the influence of these three neuromodulators exhibited striking similarities, enabling the neuron to

function robustly and consistently. Subsequently, non-physiological extracellular perturbations were introduced to the AB bursting neuron under these three neuromodulatory conditions, involving a decrease in the concentration of extracellular sodium and calcium. The effects of these perturbations varied significantly among the different neuromodulatory conditions. In some cases, the rhythm was lost, and the neuron became silent, while in others, the rhythm was sustained and nearly unaffected. This outcome suggests that, even though neuromodulators appear to exert the same external impact on the AB neuron, the underlying neuromodulatory actions, when scrutinizing the firing pattern, are quite distinct (Figure 4.3A). This implies that a rigid perturbation leads to unpredictable actions, a phenomenon attributed to the distinct ion channels targeted by these neuromodulators, resulting in diverse effects within the high-dimensional parameter set.

In conclusion, this raises a pivotal yet unanswered question: How can neuronal activity or the neuronal parameter set be modulated so that a multitude of neuromodulators, akin to physiological perturbations, modify neuronal excitability in the desired direction (Marder et al., 2014)? Several answers have been proposed, illustrated in a 2D heat map of two modulated neuronal parameters, X and Y (Figure 4.3B). The system comprises two external states, namely basal and neuromodulated states, demonstrating degeneracy, and the boundary between these states is non-trivial. In the first scenario, a stiff, similar, and state-independent neuromodulation action is applied to several points in basal states. However, it fails to produce the expected change in behavior for some points. Effectively, after the neuromodulation action, some neurons switch to the neuromodulated state while others remain in the basal state, rendering this stiff neuromodulation action unreliable. Addressing this issue can be approached in two distinct ways:

1. The neuromodulated action can remain stiff and state-independent. However, this requires that neurons in the basal state remain somehow close to the boundary between states, thanks to another regulatory mechanism that would minimize the distance with the state transitions boundary at all times. In this case, the exact same neuromodulatory action can be applied to each neuron close to the boundary to reliably switch from the basal to the neuromodulated state. However, this restricts the area that is available and reachable in the parameter space, and so, in turn, reduces the robustness brought by degeneracy.

2. Alternatively, a more intricate approach involves having a neuromodulation action that is correlated and dependent on the neuronal state. Both the parameters of the neurons and the neuromodulatory action are tuned together for a state-dependent neuromodulation. This allows the neuron access to an unrestricted degeneracy space, maximizing robustness. However, the neuromodulatory action must be tunable, in direction and/or amplitude, based on the neuronal parameters.

As previously mentioned, neuromodulation has been experimentally verified to be state-dependent (Kramer and Levitan, 1990). Therefore, the latter hypothesis is more physiologically motivated but considerably complex. Neuromodulation grapples with high-dimensional, highly nonlinear dynamical systems, targeting numerous cellular and network properties, making it challenging to unravel. For instance, even the most recent qualitative modeling attempts of brain signaling lack neuromodulation (Markram et al., 2015). This thesis aims to provide a general rule for

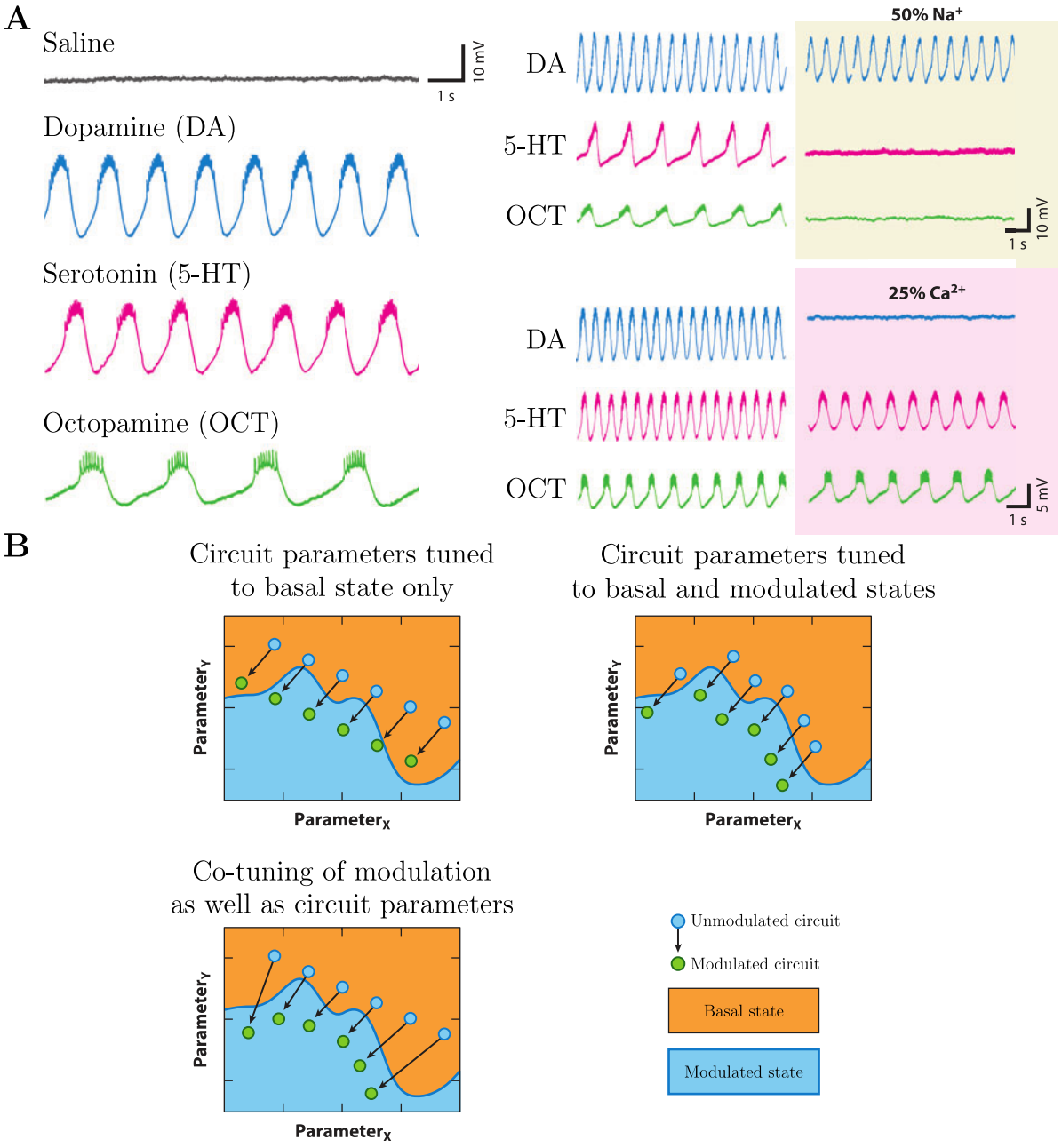

Figure 4.3: Effects of neuromodulation on neuronal parameters. A. Convergence of distinct modulatory mechanisms on single-neuron behavior. Three different neuromodulators can activate the AB neuron rhythm (left). However, when exploring non-physiological regions by decreasing the quantity of sodium ions (top right) and calcium ions (bottom right), the effects of the three neuromodulators are completely different under such conditions. **B.** How is neuromodulation tuned to produce reliable behavioral switches in variable circuits? In one scenario, a rigid neuromodulation rule with fixed magnitude and direction of modulatory changes is applied to all possible basal state parameter values (top right), leading to unreliable switches in behavior. Another scenario involves the same neuromodulatory rule, but other cellular mechanisms maintain basal parameter values close to the boundary of the modulated state (top right), potentially improving reliability. In a third scenario, the modulatory rule is state-dependent in magnitude or orientation, or both, to ensure a robust switch in behavior (bottom left). Taken from Marder et al. (2014).

neuromodulation, leveraging the last hypothesis mentioned above.

4.2 Ion channel correlations and homeostatic plasticity

4.2.1 State of the art

Throughout their lifespan, neurons must continuously adapt and evolve to maintain sustained activity and functionality, even as their inputs undergo constant change. Homeostatic plasticity refers to the ability of neurons to regulate their excitability in response to network activity, allowing them to preserve their output capacity (Davis, 2013; Turrigiano, 1999; Turrigiano and Nelson, 2004). This property can be categorized into two forms: synaptic and intrinsic (Turrigiano, 2012). Synaptic homeostatic plasticity involves neurons adjusting their synaptic strength in response to changes in input, thereby preserving network function (Davis, 2006). Intrinsic homeostatic plasticity, on the other hand, refers to neurons modulating their intrinsic electrical parameters, such as ion channel conductances, to maintain firing rates and excitability in a shifting environment, like in the case of development and aging (Davis and Bezprozvanny, 2001). In this thesis, the focus will be on intrinsic homeostatic plasticity, as the study primarily considers single cells.

Neurons use a complex array of ion channels, each likely serving overlapping and degenerate functions, yet their primary goal remains to sustain optimal functionality. Despite the ongoing turnover of transmembrane proteins, including ion channels and receptors, occurring on timescales ranging from hours to weeks, neuronal excitability must remain robust (O'Leary et al., 2013; Marder and Prinz, 2002). Intrinsic homeostatic plasticity, or homeostasis for simplicity in this thesis, serves as the critical regulatory mechanism that helps preserve this delicate balance, ensuring the continued vitality of neurons within a dynamic and fluctuating environment.

The collective body of theoretical and empirical investigations proposes that neuronal excitability adheres to a homeostatic negative feedback process, crucial for maintaining a basal level of intracellular calcium ions (O'Leary et al., 2010; Seeburg and Sheng, 2008; van Welie et al., 2004; Pratt and Aizenman, 2007). These calcium ions function as sensors, relaying information to the cell regarding the turnover of transmembrane proteins, encompassing processes such as translation, insertion, and degradation (Wierenga et al., 2006). By monitoring solely the intracellular calcium levels, the neuron orchestrates the regulation of all its ion channel conductances through homeostatic self-tuning rules (Figure 4.4A-B). This orchestration ensures the attainment of a suitable firing pattern, starting from randomized initial conditions and preserving it over time. In such models, diverse sets of ion channel conductances may yield identical external activities, underscoring the pervasive role of degeneracy (Liu et al., 1998).

In light of the singular variable governing a potentially extensive array of neuronal parameters, it is not surprising that experimental studies often reveal robust positive linear correlations in ion channel protein expressions, as quantified by the associated mRNA levels (Toledo-Rodriguez et al., 2004). Illustratively, (Tobin et al., 2009) identified a pronounced linear correlation in the mRNA encoding A-type potassium channels and H-type cyclic nucleotide-activated channels within crustacean motor neurons.

Adhering to the calcium homeostatic principle, which prescribes all neuronal parameters based on a singular variable—intracellular calcium—neurons guided purely by homeostasis would exhibit positive and robust pairwise correlations in all ion channel conductances. In O'Leary et al. (2014), the authors constructed neuronal control models, demonstrating, as anticipated, that a single neuronal type, with ion channel expression correlations emerging from the convergent action of calcium on the expression levels of different ion channels, was governed solely by homeostatic regulation. This resulted in nearly aligned ion channel conductances along a high-dimensional continuum across species (Figure 4.4C). Notably, the physiological function remained constant and sustained over time. In essence, homeostatic rules yield degenerate sets of neurons, with the degeneracy manifold confined to a one-dimensional space, irrespective of the dimensionality of the broader neuronal parameter space.

However, as observed, degeneracy is not confined to a singular dimension. Computational and experimental studies reveal that firing patterns and neuronal excitability properties can remain constant within a neuronal parameter subspace characterized by more than one manifold (Taylor et al., 2009; Goaillard and Marder, 2021). Hence, while homeostatic rules play a pivotal role in ensuring cell survival, they alone cannot comprehensively account for the full scope of neuronal degeneracy and flexibility.

4.2.2 Interplay with neuromodulation and challenges

While homeostasis and its regulatory effects are pervasive in both experimental and computational studies, recognized as a crucial physiological factor for cell survival, development, and disease, it offers only a partial explanation for the intricate landscape of neuronal dynamics (O'Leary and Wyllie, 2011). Confining homeostasis to a one-dimensional manifold, dictating strongly positive correlations among ion channels, oversimplifies the intricacies at play. Notably, the interaction of neuromodulation with this stringent homeostatic rule raises questions, given neuromodulation versatile impact on ion channel conductances and its potential to modify their correlations.

A revealing instance of the limitations imposed by a singular homeostatic rule becomes evident when comparing sets generated through homeostasis to those generated purely at random. On one side, neurons crafted solely under the influence of the previously described homeostatic rule form a point cloud in the parameter space, approximating a one-dimensional manifold with strictly positive correlations. On the other side, a set of neurons generated via Monte Carlo simulation undergoes post-processing to retain only those exhibiting the desired external behavior. Despite both sets manifesting identical firing patterns and, consequently, similar neuronal functions, the volume spanned by the purely randomly generated neurons surpasses that of the homeostatically generated set (O'Leary et al., 2013). This implies that by exclusively relying on the homeostatic rule as the sole generation mechanism, the degeneracy of the set becomes highly constrained, rendering it less versatile than its purely random counterpart.

To maximize degeneracy, an implication arises that an additional mechanism must be at play in generating neuronal sets, potentially linked to neuromodulation. The initial findings of this thesis will aim to shed light on this critical question.

An additional illustration emerges from studies such as Tapia et al. (2018), Schulz et al. (2007),

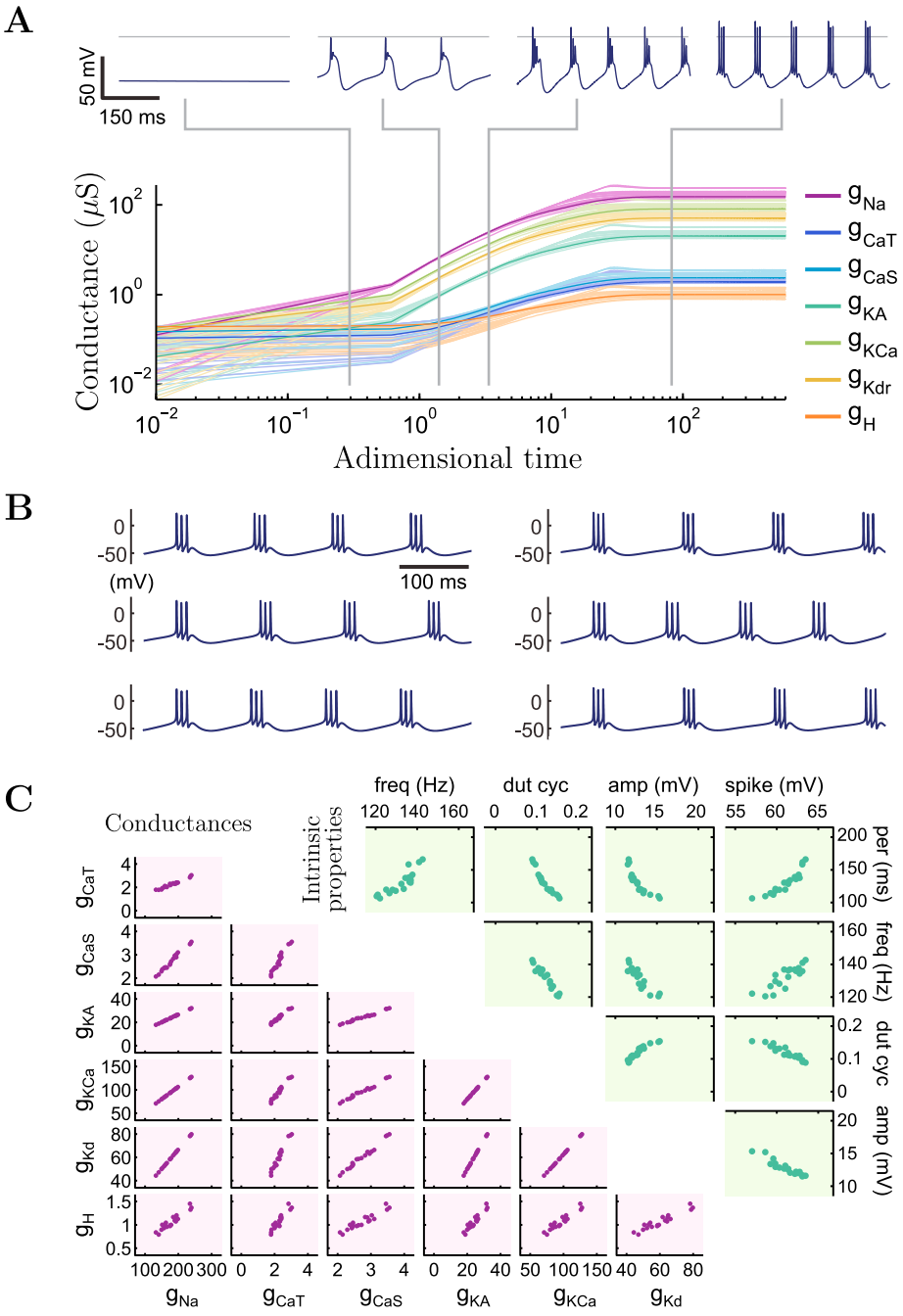

Figure 4.4: Homeostatic tuning rules create strong positive correlation in degenerate population. A. Time evolution of a self-regulating neuron implementing integral control for its seven voltage-dependent conductances using homeostatic tuning rules, *i.e.*, by maintaining predefined conductance ratios and achieving a predefined mean intracellular calcium level. **B.** Steady-state neuronal activity across different neurons. The activity is maintained, yet the values of the conductances vary. **C.** Scatter matrices of conductance distributions (bottom left) and intrinsic properties (top right) at steady state. Strong positive correlations characterize the high-dimensional conductance distribution, while intrinsic properties are constrained, indicating that the activity is maintained consistently across neurons. Adapted from O'Leary et al. (2014), with axis labels replaced in panels A and C.

and Kodama et al. (2020), emphasizing correlations among genes encoding ion channel proteins. In Schulz et al. (2007), high-order correlations in ion channel expression within stomatogastric pyloric neurons are computed. Tapia et al. (2018) explores these correlations in dopaminergic neurons of the substantia nigra in rats, while Kodama et al. (2020) identifies similar correlations in fast-spiking vestibular nucleus neurons. The consistent result across these studies is the presence of positive correlations between pairwise ion channel gene expressions, with some expressions showing no correlation. This indicates that, within experimental neuronal parameter sets, a homeostatic rule is evident, given the observable induced correlations. However, there is also compelling evidence suggesting that it does not provide a comprehensive explanation, as the reasons for the existence of uncorrelated pairwise ion channel gene expression levels remain unclear.

Nevertheless, the generation mechanism for neuronal parameter sets is not entirely obscure. In a potentially high-dimensional parameter space, it becomes apparent that the dimensionality of this space exceeds that of the space representing neuronal activity or equivalent electrophysiological phenotypes. Within this expansive parameter space, there exist manifolds along which degenerate sets proliferate. The two primary candidates for governing these sets are homeostatic regulation, which is well understood, and neuromodulation, whose dynamical effects remain unclear (Goaillard and Marder, 2021). Multivariate mutual information analysis, capable of quantifying set interactions at any dimension, reveals that slightly less than half of the total set variability in midbrain dopaminergic neuron parameter sets exists beyond pairwise correlations—outside the bounds of the homeostatic rule (Baudot and Bennequin, 2015; Baudot et al., 2019). As articulated by Goaillard and Marder (2021), authorities in ion correlations and degeneracy studies, "Despite the remarkable advances of recent years in the analyses of genes expressed in single neurons, the challenge of understanding how ion channels determine neuron and circuit resilience remains as daunting as ever".

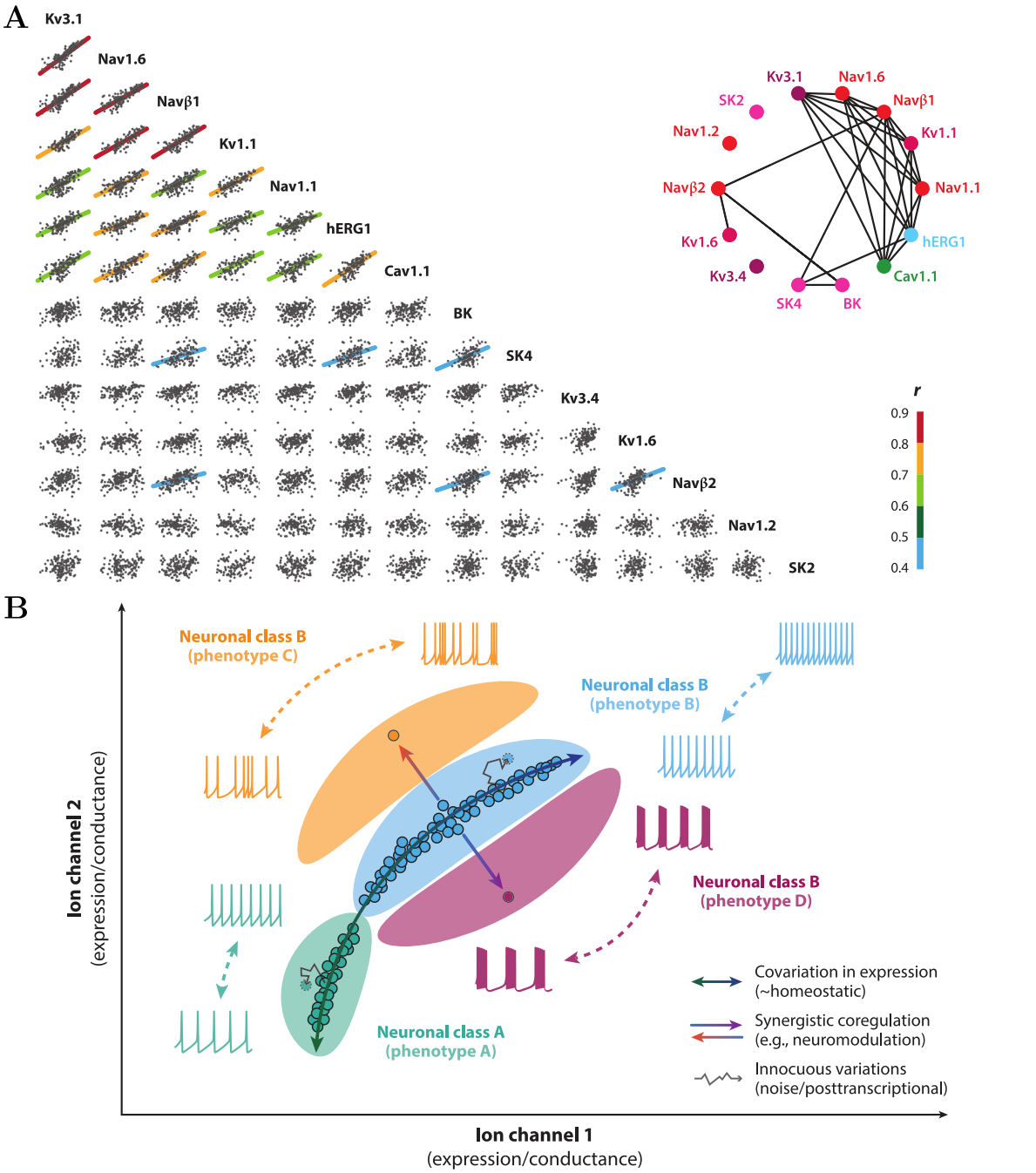

Figure 4.5: Covariation in ion channel expression and its implication in electrical phenotype. A. Pairwise correlations in ion channel mRNA expression in fast-spiking vestibular nucleus neurons. Fourteen ion channels were quantified in such neurons, plotted in a scatter matrix along with potential pairwise correlations, if significant ($r > 0.4$) (left). The correlation graph illustrates significant correlations in ion channel mRNA expression of these neurons (right). **B.** Two sets of neurons, linked in anatomy and/or function, are represented as green and blue dots within a two-dimensional framework reflecting the expression or conductance levels of two ion channels. The shaded areas delineate parameter regions associated with distinct firing behaviors, with green and blue representing control behaviors of the respective neuronal groups. Within each shaded region, the phenotype varies in quality rather than quantity, showcasing qualitatively similar yet quantitatively distinct characteristics between the two neuronal populations. Taken from Kodama et al. (2020); Goaillard and Marder (2021).

5 A good example: the stomatogastric nervous system of crabs

Historically, neuroscience breakthroughs have been achieved through the study of neuronal systems in small animals. Indeed, these small circuits are much simpler and more accessible than the complex nervous systems of larger animals capable of higher cognitive functions, such as the human brain. Despite their simplicity, simple nervous systems remarkably exhibit similar functions and mechanisms compared to more complex nervous systems, with the main differences lying in the number of neurons and connections. The very first breakthrough in cellular neuroscience was made by Hodgkin and Huxley (1952a), who recorded the first action potential ever in a giant axon of a loligo, a squid. Cephalopod and crustacean circuits are particularly easy to study due to their simplicity, making them completely tractable. This allows for a complete neuronal mapping, identifying different types of neurons and their connections, as well as neuromodulators. Moreover, in the case of the giant axon of loligos, recording is much easier given the large size of the axon compared to human ones. Thus, studying small circuits enables us to draw general conclusions and principles about how the nervous system works and its function.

In this section, the focus will be on a striking example of the study of small neuronal circuits, the stomatogastric nervous system (STNS) of crustaceans, specifically wild-caught crabs and lobsters (Figure 5.1A-B). This circuit regulates stomach contraction and is tractable. The study of wild animals captured at sea provides relevant information for neuroscience, as these animals show considerable differences in their neural characteristics while exhibiting similar behavior. This nervous system has been studied throughout the entire career of the eminent Professor Eve Marder, who made breakthrough advances in neuroscience, especially in the areas of neuromodulation, homeostasis, motor pattern generation, and degeneracy, by studying this small circuit. These advances have been proven to hold true for much more complex nervous systems.

5.1 Anatomy

This network has been briefly discussed in terms of certain observed neuronal types, and it will be more extensively described here. The stomach of crabs contains teeth that can be activated through different muscles. The different types of neurons that control these muscles are the lateral gastric (LG), dorsal gastric (DG), medial gastric (MG), gastric mill (GM), and lateral posterior gastric (LPG) neurons. They innervate muscles responsible for moving the teeth of the gastric mill (Bucher et al., 2006). It is worth noting that the LPG neuron also innervates the pyloric muscle. The activation of the medial tooth is controlled by the GM neurons, while the activation of the lateral teeth is regulated by LG and MG neurons. Conversely, DG neurons control the return path of the medial tooth, while LPG neurons control the return path of the lateral teeth. This STNS also comprises cardiac muscles and valves. The pylorus and cardio-pyloric valves are controlled by the pyloric dilator (PD) neurons and the lateral pyloric (LP) neuron. Additionally, the pylorus can be moved by the pyloric (PY) neurons. The dorsal cardiac muscles are innervated by the anterior median (AM) neuron, while the ventral cardiac ossicles muscles are innervated by

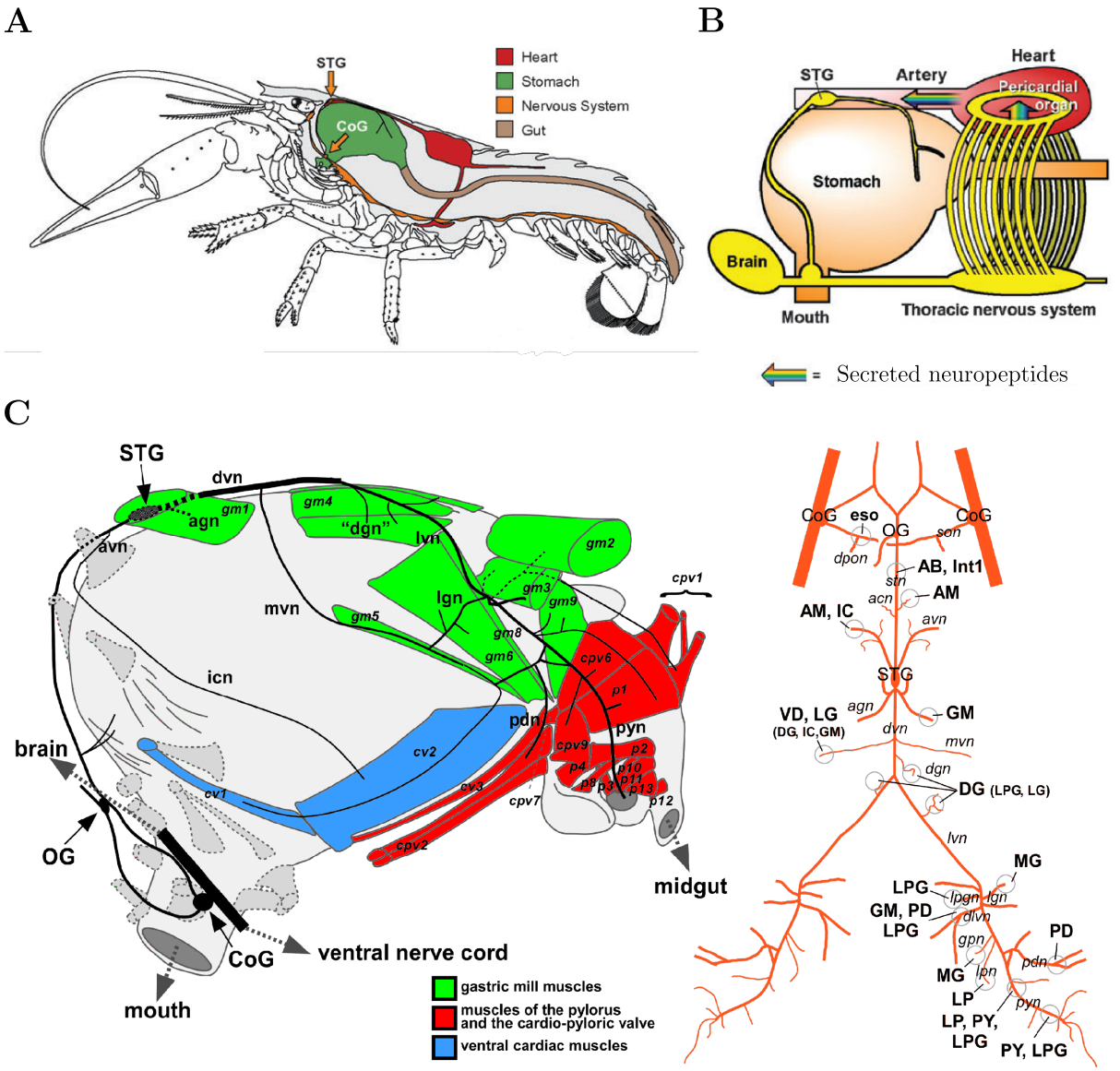

Figure 5.1: Anatomy of the STNS of crabs and lobsters. A. Side view of a lobster illustrating the anatomy of the stomach and the STNS (Stomatogastric Nervous System). CoG stands for commissural ganglion, and STG stands for stomatogastric ganglion. **B.** Neuromodulatory control of the STNS. The pericardial organ secretes neuromodulatory substances such as neuropeptides and amines. **C.** Organization of the nerves and muscles in the crab *H. americanus*. Sketch depicting muscles colored differently according to the regions of the stomach they control (left). Sketch of the STNS (right). Note that all abbreviations are not described here as they are beyond the scope of the thesis. Taken from Bucher et al. (2006); Marder and Bucher (2007).

the ventricular dilator (VD) neuron and the inferior cardiac (IC) neuron. All these neurons can be found in the stomatogastric ganglion (STG), which has nerves that extend to the muscles, providing innervation. The most significant nerve is the lateral ventricular nerve (lvn), which innervates most of the muscles mentioned above (Maynard and Dando, 1974) (Figure 5.1C).

All the neurons mentioned above have precise functions in coordinating the STNS. The morphology of neurons and the connectome of circuits (the spatial distributions of synapses, dendrites, and

axons) are crucial when studying the input-output properties of neurons (Rall et al., 1992). In Bucher et al. (2007), they characterized the morphology of every neuron belonging to the STG that plays a significant role in the two circuits of the crab STNS, creating the two crucial rhythms of that circuit—the gastric and pyloric rhythms. The main observation is that the dendritic tree can vary substantially among neuron types and even during development in large species, such as the lobster, sometimes deviating significantly from the cylindrical shape of the ganglion. Moreover, there is considerable variability in the diameter of the neuron, with variations of up to 20-fold. Thus, variability is inherent in this ganglion, both across neuron types and species.

5.2 Electrophysiology

The recording of pyloric and gastric rhythms can be achieved either through extracellular recordings of the main nerve lvn or by intracellular recordings from different types of neurons. The crab STNS contains two sub-networks that can generate two different rhythms, namely the gastric and pyloric rhythms (Weimann et al., 1991). More precisely, the pyloric rhythm is significantly faster than the gastric rhythm (Nadim et al., 1998). This implies that the STNS can be seen as a network of two coupled oscillators where the individual frequencies significantly differ from each other. The gastric mill rhythm sub-network is composed of one interneuron (Int 1), five burster neurons (GM), and six tonically firing neurons (AM, DG, LG, MG, LPG) (Selverston et al., 2009) (Figure 5.2A). The synchronization between both bursting and tonic firing subcircuits of this rhythm is orchestrated by the interneuron. On one side, it excites DG and AM cells, which, in turn, inhibit the tonic firing of GM neurons, leading them to bursting mode. On the other side, after the interneuron rapidly inhibits the LG/MG pair neurons, they undergo an increasing excitatory input, reflecting the interaction between the interneuron and the DG and AM neurons. Additionally, there exists reciprocal inhibitory connections between the LG/MG pair of neurons and the pair of LPG neurons. Thus, the interneuron has a critical synchronizing role between both subcircuits in this rhythm. Integrating everything creates a harmonically tuned rhythm with a period in the order of tens of seconds.

The main actors in the pyloric rhythms consist of bursting anterior burster (AB), VD, PY, LP, and PD neurons. More precisely, the three motor neurons LP, PY, and PD create a triphasic rhythmic pattern that can be observed all together in extracellular recordings in the lvn nerve (Hooper and Marder, 1987) (Figure 5.2B). This triphasic rhythm consists of repeating sequences of bursts one following each other from the three pyloric neurons. The resulting rhythm has a period of a bit less than a second, being at a much higher frequency than the gastric rhythm. In this rhythmic sub-network, the single AB interneuron acts as the bandleader and is pacemaking bursting mode. It dictates the rhythm for the whole network. When the AB neuron is bursting action potentials, it excites the two PD motor neurons that start firing at the same time, given the gap junctions between AB and PD neurons, represented as electrical synapses. These neurons inhibit all the other pyloric rhythm neurons, which in turn fire burst only when AB and PD neurons are silent. Moreover, the VD and LP neuron inhibit each other, forcing them to start firing bursts at different times. All in all, this produces a high-frequency bursting triphasic rhythm, where the three pyloric motor neurons start bursting at different times, with a phase difference of roughly 120°.

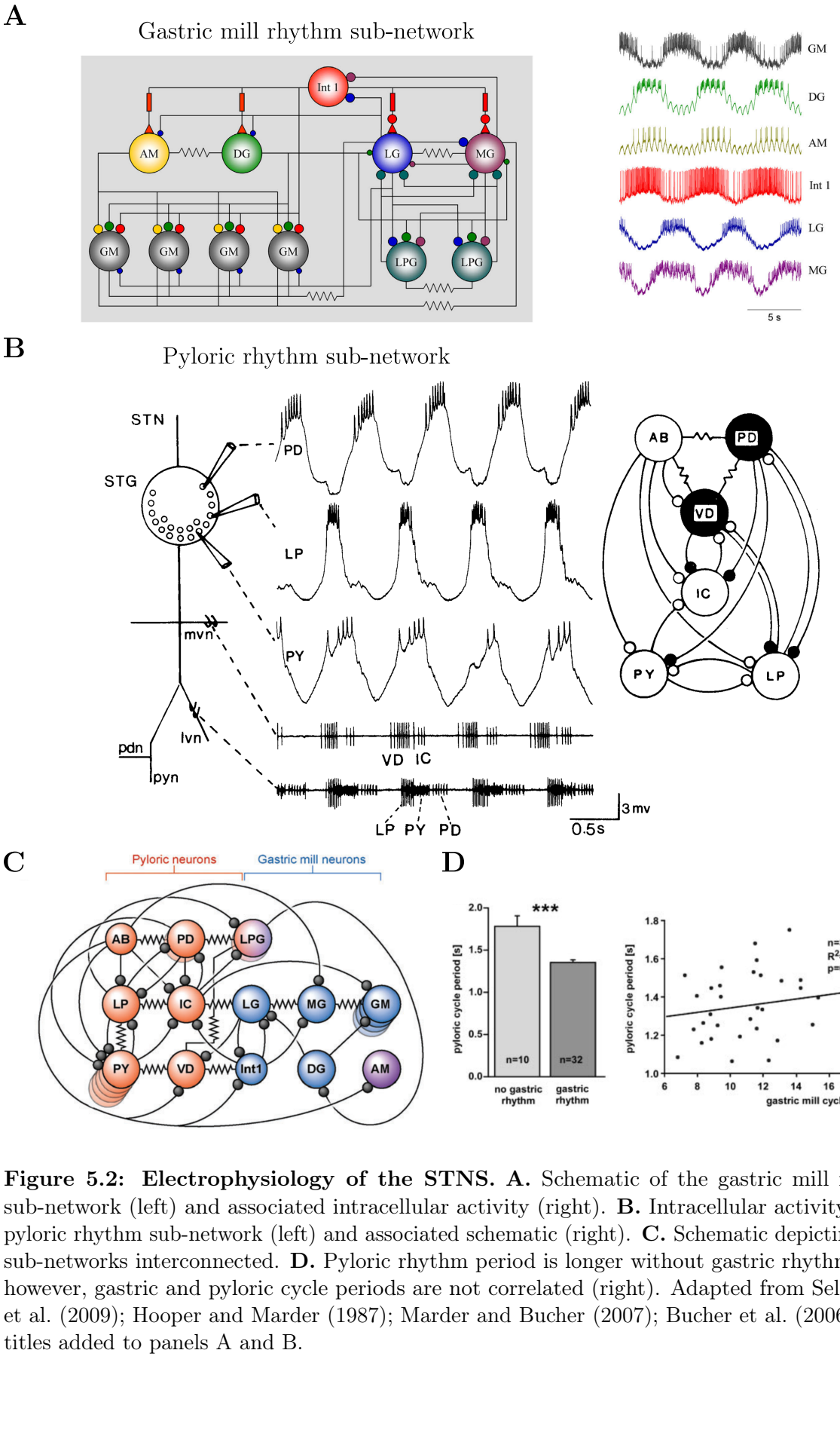

Figure 5.2: Electrophysiology of the STNS. A. Schematic of the gastric mill rhythm sub-network (left) and associated intracellular activity (right). **B.** Intracellular activity of the pyloric rhythm sub-network (left) and associated schematic (right). **C.** Schematic depicting both sub-networks interconnected. **D.** Pyloric rhythm period is longer without gastric rhythm (left); however, gastric and pyloric cycle periods are not correlated (right). Adapted from Selverston et al. (2009); Hooper and Marder (1987); Marder and Bucher (2007); Bucher et al. (2006), with titles added to panels A and B.

However, even often seen as dissociated sub-networks, both rhythms are not isolated from each other (Figure 5.2C). Indeed, there exist projections from one sub-network to another coupling these networks. However, as the frequencies of the two rhythms are very different, the interactions are complex. For instance, when the gastric mill rhythm is shut down, the frequency of the pyloric rhythm is affected, while the frequencies of both rhythms are uncorrelated across animals (Bucher et al., 2006; Hamood and Marder, 2015) (Figure 5.2D). So, studying this network allows us to better understand how neurons behave in a rhythmic circuit in biology and how such coupled oscillators with disparate frequencies can coexist in such a simple neuronal network.

5.3 The central role of neuromodulation

The gastric neuronal system of crabs is highly neuromodulated, making it a perfect candidate to study neuromodulation in a broad sense (Hamood and Marder, 2015) (Figure 5.3A). Indeed, the modulatory commissural neuron 1 is a neuron that has a neuromodulatory projection in the gastric mill rhythm sub-network that can activate it (Nadim et al., 1998). Moreover, in long-term recordings of the gastric activity in both with and without neuromodulatory input show that neuromodulation has a major role in the phase relationships between the different key players in both rhythms. Without neuromodulatory input, the gastric neuronal activity is of lower frequency, and there is a sharp decrease in the coordination between both rhythms. This leads to the conclusion that the proper functioning of this coupled oscillator neuronal network relies strongly on neuromodulatory inputs.

There exist a myriad of different neuromodulators acting in the STNS, all having a different role and actions on the rhythms (Figure 5.3B). For instance, the red pigment concentrating hormone (RPCH) has a strong impact on the functioning of the system. For instance, bath applications of RPCH increased the pyloric rhythm frequency in already self-sustained pyloric networks that exhibit an abnormally slow frequency. This suggests that this neuromodulator is crucial to maintain a proper high-frequency pyloric rhythm. Moreover, the higher the concentration, the higher the effect of this neuromodulator. In addition to this effect, RPCH is able to initiate a rhythmic pyloric pattern in abnormal circuits that were silent (Nusbaum and Marder, 1988) (Figure 5.3C). Other substances that can initiate the pyloric rhythm include dopamine, the muscarinic agonist pilocarpine, serotonin, octopamine, proctolin, and an FMRFamide-like peptide (Raper, 1979; Anderson, 1981; Marder and Paupardin-Tritsch, 1978; Marder and Eisen, 1984; Flamm and Harris-Warrick, 1986; Hooper and Marder, 1984).

Tetrodotoxin (TTX) is a neurotoxin that affects the central nervous system (Narahashi, 2001). This toxin suppresses the ability of neurons to spike by blocking sodium channels while preserving graded synaptic transmission. Studies have shown that the STNS of crabs is robust to TTX, thanks to several substances, such as dopamine, pilocarpine, and RPCH (Raper, 1979; Anderson, 1981; Hamood and Marder, 2015) (Figure 5.3D). While the spiking behavior is affected by the toxin, rhythmic non-impulse-mediated alternations still occur between key neuron antagonists in the pyloric network, thanks to the action of these substances. Although the rhythm is maintained, its frequency is much slower compared to a healthy pyloric rhythmic network.

This shows that the STNS of crabs is one of the best candidates for neuroscientists, thanks to

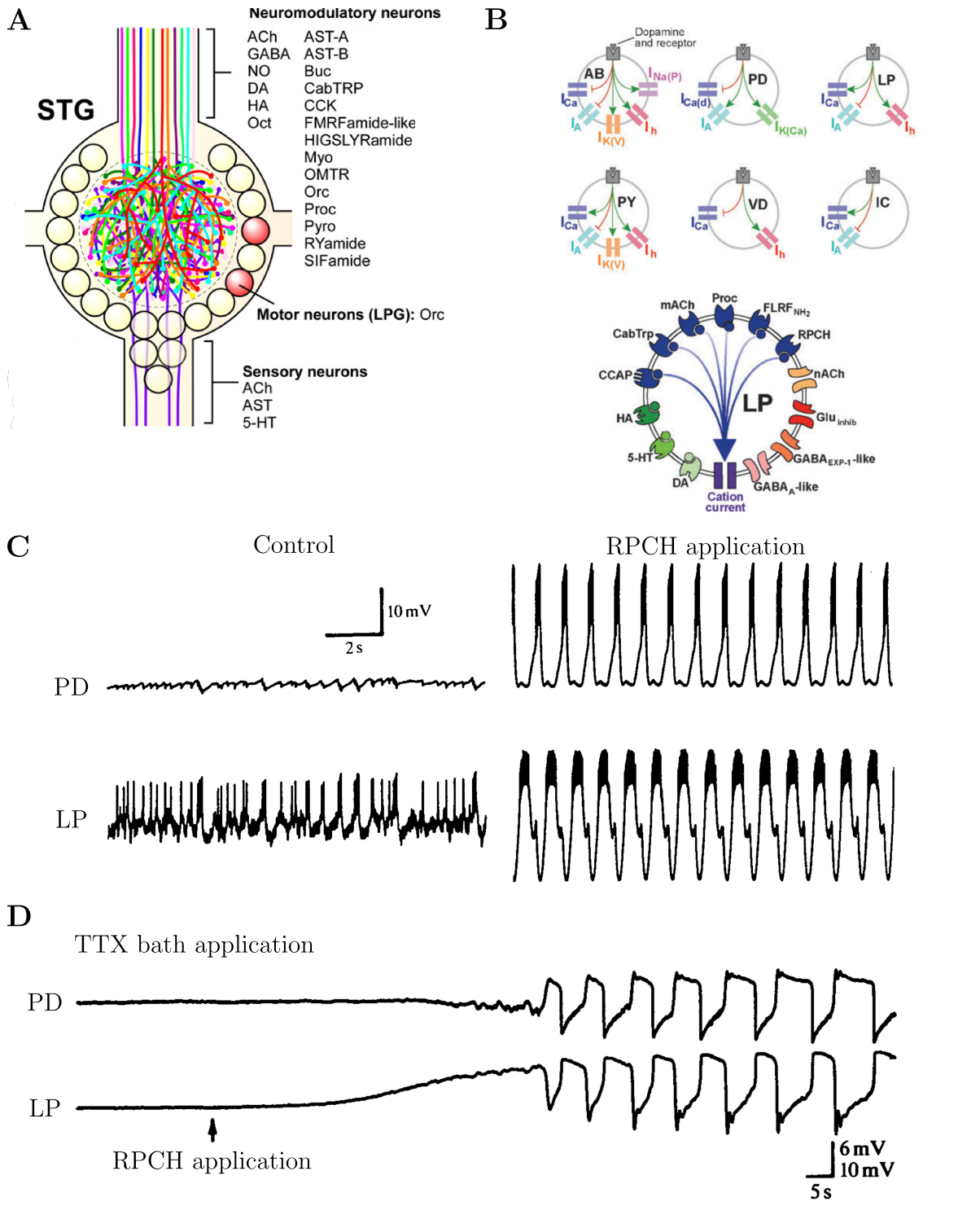

Figure 5.3: The ubiquitous role of neuromodulation in the STNS. A. More than twenty descending modulatory neurons deliver various neuromodulatory substances into the neuropil of the STG. **B.** Dopamine receptors are present in multiple neuron types of the STNS (top). However, within each cell type, dopamine modulates a different subset of ion channels, potentially in a different manner. For instance, the LP neuron has receptors for more than 10 neuromodulators, all of which may act on the same ion channel (bottom). **C.** RPCH activates the rhythm in quiescent circuits. **D.** RPCH action persists even in a TTX preparation, which typically disrupts the rhythm. Adapted from Nusbaum and Marder (1988); Marder and Bucher (2007); Marder (2012); Harris-Warrick et al. (1995b); Swensen et al. (2000); Harris-Warrick et al. (1998); Gruhn et al. (2005); Kloppenburg et al. (1999); Harris-Warrick et al. (1995a), with text added above the traces in panels C and D.

its easy accessibility and tractability. Yet much simpler than more complex neuronal networks such as the human brain, this circuit has helped throughout the years to better understand key mechanisms in neuroscience, as these are shared between simple and complex circuits. This example of the STNS will be used throughout this thesis, as many computational models have been realized on it, either from the single-neuron point of view (Liu et al., 1998) or at the whole network level (Selverston and Moulins, 2012; Marder and Bucher, 2007). Find below a summary of all the neuroscience discoveries that were made by years of study on this system (Marder and Bucher, 2007):

1. Many substances can neuromodulate neurons and circuits. Indeed, they can act on a single-cell basis or even reconfigure the whole neuronal network. Thus, the neuromodulatory targets include every single unit of the circuit and all their connections (Figure 5.3A-B).

2. Concerning the pyloric rhythm, the AB pacemaking neuron dictates the tempo of the three motor neurons. This maintaining of a constant triphasic rhythm over a given span of frequencies depends on several mechanisms.

3. Concerning the gastric mill rhythm, it is created from the circuit made by the gastric mill neurons and some external modulatory inputs. In this specific network, several connectomes can sustain similar gastric mill motor patterns across species. Moreover, within similar species, the same gastric mill rhythms can be generated through different mechanisms.

4. Some individual units within the STNS may participate in both rhythms and even switch from one pattern-generating circuit to another. Thus, studying the activity of such a neuron alone causes a loss of information concerning the identification of its role within the circuit. This phenomenon can complexify further the identification of neuronal units within more complex nervous system circuits.

5. Both modulatory inputs and direct connections from the stomatogastric ganglion can affect the motor patterns when sensory stimuli are applied. So, sensory neurons are neuromodulated as well, which is why the STNS rhythms respond to stretch.

6. The stomatogastric ganglion is formed early in crustaceans development but has a different rhythmic activity throughout the age of the animal, suggesting continuous circuit development without modifying its morphology.

7. When separated from its neuromodulatory actions for several days, the rhythmic activity eventually resumes without the help of these substances, suggesting a homeostatic mechanism that keeps the rhythmic stable under different perturbations.

8. Degeneracy is ubiquitous in such a network, where individual neurons exhibit a very different set of ion channel conductances while keeping their baseline activity. This suggests ion channel correlations that compensate for each other to always ensure proper ionic current, thus a correct firing pattern and function.

6 Summary of key concepts

Before diving into the computational introduction of this thesis, let's recap key fundamental concepts that are complex but necessary to understand clearly to avoid confounding mechanisms.

- **Neuromodulation:**
  In this thesis, neuromodulation refers to a biological cellular process in which neuromodulators bind to metabotropic receptors, often coupled to G-protein complexes. This activates potentially complex signaling cascades involving second messengers such as calcium ions. At the end of this cascade, the signaling pathway targets ion channel proteins, rapidly modifying their effective conductance, often through phosphorylation. Overall, neuromodulation is a process by which certain molecules rapidly tune a subset of ion channel conductances, resulting in changes in neuronal activity.

- **Neuromodulators:**
  In this thesis, neuromodulators are the molecules that produce a neuromodulatory effect. Note that neuropeptides, which also produce neuromodulation, are included within the definition of neuromodulators. Each neuromodulator activates different signaling cascades in different or even similar cells to affect various subsets of ion channels, leading to changes in activity. Even the same neuromodulator can activate different cascades.

- **Degeneracy:**
  In this thesis, degeneracy refers to a general concept in which several parameter combinations can lead to similar system outputs. In the case of neurons, it refers to the fact that different combinations of ion channel conductance values can lead to the same voltage activity. This has been widely observed experimentally. It differs from redundancy, which suggests the existence of an exact substitute for a given entity or mechanism.

- **Intrinsic homeostatic plasticity (or homeostasis for simplicity):**
  In this thesis, homeostasis refers to the ability of neurons to modulate their intrinsic electrical parameters, such as ion channel conductance values, to maintain firing rates and excitability in a changing environment, in response to fluctuations in network activity. It serves as a critical regulatory mechanism that helps preserve this delicate balance, ensuring the continued function of neurons in a dynamic and fluctuating environment. The model from O'Leary et al. (2014) will be used in the following.

Part II

Background in Computational Neuroscience

This chapter provides a comprehensive foundation in computational neuroscience, pivotal for a nuanced comprehension of the thesis at hand. Initially, fundamental concepts in computational neuroscience are presented, with a focus on the framework for modeling neurons. Particular emphasis is placed on conductance-based models, deemed the most physiological neuronal representations. Subsequently, the chapter extends to neurodynamics, encompassing an automated approach for dimensionality reduction of conductance-based models and the subsequent analysis of reduced models employing nonlinear system theory. Following this, an introduction to control theory is given followed by a model integrating the mechanism of homeostatic regulation is explored, with associated results. The subsequent section offers an overview of contemporary techniques in neuromodulation, underscoring a paucity of emphasis on neuromodulation within computational neuroscience. Subsequently, the chapter delves into an exhaustive discussion of dynamic input conductances, a central theme in the thesis, alongside the representation of neurons through feedback mechanisms. Finally, the chapter ends with a depiction of the three conductance-based models slated for employment within the thesis.

7 Modeling the neuronal excitability: conductance based models and networks

Modeling the electrical behavior of neurons has garnered significant interest since the seminal work of Hodgkin and Huxley in 1952 (Hodgkin and Huxley, 1952a). This modeling effort primarily involves the formulation of suitable ordinary differential equations (ODEs) or partial differential equations (PDEs) that accurately represent the dynamics of the membrane voltage, denoted as V_{m} or simply V for brevity. Prior to delving into the intricate models expounded in this thesis, it is essential to grasp the foundational principles underlying the biologically inspired modeling of neurons and the process of constructing networks composed of such models.

7.1 An electrical equivalent of the neuronal membrane

A neuron is commonly conceptualized as an electrical circuit, specifically an equivalent RC circuit. This section is dedicated to presenting a systematic approach for determining the components of such an equivalent circuit applicable to any neuron.

7.1.1 The very first conductance based model: Hodgkin and Huxley

The initial attempt to model the neuronal membrane was spearheaded by Hodgkin and Huxley in 1952 (Hodgkin and Huxley, 1952a), pioneers who also uncovered the dynamic nature of

ion permeability across the neuronal membrane. This discovery laid the groundwork for the subsequent identification of ion channels in 1955 (Hodgkin and Keynes, 1955). Their model, which comprised solely sodium and potassium channels, represented the minimal configuration required for eliciting an action potential. The modeling principles are as follows:

- The phospholipid bilayer membrane is considered quasi-impermeable to ions, and thus, it is represented as a fixed capacitance C_{m} or simply C for brevity;
- A baseline permeability of the neuronal membrane to ions exists, inducing a continuous leakage flow of ions determined by their respective electrochemical gradients. This leakage is encapsulated by fixed conductance g_{leak} producing a leakage current $I_{\mathrm{leak}} = g_{\mathrm{leak}} \cdot (V - E_{\mathrm{leak}})$ where E_{leak} is the Nernst potential of leakage ions;
- Sodium channels, crucial for action potential generation, exhibit voltage-gated behavior, with their permeability to sodium ions varying with membrane voltage. This variability is captured by a variable conductance $g_{\mathrm{Na}}(V,t)$ producing a sodium current

  $$I_{\mathrm{Na}} = g_{\mathrm{Na}} \cdot (V - E_{\mathrm{Na}})$$

  with E_{Na} the Nernst potential of sodium ions, around 50 mV (Hossain et al., 2014). When the sodium channels open (during the upstroke of the spike), their permeability to sodium ions increase and $g_{\mathrm{Na}}(V,t)$ increases as well, and vice versa.
- Similarly, potassium channels, also voltage-gated, possess a variable conductance $g_{\mathrm{Kd}}(V,t)$ producing a potassium current

  $$I_{\mathrm{Kd}} = g_{\mathrm{Kd}} \cdot (V - E_{\mathrm{K}})$$

  with E_{K} the Nernst potential of potassium ions, around -90 mV (Enyedi and Czirják, 2010). As with sodium channels, the conductance increases upon potassium channel opening during the spike downstroke and vice versa.

Note that the Nernst potential of an ion corresponds to the membrane voltage at which the net diffusion of that ion through the membrane is zero (Krishnamurthy and Chung, 2003) (Fig. 7.1A-B).

The sodium and potassium ion channel conductances had been modeled as follows

$$g_{\mathrm{Na}}(V,t) = \bar{g}_{\mathrm{Na}} \cdot m(V,t)^3 \cdot h(V,t)$$
$$g_{\mathrm{Kd}}(V,t) = \bar{g}_{\mathrm{Kd}} \cdot n(V,t)^4$$

where $\bar{g}_{\mathrm{Na}}$ and $\bar{g}_{\mathrm{Kd}}$ represent the maximum conductances of sodium and potassium ion channels, respectively (*i.e.* the values of $g_{\mathrm{Na}}(V,t)$ and $g_{\mathrm{Kd}}(V,t)$ when all the corresponding ion channels are opened). Here, m and n denote activation gating variables modeling the opening subunit of these ion channels, while h represents the inactivation gate variable of sodium channels, simulating its closing subunit. These variables, ranging from 0 (inactivated) to 1 (activated), offer a probabilistic measure of the opening and closing of the complete population of available

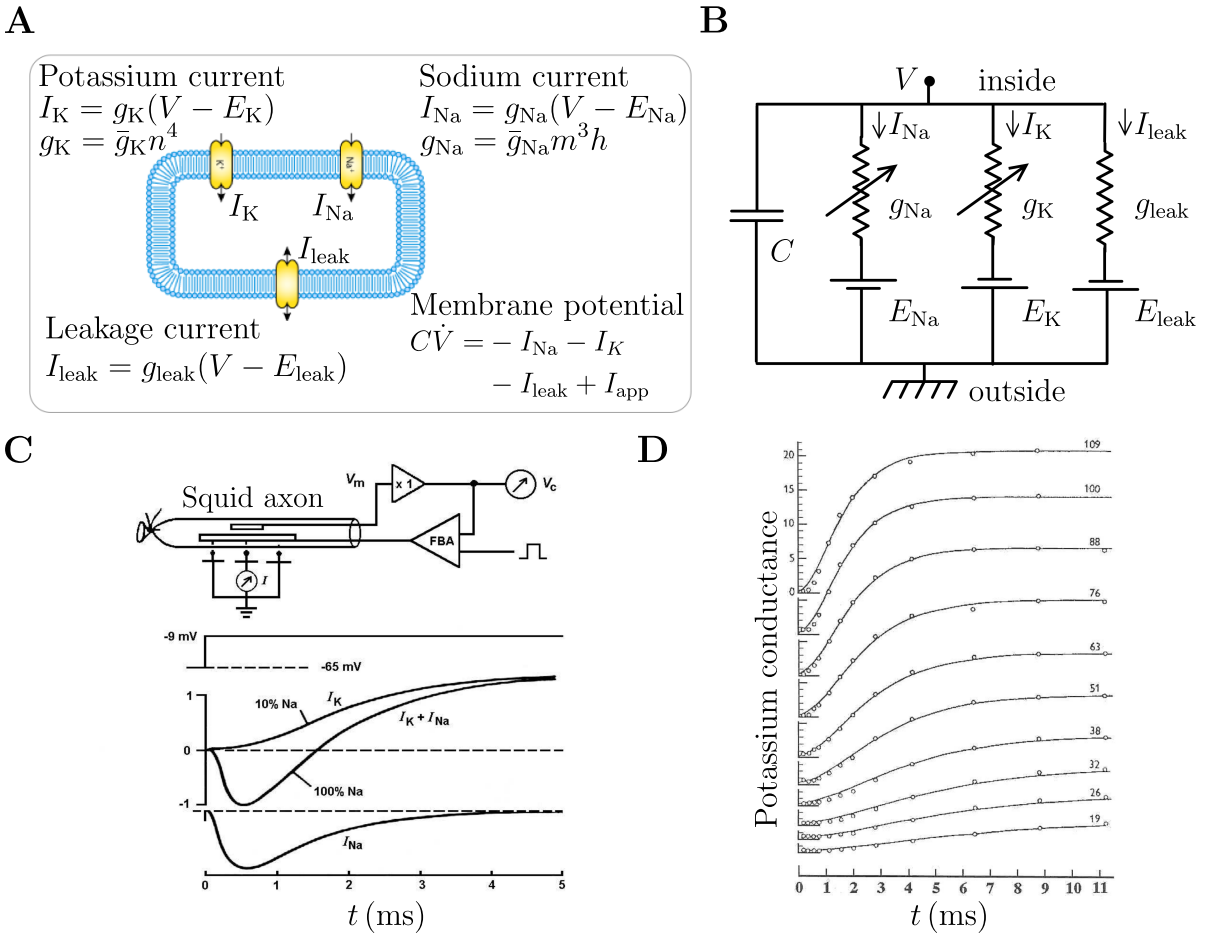

Figure 7.1: The Hodgkin and Huxley model and associated experiment. A. Biological representation of the membrane of the giant squid axon, illustrating sodium, potassium, and leakage currents. **B.** Electrical equivalent model of the giant squid axon membrane. **C.** Experimental setup for the voltage clamp experiment conducted by Hodgkin and Huxley (top). An axial wire is used to impose spatial clamp. A feedback amplifier (FBA) delivers appropriate current to maintain the membrane voltage as desired. Associated current curves for both potassium and sodium currents, along with potassium-only currents (middle). Sodium current can be reconstructed (bottom). **D.** Multiple curves depicting potassium conductance at various applied voltage steps. Adapted from Nelson and Rinzel (1995); Hunter et al. (2002), with equations added in panel A, text added in panels B and C, and axis labels added in panel D.

ion channels on the membrane. The exponents on gating variables were chosen because they best fit the dynamics of the currents. All gating variables obey first-order ODEs:

$$\dot{m} = \alpha_m(V)(1 - m) - \beta_m(V)m$$
$$\dot{h} = \alpha_h(V)(1 - h) - \beta_h(V)h$$
$$\dot{n} = \alpha_n(V)(1 - n) - \beta_n(V)n$$

where the voltage-dependent functions α_i and β_i are called the rate constants of the i-th gating

variable. Typically, they follow the form:

$$\alpha_i(V) = i_\infty(V)/\tau_i(V)$$
$$\beta_i(V) = (1 - i_\infty(V))/\tau_i(V)$$

where $i_\infty(V)$ represents the voltage dependent steady state value of the gate variable, and $\tau_i(V)$ denotes the associated voltage dependent time constant. These steady-state value functions are typically modeled as Boltzmann equations of V, resembling sigmoid functions with an image between 0 and 1. Note that the dot notation $\dot{x}$ stands for the temporal derivative $\frac{\mathrm{d}x}{\mathrm{d}t}$.

The Hodgkin and Huxley neuronal membrane model comprises 4 non-linear coupled ODEs:

$$\begin{aligned} C\dot{V} &= -\bar{g}_{\mathrm{Na}} m^3 h (V - E_{\mathrm{Na}}) - \bar{g}_{\mathrm{Kd}} n^4 (V - E_{\mathrm{K}}) - g_{\mathrm{leak}} (V - E_{\mathrm{leak}}) + I_{\mathrm{ext}} \\ \dot{m} &= \alpha_m(V)(1 - m) - \beta_m(V) m \\ \dot{h} &= \alpha_h(V)(1 - h) - \beta_h(V) h \\ \dot{n} &= \alpha_n(V)(1 - n) - \beta_n(V) n. \end{aligned}$$

The functions α_i and β_i were calibrated using experimental data from voltage-clamp experiments. In such experiments, the neuronal membrane voltage is controlled, undergoing several amplitude steps, and the resulting ionic current flowing through the membrane is measured by compensation. Distinction between sodium and potassium currents was achieved by conducting experiments in two distinct setups: one where both channels were active and another where sodium channels were pharmacologically blocked. Subtracting the current from both channels from the sodium current enabled the isolation of the potassium current (Hodgkin and Katz, 1949) (Fig. 7.1C-D).

7.1.2 Modeling any ion channel as a dynamic non linear conductance

The conceptualization of ion channels as dynamic nonlinear conductances, introduced by Hodgkin and Huxley, presents a versatile framework applicable for fitting experimental data across various types of ion channels (Skinner, 2006). Despite being over half a century old, this methodology persists in contemporary research due to its adaptability and accuracy in capturing experimental phenomena (Huxley, 2000).

Consequently, any ion channel can be modeled as a variable conductance $g_{\mathrm{ion}}(V, t)$, formulated as:

$$g_{\mathrm{ion}}(V, t) = \bar{g}_{\mathrm{ion}} \cdot m_{\mathrm{ion}}(V, t)^a \cdot h_{\mathrm{ion}}(V, t)^b, \tag{7.1}$$

where m_{ion} and h_{ion} denote the activation and inactivation gate variables of the respective ion channel, with a and b representing the associated exponents. It is noteworthy that while all ion channels possess an activation gate variable, the presence of an inactivation gate variable is not obligatory.

As previously mentioned, the dynamics of gate variables obey first-order ODEs contingent upon

membrane voltage:

$$\begin{aligned} \tau_{m,\text{ion}}(V) \cdot \dot{m}_{\text{ion}} &= m_{\text{ion},\infty}(V) - m_{\text{ion}} \\ \tau_{h,\text{ion}}(V) \cdot \dot{h}_{\text{ion}} &= h_{\text{ion},\infty}(V) - h_{\text{ion}} \end{aligned} \tag{7.2}$$

where the time constant functions $\tau_{m,\text{ion}}(V)$ and $\tau_{h,\text{ion}}(V)$, as well as the steady-state functions $m_{\text{ion},\infty}(V)$ and $h_{\text{ion},\infty}(V)$, can be parameterized using experimental voltage-clamp electrophysiology data.

This framework enables the modeling of any ion channel present in neurons across different species, relying solely on a series of voltage-clamp experiments. For instance, Wechselberger et al. (2006) developed a model for hypothalamic neurons incorporating sodium, delayed rectified potassium, hyperpolarization-activated cyclic nucleotide-gated (HCN), and A-type potassium currents. Additionally, Destexhe et al. (1998) and Liu et al. (2014) formulated models for thalamic relay neurons featuring diverse ion channels. Furthermore, Jaeger and Bower (1999) devised a model for Purkinje cells encompassing various ion channels.

An extension commonly made to the original Hodgkin and Huxley formalism involves gating variables whose steady-state function depends on another molecule necessary for ion channel activation (Abbott and Dayan, 2001). For instance, the steady-state function of the activation gate variable of calcium-dependent potassium channels (KCa) correlates with intracellular calcium concentration. This dependence arises from the fact that these channels are not solely voltage-gated but also rely on another molecule for activation.

7.1.3 Modeling any neuronal membrane as a non linear RC circuit

Once all ion channels have been characterized and parameterized, the final step in constructing a neuronal membrane model involves formulating its membrane voltage equation. Following the framework established by Hodgkin and Huxley, the neuronal membrane can be represented as a passive RC circuit in parallel with all ion channels considered in the model. This extension leads to the overarching concept of conductance-based models for neuronal membrane electrical equivalents, drawing inspiration from the Hodgkin and Huxley formalism. The voltage dynamics are governed by the following nonlinear ODE:

$$\begin{aligned} I_C &= C\dot{V} + g_{\text{leak}}(V - E_{\text{leak}}) = -I_{\text{int}} + I_{\text{ext}} \\ &= -\sum_{\text{ion}\in\mathcal{I}} g_{\text{ion}}(V,t)(V - E_{\text{ion}}) + I_{\text{ext}}, \end{aligned} \tag{7.3}$$

where C is the membrane capacitance, g_{ion} is non-negative and gated between 0 (all channels closed) and $\bar{g}_{\text{ion}}$ (all channels opened), E_{ion} and E_{leak} are the channel reversal potentials, $\mathcal{I}$ is the index set of intrinsic ionic currents, and I_{ext} is the current externally applied *in vitro* or the combination of synaptic currents (Fig. 7.2A).

Combining equations (7.1), (7.2), and (7.3) yields comprehensive conductance-based models that can be numerically solved to obtain the corresponding voltage trace. Notably, inclusion of a calcium-gated ion channel necessitates an additional ODE describing intracellular calcium

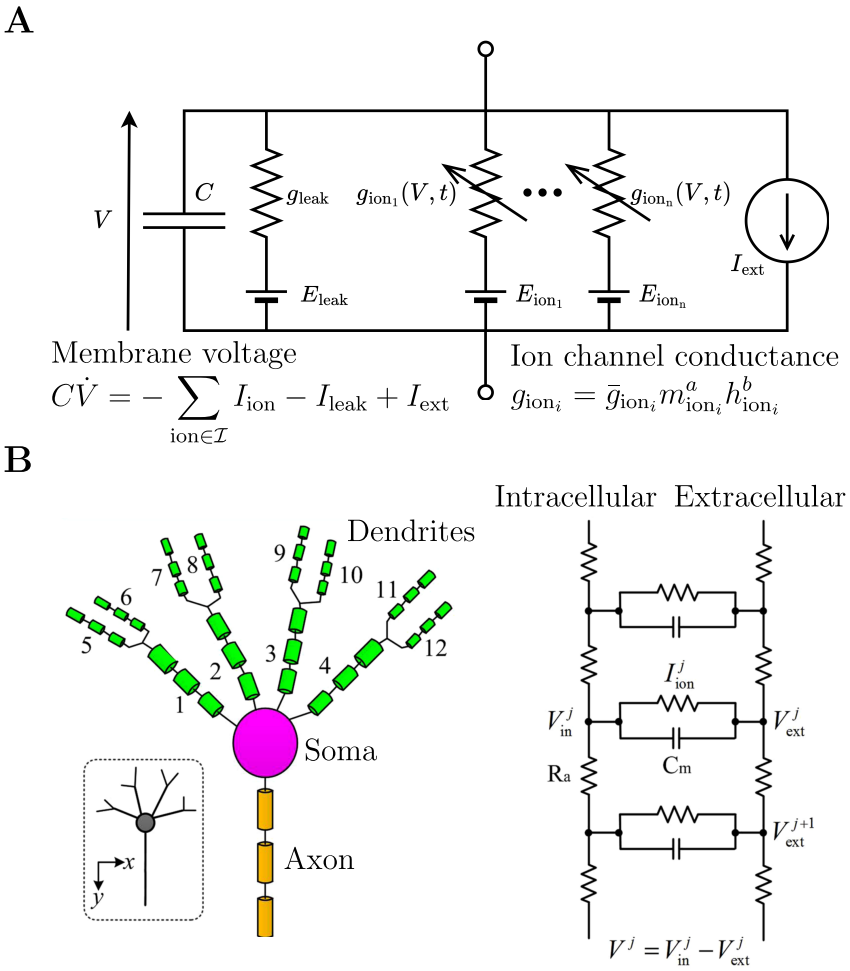

Figure 7.2: Conductance-based modeling. A. General equivalent circuit representing a membrane with n different ion channels, each modeled by a variable conductance with an associated reversal potential. **B.** Example of a multi-compartment conductance-based model that considers the morphology of the neuron. Each cylinder represents a compartment and follows the same equations as a conductance-based model. Adapted from Yi et al. (2017), with added equations and text.

dynamics, which is contingent upon the specific model.

Such conductance-based models are termed single-compartment, as neurons are depicted as a single material point in space. Advancements in modeling include the refinement to multi-compartment models, wherein neurons are divided into multiple compartments. This approach allows for the inclusion of spatial morphology, such as dendritic trees, as distinct compartments. In such models, each compartment is treated as a single-compartment model interconnected through currents obeying Ohm's law (Fig. 7.2B). For example, Zomorrodi et al. (2008) utilized a 3-compartment model for thalamocortical cells, representing the soma, proximal, and distal dendrites as separate compartments. Similarly, Halnes et al. (2011) developed a multi-compartment model of interneurons in the dorsal lateral geniculate nucleus comprising 330 compartments to depict the dendritic tree.

7.2 Conductance based models reproduce complex neuronal excitability

Conductance-based models constitute complex, highly nonlinear systems with numerous parameters, including maximal ion channel conductances. The subsequent section is dedicated to demonstrating the capability of such models to accurately replicate a diverse array of neuronal behaviors.

7.2.1 The spike firing

One characteristic of conductance-based models is their excitability, meaning they can fire spikes if the input is suprathreshold or remain inactive if the input is subthreshold. In such models, the input consists of externally applied current I_{ext}, modeling any synaptic current originating from presynaptic action potentials.

The minimal combination of ion channels necessary for excitability consists of fast sodium channels and delayed rectifier potassium channels, as in the original Hodgkin and Huxley model. At rest, with zero input, the voltage converges to the neuronal membrane resting potential, which is typically around $-60\,\text{mV}$. With positive increasing steps of external applied current, nothing happens until the input surpasses the firing threshold. Once this threshold is reached, the model begins to fire spikes periodically, and the variables of the conductance-based model enter a limit cycle attractor representing tonic firing behavior. It is noteworthy that for intermediate values of input current pulses in the subthreshold region, transient behaviors, such as firing one or several spikes, may be observed. However, these transient behaviors do not lead to sustained firing, and thus the system does not fall into a limit cycle attractor.

Looking at an individual spike, the voltage trace exhibits a sharp depolarization up to around $30\,\text{mV}$, followed by repolarization and a hyperpolarization period to a voltage lower than the baseline voltage. The spike produced by the original Hodgkin and Huxley model closely resembles a biological spike, showcasing the explanatory power of such a model. Similar to biology, this model exhibits absolute and relative refractory periods. Examining the activation gating variables, their steady-state values (at the resting potential) are relatively low, around 0.05 for m and 0.3 for n. The steady-state value of the sodium inactivation variable h is relatively high, around 0.6. This indicates that, at the resting potential, there is only a small amount of sodium and potassium current through the membrane. At the onset of the spike, the sodium activation gating variable m dramatically increases close to its maximum value of 1, opening the sodium channels and leading to an inward sodium current, causing the depolarization phase of the spike. Upon reaching the peak voltage, the sodium inactivation variable h decreases close to 0, closing the sodium channels and halting the increase in voltage. Simultaneously, the potassium activation gating variable n increases up to 0.8, opening the potassium channels and leading to an outward potassium current, which repolarizes the membrane. After the spike, all gating variables return to their steady-state values, primed to fire another spike. Overall, the Hodgkin and Huxley model mimics the biological process of an action potential using the sodium and potassium gating variables (Fig. 7.3).

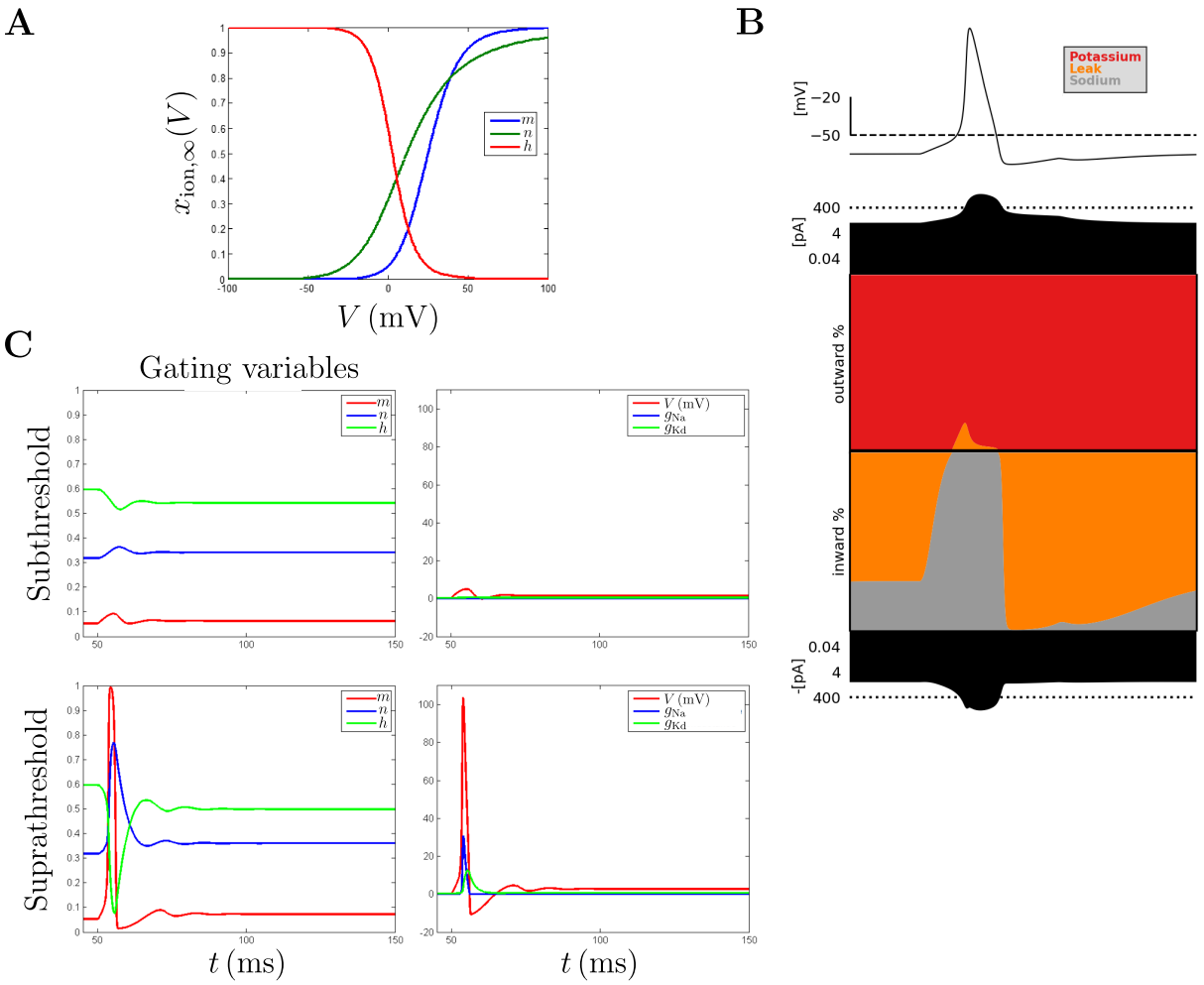

Figure 7.3: Action potential with Hodgkin and Huxley model. **A.** Steady-state functions of the three gating variables in the original Hodgkin and Huxley model. **B.** Current separation in an action potential generated by the Hodgkin and Huxley model. During the upstroke of the spike, there is a significant inward sodium current, both in relative and absolute value, whereas during the downstroke, sodium current decreases and potassium current increases in absolute value. **C.** Time evolution of gating variables (left) and voltage, along with sodium and potassium conductances (right), for subthreshold (top) and suprathreshold input (bottom) scenarios. Taken from Johnson and Chartier (2017); Jaquier et al. (2023).

It is evident that two different timescales exist in the generation of an action potential. The fast timescale involves activating the sodium channel variable m, while the slower timescale (referred to as the slow timescale) involves inactivating the sodium channels, variable h, and activating the potassium channels, variable n.

7.2.2 Reproducing key current frequency curves

The most commonly used method for classifying different neurons lies in their current-frequency (I-f) curve. Such a curve indicates the firing frequency of the neuron as a function of the constant externally applied current. As a reminder, type I neurons have a continuous I-f curve, indicating they are capable of firing at arbitrarily low frequencies. However, type II neurons have a discontinuous I-f curve, suggesting they have a minimum firing frequency. In addition

to these classical types of neurons, type II* neurons share the exact same I-f curve as type II neurons but exhibit a specific latency before the first spike. Type III neurons only fire a single spike at the beginning of the external stimulus, as a transient behavior. Hence, such neurons do not have a defined I-f curve. The original Hodgkin and Huxley model exhibits type II behavior. In other words, once the current threshold is reached, a minimum firing frequency around 50 Hz is observed. Beyond this threshold, the firing frequency increases slowly.

As observed in biology, changing the composition of ion channel types included in conductance-based models among the available variety of ion channels, as well as changing their concentration on the membrane by altering the maximum ion channel conductance $\bar{g}_{\text{ion}}$ associated, can drastically alter the behavior of the model. For instance, in Gerstner et al. (2014), the authors tuned the original sodium channel to shift its inactivation gating variable steady-state function ($h_\infty(V)$) to depolarized voltages by 20 mV compared to the original Hodgkin and Huxley model. By doing so, the authors drastically changed the nature of the sodium channel that had originally been modeled by Hodgkin and Huxley. In biology, more than 10 different types of sodium channels have been observed, in which the steady-state functions of the gating variables are slightly modified. This slight modification has a drastic effect on the model behavior, as it exhibits type I excitability. Hence, tuning the ion channel composition of the membrane in turn affects its dynamical behavior. The modified model has a continuous I-f curve, with the firing frequency increasing as the current amplitude increases beyond the threshold.

In another study (Drion et al., 2015c), the authors used an adapted Hodgkin and Huxley model, called the Connor-Stevens model (Connor et al., 1977), which is also composed of a sodium and delayed rectifier potassium channel but with an extra current: a voltage-gated potassium channel with activation and inactivation gating variables, whose timescales are slightly slower than the inactivation of sodium channels. This channel has been recognized to play an essential role in excitable cells, controlling spike timing, regulating long-term potentiation, and having a crucial role in repolarizing the cardiac action potential (Johnston, 2021). The A-type potassium current is of the form $I_{\text{A}} = \bar{g}_{\text{A}} m_{\text{A}}^3 h_{\text{A}} (V - E_{\text{K}})$ (outward). With a maximum ion channel conductance of A-type potassium channels set to zero, the Connor-Stevens model behaves similarly to the original Hodgkin and Huxley model and exhibits type II excitability. However, as the conductance $\bar{g}_{\text{A}}$ increases, the jump in the I-f curve decreases, and at some threshold value of $\bar{g}_{\text{A}}$, the model starts exhibiting type I excitability. This excitability type is observable for a range of values of $\bar{g}_{\text{A}}$. However, beyond a second threshold, the model starts exhibiting type II* excitability, with an I-f curve resembling type II but with increasing frequency jumps as $\bar{g}_{\text{A}}$ increases. Note that the applied current threshold is displaced to the right as the A-type potassium conductance increases (Fig. 7.4A).

In the same paper, the authors showed a similar behavior with another type of ion channel: the L-type calcium channels, whose current is modeled as $I_{\text{CaL}} = \bar{g}_{\text{CaL}} m_{\text{CaL}}^2 (V - E_{\text{Ca}})$ (inward). However, the transitions are observed when decreasing $\bar{g}_{\text{CaL}}$, instead of increasing it. This highlights the fact that neuronal behavior can be drastically changed by tuning the conductances of its ion channels, which is captured by conductance-based modeling. Note that type II* models also exhibit bistability. This means that for the same value of applied current, two different

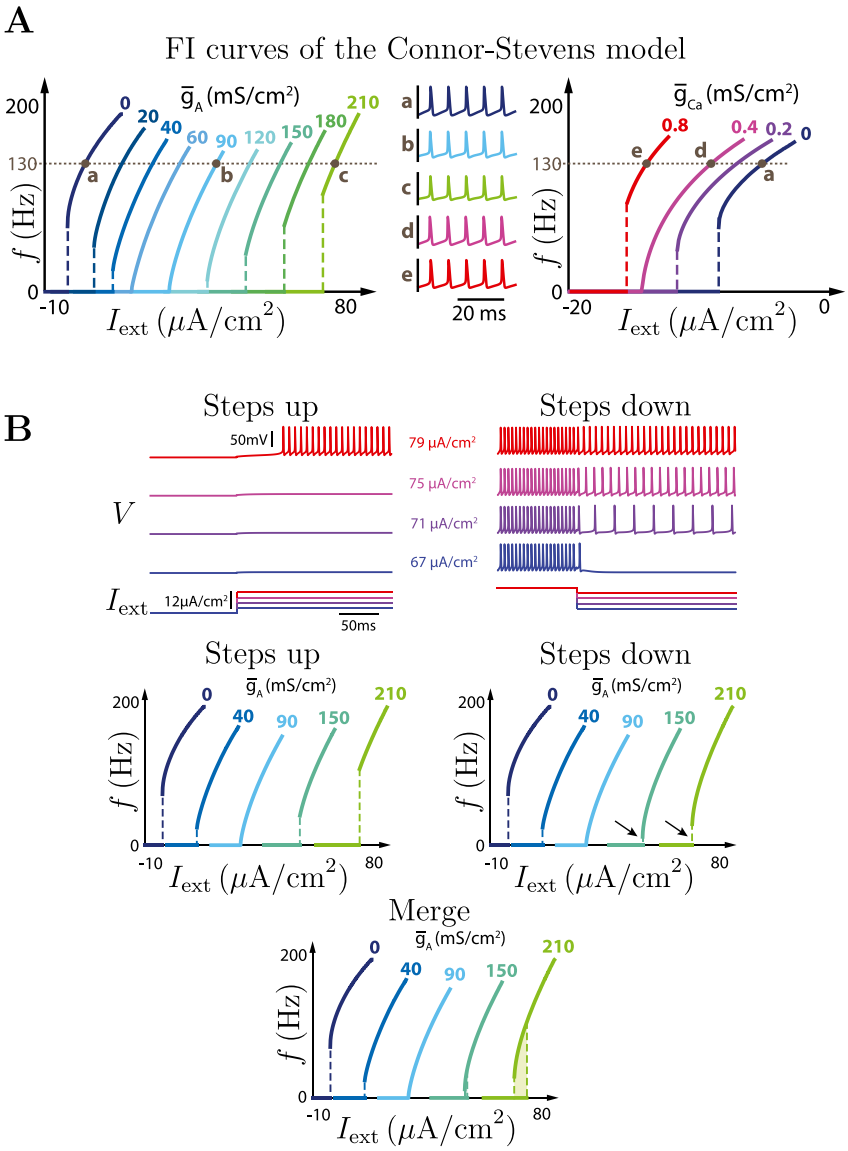

Figure 7.4: Conductance-based models reproduce key I-f curves. A. The Connor-Stevens model can manifest as type I, II, or II* depending on the conductance of A-type potassium or calcium channels. **B.** Bistability is a key characteristic of type II* neurons. By applying upward or downward steps of current to the same baseline value, distinct behaviors (silent or tonic firing) can be observed, indicative of bistability. Adapted from Drion et al. (2015c), with titles added above each plot and axis labels replaced.

behaviors can be observed (either silence or tonic firing). This difference is highlighted if the current step is up (from 0 to its studied value) or down (from a high value to its studied value). This is evidence of hysteresis in neurons (Fig. 7.4B).

7.2.3 Different types of bursting

Bursting is a critical neuronal behavior crucial for the proper functioning of many behaviors, particularly for motor pattern generation and synchronization (Selverston, 1976; Gray and McCormick, 1996). Bursting represents a dynamic state in which a neuron repeatedly fires groups of spikes, with each burst followed by a resting phase before the next burst (Izhikevich,

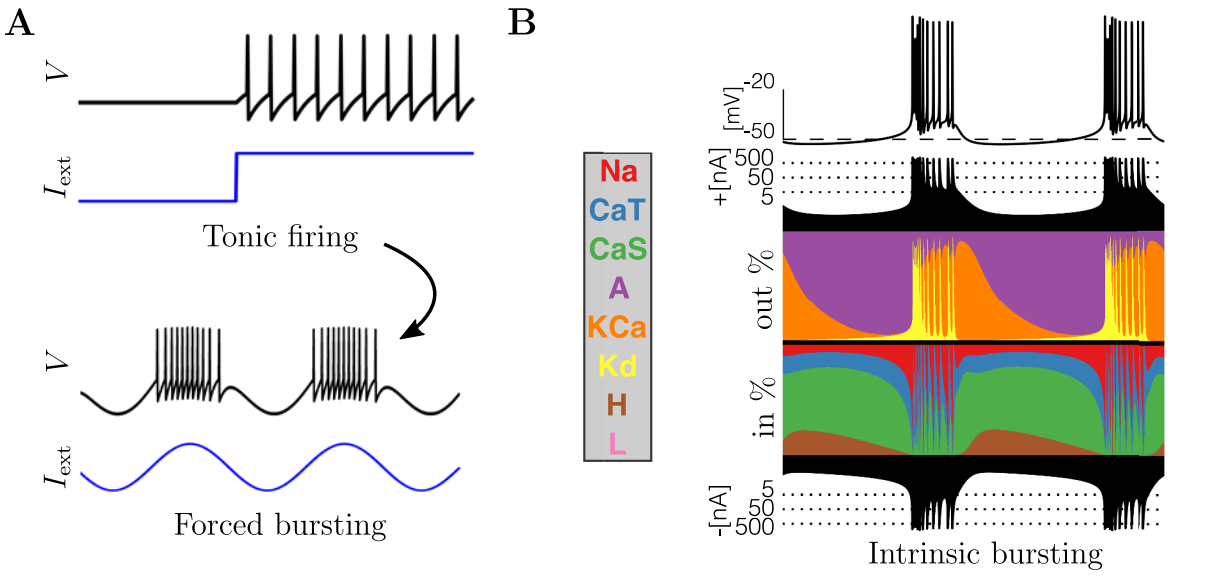

Figure 7.5: Bursting with conductance-based models. A. Forced bursting is characterized by a model displaying tonic firing subjected to oscillations in input current, leading to bursts. **B.** Intrinsic bursting occurs in the absence of input current and necessitates specific combinations of ion channels. In this scenario, the KCa current governs the initiation (when sufficiently low) and termination (when sufficiently large) of the burst. Adapted from Gangopadhyay et al. (2018); Alonso and Marder (2019), with text added below each panel.

2006). Bursting phenomena can be observed artificially even in the Hodgkin and Huxley model. By applying periodic oscillatory slow waves of current that alternately bring the neurons into subthreshold and suprathreshold regimes, one can observe packets of spikes (suprathreshold behavior) followed by periods of silence (subthreshold behavior), a technique termed forced bursting (Fig. 7.5A).

However, through an appropriate combination of ion channel types and ion channel conductances, conductance-based models are capable of autonomously reproducing most of the behaviors observed in biology, including persistent bursting (parabolic, elliptic, square wave, and pseudo-plateau), chattering, rebound bursting, etc. This phenomenon is referred to as intrinsic bursting, as no external intervention is required to induce burst mode. While a single spike generation requires only two different timescales (one for the upstroke and one for the downstroke of the spike), bursting involves a third timescale, the ultraslow timescale. This ultraslow timescale is modeled as a very slow current that accumulates during bursts. The higher this current, the more hyperpolarized the cell becomes. Eventually, when the hyperpolarization reaches a certain threshold, the spike train terminates. Subsequently, during the quiescent period, this ultraslow current slowly decreases, and once it crosses a threshold, the neuron starts to fire spikes again, initiating another burst. For instance, in an STG neuron model, this ultraslow outward current is typically a small conductance calcium-activated potassium current (SKCa) that increases during bursts, terminating them, and decreases during the quiescent period, thus facilitating the initiation of another burst (Fig. 7.5B). The generation of bursting activity, therefore, requires the integration of calcium dynamics over an ultraslow timescale, likely due to the low sensitivity of SKCa channels (Yamada et al., 1989).

7.2.4 Degeneracy

In the realm of conductance-based models, akin to biological neurons, there exists a phenomenon known as degeneracy, particularly prominent when multiple similar ion channels are involved, both in their inward/outward behavior and in their timescales. As a refresher, degeneracy refers to a property in which multiple distinct solutions exist for the same problem. In this context, it means that different combinations of conductance values within the same model can produce similar voltage activity. These distinct combinations remain indistinguishable when observing unperturbed voltage activity but can be revealed through appropriate perturbations (Alonso and Marder, 2019, 2020; Goaillard and Marder, 2021). Degeneracy should not be confused with redundancy, which implies the presence of an identical copy of the same entity or mechanism (Edelman and Gally, 2001).

Essentially, within the hyperspace of conductance-based model parameters (specifically, the space of maximum ion channel conductances), numerous clusters exist wherein the behavior is consistent, yet remarkably diverse from one another (O'Leary, 2018). This implies that while altering parameters in one direction within this hyperspace might leave the behavior unchanged, changing parameters in another direction could profoundly alter the electrical behavior of the model. In simpler terms, any modification in the maximum ion channel conductances may either drastically alter the voltage trace or leave it unaffected. Due to the high dimensionality and non-linearity inherent in conductance-based models, it remains impossible as of now to predict which direction will result in unchanged behavior (degeneracy) and which will modify the neuron behavior (akin to neuromodulation). The sole method to discern this is through model simulation and observation of the voltage trace.

A compelling illustration of such degeneracy in conductance-based modeling lies in examining the A-type potassium and L-type calcium channels described earlier in the Connor-Stevens model (Drion et al., 2015c). Through exhaustive exploration of the space of maximum ion channel conductances of A-type potassium and L-type calcium currents and by correlating the threshold current at which the neuron begins firing with its corresponding minimum observable frequency at that current, the authors underscore the degeneracy within that model. Indeed, focusing on either property (the current threshold or the minimal firing frequency) reveals a subset of the 2D parameter space where the properties remain unchanged. For instance, there are descending lines in the 2D parameter space where the minimal firing frequency remains constant. However, the configuration of the subspace for each property markedly differs from the other, significantly complicating the analysis. Essentially, maintaining one property constant necessitates a change in the other (Fig. 7.6A).

Another instance pertains to the LP neuron modeled using a multi-compartmental approach. In this model, comprising four compartments—three for the primary, secondary, and tertiary neurites, and one for the axon (Taylor et al., 2009)—substantial variability in the maximum ion channel conductances can yield identical behavior across all compartments (Zang and Marder, 2023). Remarkably, the behavior of both the primary neurite and the axon remains consistent across models that span a broad range in the parameter space of the model. The utilization of multi-compartmental models in assessing degeneracy further complicates the scenario (Fig. 7.6B

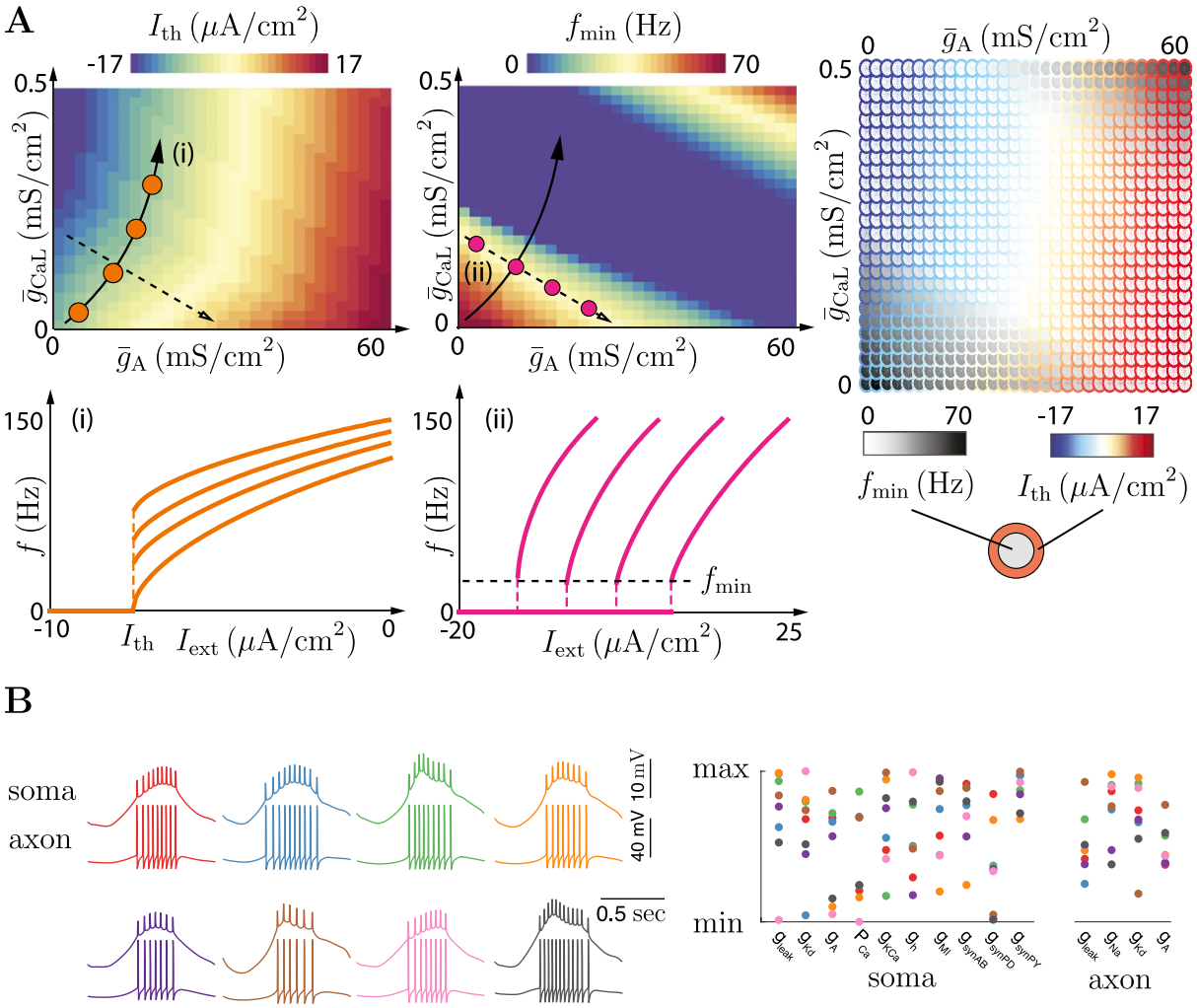

Figure 7.6: Degeneracy within conductance-based models. A. Degeneracy is evident in the Connor-Stevens model across two distinct external properties: the threshold current and the minimum frequency in tonic spiking. **B.** Degeneracy is likewise observed in a multi-compartment model of an LP neuron, occurring in both the soma and the axon. Adapted from Drion et al. (2015c); Zang and Marder (2023), with axis labels replaced and some text added to the left of panel B.

right). It is worth noting that this degenerate bursting mode of the LP neuron is implicated in the pyloric rhythm described earlier (Fig. 7.6B left).

7.3 Small neuronal networks can be modeled by interconnecting conductance based models

Another notable strength of conductance-based modeling is its ease in extending the formalism of Hodgkin and Huxley for modeling ion channels to include synaptic connections between neurons. These connections can be modeled straightforwardly and can either be inhibitory or excitatory. Additionally, conductance-based models readily accommodate the modeling of gap junctions.

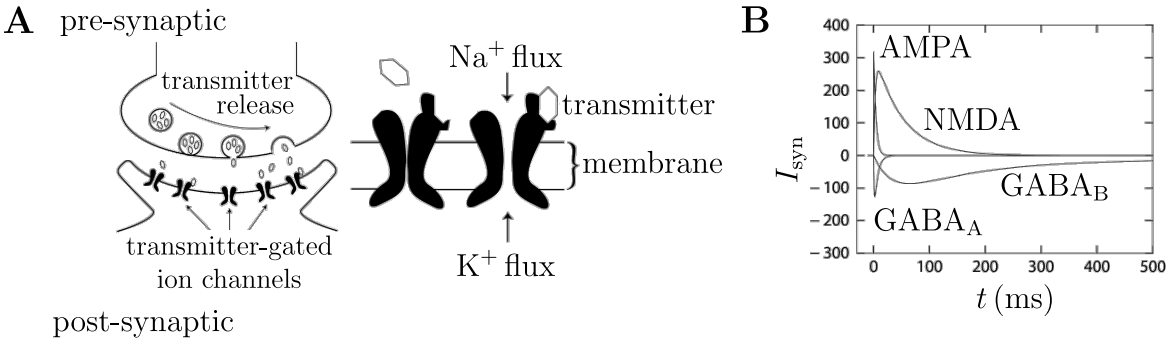

Figure 7.7: Synaptic connection in conductance-based modeling. A. Biological process through which an action potential is transmitted from a presynaptic neuron to a postsynaptic neuron using a chemical agent: neurotransmitters. **B.** Various currents produced by specific synaptic receptors. Negative currents correspond to inhibitory synapses, while positive ones correspond to excitatory synapses. Adapted from Gerstner et al. (2014), with additional text.

7.3.1 The synaptic connection / gap junction modeling

To model synaptic connections, let us designate the presynaptic conductance-based model voltage with the subscript "pre" and the postsynaptic one with the subscript "post". To integrate a synaptic connection, the postsynaptic conductance-based model voltage equation (7.3) is adjusted to incorporate a synaptic current (Gerstner et al., 2014):

$$C\dot{V}_{\text{post}} + g_{\text{leak}}(V_{\text{post}} - E_{\text{leak}}) = -\sum_{\text{ion}\in\mathcal{I}} g_{\text{ion}}(V_{\text{post}}, t)(V_{\text{post}} - E_{\text{ion}}) - I_{\text{syn}}(V_{\text{pre}}, V_{\text{post}}, t) + I_{\text{ext}}. \quad (7.4)$$

The synaptic current typically follows the form found in the Hodgkin and Huxley formalism (Richardson, 2004; Schutter, 2010):

$$I_{\text{syn}}(V_{\text{pre}}, V_{\text{post}}, t) = g_{\text{syn}}(V_{\text{pre}}, t)(V_{\text{post}} - E_{\text{syn}}), \quad (7.5)$$

where $g_{\text{syn}}(V_{\text{pre}}, t)$ represents a variable conductance modeling the synaptic ion channels following the Hodgkin and Huxley formalism, typically with a single activation gating variable (notably dependent on the presynaptic membrane voltage, *i.e.*, presynaptic action potentials), and E_{syn} denotes the Nernst potential of the synapse. It is worth mentioning that in this thesis, the maximum synaptic ion channel conductance $\bar{g}_{\text{syn}}$ will remain constant. Various models aim to modulate this parameter over time to simulate synaptic plasticity, the mechanism by which neurons alter their synaptic connections, crucial in learning processes (Morrison et al., 2008; Citri and Malenka, 2008; Feldman, 2012; Shouval, 2007; Sjöström et al., 2010; Manninen et al., 2010; Fusi and Abbott, 2007; Magee and Grienberger, 2020).

The shape of the synaptic gating variable steady-state function and time constant function can be used to describe different types of synaptic connections and associated ion channels. The parameter E_{syn} can be adjusted to differentiate between inhibitory or excitatory synapses. For inhibitory synapses, $E_{\text{syn}} \approx -75\,\text{mV}$, while for excitatory synapses, $E_{\text{syn}} \approx 0\,\text{mV}$. By doing so, a presynaptic action potential leads to postsynaptic hyperpolarization in inhibitory connections and vice versa (Destexhe and Marder, 2004). Typical inhibitory synapses utilize the neurotransmitter

γ-aminobutyric acid (GABA), prevalent in inhibitory connections in the CNS (Markram et al., 2004). The postsynaptic dendrites may exhibit various receptor types ($GABA_A$, $GABA_B$, etc.) (Fig. 7.7A-B). Excitatory synapses, on the other hand, typically involve the neurotransmitter glutamate. The postsynaptic dendrites may feature different receptor forms, such as N-methyl-D-aspartate (NMDA) or α-amino-3-hydroxy-5-methyl-4-isoxazolepropionic acid (AMPA) receptors, which are also widespread in the CNS (Hille and Catterall, 2012) (Fig. 7.7A-B).

Another type of connection modeled within the conductance-based framework is the gap junction. These junctions consist of intercellular channels facilitating direct ion and small molecule transfer between cells. Initially described as low-resistance ion channels connecting excitable cells (Goodenough and Paul, 2009), gap junctions are modeled as electrical connections (with fixed conductance) between the two neurons of interest. For two conductance-based models connected through a gap junction, their voltage equations (7.3) are modified as follows:

$$\begin{aligned} C\dot{V}_{\text{pre}} + g_{\text{leak}}(V_{\text{pre}} - E_{\text{leak}}) &= -\sum_{\text{ion}\in\mathcal{I}} g_{\text{ion}}(V_{\text{pre}}, t)(V_{\text{pre}} - E_{\text{ion}}) - \bar{g}_{\text{El}}(V_{\text{pre}} - V_{\text{post}}) + I_{\text{ext}} \\ C\dot{V}_{\text{post}} + g_{\text{leak}}(V_{\text{post}} - E_{\text{leak}}) &= -\sum_{\text{ion}\in\mathcal{I}} g_{\text{ion}}(V_{\text{post}}, t)(V_{\text{post}} - E_{\text{ion}}) - \bar{g}_{\text{El}}(V_{\text{post}} - V_{\text{pre}}) + I_{\text{ext}}, \end{aligned} \tag{7.6}$$

where $\bar{g}_{\text{El}}$ represents the value of the electrical conductance of the gap junction.

7.3.2 A basic example: half center oscillators

Half-center oscillators serve as fundamental components in central pattern generators for controlling locomotion. These oscillators comprise two bursting conductance-based models interconnected in a mutual inhibition loop. Central pattern generators are essential for generating rhythmic motor patterns for muscle contraction in animals (Doloc-Mihu and Calabrese, 2011; Calabrese, 1995). Having bursting neurons in rhythmic motor circuits is crucial, as a single spike typically does not suffice to trigger muscle contraction, whereas a burst effectively activates muscle contraction. Such circuits exhibit high reliability against noise and disturbances because, as long as the neurons are bursting, they remain in phase opposition; when one neuron fires a burst, the other is silent, and vice versa. For example, two heart interneuron (HN) models, integral to the heartbeat central pattern generator, can be interconnected in such a mutual inhibitory loop (Cymbalyuk and Calabrese, 2000). These inhibitory connections can be modeled by GABA receptors.

The robustness of half-center oscillators greatly hinges on how the two bursting neurons demonstrate post-inhibitory induced bursting (also known as post-inhibitory rebound, PIR), wherein the cessation of inhibition from one neuron triggers a burst in the previously inhibited neuron. In Dethier et al. (2015), the authors demonstrate that PIR induced by a hyperpolarization-activated cation H-type current is much less robust than PIR induced by a T-type calcium current (Fig. 7.8A-B). Under control conditions (with identical ion channel conductances and synaptic connection conductances), both mechanisms generate anti-phase oscillations. However, with variations in synaptic conductances (up to 40%) and cellular conductances (up to 20%) corresponding to biologically encountered degeneracy, oscillations are lost in the PIR induced by

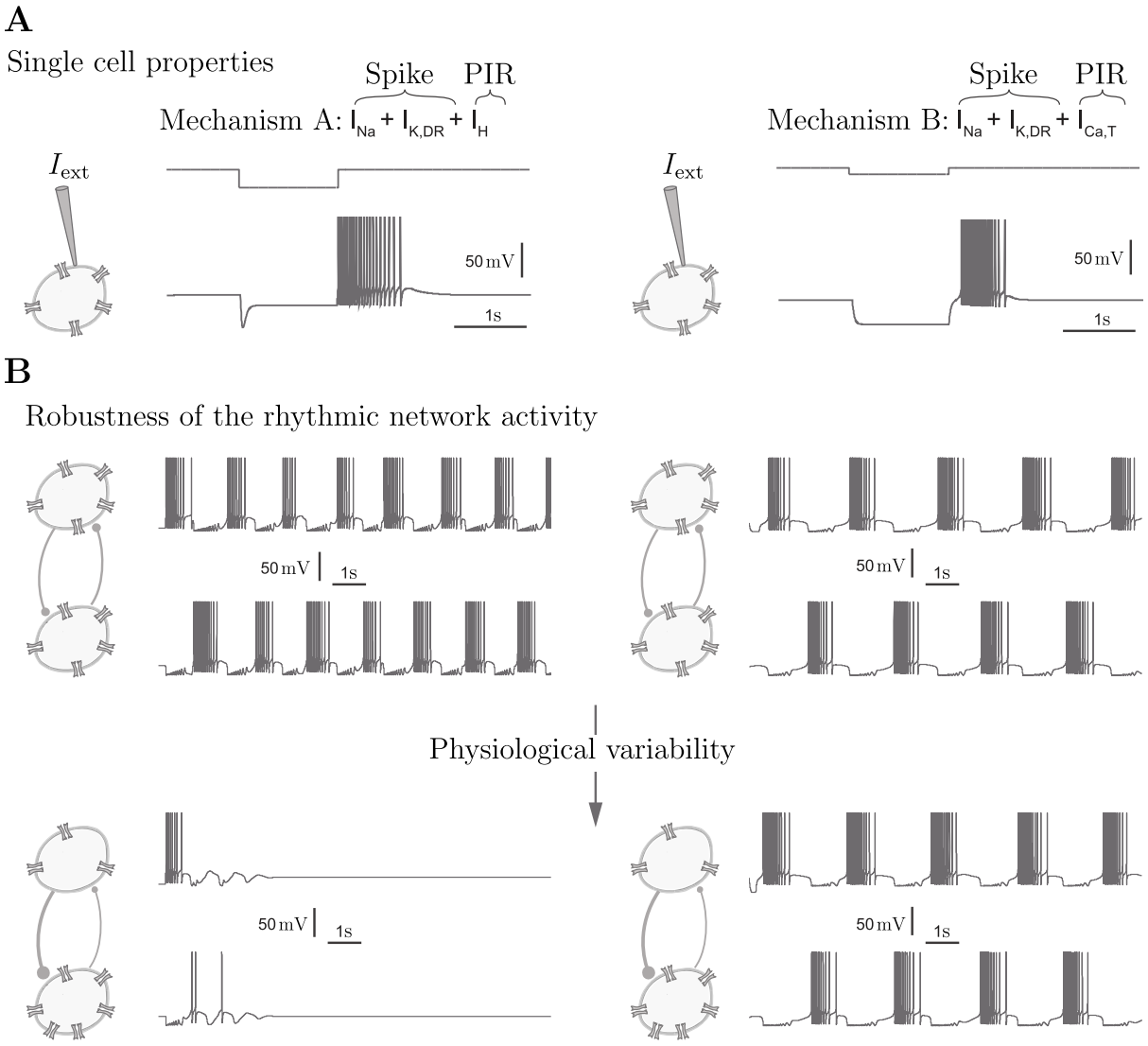

Figure 7.8: Half-center oscillators robustness depends on cellular properties. A. Various post-inhibitory rebound (PIR) mechanisms involving H or T-type calcium currents. **B.** PIR induced by H current is less resilient to physiological variability (degeneracy) compared to that produced by T-type calcium current, resulting in a more robust rhythmic activity in the latter. Adapted from Dethier et al. (2015), with titles above the traces replaced.

H currents, whereas they are sustained in the PIR induced by T-type calcium currents. This disparity primarily arises because T-type calcium channels exhibit a regenerative component, meaning that a portion of the step voltage response increasingly becomes inward (Conradi Smith, 2019). In contrast, H-type current only exhibits a decreasingly inward current component. This robustness is evident through exhaustive searches in synaptic parameters (maximum conductance and associated time constant). The PIR induced by T-type calcium current demonstrates a significantly larger zone where oscillations can be observed, with a low standard deviation in frequency when cellular conductances are modified.

8 Reduced models phase plane analysis: neurodynamics

Conductance-based models represent a cornerstone of modern computational cellular neuroscience, capable of reproducing a wide array of neuronal dynamical behaviors. They have significantly contributed to our understanding of the brain intricate workings. However, their high dimensionality and nonlinearity render them intractable. This means that predicting the electrical behavior solely from the set of ion channels and associated conductances, i.e., the model parameters, is not feasible. The theories and tools commonly employed to study nonlinear systems, such as phase plane analysis, are typically limited to two or, at most, three variables.

To establish a theoretical framework for such models, numerous researchers have endeavored to reduce their dimensionality, a pursuit initiated by the seminal work of Kepler et al. (1992). For a more comprehensive understanding beyond the scope covered in this thesis, readers are encouraged to explore the work of Izhikevich (2007).

8.1 Reducing conductance based models

The technique employed to reduce the dimensionality of conductance-based models follows a systematic procedure:

1. **Identify Timescales:** Begin by examining the complete conductance-based model and scrutinizing the time constant functions ($\tau_{\text{x,ion}}$) of all gating variables. Group gating variables with similar fast timescales together as fast gating variables. Repeat this process for slower timescales, potentially categorizing a third timescale if bursting behavior is pertinent. For example, in the original Hodgkin and Huxley model, the activation of sodium channels (m) is fast, while the inactivation of sodium channels and the activation of potassium channels (h and n respectively) are slow (Fig. 8.1);

2. **Instantaneous Fast Variables:** Fast gating variables can be made instantaneous, removing their dynamics from the model. Essentially, set the fast gating variable $x = x_\infty(V)$. By doing so, the dimensionality is reduced by the number of gating variables categorized as fast. In the Hodgkin and Huxley model, the activation of sodium channels (m) can be simplified as $m = m_\infty(V)$;

3. **Approximate Slow Variables:** For gating variables categorized as slow, retain one variable with its dynamical equation. Eliminate other slow gating variables using one of two main techniques:

    - Express other gating variables as a linear relationship with the retained slow gating variable by comparing the function $x_\infty(V)$ and finding the best linear fit. For the original Hodgkin and Huxley model, the activation of potassium channels is often kept as such, and the inactivation of sodium channel can be approximated as follows $h = 0.89 - 1.1n$ without losing a lot of information (Drion et al., 2012) (Fig. 8.1). However, as soon as the number of slow variables increase, this technique might be

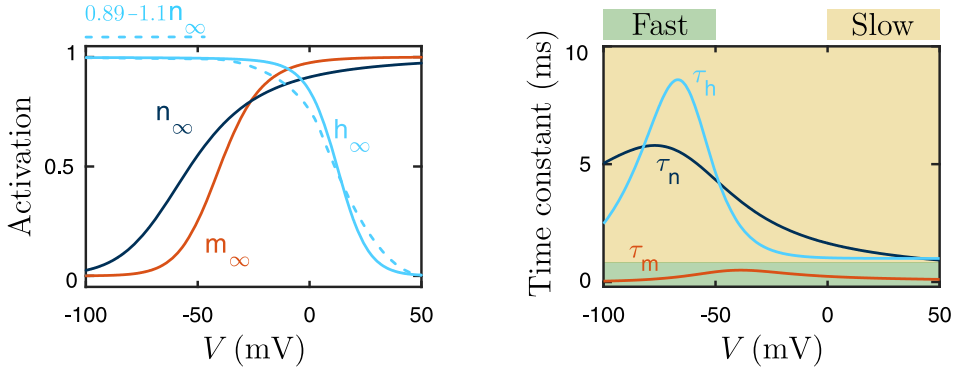

Figure 8.1: Steady-state (left) and time constant (right) functions of the original Hodgkin and Huxley model. The steady-state function of sodium inactivation can be approximated by $0.89 - 1.1n_\infty$ (left). Sodium activation gating variable is classified as fast, whereas potassium activation and sodium inactivation gating variables are classified as slow (right). Taken from Lu et al. (2023).

arduous;

- Define a slow voltage (V_s) that is the voltage that would lead to the chosen slow gating variable at steady state: $x = x_\infty(V_s)$, or $V_s = x_\infty^{-1}(x)$.Other slow gating variables can be approximated as instantaneous with respect to this slow voltage, i.e., $x = x_\infty(V_s)$. For example, in the Hodgkin and Huxley model, the inactivation of sodium currents can be approximated as $h = h_\infty(V_s)$, where $V_s = n_\infty^{-1}(n)$;

4. **Treat Ultraslow Variables:** Ultraslow gating variables can be made static as parameters and manually varied. If necessary, a third timescale and variable can be added to the reduced model using a similar protocol as in step 3. For instance, in the Hodgkin and Huxley model, bursting behavior can be achieved by incorporating a calcium-controlled potassium current. This potassium current in itself lies in the slow timescale and can be approximated as in step 3, but the calcium modulating that current lies in the ultraslow timescale and required to be a static parameter or a variable on its own.

Following this dimensionality reduction procedure, the conductance-based model is approximated by a nonlinear system with two or three variables, enabling the application of phase plane analysis to analyze the reduced models.

For the original Hodgkin and Huxley model, it can be reduced to this system of two nonlinear ODEs:

$$C\dot{V} = -\bar{g}_{\mathrm{Na}} m_\infty(V)^3(0.89 - 1.1n)(V - E_{\mathrm{Na}}) - \bar{g}_{\mathrm{Kd}} n^4(V - E_{\mathrm{K}}) - g_{\mathrm{leak}}(V - E_{\mathrm{leak}}) + I_{\mathrm{ext}}$$
$$\tau_n(V)\dot{n} = n_\infty(V) - n.$$

8.2 Phase plane analysis

Phase plane analysis serves as a pivotal tool from nonlinear systems theory for analyzing reduced models, alongside bifurcation analysis.

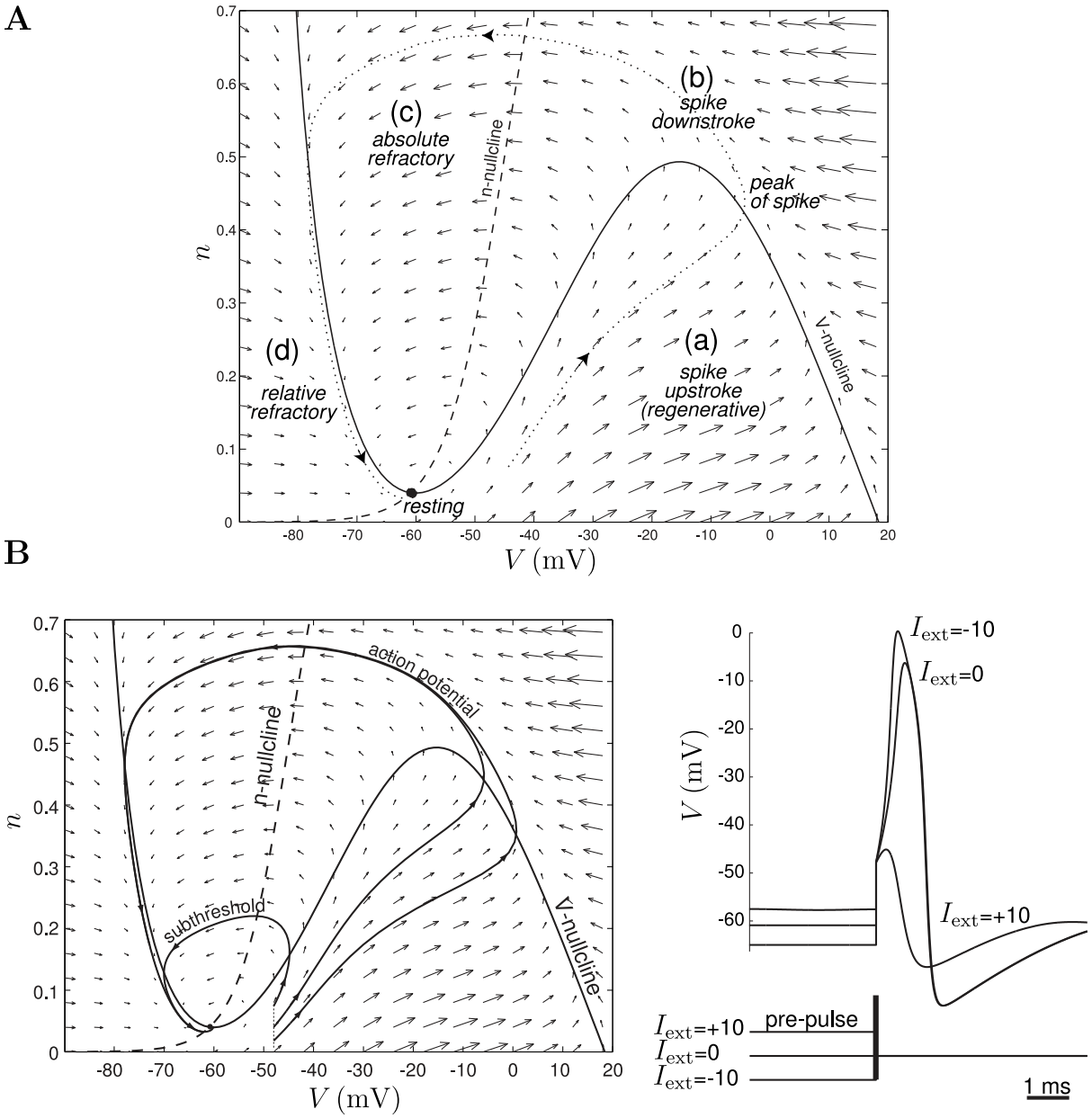

Figure 8.2: Phase plane analysis for the reduced Hodgkin and Huxley model. A. Phase plane representation of the reduced Hodgkin and Huxley model, depicting V and n as the two variables. Nullclines (solid line for V, dashed for n), vector field (arrows), and a trajectory (dotted line) are illustrated. **B.** Various trajectories corresponding to different applied currents. Subthreshold excitation results in one type of trajectory, while the triggering of a spike is depicted by the two others. Taken from Izhikevich (2007).

For a 2D nonlinear dynamical system as:

$$\dot{x_1} = f_1(x_1, x_2)$$
$$\dot{x_2} = f_2(x_1, x_2)$$

phase planes provide a 2D representation where the axes correspond to the two variables of the system, x_1 and x_2 (Terman and Izhikevich, 2008). In such a plane, three fundamental system

properties can be visualized:

1. **Nullclines:** Nullclines for a specific variable x_i represent the set $\{(x_1, x_2) \in \mathbb{R}^2 : \dot{x_i} = f_i(x_1, x_2) = 0\}$. At the crossing of nullclines, both variables rates of variation are null, indicating a fixed point, always present at the intersection of nullclines, with coordinates $(\bar{x_1}, \bar{x_2})|_{(\dot{x_1},\dot{x_2})=(0,0)}$. Stability of fixed points can be evaluated by computing the eigenvalues of the Jacobian matrix at each fixed point. Bifurcation analysis involves studying the stability of fixed points as a function of a varying parameter. For instance, a stable fixed point can be destabilized or even vanish by changing a parameter in nonlinear systems (Fig. 8.2A). For conductance-based models, increasing external current (the bifurcation parameter) modifies fixed point stability, transitioning from a stable fixed point at resting potential to a stable limit cycle attractor at threshold current, representing a bifurcation;

2. **Vector field:** The vector field comprises vectors $(\dot{x_1}, \dot{x_2})|_{(x_1,x_2)\in\mathbb{R}^2}$ (Duff, 1953), indicating the rate of change of both variables at each point in the phase plane. It provides insight into variable changes across the plane, aiding in the visual assessment of fixed point or limit cycle attractor stability (Fig. 8.2A).

3. **Trajectories:** Trajectories, represented as curves $(x_1(t), x_2(t))$, where $x_1(t)$ and $x_2(t)$ are solutions of the nonlinear system (Jenerick, 1963), illustrate system convergence relative to its initial conditions. Trajectories are valuable for observing limit cycle attractors and can be overlaid on nullclines to predict system behavior (Fig. 8.2B).

These tools are instrumental in better understanding neuronal dynamics and are commonly applied to reduced models, a field often referred to as neurodynamics.

8.3 Bifurcation analysis as an indicator of neural behavior

Understanding the loss of stability of the resting membrane potential concerning a parameter, typically the applied current, is pivotal in computational neuroscience and offers profound insights into action potential dynamics. Extensive literature explores the underlying dynamics of action potential generation through model reduction (Ermentrout, 1994; Coggan et al., 2011; Drion et al., 2012, 2015c; Courbage and Nekorkin, 2010; Franci et al., 2013; Qi et al., 2013; Yamapi et al., 2022; Bisquert, 2021; Yaru and Shenquan, 2021).

A key finding across these studies is that neuronal firing initiation involves a bifurcation where the stable fixed point is perturbed, potentially altering its stability or causing it to vanish. Various types of bifurcation, such as saddle-node (SN), saddle-node on invariant circle (SNIC), transcritical (TC), or saddle-homoclinic (SH), can lead to action potential generation. The specific type of bifurcation depends on the shape of nullclines, dictated by the set $(V, n)|_{\dot{V}=0}$, influenced by the types of ion channels present in the model.

Studies like Franci et al. (2013) and Drion et al. (2015c) have linked each excitability type (I, II, II*, or III) to specific bifurcation types (Fig. 8.3A-B). For instance, in the Connor-Stevens model:

1. With null A-type potassium channel conductance, the model is type II, and a Hopf

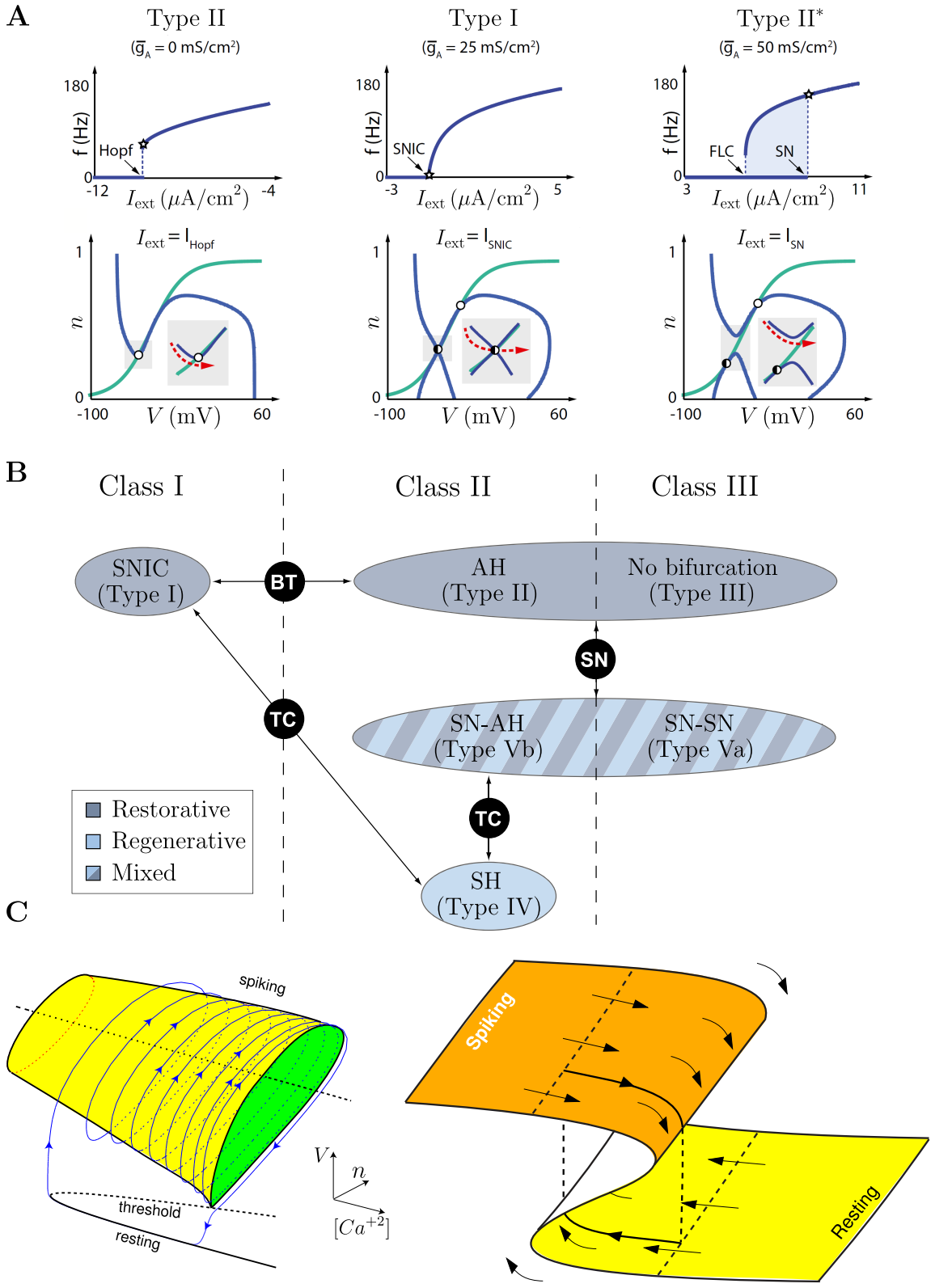

Figure 8.3: Bifurcation dictates neuronal excitability. A. Phase planes of the Connor-Stevens model illustrating Types I, II, and II* behaviors (top), along with their associated phase plane (bottom). **B.** Various bifurcations and their types. SNIC: saddle-node on invariant circle; BT: Bogdanov-Takens; AH: Andronov-Hopf; SN: saddle-node; TC: transcritical; SH: saddle-homoclinic. **C.** Three-dimensional phase plane representation of bursting, with an additional ultraslow variable. Taken from Drion et al. (2015c); Franci et al. (2013); Izhikevich (2007).

bifurcation underlies action potential generation;

2. With moderate A-type potassium channel conductance, the model is type I, and a SNIC bifurcation triggers action potentials;

3. With high A-type potassium channel conductance, the model is type II* and bistable, with fold limit cycle (FLC) or SN bifurcations driving action potential generation.

Overall, the relationship between excitability type and bifurcation type is complex, influenced by the restorative or regenerative nature of ion channels. Restorative channels provide a negative feedback at resting potential while regenerative channels provide a positive feedback at resting potential.

In the context of bursting, a similar principle applies, often involving an ultraslow variable like calcium. Calcium levels decrease during neuronal silence, triggering a bifurcation that initiates tonic firing at a bottom threshold. As calcium accumulates, another bifurcation occurs, transitioning the neuron back to a silent state, leading to continuous bursting at an upper threshold. This behavior can be visualized in a 3D phase plane (Fig. 8.3C).

9 Introduction to control theory

Before delving into intrinsic homeostatic plasticity control, a brief introduction to control theory will be provided to cover the fundamental concepts. Control theory has applications in nearly every field of engineering, including electricity, aerospace, and telecommunications, to name a few (Åström, 2002). In brief, the goals of control theory involve regulating one or more variables of an open-loop system (called a plant) using another system that can be tuned (called a controller) so that the controlled variable(s) reach target value(s) (called reference(s)) in a convenient amount of time, while remaining unaffected by external disturbances. A defining feature of control theory is that these two systems are interconnected in a feedback loop, meaning that a continuous loop can be derived from their interaction (Åström and Murray, 2021).

A prominent example of a controlled system is cruise control. In such systems, the car serves as the physical plant, with the input being the force provided by pressing the gas pedal (the control input) and the output being the variable that needs to be controlled: the velocity. The controller is a virtual system implemented within the car computer, which takes the velocity as input and outputs a force that is applied to the car. In this example, the reference is the velocity chosen by the driver on the dashboard. The controller continuously tracks the car actual velocity, compares it to the reference velocity, and outputs a force to adjust the car speed to match the reference. In addition to reference tracking, the cruise control system can counteract external forces that may affect the car (such as slopes or wind). This capability is known as disturbance attenuation (Shaout and Jarrah, 1997).

Control theory draws inspiration from biology, where feedback loops and control systems are ubiquitous. For instance, the human body regulates its internal temperature to remain as close as possible to 37°C at all times by counteracting any disturbances that may occur. When engaging in physical activity, the internal temperature rises, and the body senses this change and responds by initiating sweating to lower the temperature (Weller, 2005). Control theory is thus well-suited to be applied to neuronal models, as many feedback loops can be identified within a single cell, such as those involved in protein signaling and gene expression (Shvartsman et al., 2002; Cross and Tinkelenberg, 1991).

9.1 The usual architecture of control systems

Classical control systems are composed of various building blocks that can be either physical or virtual (Fig. 9.1A). First, on the upper branch (the process), there is the physical system to be controlled (*e.g.*, the car in the cruise control system), which outputs the controlled variable. This variable is measured by specific sensors (*e.g.*, speed sensors), with added measurement noise. The noisy measured control variable (*e.g.*, noisy velocity) is then fed to the controller. The controller may start by filtering out the measurement noise, and then it is fed into a digital computer using an analog-to-digital converter (A/D). This computer is the core of the controller and also receives the operator input (*e.g.*, the reference velocity). It computes an appropriate control input (*e.g.*, the force provided to the car) and sends it to the physical system using a digital-to-analog converter (D/A) and actuators.

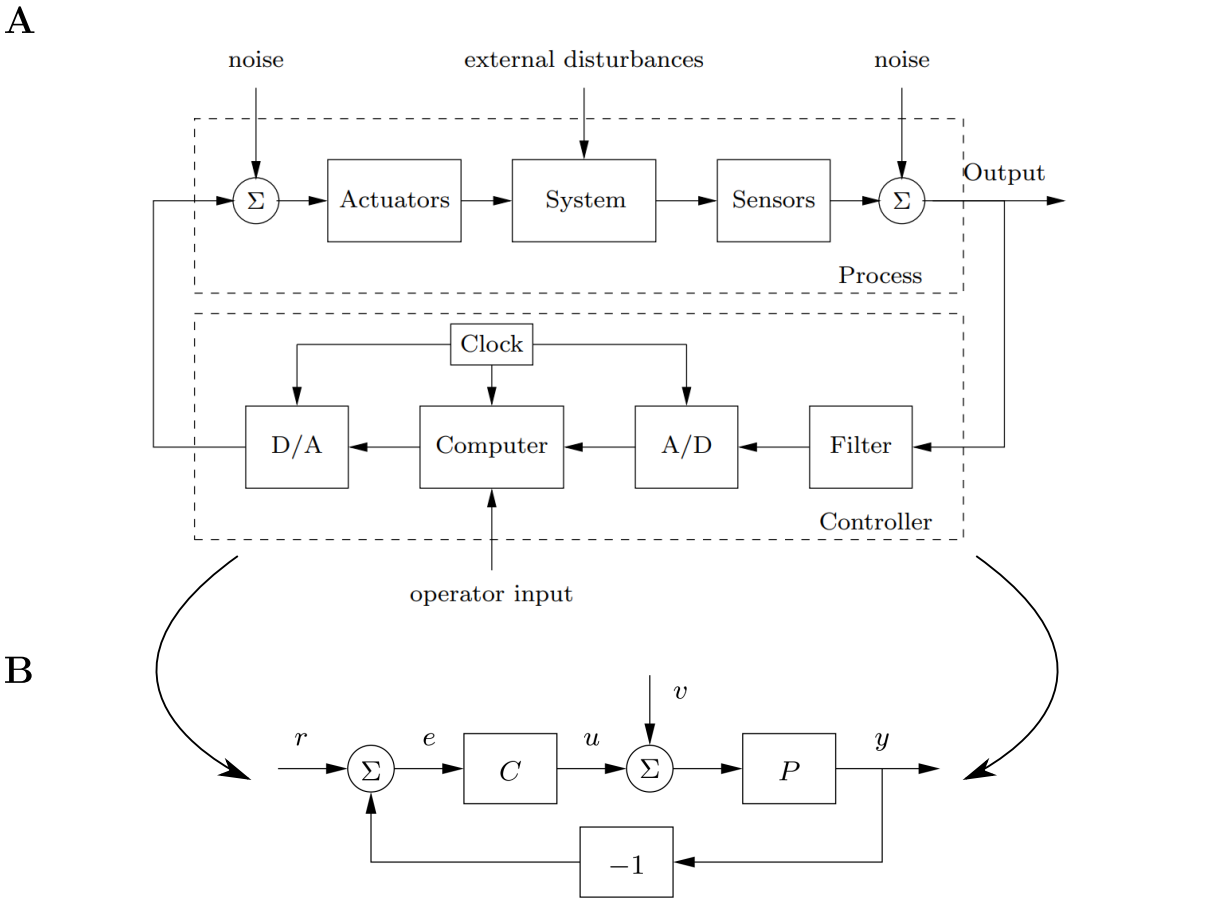

Figure 9.1: The architecture of control systems. A. Complete architecture of a physical control system. **B.** Block diagram of a control system sufficient for control theory and simulation. Taken from Åström and Murray (2021).

Such an architecture is a typical example of a physical application of a control system. In control theory and simulations, many elements essential to the physical implementation of control systems, such as actuators, sensors, and converters, can be omitted. This theoretical architecture is depicted in Fig. 9.1B, also known as a block diagram. In this diagram, r is the reference signal, y is the control variable, e is the error signal computed as $e = r - y$, u is the control input, v is the external disturbance signal (often denoted as d), C is the controller system, and P is the plant system. These two systems are modeled as a system of differential equations. Most of the time, when a system of differential equations is linear, it is not used in its raw form. Instead, linearity allows the system to be represented by a transfer function, which describes the input-output relationship (Pintelon et al., 1994). However, this thesis does not focus on transfer functions or frequency-domain analysis, as cellular neuronal systems are inherently nonlinear.

The goal of control theory is to design the system C such that e reaches zero in an adequate manner, *i.e.* by respecting the constraints of the specific application. As mentioned, these two systems are interconnected in a feedback loop. The -1 block ensures that this loop consists of negative feedback, as most engineering applications require negative feedback, characterized by a reduction of the fluctuation of the control variable (Audia and Locke, 2003). For example,

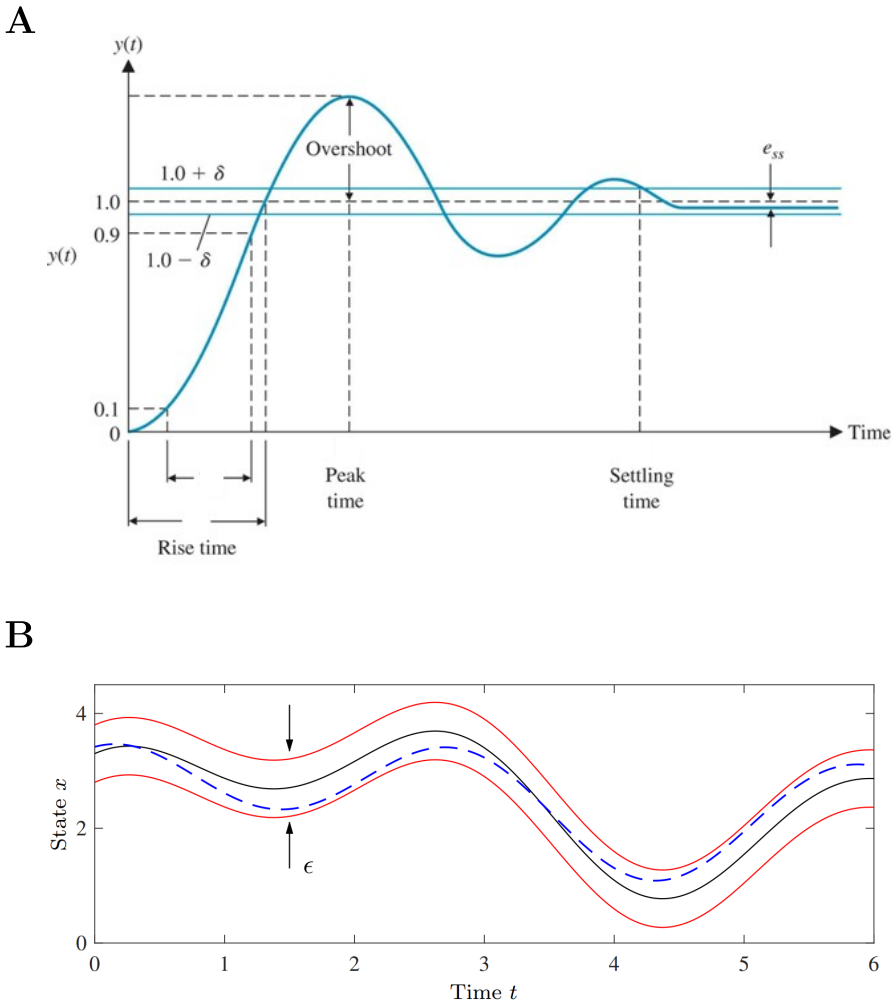

Figure 9.2: Characterizing errors in control theory. A. Step response of a typical control system, with highlighted features. The dashed line is the reference r and the solid line is the control variable y. **B.** Typical trajectory of a control system. The solid line is the reference r and the dashed line is the control variable y. Taken from Wilkerson (2016); Åström and Murray (2021).

in the cruise control system, if the speed increases due to a disturbance, the controller must counteract this increase to reduce the speed and maintain it close to the reference. Note that positive feedback is sometimes useful, especially in mixed feedback systems. Positive feedback is characterized by an amplification of the control variable. For instance, if the control variable of a positive feedback system increases, the controller will further increase it, and so on, until saturation (DeAngelis et al., 2012). There are evidence of positive feedback in biological systems (Mitrophanov and Groisman, 2008).

One typical way to assess the performance of a control system is to study its step response. This involves an instantaneous step of the reference r from 0 to 1 and observing the time evolution of the control variable. As the plant is a physical system, instantaneous attainment of the new reference value is impossible, and a dynamic transition can be observed. Characteristics of this dynamic transition include the rise time, peak time, settling time, and overshoot (Fig. 9.2A). Eventually, the control variable stabilizes (close to the reference if the controller is well-designed),

and the system reaches a steady state. A typical error observed in this regime is the steady-state error e_{ss}, which corresponds to the difference between the steady-state value of y compared to r (Butkiewicz, 1998). Ideally, this error should be null. Such a simulation is a very specific and theoretical way to assess controller performance, as real applications resemble Fig. 9.2B, with constant changes in r or persistent disturbances applied to the system that drive y from r.

9.2 A usual type of controller: Proportional–Integral (PI)

The concept of control theory is centered around designing a controller to ensure the stability of a closed-loop system while achieving the desired timing and error characteristics for the application. In this introduction, a common controller architecture known as the PI (Proportional-Integral) controller is presented.

The equation for a PI controller is given by (Desoer and Lin, 1985):

$$u(t) = K_{\text{p}} \cdot e(t) + K_{\text{i}} \cdot \int_{-\infty}^{t} e(\tau)\,\mathrm{d}\tau, \tag{9.1}$$

where $u(t)$ is the control input, $e(t)$ is the error signal, and K_{p} and K_{i} are the proportional and integral gains, respectively. This means that the control input is proportional to both the error signal and its integral. The parameters K_{p} and K_{i}, often called gains, need to be tuned to achieve the target behavior of the closed-loop system. In classical control applications, these gains remain fixed once they have been tuned.

To rewrite equation (9.1) as a set of differential equations, we use the following form (Balchen et al., 1988):

$$\begin{aligned} u &= K_{\text{p}} \cdot e + K_{\text{i}} \cdot z \\ \dot{z} &= e, \end{aligned} \tag{9.2}$$

where z is referred to as the accumulation variable.

This type of controller is highly valued in both industry and research due to its simplicity in tuning (only two gains need to be adjusted) and its ability to ensure zero steady-state error (Eitelberg, 1987). At steady state, all time derivatives are zero, and the second equation of system (9.2) simplifies to $\dot{z} = 0 = e = r - y$, ensuring that $r = y$ at steady state.

Hence, a typical block diagram of a PI controller consists of two parallel blocks (P and I) that sum up (Fig. 9.3A). As long as $K_{\text{i}} \neq 0$, zero steady-state error is ensured. However, tuning K_{i} involves a trade-off between rise time, oscillations, and settling time (Fig. 9.3B). For a low value of K_{i} (dashed line), no oscillations are observed, but the settling and rise times may be too long for the application of interest. Conversely, for a high value of K_{i} (dotted line), the rise time is significantly reduced, but untimely oscillations occur, leading to an increase in the settling time. A good tuning balances these characteristics (solid line).

To mitigate such oscillations, a third component can be introduced that incorporates the derivative of the error, leading to what is known as PID control (Knospe, 2006). This type of controller is

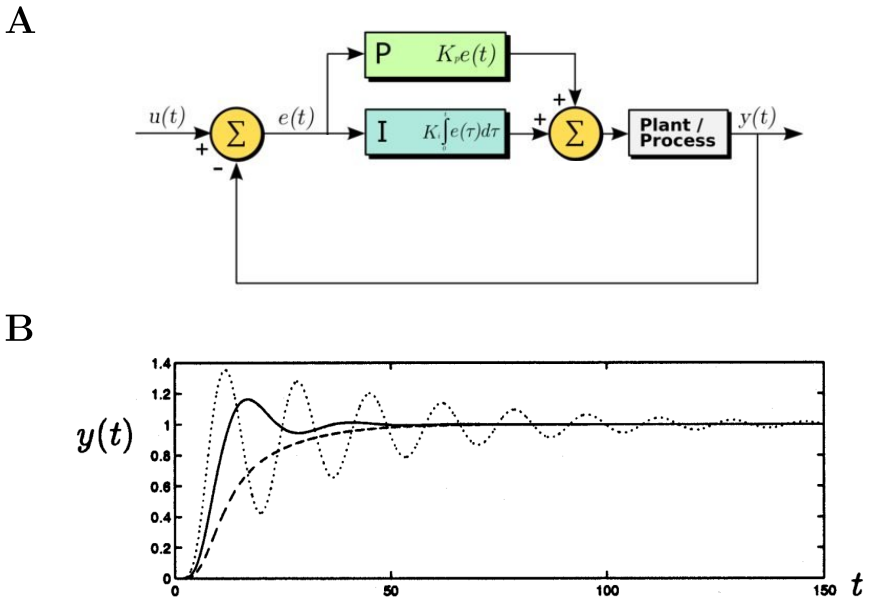

Figure 9.3: PI controller. A. Block diagram of a closed-loop system involving a PI controller. **B.** Typical step responses of a closed-loop system controlled by a PI controller, with varying values of K_i. The lowest value of K_i corresponds to the dashed line, the medium value to the solid line, and the highest value to the dotted line. Taken from Kleppinger (2021); Basilio and Matos (2002).

described by the following equation:

$$u(t) = K_\mathrm{p} \cdot e(t) + K_\mathrm{i} \cdot \int_{-\infty}^{t} e(\tau)\,\mathrm{d}\tau + K_\mathrm{d} \cdot \frac{\mathrm{d}e(t)}{\mathrm{d}t},$$

where K_d represents the derivative gain.

However, only PI control is considered in the context of this thesis, as there is evidence of this control in biological systems (Filo et al., 2023; Mairet, 2018; Frei et al., 2022).

9.3 Adaptive control

The final section of this introduction to control theory presents a more advanced concept known as adaptive control. In adaptive control, the closed-loop system includes a controller with parameters that can be adjusted by an additional mechanism, often referred to as an adjustment or adaptation mechanism (Åström, 1995). This mechanism performs parameter estimation (Annaswamy, 2023) and introduces a second feedback loop over the classical control feedback loop, allowing the controller gains to be dynamically tuned rather than remaining fixed.

This type of control is frequently used when a controller must perform well under drastically changing conditions. For instance, during an aircraft flight, its mass decreases over time due to fuel consumption, requiring all controllers to constantly adjust their parameters to adapt to the new mass of the aircraft and changing external conditions such as pressure, temperature, or asymmetric damage (Nguyen et al., 2008; Liu et al., 2010). To achieve this, the adjustment mechanism monitors r, y, and u to compute new values for the controller gains to ensure optimal

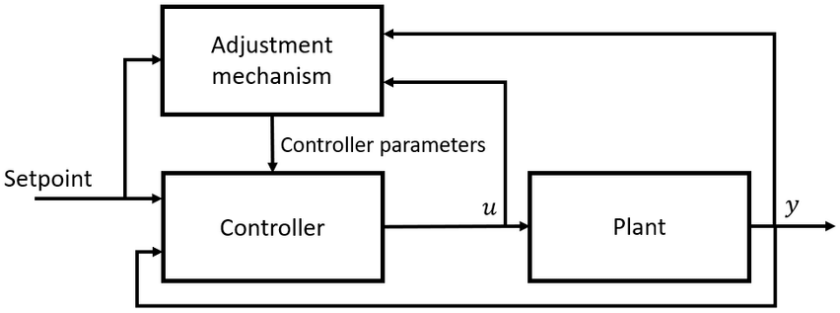

Figure 9.4: Adaptive control. A typical block diagram of a closed-loop system involving adaptive control includes an adjustment mechanism. Compared to classical control systems, this adjustment mechanism is added through a second feedback loop, which is used to adjust the parameters of the controller. Taken from Chaffre et al. (2022).

performance (Fig. 9.4).

In an adaptive PI controller, the control law is modified as follows:

$$u(t) = K_{\mathrm{p}}(t) \cdot e(t) + K_{\mathrm{i}}(t) \cdot \int_{-\infty}^{t} e(\tau)\,\mathrm{d}\tau,$$

where the proportional and integral gains, $K_{\mathrm{p}}(t)$ and $K_{\mathrm{i}}(t)$, are no longer fixed but instead adapt in real time. The specific manner in which these gains evolve depends on the design of the adaptive mechanism.

There exist many different architectures of adaptive controllers. Among them, two main families can be distinguished: Model Reference Adaptive Control (MRAC) and Model Identification Adaptive Control (MIAC), described as follows (Müller and Villegas, 2013):

- **MRAC:** This type of adaptive controller introduces an adjustment mechanism along with a reference model that defines the desired performance (Fig. 9.5A). It adjusts the control gains to ensure that the physical system follows the behavior of a predefined virtual reference model (Roy et al., 2017);
- **MIAC:** This type of adaptive controller also includes an adjustment mechanism but incorporates a system identification block that performs system identification (*i.e.*, estimating the system from output data) while the system is running (Fig. 9.5B). It adjusts the control gains based on the estimated system (Minniti et al., 2021).

However, many other adaptive control approaches exist, such as least squares support vector regression-based adaptive control, which leverages machine learning to approximate nonlinear system dynamics in real time. This approximation enables the adaptive mechanism to determine gain values that minimize an error criterion based on feedback linearization of the nonlinear system (Khooban et al., 2016). Such adaptive control strategies can be applied, for example, to regulate the speed of an electric vehicle, ensuring it tracks a desired reference even in the presence of disturbances. In the following, any controller that adjusts the gains of a pre-existing controller in real time will be referred to as adaptive.

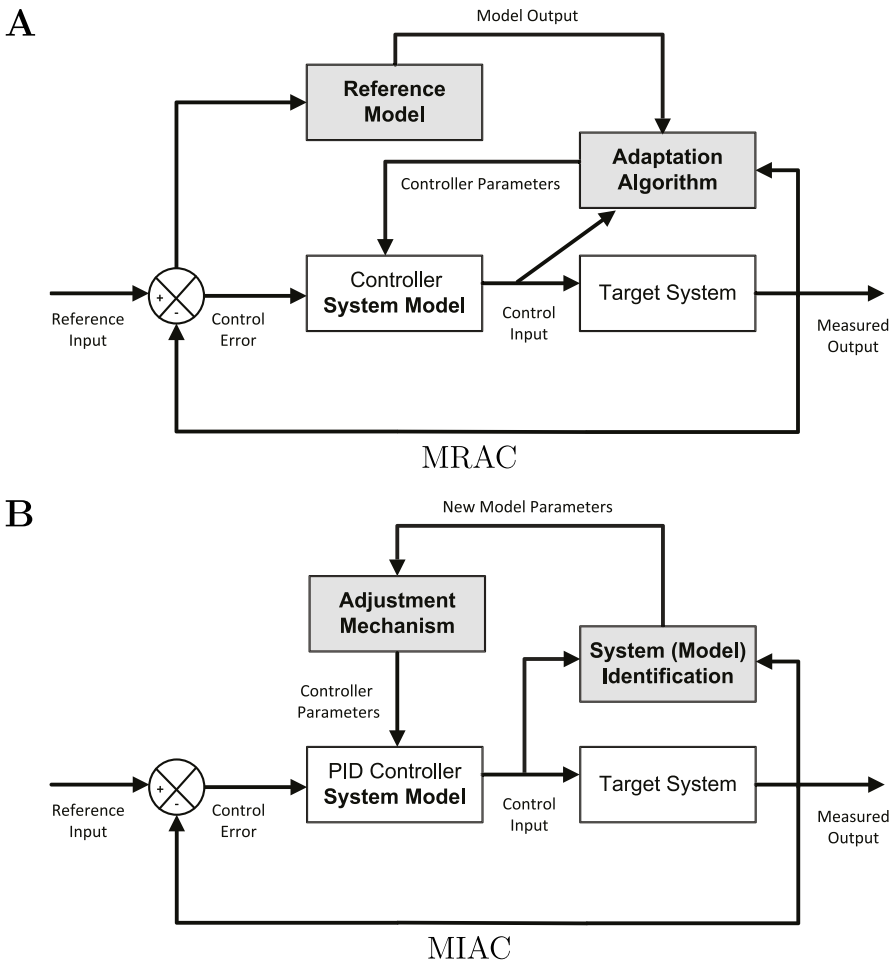

Figure 9.5: MRAC vs. MIAC. A. Block diagram of an MRAC adaptive controller. **B.** Block diagram of a MIAC adaptive controller. Adapted from Müller and Villegas (2013), with the feedback path from the output to the reference modified.

10 A model for intrinsic homeostatic control

As mentioned in the previous chapter, intrinsic homeostatic plasticity (hereafter referred to as homeostasis for simplicity) is a key mechanism by which neurons regulate ion channel expression. A mathematical model of this mechanism was proposed in O'Leary et al. (2014), describing it as a controller with an integral action on ion channel conductance. This model has been used in past studies (Levin, 2021; Goaillard and Marder, 2021; Driscoll et al., 2017; Fields and Levin, 2022; Styr and Slutsky, 2018; Gonçalves et al., 2020; Liu et al., 2016; Zenke et al., 2017; O'Leary, 2018; Keck et al., 2017; Tatti et al., 2017; Coyote-Maestas et al., 2022; Sarma et al., 2018; Jayakar et al., 2021; Marom and Marder, 2023). This homeostatic controller will be used later in the thesis.

10.1 The mathematical model

In regulating ion channel conductances, neurons rely on the expression of ion channels through their mRNA levels, given that ion channels are essentially proteins. The dynamics of protein expression, captured through mRNA levels, can be elucidated using a simple model known as the "central dogma" of molecular biology (Alon, 2007):

$$\begin{aligned} \dot{m}_{\text{ion}} &= \alpha_{m\,\text{ion}} - \beta_{m\,\text{ion}} m_{\text{ion}} \\ \dot{g}_{\text{ion}} &= \alpha_{g\,\text{ion}} m_{\text{ion}} - \beta_{g\,\text{ion}} g_{\text{ion}}, \end{aligned} \tag{10.1}$$

where m_{ion} represents the concentration of mRNA encoding ion channel g_{ion}, $\alpha_{m,\text{ion}}$ denotes the mRNA production rate, $\alpha_{g,\text{ion}}$ signifies the production rate of the ion channel using its mRNA, while $\beta_{m,\text{ion}}$ and $\beta_{g,\text{ion}}$ indicate the degradation rates of mRNA and ion channel, respectively.

The activity-dependent facet of this model lies in the fact that mRNA expression rates are contingent upon the activation of transcription factors such as CREB (Finkbeiner and Greenberg, 1998; Mermelstein et al., 2000; Mihalas et al., 2013). CREB, being calcium-dependent, is influenced by neuronal activity. In a subsequent study, O'Leary (2018) introduced a revised version of equations (10.1), where mRNA regulation is activity-dependent, and the synthesis and degradation rates of g_{ion} are consolidated into time constants:

$$\begin{aligned} \tau_{\text{ion}} \dot{m}_{\text{ion}} &= \text{Ca}_{\text{target}} - [\text{Ca}^{+2}] \\ \tau_g \dot{g}_{\text{ion}} &= m_{\text{ion}} - g_{\text{ion}}, \end{aligned} \tag{10.2}$$

where τ_{ion} denotes the ion channel type-specific time constant for mRNA production (i.e., the transcription process), $\text{Ca}_{\text{target}}$ signifies the target average intracellular calcium concentration (predefined within the cell), $[\text{Ca}^{+2}]$ represents the intracellular calcium concentration, and τ_g stands for the global time constant for protein production (the translation process). It is noteworthy that this regulatory mechanism is applicable to any type of ion channel incorporated in the model, where ion $\in \mathcal{I}$ (Fig. 10.1A).

In essence, this model functions as a monitor of the error in intracellular calcium concentration, $\text{Ca}_{\text{target}} - [\text{Ca}^{+2}]$, accumulating it within mRNAs. Consequently, it adjusts the quantity of ion

channels (and their conductance) either upward or downward if the intracellular calcium level falls below or exceeds the target value, respectively. Consequently, elevating all ion channel conductances in the neuronal model amplifies overall neuronal activity, subsequently affecting the intracellular calcium concentration, and vice versa. At steady state, the model ensures the attainment of an appropriate calcium level, as $\dot{m}_{\text{ion}} = 0$, signifying that $[\text{Ca}^{+2}] = \text{Ca}_{\text{target}}$. This form of control regulation consists in an integrative action, as the controller solely relies on error accumulation, hence its integral.

Therefore, setting equations (10.2) to steady states (where all derivatives are zero) confirms the attainment of the target intracellular calcium and $m_{\text{ion}} = g_{\text{ion}}$. However, inferring the exact value of ion channel conductances post-convergence of the controller is not feasible. Nevertheless, for each type of ion channel, over a sufficiently long period T_{SS} when steady state is approximately reached:

$$m_{\text{ion}} = \frac{1}{\tau_{\text{ion}}} \int_0^{T_{\text{SS}}} \text{Ca}_{\text{target}} - [\text{Ca}^{+2}] \, \mathrm{d}t \approx g_{\text{ion}}. \tag{10.3}$$

This implies that utilizing equation (10.3) for two different ion channels within the set $\mathcal{I}$, denoted as "ion i" and "ion j", yields:

$$\frac{g_{\text{ion}\,i}}{g_{\text{ion}\,j}} = \frac{\tau_{\text{ion}\,j}}{\tau_{\text{ion}\,i}}.$$

Consequently, distinct ratios of τ_{ion}, the transcription time constants, will result in different correlations (ratios) between each pair of ion channel conductances at steady state. Additionally, since neuronal dynamics are largely influenced by such correlations, homeostatic regulatory mechanisms like these can promote specific electrophysiological behaviors (Franci et al., 2013; Drion et al., 2012; Hudson and Prinz, 2010) (Fig. 10.1A).

In summary, this homeostasis model comprises straightforward dynamic equations that adjust ion channel conductances upwards or downwards to achieve any predefined intracellular calcium level while preserving predefined correlations between each pair of conductances embedded within the transcription time constants.

It is imperative to note that the model must have a single intracellular calcium target value. Multiple targets would result in a constant mismatch between the targets and intracellular calcium, attempting to reconcile both and ultimately leading to instability in the homeostatic controller, as this error would continuously accumulate, causing mRNA and conductances to escalate uncontrollably (Fig. 10.1B).

10.2 Results and limitations

This homeostatic control model elucidates how neurons regulate their own conductances to achieve various target behaviors by adjusting the different time constants appropriately. For example, in O'Leary (2018), diverse types of electrical behaviors were attained within the same conductance-based model. The process began with very low conductance levels, simulating a new cell devoid of any function and exhibiting silent behavior due to insufficient sodium channels to trigger spikes. Subsequently, the homeostatic model regulated the conductances using distinct predefined transcription time constants for each phenotype. Through this experiment,

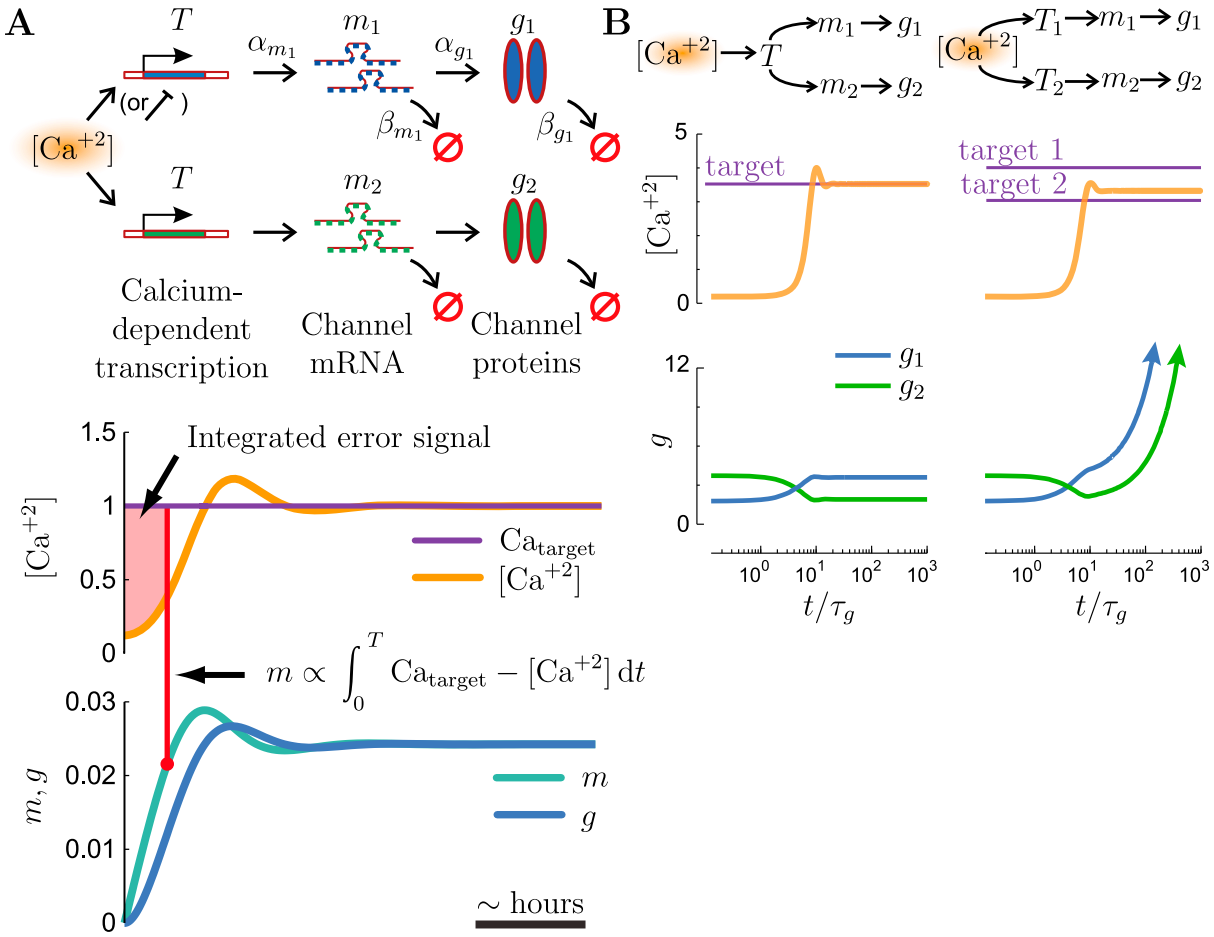

Figure 10.1: The homeostasis model. A. Illustration of the translation and transcription processes initiated by intracellular calcium signaling (top). Time evolution of mRNA and channel conductance using calcium as the signal for integral control action. **B.** A single calcium target ensures system stability. However, if two different conductances (inward and outward) have distinct calcium concentration targets, the homeostasis model may result in instability. Adapted from O'Leary et al. (2014), with axis labels replaced and text added.

the authors successfully generated a spectrum of neuronal behaviors, including type I spiking neurons, type II spiking neurons, rebound bursters, bursting pacemakers, and tonic pacemakers, all starting from randomly generated and minute conductance levels (approximately 5 orders of magnitude below their steady state values, akin to modeling a newly born neuron) (Fig. 10.2A). Furthermore, this experiment was replicated multiple times for each phenotype, employing different sets of transcription time constants. Consequently, this yielded a neuronal population for each phenotype, where points in the conductance hyperspace exhibited high correlation. Moreover, when considering pairs of conductances, the slope of the regression line corresponded closely to the ratios of transcription time constants (Fig. 10.2B).

Another notable outcome of O'Leary et al. (2014) is the applicability of these homeostatic regulation rules to neuronal networks. The authors successfully induced a robust rhythm in a pyloric network of the crustacean stomatogastric ganglion comprising three neurons (PD/AB, PY, and LP) starting from initially small random conductances. Initially, all three neurons

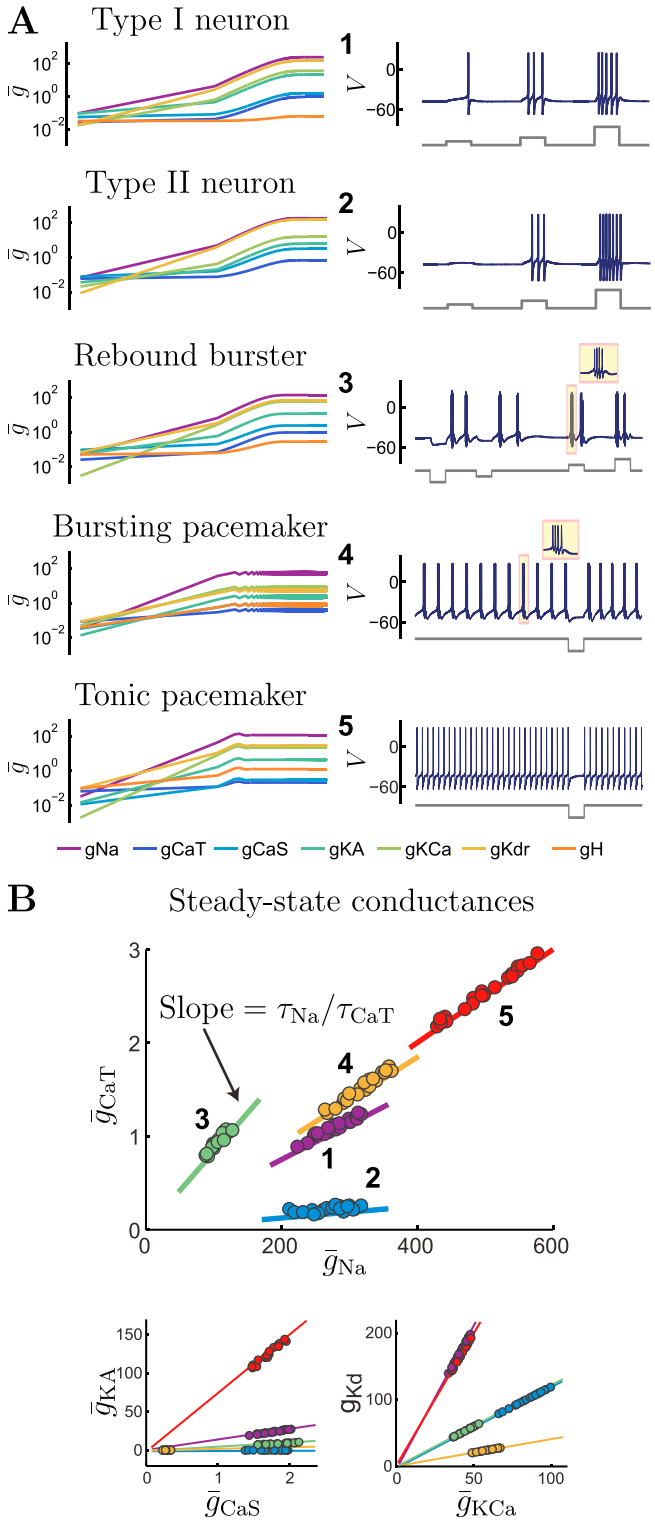

Figure 10.2: The homeostasis model allows to differentiate a same model into different excitability types. A. Example of neurons generated using the homeostasis model from the same initial population, but with different transcription time constants. **B.** At steady state, the conductances of a similar population (*i.e.*, with the same transcription time constants) align with a slope representing the ratios of their respective transcription time constants. Adapted from O'Leary et al. (2014), with axis labels replaced and text replaced on top of each trace in panel A.

were silent, but as the homeostatic tuning rules adjusted the conductances, all three neurons entered burst mode, aligning their phase patterns to produce the pyloric rhythm. Furthermore, the network displayed resilience to perturbations. For instance, when the PD/AB neuron was perturbed by a sharp increase in hyperpolarizing conductance, leading to complete silence in that neuron, allowing the homeostasis controller to regulate the conductances facilitated recovery of the pyloric rhythm within a few minutes.

"However, neurons regulated by this homeostatic controller are susceptible to perturbations, and the compensatory response to channel deletion varies depending on the cell and channel type. For example, in pacemaking bursters, the deletion of H-type channels may initially cause acute knockout (KO), but compensation mechanisms ultimately restore function. This sensitivity to deletion is a characteristic feature of these bursters. Another example is the deletion of slow calcium channels, which can lead to function loss in some cells immediately after deletion. However, in all cases, compensation preserves or restores bursting activity. In contrast, the deletion of T-type calcium channels can also result in function loss, but in this case, homeostatic compensation becomes pathological, leading to a failure to recover bursting activity (Fig. 10.3).

In conclusion, while the homeostasis controller represents a significant advancement in computational neuroscience, providing insights into homeostatic tuning rules, neurons relying solely on this mechanism lack function modulation and robustness. Therefore, it is imperative to combine the homeostatic controller with other conductance regulation mechanisms for comprehensive neural functionality.

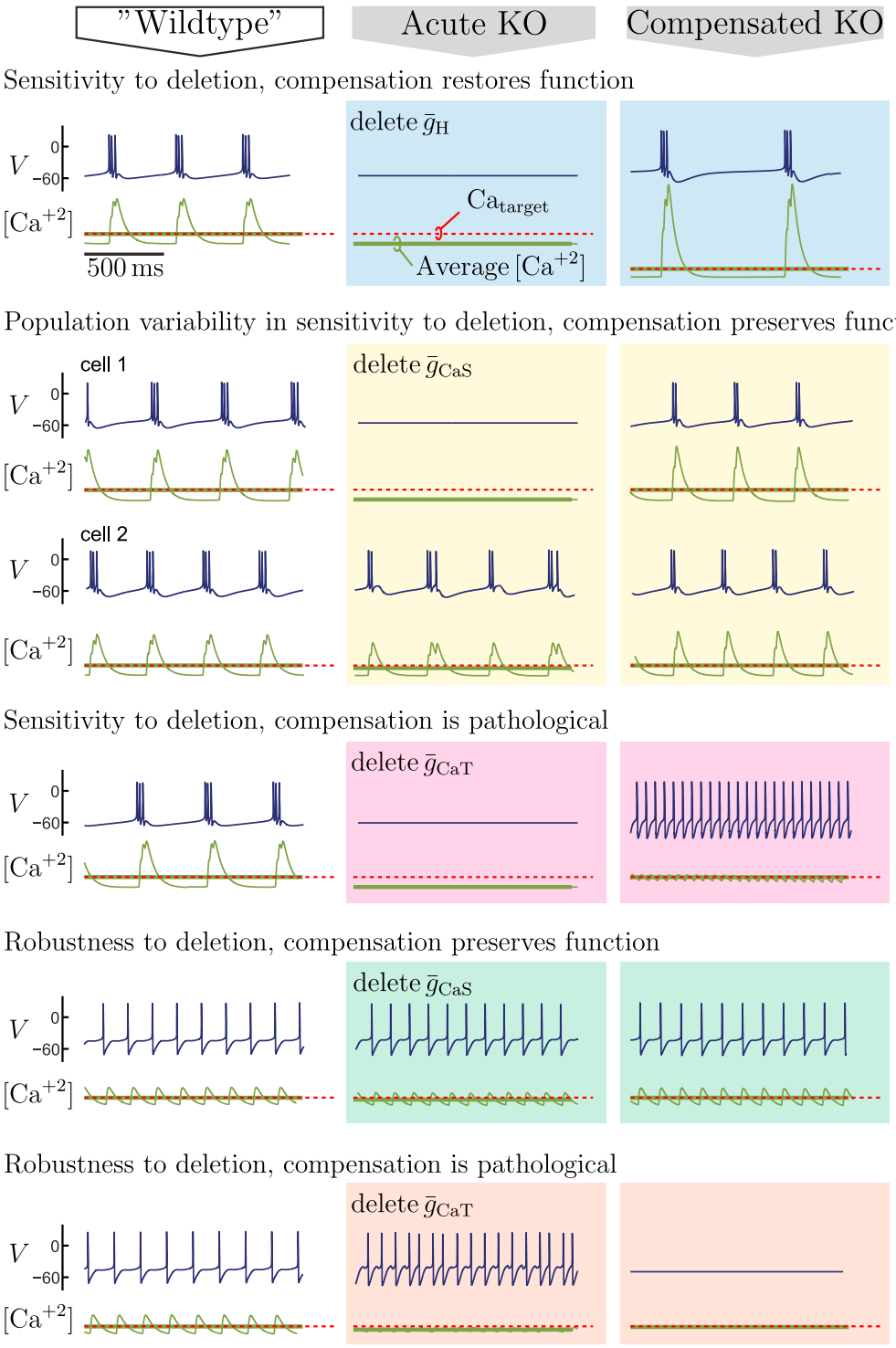

Figure 10.3: The homeostasis model compensation might be unreliable depending on cell and channel type. Electrical activity of bursting (4 top rows) or tonic (2 bottom rows) pacemakers (left). Neuronal response to channel deletion (middle). Impact of homeostatic regulation (right). Adapted from O'Leary et al. (2014), with axis labels replaced and text replaced on top of each trace.

11 Neuromodulation in conductance based models: state of the art

Neuromodulation in computational neuroscience refers to the capacity to reliably transition between different electrical activities despite variations in neuronal parameters, known as degeneracy. In biological terms, neuromodulation involves adjusting certain ion channel conductances to fine-tune the phenotype of the neuron. The preceding sections have elucidated methods for modeling neurons and circuits, as well as examining their excitability from a dynamical system perspective. Additionally, homeostatic tuning rules have been discussed, along with their advantages and limitations. Now, let us delve into state-of-the-art techniques for modulating neuronal activity.

11.1 Technique to modulate conductance based model

A pivotal aspect of neuroscience is the transition between tonic spiking and bursting activity, which holds significant importance in this thesis and serves as the focal point of this section. The conventional approach to inducing such activity switches involves modifying intrinsic and/or synaptic parameters of conductance-based models, mirroring biological mechanisms (Esser et al., 2009; Krishnan et al., 2016; Wang, 2010; Rasmussen et al., 2017). For example, González et al. (2020) adjusted the potassium leak conductance in a fixed manner to emulate the effect of acetylcholine, thereby facilitating the switch from tonic spiking to bursting. In another study (Tatsuki et al., 2016), tonic spiking to bursting transitions were modeled using a two-compartment model. Initially, the calcium-controlled potassium conductance was increased from 0.4 to 0.6, followed by an increase in NMDA conductance from 0.7 to 0.9. Additionally, the switch in activity was induced by elevating calcium conductance from 0.1 to 0.3 (Fig. 11.1). Notably, the most effective deactivation of bursting activity to date was demonstrated by Drion et al. (2019), where T-type calcium channels were deactivated to hyperpolarize the neuron.

In other studies (Wei et al., 2016; Carrillo-Medina and Latorre, 2018; Bacak et al., 2016), parameters other than conductances were altered to switch neuronal activity. This was achieved by shifting the steady-state activation function of certain currents, such as the H-type or T-type calcium current, to the right or left. Alternatively, modifying the potassium Nernst potential, by artificially altering the extracellular potassium concentration surrounding the neuron, facilitated activity switches.

In reduced models, such switches can be achieved by manipulating parameters that influence and alter the shape of nullclines, as this shape significantly impacts neuronal behavior (Van Pottelbergh et al., 2018; Izhikevich and Hoppensteadt, 2004). Although robust, this modulating technique diverges from biologically relevant methods, as reduced models serve as a dynamical approximation of neurons.

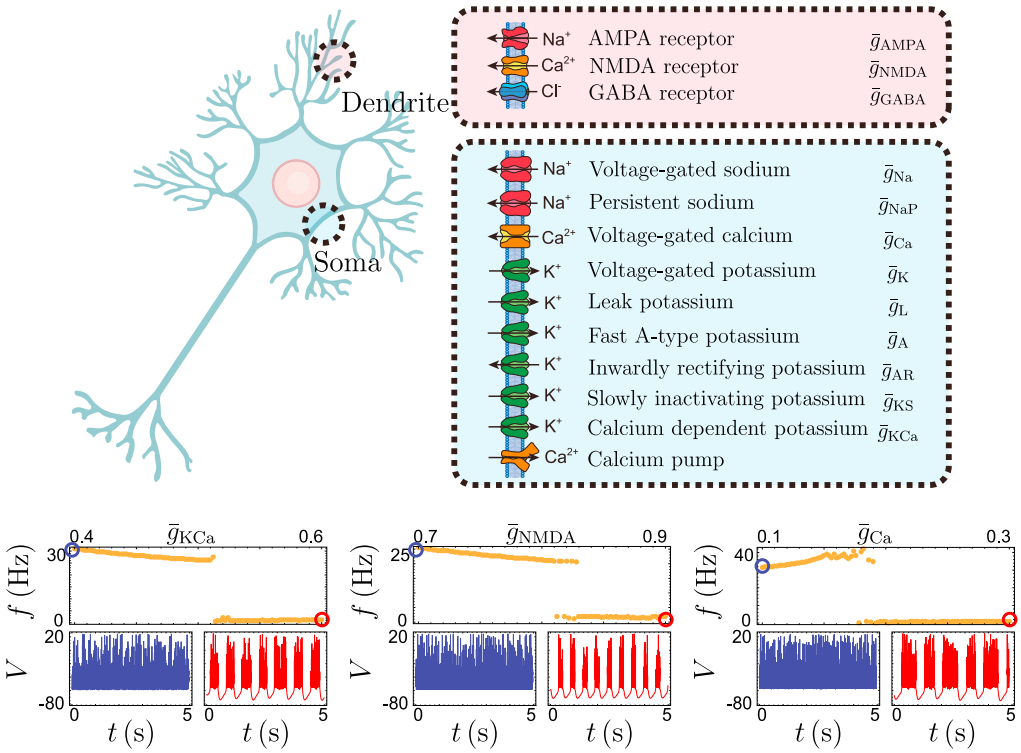

Figure 11.1: State-of-the-art neuromodulation techniques are fixed and rigid. A specific model (top) is employed to induce the transition from tonic firing to bursting (bottom). This transition is facilitated by tuning either the NMDA, calcium-controlled potassium, or voltage-gated calcium conductances in a fixed manner. However, this rigid technique has been demonstrated to be unreliable due to degeneracy. Adapted from Tatsuki et al. (2016), with axis labels replaced at the bottom.

11.2 A lack of neuromodulation in computational neuroscience: challenges

Currently, conductance-based models in neuroscience face a significant limitation: the hardcoded precise and fixed nature of transitions from tonic spiking to bursting. Such neuromodulation rules have been shown to have unreliable effect within neuronal populations with variable underlying conductances, *i.e.* degenerate neuronal population.

In contrast to this rigidity, biological neuromodulation demonstrates robustness even in the face of neuronal diversity, suggesting a need for adaptable regulatory mechanisms. Surprisingly, existing literature lacks such mechanisms, hindering our understanding of neuromodulation intricacies. For instance, even the most recent, qualitative modeling attempts of brain signaling lacks neuromodulation (Markram et al., 2015). The complexity of neuromodulation, with its involvement in high-dimensional, nonlinear dynamical systems and its impact on various cellular and network properties, compounds the challenge.

At the cellular level, neuromodulators exert their influence through metabotropic receptors, utilizing G-protein signaling pathways. This cascade of signaling events ultimately alters neuronal excitability by modifying membrane ion channel dynamics and kinetics. Importantly,

neuromodulation operates across multiple timescales, from milliseconds to hours, and functions at molecular and cellular levels to shape network-level neuronal activity.

The primary goal of this thesis is to address this gap by developing a model or controller for neuromodulation capable of dynamically regulating conductances to achieve a desired modulated phenotype based on a single signal, the neuromodulators. This endeavor seeks to bridge the divide between computational models and biological reality, offering a more nuanced understanding of neuromodulation role in neuronal function.

12 Tackling degeneracy: neurons as feedback systems and high dimensionality

12.1 Reducing the dimensionality of conductance based models: DICs

To facilitate the exploration of neuromodulation and degeneracy within high-dimensional conductance-based models, this thesis begins with dynamic input conductances (DICs), as proposed by Drion et al. (2015a). Referred to as neuronal feedback gains within this thesis, DICs serve to integrate all ion channel effects across various voltages and timescales without the need for model reduction. While the full potential of DICs may still elude many computational neuroscientists, they have proven to be immensely valuable in numerous studies aimed at comprehending neuron dynamics without sacrificing model dimensionality. Notably, they offer a means to investigate neuromodulation within circuits (Gjorgjieva et al., 2016; Sepulchre et al., 2019; Ratliff et al., 2021; Ribar and Sepulchre, 2019; Franci et al., 2018; Onasch and Gjorgjieva, 2020; Ribar and Sepulchre, 2021; Franci et al., 2020; Ergin et al., 2022; Van Pottelbergh et al., 2018; Tikidji-Hamburyan and Colonnese, 2021; Castaños and Franci, 2017; Jacquerie and Drion, 2021; Juarez-Alvarez and Franci, 2023), with many more potential applications awaiting exploration, particularly within our laboratory.

12.1.1 Mathematical definition

At steady state, the membrane voltage of a conductance-based model, hence of a neuron, is determined by Ohm's and Kirchhoff's laws, taking the form $I(V) = 0$ (Kirchhoff, 1845). The local sensitivity of the resting voltage to a small current variation ΔI can be evaluated using the Taylor expansion of the membrane voltage (Taylor, 1717):

$$\Delta V = \left(\frac{\partial I}{\partial V}\right)^{-1} \Delta I.$$

This equation underscores that the (static) input conductance $g_{\text{in}}(V) = -\frac{\partial I}{\partial V}$ dictates how the membrane voltage responds to a current variation. However, for high-dimensional conductance-based models, this equation is impractical numerically. This issue can be addressed by recognizing that neuronal activity comprises different timescales. Specifically, the action potential exhibits two timescales: a fast one for the upstroke and a slower one for the downstroke of the spike. This timescale separation is reflected in the time constant functions of gating variables. For bursting behavior, a third timescale comes into play, determined by the slowest gating kinetics. This separation of timescales can also be observed in voltage clamp experiments, where the change in current ΔI induced by a step in voltage ΔV can be divided into three timescales (f for fast, s for slow and u for ultraslow):

$$\Delta I_{\text{f}} + \Delta I_{\text{s}} + \Delta I_{\text{u}} = \Delta I,$$

leading to:

$$-g_{\mathrm{f}}(V)\Delta V - g_{\mathrm{s}}(V)\Delta V - g_{\mathrm{u}}(V)\Delta V = -g_{\mathrm{in}}(V)\Delta V,$$

and in turn:

$$g_{\mathrm{f}}(V) + g_{\mathrm{s}}(V) + g_{\mathrm{u}}(V) = g_{\mathrm{in}}(V).$$

This implies that the complete DIC can be separated into three distinct DICs corresponding to different timescales, which greatly facilitates computations. The only assumption is that, for a specific timescale j, $g_j(V)$ is the quasi-static quantity $-\frac{\partial I}{\partial V}$, meaning that current variations in faster timescales have already reached steady-state and variations in slower timescales are negligible. This approach is mathematically justified by singular perturbation theory (Fenichel, 1979).

Another advantage of DICs is their easy experimental measurability using voltage clamp experiments, without requiring knowledge of the neuron under study (Fig. 12.1A). By applying a small voltage step (often $\Delta V = 1\,\mathrm{mV}$) starting from a specific voltage V^* and measuring the current variations at the three timescales $\Delta I_j(V^*)$, experimentalists can construct the DICs by:

$$g_j(V^*) = \frac{-\Delta I_j(V^*)}{\Delta V}.$$

This analysis is fully consistent with the original work of Hodgkin and Huxley (1952a), where the activation of sodium currents models fast current variations, while the inactivation of sodium currents and activation of potassium currents model slow current variations (Fig. 12.1B).

Regarding conductance-based models, DICs can be computed using an automated method for any conductance-based model composed of any currents at any dimension. For a conductance-based model composed of variables X_i (gating variables and potentially calcium), DICs can be computed as follows:

$$\begin{aligned}
g_{\mathrm{f}}(V) &= \frac{\partial I_{\mathrm{f}}}{\partial V} = \sum_i w_{\mathrm{fs},X_i}(V) \left(\frac{\partial \dot{V}}{\partial X_i} \frac{\partial X_{i,\infty}}{\partial V} \right)\Big|_V, \\
g_{\mathrm{s}}(V) &= \frac{\partial I_{\mathrm{s}}}{\partial V} = \sum_i (w_{\mathrm{su},X_i}(V) - w_{\mathrm{fs},X_i}(V)) \left(\frac{\partial \dot{V}}{\partial X_i} \frac{\partial X_{i,\infty}}{\partial V} \right)\Big|_V, \\
g_{\mathrm{u}}(V) &= \frac{\partial I_{\mathrm{u}}}{\partial V} = \sum_i (1 - w_{\mathrm{su},X_i}(V)) \left(\frac{\partial \dot{V}}{\partial X_i} \frac{\partial X_{i,\infty}}{\partial V} \right)\Big|_V, \\
g_{\mathrm{in}}(V) &= g_{\mathrm{f}}(V) + g_{\mathrm{s}}(V) + g_{\mathrm{u}}(V),
\end{aligned} \tag{12.1}$$

where $w_{\mathrm{fs},X_i}(V)$ and $w_{\mathrm{su},X_i}(V)$ are voltage-dependent weighting factors that measure the importance of X_i in the three timescales. To compute these weights, the three timescales are chosen, often being the time constant functions $\tau(V)$ of gating variables considered as fast, slow, or ultraslow. Then, the weights are computed as logarithmic distances between the considered variable time constant $\tau_{X_i}(V)$ and the fast, slow, and ultraslow time constants. The weights are saturated to 1 if the kinetics of X_i is faster than the fast timescales and to 0 if slower. Note that DICs can be generalized to n timescales straightforwardly (Fig. 12.1A-B). Additionally,

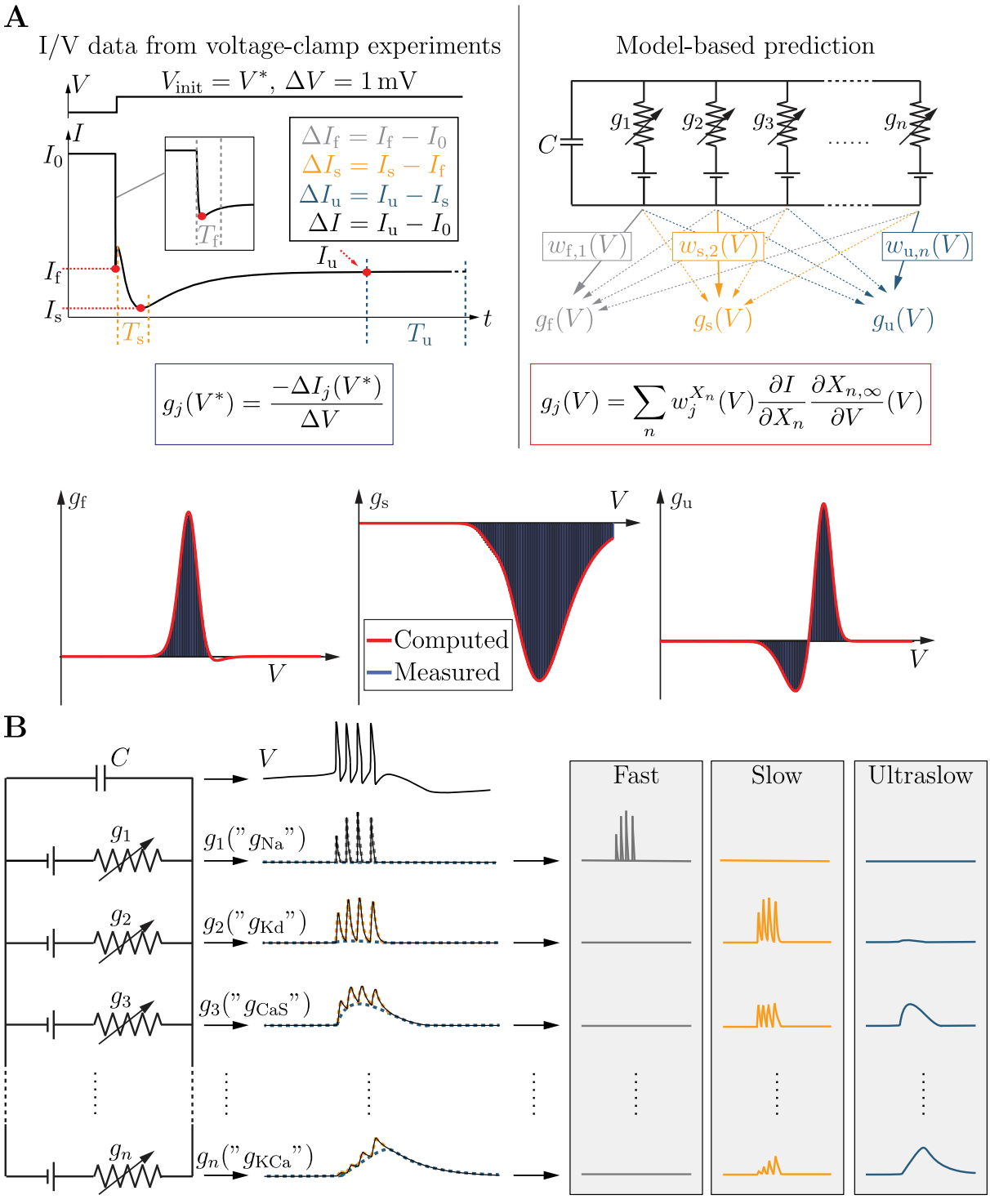

Figure 12.1: Dynamic input conductances shape neuron dynamic sensitivity. A. DICs can be computed either in voltage-clamp experiments or analytically (top). This yields either discrete or continuous functions respectively (bottom). **B.** Each ion channel contributes to multiple timescales. For example, sodium channels contribute more to the fast timescale, whereas delayed rectified potassium channels contribute more to the slow one. Taken from Drion et al. (2015a).

note that the passive properties of the membrane, captured by $\frac{\partial \dot{V}}{\partial V}$, are not included in this original definition but will be used in this thesis. Further details about changes to this DICs

definition will be explained in subsequent chapters.

Thus, the DICs from equations (12.1) are voltage-dependent linear combinations of the maximum ion channel conductance. Any current in conductance-based models can be expressed as $I_{\text{ion}}(V) = \bar{g}_{\text{ion}} m_{\text{ion}}^p h_{\text{ion}}^q (V - E_{\text{ion}}) \,\forall\, \text{ion} \in \mathcal{I}$ for which the coefficients can be computed as follows:

$$\begin{aligned}
\frac{\partial g_{\text{f}}}{\partial \bar{g}_{\text{ion}}} &= w_{\text{fs},m_{\text{ion}}} \cdot p m_{\text{ion}}^{p-1} \cdot h_{\text{ion}}^q (V - E_{\text{ion}}) + w_{\text{fs},h_{\text{ion}}} \cdot m_{\text{ion}}^p \cdot q h_{\text{ion}}^{q-1} (V - E_{\text{ion}}), \\
\frac{\partial g_{\text{s}}}{\partial \bar{g}_{\text{ion}}} &= ((w_{\text{su},m_{\text{ion}}} - w_{\text{fs},m_{\text{ion}}}) \cdot p m_{\text{ion}}^{p-1} \cdot h_{\text{ion}}^q (V - E_{\text{ion}}) \\
&\quad + (w_{\text{su},h_{\text{ion}}} - w_{\text{fs},h_{\text{ion}}}) \cdot m_{\text{ion}}^p \cdot q h_{\text{ion}}^{q-1} (V - E_{\text{ion}}), \\
\frac{\partial g_{\text{s}}}{\partial \bar{g}_{\text{ion}}} &= (1 - w_{\text{su},m_{\text{ion}}}) \cdot p m_{\text{ion}}^{p-1} \cdot h_{\text{ion}}^q (V - E_{\text{ion}}) + (1 - w_{\text{su},h_{\text{ion}}}) \cdot m_{\text{ion}}^p \cdot q h_{\text{ion}}^{q-1} (V - E_{\text{ion}}),
\end{aligned} \tag{12.2}$$

where the voltage dependency is dropped for clarity reasons.

12.1.2 DIC shape neuronal excitability

In essence, each DIC represents the voltage-dependent gain of a control feedback loop for the considered timescale. Specifically, the sign of the DIC qualitatively reflects the sign of the feedback loop, indicating either positive or negative feedback. As defined in equations (12.1), a positive value of a DIC corresponds to positive feedback, and vice versa (Fig. 12.2A). Positively feedback loops amplify small perturbations, leading to exponential growth in variables within the loop. Conversely, negative feedback minimizes perturbations, promoting stability around a reference value, such as the resting membrane voltage, akin to a cruise control system in a car (Åström and Murray, 2021).

In a bursting STG neuron model (Liu et al., 1998), the fast DIC is primarily positive around the threshold voltage (approximately $-50\,\text{mV}$). This indicates that the upstroke of the spike, occurring on the fast timescale, is primarily driven by the excitatory loop of sodium channels. Essentially, higher voltages lead to increased sodium currents, thereby elevating the voltage further. On the slow timescale, the associated DIC is predominantly negative at high voltages, reflecting the action of slow ion channels in ensuring spike repolarization and returning the voltage to its resting state. However, around the threshold voltage, a small portion of the slow DIC becomes positive, creating a slow positive feedback loop near threshold. This element of regenerative excitability is crucial for bursting behavior (Franci et al., 2013, 2014). After firing a spike and returning to resting potential, the neuron tends to fire additional spikes until the ultraslow feedback intervenes. The ultraslow DIC is mainly negative, particularly around the threshold voltage and subthreshold regions, facilitating spike adaptation and termination of bursts. Note the positive segment of the DIC in the suprathreshold region. However, this region is inconsequential for ultraslow dynamics as the neuron transiently passes through it during the spike, preventing sufficient buildup of ultraslow positive feedback before slow negative feedback sets in.

Consequently, it becomes feasible to shape the electrical activity of the neuron solely by

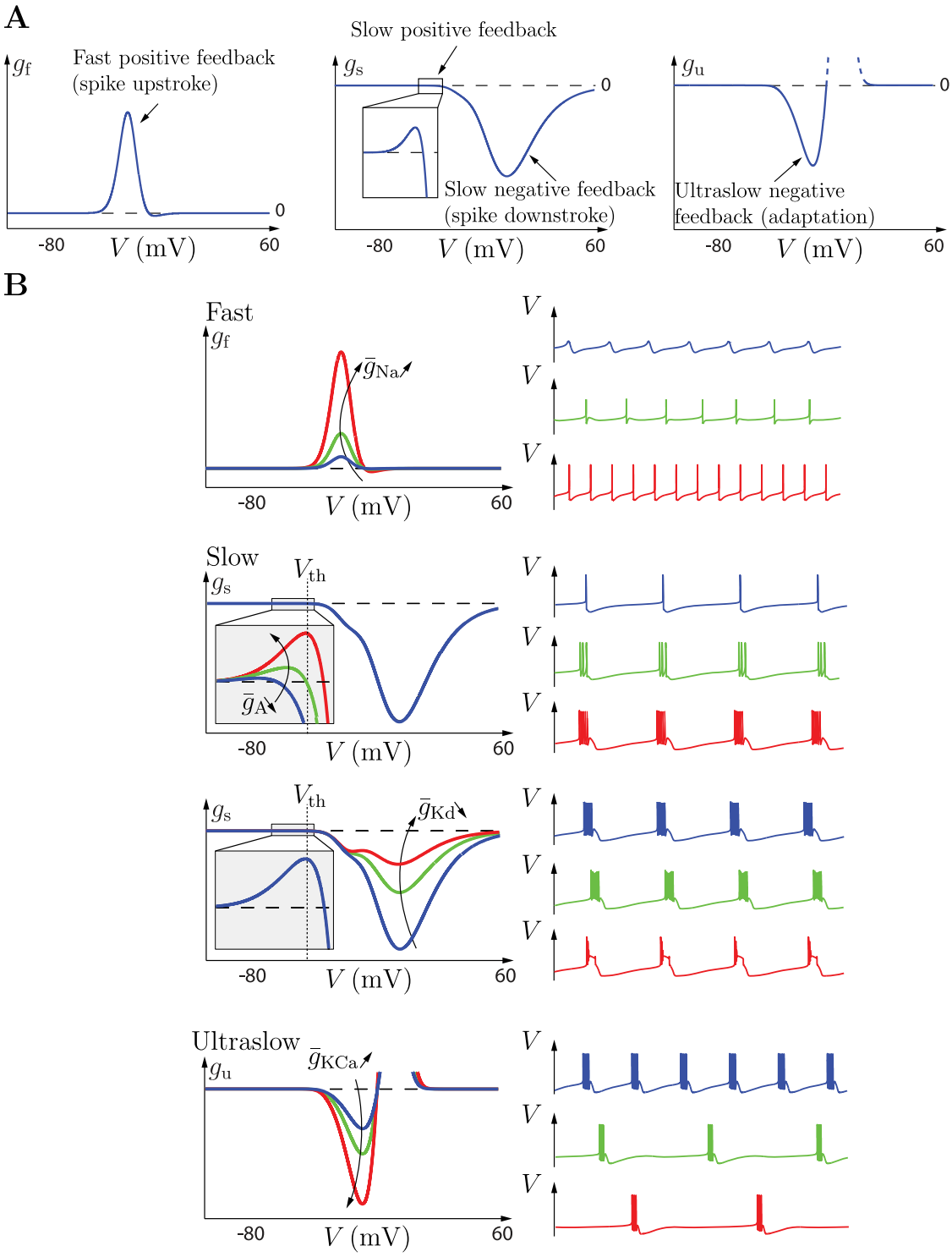

Figure 12.2: Dynamic input conductances shape neuronal activity. A. DIC curves representing the three timescales. Positive values denote positive feedback, while negative values indicate negative feedback, thus influencing neuronal activity. **B.** Variations in fast, slow, and ultraslow DICs in response to alterations in maximum ion channel conductances, accompanied by associated voltage traces. Changes near the threshold voltage signify a significant shift in neuronal excitability, whereas alterations in the suprathreshold region indicate the potential occurrence of hyperpolarized plateaus. Taken from Drion et al. (2015a).

manipulating the DICs, thereby adjusting neuron parameters. Furthermore, it becomes possible to predict phenotypic changes in response to alterations in ion channel conductance. For instance, an increase in sodium channel conductance augments the fast DIC, enhancing fast positive feedback and consequently improving the neuron spiking capability. Conversely, a reduction in A-type potassium conductance increases slow positive feedback around the threshold voltage, transitioning the electrical activity from tonic spiking to bursting in the neuron. Note the escalating burstiness as $\bar{g}_{\mathrm{A}}$ decreases further. Conversely, a decrease in delayed rectifier potassium conductance diminishes slow negative feedback at high voltages, impairing the ability to produce a proper spike downstroke, potentially leading to a depolarized plateau. Finally, an increase in calcium-controlled potassium conductance enhances ultraslow negative feedback, prolonging silent periods between bursts (Fig. 12.2B). As stated in Drion et al. (2015a), "DICs shape neuronal spiking." These findings are often oversimplified or overlook the involvement of conductances in multiple timescales. However, in general, a single ion channel influences multiple timescales, resulting in unexpected outcomes when examining only one DIC.

12.1.3 A singular value in DICs: the threshold voltage

As previously discussed, an important value in the DICs resides at the threshold voltage V_{th}. The activity beyond the suprathreshold range holds little interest, given that adequate slow negative feedback ensures spike downstrokes without necessitating depolarized plateaus. Additionally, the DICs exhibit consistent polarity around the threshold voltage, facilitating the consolidation of DIC data into singular values at V_{th}. Simplifying three entire functions into three numerical values is notably more manageable. Notably, the determination of the threshold voltage follows the algorithm outlined in Franci et al. (2013), which targets the transcritical bifurcation in conductance-based models, known for its heightened sensitivity and thus serves as the model for the threshold voltage. A more expedient method employing DICs involves computing $g_{\mathrm{in}}(V_{\mathrm{th}}) = g_{\mathrm{f}}(V_{\mathrm{th}}) + g_{\mathrm{s}}(V_{\mathrm{th}}) + g_{\mathrm{u}}(V_{\mathrm{th}}) < 0$, while ensuring that $g_{\mathrm{in}}(V_{\mathrm{th}} - \delta V) \geq 0$ with any arbitrarily small $\delta V > 0$.

This approach enables the computation of another valuable metric: the sensitivity of DIC in timescale j concerning the conductance of any ion channel $\bar{g}_{\mathrm{ion}}$ at the threshold voltage:

$$\left.\frac{\partial g_j}{\partial \bar{g}_{\mathrm{ion}}}\right|_{V=V_{\mathrm{th}}}.$$

This computation facilitates a qualitative prediction of the impact of altering any conductances on the neuronal electrical activity. For example, the positive ultraslow sensitivity to the slow calcium current CaS suggests that an increase in $\bar{g}_{\mathrm{CaS}}$ will induce a minor positive feedback near the threshold voltage, altering the burst shape. Such sensitivity analysis extends to both the threshold voltage and the up state of the neuron V_{osc} to confirm the presence of slow negative feedback in the suprathreshold region. Notably, slow and T-type calcium currents augment burstiness due to their positive impact at the threshold voltage. However, they concurrently diminish the negative feedback effect in the suprathreshold region, potentially leading to a depolarized plateau. Consequently, augmenting $\bar{g}_{\mathrm{Kd}}$ reinstates bursting, thanks to its negative influence in the suprathreshold region (Fig. 12.3).

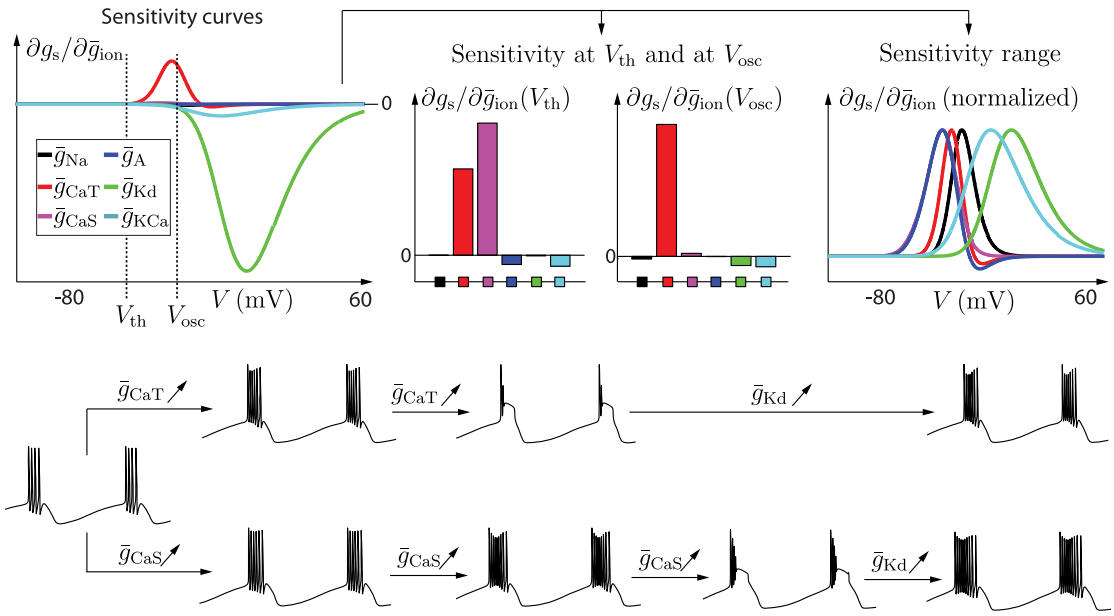

Figure 12.3: Sensitivity analysis of the slow dynamic input conductance. Sensitivity curve of the slow DIC $\partial g_s/\partial \bar{g}_{ion}$ with respect to all ion channels of an STG model, along with their values at threshold and up states (top). This sensitivity analysis can be utilized to restore bursting behavior following an increase in calcium conductances (T-type or slow). Taken from Drion et al. (2015a).

12.2 A preface to this thesis: the compensation algorithm

In the preceding section, the observation that modifying the geometrical characteristics of DICs yields corresponding alterations in electrical behavior suggests a potential utility of DICs in compensation algorithms. The premise of a compensation algorithm involves inducing a perturbation in a particular conductance and subsequently adjusting other conductances, each contributing to different timescales, to maintain the DIC values. The algorithm can be delineated as follows:

1. Initialize with a configuration of conductances that produces a reference firing pattern;
2. Compute the DICs for the configuration from step 1;
3. Select maximal ion channel conductances to counteract the perturbation, ensuring their relevance to the timescale affected. For instance, perturbation of the slow calcium conductance affects slow and ultraslow DICs, necessitating compensation via $\bar{g}_A$, $\bar{g}_{KCa}$ and $\bar{g}_{Kd}$.
4. Prescribe the DIC values to be upheld, delineating the timescale and relevant voltages of interest, such as $g_s^*(V_{th})$, $g_s^*(V_{osc})$ and $g_u^*(V_{th})$.
5. Determine the compensation conductances ($\bar{g}_A$, $\bar{g}_{KCa}$ and $\bar{g}_{Kd}$) using the perturbed conductance value. This involves solving a linear system $Ax = b$ employing any suitable method (Antsaklis and Michel, 1997). Here, x represents the vector of compensation conductances, A denotes the sensitivity matrix containing the sensitivity values of

compensation conductances at the maintained DIC values, and b signifies the vector of sustained DICs minus the influences of non-compensation conductances, including the perturbed one. For a perturbed slow calcium conductance value, $\bar{g}_{\mathrm{CaS,perturb}}$, the matrices are defined according to the model utilized in Drion et al. (2015a):

$$A = \begin{bmatrix} \frac{\partial g_{\mathrm{s}}}{\partial \bar{g}_{\mathrm{Kd}}}(V_{\mathrm{th}}) & \frac{\partial g_{\mathrm{s}}}{\partial \bar{g}_{\mathrm{A}}}(V_{\mathrm{th}}) & \frac{\partial g_{\mathrm{s}}}{\partial \bar{g}_{\mathrm{KCa}}}(V_{\mathrm{th}}) \\ \frac{\partial g_{\mathrm{s}}}{\partial \bar{g}_{\mathrm{Kd}}}(V_{\mathrm{osc}}) & \frac{\partial g_{\mathrm{s}}}{\partial \bar{g}_{\mathrm{A}}}(V_{\mathrm{osc}}) & \frac{\partial g_{\mathrm{s}}}{\partial \bar{g}_{\mathrm{KCa}}}(V_{\mathrm{osc}}) \\ \frac{\partial g_{\mathrm{u}}}{\partial \bar{g}_{\mathrm{Kd}}}(V_{\mathrm{th}}) & \frac{\partial g_{\mathrm{u}}}{\partial \bar{g}_{\mathrm{A}}}(V_{\mathrm{th}}) & \frac{\partial g_{\mathrm{u}}}{\partial \bar{g}_{\mathrm{KCa}}}(V_{\mathrm{th}}) \end{bmatrix} \qquad x = \begin{bmatrix} \bar{g}_{\mathrm{Kd}} \\ \bar{g}_{\mathrm{A}} \\ \bar{g}_{\mathrm{KCa}} \end{bmatrix},$$

$$b = \begin{bmatrix} g_{\mathrm{s}}^*(V_{\mathrm{th}}) - \left(\bar{g}_{\mathrm{Na}} \frac{\partial g_{\mathrm{s}}}{\partial \bar{g}_{\mathrm{Na}}}(V_{\mathrm{th}}) + \bar{g}_{\mathrm{CaT}} \frac{\partial g_{\mathrm{s}}}{\partial \bar{g}_{\mathrm{CaT}}}(V_{\mathrm{th}}) + \bar{g}_{\mathrm{CaS\,perturb}} \frac{\partial g_{\mathrm{s}}}{\partial \bar{g}_{\mathrm{CaS}}}(V_{\mathrm{th}})\right) \\ g_{\mathrm{s}}^*(V_{\mathrm{osc}}) - \left(\bar{g}_{\mathrm{Na}} \frac{\partial g_{\mathrm{s}}}{\partial \bar{g}_{\mathrm{Na}}}(V_{\mathrm{osc}}) + \bar{g}_{\mathrm{CaT}} \frac{\partial g_{\mathrm{s}}}{\partial \bar{g}_{\mathrm{CaT}}}(V_{\mathrm{osc}}) + \bar{g}_{\mathrm{CaS\,perturb}} \frac{\partial g_{\mathrm{s}}}{\partial \bar{g}_{\mathrm{CaS}}}(V_{\mathrm{osc}})\right) \\ g_{\mathrm{u}}^*(V_{\mathrm{th}}) - \left(\bar{g}_{\mathrm{Na}} \frac{\partial g_{\mathrm{u}}}{\partial \bar{g}_{\mathrm{Na}}}(V_{\mathrm{th}}) + \bar{g}_{\mathrm{CaT}} \frac{\partial g_{\mathrm{u}}}{\partial \bar{g}_{\mathrm{CaT}}}(V_{\mathrm{th}}) + \bar{g}_{\mathrm{CaS\,perturb}} \frac{\partial g_{\mathrm{u}}}{\partial \bar{g}_{\mathrm{CaS}}}(V_{\mathrm{th}})\right) \end{bmatrix}.$$

To illustrate this approach, perturbations can be applied to the slow calcium conductance, either augmenting or diminishing it. Absent compensation, the functional integrity is compromised post-perturbation. Conversely, activation of the compensation algorithm ensures preservation of the reference firing pattern throughout and following the perturbation. Nonetheless, it is noteworthy that the compensation algorithm may yield negative values for compensation conductances. Saturating these to zero is imperative for model stability, as negative ion channel conductances may disrupt simulations. Additionally, such saturation holds biological relevance, as negative ion channel concentrations are untenable. In the presented example, the perturbation entails a modification of conductances (Fig. 12.4). However, the compensation algorithm remains applicable even when perturbations are directed at the steady-state functions of any gating variables, as such alterations are encompassed within the DICs.

12.3 Feedback representation of neurons: mixed feedback systems

The introduction of DICs in neurological discourse has illuminated the conceptualization of neurons as feedback systems. Each DIC serves as an indicator of the feedback gain pertinent to its respective timescale, characterized both quantitatively (by its magnitude) and qualitatively (by its polarity). Recently, the notion of mixed-feedback systems, wherein negative and positive feedback mechanisms operate across various spatial and temporal scales, has emerged as a cornerstone in neuromorphic engineering. This field endeavors to fabricate electronic circuits emulating biological counterparts for information processing, with a focus on achieving high energy efficiency and resilience. Notably, biological neurons encompass both types of feedback, as articulated in Sepulchre et al. (2019): "Feedback shapes the sensitivity of an input-output behavior. Positive feedback is a source of ultra-sensitivity, memory, and discrete signaling. Negative feedback is a source of infra-sensitivity, linearity, and continuous signaling." Additionally, it has been demonstrated that the excitability exhibited by neurons results from mixed-feedback mechanisms, necessitating localized positive feedback coupled with broader, slower negative feedback (Sepulchre

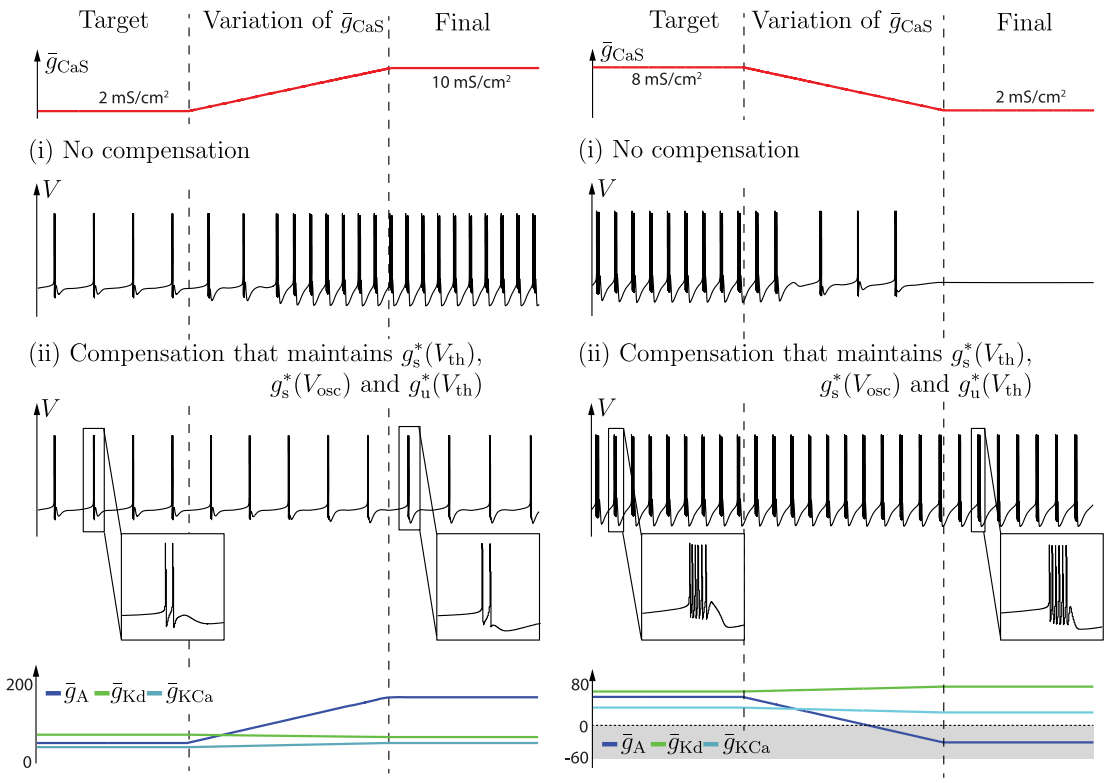

Figure 12.4: The compensation algorithm. Changes in the conductance of the slow calcium current lead to loss of function in a tonic spiking (top left) and a bursting (top right) neuron. This can be compensated for using A-type, delayed rectified, and calcium-controlled potassium conductances in both cases (bottom) to ensure functional preservation. Taken from Drion et al. (2015a).

et al., 2018).

Recently, the depiction of neurons as mixed-feedback systems has garnered considerable interest in the development of neuromorphic control systems. Persistent efforts are directed towards establishing a robust theoretical framework to facilitate the creation of systems that are adaptive, implantable in electronic circuits, and amenable to simulation. Notably, the contributions of Thomas Chaffey, Rodolphe Sepulchre, and others have been instrumental in advancing the theoretical understanding of monotone operators, a fundamental aspect of mixed-feedback systems (Chaffey et al., 2023b; Chaffey and Sepulchre, 2023; Chaffey et al., 2023c; Das et al., 2022; Chaffey, 2022; Sepulchre et al., 2022; Chaffey et al., 2023a). They have also developed methodologies for systems integrating positive feedback with negative conductance and devised efficient simulation techniques inspired by optimization theory.

Building upon this theoretical foundation, mixed-feedback systems can be designed straightforwardly by integrating suitable positive and negative feedback loops into the passive membrane of a neuron, modeled as an RC circuit (Fernandez Lorden et al., 2023) (Fig. 12.5A). Recent advancements include achieving robust control of a pendulum using mixed feedback systems, demonstrating the ability to robustly control a pendulum solely through models mimicking action potentials. This approach mirrors biological processes by employing event-based processing and control through analog events, rather than continuous digital control

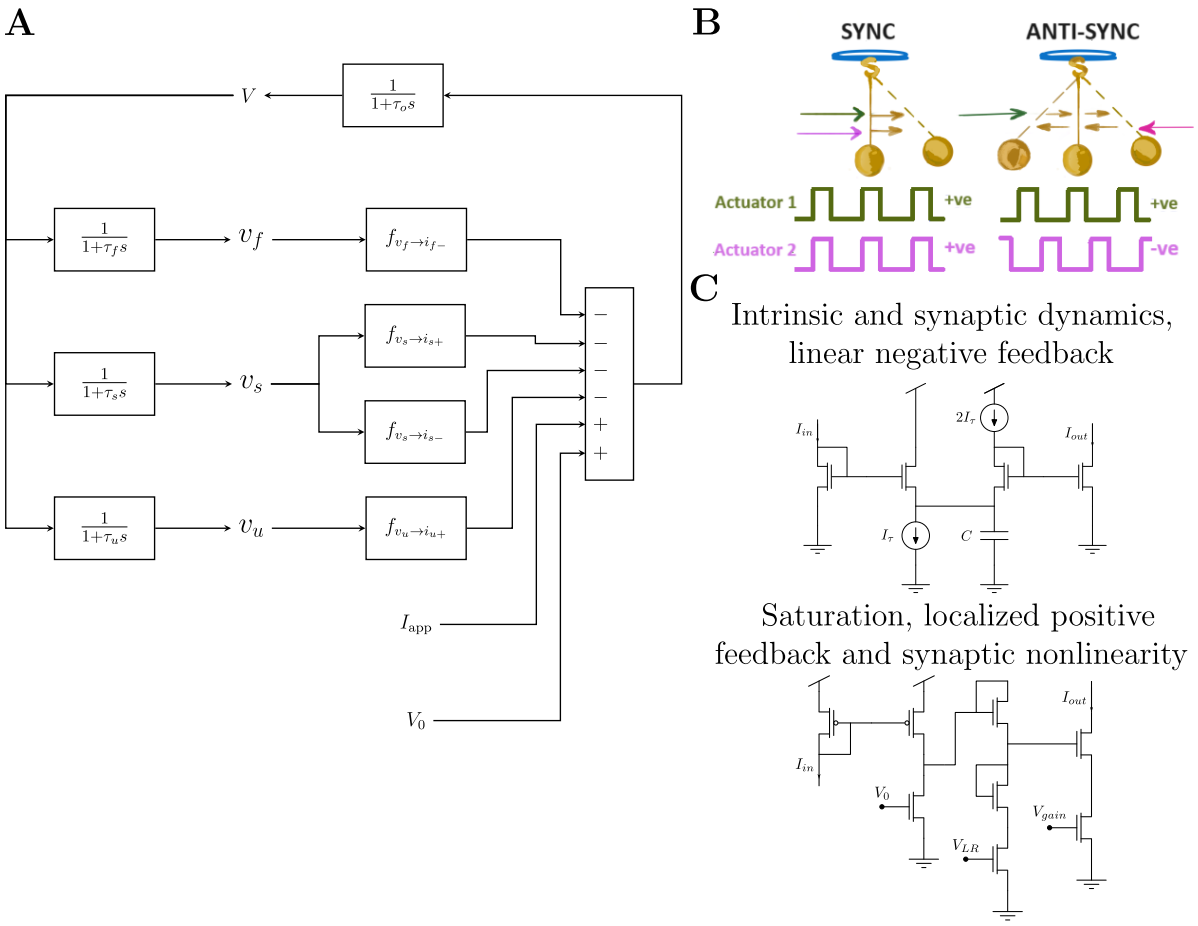

Figure 12.5: Mixed feedback systems and neuromorphic engineering. A. Illustration of a mixed feedback system mimicking neurons, showcasing their excitability and ability to spike in tonic or bursting modes. **B.** Recent application of such mixed feedback system for the control of a pendulum using various synchronization patterns of different neurons. **C.** Electronic implementation of a mixed feedback system in CMOS technology. Adapted from Fernandez Lorden et al. (2023); Schmetterling et al. (2024); Mendolia et al. (2023), with titles added on top of each schematic in panel C.

(Schmetterling et al., 2024) (Fig. 12.5B). Analog neurons implemented in silicon chips, inspired by mixed feedback theory, exemplify another avenue of exploration in this field (Mendolia et al., 2023) (Fig. 12.5C). Given the increasing urgency surrounding energy efficiency in artificial intelligence and control, further developments in neuromorphic control hold promise for the emergence of fully automated robots and AI systems reliant on mixed-feedback mechanisms involving spiking neurons.

13 Specific models used in this thesis

While the results in this thesis aim for broad applicability, three models from existing literature have been selected to illustrate them. These models were chosen for their high dimensionality and ability to show degeneracy and different types of electrical activity, such as regular firing and bursting, which are the main focuses of this thesis.

13.1 Stomatogastric neuron from crabs

The model discussed here originates from Liu et al. (1998) and represents neurons found in the stomatogastric (STG) ganglion of crustaceans. It enables the examination of various neuron types within the ganglion, including PY, PD, AB, and others. These neurons primarily contribute to rhythmic circuits responsible for generating rhythmic signals that trigger the contraction of stomach muscles in crustaceans. Their typical firing pattern involves pacemaking bursting.

13.1.1 Equations

The voltage equation of the STG model writes:

$$\begin{aligned} C\dot{V} = &- \bar{g}_{\mathrm{Na}} m_{\mathrm{Na}}^3 h_{\mathrm{Na}} (V - E_{\mathrm{Na}}) - \bar{g}_{\mathrm{CaT}} m_{\mathrm{CaT}}^3 h_{\mathrm{CaT}} (V - E_{\mathrm{Ca}}) - \bar{g}_{\mathrm{CaS}} m_{\mathrm{CaS}}^3 h_{\mathrm{CaS}} (V - E_{\mathrm{Ca}}) \\ &- \bar{g}_{\mathrm{A}} m_{\mathrm{A}}^3 h_{\mathrm{A}} (V - E_{\mathrm{K}}) - \bar{g}_{\mathrm{KCa}} m_{\mathrm{KCa}}^4 (V - E_{\mathrm{K}}) - \bar{g}_{\mathrm{Kd}} m_{\mathrm{Kd}}^4 (V - E_{\mathrm{K}}) \\ &- \bar{g}_{\mathrm{H}} m_{\mathrm{H}} (V - E_{\mathrm{H}}) - g_{\mathrm{leak}} (V - E_{\mathrm{leak}}) + I_{\mathrm{app}}, \end{aligned}$$

where the dot notation represents the time derivative, C is the membrane capacitance, Na stands for the sodium current, CaT for the T-type calcium current, CaS for the slow calcium current, A for the A-type potassium current, KCa for the calcium-controlled potassium current, Kd for the delayed rectified potassium current, H for the H current, and leak for the leakage current. All E values denote the channel reversal Nernst potentials, and I_{app} represents the externally applied current. The parameters of interest are the maximum ion channel conductances $\bar{g}$, expressed in $\mathrm{mS/cm^2}$, corresponding to the ion channel conductance when fully opened. Additionally, all m and h variables represent activation and inactivation gate variables, respectively, following first-order lag equations that are voltage-dependent. Notably, the KCa gating variable also depends on intracellular calcium concentration $[\mathrm{Ca}^{+2}]$, and its dynamical equation writes:

$$20 \cdot [\dot{\mathrm{Ca}}^{+2}] = -0.94 \left[\bar{g}_{\mathrm{CaT}} m_{\mathrm{CaT}}^3 h_{\mathrm{CaT}} (V - E_{\mathrm{Ca}}) + \bar{g}_{\mathrm{CaS}} m_{\mathrm{CaS}}^3 h_{\mathrm{CaS}} (V - E_{\mathrm{Ca}}) \right] - [\mathrm{Ca}^{+2}] + 0.05.$$

The time constants, steady-state functions of gating variables, and Nernst reversal potential values are detailed in Appendix B1.

13.1.2 Typical firing patterns

The typical firing patterns of this model encompass tonic firing, characterized by a relatively high frequency (approximately 15 Hz), as well as pacemaking bursting, that can exhibit between 2 and 5 spikes per burst (Fig. 13.1).

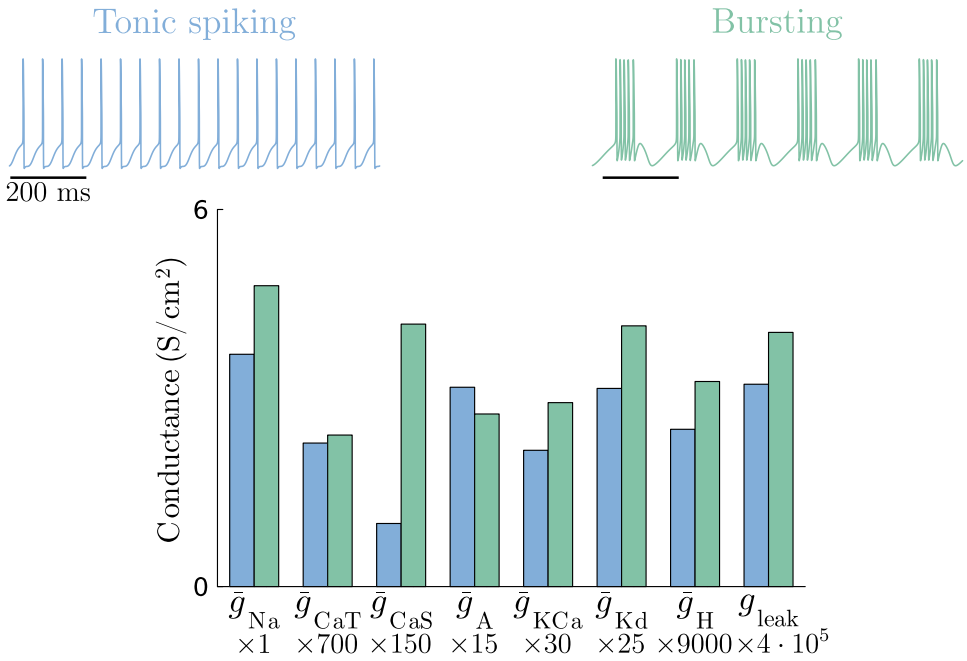

Figure 13.1: The stomatogastric model firing patterns. Tonic spiking (blue) and bursting (green) typical voltage traces of the STG model (top), along with associated conductance values (bottom).

13.2 Dopaminergic neurons

The model described here is derived from Qian et al. (2014) and represents midbrain dopaminergic (DA) neurons, renowned for their capacity to fire spikes at a highly consistent rate, typically around 1 Hz. These neurons play a crucial role in providing the brain with dopamine, a vital neuromodulator. Pacemaking firing serves to sustain a baseline level of dopamine, while burst mode activation allows for the release of additional dopamine when needed. It is worth noting that, compared to the original publication, SK channels were omitted from the model to facilitate bursting activity.

13.2.1 Equations

The voltage equation of the DA model writes:

$$\begin{aligned} C\dot{V} = &- \bar{g}_{\mathrm{Na}} m_{\mathrm{Na}}^3 h_{\mathrm{Na}} (V - E_{\mathrm{Na}}) - \bar{g}_{\mathrm{Kd}} m_{\mathrm{Kd}}^3 (V - E_{\mathrm{K}}) - \bar{g}_{\mathrm{CaL}} m_{\mathrm{CaL}}^2 (V - E_{\mathrm{Ca}}) \\ &- \bar{g}_{\mathrm{CaN}} m_{\mathrm{CaN}} (V - E_{\mathrm{Ca}}) - \bar{g}_{\mathrm{ERG}} m_{\mathrm{ERG}} (V - E_{\mathrm{K}}) - g_{\mathrm{leak}} (V - E_{\mathrm{leak}}) \\ &- \bar{g}_{\mathrm{NMDA}} \frac{(V - E_{\mathrm{NMDA}})}{1 + Mg \cdot exp(-0.08V)/10} + I_{\mathrm{app}}, \end{aligned}$$

where CaL represents the L-type calcium current, CaN the N-type calcium current, ERG the ERG current, and NMDA the NMDA current. Additionally, Mg denotes the extracellular magnesium concentration, assumed to be a constant of 1.4 µM.

The time constants, steady-state functions of gating variables, and Nernst reversal potential values are detailed in Appendix B2.

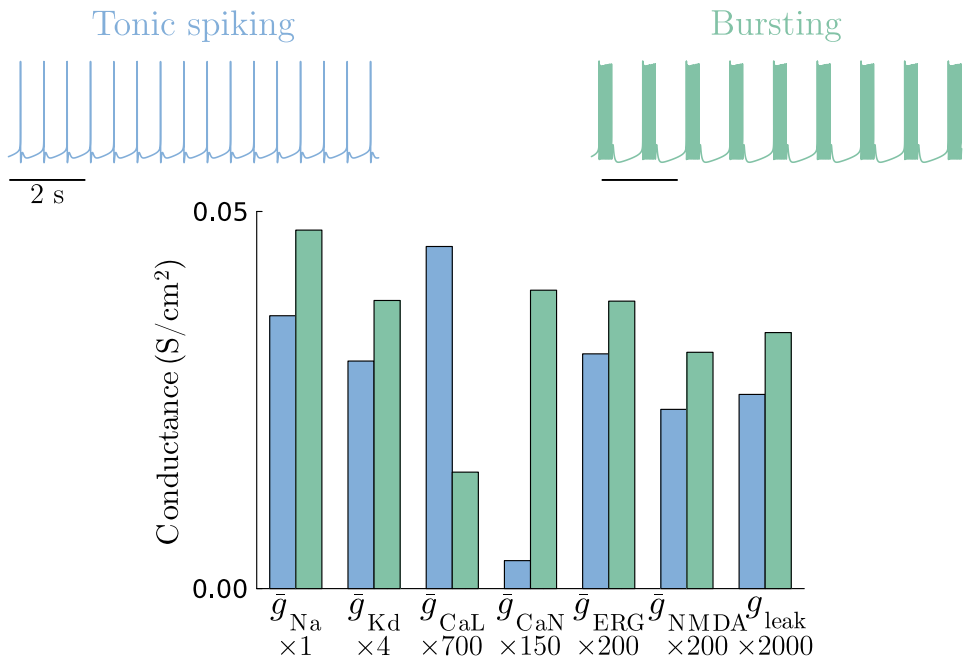

Figure 13.2: The dopaminergic model firing patterns. Tonic spiking (blue) and bursting (green) typical voltage traces of the DA model (top), along with associated conductance values (bottom).

13.2.2 Typical firing patterns

The typical firing patterns of this model comprise pacemaking firing, characterized by a highly regular frequency (approximately 1 Hz), as well as pacemaking bursting, typically featuring around ten spikes per burst (Fig. 13.2).

13.3 Aplysia neurons

The model discussed here is adapted from Plant and Kim (1976) (further refined in Plant (1981)) and represents neuron R15, situated in the abdominal ganglion of the gastropod mollusk *Aplysia californica* (Sieling and Butera, 2011). This neuron was among the first autonomously bursting neurons to undergo extensive electrophysiological study. Its bursting activity plays a pivotal role in the process of egg laying, a process occurring over a timescale of minutes (Alevizos et al., 1991). However, under typical *in vivo* conditions, these neurons do not exhibit bursting behavior.

13.3.1 Equations

The voltage equation of the aplysia model writes:

$$\begin{aligned} C\dot{V} = &- \bar{g}_{\mathrm{Na}} m_{\mathrm{Na},\infty}(V)^3 h_{\mathrm{Na}} (V - E_{\mathrm{Na}}) - \bar{g}_{\mathrm{Kd}} m_{\mathrm{Kd}}^4 (V - E_{\mathrm{K}}) - \bar{g}_{\mathrm{TTX}} m_{\mathrm{TTX}} (V - E_{\mathrm{Na}}) \\ &- \bar{g}_{\mathrm{KCa}} \frac{[\mathrm{Ca}^{+2}]}{0.5 + [\mathrm{Ca}^{+2}]} (V - E_{\mathrm{K}}) - g_{\mathrm{leak}} (V - E_{\mathrm{leak}}) + I_{\mathrm{app}}, \end{aligned} \tag{13.1}$$

where TTX represents the TTX-resistant inward current with slow activation. Note the instantaneous sodium activation gating variable. Notably, the KCa conductance depends on

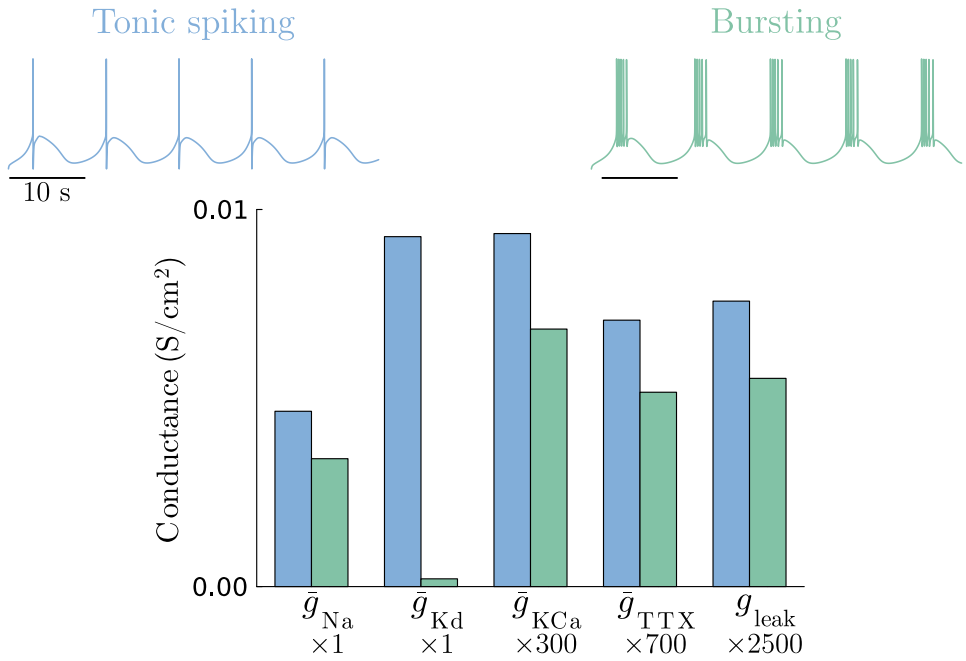

Figure 13.3: The aplysia R15 model firing patterns. Tonic spiking (blue) and bursting (green) typical voltage traces of the Plant model (top), along with associated conductance values (bottom).

intracellular calcium concentration $[\mathrm{Ca}^{+2}]$, and its dynamical equation writes:

$$3333 \cdot [\dot{\mathrm{Ca}}^{+2}] = -0.0085\,[\bar{g}_{\mathrm{TTX}} m_{\mathrm{TTX}} (V - E_{\mathrm{Ca}})] - [\mathrm{Ca}^{+2}].$$

The time constants, steady-state functions of gating variables, and Nernst reversal potential values are detailed in Appendix B3.

13.3.2 Typical firing patterns

The typical firing patterns of this model encompass pacemaking parabolic bursting, characterized by a very slow interburst frequency (approximately 0.1 Hz), with tens of spikes per burst, as well as tonic firing occurring at a frequency of a similar order of magnitude (Fig. 13.3).

Part III

Scientific results

This chapter focuses on the scientific results of this thesis, which can be summarized in four main points:

1. The first focus of this thesis is on exploring and understanding the foundations of neuronal degeneracy, as well as its behavior under neuromodulation. As a reminder, degeneracy refers to the property where distinct combinations of conductance values result in the same voltage activity. Although such phenomena have been studied experimentally, primarily in Marder Lab, no mechanistic explanations have been formulated to date. In computational neuroscience, the challenge lies in analyzing highly dimensional and nonlinear models, such as conductance-based models. The initial step involves formulating a mechanistic proposal for neuronal degeneracy and examining its behavior under neuromodulation. The results of this research have been published in an article (Fyon et al., 2024). I also had the opportunity to present these findings at the Annual Meeting of the Society for Neuroscience (SfN) held online in 2021 (Fyon and Drion, 2021).

2. With an understanding of neuronal degeneracy, the study then advances to robust neuromodulation. Robust neuromodulation refers to the consistent effect of neuromodulators (robust changes in firing activity), despite a highly heterogeneous neuronal population. Essentially, neurons that exhibit degeneracy respond similarly to the same amount of a particular neuromodulator. The next step of this thesis is to develop a general model of neuromodulation that can be integrated with any conductance-based model, based on the previously formulated mechanistic explanation of neuronal degeneracy. The results of this research have been published in an article (Fyon et al., 2023). I also had the opportunity to present these findings at the International Federation of Automatic Control (IFAC) World Congress in Yokohama, Japan, 2023.

3. This thesis also delves into further analyzing the behavior of this new model of neuromodulation across different types of conductance-based models, and its interaction with the widely accepted O'Leary model of homeostasis. The interplay between neuromodulation and homeostasis is crucial in neuroscience, as it enables neurons to adapt to external stimuli (neuromodulation) while maintaining basal cellular activity essential for survival (homeostasis). It is vital that our model of neuromodulation is both general and compatible with existing models of homeostasis to construct a comprehensive neuron model that includes both neuromodulation and homeostasis. This study illustrates how ion channel conductances behave when these two mechanisms operate in concert to achieve robust neural function. The results of this research have been published in a preprint (Fyon and Drion, 2024b). I also had the opportunity to present these findings at the Bernstein Conference in Berlin, Germany, 2023 (Fyon and Drion, 2023).

4. Lastly, this chapter focuses on developing an automatic way of designing any Central Pattern Generators (CPGs) that can switch smoothly to one rhythm to another using only neuromodulation. CPGs are self organized neuronal circuits that can produce a rhythmic output, without rhythmic input (Selverston, 2010). It is often composed of rebound bursters or autonomously bursting neurons connected using inhibitory synapses. The simplest example is the half center oscillator, that produces a simple rhythm without any input. Designing a method for more complex rhythms seemed necessary, as no design rules have been formulated to date. I had the opportunity to present these findings at 43rd Benelux Meeting on Systems and Control in Blankenberge, Belgium, 2024 (Fyon and Drion, 2024a). I also had the opportunity to present these findings at the Federation of European Neuroscience Societies (FENS) Forum in Vienna, Austria, 2024 (Fyon and Drion, 2024c).

14 Dimensionality reduction of neuronal degeneracy reveals two interfering physiological mechanisms

This section is adapted from:
A. Fyon, A. Franci, P. Sacré, G. Drion,
Dimensionality reduction of neuronal degeneracy reveals two interfering physiological mechanisms,
PNAS Nexus,
Volume 3, Issue 10,
2024,
pgae415,
https://doi.org/10.1093/pnasnexus/pgae415
(https://academic.oup.com/pnasnexus/article/3/10/pgae415/7762142)
Fyon et al. (2024)

14.1 Preface

Before delving to neuromodulation modeling, this thesis focuses on the identification and quantification of mechanisms underlying degeneracy. The initial phase involves identifying functional variables that uniquely determine neuronal activity and can be correlated with degenerate physiological variables (such as ion channel density, etc.). Having this set of variables is crucial before delving into the design of the neuromodulation controller, as non-degenerate references and variables are necessary to address any ambiguities related to neuronal parameter heterogeneity. To achieve this goal, we worked with families of high-dimensional conductance-based models with random intrinsic conductance values taken in large sets, starting with the STG model published in Liu et al. (1998) and a DA neuron model published in Qian et al. (2014). We applied recent analysis tools (DICs) that were developed in my host research group (Drion et al., 2015a), which provide a promising angle of attack. One expected outcome of this section is the creation of an algorithm capable of automatically tuning a subset of ion

channels in conductance-based models in response to a neuromodulatory signal to achieve reliable neuromodulation in highly variable cells.

14.2 Introduction

A remarkable property of nervous systems is their ability to maintain stable functions despite large variability and turnover of the underlying physiological components. This observation has led to the understanding that neuron electrophysiological properties are shaped by the coordinated expression of potentially large subsets of ion channels (Goaillard and Marder, 2021), which represent a substantial challenge in any attempt to link ion channel properties with neuron electrophysiological signature.

In recent decades, a combination of experimental and computational work has provided insights into the relationship between the densities of ion channels and neuronal signaling. First, it has been clarified that different combinations of ion channels can lead to similar activity despite substantial variation in channel densities (Achard and De Schutter, 2006; Alonso and Marder, 2019; Prinz et al., 2004; Swensen and Bean, 2005; Taylor et al., 2009), as a result of functional overlap in channel voltage- and time-dependent properties (Drion et al., 2015a; Goaillard and Marder, 2021). Second, it has been shown experimentally that ion channel expression correlates positively in the same neuron type, while the correlation graphs vary among different neuron types (Amendola et al., 2012; Liss et al., 2001; Schultz, 2007; Schulz et al., 2006b, 2007; Tobin et al., 2009). It has been revealed that these positive correlations in ion channel expression emerge from physiologically plausible homeostatic rules (O'Leary et al., 2014). One could thus argue that specific correlation graphs in channel expression are an important neuronal signature. Third, reliable neuromodulation has been shown to often occur through a concomitant action on several channel subtypes (Amendola et al., 2012; Grashow et al., 2009; Marder and Bucher, 2007; Nadim and Bucher, 2014; Schulz et al., 2006a), which highlights the importance of understanding the mechanisms that link the density of ion channels and neuronal signaling.

Although this body of work has deepened our understanding of how ion channels shape neuronal activity, many important questions remain. First, although most studies have reported positive correlations in ion channel expression, studies on correlations in actual conductance values have revealed a less clear picture. Correlations in conductance values are observed, but the intensity of the correlation can vary and it can be either positive or negative depending on the ion channel subtype and neuron subtype (Iacobas et al., 2019; Khorkova and Golowasch, 2007; Kodama et al., 2020; Tapia et al., 2018). In addition, correlations in both ion channel expression and conductance values can be dependent on activity and neuromodulation (Santin and Schulz, 2019; Temporal et al., 2012). Given these negative correlations in conductance values, the question arises of what potentially complex mechanism might link channel expression and conductance value. Here, we attempt to answer this question by analyzing how positive and negative conductance correlations arise in highly degenerate parameter sets of two different conductance-based models. We show that pairwise correlations in channel conductance are the result of two interfering mechanisms. Such interference is activity-dependent, which results in activity-dependent correlation levels. Another unanswered question involves the fact that, at present, our understanding of how ion

channels shape neuronal activity remains largely qualitative. The lack of a concrete mechanistic understanding makes it extremely difficult to quantify how specific changes in ion channel density affect neuronal output, which in turn makes the study of reliable neuromodulation laborious. Here, we provide such a mechanistic understanding through a dimensionality reduction analysis of the two degenerate parameter sets. The geometry of the principal components found by dimensionality reduction methods is fully explained by the geometry of the sensitive directions in the maximal conductance space, as revealed by using feedback control ideas (Drion et al., 2015a). This analysis permits the derivation of a simple, physiologically plausible rule explaining how neuromodulation can be achieved reliably in highly degenerate neurons.

14.3 Results

14.3.1 Neuronal degeneracy in conductance-based models is associated with variable pairwise correlations in channel conductances

We first created variable sets of conductances leading to stable firing patterns in two different neuron conductance-based models (Fig. 14.1): a stomatogastric (STG) neuron model (Liu et al., 1998) (left) and a dopaminergic (DA) neuron model (adapted from Qian et al. (2014)) (right). All simulations and analyses were performed on these two different models to avoid uncovering model-specific features, but rather to focus on general properties. Each parameter set was created through random sampling followed by a post-processing procedure that selected models sharing specific firing pattern characteristics (Prinz et al., 2004). Each model was first studied in its nominal firing pattern: burst firing for the STG neuron model, and slow tonic spiking for the DA neuron model (see Materials and Methods). An example of each firing pattern is shown at the top, right of each panel in Fig. 14.1A.

Fig. 14.1A shows a scatter plot matrix of ion channel maximal conductances for a subset of ion channel types in both models, as well as the correlation computed for each pair. As observed in previous experimental and computational work (Goaillard and Marder, 2021; Khorkova and Golowasch, 2007), correlations can vary markedly between different pairs of conductances, from strongly positive (such as $\bar{g}_{\mathrm{Na}}$ and $\bar{g}_{\mathrm{A}}$ in STG model), to negative (such as $\bar{g}_{\mathrm{A}}$ and $\bar{g}_{\mathrm{Kd}}$ in STG model), or seemingly uncorrelated. This highlights the strong degeneracy of both conductance-based models, despite the fact that they maintain their respective firing activity using different types of ion channels.

To gain deeper insights into how conductances correlate to maintain robust and consistent firing activity, we represent the pairwise correlations between all conductances using correlation graphs (Fig. 14.1B). Each node represents a conductance, the thickness of the edges connecting each node represents the strength of the correlation, and the color of each edge represents the correlation sign (red for positive and blue for negative). These two graphs show similar trends for the two models: correlations between ion channels are mostly positive, but there are also negative correlations in a small subset of conductance pairs. This is intriguing for two reasons.

First, to maintain similar firing activity, one would expect conductances that are sources of currents of the same sign to correlate negatively, whereas conductances that are sources of currents

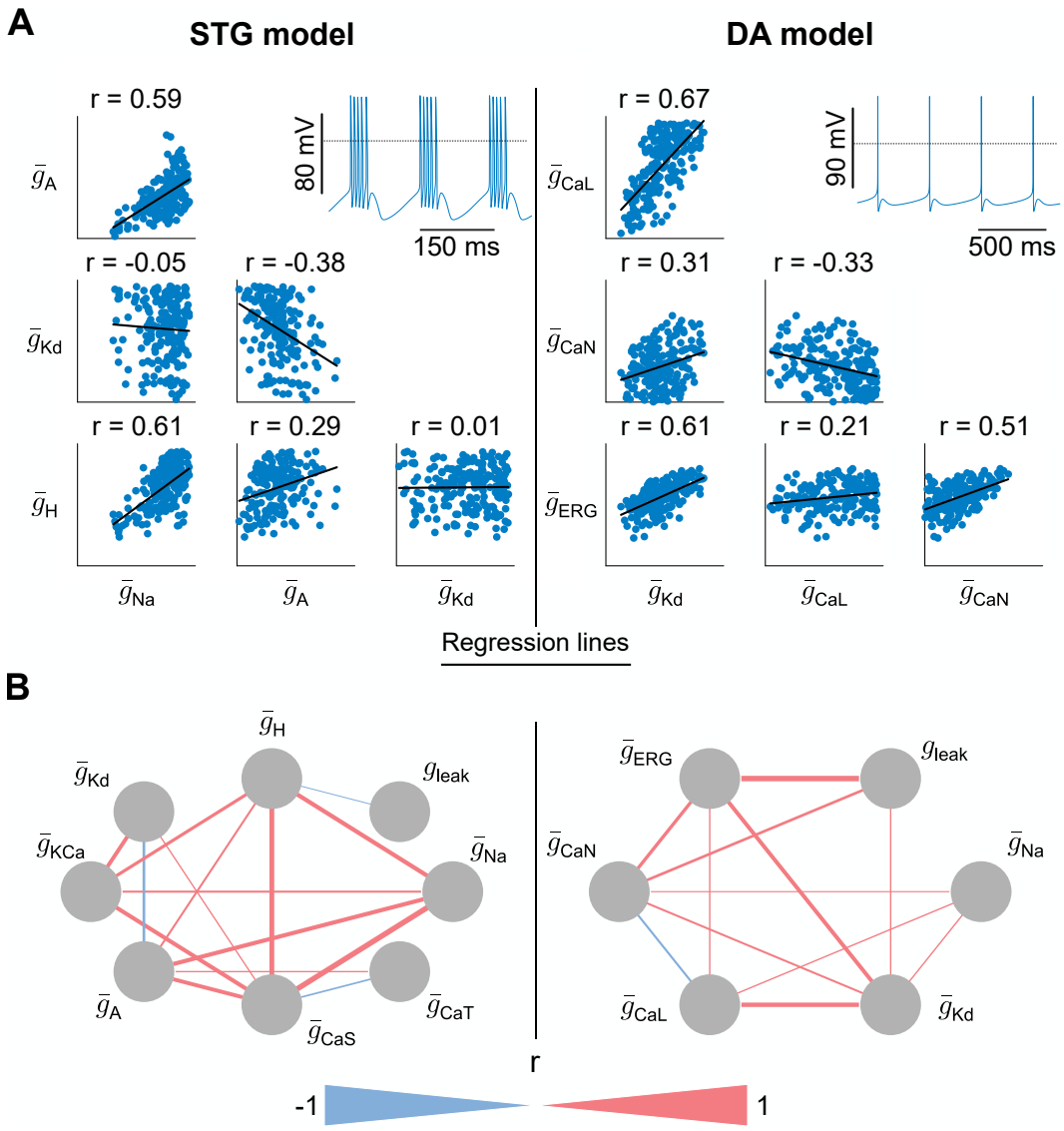

Figure 14.1: Neuronal degeneracy in conductance-based models is associated with variable pairwise correlations in channel conductances.
(A) Scatter plot matrices of random sampling populations in the conductance spaces for the STG model (left) and the DA model (right), along with regression lines. The pairs depicted here do not represent all conductances of the models and are randomly chosen to illustrate the variable correlations, expressed by the Pearson correlation coefficient (r). All conductances are expressed in mS/cm^2. The bottom left corner of each scatter plot represents the origin of the conductance space. For the STG model, $\bar{g}_{\mathrm{A}}$ ranges up to 600, $\bar{g}_{\mathrm{Kd}}$ to 350, $\bar{g}_{\mathrm{H}}$ to 0.7 and $\bar{g}_{\mathrm{Na}}$ to 8000. For the DA model, $\bar{g}_{\mathrm{CaL}}$ ranges up to 0.1, $\bar{g}_{\mathrm{CaN}}$ to 0.12, $\bar{g}_{\mathrm{ERG}}$ to 0.25 and $\bar{g}_{\mathrm{Kd}}$ to 20. The dotted line on the voltage traces corresponds to 0 mV.
(B) Correlation graphs of all conductances of the random sampling populations for the STG model (left) and DA model (right). A blue (red) line indicates a negative (positive) pairwise correlation. The thickness of the line represents the absolute value of the correlation. Correlations below a certain threshold, corresponding to the inverse of the number of conductances in the considered model (1/8 and 1/6 in the STG and DA models respectively), are not shown.

of the opposite sign would correlate positively. This would allow the global transmembrane current, hence excitability, to be maintained at a steady level. However, this is not what is observed in Fig. 14.1B. If we take the example of $\bar{g}_{\mathrm{CaS}}$ in the STG model, which is a source

of inward current, it can correlate either negatively or positively with other sources of inward currents ($\bar{g}_{\mathrm{CaT}}$ and $\bar{g}_{\mathrm{Na}}$, respectively). Likewise, outward current sources can correlate either negatively or positively with other outward sources (i.e. $\bar{g}_{\mathrm{Kd}}$ with $\bar{g}_{\mathrm{A}}$ and $\bar{g}_{\mathrm{KCa}}$ in the STG model). The same observation can be made for the DA neuron model.

Second, experimental studies on the correlation between ion channel mRNA and computational models of neuronal homeostasis have uncovered the existence and emergence of neuron-dependent, strictly positive correlations in channel densities (Goaillard and Marder, 2021; O'Leary et al., 2013; Tobin et al., 2009). A similar trend emerges from our data set, where the vast majority of correlations are indeed positive. However, in opposition to homeostasis models and in agreement with experimental data (Khorkova and Golowasch, 2007), negative correlations are also observed, suggesting that correlations emerging from homeostatic rules are important for the maintenance of robust firing activity, but that some other mechanisms must be at play.

14.3.2 A few principal components capture neuronal degeneracy but do not single out channel functions

As pairwise correlations between conductances alone did not provide much insight into how ion channels correlate to maintain robust firing activity, we performed principal component analysis (PCA) of both random sampling sets in an attempt to uncover low-dimensional subspaces in the data. We observed that a limited number of principal components, namely, four for the STG model and three for the DA model, accounts for more than 80% of the total variances in the data (Fig. 14.2A). We chose to focus our analysis on these significant principal components. The first principal component accounted for approximately 40% of the variance in both models. This observation is encouraging, as it shows that the mechanisms that drive conductance joint distribution in neuron models are low-dimensional, which is key for interpretability.

We then extracted the contribution of each conductance in each of the principal components, with the hope of observing a pattern that would allow us to make predictions on the biophysics behind these components (Fig. 14.2B). However, the results were difficult to interpret, as a variety of conductances contributed to the different principal components for both models. Moreover, conductances that made substantial contributions to the first principal component in one model did not do so in the other (*e.g.*, see the role of $\bar{g}_{\mathrm{Na}}$ or g_{leak} in the two models), which prevented the extraction of a model-independent rule from a naive analysis focusing on the role of single conductances. Although this last observation might seem unsurprising, as both models relate to different neurons exhibiting different firing patterns from different ion channels, we still aim to find some common, general mechanisms that might rule the degeneracy in ion channel conductances.

14.3.3 Dominant principal component captures homogeneous scaling of maximal conductances

As the first principal component (PC1) accounted for a large portion of the variability in the data for both models (approximately 40 %), we further analyzed its role by creating scatter plots of conductance values for a subset of four conductances that play dominant roles in PC1 (Fig. 14.3A). Interestingly, according to these scatter plots, all conductances that play significant

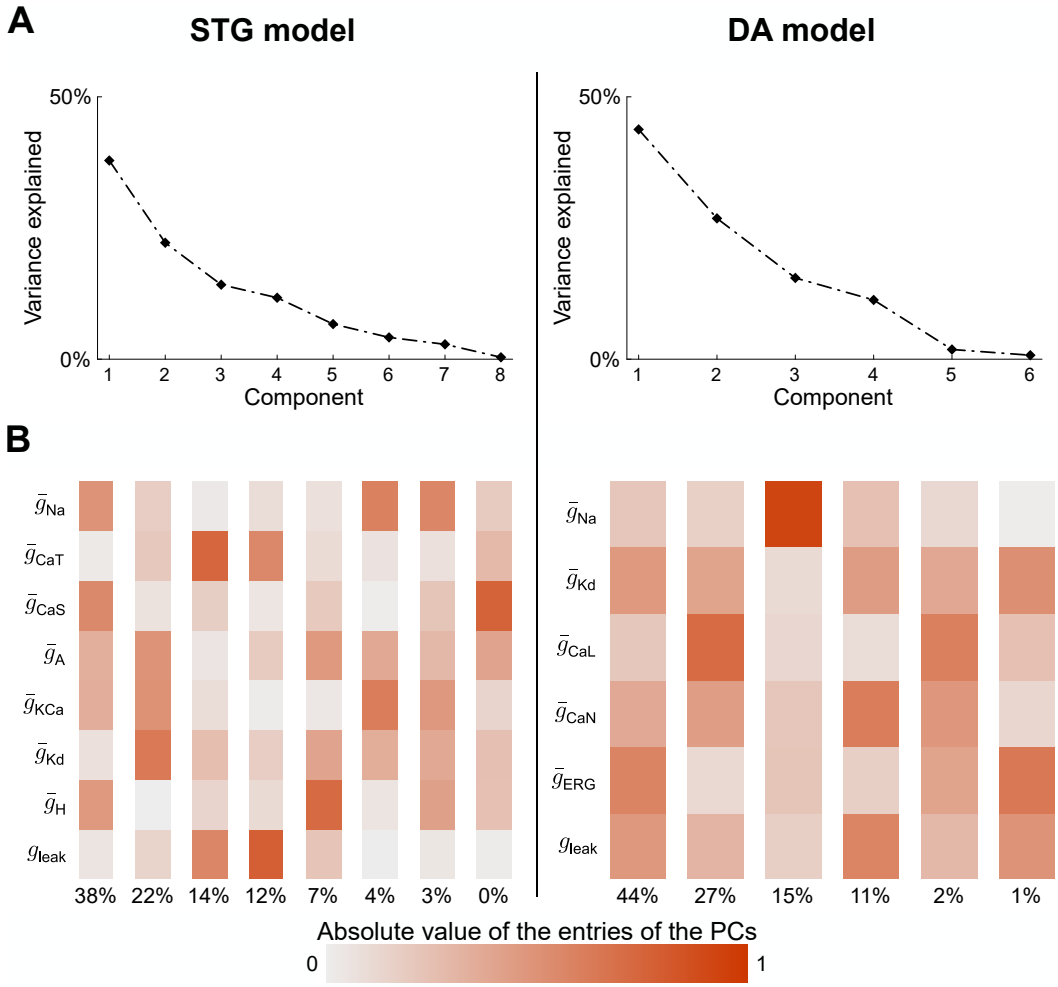

Figure 14.2: A few principal components capture neuronal degeneracy but do not single out channel functions.
(A) Scree plot of PCA applied to the conductance spaces of random sampling populations for the STG model (left) and the DA model (right).
(B) Absolute values of the entries of the PCs in the conductance space for the STG model (left) and the DA model (right).

roles in PC1 are strongly positively correlated with each other in both models. This is highly reminiscent of previous observations in channel mRNA data or the channel correlations emerging from models of neuronal homeostasis (Marder and Goaillard, 2006; O'Leary et al., 2013; O'Leary et al., 2014). In particular, such positive correlations follow a direction passing roughly through the origin.

This direction is close to the homogeneous scaling direction in the maximal conductances. The direction of homogeneous scaling corresponds to the total least squares regression direction without intercept, *i.e.*, to the direction connecting the origin of the conductance space to the center of mass of the degeneracy set. This center of mass represents the means of every type of conductance across the population. While pairwise homogeneous scaling is only evident in a subset of ion channels, this observation extends to the entire conductance space. The alignment between PC1 and homogeneous scaling in the full conductance space was robustly confirmed in both the STG and the DA models, with a notable 0.8 alignment in the former and a remarkable

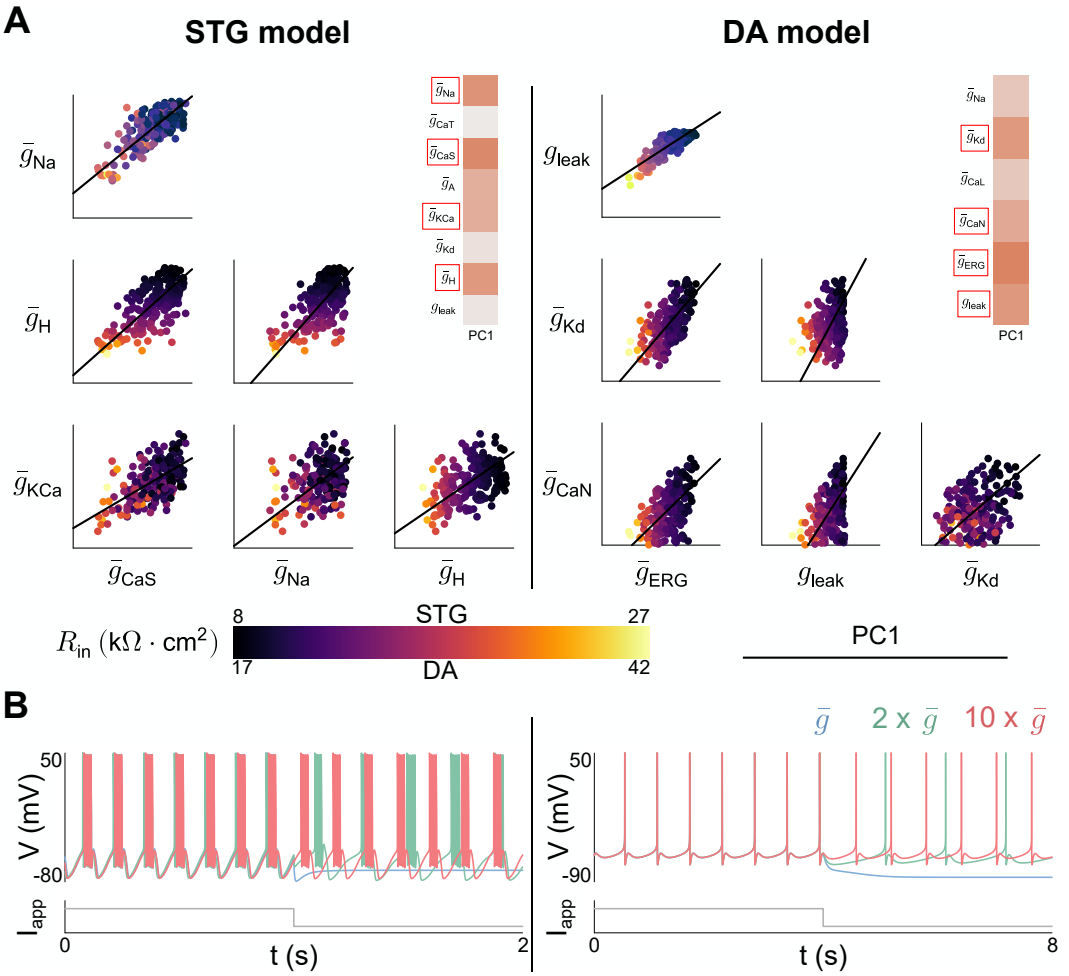

Figure 14.3: Dominant principal component captures homogeneous scaling of maximal conductances.
(A) Scatter plot matrices of random sampling populations in the conductance spaces for the STG model (left) and the DA model (right) along with the direction of PC1, color coded based on the input resistance. The scatter plots shown are associated with the conductances having the largest entries (in absolute value) in the first PC. All conductances are expressed in mS/cm^2. The bottom left corner of each 2D subspace represents the origin of the conductance space. For the STG model, $\bar{g}_{Na}$ ranges up to 8000, $\bar{g}_H$ to 0.7, $\bar{g}_{KCa}$ to 250 and $\bar{g}_{CaS}$ to 50. For the DA model, g_{leak} ranges up to 0.02, $\bar{g}_{Kd}$ to 20, $\bar{g}_{CaN}$ to 0.12 and $\bar{g}_{ERG}$ to 0.25.
(B) Simulations illustrating the effect of homogeneous scaling for the STG model (left) and the DA model (right). A random model from the scatter plot in (A) receives an inhibitory input (blue). The same experiment is then conducted with all conductances multiplied by 2 (green) and 10 (red).

0.9 alignment in the latter. This alignment was computed as the dot product between the unit vectors along PC1 and homogeneous scaling direction. Alternatively, it can be interpreted as the cosine of the angle formed by these two directions in the high-dimensional space of conductances.

The dominant role of homogeneous scaling of conductances in neuronal degeneracy can be understood by its functional significance. Such homogeneous scaling can emerge from homeostatic models of ion channel expression, where the slope between a pair of conductances correlates with the type of neuronal activity (O'Leary et al., 2014). This slope is determined by the ratio of

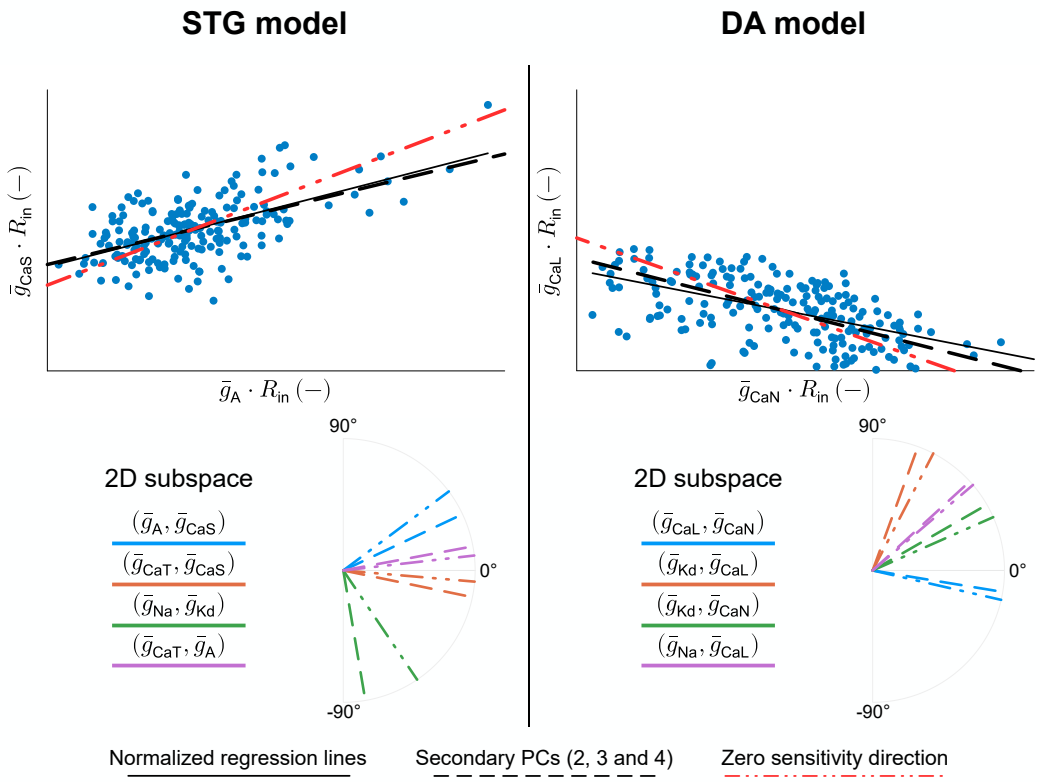

Figure 14.4: Normalization of the dataset by the input resistance reveals that the secondary principal components capture variable conductance ratios that maintain neuronal activity.
Scatter plots (top) of random sampling populations in the $(\bar{g}_{\mathrm{A}}, \bar{g}_{\mathrm{CaL}})$ 2D subspace for the STG model (left) and the $(\bar{g}_{\mathrm{CaL}}, \bar{g}_{\mathrm{CaN}})$ 2D subspace for the DA model (right) , normalized by the input resistance, along with the regression lines of the normalized dataset (solid line), secondary PCs of the non-normalized dataset (dashed line), and the zero sensitivity direction (dash-dotted line). The bottom left corners of the scatter plots represent the origin of the conductance space, and the ranges are irrelevant. Polar plots of secondary PCs and the zero sensitivity direction in randomly chosen 2D subspaces of the conductance space (bottom).

regulation time constants. Homogeneous scaling also permits modulation of the neuron response to external inputs while its intrinsic firing pattern is maintained unaffected. Indeed, increasing all conductances by a common factor permits an increase in the global membrane permeability, which decreases the responsiveness to external input through a decrease in input resistance R_{in} (Fig. 14.3B). As indicated by the color coding in Fig. 14.3A, the direction of PC1, which represents homogeneous scaling, aligns with the variability in neuron input resistance in both models. At the same time, it does not affect the ratio between channel conductances, thus maintaining firing activity. Therefore, homogeneous scaling plays a critical role in excitability modulation and homeostasis.

14.3.4 Normalization of the datasets by the input resistance reveals that the secondary principal components capture variable conductance ratios

Analysis of the remaining meaningful principal components (PC2, PC3, and PC4 in the STG model, and PC2 and PC3 in the DA model) should shed light on the physiological origin of most

of the remaining variance in the data. However, these principal components have highly variable slopes in the different conductance planes, making the analysis less straightforward than for PC1. The effect of homogeneous scaling is intertwined with the other potential origins of degeneracy in neuron model populations, which complicates matters further.

To circumvent this problem, we removed the effect of PC1 by normalizing the dataset by neuron input resistance, thereby eliminating the effect of homogeneous scaling. This was achieved by multiplying each conductance by R_{in} (*i.e.* dividing by the input conductance g_{in}). The regression lines of the normalized dataset almost perfectly coincide with the secondary PCs of the non-normalized dataset (Fig. 14.4), demonstrating that normalization by input resistance effectively suppresses the effect of PC1.

Once the effect of homogeneous scaling is removed, the remaining variability corresponds to changes in conductance ratios that do not impact neuron input resistance. Degeneracy in conductance ratios can be quantified by leveraging the concept of dynamic input conductances (DICs) (Drion et al., 2015a), which provides a way of linking channel conductance ratios with firing activity. In short, it was shown that the dynamical effects of ion channel gating on neuron activity could be captured by a few voltage-dependent conductance curves (DIC) acting on separate timescales. For a bursting neuron, three timescales are sufficient: a fast timescale characterizing spike upstroke; a slow timescale characterizing spike downstroke, neuron excitability type and rest-spike bistability; and an ultraslow timescale characterizing burst parameters such as period and duty cycle. The value of each DIC at the threshold potential on each timescale determines firing activity, and each parameter set leading to similar DIC values leads to similar firing activities. We exploited this last property to understand the variability that remains in the normalized dataset by identifying directions of zero sensitivity in the maximal conductance space, *i.e.*, directions along which changes in maximal conductances do not affect DIC values at threshold, and hence lead to similar spiking behavior (Drion et al., 2015a).

We then verified if variability in conductance ratio leading to similar DIC values was the dominant source of degeneracy in the normalized dataset by computing zero sensitivity directions of the slow DIC in both STG and DA neuron models and comparing these directions with the secondary principal components of the original dataset (PC2, PC3, and PC4). Indeed, we found that the effect of the slow DIC was dominant on degeneracy, as the slow DIC is the main player in determining neural excitability types by governing spiking-to-bursting transitions and the regulation of cellular rest-spike bistability (for further details, see Materials and Methods). In both models, the zero-sensitivity directions strongly align with one of the secondary principal components in the original random sampling set (Fig. 14.4), and thus with the regression line of the normalized dataset. This confirmed that the second origin of degeneracy in ion channel expression can be explained by the existence of variable conductance ratios that create similar membrane dynamical properties.

Degeneracy in conductance ratios is also functionally significant for robust neuronal signaling. Relying on different conductance ratios to create similar firing activity allows the creation of heterogeneity in response to external perturbations such as changes in temperature or pH (Haley et al., 2018; Rinberg et al., 2013), as well as specific ion channel blockades or dysfunction,

which increases neuronal robustness. It also creates variable responses to exogenous neuroactive drugs, and allows for compensation during long-lasting drug exposure or a genetic defect in the expression of a specific channel.

14.3.5 An alternative approach to building degenerate parameter sets allows the effect of homogeneous scaling to be separated from variability in conductance ratios

To better understand how homogeneous scaling and variability in conductance ratios interfere with each other, we constructed a new dataset that allowed us to separate these two effects. We created datasets of similar firing patterns by allowing randomness in all conductances but one per timescale, and adapting the remaining conductances to ensure that DIC values are kept constant (for further details, see Materials and Methods). Importantly, to be able to separate the effect of homogeneous scaling from other sources of ion channel degeneracy, we normalized DIC values by g_{leak}. This normalization allows the creation of variable conductance ratios that barely affects homogeneous scaling, which is itself mostly captured through variability in g_{leak}. We decided to perform normalization using g_{leak} instead of R_{in} for computational efficiency, as R_{in} depends on all conductances and is voltage-dependent. Note that homogeneous scaling is equally well captured using R_{in} or g_{leak}, since the leak conductance is the dominant current source below the threshold potential in both models.

The dataset constructed using this approach created neurons exhibiting similar firing activities (see supplementary Fig.) and showed close qualitative similarities to the dataset produced through random sampling in both models: pairwise correlations in channel conductances are highly variable between channel pairs, with a positive correlations dominating but negative correlations also being found, while the first principal component aligns with homogeneous scaling and the second principal component has highly variable slopes in the different conductance planes (Fig. 14.5A).

This dataset is easily seen to be generated by two subspaces in the maximal conductance space (Fig. 14.5B): one characterized by variability solely in g_{leak} (triangles in Fig. 14.5B) and the other exhibiting variability exclusively in voltage-gated conductance ratios along DIC zero sensitivity directions (crosses in Fig. 14.5B). Variability in g_{leak} only creates a degenerate dataset with strong, strictly positive correlations between conductance pairs, which isolates the effect of homogeneous scaling in channel conductances. Regression slopes of these subsets strongly align with the first principal component of the randomly sampled dataset. Variability limited to voltage-gated conductances (and fixed g_{leak}) creates a degenerate dataset that also shows strong pairwise correlations. However, these correlations can be either positive or negative, and their regression slopes do not intersect the origin. Within this subset, the correlation between pairs of conductances arises from their distinct roles in shaping DIC values at threshold, and the slow DIC in particular. Channels that have an opposite effect on the slow DIC show a positive correlation ($\bar{g}_{\text{CaS}}$ and $\bar{g}_{\text{A}}$ in the STG), whereas channels that have similar effects show a negative correlation ($\bar{g}_{\text{CaL}}$ and $\bar{g}_{\text{CaN}}$ in the DA model). The regression slopes within this subset strongly align with the second principal component (PC2) of the complete dataset (compare PC2 in Fig. 14.5A with crosses in Fig. 14.5B).

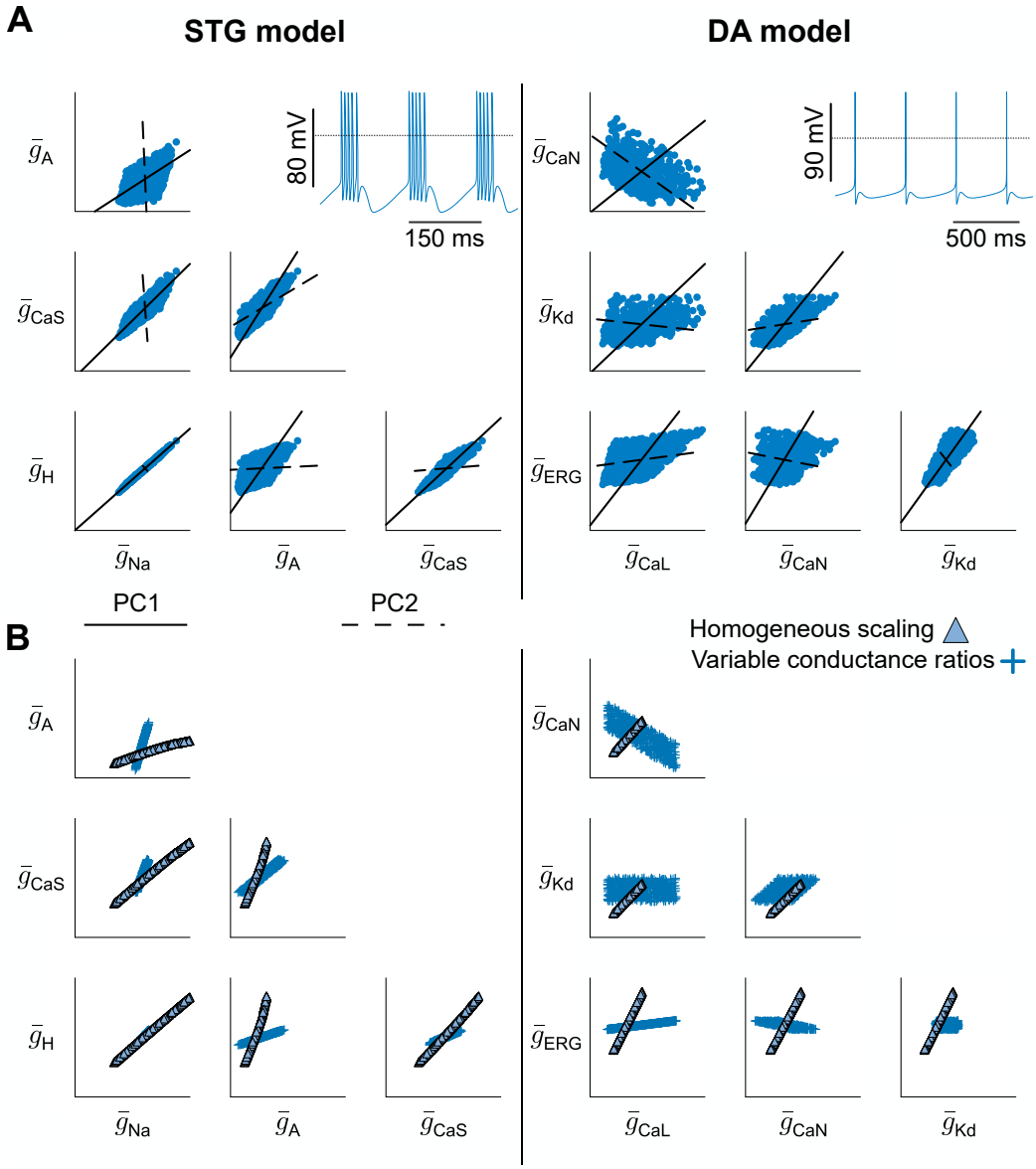

Figure 14.5: An alternative approach to building degenerate parameter sets allows the effect of homogeneous scaling to be separated from variability in conductance ratios.

(A) Scatter matrices of custom generated populations in the conductance spaces for the STG model (left) and the DA model (right) along with the directions of PC1 and PC2. The 2D subspaces shown here do not represent all conductances of the models and are randomly chosen. All conductances are expressed in mS/cm^2. The bottom left corner of each 2D subspace represents the origin of the conductance space. For the STG model, $\bar{g}_{\mathrm{A}}$ ranges up to 600, $\bar{g}_{\mathrm{CaS}}$ to 50, $\bar{g}_{\mathrm{H}}$ to 0.7 and $\bar{g}_{\mathrm{Na}}$ to 8000. For the DA model, $\bar{g}_{\mathrm{CaN}}$ ranges up to 0.12, $\bar{g}_{\mathrm{Kd}}$ to 20, $\bar{g}_{\mathrm{ERG}}$ to 0.25 and $\bar{g}_{\mathrm{CaL}}$ to 0.1. The dotted line on the voltage traces corresponds to the 0 mV line.

(B) Scatter matrices of custom generated populations in the conductance spaces for the STG model (left) and the DA model (right), isolating the effects of homogeneous scaling only (resp. variability in conductance ratios) shown as triangles (resp. crosses). The 2D subspaces are the same as in (A). All conductances are expressed in mS/cm^2. The bottom left corner of each 2D subspace represents the origin of the conductance space. For the STG model, $\bar{g}_{\mathrm{A}}$ ranges up to 600, $\bar{g}_{\mathrm{CaS}}$ to 50, $\bar{g}_{\mathrm{H}}$ to 0.7 and $\bar{g}_{\mathrm{Na}}$ to 8000. For the DA model, $\bar{g}_{\mathrm{CaN}}$ ranges up to 0.12, $\bar{g}_{\mathrm{Kd}}$ to 20, $\bar{g}_{\mathrm{ERG}}$ to 0.25 and $\bar{g}_{\mathrm{CaL}}$ to 0.1.

This alternative approach to building degenerate parameter datasets shows that variable pairwise correlations in channel conductances could result from the interaction of two distinct factors: homogeneous scaling, which maintains the ratio between ion channel conductances; and variable conductance ratio, which leads to similar DIC values and hence similar membrane dynamical properties.

14.3.6 Variability from both homogeneous scaling and variable conductance ratios blurs the connection between conductance correlation and function

Our analysis so far shows that variability from homogeneous scaling creates strong positive correlations in channel conductances. Meanwhile, variability in voltage-gated conductance ratios also leads to strong correlations in channel conductances, but these can be either positive or negative depending on the channel pair (Fig. 14.6A). When both types of variability are present within a neuron population, these two correlation mechanisms interfere with each other to create highly variable levels of correlations between channel pairs (Fig. 14.6B). If both types of variability create positive correlations, the interference is minimal, and the global correlation in channel conductance remains strong (Fig. 14.6, left). However, if the variability in conductance ratios creates a negative correlation, the interference is consequential, and the global correlation in channel conductance becomes weak (Fig. 14.6, right). This observation is of interest, as it shows that the variable pairwise correlation observed in channel conductance values originate from potentially competing effects rather than from an actual uncorrelated role in our datasets.

From an experimental perspective, this analysis helps us to understand how recorded ion channel conductances are correlated. Homogeneous scaling always results in a strong positive correlation. Therefore, an overall positive correlation would indicate that the channels are functionally antagonistic, as their variable conductance ratios align with the direction of homogeneous scaling. Conversely, if the overall correlation is non-significant or slightly negative, this suggests that the channels are either functionally uncorrelated or agonistic. In these cases, the positive correlation from homogeneous scaling is counteracted by variability in conductance ratios, leading to a null or negative correlation, respectively. Experimentally, the normalization of channel conductances by input resistance can reveal correlations arising solely from variable conductance ratios, thus dissociating the two sources of degeneracy (see additional material for other 2D subspaces).

14.3.7 Variability in pairwise correlations in conductance values is neuromodulation-dependent

The variability in channel pairwise correlation level is therefore linked to the relative slope of the correlations created by both variability types, homogeneous scaling and variable conductance ratios. This has an interesting consequence when one studies the effect of neuromodulation on the correlation in channel conductance. To illustrate this consequence, we performed a simple computational experiment where we neuromodulated the excitability state of both models from spiking to light bursting to strong bursting (Fig. 14.7). In both cases, the neuromodulator affects the maximal conductance of two channel types: $\bar{g}_{\mathrm{A}}$ and $\bar{g}_{\mathrm{CaS}}$ in the STG model, and $\bar{g}_{\mathrm{CaL}}$ and $\bar{g}_{\mathrm{CaN}}$ in the DA model (Fig. 14.7A).Those conductances are known to affect the burstiness of

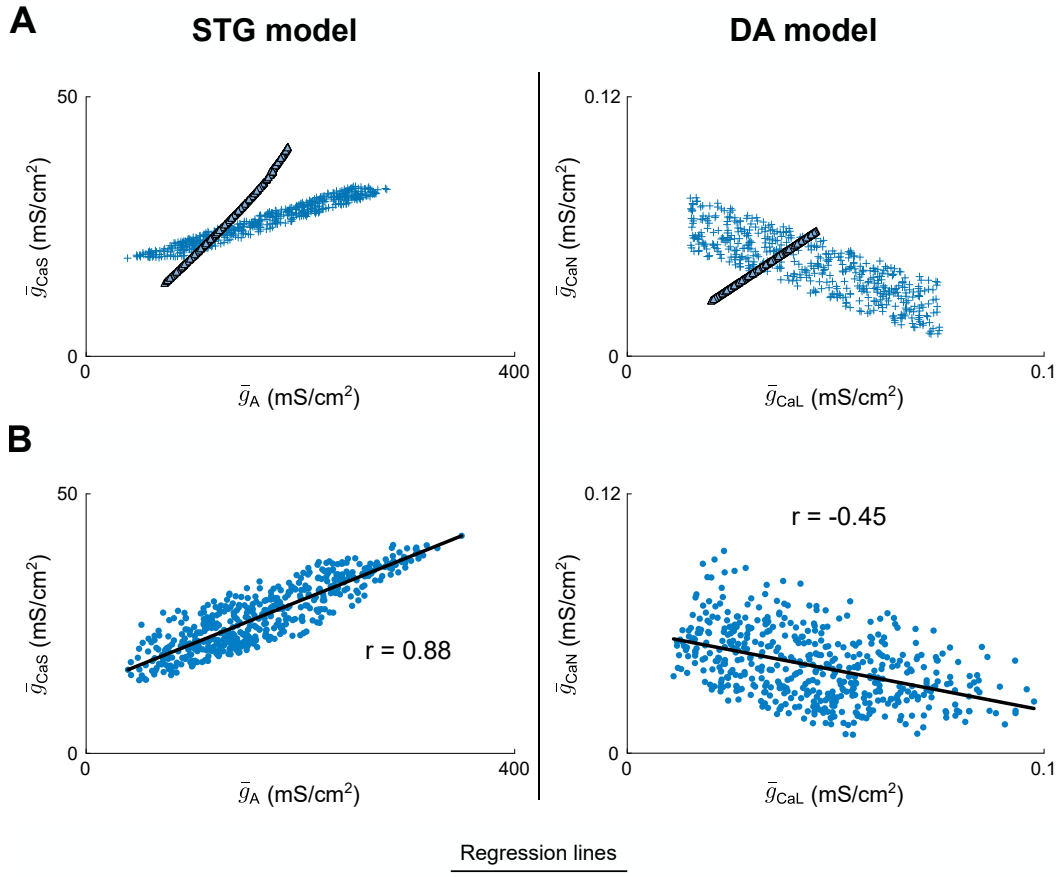

Figure 14.6: Variability from both homogeneous scaling and variable conductance ratios blurs the connection between conductance correlation and function.
(A) Scatter plots of custom generated populations separated into triangles (homogeneous scaling only) and crosses (variability in conductance ratios only) in the $(\bar{g}_{\mathrm{A}}, \bar{g}_{\mathrm{CaL}})$ 2D subspace for the STG model (left) and the $(\bar{g}_{\mathrm{CaL}}, \bar{g}_{\mathrm{CaN}})$ 2D subspace for the DA model (right).
(B) Scatter plots of the full variability custom generated populations in the same 2D subspace as in (A) for both the STG model (left) and the DA model (right), along with regression lines and Pearson correlation coefficients.

the respective neuron models. To create robust neuromodulation in degenerate neurons, we modulated the datasets of Fig. 14.5A by modifying the target threshold value for the slow DIC and used the algorithm of Drion et al. (2015a) to compute the neuromodulated conductance values for each neuron of the dataset (see Materials and Methods). The resulting data points are shown in the scatter plots at the top of Fig. 14.7B. The dot color quantifies neuron burstiness, showing that the three firing patterns are robustly attained and well separated.

In both models, neuromodulation of neuron excitability strongly affects the level of pairwise correlations (Fig. 14.7B). In the STG model, the correlation between $\bar{g}_{\mathrm{A}}$ and $\bar{g}_{\mathrm{CaS}}$ is strongly positive in spiking (r = 0.93), peaks in light bursting (r = 0.97), and decreases in strong bursting (r = 0.88). Meanwhile, in the DA model, the correlation between $\bar{g}_{\mathrm{CaL}}$ and $\bar{g}_{\mathrm{CaN}}$ is negative in spiking (r = -0.45), becomes less negative in light bursting (r = -0.11), and the two conductances appear uncorrelated in strong bursting (r = 0.03). Pairwise correlations in ion channel conductances therefore appear neuromodulation-dependent.

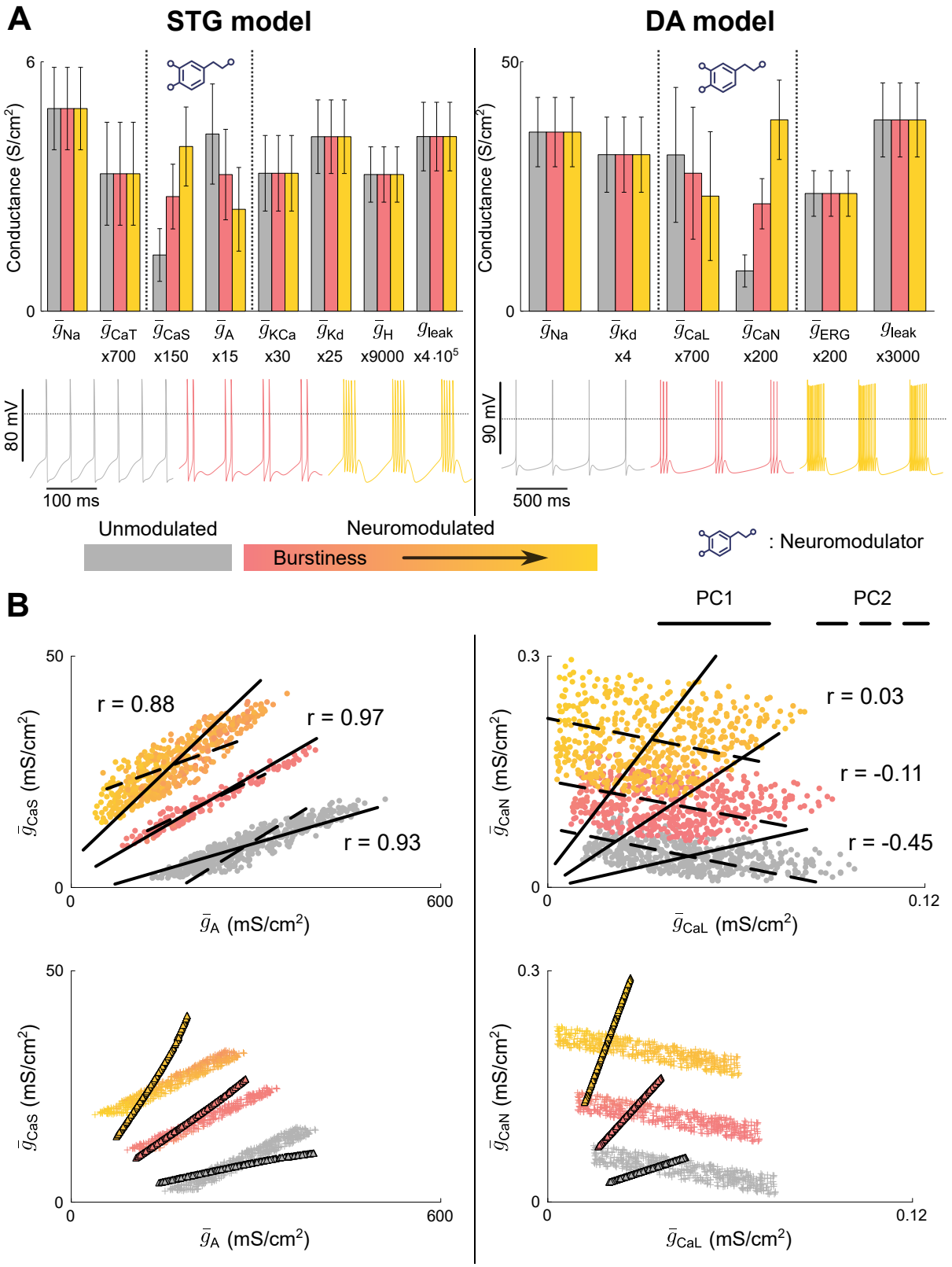

Figure 14.7: Variability in pairwise correlations in conductance values is neuromodulation-dependent.

The caption is on the next page.

Figure 14.7: (A) Bar plot of conductance values for custom generated populations in the three phenotypes considered for the STG model (right) and the DA model (left). The dotted line on the voltage traces corresponds to 0 mV.
(B) Scatter plots of full variability custom generated populations in the neuromodulated 2D space for both the STG model (left) and the DA model (right) across three neuromodulated states, along with PC1, PC2, and Pearson correlation coefficients (top). Scatter plots of separated custom generated populations in the neuromodulated 2D space for both the STG model (left) and the DA model (right) across three neuromodulated states (bottom).

The origin of these neuromodulation-dependent changes in pairwise correlations can be explained by plotting the first two principal components (PC1 and PC2) on the scatter plots and observing the effect of neuromodulation on them. On the one hand, neuromodulation creates a rotation of PC1 around the origin, which affects its slope. In the projections of Fig. 14.7B, the slope of PC1 increases when neurons switch from spiking to bursting in both models. This effect is consistent with the results obtained from homeostatic models of ion channel expression (O'Leary et al., 2014). On the other hand, neuromodulation creates a translation of PC2, and the slope is barely affected. As a result, the relative slopes between PC1 and PC2 depend on neuron neuromodulatory state, which affects the global correlation level.

In the STG model, both PC components have a positive slope. In spiking, PC1 has a flatter slope than PC2, which slightly widens the data cloud. As the model switches to bursting mode, the slope of PC1 increases and the two slopes become almost identical in light bursting. In this state, the two principal components align, which creates a strong correlation between the channel pair. As the model further increases its burstiness, the steepness of the slope of PC1 increases further and it becomes steeper than that of PC2. The two principal components disalign again and the correlation between the channel pair decreases. A similar observation can be made in the DA model, except that here PC2 has a negative slope. As a result, PC1 and PC2 become more and more orthogonal as burstiness increases, which reduces the correlation level, and even destroys the channel pairwise correlation in a strong bursting state.

As identified above, PC1 relates to the homogeneous scaling of conductances, whereas PC2 relates to the variability in the ratio between voltage-dependent conductances. To further demonstrate this link, we reproduced the three neuromodulatory states in two subsets where we isolated variability derived from homogeneous scaling (triangles in the bottom panels of Fig. 14.7B) from variability in conductance ratios (crosses in the bottom panels of Fig. 14.7B). We used the same algorithm as for the full dataset to create robustly neuromodulated states. The results from both models clearly show that robust neuromodulation is achieved through a rotation of the data points in the conductance space if variability derives from homogeneous scaling, whereas it is achieved through a translation of the data points if variability involves the ratio between voltage-dependent conductances.

This observation can be interpreted physiologically and provides significant insights into the requirements for robust neuromodulation in variable neurons. If robust neuromodulation is achieved through a rotation in the conductance space, it means that the robust neuromodulation rule is multiplicative: $\bar{g}_{i,\mathrm{MOD}} = \alpha_i \cdot \bar{g}_{i,\mathrm{init}}$ where α_i is set by the concentration of neuromodulator.

The rule is multiplicative in the case of variability through homogeneous scaling, because neurons having twice the maximal conductance values require twice the change in conductance to achieve a similar firing pattern, owing to the change in input resistance. If robust neuromodulation is achieved through a translation in the conductance space, it means that the robust neuromodulation rule is additive: $\bar{g}_{i,\mathrm{MOD}} = \bar{g}_{i,\mathrm{init}} + \beta_i$ where β_i is also set by the neuromodulator concentration. The rule is additive in the case of variability in conductance ratios only because a similar firing pattern is achieved through a similar change in the normalized DIC values, which is created by the same change in maximal conductances. As a result, robust neuromodulation can be achieved through a simple, direct rule if only one type of variability is present in the neuronal population. However, derivation of a direct rule is impossible if both variability types are present in the population, which is likely considering the physiological significance of both types. Such a rule would indeed need to be both additive and multiplicative with a neuron-dependent ratio between both effects. Robust neuromodulation therefore requires an indirect rule involving a second messenger in highly degenerate neurons, which is precisely the mechanism observed in G protein-coupled receptor signaling.

14.3.8 A simple indirect rule for robust neuromodulation in highly degenerate neurons

We showed that robust neuromodulation in highly degenerate cells cannot rely on a simple rule directly targeting ion channels, but rather requires a more complex rule involving a second messenger. This raises the questions of how complex a rule for reliable neuromodulation should be, and whether a general, model-independent rule could be derived. In an attempt to answer these questions, we used the algorithm developed above to construct reliable neuromodulatory paths in degenerate neurons for both STG and DA models, moving from tonic spiking to bursting of increasing burstiness (Fig. 14.8). Similarly to the case presented above, the neuromodulatory algorithm targeted $\bar{g}_{\mathrm{A}}$ and $\bar{g}_{\mathrm{CaS}}$ in the STG model, and $\bar{g}_{\mathrm{CaL}}$ and $\bar{g}_{\mathrm{CaN}}$ in the DA model. Many reliable neuromodulatory paths could be achieved in both models using a simple rule whose objective is to increase the target threshold value for the slow DIC while moving from tonic spiking to bursting, while keeping the ultraslow DIC value constant to maintain spiking and bursting periods (Drion et al., 2015a) (see Materials and Methods). Fig. 14.8 plots the neuromodulatory pathways in the $(\bar{g}_{\mathrm{CaS}}, \bar{g}_{\mathrm{A}})$ plane (resp. $(\bar{g}_{\mathrm{CaL}}, \bar{g}_{\mathrm{CaN}})$ plane) for the STG model (resp. DA model) and examples of neuromodulated neuronal traces.

Interestingly, although a simple direct rule cannot be used, the indirect rule resulted in linear neuromodulatory paths for both models, where the direction of neuromodulation is constant and only varies between neurons of different types. The nonlinearity occurs in the distance the neuron has to move in the direction to switch activity, which is affected by parameter variability (see the variability in the color transitions of Fig. 14.8 top). These results highlight that, even in the case of maximal degeneracy in neuron parameters, the relative change in maximal conductances of ion channels targeted by the same neuromodulatory receptor can be hard wired in a neuron type, creating a robust neuromodulatory path. The second messenger then has the role of controlling the movement along that neuromodulatory path that would lead to the target activity, strongly reducing the complexity of the reliable neuromodulation process. Such control could for example

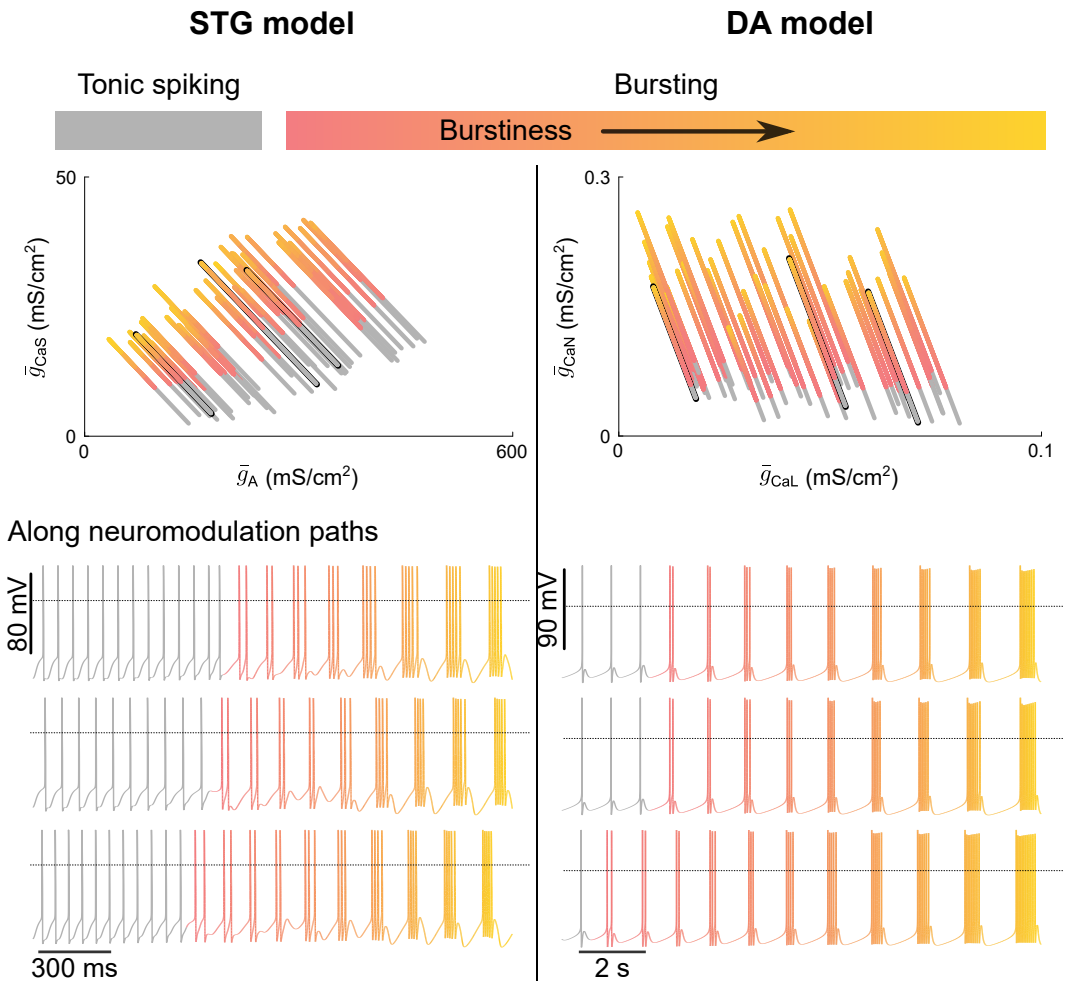

Figure 14.8: A simple indirect rule for robust neuromodulation in highly degenerate neurons.
Neuromodulatory paths of custom generated populations for a gradually continuous neuromodulation application in the neuromodulated 2D subspace (top). Each line corresponds to one neuron continuously undergoing neuromodulation. Three randomly chosen neuron voltage traces along their neuromodulation paths (bottom). The dotted line on the voltage traces corresponds to 0 mV.

be implemented by sensing neuronal activity through intracellular calcium oscillations, as already suggested in homeostatic models (Liu et al., 1998; O'Leary et al., 2014), or by sensing membrane voltage (Santin and Schulz, 2019), creating activity-dependent changes in targeted maximal conductances. Substantial evidence of such activity-dependent neuromodulatory mechanisms involving intracellular calcium can be found in the literature on experimental studies (Kramer and Levitan, 1990; Marder et al., 2014; Raymond et al., 1992; Walters and Byrne, 1984).

14.4 Discussion

14.4.1 Two physiologically relevant sources of neuronal variability govern ion channel degeneracy

To uncover how so many different neuron types emerge, as well as the mechanisms underlying neuromodulation and variable neuronal response to neuroactive drugs, it is critical to understand how ion channels shape neuronal excitability (Amendola et al., 2012; Grashow et al., 2009; Nadim and Bucher, 2014; Schulz et al., 2006a; Tobin et al., 2009). However, the connection between ion channels and neuronal signaling is complex due to channel degeneracy, and despite considerable advances made on the subject through experimental, computational, and mathematical work, a mechanistic understanding of ion channel variability and degeneracy in neurons remains elusive (Achard and De Schutter, 2006; Alonso and Marder, 2019; Prinz et al., 2004; Swensen and Bean, 2005; Taylor et al., 2009). Here, we showed that neuronal variability can be separated into two quantifiable, physiological components: homogeneous scaling of conductances and variability in conductance ratios.

Homogeneous scaling refers to the fact that neurons can exhibit similar activity if the relative difference in their channel maximal conductances is similar for all channels expressed at the membrane, whereby conductance ratios are maintained. This property has been observed experimentally in channel expression and shown to emerge from homeostatic rules (Marder and Goaillard, 2006; O'Leary et al., 2013; O'Leary et al., 2014). In this case, intrinsic characteristics are maintained, but extrinsic excitability is altered due to differences in neuron input resistance. Variability in conductance ratios refers to the fact that neurons having a similar input resistance can exhibit similar activity with different ratios in their voltage-gated conductances. In this case, intrinsic characteristics are maintained, but the response to perturbations such as in temperature as well as channel blockade is altered due to differences in the relative role of each channel subtype on excitability.

Both sources of channel variability are physiologically relevant. Homogeneous scaling is central for network homeostasis, as it permits the tuning of neuron input/output response while keeping the intrinsic properties of neurons stable (O'Leary and Wyllie, 2011). Homogeneous scaling also permits compensation for changes in membrane capacitance. On the other hand, variability in conductance ratios permits improvement of the robustness against external perturbations by creating an heterogeneous response to perturbations affecting specific channel functions at the network level (Drion et al., 2015c). It could also lead to variable inter-individual responses to neuroactive drugs.

The contributions of variability from homogeneous scaling and conductance ratios are intertwined in any neuron degenerate dataset, making any attempt at quantification difficult. Combining dimensionality reduction analysis and recent insights into the reduced dynamics of conductance-based models, we were able to separate the contributions of the two sources of variability, allowing the establishment of a mechanistic understanding of how variable ion channels can lead to specific neuronal activity. This enabled an understanding of the origin of ion channel variable pairwise correlations and the derivation of a robust indirect rule for reliable neuromodulation in degenerate

neurons.

14.4.2 Variable channel correlations arise from the interference between homogeneous scaling and variability in conductance ratios

Separating the effects of homogeneous scaling and variability in conductance ratios allowed analysis of the roles of the two sources of variability on channel pairwise correlations. Homogeneous scaling creates strictly positive correlations between all ion channels, and different firing patterns/neuron subtypes lead to different regression slopes, as observed in the channel expression data and homeostatic models of neuronal excitability (O'Leary et al., 2014). These positive correlations come from the passive role of ion channels on membrane properties through Ohm's law: an increase of any channel conductance decreases the membrane input resistance. Other channels thus have to increase their conductance to maintain their effect on membrane potential variations.

On the other hand, variability in conductance ratios creates both positive and negative correlations between ion channel subsets, but not all ion channels. Ion channels correlate to maintain neuronal dynamics if their gating, representing either activation or inactivation, occurs on a similar timescale. The sign of the correlation is determined by the relative feedback provided by each channel gating on membrane potential variations, which is a key determinant of neuron dynamical properties as quantified by dynamic input conductances, for example (Drion et al., 2015a). Specifically, activation of inward current and inactivation of outward current produce positive feedback, whereas activation of outward current and inactivation of inward current produce negative feedback. Two channels producing opposite feedbacks on a similar timescale will correlate positively (such as *e.g.* $\bar{g}_{\mathrm{A}}$ and $\bar{g}_{\mathrm{CaS}}$ in the STG model), whereas two channels producing similar feedbacks will correlate negatively (such as *e.g.* $\bar{g}_{\mathrm{CaL}}$ and $\bar{g}_{\mathrm{CaN}}$ in the DA model).

When both sources of variability are present in a neuron degenerate set, the two types of correlations interfere with each other. When the correlation emerging from variability in conductance ratio is positive, both regression lines have a positive slope, creating an overall positive correlation whose intensity depends on the alignment of the regression lines. However, when the correlation emerging from variability in conductance ratio is negative, both regression lines have opposite signs, which can lead to an uncorrelation between two conductances even though there is a strong correlation between their role in neuron dynamics and passive properties. This situation could be indistinguishable from two channels that actually do not correlate due to a lack of action on a similar timescale. Therefore, variable correlations in channel conductances in a degenerate dataset do not always relate to correlated or uncorrelated functions, but could also arise from highly correlated functions of opposite signs.

14.4.3 The importance of indirect neuromodulatory pathways for reliable neuromodulation in variable neurons

One prominent issue arising from channel degeneracy involves how neuromodulation could be reliable across neurons when it acts on degenerate conductances (Grashow et al., 2009; Marder, 2012; Marder and Bucher, 2007; Marder et al., 2014; Nadim and Bucher, 2014; Schulz et al.,

2006a). We showed that a simple direct rule for reliable neuromodulation could be derived if either homogeneous scaling or variability in conductance ratios, but not both, was present in a dataset. Indeed, homogeneous scaling requires a simple multiplicative rule due to its effect on input resistance, whereas variability in conductance ratios requires an additive rule. There is no direct rule if both variability types exist, as it would need to be both additive and multiplicative with a neuron-dependent ratio between the two effects.

We showed that a simple indirect rule could produce reliable neuromodulation when both sources of variability are present in the dataset. This rule is indirect in the sense that it uses an intermediate signaling pathway to connect neuromodulation concentration with changes in channel conductances. In our computational study, this intermediate pathway encodes the values of the slow and ultraslow dynamic input conductances around the threshold potential: neuromodulator concentration tunes the target values for both dynamic conductances, and a subset of ion channels are in turn modulated to reach these new targets. The presence of an intermediate messaging pathway is a core property of GPCR signaling, making such an indirect rule physiologically plausible. Our work provides a quantitative framework that provides a new angle of attack to study how intermediate signaling pathways could lead to reliable neuromodulation in degenerate neurons.

14.5 Material and Methods

14.5.1 Programming language

The Julia programming language was used in this work (Bezanson et al., 2017). Numerical integration was realized using *DifferentialEquations.jl*. Regression lines and correlations were computed using *Statistics.jl*. PCA was conducted using *LinearAlgebra.jl*.

14.5.2 Conductance-based models

For all experiments, single-compartment conductance-based models were employed. These models articulate an ordinary differential equation for the membrane voltage V, where N ion channels are characterized as nonlinear dynamic conductances, and the phospholipid bilayer is represented as a passive resistor-capacitance circuit. Mathematically, the voltage-current relationship of any conductance-based neuron model is expressed as follows:

$$\begin{aligned} I_C &= C\frac{\mathrm{d}V}{\mathrm{d}t} + g_{\mathrm{leak}}(V - E_{\mathrm{leak}}) = -I_{\mathrm{int}} + I_{\mathrm{ext}} \\ &= -\sum_{\mathrm{ion}\in\mathcal{I}} g_{\mathrm{ion}}(V,t)(V - E_{\mathrm{ion}}) + I_{\mathrm{ext}}. \end{aligned}$$

Here, C represents the membrane capacitance, g_{ion} denotes the considered ion channel conductance and is non-negative, gated between 0 (all channels closed) and $\bar{g}_{\mathrm{ion}}$ (all channels open), E_{ion} and E_{leak} are the channel reversal potentials, $\mathcal{I}$ is the index set of intrinsic ionic currents considered in the model, and I_{ext} is the current externally applied *in vitro*, or the combination of synaptic currents. Each ion channel conductance is nonlinear and dynamic, represented by $g_{\mathrm{ion}}(V,t) = \bar{g}_{\mathrm{ion}} m_{\mathrm{ion}}^a(V,t) h_{\mathrm{ion}}^b(V,t)$, where m_{ion} and h_{ion} are variables gated between 0 and 1,

modeling the opening and closing gates of ion channels, respectively. Throughout this study, both the isolated crab STG neuron model (Liu et al., 1998) and the adapted DA neuron model (Qian et al., 2014) (where SK channels had been blocked to enable bursting) were employed.

The STG model consists of seven ion channels that operate on various time scales: fast sodium channels ($\bar{g}_{\mathrm{Na}}$); delayed-rectifier potassium channels ($\bar{g}_{\mathrm{Kd}}$); T-type calcium channels ($\bar{g}_{\mathrm{CaT}}$); A-type potassium channels ($\bar{g}_{\mathrm{A}}$); slow calcium channels ($\bar{g}_{\mathrm{CaS}}$); calcium controlled potassium channels ($\bar{g}_{\mathrm{KCa}}$); and H channels ($\bar{g}_{\mathrm{H}}$).

The DA model consists of six ion channels that operate on various time scales: fast sodium channels ($\bar{g}_{\mathrm{Na}}$); delayed-rectifier potassium channels ($\bar{g}_{\mathrm{Kd}}$); L-type calcium channels ($\bar{g}_{\mathrm{CaL}}$); N-type calcium channels ($\bar{g}_{\mathrm{CaN}}$); ERG channels ($\bar{g}_{\mathrm{ERG}}$); and NMDA channels ($\bar{g}_{\mathrm{NMDA}}$). Note that, owing to the multicellular nature of NMDA channels, they were excluded from this study but were still used for simulations with baseline values.

14.5.3 Random sampling sets

Random sampling sets consist of 200 neuron models with varying maximum ion channel conductances. These sets were created by generating numerous random points in the space of maximum ion channel conductances (within specified ranges). Subsequently, the models underwent post-processing based on their firing patterns, with only those fitting the desired phenotype being retained. For the STG models, post-processing involved considerations of peak and hyperpolarized voltages, intra- and interburst frequencies, the number of spikes per burst, and burstiness (computed as in Franci et al. (2018)). Meanwhile, the DA models were post-processed based on their peak and hyperpolarized voltages and spike frequency.

14.5.4 Dynamic input conductances (DICs)

DICs consist of three voltage-dependent conductances that separate according to timescales: one fast, one slow, and one ultraslow, denoted as $g_{\mathrm{f}}(V)$, $g_{\mathrm{s}}(V)$, and $g_{\mathrm{u}}(V)$, which can be computed as linear functions of the maximal conductance vector $\bar{g}_{\mathrm{ion}} \in \mathbb{R}^N$ of an N-channel conductance-based model at each voltage level V:

$$[g_{\mathrm{f}}(V); g_{\mathrm{s}}(V); g_{\mathrm{u}}(V)] = f_{\mathrm{DIC}}(V) = S(V) \cdot \bar{g}_{\mathrm{ion}}\,,$$

where $S(V) \in \mathbb{R}^{3\times N}$ is a sensitivity matrix that can be built by: $S_{i\,j}(V) = -\left(w_{i\,j} \cdot \frac{\partial \dot{V}}{\partial X_j} \frac{\partial X_{j,\infty}}{\partial V}\right) / g_{\mathrm{leak}}$, where i denotes the timescale, X_j are gating variables of the j-th channel of the considered model and $w_{i\,j}$ is a timescale-dependent weight which is computed as the logarithmic distance of the time constant of X_j and the timescale i (Drion et al., 2015a). While the complete curve of the DICs may be of interest, only its value at the threshold voltage V_{th} is used, as the values and signs of the DICs at V_{th} reliably determine the firing pattern (Drion et al., 2015a). Thus, the following linear system $f_{\mathrm{DIC}}(V_{\mathrm{th}}) = S(V_{\mathrm{th}}) \cdot \bar{g}_{\mathrm{ion}}$ makes the link between ion channel conductances and neuronal activity.

14.5.5 An efficient method to build sets that allow the separation of the two sources of degeneracy

Throughout this study, a novel method for generating degenerate datasets of conductance-based models has been developed, which was proven to be significantly faster than the random sampling approach (all figures were created using a dataset of 500 neurons). The methodology for a N-channel conductance-based model can be summarized as follows:

1. The leakage conductance g_{leak} is drawn from a physiological uniform distribution: $g_{\text{leak}} \sim \mathcal{U}\left(g_{\text{leak min}}, g_{\text{leak max}}\right)$;
2. $N-3$ maximum ion channel conductances are drawn from a physiological uniform distribution that is proportional to g_{leak}: $\bar{g}_{\text{ion}} \sim \frac{g_{\text{leak}}}{(g_{\text{leak min}}+g_{\text{leak max}})/2} \cdot \mathcal{U}^{N-3}\left(\bar{g}_{\text{unmod min}}, \bar{g}_{\text{unmod max}}\right)$;
3. The three remaining maximum ion channel conductances are computed using the linear system $f_{\text{DIC}}(V_{\text{th}}) = S(V_{\text{th}}) \cdot \bar{g}_{\text{ion}}$, in which $f_{\text{DIC}}(V_{\text{th}})$ are fixed by the user to chose the firing pattern of the population.

The normalization by g_{leak} in (ii) allows the combination of the effects of homogeneous scaling and variability in conductance ratios. The subsequent sets, each targeting either homogeneous scaling or conductance ratio, were generated by using shared deterministic values for g_{leak} or for the $N-3$ maximum ion channel conductances, respectively. The zero sensitivity directions of slow dynamical membrane properties were computed using the equations for the slow dynamic input conductance, where the two ion channel conductances of interest were treated as variables along this direction.

14.5.6 Neuromodulation algorithm

As a result of this newly developed method for generating degenerate neuronal sets, neuromodulation of these sets is achieved by manipulating the linear system $f_{\text{DIC}}(V_{\text{th}}) = S(V_{\text{th}}) \cdot \bar{g}_{\text{ion}}$. Once a population is created, the values of $f_{\text{DIC}}(V_{\text{th}})$ can be adjusted, and the linear system can be solved for certain ion channel conductances (the modulated ones) to achieve a new firing pattern. Specifically, two maximum conductances are recalculated by tuning the value of the slow dynamic input conductance while the ultraslow dynamic input conductance is kept unchanged. The latest results were obtained by continuously adjusting this slow dynamic input conductance value.

14.6 Supplementary Material

14.6.1 Simulation details for the two conductance based models

Throughout the entire section, two high-dimensional conductance-based models have been employed. First, the voltage equation for the Stomatogastric Ganglion (STG) neuron model, as

proposed by Liu et al. (1998), is expressed as follows:

$$\begin{aligned} C\dot{V} = &- \bar{g}_{\mathrm{Na}} m_{\mathrm{Na}}^3 h_{\mathrm{Na}} (V - E_{\mathrm{Na}}) - \bar{g}_{\mathrm{CaT}} m_{\mathrm{CaT}}^3 h_{\mathrm{CaT}} (V - E_{\mathrm{Ca}}) - \bar{g}_{\mathrm{CaS}} m_{\mathrm{CaS}}^3 h_{\mathrm{CaS}} (V - E_{\mathrm{Ca}}) \\ &- \bar{g}_{\mathrm{A}} m_{\mathrm{A}}^3 h_{\mathrm{A}} (V - E_{\mathrm{K}}) - \bar{g}_{\mathrm{KCa}} m_{\mathrm{KCa}}^4 (V - E_{\mathrm{K}}) - \bar{g}_{\mathrm{Kd}} m_{\mathrm{Kd}}^4 (V - E_{\mathrm{K}}) \\ &- \bar{g}_{\mathrm{H}} m_{\mathrm{H}} (V - E_{\mathrm{H}}) - g_{\mathrm{leak}} (V - E_{\mathrm{leak}}) + I_{\mathrm{app}}, \end{aligned} \tag{14.1}$$

where the dot notation represents the time derivative, C is the membrane capacitance, Na stands for the sodium current, CaT for the T-type calcium current, CaS for the slow calcium current, A for the A-type potassium current, KCa for the calcium-controlled potassium current, Kd for the delayed rectified potassium current, H for the H current, and leak for the leakage current. All E values denote the channel reversal Nernst potentials, and I_{app} represents the externally applied current. The parameters of interest are the maximum ion channel conductances $\bar{g}$, expressed in mS/cm^2, corresponding to the ion channel conductance when fully opened. Additionally, all m and h variables represent activation and inactivation gate variables, respectively, following first-order lag equations that are voltage-dependent. Notably, the KCa gating variable also depends on intracellular calcium concentration, and its ordinary differential equation (ODE) can be found in Liu et al. (1998). For all STG voltage traces in this article, equation (14.1) and subsequent gate variable equations are numerically integrated using the Julia language (Bezanson et al., 2017).

Second, the voltage equation for the Dopaminergic (DA) neuron model, adapted from Qian et al. (2014) (with the SK channels blocked), is given by:

$$\begin{aligned} C\dot{V} = &- \bar{g}_{\mathrm{Na}} m_{\mathrm{Na}}^3 h_{\mathrm{Na}} (V - E_{\mathrm{Na}}) - \bar{g}_{\mathrm{Kd}} m_{\mathrm{Kd}}^3 (V - E_{\mathrm{K}}) - \bar{g}_{\mathrm{CaL}} m_{\mathrm{CaL}}^2 (V - E_{\mathrm{Ca}}) \\ &- \bar{g}_{\mathrm{CaN}} m_{\mathrm{CaN}} (V - E_{\mathrm{Ca}}) - \bar{g}_{\mathrm{ERG}} m_{\mathrm{ERG}} (V - E_{\mathrm{K}}) - g_{\mathrm{leak}} (V - E_{\mathrm{leak}}) \\ &- \bar{g}_{\mathrm{NMDA}} \frac{(V - E_{\mathrm{NMDA}})}{1 + Mg \cdot \exp(-0.08V)/10} + I_{\mathrm{app}}, \end{aligned} \tag{14.2}$$

where CaL represents the L-type calcium current, CaN the N-type calcium current, ERG the ERG current, and NMDA the NMDA current. Additionally, Mg denotes the extracellular magnesium concentration, assumed to be a constant of 1.4 µM. For all dopaminergic (DA) voltage traces in this article, equation (14.2) and subsequent gate variable equations are numerically integrated using the Julia language (Bezanson et al., 2017). It is important to note that the NMDA ion channel is not discussed in the article and is treated with a constant maximum conductance scaled by the leakage current.

14.6.2 Computation details for the Dynamic Input Conductances (DICs)

This article employs the concept of Dynamic Input Conductances (DICs) introduced in Drion et al. (2015a). DICs consist of three voltage-dependent conductances that separate according to timescales: one fast, one slow, and one ultraslow. These DICs have been demonstrated to shape neuronal spiking. Specifically, based on specific values of the DICs, it becomes possible to predict the firing pattern of the neuron. The computation of the DICs in this article has been improved compared to Drion et al. (2015a), and this enhancement will be detailed in the following sections.

The DICs are three voltage-dependent conductances, denoted as $g_{\mathrm{f}}(V)$, $g_{\mathrm{s}}(V)$, and $g_{\mathrm{u}}(V)$, which can be computed as linear functions of the maximal conductance vector $\bar{g}_{\mathrm{ion}} \in \mathbb{R}^N$ of an N-channel conductance-based model at each voltage level V

$$\begin{bmatrix} g_{\mathrm{f}}(V) \\ g_{\mathrm{s}}(V) \\ g_{\mathrm{u}}(V) \end{bmatrix} = f_{\mathrm{DIC}}(V) = S(V) \cdot \bar{g}_{\mathrm{ion}}\,, \tag{14.3}$$

where $S(V) \in \mathbb{R}^{3\times N}$ is a sensitivity matrix that can be built by (line per line)

$$S_{\mathrm{f}\,j}(V) = -\left(w_{\mathrm{fs},X_j} \cdot \frac{\partial \dot{V}}{\partial X_j} \frac{\partial X_{j,\infty}}{\partial V} \right) \Big/ g_{\mathrm{leak}}, \tag{14.4}$$

$$S_{\mathrm{s}\,j}(V) = -\left((w_{\mathrm{su},X_j} - w_{\mathrm{fs},X_j}) \cdot \frac{\partial \dot{V}}{\partial X_j} \frac{\partial X_{j,\infty}}{\partial V} \right) \Big/ g_{\mathrm{leak}}, \tag{14.5}$$

$$S_{\mathrm{u}\,j}(V) = -\left((1 - w_{\mathrm{su},X_j}) \cdot \frac{\partial \dot{V}}{\partial X_j} \frac{\partial X_{j,\infty}}{\partial V} \right) \Big/ g_{\mathrm{leak}}, \text{ with } j = 1:N, \tag{14.6}$$

where equations (14.4), (14.5), and (14.6) represent the computation of rows 1, 2, and 3, respectively, of the matrix $S(V)$ — that is, the computation of the fast, slow, and ultraslow DICs. The weighing factors w_{fs,X_j} and w_{su,X_j} are computed following the method outlined in Drion et al. (2015a), where X_j corresponds to the gating variable(s) (activation and/or inactivation) of the current with index j, and $X_{j,\infty}$ denotes the steady-state function(s) of the considered gating variable lag equation(s). It is important to note that if the current j has both activation and inactivation variables, the column S_j corresponds to the sum of equations (14.4) through (14.6) over the two gating variables of the current j.

While the complete curve of the DICs may be of interest, only its value at the threshold voltage V_{th} is used, as the values and signs of the DICs at V_{th} reliably determine the neuronal firing pattern (Drion et al., 2015a). In the following sections, the voltage dependency of all variables will be disregarded, as functions are only evaluated at V_{th}. The threshold voltage is computed as $g_{\mathrm{in}}(V_{\mathrm{th}}) = g_{\mathrm{f}}(V_{\mathrm{th}}) + g_{\mathrm{s}}(V_{\mathrm{th}}) + g_{\mathrm{u}}(V_{\mathrm{th}}) < 0$, while ensuring that $g_{\mathrm{in}}(V_{\mathrm{th}} - \delta V) \geq 0$ with any arbitrarily small $\delta V > 0$. It is important to note that this algorithm might fail for the DA neuron model, where the default $V_{\mathrm{th}} = -55.5$ mV.

14.6.3 Computation details for the random sampling sets

For both models, random sampling sets consist of randomly drawing maximum ion channel conductances, *i.e.*, generating a point in the conductance space, numerically integrating the model equations, and retaining the point in the set if its phenotype is correct until the set reaches 200 neurons, according to different criteria. For the STG model, a bursting behavior is desired, so post-processing is carried out on:

- Peak voltage (between 49.9 mV and 49.95 mV);
- Low voltage (between -76 mV and -69 mV);

- Number of spike per burst (5);
- Burstiness (between 3000 Hz^2 and 7000 Hz^2);
- Interburst frequency (between 8.8 Hz and 9.9 Hz);
- Intraburst frequency (between 70 Hz and 140 Hz);

with the burstiness computed as in Franci et al. (2018).

For the DA model, a pacemaking tonic spiking behavior is desired, so post-processing is carried out on:

- Peak voltage (between 54 mV and 58.5 mV);
- Low voltage (between -80.5 mV and -77.5 mV);
- Spiking frequency (between 1.75 Hz and 1.95 Hz).

To generate a random point in the parameter space for each N-channel conductance-based model, each conductance was drawn from a uniform random distribution $\bar{g}_{\text{ion}} \sim \mathcal{U}^N(0, \bar{g}_{\text{ion max}})$ and $g_{\text{leak}} \sim \mathcal{U}(0, g_{\text{leak max}})$, with $\bar{g}_{\text{ion max}}$ and $g_{\text{leak max}}$ are equal to the corresponding values in Tables 14.1 and 14.2 for the STG and DA models, respectively. It is noteworthy that, for the DA model, the NMDA conductance is computed as $\bar{g}_{\text{NMDA}} = g_{\text{leak}} \cdot 0.12/0.013$, *i.e.*, a baseline value of 0.12 scaled by the leakage conductance to achieve homogeneous scaling.

Current name	Na	CaT	CaS	A	KCa	Kd	H	leak
$\bar{g}_{\text{ion max}}$ or $g_{\text{leak max}}$	8000	12	50	600	250	350	0.7	0.02

Table 14.1: Right boundary of the uniform distribution for all maximum ion channel conductances of the STG model.

Current name	Na	Kd	CaL	CaN	ERG	leak
$\bar{g}_{\text{ion max}}$ or $g_{\text{leak max}}$	60	20	0.1	0.12	0.25	0.02

Table 14.2: Right boundary of the uniform distribution for all maximum ion channel conductances of the DA model.

14.6.4 Additional 2D subspaces of the random sampling datasets normalized by the input resistance

Fig. 14.9 depicts a scatter matrix of the random sampling datasets normalized by the input resistance for the 2D subspaces of Fig. 5 from the main manuscript. This visualization highlights that normalizing by the input resistance effectively removes the effect of homogeneous scaling, leaving only mechanistic correlations that might arise from the ion channels.

On one hand, antagonist channels reveal positive correlations once normalized (*e.g.*, see $\bar{g}_{\text{A}}$ and $\bar{g}_{\text{CaS}}$ for the STG model and $\bar{g}_{\text{Kd}}$ and $\bar{g}_{\text{CaL}}$ for the DA model). Such correlations within the variability of conductance ratios align with homogeneous scaling, leading to overall positive correlations in the random sampling datasets (see Fig. 1 of the main manuscript).

On the other hand, agonist channels reveal negative correlations once normalized (*e.g.*, $\bar{g}_{\mathrm{CaL}}$ and $\bar{g}_{\mathrm{CaN}}$ for the DA model). Such correlations within the variability of conductance ratios oppose homogeneous scaling, leading to overall negative or nonexistent correlations in the random sampling datasets, depending on the strength of homogeneous scaling (see Fig. 1 of the main manuscript).

A last case is when the channels are not correlated mechanistically, such as the pair including ultraslow channels like $\bar{g}_{\mathrm{H}}$ for the STG model or $\bar{g}_{\mathrm{ERG}}$ for the DA model. As the dynamics of such channels lie in another timescale than other channels, the correlation within the normalized dataset is nonexistent. When combined with homogeneous scaling, this may lead to either a nonexistent correlation or a slight positive correlation, depending on the strength of homogeneous scaling (see Fig. 1 of the main manuscript).

Note that input resistance have been computed as the sum of the ion channel conductances at $-60\,\mathrm{mV}$ for the STG model and $-55.5\,\mathrm{mV}$ for the DA model.

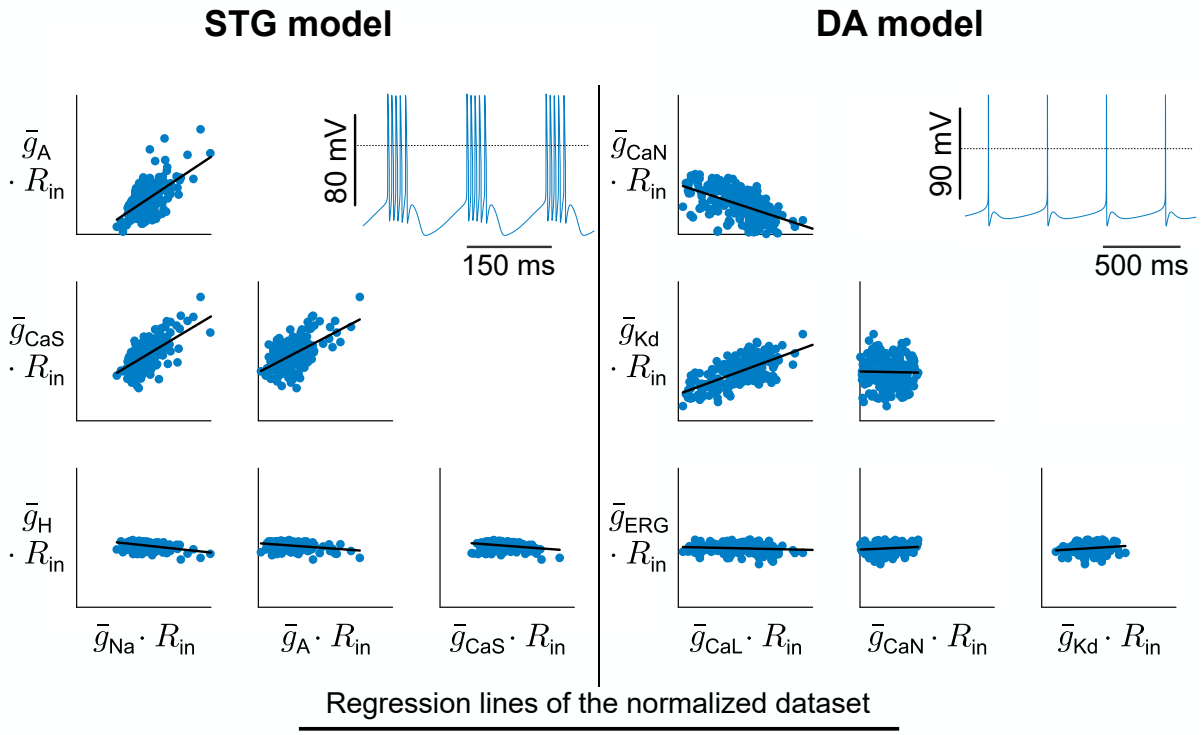

Figure 14.9: Scatter matrices of random sampling populations in the conductance spaces normalized by the input resistance for the STG model (left) and the DA model (right) along with the directions of the regression lines. The 2D subspaces shown here do not represent all conductances of the models and are chosen to be the same as in Fig. 5 of the main manuscript. All normalized conductances are dimensionless. The bottom left corner of each 2D subspace represents the origin of the conductance space, and ranges are irrelevant. The dotted line on the voltage traces corresponds to the 0 mV line.

14.6.5 Computation details for the efficient method to build degeneracy sets that allows to remove the effect of homogeneous scaling

Throughout this study, a novel method for generating degenerate datasets of conductance-based models has been developed, proving to be significantly faster than the random sampling approach (all figures were created using a dataset of 500 neurons). The methodology for an N-channel conductance-based model can be summarized as follows:

1. The leakage conductance g_{leak} is drawn from a physiological uniform distribution: $g_{\text{leak}} \sim \mathcal{U}\left(g_{\text{leak min}}, g_{\text{leak max}}\right)$;
2. N - 3 maximum ion channel conductances are drawn from a physiological uniform distribution that is proportional to g_{leak}: g_{leak}: $\bar{g}_{\text{ion}} \sim \frac{g_{\text{leak}}}{(g_{\text{leak min}}+g_{\text{leak max}})/2} \cdot \mathcal{U}^{N-3}\left(\bar{g}_{\text{unmod min}}, \bar{g}_{\text{unmod max}}\right)$
3. The 3 remaining maximum ion channel conductances are computed using the compensation algorithm described in Drion et al. (2015a), and detailed just below.

So, the maximal conductance vector $\bar{g}_{\text{ion}} \in \mathbb{R}^N$ of a N-channel conductance-based model can be split in two parts: $\bar{g}_{\text{ion random}} \in \mathbb{R}^{N-3}$ that corresponds to the N - 3 randomly initialized maximum conductances in step 2 (proportional to g_{leak}), and $\bar{g}_{\text{ion compensated}} \in \mathbb{R}^3$ which corresponds to the 3 maximum conductances computed in step 3. The same split can be applied to S: $S_{\text{random}} \in \mathbb{R}^{3\times N-3}$ and $S_{\text{compensated}} \in \mathbb{R}^{3\times 3}$. By doing so, the DIC equation (14.3) can be written as:

$$\begin{aligned} f_{\text{DIC}} &= S_{\text{random}} \cdot \bar{g}_{\text{ion random}} + S_{\text{compensated}} \cdot \bar{g}_{\text{ion compensated}} \\ \iff S_{\text{compensated}} \cdot \bar{g}_{\text{ion compensated}} &= f_{\text{DIC}} - S_{\text{random}} \cdot \bar{g}_{\text{ion random}}. \end{aligned} \tag{14.7}$$

If values of the DIC at threshold voltage are specified, equation (14.7) consists of a system of 3 equations with 3 unknowns, *i.e.*, $\bar{g}_{\text{ion compensated}}$. For this system to be solved, $S_{\text{compensated}}$ must be of full rank. This means that the compensated ion channels must have a significant impact on the three timescales defined by the DICs. For the STG model, the compensated ones are the sodium (fast), A-type potassium (slow), and H (ultraslow) currents. For the DA model, the compensated ones are the sodium (fast), N-type calcium (slow), and ERG (ultraslow) currents.

So, the inputs of this algorithm consist of an a priori threshold voltage (which can be computed after using the algorithm described above), the values of the 3 DICs at the threshold voltage (these will specify the desired firing pattern), and all the boundaries of the uniform distributions. Note that, very often, a linear relation can be found between the value of the slow DIC at the threshold voltage and the corresponding value of the fast DIC. Tables 14.3, 14.4, and 14.5 contain all the parameters for the generated sets in the article. Also, note that the NMDA conductances follow the same formula as in random sampling sets.

Fig. 14.10 depicts the firing pattern characteristics, including inter- and intra-burst frequencies, duty cycle for the STG model, and spiking frequency for the DA model, at the population level for the sets generated by DICs. This visualization demonstrates the similarity of these neurons to those from the random sampling sets in terms of phenotype variability.

	V_{th}	$g_{\text{f}}(V_{\text{th}})$	$g_{\text{s}}(V_{\text{th}})$	$g_{\text{u}}(V_{\text{th}})$
STG model	-50 mV	-$g_{\text{s}}(V_{\text{th}})$ - 2.2	-8	4
DA model	-55.5 mV	-3.9·$g_{\text{s}}(V_{\text{th}})$ - 11	0.5	5

Table 14.3: Inputs for the DIC set generation algorithm for both models.

Current name	CaT	CaS	KCa	Kd	leak
$\bar{g}_{\text{ion min}}$ or $g_{\text{leak min}}$	2	6	140	70	0.007
$\bar{g}_{\text{ion max}}$ or $g_{\text{leak max}}$	7	22	180	140	0.014

Table 14.4: Boundaries of the uniform distribution for all maximum ion channel conductances of the STG model.

Current name	Kd	CaL	leak
$\bar{g}_{\text{ion min}}$ or $g_{\text{leak min}}$	0.015	6	0.008667
$\bar{g}_{\text{ion max}}$ or $g_{\text{leak max}}$	0.075	10	0.017334

Table 14.5: Boundaries of the uniform distribution for all maximum ion channel conductances of the DA model.

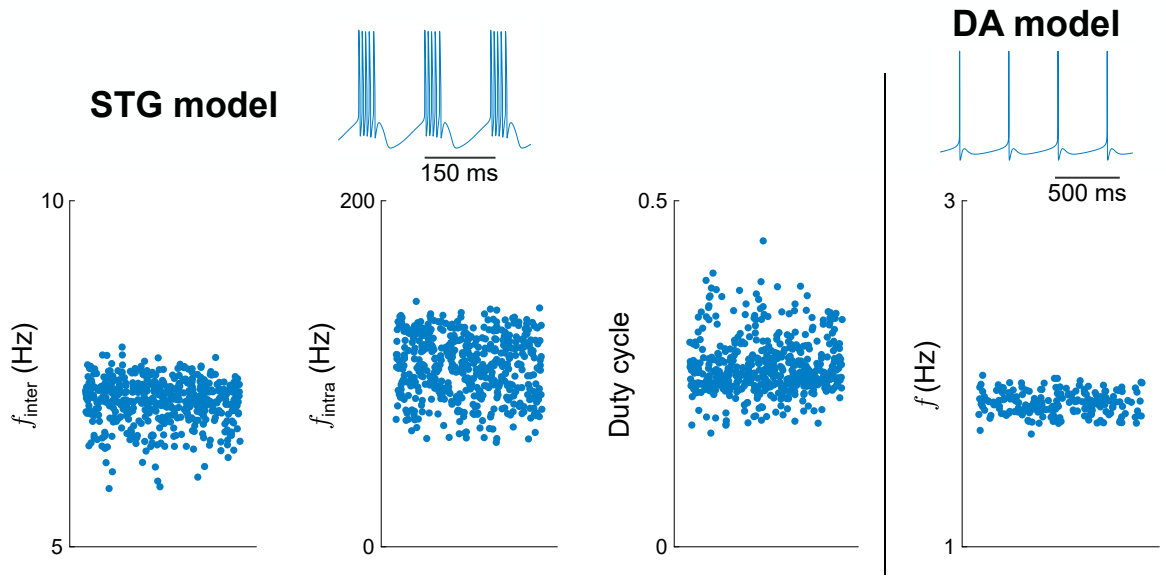

Figure 14.10: Firing pattern characteristics for the full variability DICs generated sets for both model.
On the left, the interburst frequencies, intraburst frequencies, and duty cycles of the DICs generated STG neurons are depicted. On the right, the spiking frequencies of the DICs generated DA neurons are depicted.

For the homogeneous scaling sets only, the boundaries $\bar{g}_{\text{ion random}}$ of the uniform distributions coincide to only keep the scaling with respect to g_{leak}, *i.e.*, $\bar{g}_{\text{ion min}} = \bar{g}_{\text{ion max}}$. Tables 14.6 and 14.7 contain these these boundaries for the homogeneous scaling-only generated sets in the article.

Current name	CaT	CaS	KCa	Kd
$\bar{g}_{\text{ion min}}$ or $\bar{g}_{\text{ion max}}$	3.5	11	160	110

Table 14.6: Boundaries of the uniform distribution for all maximum ion channel conductances of the STG model, for the homogeneous scaling only set.

Current name	Kd	CaL
$\bar{g}_{\text{ion min}}$ or $\bar{g}_{\text{ion max}}$	0.03	6

Table 14.7: Boundaries of the uniform distribution for all maximum ion channel conductances of the DA model, for the homogeneous scaling only set.

The last sets generated in this article consist of those where full variability is retained, except for homogeneous scaling. This implies that only the variability in conductance ratios is preserved. To achieve this, the boundaries of the uniform distribution for the leakage conductance coincide, *i.e.*, $g_{\text{leak min}} = g_{\text{leak max}}$. Consequently, g_{leak} is a constant. For the STG model, $g_{\text{leak}} = 0.01$, while for the DA model, $g_{\text{leak}} = 0.013$.

14.6.6 Computation details for the neuromodulation algorithm

A neuromodulation algorithm can be used to neuromodulate a degenerate set that has been initialized without the method previously described. This neuromodulation algorithm is greatly inspired by the set generation method described above.

Two conductances can be chosen to be neuromodulated in each model: $\bar{g}_{\text{CaS}}$ and $\bar{g}_{\text{A}}$ for the STG model, and $\bar{g}_{\text{CaL}}$ and $\bar{g}_{\text{CaN}}$ for the DA model. Moreover, neuromodulation is only applied to the slow and ultraslow DICs in this section, as the transition from tonic spiking to bursting is studied. This means that the first row of S is dropped, resulting in a new matrix $S_{\text{su}} \in \mathbb{R}^{2\times N}$ corresponding to the second and third rows of S.

So a similar split can be made for the maximal conductance vector $\bar{g}_{\text{ion}} \in \mathbb{R}^N$ of an N-channel conductance-based model and its reduced sensitivity matrix S_{su}: $\bar{g}_{\text{ion unmod}} \in \mathbb{R}^{N-2}$ corresponds to the $N-2$ unmodulated (unchanged) maximum conductances and $\bar{g}_{\text{ion mod}} \in \mathbb{R}^2$ corresponds to the 2 maximum conductances that are neuromodulated, along with their corresponding columns in S_{su}. Additionally, $S_{\text{su unmod}} \in \mathbb{R}^{2\times N-2}$ and $S_{\text{su mod}} \in \mathbb{R}^{2\times 2}$. By doing so, the DIC equation (14.3) can be written as

$$\begin{aligned} \begin{bmatrix} g_{\text{s}} \\ g_{\text{u}} \end{bmatrix} &= f_{\text{su DIC}} = S_{\text{su unmod}} \cdot \bar{g}_{\text{ion unmod}} + S_{\text{su mod}} \cdot \bar{g}_{\text{ion mod}} \\ \iff S_{\text{su mod}} \cdot \bar{g}_{\text{ion mod}} &= f_{\text{su DIC}} - S_{\text{su unmod}} \cdot \bar{g}_{\text{ion unmod}}. \end{aligned} \tag{14.8}$$

If values of the slow and ultraslow DICs at the threshold voltage are specified, equation (14.8) consists of a system of 2 equations with 2 unknowns, *i.e.*, $\bar{g}_{\text{ion mod}}$. For this system to be solved, $S_{\text{su mod}}$ must be of full rank, meaning that the neuromodulated ion channels must have a significant impact on the two timescales defined by the DICs.

If the values of the slow and ultraslow DICs are the same as in the set generation mechanism, the computed neuromodulated conductances match the original ones. However, as soon as the DIC values are modified, the modulated conductances will be tuned to match the desired DIC values, *i.e.*, the desired firing pattern. In this article, we showed that neuromodulation (for the tonic spiking to bursting transition) is robust when the ultraslow DIC value is kept constant (the same as in the generation mechanism) and when the slow DIC value is tuned to achieve different

firing patterns. Concerning the STG model, $g_s = 5$ for the tonic spiking set and $g_s = -2$ for the light bursting set. Regarding the DA model, $g_s = -1.5$ for the light bursting set and $g_s = -4$ for the strong bursting set.

For Figure 8, the same neuromodulation was used, but with continuous variation from one extreme value of g_s to another. Steps of 0.02 in g_s were used for the STG model, while steps of 0.005 in g_s were used for the DA model.

14.7 Data availability

All code and data can be found on the first author GitHub (https://github.com/arthur-fyon/CORR_2024) (Fyon, 2024).

14.8 Postface

In summary, this work provides a mechanistic understanding of neuronal degeneracy and its behavior under neuromodulation. Leveraging this knowledge, an efficient algorithm has been developed to generate a degenerate population and neuromodulate it. This algorithm is highly versatile and can be applied to any conductance-based model, provided it has enough ion channels to exhibit degeneracy.

Building on this foundation, the next part of this thesis focuses on developing a real-time model of neuromodulation inspired by the previous algorithm, as well as studying its interaction with homeostasis. This model can be easily integrated with any conductance-based model. In the following sections, neurons (or conductance-based models) are viewed as control systems, with the passive membrane as the plant and the active ion channels as the controller. This perspective is intended to facilitate the introduction of the neuromodulation model as an adaptive controller of ion channels.

15 Reliable neuromodulation from adaptive control of ion channel expression

This section is adapted from:
A. Fyon, P. Sacré, A. Franci, G. Drion,
Reliable neuromodulation from adaptive control of ion channel expression,
IFAC-PapersOnLine,
Volume 56, Issue 2,
2023,
Pages 458-463,
ISSN 2405-8963,
https://doi.org/10.1016/j.ifacol.2023.10.1610.
(https://www.sciencedirect.com/science/article/pii/S2405896323020189)
Fyon et al. (2023)

15.1 Preface

The first part of this chapter addresses reliable neuromodulation in a heterogeneous population of neurons. We developed a computational algorithm based on DICs theory that computes neuromodulated conductance values for each neuron to achieve a target firing pattern. However, this algorithm remains purely theoretical, with no direct biological interpretation.

Building on the mechanisms identified earlier, this section introduces a physiologically plausible GPCR-based molecular controller for neuromodulation. The approach relies on intracellular signals as physiological sensors, offering a functional approximation of previously extracted parameters. These signals enable the construction of a feedback control system at the level of second messengers and intracellular signaling pathways.

To ensure reliable neuromodulation, a feedback controller that is not adaptive was designed at the molecular level. Additionally, an adaptive mechanism was introduced to adjust a subset of intrinsic gains, specifically ion channel conductances, to produce consistent voltage activity despite degeneracy. This controller modifies ion channel properties to bring physiological sensor signals close to predefined reference values using adaptive control principles.

Finally, mechanisms linking neuromodulator concentration to target activity states were incorporated. Neuromodulator levels dynamically influence reference values at the second messenger level, enabling modulation of neuronal activity. In this context, reliability refers to the controller robustness to degeneracy, ensuring that any degenerate neuron reaches the desired neuromodulated activity. A robust controller, in this context, should be understood as one that produces reliable outcomes despite degeneracy, rather than the more common interpretation in control theory, which refers to a controller design explicitly addressing uncertainty.

15.2 Introduction

Cerebral activity is continuously shaped through the action of numerous neuromodulators and neuropeptides such as dopamine, serotonin, and histamine (Bargmann and Marder, 2013; Marder et al., 2014). These molecules dynamically affect the intrinsic properties and activity of single neurons and the strengths and dynamics of synaptic connections, providing means to constantly adapt a neuronal network activity in response to ever-changing needs, contexts, and environments (Marder and Calabrese, 1996; McCormick et al., 2020). Neuromodulators mainly act by changing the density, dynamics, and kinetics of transmembrane ion channels. The signaling of the entire brain therefore strongly depends on the robustness and reliability of neuromodulation actions at the molecular and cellular levels.

Although the ubiquity of neuromodulator action in all nervous systems has been acknowledged several decades ago, the mechanisms underlying their reliable action still remain elusive, particularly because they indirectly target the intrinsic properties of highly heterogeneous neurons (Marder et al., 2014). Neuromodulators act through the activation of metabotropic receptors. These receptors affect ion channels through second messengers that trigger complex and varied signaling cascades, eventually resulting in a wide range of effects depending on the neuron type. Many neuromodulators can target the same subset of ion channels, potentially leading to interfering effect (Marder and Bucher, 2007). Ion channel densities have been shown to be highly variable even in neurons of the same types, sometimes varying up to 5 folds (Schulz et al., 2006b). These observations raise the question of how neuromodulators can reliably work at the whole brain level whilst indirectly targeting these variable properties at the molecular and cellular levels.

In this work, we explore how reliable neuromodulation can be achieved through a simple intracellular feedback control system whose reference activity is set by the neuromodulator concentration level. This intracellular control system is motivated by the structure of metabotropic receptor signaling and exploits, rather than being affected by, variability in ion channels density. The resulting adaptive feedback control system is similar to a recently proposed adaptive conductance control system (Schmetterling et al., 2022) but with some key differences. First, the proposed control system is biologically plausible. As such, it provides a new mean to connect biological and engineered neuronal systems. Second, it does not require the knowledge of a reference membrane potential trajectory and to compare this reference trajectory with the neuron membrane potential trajectory. Rather, it exploits the mapping from neuronal intrinsic feedback gains to neuronal behavior (Drion et al., 2015a) to use simpler, *i.e.*, constant, references for those gains, which makes sensing and action more parsimonious. Third, the proposed model is fully compatible with existing models of neuronal homeostatic control (O'Leary et al., 2014).

The paper is organized as follows. Section 15.3 reviews the biology of neuromodulation-mediated neuronal regulation and translates it into an adaptive control scheme. Section 15.4 translates the derived control scheme into equations, partly relying on dynamic input conductance theory (Drion et al., 2015a). Section 15.5 presents numerical results and discuss their relevance in terms of reliable neuromodulation. Conclusions and perspective are discussed in Section 15.6.

15.3 Neurons as adaptive neuromodulation-controlled systems

15.3.1 Neuronal excitability and neuromodulation from an adaptive feedback control perspective

Excitability is a dynamical property that is fundamental to neurons. Yet intuitive, excitability is mathematically challenging since neurons are nonlinear, often high-dimensional, and their dynamics exhibit complex kinds of attractors, like limit cycles with multiples characteristic timescales. This makes the study of excitability and its modulation often hardly tractable, particularly when using neuron models made of high-dimensional nonlinear systems of ordinary differential equations.

Looking at neuronal excitability as a feedback control system permits to overcome this complexity by merging the effects of the many voltage-gated ion channels into a set of feedback gains acting on a few timescales (Drion et al., 2015a). Neuronal dynamics can indeed be modeled as a control system where many voltage-gated (and some calcium-gated) ion channels define a controller that outputs a control signal I_{int} to a passive membrane, representing the plant (Drion et al., 2015b) (Fig. 15.1, blue block).

The controller is tuned by the balance of many different types of ion channels, whose voltage-gating mechanisms can be sources of positive or negative feedback acting on different timescales. In a bursting neuron, the many timescales of channel gating can be merged into three sharply separated timescales, which we call fast, slow, and ultraslow. The feedback actions of all channel variables acting on a similar timescale balance each other to define a voltage-dependent feedback gain in each timescale. Dynamic input conductance (DIC) theory can be used to compute these gains (Drion et al., 2015a). In this way, excitability and its modulation emerge from the balance of positive and negative feedback loops at only three different timescales, which drastically lowers the dimensionality of the problem and makes it amenable to rigorous mathematical analysis through bifurcation and singularity theory (Franci et al., 2019).

The feedback control viewpoint of neuronal dynamics permits to study the mechanisms of reliable neuromodulation in a tractable way. Indeed, the primary targets of neuromodulators are ion channel densities (Marder et al., 2014), which themselves determine the feedback gains of the controller on each timescale. Neuromodulation can thus be understood as an input to an adaptive control block whose main role is to tune neuron behavior by adapting the feedback gains of the neuronal controller in a functionally relevant way, as depicted in Fig. 15.1, red block.

The neuromodulatory inputs to the adaptive block represents the neuromodulation concentration in the vicinity of the neuron. The adaptive control layer also receives ion channel conductance values $\bar{g}_{\text{ion}}$ as an input. Biologically, this input could be the output of a further neuronal adaptive control block, most naturally, a homeostatic control one (O'Leary et al., 2014), that reads the neuron outputs (membrane potential V and intracellular calcium concentration $[Ca]^{2+}$) and maps them to overall level of ion channel conductances to maintain excitability levels into safe bounds. We omit this block in the present work.

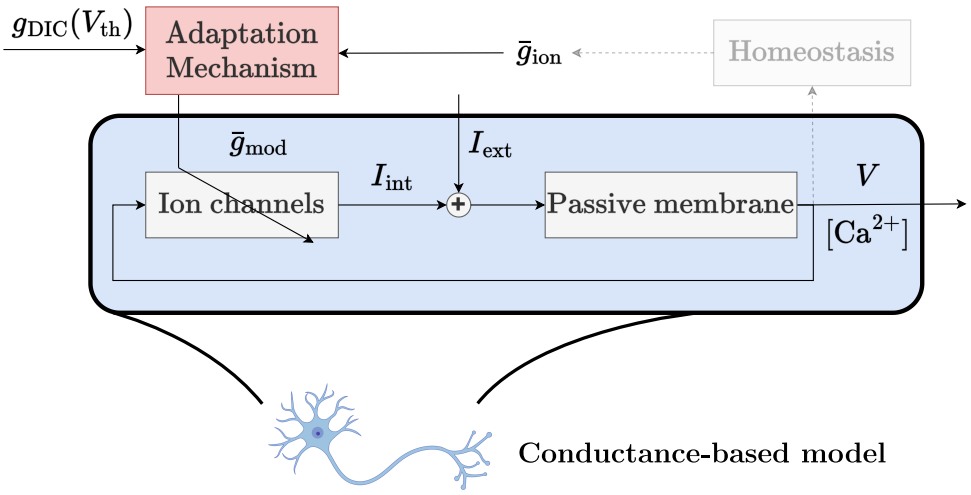

Figure 15.1: Neuronal excitability and neuromodulation from an adaptive feedback control perspective. High level block diagram of the adaptive neuronal controller. The blue block depicts the typical structure of a conductance based model from the feedback control perspective. A neuron is composed of a controller, *i.e.*, voltage and calcium controlled active ion channels, that produces an intrinsic current I_{int}, and a plant, *i.e.*, the passive membrane. *In vitro*, an external current I_{ext} can also be applied to excite the neuron. The red block lumps all the biological mechanisms that regulate ion channel conductances and that act as an adaptive layer onto the neuronal controller. Neuromodulator concentration $[nmod]$ can be modeled as an input to this adaptive block. See text for more details.

15.3.2 The neuromodulation adaptive control layer

Using the proposed viewpoint of neuromodulation and exploiting the indirect properties of cell signaling, we derived the adaptation mechanism system of Fig. 15.2. The proposed adaptation mechanism consists of two blocks: a reference generator block and a reference tracking block, *i.e.* a feedforward block and a feedback block respectively. The outputs of this neuromodulation-dependent adaptive system are ion channel conductances that tune neuronal feedback gains.

The feedforward block represents the activation of a metabotropic receptor that sets a neuromodulation dependent target for neuronal excitability properties by setting a reference signal for the modulated ion channels conductances (Fig. 15.2, blue block). Using DIC theory, setting a target for neuronal excitability properties is equivalent to setting targets, encoded in the vector $g_{\mathrm{DIC}}(V_{\mathrm{th}})$, for the neuron feedback gains at threshold voltage V_{th} where the neuronal behavior is maximally sensitive. A molecular network, triggered by the metabotropic receptor activation, maps these target gains into references $\bar{g}_0$ for the modulated channel conductances.

Reference ion channel conductance serves as the input of a PI regulated protein translation control system that creates new transmembrane proteins that are transported to the membrane by diffusion or active trafficking (O'Leary et al., 2014). The transport mechanism is modeled using two compartments representing the intracellular and membrane domains. Ion channel movement between the two compartments is modeled by simple passive diffusion, and ion channel turnover is accounted for by introducing a continuous degradation of transmembrane proteins in the intracellular domain (Fig. 15.2, purple block). For each modulated conductance, a positive translation control signal representing the synthesizing of new transmembrane proteins

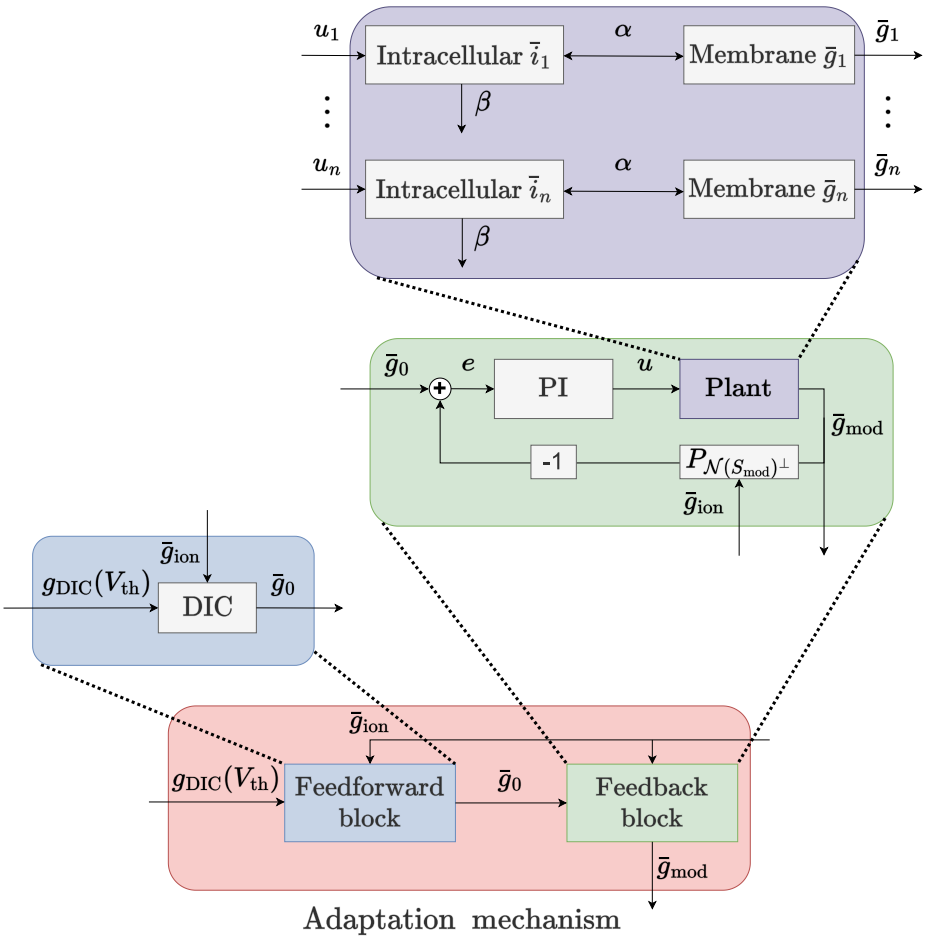

Figure 15.2: The neuromodulation adaptive control layer. Detailed block diagram of the adjustment mechanism, red block of Figure 15.1. It is composed of two sub-blocks: a reference generator (feedforward) block in blue and a reference tracking (feedback) block in green. The feedforward block models a cell signaling cascade that maps target neuronal gains $g_{\text{DIC}}(V_{\text{th}})$ at threshold voltage V_{th} to a reference signal $\bar{g}_0$ for modulated ion channel conductances. The feedback block regulates ion channel conductances through a classical PI negative feedback control loop of a molecular plant describing ion channel protein translation, trafficking, and membrane turnover. See text for details.

is computed by a classical negative feedback controller aiming at matching the ion channel conductance to its reference (Fig. 15.2, green block).

The projection matrix $P_{\mathcal{N}(S_{\text{mod}})^\perp}$ appearing in the feedback block is a mathematical abstraction of ion channel degeneracy, meaning that many ion channel combinations can lead to the same excitability type, *i.e.*, the same neuronal gains. Degeneracy can be understood as the existence of a subspace of ion channel conductances in which excitability properties do not change. Only regulation with respect to this subspace is relevant for tuning excitability and this is obtained by projection through $P_{\mathcal{N}(S_{\text{mod}})^\perp}$. We derive an expression for $P_{\mathcal{N}(S_{\text{mod}})^\perp}$ in the next section. Biologically, a molecule regulatory network can implement the mapping defined by $P_{\mathcal{N}(S_{\text{mod}})^\perp}$.

15.4 Putting biology into equations

This section is dedicated to put the blocks of Figures 15.1 and 15.2 into equations.

15.4.1 Neurons as electrical circuits: the conductance-based framework

Mathematical modeling of neuronal excitability was pioneered by Hodgkin and Huxley (Hodgkin and Huxley, 1952b). Models based on the Hodgkin-Huxley formalism are known as conductance-based models as they represent the neuronal membrane as an equivalent resistor-capacitor circuit. These models are a biophysical representation of an excitable cell in which current flowing across the membrane is split into two quantities: I_C due to charging of the membrane capacitance and I_{int} due to movement of ions across the membrane through different ion channels. In addition to leakage channels modeled by constant conductances, each modeled ion channel type is represented by a voltage- and time-dependent conductance $g_{\text{ion}}(V,t)$ whose maximum value $\bar{g}_{\text{ion}}$ is determined by the number of ion channels available at the membrane. Voltage- and time-dependence of ion channel conductances is determined by their dynamic opening and closing in response to changes in membrane potential, a phenomenon called gating. These models have proved successful to capture a variety of complex neuronal phenomena like excitability and its modulation, degeneracy, and homeostatic regulation (Marder et al., 2014).

Mathematically, the voltage current relationship of any conductance-based neuron model writes

$$\begin{aligned} I_C &= C\frac{\mathrm{d}V}{\mathrm{d}t} + g_{\text{leak}}(V - E_{\text{leak}}) = -I_{\text{int}} + I_{\text{ext}} \\ &= -\sum_{\text{ion}\in\mathcal{I}} g_{\text{ion}}(V,t)(V - E_{\text{ion}}) + I_{\text{ext}}, \end{aligned}$$

where C is the membrane capacitance, g_{ion} is non-negative and gated between 0 (all channels closed) and $\bar{g}_{\text{ion}}$ (all channels opened), E_{ion} and E_{leak} are the channel reversal potentials, $\mathcal{I}$ is the index set of intrinsic ionic currents, and I_{ext} is the current externally applied *in vitro* or the combination of synaptic currents.

In this paper, we focus our study of reliable neuromodulation on a stomatogastric (STG) neuron conductance-based model (Liu et al., 1998), but the proposed mechanisms are general. Thanks to the plethora of modulatory transmitters and neuropeptides flowing through the STG ganglion, STG neurons provide a prototypical test-bed for neuromodulation studies (Marder et al., 2014). In the chosen STG neuron model, transitions between tonic spiking and bursting activities are of particular interest, as they relate to important behavioral switches in the STG ganglion (Meyrand et al., 1994).

15.4.2 Mapping ion channel conductances to neuronal feedback gains

The few feedback gains determining neuronal behavior are constructed from the voltage-dependent DIC (Drion et al., 2015a). DICs are three voltage-dependent conductance curves $g_{\text{f}}(V), g_{\text{s}}(V), g_{\text{u}}(V)$ that can be computed as linear functions of the maximal conductance vector $\bar{g}_{\text{ion}}$ of the neuron model at each V

$$\begin{bmatrix} g_{\text{f}}(V) \\ g_{\text{s}}(V) \\ g_{\text{u}}(V) \end{bmatrix} = f_{\text{DIC}}(V) = S(V)\cdot\bar{g}_{\text{ion}}\,, \tag{15.1}$$

where $S(V)$ is a sensitivity matrix that can be built using the methods in Drion et al. (2015a). Because of the specific feedback structure of conductance-based models, DICs shape neuronal spiking behavior and the three DICs differ in the timescale at which this shaping happens: fast $g_{\mathrm{f}}(V)$, slow $g_{\mathrm{s}}(V)$, and ultraslow $g_{\mathrm{u}}(V)$.

Values and signs of the DICs at specific voltages, mainly the threshold voltage V_{th}, reliably determine the neuronal firing pattern (Drion et al., 2015a). For instance, a negative $g_{\mathrm{f}}(V_{\mathrm{th}})$, which corresponds to a local fast positive feedback, indicates that the neuron is able to fire a spike spontaneously around threshold voltage. A positive $g_{\mathrm{s}}(V_{\mathrm{th}})$, which corresponds to a slow negative feedback, indicates that, right after a spike, the neuron will tend to attenuate the excitation and bring back the neuron to rest voltage, while a negative $g_{\mathrm{s}}(V_{\mathrm{th}})$ indicates that the neuron will tend to fire other spikes to initiate a burst. In the case of bursting neuron, $g_{\mathrm{u}}(V_{\mathrm{th}})$ is always positive and is an indicator of the interburst frequency as well as the duty cycle, *i.e.*, ultraslow negative feedback.

15.4.3 The reference generator block: mapping target feedback gains to reference ion channel conductances

The reference generator block of the proposed adaptation mechanism transforms neuronal feedback gain reference trajectories into ion channel conductance reference trajectories. That is, it transforms a functionally relevant reference signal, linked to the excitability type of the neuron, into a molecular reference signal that the feedback block can track.

The neuronal feedback gains are linked to ion channel maximal conductance through DICs. Target neuronal activity is defined as $g_{\mathrm{DIC}}(V_{\mathrm{th}}) = [f_{\mathrm{DIC}}(V_{\mathrm{th}})]_{t\in\mathcal{T}}$ with $\mathcal{T}$ being the set of timescales, *i.e.* $\mathcal{T} = \{f, s, u\}$ and t being the modulated timescales (neuromodulator dependent). Given this target neuronal activity $g_{\mathrm{DIC}}(V_{\mathrm{th}}) \in \mathbb{R}^p$ for $p \leq 3$ neuronal feedback gains, and if there are n modulated conductances, (15.1) defines a linear system of p equations in n unknowns. Because each modulator affects many conductances, in general $p \leq n$ and the system might be underdetermined, which leads to an infinite number of solutions (a whole subspace) in accordance with biological observation of ion channel degeneracy.

More formally, if the neuron expresses N types of ion channels, of which n are modulated and $m = N - n$ are unmodulated, the complete sensitivity matrix $S(V)$ used in the computation of the DICs at voltage V and the complete maximum ion channel conductance vector $\bar{g}_{\mathrm{ion}}$ can be split in modulated ($S_{\mathrm{mod}}(V) \in \mathbb{R}^{p\times n}$, $\bar{g}_{\mathrm{mod}} \in \mathbb{R}^n$) and unmodulated ($S_{\mathrm{unmod}}(V) \in \mathbb{R}^{p\times m}$, $\bar{g}_{\mathrm{unmod}} \in \mathbb{R}^m$) components. Then the mapping from maximal conductances to DICs at threshold voltage can then be written as

$$g_{\mathrm{DIC}}(V_{\mathrm{th}}) = \begin{bmatrix} S_{\mathrm{mod}}(V_{\mathrm{th}}) & S_{\mathrm{unmod}}(V_{\mathrm{th}}) \end{bmatrix} \cdot \begin{bmatrix} \bar{g}_{\mathrm{mod}} \\ \bar{g}_{\mathrm{unmod}} \end{bmatrix}.$$

As only the threshold voltage is used, we drop voltage dependence of coefficient matrices and DICs in what follows. Isolating the unknowns modulated ion channel reference, the system

becomes

$$S_{\text{mod}} \cdot \bar{g}_{\text{mod}} = g_{\text{DIC}} - S_{\text{unmod}} \cdot \bar{g}_{\text{unmod}} =: g_{\text{DIC}_\text{r}} \,. \tag{15.2}$$

Under the assumption that $n \geq p$ and S_{mod} has full row rank, the solution set to (15.2) is

$$\{\ \bar{g}_{\text{mod}} \mid S_{\text{mod}} \cdot \bar{g}_{\text{mod}} = g_{\text{DIC}_\text{r}}\ \} = \{\ \bar{g}_0 + z \mid z \in \mathcal{N}(S_{\text{mod}})\ \}\,,$$

where $\bar{g}_0$ is any solution, *i.e.*, $S_{\text{mod}} \cdot \bar{g}_0 = g_{\text{DIC}_\text{r}}$ and $\mathcal{N}(S_{\text{mod}})$ is the nullspace of S_{mod}, *i.e.*,

$$\mathcal{N}(S_{\text{mod}}) = \{z \in \mathbb{R}^n \mid S_{\text{mod}} z = 0\}.$$

An important particular solution, that has the smallest norm as compared to any other solution, is

$$\bar{g}_0 = S_{\text{mod}}^T (S_{\text{mod}} S_{\text{mod}}^T)^{-1} \cdot g_{\text{DIC}_\text{r}} =: S_{\text{mod}}^+ \cdot g_{\text{DIC}_\text{r}}\,, \tag{15.3}$$

where S_{mod}^+ is the Moore-Penrose generalized inverse of S_{mod} (Golub and Van Loan, 2013). The matrix

$$S_{\text{mod}}^+ S_{\text{mod}} = P_{\mathcal{N}(S_{\text{mod}})^\perp} \tag{15.4}$$

gives the projection onto the orthogonal complement of $\mathcal{N}(S_{\text{mod}})$. Equation 15.3 provides a reference values $\bar{g}_0$ for modulated ion channel conductances to the neuron to the desired excitability type. Biologically a molecular regulatory network can implement this equation. Note that the feedforward block depends and therefore must access the overall conductance state $\bar{g}_{\text{ion}}$ of the neuron. This means that the feedforward block adapts to any change in the conductance of unmodulated ion channels. Because a neuron cannot measure its own ion channel conductance levels, the dependence of the proposed adaptation mechanism in $\bar{g}_{\text{ion}}$ is not biologically plausible. We will address this issue in future works, by using signals measurable by the neuron such as V or $[\text{Ca}^{2+}]$ and adding a homeostatic control loop inspired by O'Leary et al. (2014) whose output provides a biological version of $\bar{g}_{\text{ion}}$. Putting together homeostasis and molecular regulatory network is an idea already explored in Franci et al. (2020) to make the homeostatic controller in O'Leary et al. (2014) robust to unmatched disturbances.

15.4.4 The feedback block: ion channel conductance regulation and membrane turnover

The feedback block takes the form of a classical PI control system with gains K_p and K_i controlling a plant describing the molecular dynamics of each modulated ion channel. The input of the PI controller is an error signal vector $e \in \mathbb{R}^n$. The dynamics describing ion channel creation and transport are modeled as a linear two compartments (the intracellular and membrane ones, with state variables $\bar{i} \in \mathbb{R}^n$ and $\bar{g}_{\text{mod}} \in \mathbb{R}^n$, respectively) model communicating at rate α and with continuous degradation of intracellular ion channels at rate β, biologically motivated by the membrane turnover. The control input ($u \in \mathbb{R}^n$) consists in a controlled translation mechanism that synthesizes intracellular ion channels ready to integrate the membrane through diffusion and to participate in excitability shaping of the neuron.

The dynamics of the feedback block for n neuromodulated ion channel writes

$$\dot{\bar{i}}_j = \alpha \cdot \bar{g}_j - (\alpha + \beta) \cdot \bar{i}_j + u_j$$
$$\dot{\bar{g}}_j = \alpha \cdot \bar{i}_j - \alpha \cdot \bar{g}_j, \quad j = 1, \ldots, n.$$

The control u_j is generated by a PI controller

$$u_j(t) = K_\mathrm{p} \cdot e_j(t) + K_\mathrm{i} \cdot \int_0^t e_j(\tau)\, d\tau. \tag{15.5}$$

To ensure that the steady-state value imposed by the PI controller for the modulated ion channels will make the neuronal feedback gains match the target ones, the error vector e in (15.5) is defined as

$$e = r - y := \bar{g}_0 - P_{\mathcal{N}(S_\mathrm{mod})^\perp} \cdot \bar{g}_\mathrm{mod}\,,$$

where $r = \bar{g}_0$ is the reference of the feedback block and $y = P_{\mathcal{N}(S_\mathrm{mod})^\perp} \bar{g}_\mathrm{mod}$ is its output. Thanks to PI action, the overall system will reach steady state when the error vector is identically zero, *i.e.*, when $e = 0_n$. By developing e using (15.3) and (15.4), one has

$$e = S_\mathrm{mod}^+ \cdot g_{\mathrm{DIC_r}} - S_\mathrm{mod}^+ S_\mathrm{mod} \cdot \bar{g}_\mathrm{mod}.$$

Imposing $e = 0_n$ leads

$$S_\mathrm{mod}^+ S_\mathrm{mod} \cdot \bar{g}_\mathrm{mod}^* = S_\mathrm{mod}^+ \cdot g_{\mathrm{DIC_r}}\,,$$

where $\bar{g}_\mathrm{mod}^*$ denote the modulated conductance values at steady state. Multiplying both sides of the last equality from the left by S_mod gives

$$\underbrace{S_\mathrm{mod} S_\mathrm{mod}^+}_{I_p} S_\mathrm{mod} \cdot \bar{g}_\mathrm{mod}^* = \underbrace{S_\mathrm{mod} S_\mathrm{mod}^+}_{I_p} \cdot g_{\mathrm{DIC_r}}$$

and therefore

$$S_\mathrm{mod} \cdot \bar{g}_\mathrm{mod}^* = g_{\mathrm{DIC_r}}, \tag{15.6}$$

which means that, at steady state, the overall system will converge towards values of neuromodulated ion channels that match the actual model DICs with the target ones, even if the system (15.2) is underdetermined. Therefore, the adaptive neuromodulation-controlled system ensure that, with n ($\geq p$) appropriate neuromodulated ion channels (S_mod full row rank), the excitability of the neuron can be shaped by fixing neuronal feedback gains. The adaptation mechanism, and especially the feedback block, is ensured to be stable as long as the PI feedback is slow enough. Under-determinacy of (15.2) implies that the steady-state solution enforced by the PI controller is not unique, which provides a new mechanistic explanation for neuronal degeneracy.

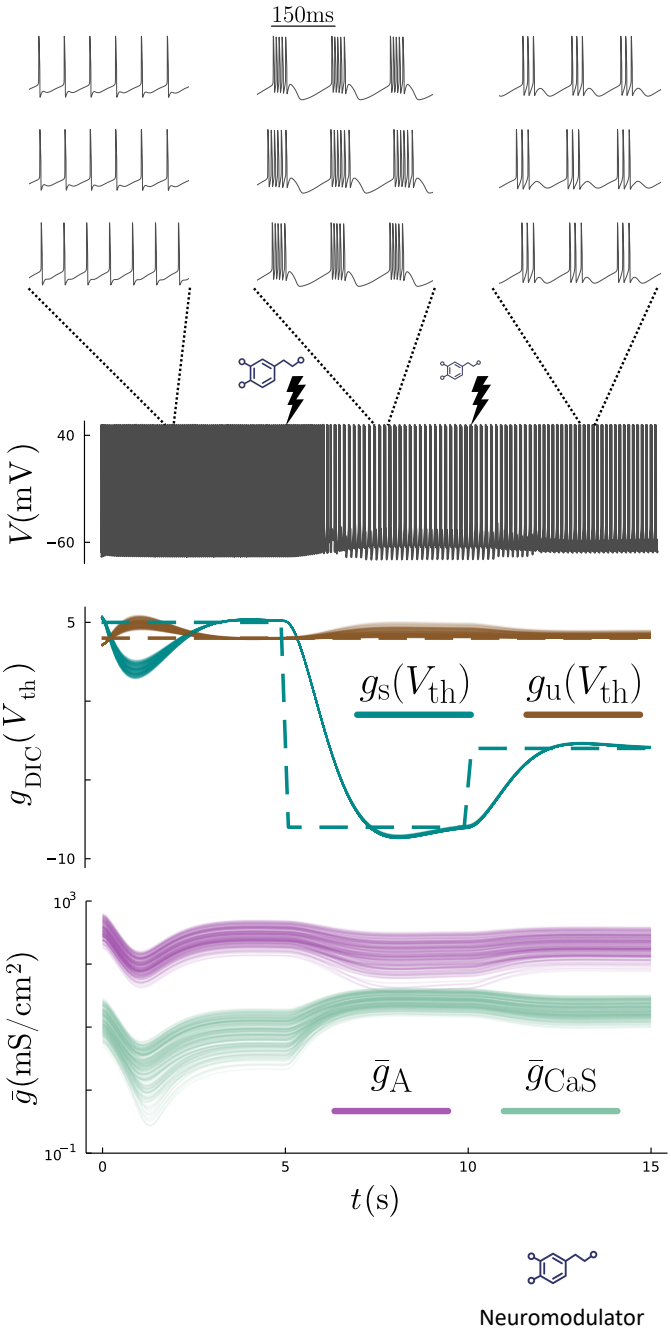

Figure 15.3: Reliable neuromodulation from adaptive gain control. Virtual experiment of the adjustment mechanism applied to 200 STG models with heterogeneous nominal parameters. In this experiment, three different states are targeted during the three different thirds of the simulation, respectively tonic spiking, strong bursting and light bursting (triplets). A typical V trace for each third of the simulation is shown on top for three randomly chosen model neurons with different parameter values, which proves the robustness of the modulation mechanism to heterogeneity. We simulated a bath application with a strong increase in the neuromodulator concentration at $t = 5\,\mathrm{s}$ and a slight decrease at $t = 10\,\mathrm{s}$. This modulation is achieved by maintaining $g_\mathrm{u}(V_\mathrm{th})$ constant and by regulating $g_\mathrm{s}(V_\mathrm{th})$ through the proposed neuromodulation control scheme. Target values of DICs are depicted in dashed lines while actual values of neuronal feedback gains are depicted in full lines. The target $g_\mathrm{s}(V_\mathrm{th})$ is achieved by modulating only two slow ion channel conductances, namely $\bar{g}_\mathrm{A}$ and $\bar{g}_\mathrm{CaS}$, bottom.

15.5 Reliable neuromodulation from adaptive gain control

The robustness of the proposed adaptive gain control scheme was tested in simulation on neurons having highly variable sets of maximal conductances, in agreement with biological data. We focus our simulation on neuromodulation-dependent spiking to bursting transitions, with slow calcium and A type potassium channels ($\bar{g}_{\mathrm{CaS}}$ and $\bar{g}_{\mathrm{A}}$, respectively) as targets of neuromodulators. Spiking to bursting transitions are controlled by specific values of $g_{\mathrm{s}}(V_{\mathrm{th}})$ and $g_{\mathrm{u}}(V_{\mathrm{th}})$ (Drion et al., 2015a). $g_{\mathrm{f}}(V_{\mathrm{th}})$ is chosen to not be controlled, as it correlates with spike upstroke but does not affect spiking to bursting transitions. Therefore, the problem results in a two dimensional linear system where the unknowns are the ion channel conductance reference trajectories, and solutions of (15.6) are uniquely determined.

These simulations reproduce a bath application that is constructed as follows (Fig. 15.3): first, no neuromodulator is applied to the neurons, which is emulated by setting the value of $g_{\mathrm{s}}(V_{\mathrm{th}})$ to a positive value. In that state, the target activity is single spike firing. After 5 seconds, $g_{\mathrm{s}}(V_{\mathrm{th}})$ is set to a strongly negative value, emulating the application of a strong concentration of a bursting-inducing neuromodulator, such as proctoline or pilocarpine. $g_{\mathrm{s}}(V_{\mathrm{th}})$ is then reduces to a less negative value at 10 seconds to model a decrease in neuromodulator concentration. The target value for $g_{\mathrm{u}}(V_{\mathrm{th}})$ is kept constant during the whole simulation, as we consider that the neuromodulator only tunes the slow conductance value. It is important to note that $g_{\mathrm{s}}(V_{\mathrm{th}})$ is the only externally modified input to the model in this virtual experiment, every other inputs and parameters, including channel maximal conductances being autonomously tuned by the adaptive control mechanism.

Figure 15.3 shows simulation results for 200 highly variable parameter sets of maximal conductance values. In all these models, the adaptive control system is capable of reliably reaching the three target firing activities corresponding to the three neuromodulation levels by tuning the maximal conductance values $\bar{g}_{\mathrm{CaS}}$ and $\bar{g}_{\mathrm{A}}$ in a neuron-dependent manner. This shows that such simple yet carefully designed adaptive controller targeting two scalar reference gain values is capable of reliably controlling the behavior of a complex neuron model. The same experiment showed similar results on a dopaminergic neuron model, which illustrates the generality of the proposed approach.

15.6 Conclusions

In this work, we designed an adaptive control mechanism that achieves reliable neuromodulation in highly heterogeneous neurons. The control mechanism is motivated by the specific structure of molecular signaling triggered by neuromodulators, which involves second messenger and intracellular signaling cascades in molecular regulatory networks to link changes in neuromodulator concentration to changes in ion channel maximal conductances. We showed that despite the high complexity and dimensionality of neuronal dynamics, reliable neuromodulation could be achieved by tuning the values of a few neuron feedback gains acting on different timescales and localized around threshold potential. A feedforward mechanism transforms these target gains into neuron-dependent targets for the maximal conductance of a subset of neuromodulated ion channels. Future work will aim at coupling the proposed control scheme with previously published

homeostatic neuronal control schemes and at the implementation of the resulting controller in neuromorphic hardware.

15.7 Supplemental material

Table 15.1: Parameter values

Parameter	Value	Units
α	$5 \cdot 10^{-3}$	ms^{-1}
β	$5 \cdot 10^{-3}$	ms^{-1}
K_p	$3 \cdot 10^{-4}$	ms^{-1}
K_i	$5 \cdot 10^{-6}$	ms^{-1}

15.8 Postface

In the context of this thesis, the robust neuromodulation algorithm developed in the first section, initially lacking biological interpretation, is transformed into a biologically interpretable bio-controller for neuromodulation. This adaptive controller is designed for generality, enabling its application to any conductance-based model while closely replicating the performance of biological systems, as shown in Fig. 15.3. To demonstrate this generality, spiking-to-bursting transitions were applied to both a dopaminergic neuron model (Qian et al., 2014) and an Aplysia R15 neuron model (Plant and Kim, 1976), illustrated in Fig. 15.4.

Remarkably, despite the differences between these conductance-based models, the adaptive neuromodulation controller robustly tuned the firing patterns from tonic spiking to bursting. This was achieved by modulating two slow conductances ($\bar{g}_\mathrm{CaL}$ and $\bar{g}_\mathrm{CaN}$) in the dopaminergic model to adjust $g_\mathrm{s}(V_\mathrm{th})$ while maintaining $g_\mathrm{u}(V_\mathrm{th})$ constant, similar to the approach used in the STG model. In contrast, the Aplysia neuron model, characterized by low degeneracy and significant timescale separation, required modulation of only one conductance ($\bar{g}_\mathrm{Kd}$) to achieve robust bursting without the need to explicitly maintain $g_\mathrm{u}(V_\mathrm{th})$.

This neuromodulation controller is not limited to transitions from tonic spiking to bursting; it can also modulate neuronal activity in diverse ways by appropriately adjusting the corresponding DIC values. For example, the burstiness of bursting neurons can be modulated using this adaptive neuromodulation control. Fig. 15.5 illustrates how burstiness is robustly increased in degenerate populations of DA and STG neuron models by maintaining $g_\mathrm{s}(V_\mathrm{th})$ constant while slightly decreasing $g_\mathrm{u}(V_\mathrm{th})$, thereby reducing the strength of the ultraslow negative feedback.

As shown, the same conductances were used to achieve this modulation, resulting in an increased number of spikes per burst and a higher duty cycle in both bursting behaviors. This demonstrates the generality of the adaptive neuromodulation control, as it can be robustly applied to any neuron model to modulate activity in a physiologically meaningful way.

In addition to its robustness, this adaptive controller of neuromodulation is biologically relevant, and a biological interpretation is given in Fig. 15.6. Fig. 15.6A depicts a direct comparison between the biological neuromodulation process and the block diagram of the neuromodulation controller. In biology, most neuromodulators bind to G-protein coupled receptors (GPCR)

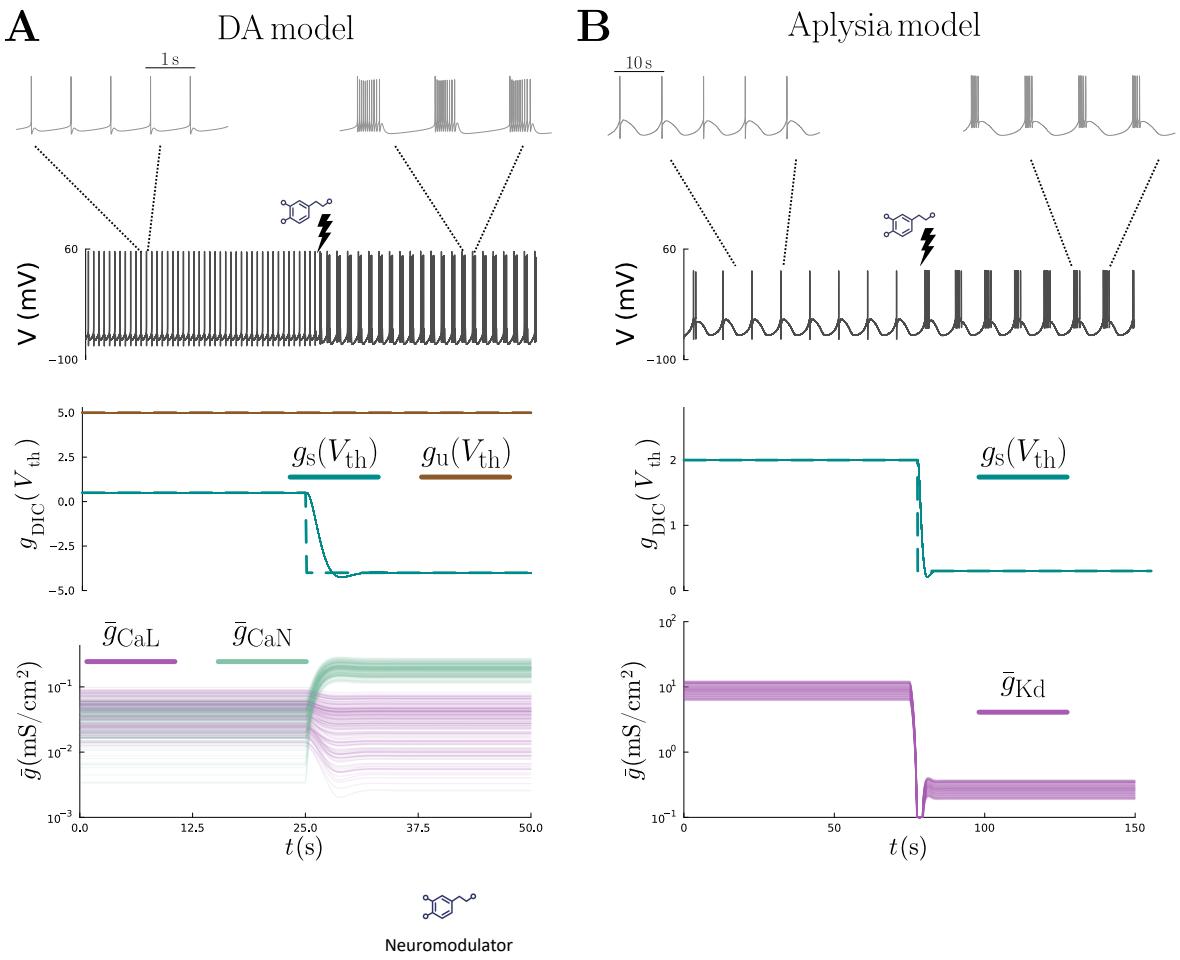

Figure 15.4: Reliable neuromodulation through adaptive gain control in DA and Aplysia models. Virtual experiments demonstrating the neuromodulation mechanism applied to 200 DA (A) and Aplysia (B) neuron models with heterogeneous nominal parameters. In this experiment, two distinct states—tonic spiking and strong bursting—are targeted. A representative voltage trace (V) for each half of the simulation is shown at the top for one randomly selected neuron. At the midpoint of the simulation, a simulated bath application induces a significant increase in neuromodulator concentration. This modulation is achieved by maintaining $g_{\mathrm{u}}(V_{\mathrm{th}})$ constant while regulating $g_{\mathrm{s}}(V_{\mathrm{th}})$ through the proposed neuromodulation control scheme. The dashed lines represent target DIC values, while solid lines indicate the actual neuronal feedback gains. In the DA model, the target $g_{\mathrm{s}}(V_{\mathrm{th}})$ is achieved by modulating two slow ion channel conductances, $\bar{g}_{\mathrm{CaL}}$ and $\bar{g}_{\mathrm{CaN}}$ (bottom). In contrast, the Aplysia model, characterized by low degeneracy and significant timescale separation, required modulation of only a single slow ion channel conductance, $\bar{g}_{\mathrm{Kd}}$, to robustly transition between states.

and initiate a complex signaling cascade using second messengers such as calcium ($[Ca^{+2}]$) or cyclic adenosine monophosphate (cAMP) (Chen et al., 2006; Xia and Storm, 1997; Spangler and Bruchas, 2017). This cascade may activate various cellular mechanisms, eventually altering the ionic conductance of a subset of ion channels on the neuronal membrane. In the adaptive neuromodulation controller, neurons are viewed as feedback models, where ion channels act as intrinsic neuronal controllers producing an ionic current based on membrane potential, modeled as nonlinear conductances. The passive bilayer of phospholipids is considered the "plant" modeled as a linear RC circuit. The adaptive controller takes as input the concentration of specific

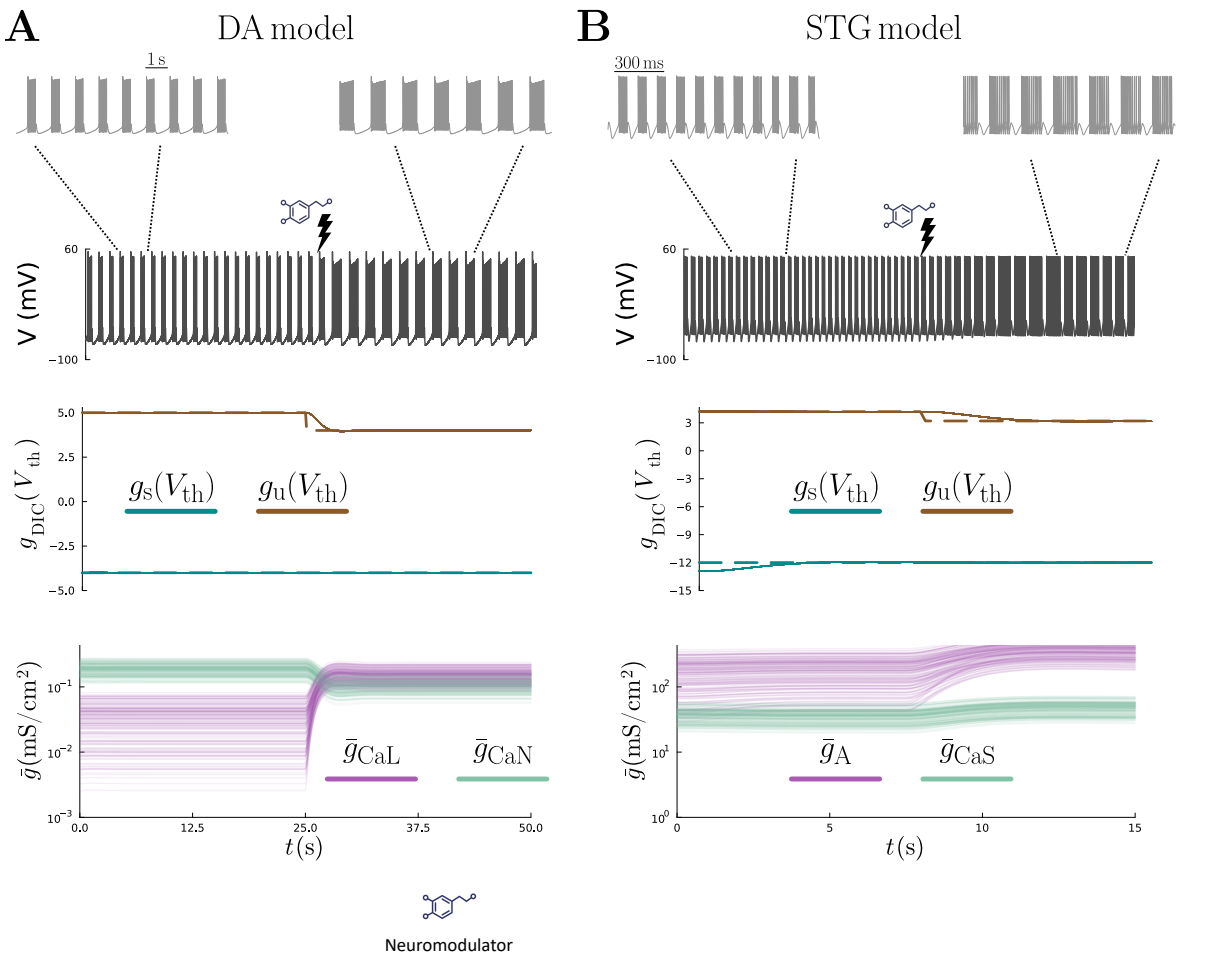

Figure 15.5: Reliable bursting neuromodulation through adaptive gain control in DA and STG models. Virtual experiments demonstrate the neuromodulation mechanism applied to 200 DA (A) and STG (B) neuron models with heterogeneous nominal parameters. In this experiment, two distinct bursting states are targeted. Representative voltage traces (V) for each half of the simulation are shown at the top for a randomly selected neuron. At the midpoint of the simulation, a simulated bath application induces a significant increase in neuromodulator concentration, resulting in enhanced burstiness. This modulation is achieved by maintaining $g_{\mathrm{s}}(V_{\mathrm{th}})$ constant while regulating $g_{\mathrm{u}}(V_{\mathrm{th}})$ through the proposed neuromodulation control scheme. Dashed lines represent the target DIC values, while solid lines indicate the actual neuronal feedback gains. In the DA model, the target $g_{\mathrm{u}}(V_{\mathrm{th}})$ is achieved by modulating two slow ion channel conductances, $\bar{g}_{\mathrm{CaL}}$ and $\bar{g}_{\mathrm{CaN}}$ (bottom). In contrast, $\bar{g}_{\mathrm{A}}$ and $\bar{g}_{\mathrm{CaS}}$ are modulated in the STG model.

neuromodulators, modeled as target neuronal feedback gains (*i.e.* target firing pattern), at the entry of a first reference generator block, analogous to the GPCR complex. This block transforms neuronal feedback gain references into reference values of neuromodulated maximum ion channel conductances $\bar{g}_0$, utilizing the DIC theory (Drion et al., 2015a). The second block of the adaptive controller is reference tracking, where actual values of maximum ion channel conductances that are neuromodulated ($\bar{g}_{\mathrm{mod}}$) are tracked to their reference values using PI control, reflecting integrative and proportional actions observed in biology (Tellam et al., 2000; Robinson, 1989). In biology, this function is fulfilled by the complex signaling cascade, serving as a negative feedback controller to adjust the effective values of modulated conductances. Once

modulated conductances reach their reference values, neuromodulated activity is achieved.

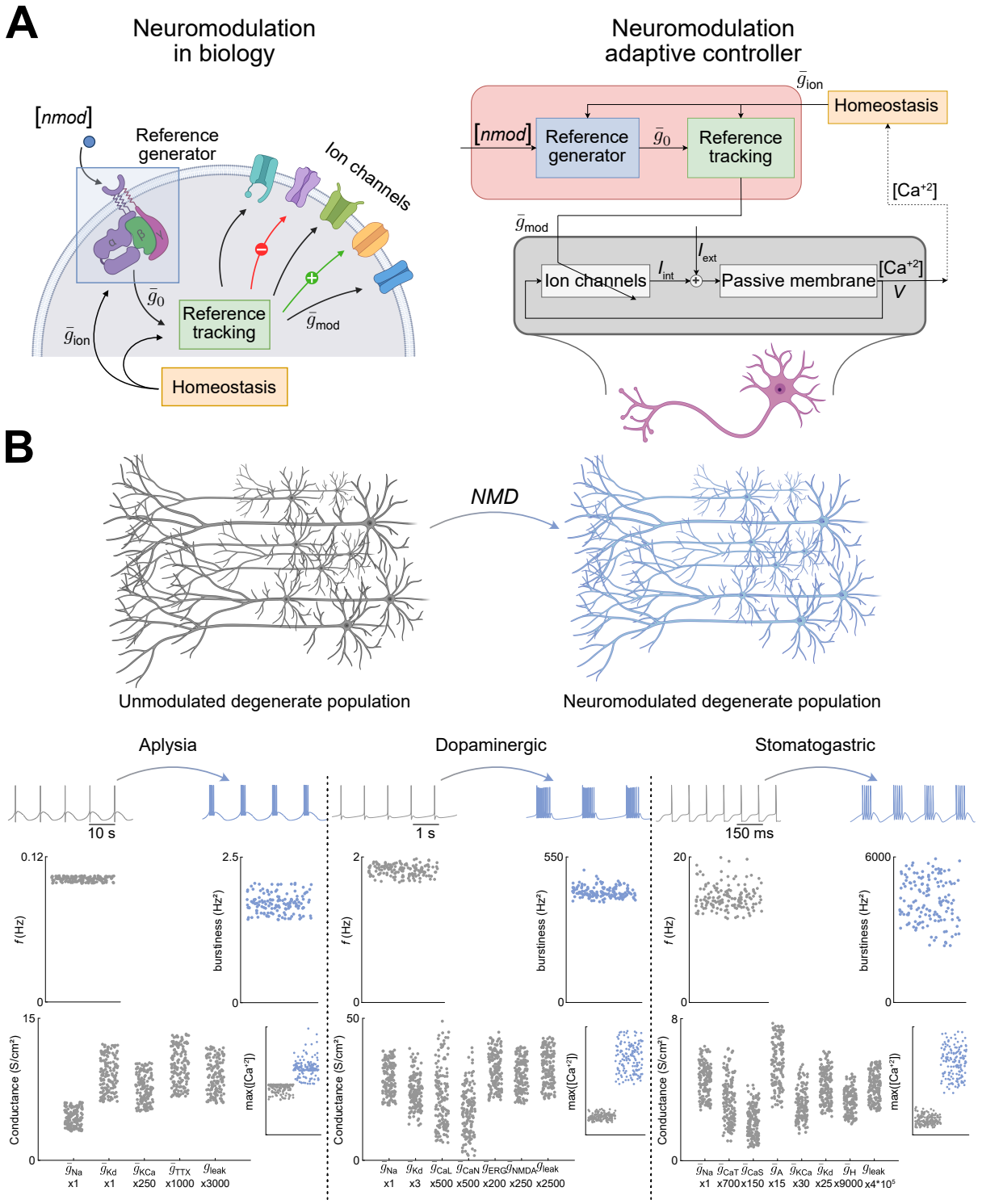

Figure 15.6: A biological interpretation of the adaptive neuromodulation controller. **A.** One-to-one comparison between biological neurons (left) and the block diagram of the adaptive neuromodulation controller (right). **B.** Populations of Aplysia R15, DA, and STG neuron models are robustly neuromodulated from tonic spiking to bursting (top), despite exhibiting significant degeneracy in their intrinsic parameters (bottom). However, this transition results in an increase in intracellular calcium levels, which, if prolonged, could lead to cell apoptosis. This strongly suggests that the adaptive neuromodulation controller should be integrated with a homeostatic controller, whose primary role is to preserve cell viability by regulating intracellular calcium.

Fig. 15.6B illustrates the results of the adaptive neuromodulation controller on three different conductance-based models: a model of R15 neuron in the Aplysia, a DA neuron model, and a STG neuron model. For each model, degenerate populations expressing tonic spiking at common frequencies were generated. Transitions from tonic spiking (gray) to bursting (blue) were simulated using the adaptive neuromodulation controller by tuning the slow neuronal feedback gain from positive to negative values. The neuromodulated conductances for the Aplysia, DA and STG models were respectively $\bar{g}_{\mathrm{Kd}}$; $\bar{g}_{\mathrm{CaL}}$ and $\bar{g}_{\mathrm{CaN}}$; $\bar{g}_{\mathrm{CaS}}$ and $\bar{g}_{\mathrm{A}}$. These transitions were achieved for every neuron in the population, indicating similar bursting behavior after neuromodulation among a population (Fig. 15.6B bottom, on top of each neuron panel), despite large initial differences in ionic conductances (Fig. 15.6B bottom, on bottom left of each neuron panel). This highlights the robustness of this neuromodulation model with respect to variability in neuronal parameters, *i.e.*, degeneracy.

However, when neuromodulation is applied alone, the maximal level of intracellular calcium can significantly increase during tonic spiking to bursting transitions, as there are no homeostatic compounds in pure neuromodulation (Fig. 15.6B bottom, on bottom right of each neuron panel). This elevation in calcium levels may lead to cellular dysfunctions and eventual cell apoptosis (Orrenius et al., 2003; Krebs, 1998). Therefore, the interaction between homeostasis tuning rules and neuromodulation is crucial to create a function modulatory system combined with a self-regulatory system that maintains adequate levels of intracellular calcium and ionic conductances within the cell to achieve functional duration.

16 Neuromodulation and homeostasis: complementary mechanisms for robust neural function

This section is adapted from:
A. Fyon, G. Drion,
Neuromodulation and homeostasis: Complementary mechanisms for robust neural function,
ArXiv preprint,
https://arxiv.org/abs/2412.04172v1
Fyon and Drion (2024b)

16.1 Preface

Developing such a model of neuromodulation offers advantages over its static algorithmic version, particularly as it can operate in real time. One key benefit is the ability to couple this model with a previously developed homeostatic controller model (O'Leary et al., 2014) to analyze their interaction and demonstrate the necessity of such a controller. Understanding the dynamic interaction between neuromodulation and homeostasis is of great interest in experimental neuroscience, and computationally studying this interaction could assist in designing new experiments and interpreting their results. This section is dedicated to analyzing this interaction at both the neuron and circuit levels.

16.2 Introduction

Brain activity is continuously shaped by neuromodulators and neuropeptides, including dopamine, serotonin, and histamine (Bargmann and Marder, 2013; Marder et al., 2014). Neuromodulators dynamically influence single-neuron activity, input-output properties, and synaptic connection strength and dynamics, enabling neuronal networks to adapt to changing needs, contexts, and environments (Marder and Calabrese, 1996; Marder and Bucher, 2001; McCormick et al., 2020). To achieve this modulation, neuromodulators dynamically reshape the density, dynamics, and kinetics of many single cell transmembrane proteins, making whole brain functional signaling strongly dependent on the robustness and reliability of neuromodulation mechanisms at the molecular and cellular levels (Nadim and Bucher, 2014; Hooper and Marder, 1984). While experimental studies underscore the ubiquity of neuromodulation across nervous systems, the fundamental principles underlying this mechanism remain incompletely understood. As such, studying neuromodulation is a very arduous task, both experimentally and computationally, which explains our limited understanding of its underlying mechanisms.

Neuromodulation coexists with cellular homeostasis, a mechanism that gradually adjusts neuronal membrane properties to maintain a target activity level (Desai, 2003; Marder and Goaillard, 2006; O'Leary et al., 2013). Neuronal cells are dependent on homeostatic mechanisms to maintain optimal functionality throughout the extended useful life of mammals (Marder, 2011). Despite continuous turnover of transmembrane proteins, such as ion channels and receptors, occurring on varying temporal scales ranging from hours to weeks (O'Leary and Wyllie, 2011), the robustness

and excitability of neurons must remain undisturbed (Marder and Prinz, 2002). By monitoring only intracellular calcium levels, the neuron orchestrates the regulation of all its ion channel conductances through homeostatic self-tuning rules (O'Leary et al., 2010; Pratt and Aizenman, 2007). This raises the question of how two different mechanisms acting on the same targets (ion channels), each potentially having divergent goals, can co-exist and complement each other harmoniously (Marder et al., 2014; Marder and Prinz, 2002).

We propose to study this interaction between neuromodulation and homeostasis computationally, using conductance-based models. Conductance-based models provide an electrical representation of the neuronal membrane, where the membrane is modeled as an RC circuit, while the ion channels are modeled as non-linear conductances (Izhikevich, 2007). These models are the closest equivalent of biological neurons, thanks to their ability to model any ion channel from experimental data following a methodology first proposed by Hodgkin and Huxley (Hodgkin and Huxley, 1952b). There exists a myriad of different conductance-based models that model various types of neuronal cells (Liu et al., 1998; Qian et al., 2014; Plant, 1981; Wechselberger et al., 2006; Drion et al., 2011; Katori et al., 2010; Megwa et al., 2023).

On the one hand, a homeostatic controller has been developed by O'Leary et al. (2014) and can be applied on top of any conductance-based model. In this controller, the neuron can adjust all ionic conductances up or down depending on its average intracellular calcium level. If the calcium level is lower than a reference value, ionic conductances are increased following homeostatic tuning rules and vice versa. Such rules force the tuning of ionic conductances along a single axis, that is, by preserving conductance ratios or correlations. On the other hand, Fyon et al. (2023) has developed a reliable neuromodulation controller and can also be applied to any conductance-based model. This controller can robustly tune the external activity of neurons, which means that neurons with various sets of ion channel properties that lead to similar firing activities (a property called degeneracy (Drion et al., 2015c)) can be neuromodulated using the same control action. In this study, we first examine the interaction between homeostasis and sharp neuromodulation, emphasizing that improperly combining the homeostatic controller with neuromodulation may result in unreliable outcomes. Subsequently, we expand our analysis to explore the interaction between the homeostatic controller and a neuromodulation controller, both at the single-cell level and in rhythmic networks. This approach enables the development of a combined controller that integrates the strengths of both individual controllers, facilitating robust modulation and preservation of neuronal function.

16.3 Results

16.3.1 Current model of homeostasis can lead to pathological excitability in the presence of sharp neuromodulation

This study employs a stomatogastric ganglion (STG) neuron conductance model (Liu et al., 1998) to explore the interaction between homeostasis and neuromodulation. These neurons contribute to rhythmic circuits that generate signals triggering stomach muscle contractions in crustaceans. This model was chosen for its ability to produce diverse firing patterns—ranging from tonic spiking to bursting, including single-spike bursting—and its rich combination of ion

channels enabling degeneracy. The model includes classical fast sodium and delayed rectified potassium channels, A-type and calcium-activated potassium channels, T-type and slow calcium channels as well as hyperpolarization-activated H-channels. We first study the interaction between state-of-the-art model homeostasis (O'Leary et al., 2014) and sharp neuromodulation (Fyon et al., 2024). We define *sharp neuromodulation* as a direct change in a subset of ion channel maximal conductances, which results in functional modulation. In the context of this work, we focus on a robust transition from tonic spiking to bursting in degenerate neurons, *i.e.*, neurons exhibiting similar firing activities from different underlying channel conductances.

First, we sharply neuromodulated a set of degenerate neurons from tonic spiking to bursting by directly modifying the maximal conductances of A-type potassium $\bar{g}_A$ and slow calcium $\bar{g}_{CaS}$, then allowed homeostatic compensation to take its course. Three example traces with a time evolution of maximal conductances are provided in Fig. 16.1, left, whereas Fig. 16.1, right show trajectories in the $\bar{g}_{\mathrm{CaS}}$-$\bar{g}_{\mathrm{A}}$ plane. As can be seen in the figure, although the initial tonic firing and the sharply neuromodulated bursting activities are very similar in all three neurons, homeostatic compensation has very variable and unreliable effects. Depending on the initial conductance state, neuromodulation shifts the neuron to a new state where homeostatic compensation can lead to pathological (Fig. 16.1A), functionally preserved (Fig. 16.1B), or unphysiological (Fig. 16.1C) behaviors. This interesting result highlights an important property of neuronal degeneracy: although distinct channel subsets can produce similar neuronal behaviors, neurons may respond differently to perturbations, such as sharp neuromodulation.

To better understand the reasons behind this unreliability, both mechanisms must be discussed in detail. In the homeostatic model (O'Leary et al., 2014), the cell senses its own intracellular calcium level and averages it over time. If the mean intracellular calcium falls below a predefined target value, RNA transcription and ion channel protein translation are triggered to increase all ionic conductance values, and vice versa. Specifically, increasing calcium ion channel conductances leads to more calcium ions entering the cell. This implies that homeostasis induces changes in all conductance values (Fig. 16.1 left), which leads to a linear motion in the conductance plane (Fig. 16.1 right). This phenomenon happens on a relatively slow timescale, which can last up to days (O'Leary et al., 2010). Notably, the RNA transcription time constants, denoted by τ_m, vary across different ion channels and cell types. Steady-state mathematical analysis has shown that these differing time constants tune correlations in ion channel conductances. For two ion channels i and j, steady-state analysis yields $\bar{g}_i/\bar{g}_j \approx \tau_{m_j}/\tau_{m_i}$. This indicates that homeostatic tuning rules maintain ratios of ionic conductances and their correlations while adjusting their values in response to intracellular calcium levels. In the ionic conductance space, these rules allow neurons to navigate along a one-dimensional line, where the slope of this line in two dimensions is determined by the ratios of mRNA transcription time constants. This phenomenon, known as homogeneous scaling, involves proportionally increasing or decreasing all ionic conductances by the same multiplicative factor.

On the other hand, sharp neuromodulation is implemented by transiently applying the algorithm of Fyon et al. (2024). This neuromodulation also produces changes in conductance values (Fig. 16.1 left), resulting in motion within the conductance plane in a direction different from

homogeneous scaling (Fig. 16.1 right) to reach a new firing activity. However, neuromodulation only affects a subset of ion channels, not all (Marder, 2012). Furthermore, the timescale of neuromodulation is much faster than that of homeostasis, lasting for a maximum of a few minutes (Marder et al., 2014). In addition, neuromodulation tunes correlations between neuromodulated ion channels, rather than preserving them (Fyon et al., 2024).

Coupling homeostasis and neuromodulation in this way is problematic because homeostasis preserves correlations and regulates calcium, whereas neuromodulation adjusts correlations to modulate neuronal function. In Fig. 16.1, sharp neuromodulation is applied to three different STG models with distinct initial ionic conductances. Initially, all neurons exhibited tonic firing due to homeostatic regulation, with RNA transcription time constants selected to produce tonic spiking neurons. Neuromodulation was then applied instantaneously, leading to a transition from tonic spiking to bursting in all cases (Fig. 16.1). These transitions drastically increase intracellular calcium concentration. From the perspective of homeostatic tuning rules, this constitutes a disturbance, as it alters the conductance ratios between $\bar{g}_{\mathrm{CaS}}$ and $\bar{g}_{\mathrm{A}}$. Although this disturbance is necessary for adaptation and functional modulation, the outcome of homeostasis in response to this biological disturbance is unpredictable. Indeed, as the homeostatic controller was initially designed to produce tonic spiking neurons, it tends to preserve the predefined correlations that produce such behavior. However, neuromodulation changes the firing activity, leading to a mismatch between actual conductance values and the encrypted conductance ratios.

In Fig. 16.1A, homeostatic compensation results in pathological behavior, characterized by irregular bursting with a hyperpolarized plateau, failing to achieve either bursting or tonic spiking. In Fig. 16.1B, the modulated behavior (bursting) is maintained after homeostatic compensation. In Fig. 16.1C, homeostatic compensation leads to unphysiological values of $\bar{g}_{\mathrm{A}}$, tending towards negative values. Even when $\bar{g}_{\mathrm{A}}$ is constrained to be non-negative, the resulting electrical behavior is pathological, failing to exhibit either tonic spiking or bursting. This toy experiment highlights that homeostasis and sharp neuromodulation can interfere pathologically.

Such behavior was predicted in O'Leary et al. (2014), where the authors demonstrate that their homeostasis model can lead to various outcomes in response to disturbances, such as channel deletions. Initially, the deletion itself may directly affect neuronal function, either preserving it or causing its loss. Subsequently, homeostatic compensation can either preserve or restore function, but it may also lead to pathological behaviors, such as functional deletion. This result suggests that any disturbance applied to the conductance ratios—even physiological ones such as neuromodulation—can lead to problematic behaviors.

16.3.2 Controlled neuromodulation and homeostasis naturally lead to robust neuronal function

In biological systems, homeostasis and neuromodulation collaborate to ensure robust and modular neural function. These mechanisms operate on different timescales: neuromodulation acts within seconds or minutes (Werner and Mitterauer, 2014), while homeostatic compensation may take hours or even days (Marder and Prinz, 2002). However, in computational models, the goals of neuromodulation and homeostatic controllers often seem discordant. Neuromodulation typically

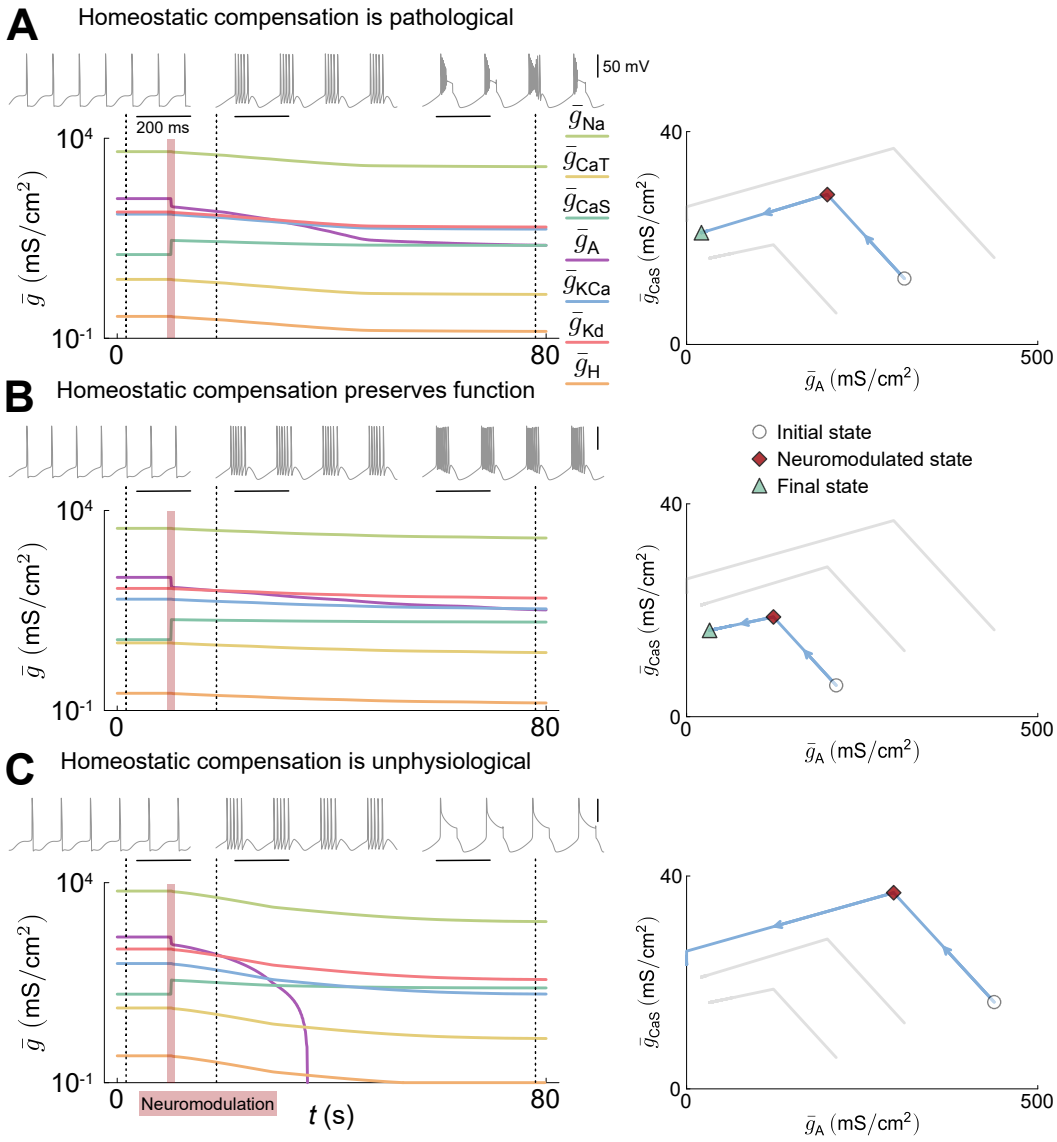

Figure 16.1: Current model of homeostasis can lead to pathological excitability in the presence of sharp neuromodulation. A. Time evolution of all conductances in the STG model, shown on a logarithmic scale, when homeostasis is applied with sharp neuromodulation (instantaneous changes in $\bar{g}_{\mathrm{CaS}}$ and $\bar{g}_{\mathrm{A}}$ within the red region) (left). Corresponding trajectory in the modulated conductance space (right). The white circle represents the initial condition (tonic spiking), the red diamond marks the neuromodulated state (bursting) immediately after the sharp modulation, and the green triangle denotes the final state after homeostasis has converged. In this case, homeostatic compensation is pathological, resulting in irregular bursting. **B.** Same as in panel A, but with different degenerate initial conditions. Here, homeostatic compensation preserves the neuromodulated function. **C.** Same as in panel A, with another set of degenerate initial conditions. In this case, homeostatic compensation results in negative values of $\bar{g}_{\mathrm{A}}$ (saturated at 0), leading to pathological behavior characterized by one-spike bursting.

adjusts conductance ratios, while homeostasis seeks to maintain these ratios and guide the neuron through homogeneous scaling. Consequently, applying sharp neuromodulation to any homeostatic conductance-based model can lead to instability, as neuromodulation disrupts the references and control actions of the homeostasis controller (Fig. 16.2A).

To model the actions of both mechanisms within a single cell, we include a more advanced neuromodulation model, referred to as the neuromodulation controller, as developed in Fyon et al. (2023). This controller can be coupled with any conductance-based model, allowing modulation of its neuronal function, such as its firing pattern, to mimic biological neuromodulation. We call this type of neuromodulation *controlled neuromodulation*, in contrast to the sharp neuromodulation discussed above. The neuromodulation controller adjusts target channel conductances, providing continuous and consistent modulation rather than instantaneous, rigid changes.

Fig. 16.2B illustrates the results of transitions from tonic spiking to bursting when applied to a degenerate population of STG neuron models. Initially, all neurons exhibit tonic firing mode, and homeostasis adjusts the conductances to achieve a predefined calcium level along a first tonic spiking homogeneous scaling line. Midway through the simulation, controlled neuromodulation is applied to switch all neurons to bursting mode, which now occurs through a controlled adjustment of $\bar{g}_{\mathrm{CaS}}$ and $\bar{g}_{\mathrm{A}}$. Consequently, intracellular calcium levels rise sharply, and conductance ratios involving one or both neuromodulated ionic conductances are adjusted. Finally, with the reshaped RNA time constants, the homeostasis controller adjusts all conductances to restore an appropriate calcium level, while controlled neuromodulation preserves neuromodulated conductance ratios along a second bursting homogeneous scaling line. Ultimately, the neuronal population reaches a new state where the neuromodulated function is preserved and intracellular calcium levels are back to their target value.

Simulations were also performed on a midbrain dopaminergic neuron model (adapted from Qian et al. (2014)) to demonstrate the generality of our results (Fig. 16.2C). As with the previous simulations, a transition from tonic spiking (pacemaking) to strong bursting was induced midway through by modulating the N-type and L-type calcium conductances ($\bar{g}_{\mathrm{CaN}}$ and $\bar{g}_{\mathrm{CaL}}$) using controlled neuromodulation. Homeostatic compensation was continuously applied to maintain proper calcium levels, resulting in a reliable and robust outcome despite initial degeneracy within the population.

16.3.3 Why do controlled neuromodulation and homeostasis lead to robust neural function?

Fig. 16.3A shows the trajectories of the simulations from Fig. 16.2B in the plane of modulated conductances, $\bar{g}_{\mathrm{CaS}}$ and $\bar{g}_{\mathrm{A}}$, during tonic spiking homeostatic compensation for both sharp and controlled neuromodulation. Initially, the modulated conductances of every neuron in the population grow along the homogeneous scaling direction in tonic spiking mode, as the calcium levels are below the threshold value. This homogeneous scaling corresponds to a line intersecting the origin, with variability due to the degeneracy in conductance ratios within the population. During neuromodulation, all conductances are adjusted to tune their ratios and achieve bursting (Fig. 16.3B). Importantly, all neuromodulatory actions occur along the same direction, but with varying magnitudes depending on the state of the neuron (Fyon et al., 2024). As a result, calcium levels increase drastically for each neuron in the population. Once the neuromodulatory action ends, the outcome depends on the type of neuromodulation applied (Fig. 16.3C).

In the case of sharp neuromodulation, during the homeostatic action in the bursting phase,

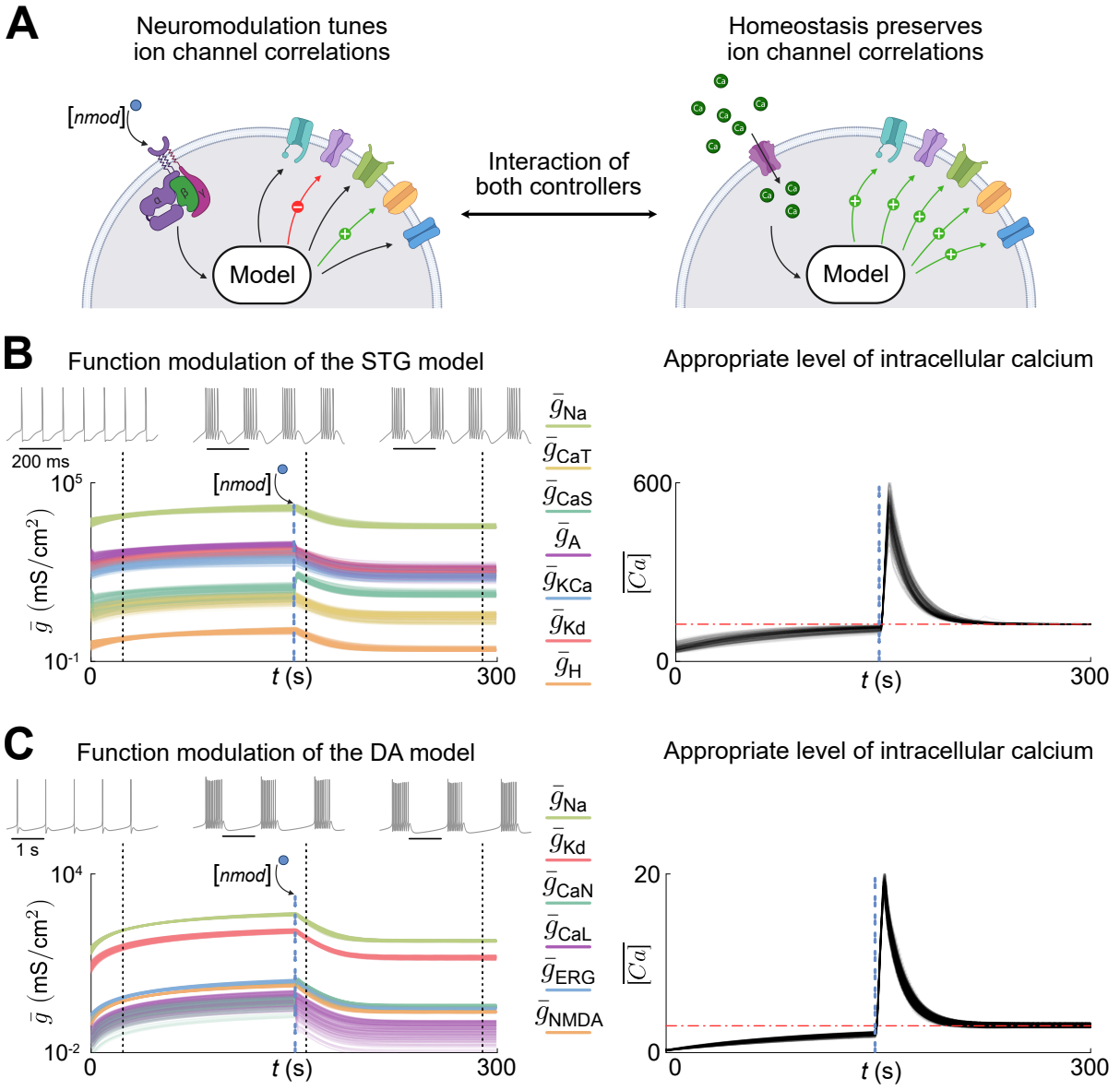

Figure 16.2: Controlled neuromodulation and homeostasis naturally lead to robust neuronal function. A. Schematic representation of neuromodulation (left) and homeostasis (right) cascades. Neuromodulators bind to G-protein receptors, triggering complex signaling pathways that selectively affect subsets of ion channels. In contrast, homeostasis senses intracellular calcium levels and regulates them by adjusting all conductances uniformly. **B.** Time evolution of all conductances in the STG model, displayed on a logarithmic scale, during homeostasis with controlled neuromodulation (controlled changes in $\bar{g}_{\mathrm{CaS}}$ and $\bar{g}_{\mathrm{A}}$ starting at the dashed blue line) for a degenerate population of 200 models (left). The corresponding mean intracellular calcium concentration over time (right) shows the target value (red dash-dotted line) is maintained both before and after controlled neuromodulation. **C.** Same as panel B, but for a DA model where controlled neuromodulation affects $\bar{g}_{\mathrm{CaN}}$ and $\bar{g}_{\mathrm{CaL}}$.

the homeostatic controller acts alone and tends to maintain the same conductance ratios as in tonic spiking (Fig. 16.3C left). This leads to a reduction in calcium levels, but, as seen in Fig. 16.1, its effects are unreliable and undesirable. Specifically, for most neurons in the population, the homeostatic controller reduces $\bar{g}_{\mathrm{A}}$ towards negative values (saturated at 0 to

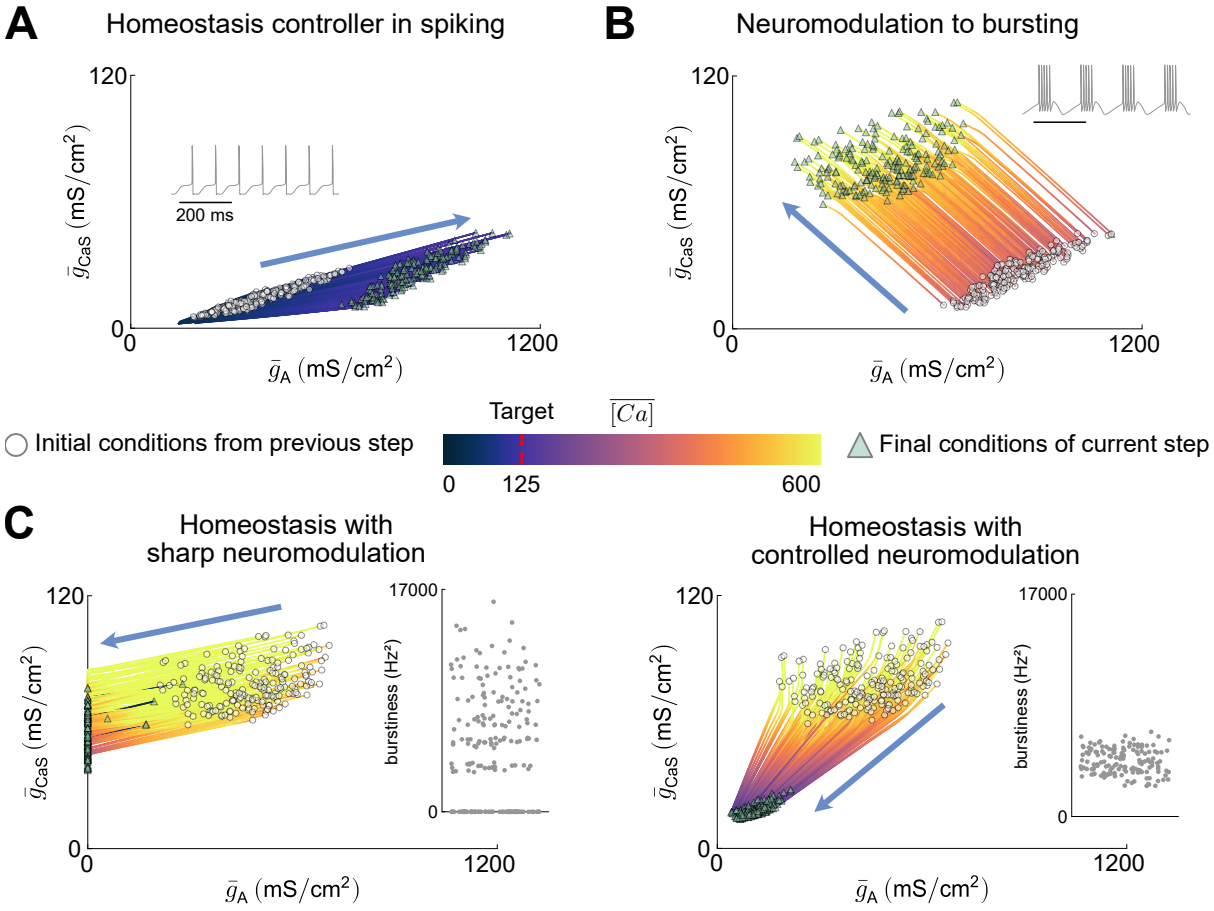

Figure 16.3: Why do controlled neuromodulation and homeostasis lead to robust neural function? A. Trajectories of the STG population from Fig. 16.2 in the modulated conductance space during homogeneous scaling in tonic spiking only. As expected from homeostasis, all neurons move in the same direction. White circles represent the initial conditions at the start of the step, and the green triangle marks the final conditions. **B.** Same as panel A, but during the brief period when neuromodulation is active. All trajectories are parallel to one another. **C.** Same as panels A and B, but during the homeostasis phase following neuromodulation. The outcome depends on the type of neuromodulation: sharp (left) or controlled (right). Sharp neuromodulation results in non-robust outcomes, whereas controlled neuromodulation preserves robust neural function.

avoid model instability) to bring $\bar{g}_{\text{CaS}}$ into an appropriate range. This regulation causes the neuron to move away from the robust bursting behavior, resulting in heterogeneous changes in the activity of the population.

In the case of controlled neuromodulation, the homeostatic and neuromodulation controllers work together to maintain the new conductance ratios corresponding to bursting (Fig. 16.3C right). This results in a new homogeneous scaling following these updated conductance ratios in bursting, which translates into trajectories that move toward the origin of the axes, as would be expected in tonic spiking. Homogeneous scaling during bursting differs across the population due to initial degeneracy. The difference between the two homogeneous scalings (tonic spiking and bursting) is driven by the neuromodulatory action, ensuring that the neuromodulated behavior (bursting) is not lost.

In the first section, when the homeostasis controller was combined with sharp neuromodulation, unreliable outcomes were observed. To explain this behavior, we use a schematic representation of the modulated conductance plane (Fig. 16.4A). In this plane, different values of $\bar{g}_{\mathrm{CaS}}$ and $\bar{g}_{\mathrm{A}}$ can lead to similar mean intracellular calcium concentration. These values can be highlighted using calcium isoclines (green dashed lines in Fig. 16.4A). Likewise, different values of $\bar{g}_{\mathrm{CaS}}$ and $\bar{g}_{\mathrm{A}}$ can lead to similar firing activity. These values can be highlighted using activity isoclines (blue dashed lines in Fig. 16.4A). Calcium isoclines are parallel one to each other, whereas activity isoclines pass through the origin and rotate around this point. This behavior is explained by homeostatic tuning rules and homogeneous scaling, as different conductance ratios lead to different firing patterns. Initially, the neuron operates in the target spiking mode at the target calcium level, corresponding to the intersection of the spiking and the target calcium isoclines. When sharply neuromodulating the neuron, the modulated conductances change, and the neuron shifts to another state, now reaching a new target strong bursting isocline, which intersects a higher calcium isocline. Homeostasis then kicks in to reduce the calcium level to its target value. However, in the homeostatic controller, the "native" tonic spiking direction is encrypted, leading to changes in conductances along the spiking isocline. As a result, the neuron moves away from the bursting isocline, potentially disrupting the new function. This explains why sharp neuromodulation is incompatible with the homeostasis controller.

To harmonize the actions of both controllers and achieve robust functional modulation, we leverage the significant difference in their timescales. Neuromodulation controls the modulated ionic conductances, while homeostatic tuning rules regulate all ionic conductances over a slower timescale to maintain an appropriate calcium level. In the modulated conductance plane (Fig. 16.4B), the initial and neuromodulated states are the same as in Fig. 16.4A. However, in the case of controlled neuromodulation, both homeostatic and neuromodulatory controllers are active. Specifically, when homeostasis reduces the calcium level and shifts the neuron away from the bursting isocline, the neuromodulation action counteracts this perturbation in function by bringing the neuron back to the bursting isocline, preserving its function. The neuromodulatory controller operates several orders of magnitude faster than the homeostatic controller. As a result, fast corrections from the former render perturbations from the latter infinitesimal, leading to changes in the conductance ratio along the target activity isocline (strong bursting in this example). Ultimately, the neuron stabilizes at the intersection of the target calcium and target activity isoclines, where both controllers meet their objective.

16.3.4 Controlled neuromodulation and homeostasis ensure the preservation of function under physiologically recoverable disturbances

By employing this tandem of controllers, neuronal function becomes robust to channel blockade, provided that the channel deletion is compensable. While homeostasis compensation alone might lead to unreliable recovery from channel blockade, incorporating controlled neuromodulation somehow stabilizes the neuron response to such blockade, even in the case of highly degenerate neuronal populations. Furthermore, if the channel blockade is physiologically recoverable—meaning the function of the blocked channel can be restored using other channels—there exists an optimal combination of neuronal feedback gains to preserve

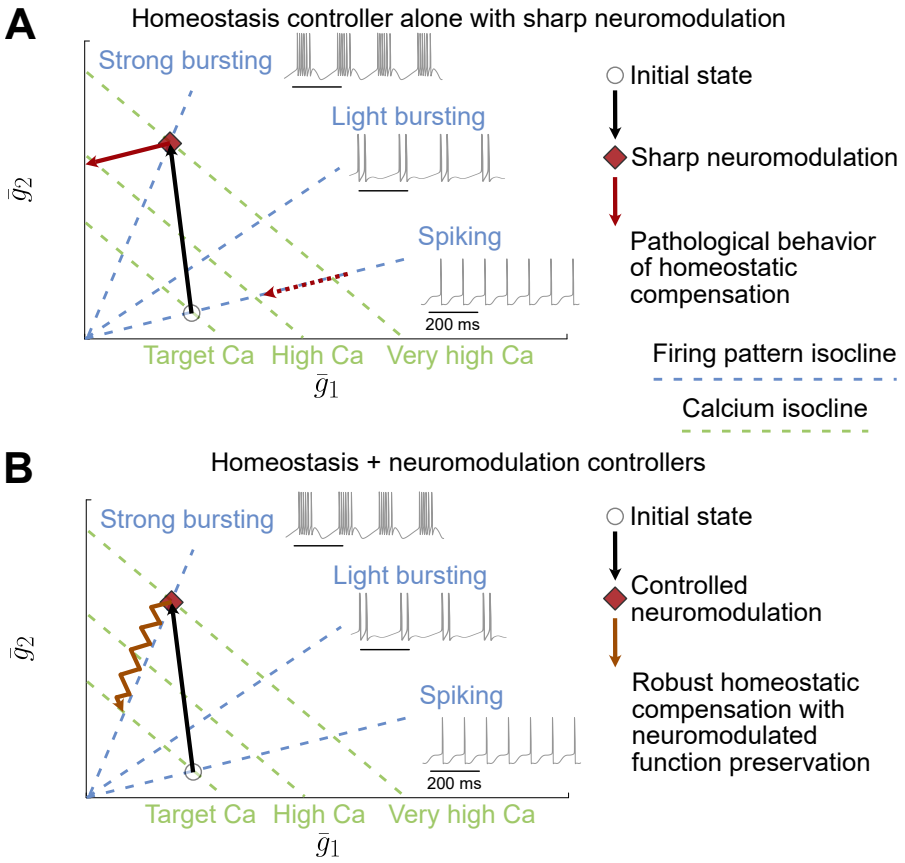

Figure 16.4: Schematic explanation of why controlled neuromodulation integrates better with homeostasis compared to sharp neuromodulation. A. Schematic of the modulated conductance space for homeostasis combined with sharp neuromodulation. Initially (white circles), the neuron spikes at the target calcium level, located at the intersection of the firing pattern isocline (dashed blue lines) and the calcium level isocline (dashed green lines). Following sharp neuromodulation to a new firing pattern (red diamond), calcium levels sharply increase. Homeostasis reduces calcium (solid red arrow) by moving along the same direction as before neuromodulation (dashed red arrow), causing the neuron to deviate from the neuromodulated firing pattern isocline. **B.** Same as panel A, but with controlled neuromodulation. The initial steps are identical, but after neuromodulation, as homeostasis acts to reduce calcium, controlled neuromodulation simultaneously adjusts to keep the neuron on the neuromodulated firing pattern isocline (sawtooth red arrow). Because controlled neuromodulation operates on a much faster timescale than homeostasis, the neuron remains on the neuromodulated firing pattern isocline throughout.

that function. In essence, if one channel is blocked, a specific concentration of particular neuromodulators can preserve the function.

For example, in Fig.16.5, various channel blockades are applied to a degenerate population of STG conductance-based models equipped with the combined homeostasis/neuromodulation tandem of controllers. The target behavior of the population is regular bursting. In Fig.16.5A, H-type channels are blocked. Here, the function is preserved even immediately after the blockade, without requiring compensation. Subsequently, the combined regulation of homeostasis and controlled neuromodulation maintains this function by restoring the neuron to an appropriate calcium level on a population-wide scale. In Fig. 16.5B and C, T-type calcium and calcium-

controlled potassium channels are blocked, respectively. In these cases, the blockade results mostly in the loss of bursting function. However, by allowing the homeostasis/neuromodulation pair of controllers to compensate, the function is largely recovered, albeit with irregular bursting patterns in some neurons. Additionally, intracellular calcium levels stabilize at their target values. This preservation of functions is feasible because the actions of H-type, T-type calcium, and calcium-controlled potassium channels are degenerate and can be compensated for using other channels present within the cell. The STG neuron model incorporates numerous channels operating on slow and ultraslow timescales, enabling the compensation for lost channels in these timescales. It is worth noting that only the loss of the calcium-controlled potassium channel has been compensated using different neuronal feedback gain values, *i.e.*, different concentrations of various neuromodulators, as in control conditions.

However, the blockade of fast transient sodium channels is irrecoverable (Fig. 16.5D), as these channels are crucial for initiating spikes on a fast timescale. Once the blockade is applied, compensation cannot restore spikes because the action of sodium channels is non-degenerate and occurs on the fast timescale of the neuron. Similarly, achieving the appropriate intracellular calcium level becomes unattainable. A comparable outcome would result from the blockade of delayed rectified potassium channels, which are responsible for the downstroke of the spikes.

16.3.5 Central pattern generator networks can be robustly modulated to orchestrate their rhythmic output

The application of this tandem of controllers extends even to networks, particularly central pattern generators (CPGs). CPGs are self-organized neuronal circuits mainly composed of bursting neurons connected primarily through inhibitory connections, capable of generating rhythmic output without external input (Yuste et al., 2005; Guertin, 2009). One extensively studied circuit is responsible for the pyloric and gastric mill rhythms in crustaceans, observed in the stomatogastric ganglion. This network exhibits two rhythms at different speeds: the fast pyloric rhythm and the slow gastric mill rhythm. These rhythmic outputs are vital for coordinating muscle contractions in the stomach for digestion, among other functions. A minimalist network model of such a bi-rhythmic circuit is investigated in Fig. 16.6 (Gutierrez et al., 2013; Drion et al., 2019). It comprises two half-center oscillators operating at different speeds, connected via a central neuron. Half-center oscillators consist of two bursting neurons connected in mutual inhibition, enabling them to fire anti-phase bursts. In the network scheme, the purple and blue neurons constitute the fast half-center oscillator (representing the pyloric rhythm), while the green and yellow neurons form the slow half-center oscillator (representing the gastric mill rhythm). The red neuron serves as the central one, also in bursting mode. It has been demonstrated that the gastric mill rhythm requires a neuromodulatory input to be activated (Selverston et al., 2009).

In this study, the gastric mill rhythm can be reliably induced by the pair of controllers, but not with homeostasis combined with sharp neuromodulation. Under control conditions (Fig. 16.6A), *i.e.*, without neuromodulatory input to the gastric mill rhythm, only the pyloric rhythm is active and the central neuron consistently bursts. In particular, variability in conductances is observed in this network (Fig. 16.6A right). When neurons are equipped with homeostasis only, activation

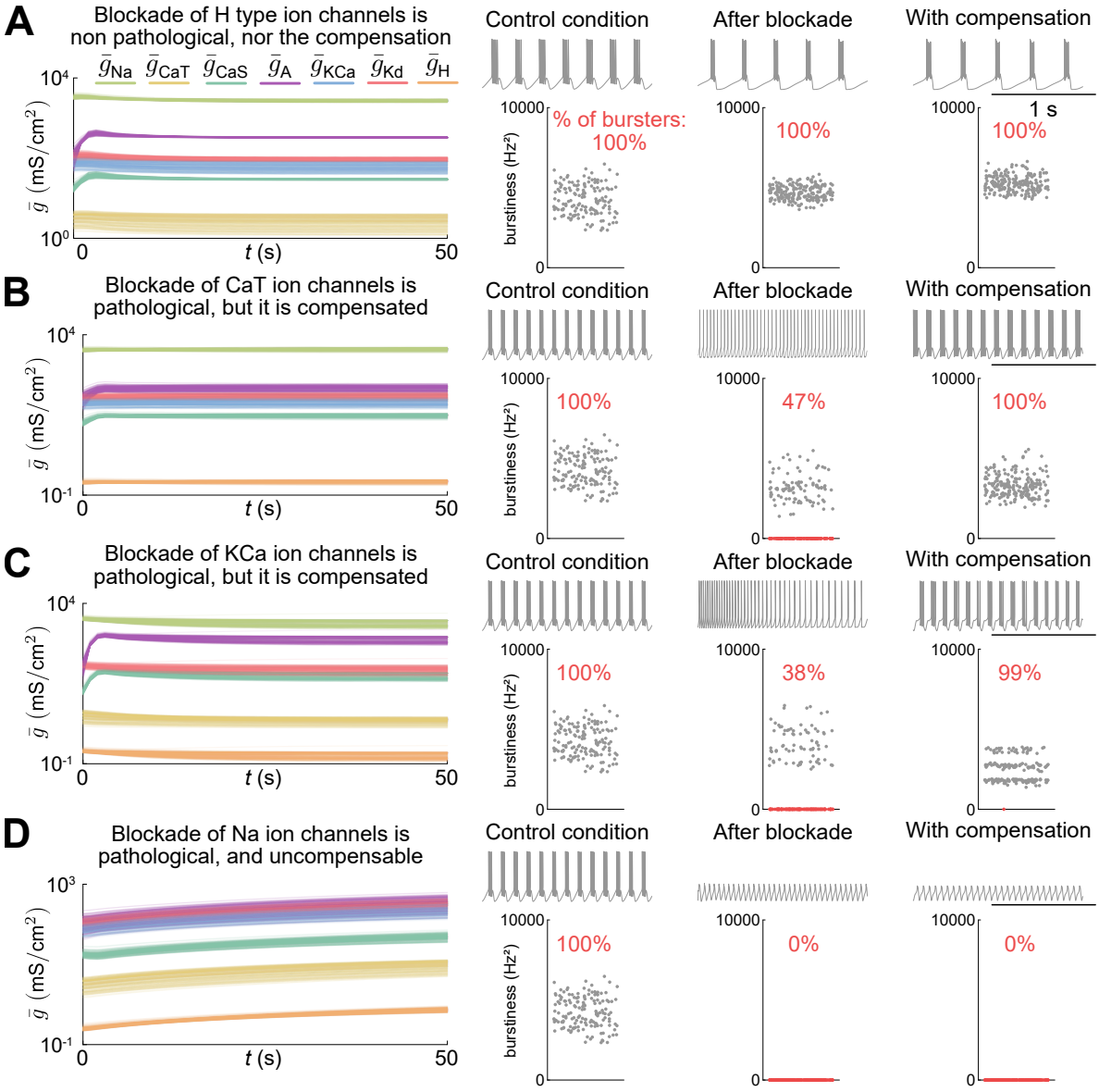

Figure 16.5: Controlled neuromodulation and homeostasis ensure the preservation of function under physiologically recoverable disturbances. A. Time evolution of all conductances in the STG model, displayed on a logarithmic scale, during homeostasis with controlled neuromodulation (controlled changes in $\bar{g}_{\mathrm{CaS}}$ and $\bar{g}_{\mathrm{A}}$ starting at the dashed blue line) for a degenerate population of 200 models with H-type ion channel blockade (left). The corresponding distribution of behaviors before the blockade, immediately after the blockade, and following compensation (right) demonstrates the effect of the blockade. In this case, no neurons lose bursting due to the channel blockade or compensation. **B.** Same as panel A, but with a CaT channel blockade. The blockade causes half of the neurons to lose bursting; however, all neurons recover bursting with compensation. **C.** Same as panel A, but with a KCa channel blockade. The blockade causes more than half of the neurons to lose bursting, but nearly all recover bursting with compensation. **D.** Same as panel A, but with a Na channel blockade. The blockade causes all neurons to lose bursting, and compensation does not restore bursting due to the non-degenerate essential role of Na channels.

of sharp neuromodulation for the gastric mill rhythm leads to rapid loss of function, due to the unreliability of this combination (Fig. 16.6B middle). However, when neurons undergo controlled

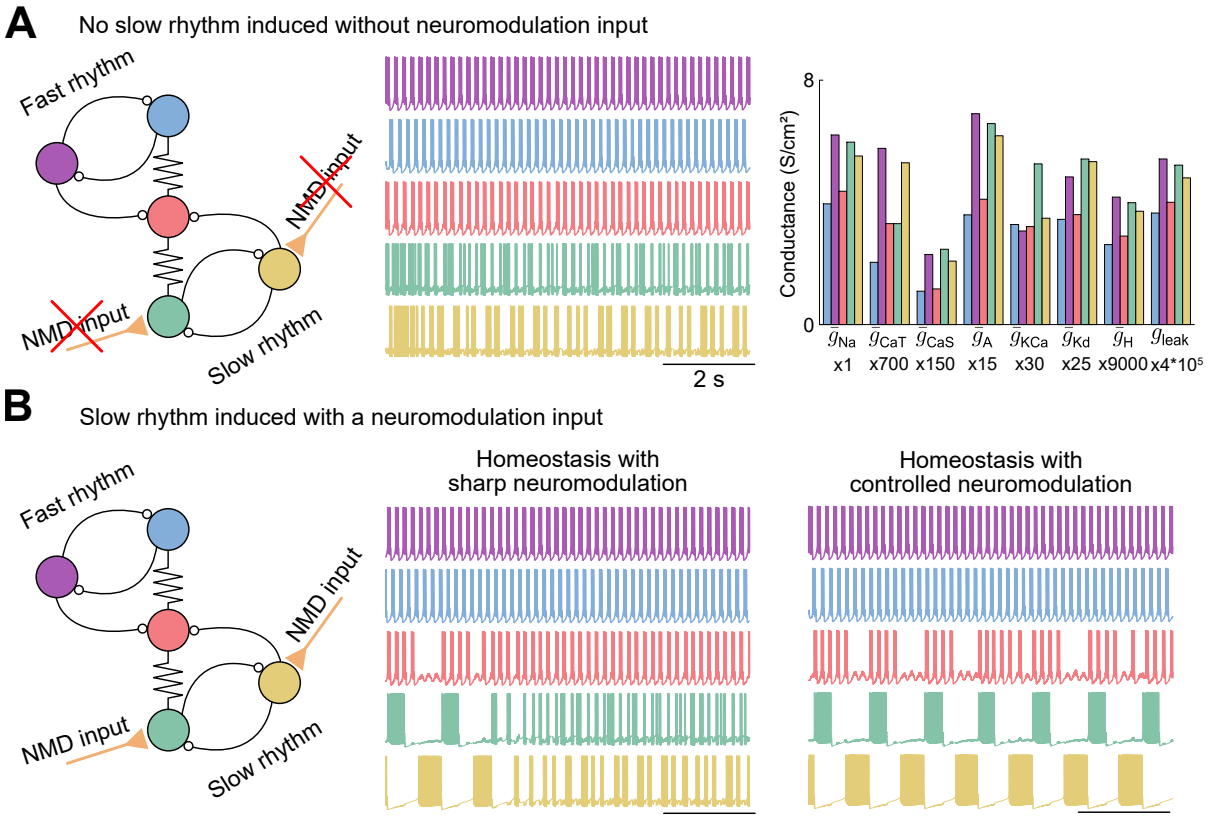

Figure 16.6: Central pattern generator networks can be robustly modulated to orchestrate their rhythmic output. A. Control condition of the simplified pyloric/gastric mill rhythm network (left), inspired from Gutierrez et al. (2013). Without neuromodulation, the fast rhythm is active (top two traces, middle), while the slow rhythm is inactive (bottom two traces, middle). In this case, all neurons in the network exhibit degenerate conductances (right). **B.** Schematic representation of the activated slow rhythm network (left), modulated by either sharp neuromodulation (middle) or controlled neuromodulation (right). With sharp neuromodulation, the slow rhythm fails due to its unreliability, whereas controlled neuromodulation sustains the slow rhythm.

neuromodulation, the gastric mill rhythm is successfully induced and sustained (Fig. 16.6B right). Despite the degeneracy of neurons, characterized by significant variability in conductance ratios, the network achieves rhythmic output with appropriate intracellular calcium levels. This toy experiment demonstrates that such a tandem of controllers can be applied in computational models to modulate and maintain not only single cell activity but also network-level activity.

16.4 Discussion

The efficient and robust integration of homeostasis and neuromodulation in neurons remains an open question with several proposed hypotheses (Marder et al., 2014; Marder and Bucher, 2005; Cunha, 2001). The improper integration of these mechanisms—for example, combining sharp neuromodulation with a homeostatic controller—can lead to negative interactions. Such interactions may result in unreliable behaviors or numerical instabilities.

In contrast, pairing a homeostatic controller with controlled neuromodulation ensures reliable

neural function modulation while maintaining appropriate calcium levels. This approach draws inspiration from biology, where neuromodulation is known to be activity-dependent, as observed experimentally (Kramer and Levitan, 1990; Raymond et al., 1992). Specifically, the neuromodulation controller models the role of G-protein-coupled receptors and second messengers, embedding feedback in the metabolic neuromodulation cascade (Marcus and Bruchas, 2023; Scheler, 2004). This reliable interaction can be extended to neural circuits, such as the gastric mill circuit in crabs, to produce robust network-level functionality (Marder et al., 2014).

However, the success of this interaction critically depends on a point in the conductance space where both controllers converge. This point represents a neural activity pattern that supports neuromodulated firing while maintaining homeostatic calcium levels. As shown in Fig. 16.4, this intersection of the strong bursting isocline (the target of controlled neuromodulation) and the target calcium level (the goal of homeostatic control) represents the convergence point. When such a point is absent—*e.g.*, during sodium channel blockade (Fig. 16.5)—neither neuromodulated activity nor calcium homeostasis is sustained. This may lead to pathological compensations, where one controller prioritizes calcium regulation at the cost of abandoning the desired firing pattern (Starmer et al., 1991; Grant et al., 1984; Anger et al., 2001). Furthermore, discontinuities in the neuromodulated firing pattern may lead to transient pathological behaviors.

Maximizing convergence between these control mechanisms requires increasing the likelihood of both an intersection and a continuous path in conductance space. We hypothesize that this can be achieved by maximizing neuronal degeneracy (Whitacre, 2010; Rathour and Narayanan, 2019; Whitacre and Bender, 2010; Prinz, 2017; Goaillard and Marder, 2021). Higher degeneracy increases the likelihood that the functional and dynamical role of one ion channel can be compensated by others, thereby preserving both the path and the intersection. This underscores the essential role of degeneracy in enabling robust neural functions that can be modulated.

Finally, this study underscores the potential risks associated with pharmacological ion channel blockade (X Cubeddu, 2016; DeWitt and Waksman, 2004; Imbrici et al., 2018). If neuronal degeneracy is insufficient, such interventions may disrupt neuron ability to maintain robust neuromodulation. Instead, we propose targeting elements within the neuromodulation cascade—such as second messengers or other components of the control loop—as more reliable pharmacological strategies. Such interventions would preserve the dynamics of controlled neuromodulation, providing a more robust alternative to direct ion channel blockade.

16.5 Material and Methods

16.5.1 Programming language

The Julia programming language was used in this work (Bezanson et al., 2017). Numerical integration was realized using *DifferentialEquations.jl*.

16.5.2 Conductance-based models

For all experiments, single-compartment conductance-based models were employed. These models articulate an ordinary differential equation for the membrane voltage V, where N ion channels

are characterized as nonlinear dynamic conductances, and the phospholipid bilayer is represented as a passive resistor-capacitance circuit. Mathematically, the voltage-current relationship of any conductance-based neuron model is expressed as follows:

$$\begin{aligned} I_C &= C\frac{\mathrm{d}V}{\mathrm{d}t} + g_{\text{leak}}(V - E_{\text{leak}}) = -I_{\text{int}} + I_{\text{ext}}, \\ &= -\sum_{\text{ion}\in\mathcal{I}} g_{\text{ion}}(V,t)(V - E_{\text{ion}}) + I_{\text{ext}}. \end{aligned}$$

Here, C represents the membrane capacitance, g_{ion} denotes the considered ion channel conductance and is non-negative, gated between 0 (all channels closed) and $\bar{g}_{\text{ion}}$ (all channels open), E_{ion} and E_{leak} are the channel reversal potentials, $\mathcal{I}$ is the index set of intrinsic ionic currents considered in the model, and I_{ext} is the current externally applied *in vitro*, or the combination of synaptic currents. Each ion channel conductance is nonlinear and dynamic, represented by $g_{\text{ion}}(V,t) = \bar{g}_{\text{ion}} m_{\text{ion}}^a(V,t) h_{\text{ion}}^b(V,t)$, where m_{ion} and h_{ion} are variables gated between 0 and 1, modeling the opening and closing gates of ion channels, respectively. Throughout this study, both the isolated crab STG neuron model (Liu et al., 1998) and the adapted DA neuron model (Qian et al., 2014) (where SK channels had been blocked to enable bursting) were employed.

The STG model consists of seven ion channels that operate on various time scales: fast sodium channels ($\bar{g}_{\text{Na}}$); delayed-rectifier potassium channels ($\bar{g}_{\text{Kd}}$); T-type calcium channels ($\bar{g}_{\text{CaT}}$); A-type potassium channels ($\bar{g}_{\text{A}}$); slow calcium channels ($\bar{g}_{\text{CaS}}$); calcium controlled potassium channels ($\bar{g}_{\text{KCa}}$); and H channels ($\bar{g}_{\text{H}}$).

The DA model consists of six ion channels that operate on various time scales: fast sodium channels ($\bar{g}_{\text{Na}}$); delayed-rectifier potassium channels ($\bar{g}_{\text{Kd}}$); L-type calcium channels ($\bar{g}_{\text{CaL}}$); N-type calcium channels ($\bar{g}_{\text{CaN}}$); ERG channels ($\bar{g}_{\text{ERG}}$); and NMDA channels ($\bar{g}_{\text{NMDA}}$). Note that, owing to the multicellular nature of NMDA channels, they were excluded from this study but were still used for simulations with baseline values.

16.5.3 The homeostatic controller

The homeostatic controller adjusts all conductances using an integration rule described in O'Leary et al. (2014). Let $\bar{g}_i$ denote the conductance of ion channel $i \in [1, N]$, and m_i the corresponding mRNA concentration. The dynamics of the homeostatic controller are governed by the following equations:

$$\begin{aligned} \tau_i \dot{m}_i &= [Ca^{+2}]_{\text{target}} - [Ca^{+2}], \\ \tau_g \dot{\bar{g}}_i &= m_i - \bar{g}_i, \end{aligned}$$

where $[Ca^{+2}]$ and $[Ca^{+2}]_{\text{target}}$ represent the intracellular calcium concentration and its target value, respectively. In essence, the calcium concentration error is integrated into the mRNA levels, which subsequently modulate the corresponding channel conductances. This regulation aims to bring the calcium concentration to its target value, as higher channel conductances (particularly calcium-conducting ones) facilitate greater calcium influx. Starting from any initial condition, this controller drives the cell along a line in conductance space known as the homogeneous

scaling line. This line passes through both the initial condition and the origin of the conductance space axes. Steady-state analysis reveals that the conductance ratios remain invariant, such that $\frac{\bar{g}_i}{\bar{g}_j} = \frac{\tau_j}{\tau_i}$. This invariance ensures that the relative scaling of conductances is preserved during homeostatic compensation. Consequently, the cell conductance properties develop along the homogeneous scaling beam defined by these ratios.

16.5.4 The neuromodulation controller

The neuromodulation controller adjusts a subset of n conductances, denoted as $\bar{g}_{\text{mod}} \in \mathbb{R}^n$ with $n < N$, using the algorithm introduced in Fyon et al. (2023). This controller employs the concept of Dynamic Input Conductances (DICs) to determine target values for $\bar{g}_{\text{mod}}$ based on the input neuromodulator concentration, represented as $\bar{g}_0\left([\text{nmod}]\right) \in \mathbb{R}^n$. The error between the target and the current values, e_{mod}, drives a Proportional-Integral (PI) controller, which updates $\bar{g}_{\text{mod}}$ to track the desired reference. The controller dynamics are described by the following equations:

$$
\begin{aligned}
e_{\text{mod}} &= \bar{g}_0\left([\text{nmod}]\right) - \bar{g}_{\text{mod}}, \\
\dot{\bar{g}}_{\text{mod}} &= f\left(K_p \cdot e_{\text{mod}} + K_i \cdot \int e_{\text{mod}} \mathrm{d}t\right),
\end{aligned}
$$

where K_p and K_i are the proportional and integral gains of the PI controller, respectively. In summary, the controller adjusts the modulated conductances $\bar{g}_{\text{mod}}$ in response to the local concentration of neuromodulator, producing new reference values for these conductances to fine-tune the cell firing pattern—effectively neuromodulating it. This neuromodulator controller produces changes in conductance ratios that are normally preserved within the homeostatic controller. The new reference values depend on the neuromodulator concentration, the type of neuron, and the cell current state, characterized by the full set of conductances $\bar{g}_{\text{ion}} \in \mathbb{R}^N$. The computation of these references is achieved through DICs, which encapsulate this complexity.

DICs consist of three voltage-dependent conductances that separate according to timescales: one fast, one slow, and one ultraslow, denoted as $g_{\text{f}}(V)$, $g_{\text{s}}(V)$, and $g_{\text{u}}(V)$, which can be computed as linear functions of the maximal conductance vector $\bar{g}_{\text{ion}} \in \mathbb{R}^N$ of an N-channel conductance-based model at each voltage level V:

$$
[g_{\text{f}}(V); g_{\text{s}}(V); g_{\text{u}}(V)] = f_{\text{DIC}}(V) = S(V) \cdot \bar{g}_{\text{ion}}\,,
$$

where $S(V) \in \mathbb{R}^{3\times N}$ is a sensitivity matrix that can be built by: $S_{i\,j}(V) = -\left(w_{i\,j} \cdot \frac{\partial \dot{V}}{\partial X_j} \frac{\partial X_{j,\infty}}{\partial V}\right) / g_{\text{leak}}$, where i denotes the timescale, X_j are gating variables of the j-th channel of the considered model and $w_{i\,j}$ is a timescale-dependent weight which is computed as the logarithmic distance of the time constant of X_j and the timescale i (Drion et al., 2015a). While the complete curve of the DICs may be of interest, only its value at the threshold voltage V_{th} is used, as the values and signs of the DICs at V_{th} reliably determine the firing pattern (Drion et al., 2015a). Thus, the following linear system $f_{\text{DIC}}(V_{\text{th}}) = S(V_{\text{th}}) \cdot \bar{g}_{\text{ion}}$ makes the link between ion channel conductances and neuronal activity.

16.6 Data availability

All code and data can be found on the first author GitHub (https://github.com/arthur-fyon/BIOCONTROL_2025).

16.7 Postface

To summarize these three scientific result parts, this thesis explores neuronal dynamics by studying the distributions of ion channels within a degenerate population undergoing robust neuromodulation. First, the mechanisms governing ion channel distributions in a degenerate population were uncovered. Specifically, homogeneous scaling preserves correlations between pairs of ion channels, while variable conductance ratios adjust them. When both mechanisms are aligned, a positive apparent correlation emerges; however, when they are misaligned, the apparent correlation may disappear or even become negative. Leveraging this knowledge, an efficient algorithm was designed to generate a degenerate population of thousands of neurons within seconds. This is crucial for the subsequent results, as robust neuromodulation must be studied in degenerate populations. By fine-tuning this algorithm, a sharp neuromodulation algorithm was also developed, enabling the computation of new ion channel conductances to switch from one firing pattern to another in a static manner. This finding paved the way for understanding how ion channel correlations are altered under neuromodulation and provided insights into the direction and manner in which ion channel conductances are modified.

The need to improve this static, sharp version of the neuromodulation algorithm then became evident. Consequently, a real-time adaptive controller, inspired by this algorithm, was developed to neuromodulate any conductance-based model in real time. This model is both biologically and mathematically grounded, and its performance closely mimics biological neuromodulation in a degenerate population. Finally, further insights were gained into how this neuromodulation controller interacts with a previously published homeostasis controller. Experimental and computational evidence demonstrated that both controllers work in harmony to ensure robust neural function, with all the instabilities and unphysiological behaviors observed when homeostasis was combined with sharp neuromodulation being eliminated. Moreover, this tandem of controllers is easily adaptable to any conductance-based model and any neuronal circuit composed of degenerate neurons.

17 Application of neuromodulation on central pattern generators, a general framework

In Drion et al. (2019) and Fyon and Drion (2024b), neuromodulation and homeostasis are applied to a small neuronal circuit known as a central pattern generator (CPG) to facilitate transitions between different rhythms. CPGs are self-organizing neuronal circuits capable of generating rhythmic output in the absence of rhythmic input (Selverston, 2010). Numerous vital biological functions, including breathing, digestion, and walking, rely on the orchestration of robust and adaptable rhythmic patterns. Bursting inhibitory neural circuits have traditionally been acknowledged as the cornerstone responsible for initiating and regulating these patterns. A fundamental example is the half-center oscillator, which produces a basic rhythm without external input. This section introduces a novel method for constructing a neuromodulated CPG that can reliably switch between rhythms.

17.1 Central pattern generators and challenges

In biological systems, CPG-based locomotion control involves several components (Fig. 17.1A) (Dutta et al., 2019):

- **The brain**, including regions such as the basal ganglia, acts as a higher control entity capable of modulating rhythmic patterns;
- **The spinal locomotor system**, which comprises various CPGs, generates rhythmic outputs based on the non-rhythmic higher control signals from the brain;
- **The musculoskeletal system**, which converts the rhythmic neuronal signals into effective motion through motor neurons and neuromuscular junctions, the synaptic connections between motor nerve terminals and muscles (Engel, 2008);
- **The sensory feedback loop**, which integrates environmental feedback to adjust the rhythmic behavior of the CPGs, along with the higher control signals.

Such signal flow architecture can be translated into bio-inspired CPG-based robotic locomotion control (Fig. 17.1B), as demonstrated by Dutta et al. (2019) using coupled insulator-to-metal phase-transition nano-oscillators. Both biological and technological systems utilizing this architecture are capable of generating complex rhythmic outputs and transitioning between different rhythms. For example, the ability to switch between walking, running, and other movements is natural for healthy humans and can be emulated in artificial bio-inspired systems.

Rhythmic transitions in biological systems are known to be triggered by neuromodulatory inputs from higher neuronal regions, as shown in studies of invertebrates (Marder and Calabrese, 1996; Marder and Bucher, 2001). In artificial systems, however, rhythmic transitions typically involve altering the connections within the CPG network (Barron-Zambrano et al., 2010). Different rhythmic patterns are associated with distinct network architectures, or connectomes. These static connectomes often face challenges such as vulnerability to disruption, limited flexibility, and difficulties in external manipulation. Rapid and localized transitions in rhythmic patterns

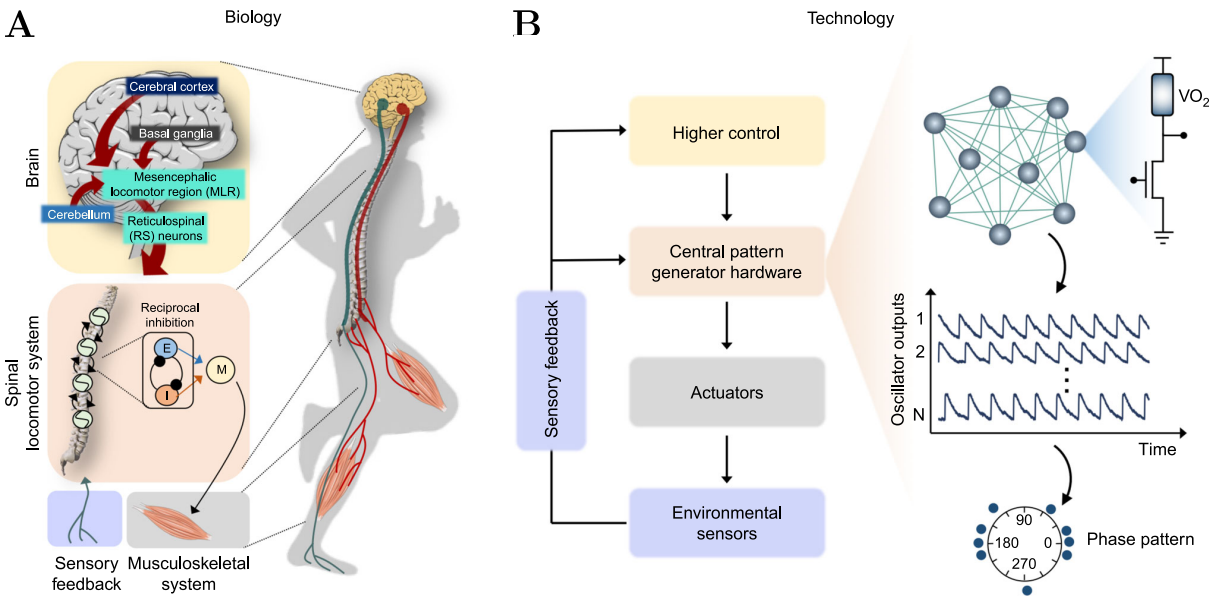

Figure 17.1: CPG-based locomotion control. A. Illustration of CPG-based locomotion control in humans, highlighting the flow of signals between different components. **B.** Technological system for locomotion control, inspired by biological CPG-based mechanisms. Taken from Dutta et al. (2019)

cannot rely solely on changes in synaptic connectivity through plasticity.

To address these challenges, our study proposes a novel approach: integrating neuromodulation to enable dynamic pattern reconfiguration within fixed connectome networks of conductance-based models. This method aims to overcome the limitations of static network architectures by allowing for more flexible and rapid adjustments in rhythmic behavior.

17.2 Including neuromodulation in central pattern generators

By introducing a neuromodulatory network alongside a rhythmic network, which encodes various patterns within its connectome, transitions between different patterns are facilitated seamlessly.

17.2.1 The neuromodulated central pattern generator architecture

The proposed architecture consists of three interconnected entities arranged in a top-down fashion (Fig. 17.2):

- A neuromodulatory input projects to a neuromodulated network composed of bursting neurons and inhibitory synapses. This input allows the neuromodulated network neurons to switch between tonic spiking and bursting. The neuromodulation controller, as described in Fyon et al. (2023), is designed to be robust to variations in neuronal parameters;
- The neuromodulated network projects to the motor neurons network through inhibitory synapses. These inhibitory projections induce rhythmic patterns within the motor neurons network. The neuromodulatory input modifies the behavior of the neuromodulated network, which in turn alters the strength of the inhibitory connections to the motor neurons network,

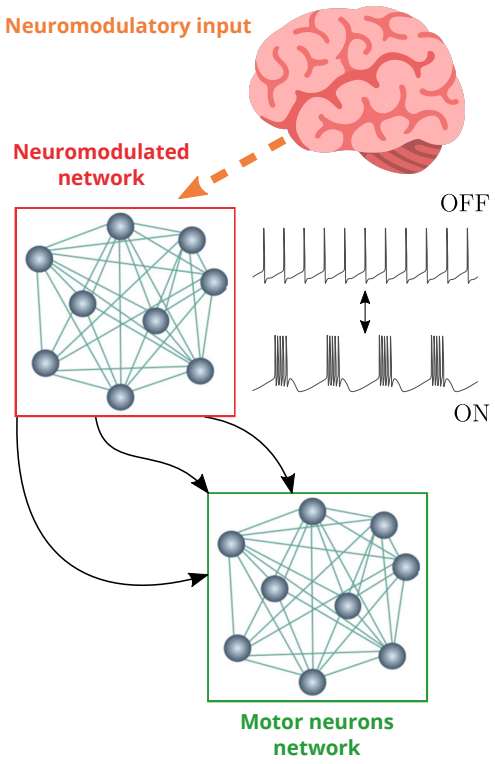

Figure 17.2: The neuromodulated central pattern generator architecture. Top-down hierarchy of the proposed neuromodulated CPG architecture, illustrating the interaction between the neuromodulatory input, neuromodulated network, and motor neurons network.

thereby enabling a switch in rhythmic patterns;

- The motor neurons network consists of bursting neurons that activate the muscles and include inhibitory synapses.

Thus, rhythmic transitions occur through the modulation of specific neuromodulatory neurons, which switch between bursting and tonic firing states. This approach ensures that the pattern shift remains robust even with variations in neuronal parameters. A notable application of our research is in the regulation of locomotion.

17.2.2 Application to robust gait control

The practical implications of our approach for quadruped gait control are demonstrated in this section, focusing on the trot-to-gallop transition. This innovative method allows us to analyze the trot and gallop rhythms encoded by the connectome while enabling external modulation through neuromodulatory mechanisms. Our work aims for broad applicability, with potential impacts on various fields within computational neuroscience.

17.2.2.1 Gait: gallop and trot

To demonstrate the effectiveness of the proposed architecture for a neuromodulated CPG, we applied it to a simplified quadruped model that switches between two rhythmic patterns: gallop and trot (Fig 17.3A).

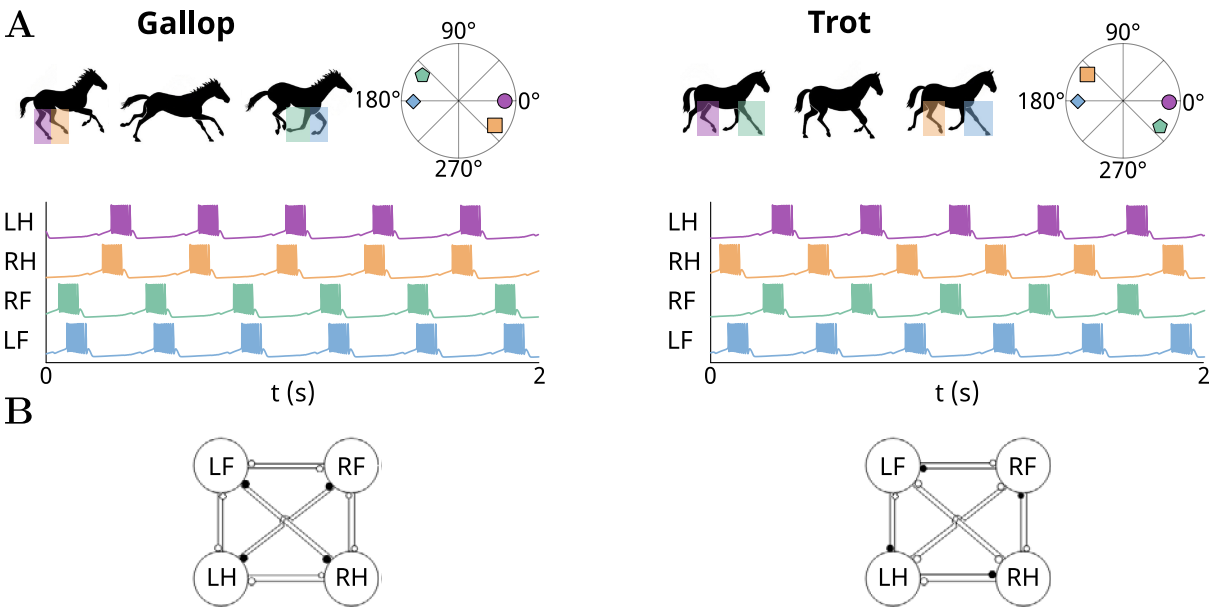

Figure 17.3: Gait: gallop and trot. A. Trot and gallop rhythms with associated phase patterns (top) along with the corresponding behaviors of bursting motor neurons for each leg (bottom). **B.** State-of-the-art artificial neuronal structure featuring distinct connectomes for each rhythm. Black dots represent excitatory synapses, and white dots represent inhibitory synapses. Labels: L for left, R for right, F for front, and H for hip. Taken from Barron-Zambrano et al. (2010).

These rhythms are intuitively understandable: in the trot gait, the diagonally opposed legs are activated alternately, while in the gallop gait, both the front or both the hind legs are activated together. In the literature, transitions between these rhythms in artificial neuronal systems are typically achieved by altering the network connectome (Fig 17.3B) (Barron-Zambrano et al., 2010).

17.2.2.2 The importance of symmetry

Following the architecture described above, a minimal solution would include four motor neurons and two neurons in the neuromodulated network, one for each rhythm (Fig. 17.4). Note that both left and right motor neurons are never activated simultaneously, which is why the motor network includes mutual inhibition loops to hardcode this rhythmic feature.

In gallop mode, the gallop coding neuron in the neuromodulated network (pale red) bursts (thus activating it), while the trot coding neuron (pale gray) exhibits tonic spiking (thus deactivating it), and vice versa. The inhibition force of a burst is much greater than that of a single spike.

If we approximate a single spike as having negligible inhibitory force, the architecture proposed in Fig. 17.4 should work ideally. For example, in gallop mode, the gallop coding neuron inhibits the LF and RF neurons, causing them to be silent and thereby activating the LH and RH neurons simultaneously, which results in the gallop rhythm. The same reasoning applies to trot mode. However, during simulation, neither gallop nor trot rhythms are sustained perfectly. This issue arises because the RF neuron sometimes fails to initiate a burst (red circles in Fig. 17.4), disrupting the rhythm. While the inhibitory force of a single spike is small, it is not zero. As

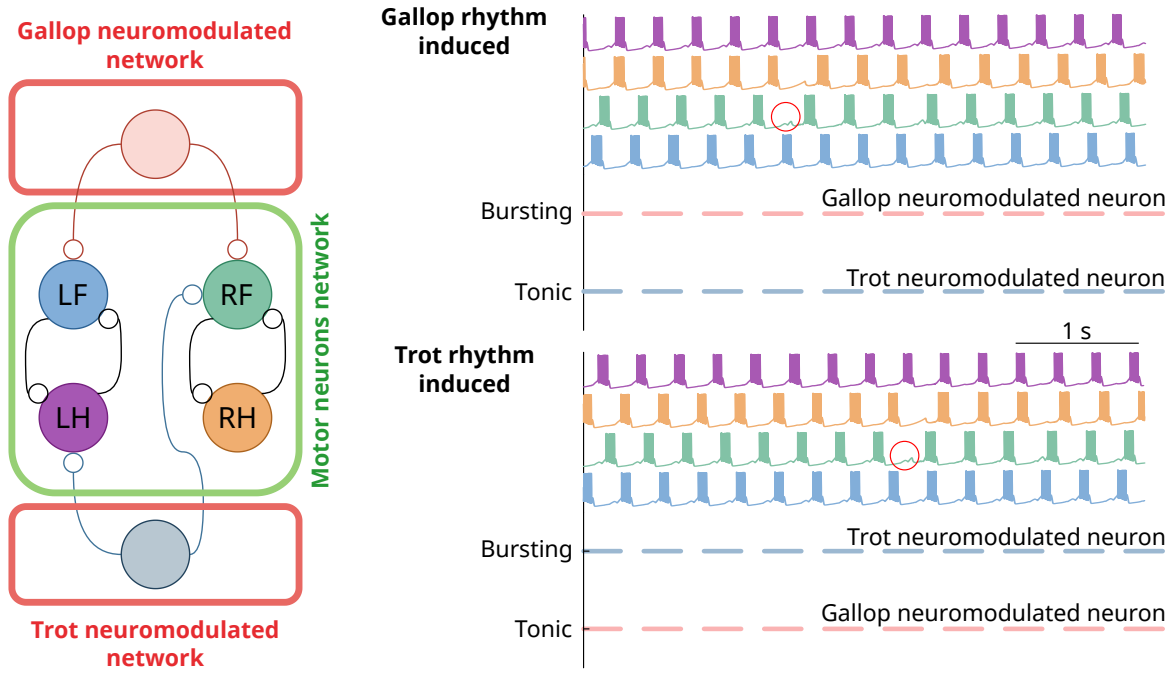

Figure 17.4: Asymmetric gait control. Minimal architecture including four motor neurons and two neurons in the neuromodulated network, one for each rhythm in the toy gait control example (left). Voltage traces of the four motor neurons during gallop and trot rhythms, without switching, are shown on the right. The red circles indicate the failure of the RF neuron to initiate a burst, thus sustaining the rhythm.

the RF neuron continually receives more inhibition compared to the other motor neurons, it can occasionally be excessively inhibited and unable to initiate its burst. This example underscores the importance of symmetry in the projections from the neuromodulated network to the motor network.

Following this idea, a minimal solution that maintains this symmetry would include the same motor network but an augmented neuromodulated network with four neurons—two for each rhythm—arranged in mutual inhibition loops (Fig. 17.5).

In this symmetric architecture, the same reasoning where the force of inhibition from a single spike is negligible can be applied to show that activating either the gallop or trot neuromodulated network effectively induces the respective rhythm in the motor neurons. Thanks to this symmetry in the projection from the neuromodulated to the motor networks, both rhythms can be sustained perfectly (Fig. 17.5 top). Furthermore, transitions from one rhythm to another can be achieved with a fixed connectome. Fig. 17.5 illustrates the phase patterns of the motor neurons during a transition from gallop to trot. This transition is triggered by switching the gallop coding neurons from bursting to tonic spiking (deactivating them) and the trot coding neurons from tonic spiking to bursting (activating them). Such a symmetric architecture can reliably produce rhythmic switches without modifying the connectome of the CPG, relying solely on neuromodulation.

The previous experiment was conducted using identical neurons in both the neuromodulated and motor networks, meaning that all neurons had the same unmodulated conductance values. To demonstrate the robustness of this architecture, 200 networks were generated with neurons

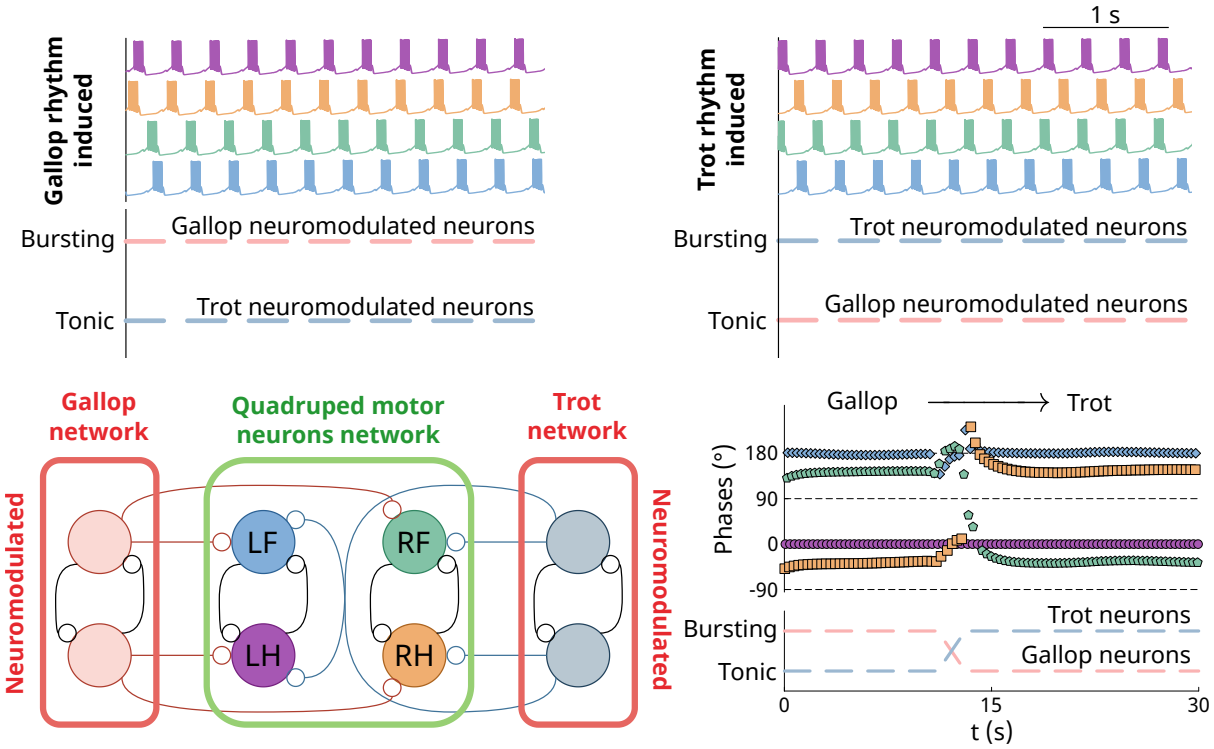

Figure 17.5: Symmetric gait control. Voltage traces of the four motor neurons during gallop and trot rhythms, without switching, for the symmetric architecture (top). The minimal architecture includes four motor neurons and four neurons in the neuromodulated network—two for each rhythm—in the toy gait control example (bottom left). Phase patterns during the transition from gallop to trot of the motor neurons are shown (bottom right).

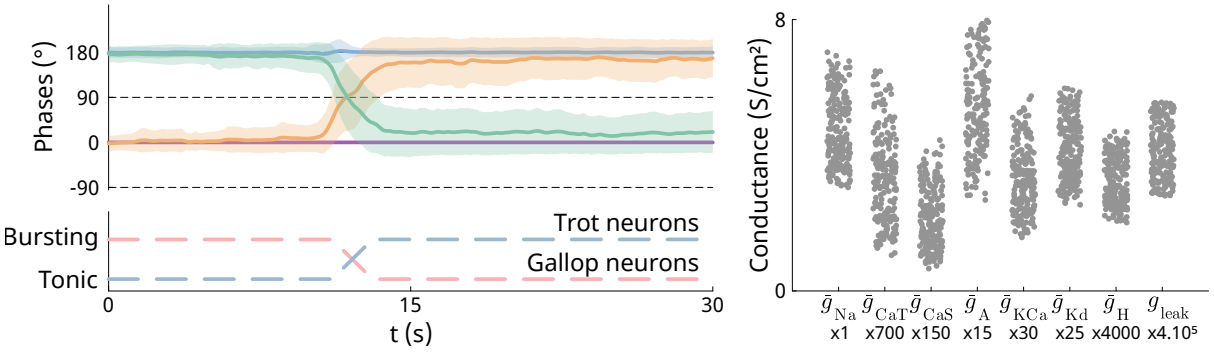

Figure 17.6: Symmetric gait control with variable conductances. Phase patterns of the motor neurons undergoing the transition from gallop to trot are shown (left). The solid line represents the mean across the population of networks, while the shaded areas indicate the minimal and maximal values. Distributions of ionic conductances across the neuronal population (right).

having varying conductance values, using the algorithm described in Fyon et al. (2024). These networks, despite having identical connectomes in terms of structure and synaptic strengths, underwent the same gallop-to-trot transitions using only neuromodulation. The results of this experiment are shown in Fig. 17.6.

Despite conductance variability up to fivefold across all neurons, the rhythmic patterns are robustly maintained by the model. The transition from one pattern to another (such as from

gallop to trot) is achieved reliably without modifying the connectome or involving synaptic plasticity. This underscores the robustness of our method to variations in neuronal parameters. While these simulations specifically address gallop-to-trot gait control, the proposed architecture is designed for broad applicability. By carefully designing both the neuromodulated and motor networks and ensuring symmetric projections between them, this approach can be adapted to any CPG. This method could pave the way for a new generation of bio-inspired locomotion control in neuromorphic systems.

Part IV

Methodological result

This chapter focuses on one methodological result of this thesis, which can be summarized here below:

1. The method that have been developed in this thesis consists in a Julia package that allows the user to easily initialize any conductance based models, to compute its Dynamic Input Conductances (DICs), and to simulate it with or without the neuromodulation controller developed in the last chapter. This package is very new and completely open source, and will continue to be developed to include more features in future years.

18 A Julia package to easily use the results of this thesis

As discussed in the previous chapter, the theory of Dynamic Input Conductances (DICs) is extremely powerful when applied appropriately and can be generalized to any conductance-based models. It can be utilized to analyze the dynamic behavior of neurons, as demonstrated in the original paper (Drion et al., 2015a), to study the rules of degeneracy within a degenerate neuronal population, as explored in Fyon et al. (2024), or even to develop a neuromodulation controller compatible with homeostasis, as shown in Fyon et al. (2023).

For nearly a decade, the theory of DICs remained relatively obscure, used primarily by the few researchers who developed it, mainly to analyze and understand dynamic behavior. One of the main reasons for its limited adoption is the difficulty in implementing the DIC equations, as follows:

$$
\begin{aligned}
g_{\mathrm{f}}(V) &= \frac{\partial I_{\mathrm{f}}}{\partial V} = \sum_i w_{\mathrm{fs},X_i}(V) \left(\frac{\partial \dot{V}}{\partial X_i} \frac{\partial X_{i,\infty}}{\partial V} \right)\Big|_V, \\
g_{\mathrm{s}}(V) &= \frac{\partial I_{\mathrm{s}}}{\partial V} = \sum_i (w_{\mathrm{su},X_i}(V) - w_{\mathrm{fs},X_i}(V)) \left(\frac{\partial \dot{V}}{\partial X_i} \frac{\partial X_{i,\infty}}{\partial V} \right)\Big|_V, \\
g_{\mathrm{u}}(V) &= \frac{\partial I_{\mathrm{u}}}{\partial V} = \sum_i (1 - w_{\mathrm{su},X_i}(V)) \left(\frac{\partial \dot{V}}{\partial X_i} \frac{\partial X_{i,\infty}}{\partial V} \right)\Big|_V, \\
g_{\mathrm{in}}(V) &= g_{\mathrm{f}}(V) + g_{\mathrm{s}}(V) + g_{\mathrm{u}}(V).
\end{aligned} \tag{18.1}
$$

Indeed, the quantities $\frac{\partial \dot{V}}{\partial X_i} \frac{\partial X_{i,,\infty}}{\partial V}$, although very general, can be challenging to develop, particularly for users who are not well-versed in conductance-based models. These expressions involve

derivatives that can be computed analytically, numerically (Whitaker and Pigford, 1960), or symbolically (Tobey, 1971). In any case, the user must have a solid understanding of either mathematical analysis or numerical analysis to effectively use DIC theory and, consequently, the neuromodulation controller developed in this thesis.

To address this challenge, we decided to develop a Julia package, *NmodController*, which is available on my GitHub (https://github.com/arthur-fyon/NmodController.jl). As will be demonstrated in this section, this package allows users to easily initialize any conductance-based model, automatically compute the DICs, and simulate the neuron, with or without the neuromodulation controller.

18.1 Benefits of the Julia programming language

This thesis was entirely developed in the Julia programming language (Bezanson et al., 2017). Although relatively new, Julia is already a mature language that offers several advantages over others (Cabutto et al., 2018). Here is a non-exhaustive list:

1. **Speed**: Julia is designed for high-performance computing, compiling everything into efficient native code, which results in extremely fast execution.
2. **Dynamic Typing**: Julia is dynamically typed, making coding in Julia highly interactive, similar to other languages like MATLAB (Matlab, 2012).
3. **Reproducibility**: Julia supports reproducible environments, ensuring that experiments can be replicated consistently.
4. **Open Source**: Julia is open source with a large community of contributors. The source code is freely available on GitHub.

To use the package, follow these steps:

1. Download Julia v1.6.X or later, if you have not already.
2. Add the *NmodController* module by entering the following at the Julia REPL:

```
]add https://github.com/arthur-fyon/NmodController.jl
```

The remainder of this section will demonstrate how to use this package.

18.2 Initializing an ionic current

"In conductance-based models, an ionic current, I_{ion}, is described by its voltage-dependent conductance, g_{ion}, and its Nernst reversal potential, E_{ion}:

$$I_{\text{ion}} = g_{\text{ion}}(V) \cdot (V - E_{\text{ion}}).$$

The voltage-dependent conductance is defined by its maximum value, $\bar{g}_{\text{ion}}$, and up to two gating variables: one activation, $m_{\text{ion}}(V)$, and one inactivation, $h_{\text{ion}}(V)$, each varying between 0 and 1.

For a current with two gating variables, this relationship is expressed as:

$$g_{\text{ion}}(V) = \bar{g}_{\text{ion}} \cdot m_{\text{ion}}^{a}(V) \cdot h_{\text{ion}}^{b}(V).$$

It is important to note that the maximum ion channel conductance, $\bar{g}_{\text{ion}}$, is not stored within the current data structure but rather within the conductance-based model data structure.

Each gating variable dynamics follow a basic first-order ordinary differential equation (ODE), where both the time constant, $\tau_{m_{\text{ion}}}$, and the steady-state value, m_{ion_∞} are voltage-dependent:

$$\dot{m}_{\text{ion}} = \frac{m_{\text{ion}_\infty}(V) - m_{\text{ion}}}{\tau_{m_{\text{ion}}}(V)}.$$

In *NmodController.jl*, an ionic current can be represented by the `IonCurrent` type. To facilitate the initialization of this data structure, it is strongly recommended to use `initializeCurrent()` with the appropriate arguments.

Example 1

The following lines of code demonstrate how to initialize a sodium current with two gating variables. This current is described by:

$$I_{\text{Na}} = \bar{g}_{\text{Na}} \cdot m_{\text{Na}}^{3} \cdot h_{\text{Na}} \cdot (V - E_{\text{Na}}).$$

```
# First initializing the converging values and time constant functions
boltz(V, A, B) = 1 / (1 + exp((V+A) / B))
tauX(V, A, B, D, E) = A - B / (1 + exp((V+D) / E))

mNa_inf(V) = boltz(V, 25.5, -5.29)
tau_mNa(V) = tauX(V, 1.32, 1.26, 120., -25.)
hNa_inf(V) = boltz(V, 48.9, 5.18)
tau_hNa(V) = (0.67 / (1 + exp((V+62.9)/-10.0))) * (1.5 + 1 / (1+exp((V+34.9)/3.6)))

# Initializing Nernst reversal potential
ENa = 50.

using NmodController
NaCurrent = initializeCurrent("Na", ENa, numberOfGatings=2, exponents=[3, 1],
    activationSteadyStateGating=mNa_inf, activationTimeConstant=tau_mNa,
    inactivationSteadyStateGating=hNa_inf, inactivationTimeConstant=tau_hNa)
```

Example 2

Sometimes, the steady-state value of a gating variable may depend on intracellular calcium levels. The following lines of code demonstrate how to initialize a calcium-controlled potassium current

with a single gating variable. This current is described by:

$$I_{\text{KCa}} = \bar{g}_{\text{KCa}} \cdot m_{\text{KCa}}^4 \cdot (V - E_{\text{KCa}}),$$

where the dynamics of m_{KCa} are given by:

$$\dot{m}_{\text{KCa}} = \frac{m_{\text{KCa}_\infty}(V, Ca) - m_{\text{KCa}}}{\tau_{m_{\text{KCa}}}(V)}.$$

As shown, m_{KCa_∞} depends on both voltage and calcium levels, and this dependency must be specified when using `initializeCurrent()`.

```
# First initializing the converging value and time constant functions
boltz(V, A, B) = 1 / (1 + exp((V+A) / B))
tauX(V, A, B, D, E) = A - B / (1 + exp((V+D) / E))

mKCa_inf(V, Ca) = (Ca / (Ca+3)) * (1 / (1+exp((V+28.3)/-12.6)))
tau_mKCa(V) = tauX(V, 90.3, 75.1, 46., -22.7)

# Initializing Nernst reversal potential
EK = -80.

using NmodController
KCaCurrent = initializeCurrent("KCa", EK, exponents=4,
    activationSteadyStateGating=mKCa_inf, activationTimeConstant=tau_mKCa,
    calciumDependency=true)
```

Example 3

Another specific case occurs when the time constant does not depend on voltage. In such instances, you can provide the time constant as a `Float64` or `Int64` argument to `initializeCurrent()`. Additionally, the steady-state value of the gating variable may depend on magnesium. To handle this, follow the example below. The following lines of code demonstrate how to initialize an instantaneous magnesium-dependent NMDA current with one gating variable. This current is expressed as:

$$I_{\text{NMDA}} = \bar{g}_{\text{NMDA}} \cdot m_{\text{NMDA}} \cdot (V - E_{\text{NMDA}}),$$

where the dynamics of m_{NMDA} are given by:

$$m_{\text{NMDA}} = m_{\text{NMDA}_\infty}(V, Mg).$$

As shown, m_{NMDA_∞} depends on both voltage and magnesium, and this dependency must be specified when using `initializeCurrent()`.

```
# First initializing the converging value and time constant functions
NMDA_inf(V, Mg) = 1 / (1 + Mg*exp(-0.08*V)/10.)
```

```
tau_NMDA(V) = 1e-10 # Never equal to zero, this might be fixed later on

# Initializing Nernst reversal potential
ENMDA = 0.

using NmodController
NMDACurrent = initializeCurrent("NMDA", ENMDA, exponents=1,
    activationSteadyStateGating=NMDA_inf, activationTimeConstant=tau_NMDA,
    MgDependency=true)
```

18.3 Initializing a complete conductance based model

18.3.1 Classical conductance based model without intracellular calcium dynamic

Once all ionic current data structures have been initialized, a complete conductance-based model can be described. The voltage equation for such a model, without any externally applied current, is given by:

$$\dot{V} = (1/C) \cdot (-\sum_{\text{ion}} I_{\text{ion}} - I_{\text{leak}}),$$

where C is the membrane capacitance, and the leak current I_{leak} is defined as:

$$I_{\text{leak}} = g_{\text{leak}}(V - E_{\text{leak}}).$$

All other equations in the model pertain to the dynamics of the gating variables, as previously described.

In *NmodController.jl*, a conductance-based model can be encapsulated within a `NeuronCB` type. To assist with initializing this data structure, it is strongly recommended to use `initializeNeuronModel()` with the appropriate arguments.

Example

The following lines of code demonstrate how to initialize a conductance-based model with two ionic currents: a fast sodium current and a rectified delayed potassium current, corresponding to the original Hodgkin and Huxley model. The voltage equation for this model is expressed as:

$$\dot{V} = (1/C) \cdot (-I_{\text{Na}} - I_{\text{Kd}} - I_{\text{leak}}).$$

```
# First wrapping all ionic currents in a vector
ionCurrents = [NaCurrent, KdCurrent]

# Initializing leakage reversal potential and leakage conductance
Eleak = -50.
gleak = 0.01
```

```
# Initializing all the maximum ion channel conductances
bar_g = [100., 10.]

using NmodController
HHmodel = initializeNeuronModel(ionCurrents, C=0.1, leakageConductance=gleak,
    reversalLeakagePotential=Eleak, maximumConductances=bar_g)
```

Note that the argument `maximumConductances` is optional and corresponds to a vector containing all the maximum ion channel conductances, $\bar{g}_{\text{ion}}$. If `maximumConductances` is not provided, it will be automatically filled with `NaN` values.

18.3.2 Intracellular calcium dynamic in a conductance based model

When at least one ionic current is calcium-dependent, an additional ODE must be included to describe the dynamics of intracellular calcium. This equation typically takes the form:

$$\tau_{\text{Ca}} \cdot [\dot{Ca}] = \sum_{\text{ion}\,Ca} e_{\text{ion}\,Ca} I_{\text{ion}\,Ca} - [Ca] + Ca_{\text{eq}},$$

where $I_{\text{ion}\,Ca}$ represents the calcium current in the model, and $e_{\text{ion}\,Ca}$ is its associated coefficient.

In *NmodController.jl*, intracellular calcium dynamics can be represented using a `CalciumDynamic` type. To assist with initializing this data structure, it is strongly recommended to use `initializeCalciumDynamics()` with the appropriate arguments.

Example

The following lines of code illustrate how to initialize a conductance-based model with five ionic currents: a fast sodium current, a rectified delayed potassium current, a calcium-controlled potassium current, a T-type calcium current, and a slow calcium current. Note that the calcium-controlled potassium current is unique in that it depends on both voltage and intracellular calcium. The voltage equation for this model is given by:

$$\dot{V} = (1/C) \cdot (-I_{\text{Na}} - I_{\text{Kd}} - I_{\text{KCa}} - I_{\text{CaS}} - I_{\text{CaT}} - I_{\text{leak}}).$$

The associated calcium dynamics are described by:

$$\tau_{\text{Ca}} \cdot [\dot{Ca}] = -0.94 \cdot I_{\text{CaT}} - 0.94 \cdot I_{\text{CaS}} - [Ca] + Ca_{\text{eq}},$$

with $\tau_{\text{Ca}} = 20$ and $Ca_{\text{eq}} = 0.05$.

```
# First wrapping all ionic currents in a vector
ionCurrents = [NaCurrent, KdCurrent, KCaCurrent, CaTCurrent, CaSCurrent]

# Initializing leakage reversal potential and leakage conductance
Eleak = -50.
```

```
gleak = 0.01

# Initializing all the maximum ion channel conductances
bar_g = [100., 10., 10., 1., 1.]

using NmodController
CaDyn = initializeCalciumDynamics(["CaT", "CaS"], [-0.94, -0.94], 0.05, 20)
CBmodel = initializeNeuronModel(ionCurrents, C=0.1, calciumDynamics=CaDyn,
    leakageConductance=gleak, reversalLeakagePotential=Eleak, maximumConductances=bar_g)
```

18.4 Computations on conductance based model

18.4.1 Computing dynamic input conductances (DICs)

DICs are three voltage-dependent conductance curves, $g_{\mathrm{f}}(V)$, $g_{\mathrm{s}}(V)$, and $g_{\mathrm{u}}(V)$, which can be computed as linear functions of the maximal conductance vector $\bar{g}_{\mathrm{ion}}$ for each voltage V. By encapsulating these three dynamic input conductances in a vector $g_{\mathrm{DIC}}(V)$, the linear combination is expressed as:

$$g_{\mathrm{DIC}}(V) = S(V) \cdot \bar{g}_{\mathrm{ion}},$$

where $S(V)$ is the sensitivity matrix. These mathematical functions can be constructed as detailed in Drion et al. (2015a).

Due to the specific feedback structure of conductance-based models, DICs influence neuronal spiking behavior, and the three types of DICs differ in the timescale of their effects: fast $g_{\mathrm{f}}(V)$, slow $g_{\mathrm{s}}(V)$, and ultraslow $g_{\mathrm{u}}(V)$. The values and signs of the DICs at particular voltages, especially the threshold voltage V_{th} are crucial for determining the neuronal firing pattern. For example, a negative $g_{\mathrm{f}}(V_{\mathrm{th}})$, indicative of local fast positive feedback, suggests that the neuron can spontaneously fire a spike near the threshold voltage. Conversely, a positive $g_{\mathrm{s}}(V_{\mathrm{th}})$, corresponding to slow negative feedback, indicates that after a spike, the neuron will likely reduce excitation and return to its resting voltage. A negative $g_{\mathrm{s}}(V_{\mathrm{th}})$ suggests the neuron may fire additional spikes, initiating a burst. In bursting neurons, $g_{\mathrm{u}}(V_{\mathrm{th}})$ is always positive and reflects the interburst frequency and duty cycle, representing ultraslow negative feedback.

After initializing the conductance-based model using *NmodController.jl*, you can compute the DICs or sensitivity matrix using the function `computeDICs()`. Simply provide your model and specify the three time constant functions corresponding to the fast, slow, and ultraslow timescales for DIC computation. This function eliminates the need for manual, complex calculations.

Example 1

The following lines of code illustrate how to compute DICs using a predefined conductance-based model named `neuron`. It is important to note that you must specify the maximum ion channel conductances when initializing the conductance-based model in order to compute the DICs.

```
# First initializing the three timescales
```

```
tauX(V, A, B, D, E) = A - B / (1 + exp((V+D) / E))
tauFast(V) = tauX(V, 1.32, 1.26, 120., -25.)
tauSlow(V) = boltz(V, 12.3, -11.8)
tauUltraslow(V) = 100.

using NmodController
gf, gs, gu = computeDICs(neuron, tauFast, tauSlow, tauUltraslow)
```

Example 2

The following lines of code demonstrate how to compute the sensitivity matrix using a predefined conductance-based model named `neuron`.

```
# First initializing the three timescales
tauX(V, A, B, D, E) = A - B / (1 + exp((V+D) / E))
tauFast(V) = tauX(V, 1.32, 1.26, 120., -25.)
tauSlow(V) = boltz(V, 12.3, -11.8)
tauUltraslow(V) = 100.

using NmodController
S = computeDICs(neuron, tauFast, tauSlow, tauUltraslow, onlyS=true)
```

Note that two additional optional arguments can be specified in the `computeDICs()` function:

1. `tauCa`, which is a number representing the timescale of the intracellular calcium dynamics (typically large, as calcium dynamics are ultraslow);
2. `scaled`, a boolean argument that is automatically set to `true`. When enabled, this argument scales the DICs or sensitivity matrix by the leakage conductance of the conductance-based model, making them dimensionless. This scaling is strongly recommended.

18.4.2 Computing threshold voltage

As mentioned earlier, the threshold voltage V_{th} plays a crucial role when working with DICs. To determine this value, we need the DICs, as the threshold voltage is defined as the zero-crossing point where the global input conductance $g_{\text{in}}(V) = g_{\text{f}}(V) + g_{\text{s}}(V) + g_{\text{u}}(V)$ transitions from positive to negative. After computing the DICs using *NmodController.jl*, the threshold voltage can be calculated using the `computeThresholdVoltage()` function.

Example

The following lines of code demonstrate how to compute the threshold voltage using a predefined conductance-based model named `neuron`.

```
# First initializing the three timescales
tauX(V, A, B, D, E) = A - B / (1 + exp((V+D) / E))
tauFast(V) = tauX(V, 1.32, 1.26, 120., -25.)
```

```
tauSlow(V) = boltz(V, 12.3, -11.8)
tauUltraslow(V) = 100.

using NmodController
gf, gs, gu = computeDICs(neuron, tauFast, tauSlow, tauUltraslow)
Vth = computeThresholdVoltage(gf, gs, gu)
```

18.5 Simulating conductance based models

18.5.1 Simulating uncontrolled conductance based models

The most compelling aspect of conductance-based models becomes evident when integrating their ODEs. Indeed, the voltage solution can accurately reproduce neuronal activity, making it a key tool in both computational neuroscience and neuromorphic engineering. To facilitate this, *NmodController.jl* integrates seamlessly with *DifferentialEquations.jl*, a Julia package dedicated to the efficient numerical solution of differential equations.

NmodController.jl simplifies the simulation of conductance-based models by providing a convenient method to generate the ODE function required by *DifferentialEquations.jl*. This is done through the function `writeUncontrolledODEs()`. To use this function, simply provide your model as an argument. Additionally, you can specify the optional argument `filename` to save the ODE function in a newly created *.jl* file.

Example

The following lines of code demonstrate how to generate the ODE function file using a predefined conductance-based model named `neuron`.

```
using NmodController
writeUncontrolledODEs(neuron, filename="neuron_ODE.jl")
```

To define your ODE problem, include the newly created *.jl* file and specify the ODE function (which defaults to `CBModelODEs`) as an argument to the `ODEProblem()` function from the *DifferentialEquations.jl* suite. You will also need to provide simulation parameters, initial conditions, and the time span for integration. Finally, solve the ODE problem using the `solve()` function from *DifferentialEquations.jl*.

18.5.2 Simulating controlled conductance based models

In Fyon et al. (2023), a neuromodulation adaptive controller that is robust to neuronal degeneracy is proposed that can be applied to any conductance-based model. This controller allows for the adjustment of p DICs at any voltage (typically, the threshold voltage is used, as DICs at this voltage shape neuronal activity) with n ionic currents. By selecting appropriate neuromodulated maximum ion channel conductances and the DICs to control, any desired physiological firing pattern can be achieved by setting the DICs accordingly. Note that $p \leq n$ to ensure that the linear system behind the controller has a solution.

To facilitate the simulation of neuromodulated conductance-based models, *NmodController.jl* provides a straightforward way to generate the ODE function required for solvers from *DifferentialEquations.jl*. Use the function `writeControlledODEs()` and specify your model, the names of the conductances to neuromodulate, and the DICs to control. The ODE function will be saved in a newly created *.jl* file, which you can name using the optional `filename` argument.

Example

The following lines of code demonstrate how to generate the ODE function file using a predefined conductance-based model named `neuron`.

```
using NmodController
writeControlledODEs(neuron, ["ion1", "ion2", "ion3"], ["f", "s", "u"],
    filename="ControlledNeuron_ODE.jl")
```

To define your ODE problem, include the newly created *.jl* file and specify the ODE function (which defaults to `ControlledCBModelODEs`) as an argument to the `ODEProblem()` function from the *DifferentialEquations.jl* suite. You will also need to provide simulation parameters, initial conditions, and the time span for integration. Finally, solve the ODE problem using the `solve()` function from *DifferentialEquations.jl*.

18.6 Example on existing models in the literature

In the following subsections, we will present examples of simulations and figures that can be easily generated using *NmodController.jl* for the two primary models discussed in this thesis: the STG and DA models (Liu et al., 1998; Qian et al., 2014). The source code used to generate these figures is provided in Appendices C1 and C2.

18.6.1 The STG model

Once the STG model is initialized, computing DICs, the sensitivity matrix, or the threshold voltage becomes straightforward. For comparison, we will use two STG models with different maximum ion channel conductances: `STG_spiking`, which exhibits a tonic spiking behavior, and `STG_bursting`, which exhibits a bursting behavior.

The parameters for `STG_spiking` are:

- Sodium current: $\bar{g}_{\mathrm{Na}} = 4000$;
- T-type calcium current: $\bar{g}_{\mathrm{CaT}} = 3$;
- Slow calcium current: $\bar{g}_{\mathrm{CaS}} = 4$;
- A-type potassium current: $\bar{g}_{\mathrm{A}} = 175$;
- Calcium controlled potassium current: $\bar{g}_{\mathrm{KCa}} = 110$;
- Delayed rectified potassium current: $\bar{g}_{\mathrm{Kd}} = 137$;
- H type current: $\bar{g}_{\mathrm{H}} = 0.3$;

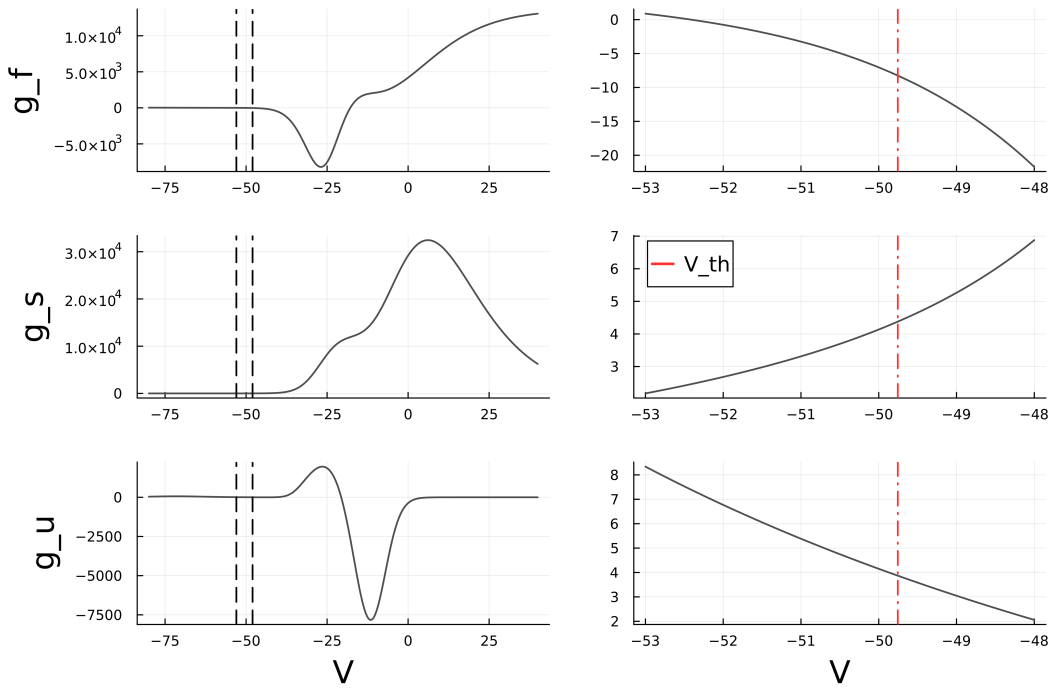

Figure 18.1: DIC curves for `STG_spiking`. Left: complete DIC curves. Right: Zoomed DIC curves around the threshold voltage

- Leakage current: $g_{\text{leak}} = 0.01$;

The parameters for `STG_bursting` are:

- Sodium current: $\bar{g}_{\text{Na}} = 4000$;
- T-type calcium current: $\bar{g}_{\text{CaT}} = 3$;
- Slow calcium current: $\bar{g}_{\text{CaS}} = 19$;
- A-type potassium current: $\bar{g}_{\text{A}} = 70$;
- Calcium controlled potassium current: $\bar{g}_{\text{KCa}} = 110$;
- Delayed rectified potassium current: $\bar{g}_{\text{Kd}} = 137$;
- H type current: $\bar{g}_{\text{H}} = 0.3$;
- Leakage current: $g_{\text{leak}} = 0.01$;

Figures 18.1 and 18.2 show the DIC curves of the STG model with spiking and bursting behaviors, respectively.

As mentioned earlier, the primary difference between a spiking and a bursting neuron is found in the slow DIC, particularly in its sign around the threshold voltage. In spiking neurons, the slow DIC is positive around the threshold, while in bursting neurons, it is negative.

Simulation is also simplified when using *NmodController.jl*. First, we will simulate the `STG_spiking` model, which exhibits a tonic spiking behavior with the parameters listed above. With just a few

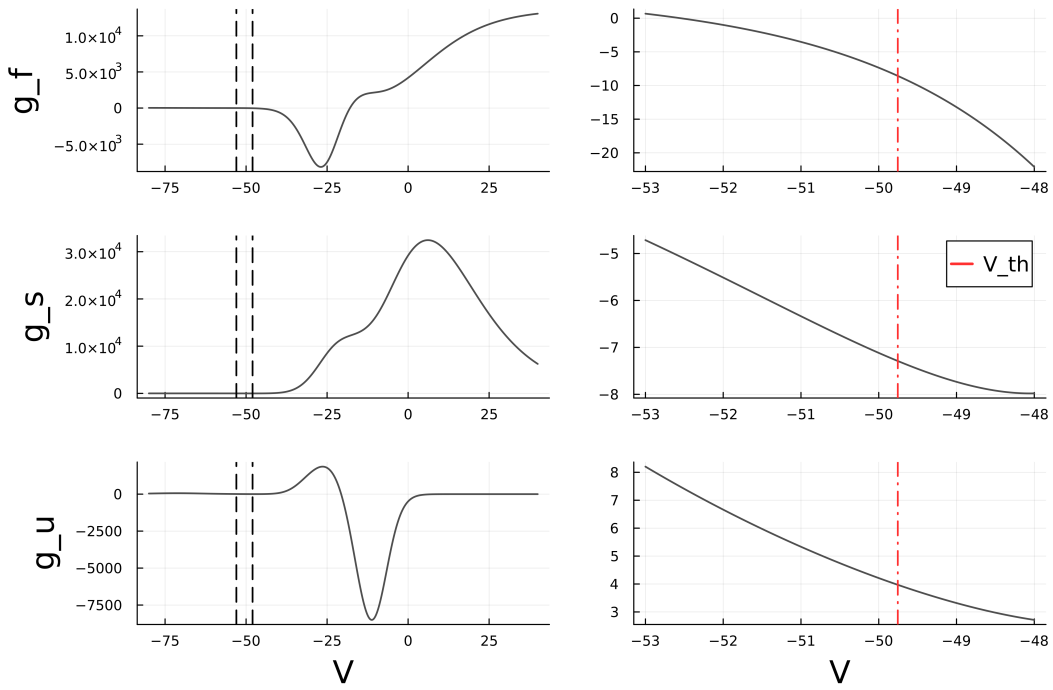

Figure 18.2: DIC curves for `STG_bursting`. Left: complete DIC curves. Right: Zoomed DIC curves around the threshold voltage

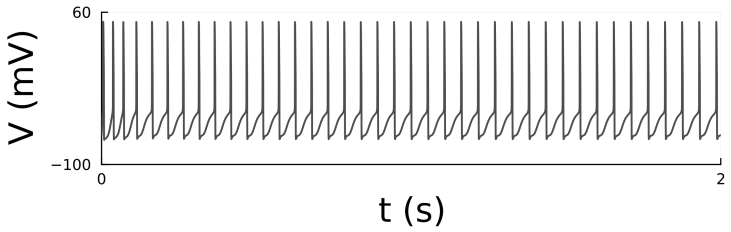

Figure 18.3: Voltage trace for `STG_spiking`.

lines of code, Figure 18.3 can be generated, displaying a voltage trace characteristic of typical tonic spiking behavior.

As demonstrated in Fyon et al. (2023), the slow and ultraslow DICs of the STG model can be controlled by the slow calcium and A-type potassium currents to achieve a robust transition from tonic spiking to bursting. With just a few lines of code, Figure 18.4 can be generated, illustrating the voltage trace of the neuromodulated `STG_spiking` model, which exhibits a typical tonic spiking to bursting transition behavior.

18.6.2 The DA model

Once the DA model is initialized, computing DICs, the sensitivity matrix, or the threshold voltage becomes straightforward. For comparison, we will use two DA models with different maximum ion channel conductances: `DA_spiking`, which exhibits a tonic spiking behavior, and `DA_bursting`, which exhibits a bursting behavior.

The parameters for `DA_spiking` are:

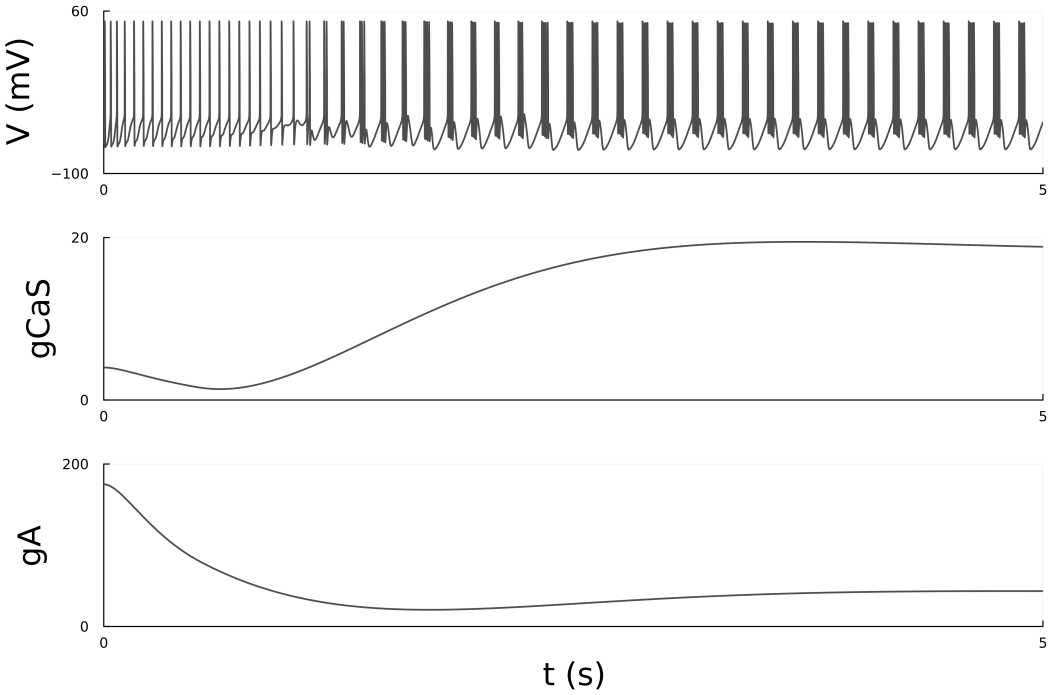

Figure 18.4: Voltage trace for neuromodulated `STG_spiking`.

- Sodium current: $\bar{g}_{\mathrm{Na}} = 30$;
- Delayed rectified potassium current: $\bar{g}_{\mathrm{Kd}} = 5$;
- L-type calcium current: $\bar{g}_{\mathrm{CaL}} = 0.03$;
- N-type calcium current: $\bar{g}_{\mathrm{CaN}} = 0.03$;
- ERG current: $\bar{g}_{\mathrm{ERG}} = 0.12$;
- NMDA current: $\bar{g}_{\mathrm{NMDA}} = 0$;
- Leakage current: $g_{\mathrm{leak}} = 0.01$.

The parameters for `DA_bursting` are:

- Sodium current: $\bar{g}_{\mathrm{Na}} = 30$;
- Delayed rectified potassium current: $\bar{g}_{\mathrm{Kd}} = 5$;
- L-type calcium current: $\bar{g}_{\mathrm{CaL}} = 0.02$;
- N-type calcium current: $\bar{g}_{\mathrm{CaN}} = 0.15$;
- ERG current: $\bar{g}_{\mathrm{ERG}} = 0.12$;
- NMDA current: $\bar{g}_{\mathrm{NMDA}} = 0$;
- Leakage current: $g_{\mathrm{leak}} = 0.01$.

Note that the NMDA current conductance is set to 0 since it is not involved in intrinsic neuronal excitability, as it specifically involves NMDA receptors.

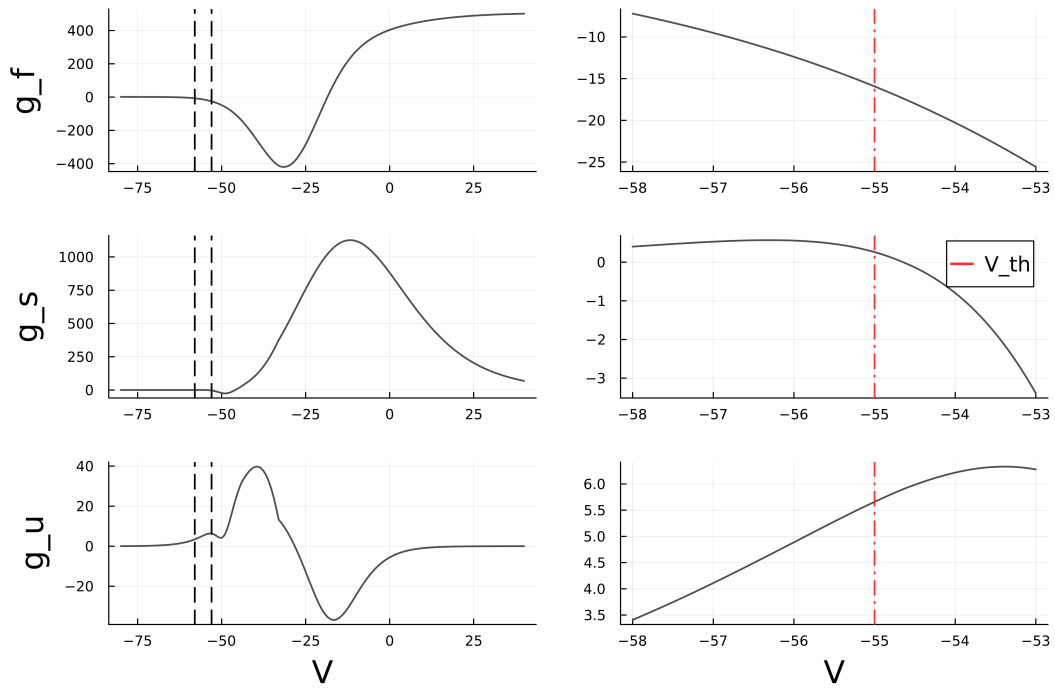

Figure 18.5: DIC curves for `DA_spiking`. Left: complete DIC curves. Right: Zoomed DIC curves around the threshold voltage

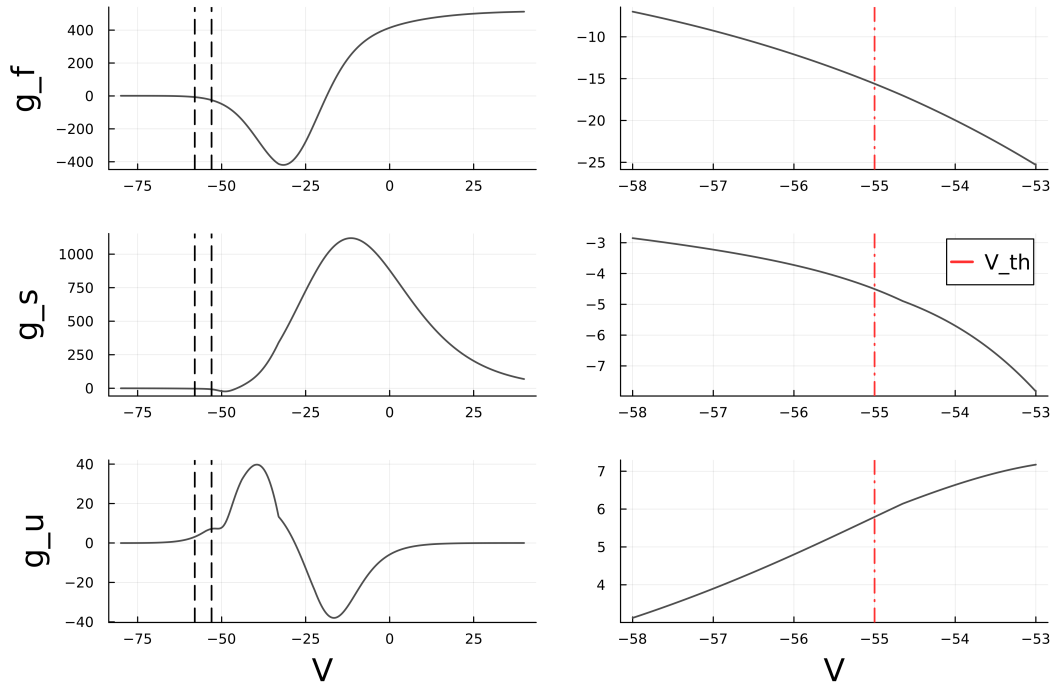

Figure 18.6: DIC curves for `DA_bursting`. Left: complete DIC curves. Right: Zoomed DIC curves around the threshold voltage

Figures 18.5 and 18.6 show the DIC curves of the DA model with spiking and bursting behaviors, respectively.

Again, the primary difference between a spiking and a bursting neuron is found in the slow DIC,

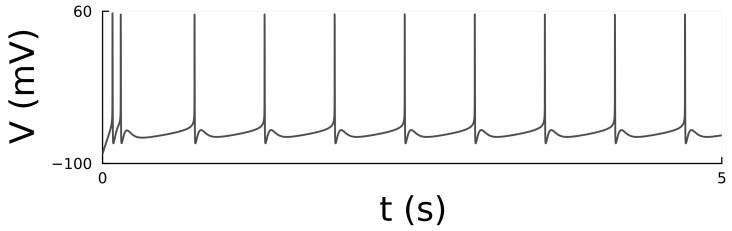

Figure 18.7: Voltage trace for `DA_spiking`.

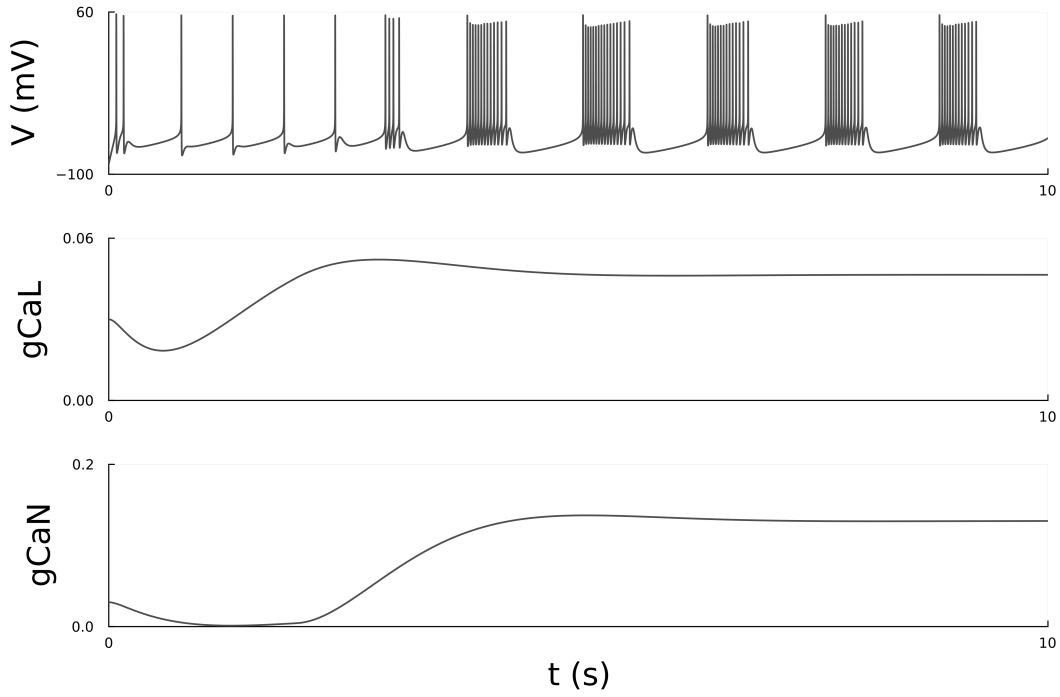

Figure 18.8: Voltage trace for neuromodulated `DA_spiking`.

particularly in its sign around the threshold voltage. In spiking neurons, the slow DIC is positive around the threshold, while in bursting neurons, it is negative.

Simulation is also simplified when using *NmodController.jl*. First, we will simulate the `DA_spiking` model, which exhibits a tonic spiking behavior with the parameters listed above. With just a few lines of code, Figure 18.7 can be generated, displaying a voltage trace characteristic of typical tonic spiking behavior.

The slow and ultraslow DICs of the DA model can be controlled by the L-type and N-type calcium currents to achieve a robust transition from tonic spiking to bursting. With just a few lines of code, Figure 18.8 can be generated, illustrating the voltage trace of the neuromodulated `DA_spiking` model, which exhibits a typical tonic spiking to bursting transition behavior.

18.7 Conclusion and perspectives

All in all, this Julia package enables users to instantiate any conductance-based model, compute its DICs, and simulate it (with or without the neuromodulation controller) with minimal knowledge

of Julia or programming in general. It serves as an efficient tool to disseminate the primary outcome of this thesis—the neuromodulation controller—and the underlying theory of DICs. Additionally, it encourages computational neuroscience researchers to apply DIC theory for more thorough model analysis, as demonstrated in this thesis.

In the near future, this package will be enhanced with features such as:

- The ability to compute more than three DICs, extending up to n;
- Support for initializing non-conventional ionic currents, like the ERG current in the DA model;
- Simulation capabilities without explicitly relying on *DifferentialEquations.jl*, integrating all relevant simulation code within *NmodController.jl*;
- The ability to simulate both the neuromodulation and homeostasis controllers on any neuron, reproducing the results from Fyon and Drion (2024b) using the package;
- User feedback-driven improvements to refine and optimize the package.

Part V

Conclusion

19 Summary

This thesis can be summarized in three main results, each flowing into the next.

19.1 Functional variable identification and degeneracy mechanisms in neuronal activity

The initial phase of this thesis focuses on identifying functional variables that uniquely characterize neuronal activity and correlate with degenerate physiological variables (*e.g.*, ion channel density). Establishing this set of variables is essential prior to designing a neuromodulation controller, as non-degenerate references and variables are required to resolve ambiguities stemming from neuronal parameter heterogeneity.

Through dimensionality reduction, specifically Principal Component Analysis (PCA), applied to populations of degenerate neurons, two physiological mechanisms underlying neuronal variability are revealed. These populations were generated by a random conductance search across two conductance-based models: one from the stomatogastric ganglion (STG) of the crab and the other from a dopaminergic neuron (DA). The post-processing step ensured a fixed phenotype across neurons, resulting in external homogeneity but internal heterogeneity, without assuming specific degeneracy mechanisms.

The first identified mechanism is homogeneous scaling of maximal ion channel conductances, where conductances are scaled by a common factor, determining the slope of a regression line. This is captured by the dominant PCA component in both models and can arise from homeostatic ion channel expression models, where the slope between conductances correlates with neuronal activity type. The second mechanism, captured by secondary PCA components, involves degeneracy in conductance ratios associated with neuronal dynamical properties. This cryptic variability only becomes apparent when perturbations, such as ion channel blockades, are introduced in neurons with variable conductance ratios.

Interestingly, these two mechanisms—homogeneous scaling and degenerate conductance ratios—may compete. Variability from both mechanisms leads to neuromodulation-dependent correlations or uncoupling of conductance values. When the manifolds of these mechanisms align, pairwise conductance correlations are high; when misaligned, correlations diminish. These correlations vary with the neuromodulated state. Under neuromodulation, homogeneous scaling rotates around the origin of parameter space, while variable conductance ratios translate within the space, leading to changes in alignment and corresponding shifts in correlation values.

This study suggests that neuromodulation of degenerate neuronal populations cannot be simplified to purely multiplicative or additive rules, as the underlying degeneracy emerges from these

two distinct mathematical operations. However, the resulting neuromodulation rule is still straightforward but indirect. Neuromodulation follows a linear trajectory, though the path length varies between neurons. This indicates that the direction of neuromodulation is neuron-type-dependent, while the step length is determined by neuronal parameters. Furthermore, this work facilitates the development of algorithms capable of generating degenerate neuronal populations within seconds, a significant improvement over the random search techniques that require hours. The algorithm has also been adapted to modulate existing degenerate populations by computing new values for modulated conductances.

19.2 Development of a GPCR-based molecular controller for reliable neuromodulation

Building on the previously developed algorithms, a GPCR-based molecular controller was designed to achieve reliable neuromodulation in neuron models exhibiting high variability. The use of Dynamic Input Conductances (DICs) as control variables allowed the translation of a pre-defined neuromodulation rule into an online controller. This controller is capable of dynamically regulating neuronal activity in real time, using human-understandable references and neuromodulator concentrations as control benchmarks.

Treating neuronal excitability as a feedback control system addresses the inherent complexity of neuromodulation by consolidating the effects of multiple voltage-gated ion channels into a set of feedback gains operating on various timescales. In this framework, neuronal dynamics are modeled as a control system, where voltage-gated (and some calcium-gated) ion channels function as a controller that generates control signals, acting on a passive membrane that serves as the plant. This feedback control perspective simplifies the investigation of neuromodulation by reducing the complexity of neuronal dynamics to a manageable system.

The primary targets of neuromodulators are ion channel densities, which determine the feedback gains of the controller on each timescale. Neuromodulation can therefore be viewed as an input to an adaptive control block, whose function is to fine-tune neuronal behavior by adjusting the feedback gains in a functionally relevant manner. The inputs to this adaptive control block correspond to neuromodulator concentration near the neuron and ion channel conductance values. Biologically, these inputs could originate from an additional neuronal adaptive control mechanism, such as a homeostatic control block, which reads neuronal outputs (membrane potential and intracellular calcium concentration) and regulates ion channel conductances to maintain neuronal excitability within safe physiological limits.

From this neuromodulation perspective, an adaptation mechanism was derived. The proposed system consists of two main components: a reference generator block and a reference tracking block (feedforward and feedback, respectively). The outputs of this neuromodulation-dependent adaptive system are ion channel conductance levels that modulate neuronal feedback gains.

The feedforward block represents the activation of a metabotropic receptor, which sets neuromodulation-dependent targets for neuronal excitability by generating a reference signal for modulated ion channel conductances. A molecular network, activated by the metabotropic

receptor, maps these target gains into specific references for ion channel conductances. These reference conductances are input into a proportional-integral (PI) regulated protein translation control system, which synthesizes new transmembrane proteins and facilitates their transport to the membrane through diffusion or active trafficking. Ion channel movement between intracellular and membrane compartments is modeled as passive diffusion, while ion channel turnover accounts for continuous degradation of transmembrane proteins in the intracellular domain. For each modulated conductance, a positive translation control signal, representing the synthesis of new transmembrane proteins, is computed by a classical negative feedback controller, which seeks to match the ion channel conductance to its reference value.

The robustness to neuronal degeneracy of this adaptive gain control scheme was tested through simulations involving neurons with highly variable maximal conductance values, consistent with biological data. The results demonstrate that the proposed neuromodulation adaptive control system closely replicates the biological feedback mechanisms of neuromodulation. Despite significant variability in intrinsic ion channel conductances, the neuromodulated neurons exhibited minimal variability in their phenotypic properties.

19.3 Interaction between neuromodulation and homeostatic regulation in neurons and robotics applications

After validating the neuromodulation adaptive controller, we explored its interaction with a previously published model of intrinsic homeostatic plasticity.

Neurons and circuits demonstrate an exceptional ability to regulate and maintain their electrical signaling properties despite various disturbances, such as protein turnover or external perturbations. This critical functionality is achieved through homeostatic regulation, exemplified by a model that maintains intracellular calcium levels by adjusting the conductances of all ion channels, either increasing or decreasing them, while preserving predefined correlations between conductances (O'Leary et al., 2014).

The two computational models—neuromodulation and homeostasis—offer contrasting regulatory approaches. Neuromodulation primarily alters the correlations between pairs of conductances within a subset of neuromodulated ion channels, impacting neuronal dynamics. In contrast, homeostatic regulation adjusts all conductances in the same direction to maintain a target calcium level, thus modifying passive neuronal properties while preserving existing correlations. Despite these differences, biological neurons integrate both mechanisms robustly. We aimed to understand the computational mechanisms underlying the successful interaction of neuromodulation and homeostasis. Homeostatic regulation alone can lead to pathological loss of function in response to disturbances. However, when combined effectively with neuromodulation, this loss of function is mitigated. The synergy between neuromodulation and homeostasis enables the robust achievement and maintenance of a desired firing pattern, provided as input to the model.

Additionally, we applied the combined neuromodulation controller and homeostasis to achieve gait control in a quadruped robot that is robust to neuronal degeneracy. Traditionally, gait control and transitions between rhythmic patterns, such as from trot to gallop, have been associated

with distinct network architectures, or connectomes. However, such networks face challenges, including susceptibility to disruption, limited adaptability, and difficulty in external manipulation due to their static nature. To overcome these limitations, we developed an innovative approach: integrating neuromodulation to allow dynamic reconfiguration of rhythmic patterns encoded by fixed connectome networks.

By introducing a neuromodulatory network alongside a pre-existing rhythmic network that encodes various patterns in its connectome, we can facilitate seamless transitions between patterns. This transition is achieved by modulating specific neuromodulatory neurons, switching them between bursting and tonic firing states. Remarkably, this pattern shift remains robust, even in the presence of neuronal parameter variability. One significant application of this work lies in the control of locomotion.

Both the neuromodulatory and rhythmic networks utilize half-center oscillators to maintain symmetry, which prevents pattern disruptions caused by neuromodulatory-rhythmic asymmetries. This approach allows us to dissociate the trot and gallop rhythms hardwired in the connectome while providing external modulation through neuromodulatory mechanisms. The implications of this neuromodulatory network extend beyond locomotion control, with potential applications in neuromorphic engineering, including the control of neuromorphic robots and the modulation of spiking neural networks.

19.4 Broadcasting these models: a Julia package

In parallel with these research efforts, we have developed a Julia package, available on GitHub, to facilitate broader access to the research and models. This package allows users to begin with any specified conductance-based models and compute DICs, enabling the simulation of both uncontrolled and controlled versions of the neuron using the controller developed in the second part of this summary. This tool provides an efficient and straightforward means for global distribution of these models, allowing other researchers to rapidly and easily reproduce the results.

20 Future work

Throughout this thesis, a computational approach is employed to explore a fundamental domain in neuroscience and its interaction with various mechanisms, *i.e.* neuromodulation. Computational tools allow for the simulation of experiments by simply adjusting parameters and equations, providing a more efficient alternative to experimental validation, which can take months. While these tools are powerful, they remain constrained by the limitations of current computational resources, though these are rapidly advancing (Poirazi and Papoutsi, 2020). Nevertheless, it is important to acknowledge the inherent limitations of computational neuroscience compared to experimental validation. Therefore, a key focus of future work will be to further refine the neuromodulation controller through both experimental and neuromorphic engineering validation. Such validation will enhance the controller ability to capture the complexities of neuromodulation and behavioral adaptation.

20.1 Experimental validation of the neuromodulation controller

First, experimental validation of the feedback control mechanism in neuromodulation must be conducted. A straightforward approach would involve working on isolated neurons from the crab stomatogastric system, primarily in current clamp mode, as performed in the Marder Lab (Brandeis University, MA, USA). Experimental protocols could follow those described in Grashow et al. (2009), and two experiments are proposed.

In the first experiment, a fixed concentration of a neuromodulator such as serotonin or oxotremorine will be applied to an isolated neuron (via bath application). Neuronal activity will be measured under two conditions: a control condition and one where the neuron is initially perturbed by a constant inhibitory or excitatory current (the perturbation is maintained throughout the experiment). The neuromodulated states between the two conditions can then be compared to observe whether the perturbation attenuates or disappears in the neuromodulated state. This would suggest that the neuromodulator adapts its effect to varying experimental conditions, implying feedback action in neuromodulation.

In the second experiment, a biological neuron will be connected to an artificial system involving the neuromodulation controller through dynamic clamp (Sharp et al., 1993). The biological neuron membrane potential will be fed in real time to the artificial system, which compares it to a target activity predefined by the experimenter. The artificial control system will then dynamically adjust 2 or 3 artificial conductances inserted into the neuron membrane until the measured activity matches the target.

On one hand, this approach will allow us to verify whether such control mechanisms can achieve reliable neuromodulation in biological cells. On the other hand, it will enable a comparison of injected artificial conductances over time across experiments, providing insight into whether reliable neuromodulation depends on neuron-specific modifications in ion channel densities. These are just examples of potential experiments that could be conducted in the Marder Lab, with many other possibilities that could be explored.

20.2 Investigating the role of neuronal morphology in neuromodulation

One aspect briefly mentioned earlier in this thesis, but not explored in the results, is the influence of neuronal morphology on its voltage activity. The shape of the dendritic tree, the number of dendrites, and other morphological factors are linked to neuronal function and activity (Van Ooyen et al., 1995; Yelnik et al., 1991). For example, Purkinje cells from the cerebellum and pyramidal cells from the hippocampus exhibit very distinct morphologies and functions (Vida et al., 2018; Hirano, 2018).

In this thesis, the focus has been primarily on uncovering general neuromodulatory mechanisms related to the intrinsic electrical properties of neurons, such as ion channels, rather than on morphology. Our modeling approach does not simulate full neurons but instead focuses on a small piece of membrane at a recording site, neglecting information propagation within the neuron.

While this approach does not directly account for the effects of morphology on neuromodulation, the existing adaptive controller for neuromodulation could potentially be expanded to investigate these effects, albeit with some adjustments. Currently, we model single-compartment neurons, where only the recording site is considered. To incorporate full morphological details such as cable properties, multi-compartment models are required, where neurons are divided into distinct compartments to represent structures like dendritic trees. Each compartment is modeled as a single-compartment system, interconnected through currents that follow Ohm's law.

Thus, the current neuromodulation controller is limited to modulating conductances within single-compartment models, as the DICs theory was originally developed for this scope. A natural next step would be to extend the DICs theory to multi-compartment models, defining a separate DIC for each compartment and establishing the connections between them. Once this extension is developed, the neuromodulation controller can be adapted to modulate conductances in each compartment independently.

Such advances could provide deeper insights into how neuromodulation interacts with neuronal morphology. For instance, to effectively modulate activity along the axon, should only specific dendrites be targeted, or does the entire dendritic tree and soma require changes to the modulated conductance? Addressing these questions computationally could lead to novel experimental studies and further our understanding of neuromodulation's spatial effects within neurons.

20.3 Neuromorphic engineering validation of the neuromodulation controller

On the other side of the neuroengineering spectrum, neuromorphic engineering is an emerging field that bridges tools from computer science, engineering, and biology. Its primary focus is the development of electronic devices and robots inspired by biological brains. Below are some potential applications where the neuromodulation controller could be validated.

20.3.1 Neuromorphic machine learning

Neuromorphic machine learning draws inspiration from the human brain to develop algorithms and models that emulate biological neural networks. Unlike conventional machine learning, which often relies on large datasets and centralized processing, neuromorphic machine learning emphasizes decentralized, event-driven computation (Yoo and Shoaran, 2021). By mimicking the brain parallel and distributed processing capabilities, neuromorphic systems exhibit enhanced energy efficiency and adaptability. These systems often utilize Spiking Neural Networks (SNNs) and event-based sensors, enabling real-time processing of sensory data and facilitating rapid decision-making in dynamic environments (Ghosh-Dastidar and Adeli, 2009; Tavanaei et al., 2019; Yamazaki et al., 2022).

Current SNNs employ basic, simple integrate-and-fire models that lack many of the advantages of biological neurons (Dora and Kasabov, 2021). One key characteristic of interest is adaptation, as integrate-and-fire models only produce single spikes, making them rigid. Incorporating the neuromodulation controller into SNNs could broaden the range of firing patterns these artificial neurons can exhibit, potentially improving the adaptability and performance of current SNNs. This line of research will likely be pursued in our lab.

20.3.2 Bio-inspired control and neuromorphic robotics

Bio-inspired control applies principles from biological systems to design innovative control strategies. Drawing inspiration from nature, it harnesses the efficiency and adaptability observed in living organisms. By mimicking behaviors found in animals and ecosystems, bio-inspired control systems create autonomous and adaptive mechanisms (Zeng et al., 2018; Wang et al., 2019). Meanwhile, neurorobotics—a dynamic field at the intersection of cognitive neuroscience, robotics, engineering, and artificial intelligence—aims to develop autonomous neural systems that can be embodied in robots, enabling them to learn and adapt to changing environments (Park et al., 2020a; Aitsam et al., 2022; Bartolozzi et al., 2022). The intersection of these two fields could lead to robots that utilize bio-inspired control to replicate biological functions such as gait (Still et al., 2006).

Our approach in building neuromodulated central pattern generators (CPGs) could be explored from a bio-inspired control perspective. If applicable, this control could be embedded into robots to create biologically plausible machines that mimic the gait and adaptability of living organisms. This research will likely be pursued in our lab.

20.3.3 Neuromorphic electronics

Neuromorphic electronics mimics the brain structure and function to create systems capable of adapting and processing information in ways similar to biological neural networks. Unlike traditional computing, which relies on binary and sequential processing, neuromorphic electronics replicate parallel, event-driven processing for greater energy efficiency and learning potential (Mead, 1990; Neftci et al., 2013). These devices have applications in AI, robotics, and brain-machine interfaces. Although replicating biological brains in digital computers is challenging due to their analog nature, mathematical models and analog electronic circuits using transistors can

capture key neuronal operations. Such electronic circuits could form the basis for efficient SNN implementation (Chicca et al., 2014).

A significant challenge in this field is the variability introduced by the manufacturing process of semiconductor chips, which can produce transistors with substantial differences (Borkar, 2005). This variability leads to a degenerate neuronal population, making it difficult to tune firing patterns for adaptability. Experiments in this area could provide an ideal framework for electronically validating the neuromodulation controller, thus refining its design. This research will likely be conducted in our lab.

21 Conclusion

Neuromodulation is a crucial process in neuroscience that enables individuals to adapt to changing environments. However, given that neurons exhibit variability yet produce similar electrical activity—a property known as degeneracy—it raises the question of how a single neuromodulator can produce reliable effects across a diverse neuronal population. This thesis employs biophysical neuron models to investigate how neuromodulators achieve reliable adaptability in such degenerate neuronal populations.

References

Abbott, L. F. and Dayan, P. (2001). Theoretical neuroscience. *Comput Math Model Neural*, 60:489–95.

Achard, P. and De Schutter, E. (2006). Complex parameter landscape for a complex neuron model. *PLoS Computational Biology*, 2(7):e94.

Adams, W. (1985). Slow depolarizing and hyperpolarizing currents which mediate bursting in aplysia neurone r15. *The Journal of Physiology*, 360(1):51–68.

Ahn, M., Beacham, D., Westenbroek, R. E., Scheuer, T., and Catterall, W. A. (2007). Regulation of nav1. 2 channels by brain-derived neurotrophic factor, trkb, and associated fyn kinase. *Journal of Neuroscience*, 27(43):11533–11542.

Aitsam, M., Davies, S., and Di Nuovo, A. (2022). Neuromorphic computing for interactive robotics: A systematic review. *IEEE Access*, 10:122261–122279.

Alevizos, A., Weiss, K., and Koester, J. (1991). Synaptic actions of identified peptidergic neuron r15 in aplysia. i. activation of respiratory pumping. *Journal of Neuroscience*, 11(5):1263–1274.

Alon, U. (2007). Network motifs: Theory and experimental approaches. *Nature Reviews Genetics*, 8(6):450–461.

Alonso, L. M. and Marder, E. (2019). Visualization of currents in neural models with similar behavior and different conductance densities. *eLife*, 8:e42722.

Alonso, L. M. and Marder, E. (2020). Temperature compensation in a small rhythmic circuit. *eLife*, 9:e55470.

Amendola, J., Woodhouse, A., Martin-Eauclaire, M.-F., and Goaillard, J.-M. (2012). Ca2+/camp-sensitive covariation of ia and ih voltage dependences tunes rebound firing in dopaminergic neurons. *Journal of Neuroscience*, 32(6):2166–2181.

Anderson, W. W. (1981). *Synaptic mechanisms generating nonspiking network oscillations in the stomatogastric ganglion of the lobster, panulirus interruptus.* PhD thesis, University of Oregon.

Anger, T., Madge, D. J., Mulla, M., and Riddall, D. (2001). Medicinal chemistry of neuronal voltage-gated sodium channel blockers. *Journal of Medicinal Chemistry*, 44(2):115–137.

Annaswamy, A. M. (2023). Adaptive control and intersections with reinforcement learning. *Annual Review of Control, Robotics, and Autonomous Systems*, 6(1):65–93.

Antsaklis, P. J. and Michel, A. N. (1997). *Linear systems*, volume 8. Springer.

Åström, K. J. (1995). Adaptive control. In *Mathematical system theory: The influence of RE Kalman*, pages 437–450. Springer.

Åström, K. J. (2002). Control system design lecture notes for me 155a. *Department of Mechanical and Environmental Engineering University of California Santa Barbara*, 333.

Åström, K. J. and Murray, R. (2021). *Feedback systems: An introduction for scientists and engineers*. Princeton university press.

Audia, P. G. and Locke, E. A. (2003). Benefiting from negative feedback. *Human Resource Management Review*, 13(4):631–646.

Ávila-Åkerberg, O., Krahe, R., and Chacron, M. (2010). Neural heterogeneities and stimulus properties affect burst coding in vivo. *Neuroscience*, 168(1):300–313.

Bacak, B. J., Segaran, J., and Molkov, Y. I. (2016). Modeling the effects of extracellular potassium on bursting properties in pre-bötzinger complex neurons. *Journal of Computational Neuroscience*, 40:231–245.

Baines, R. A., Uhler, J. P., Thompson, A., Sweeney, S. T., and Bate, M. (2001). Altered electrical properties in drosophilaneurons developing without synaptic transmission. *Journal of Neuroscience*, 21(5):1523–1531.

Balchen, J. G., Ljungquist, D., and Strand, S. (1988). Predictive control based upon state space models. In *1988 American Control Conference*, pages 2174–2179. IEEE.

Bargmann, C. I. (2012). Beyond the connectome: How neuromodulators shape neural circuits. *Bioessays*, 34(6):458–465.

Bargmann, C. I. and Marder, E. (2013). From the connectome to brain function. *Nature Methods*, 10(6):483–490.

Barnett, M. and Larkman, P. (2007). The action potential. *Practical Neurology*, 7:192–7.

Barron-Zambrano, J. H., Torres-Huitzil, C., and Girau, B. (2010). Hardware implementation of a cpg-based locomotion control for quadruped robots. In *International Conference on Artificial Neural Networks*, pages 276–285. Springer.

Bartolozzi, C., Indiveri, G., and Donati, E. (2022). Embodied neuromorphic intelligence. *Nature Communications*, 13(1):1024.

Basilio, J. C. and Matos, S. (2002). Design of pi and pid controllers with transient performance specification. *IEEE Transactions on education*, 45(4):364–370.

Bastian, J., Chacron, M. J., and Maler, L. (2002). Receptive field organization determines pyramidal cell stimulus-encoding capability and spatial stimulus selectivity. *Journal of Neuroscience*, 22(11):4577–4590.

Baudot, P. and Bennequin, D. (2015). The homological nature of entropy. *Entropy*, 17(5):3253–3318.

Baudot, P., Tapia, M., Bennequin, D., and Goaillard, J.-M. (2019). Topological information data analysis. *Entropy*, 21(9):869.

Begenisich, T. and Cahalan, M. (1980). Sodium channel permeation in squid axons. i: Reversal potential experiments. *The Journal of Physiology*, 307(1):217–242.

Bernstein, J. J. (1970). Anatomy and physiology of the central nervous system. In Hoar, W. and Randall, D., editors, *The nervous system, circulation, and respiration*, volume 4 of *Fish Physiology*, pages 1–90. Academic Press.

Berridge, C. W. (2008). Noradrenergic modulation of arousal. *Brain Research Reviews*, 58(1):1–17.

Bertram, R., Rhoads, J., and Cimbora, W. P. (2008). A phantom bursting mechanism for episodic bursting. *Bulletin of Mathematical Biology*, 70:1979–1993.

Bezanson, J., Edelman, A., Karpinski, S., and Shah, V. B. (2017). Julia: A fresh approach to numerical computing. *SIAM Review*, 59(1):65–98.

Bisquert, J. (2021). A frequency domain analysis of the excitability and bifurcations of the fitzhugh–nagumo neuron model. *The Journal of Physical Chemistry Letters*, 12(45):11005–11013.

Borkar, S. (2005). Designing reliable systems from unreliable components: The challenges of transistor variability and degradation. *IEEE Micro*, 25(6):10–16.

Borst, J. G. G. and Sakmann, B. (1999). Effect of changes in action potential shape on calcium currents and transmitter release in a calyx-type synapse of the rat auditory brainstem. *Philosophical Transactions of the Royal Society of London. Series B: Biological Sciences*, 354(1381):347–355.

Bradley, C., Nydam, A. S., Dux, P. E., and Mattingley, J. B. (2022). State-dependent effects of neural stimulation on brain function and cognition. *Nature Reviews Neuroscience*, 23(8):459–475.

Brette, R. and Destexhe, A. (2012). Intracellular recording. *Handbook of Neural Activity Measurement*, pages 44–91.

Brzosko, Z., Mierau, S. B., and Paulsen, O. (2019). Neuromodulation of spike-timing-dependent plasticity: Past, present, and future. *Neuron*, 103(4):563–581.

Bucher, D., Johnson, C. D., and Marder, E. (2007). Neuronal morphology and neuropil structure in the stomatogastric ganglion of the lobster, homarus americanus. *Journal of Comparative Neurology*, 501(2):185–205.

Bucher, D. and Marder, E. (2013). Snapshot: Neuromodulation. *Cell*, 155(2):482–482.

Bucher, D., Taylor, A. L., and Marder, E. (2006). Central pattern generating neurons simultaneously express fast and slow rhythmic activities in the stomatogastric ganglion. *Journal of Neurophysiology*, 95(6):3617–3632.

Butkiewicz, B. S. (1998). Steady-state error of a system with fuzzy controller. *IEEE Transactions on Systems, Man, and Cybernetics*, 28(6):855–860.

Buzsáki, G. (2006). *Rhythms of the brain*. Oxford Academic, online edition edition. DOI: https://doi.org/10.1093/acprof:oso/9780195301069.001.0001.

Cabutto, T. A., Heeney, S. P., Ault, S. V., Mao, G., and Wang, J. (2018). An overview of the julia programming language. In *Proceedings of the 2018 International Conference on Computing and Big Data*, pages 87–91.

Calabrese, R. L. (1995). Half-center oscillators underlying rhythmic movements. *Nature*, 261:146–148.

Capogrosso, M., Milekovic, T., Borton, D., Wagner, F., Moraud, E. M., Mignardot, J.-B., Buse, N., Gandar, J., Barraud, Q., Xing, D., et al. (2016). A brain–spine interface alleviating gait deficits after spinal cord injury in primates. *Nature*, 539(7628):284–288.

Carrillo-Medina, J. L. and Latorre, R. (2018). Detection of activation sequences in spiking-bursting neurons by means of the recognition of intraburst neural signatures. *Scientific Reports*, 8(1):16726.

Castaños, F. and Franci, A. (2017). Implementing robust neuromodulation in neuromorphic circuits. *Neurocomputing*, 233:3–13.

Catterall, W. A. (1995). Structure and function of voltage-gated ion channels. *Annual Review of Biochemistry*, 64(1):493–531.

Chadderton, P., Margrie, T. W., and Häusser, M. (2004). Integration of quanta in cerebellar granule cells during sensory processing. *Nature*, 428(6985):856–860.

Chaffey, T. (2022). *Input/output analysis: Graphical and algorithmic methods*. PhD thesis, Cambridge University.

Chaffey, T., Banert, S., Giselsson, P., and Pates, R. (2023a). Circuit analysis using monotone+ skew splitting. *European Journal of Control*, 74:100854.

Chaffey, T., Forni, F., and Sepulchre, R. (2023b). Graphical nonlinear system analysis. *IEEE Transactions on Automatic Control*.

Chaffey, T. and Sepulchre, R. (2023). Monotone one-port circuits. *IEEE Transactions on Automatic Control*.

Chaffey, T., van Waarde, H. J., and Sepulchre, R. (2023c). Relaxation systems and cyclic monotonicity. In *2023 62nd IEEE Conference on Decision and Control (CDC)*, pages 1673–1679. IEEE.

Chaffre, T., Moras, J., Chan-Hon-Tong, A., Marzat, J., Sammut, K., Le Chenadec, G., and Clement, B. (2022). Learning-based vs model-free adaptive control of a mav under wind gust. In *Informatics in Control, Automation and Robotics: 17th International Conference, ICINCO 2020 Lieusaint-Paris, France, July 7–9, 2020, Revised Selected Papers*, pages 362–385. Springer.

Chapin, J. K. (2004). Using multi-neuron population recordings for neural prosthetics. *Nature Neuroscience*, 7(5):452–455.

Chen, Y., Frank, H. Y., Surmeier, D. J., Scheuer, T., and Catterall, W. A. (2006). Neuromodulation of na+ channel slow inactivation via camp-dependent protein kinase and protein kinase c. *Neuron*, 49(3):409–420.

Chevaleyre, V. and Siegelbaum, S. A. (2010). Strong ca2 pyramidal neuron synapses define a powerful disynaptic cortico-hippocampal loop. *Neuron*, 66(4):560–572.

Chicca, E., Stefanini, F., Bartolozzi, C., and Indiveri, G. (2014). Neuromorphic electronic circuits for building autonomous cognitive systems. *Proceedings of the IEEE*, 102(9):1367–1388.

Choquet, D. and Triller, A. (2013). The dynamic synapse. *Neuron*, 80(3):691–703.

Citri, A. and Malenka, R. C. (2008). Synaptic plasticity: Multiple forms, functions, and mechanisms. *Neuropsychopharmacology*, 33(1):18–41.

Cobb, S., Halasy, K., Vida, I., Nyiri, G., Tamás, G., Buhl, E., and Somogyi, P. (1997). Synaptic effects of identified interneurons innervating both interneurons and pyramidal cells in the rat hippocampus. *Neuroscience*, 79(3):629–648.

Coggan, J. S., Ocker, G. K., Sejnowski, T. J., and Prescott, S. A. (2011). Explaining pathological changes in axonal excitability through dynamical analysis of conductance-based models. *Journal of Neural Engineering*, 8(6):065002.

Connor, J. A., Walter, D., and McKowN, R. (1977). Neural repetitive firing: Modifications of the hodgkin-huxley axon suggested by experimental results from crustacean axons. *Biophysical Journal*, 18(1):81–102.

Conradi Smith, G. D. (2019). Regenerative ionic currents and bistability. *W&M ScholarWorks*.

Courbage, M. and Nekorkin, V. I. (2010). Map based models in neurodynamics. *International Journal of Bifurcation and Chaos*, 20(06):1631–1651.

Coyote-Maestas, W., Nedrud, D., He, Y., and Schmidt, D. (2022). Determinants of trafficking, conduction, and disease within a k+ channel revealed through multiparametric deep mutational scanning. *eLife*, 11:e76903.

Crabtree, J. W. (2018). Functional diversity of thalamic reticular subnetworks. *Frontiers in Systems Neuroscience*, 12:41.

Cross, F. R. and Tinkelenberg, A. H. (1991). A potential positive feedback loop controlling cln1 and cln2 gene expression at the start of the yeast cell cycle. *Cell*, 65(5):875–883.

Cunha, R. (2001). Adenosine as a neuromodulator and as a homeostatic regulator in the nervous system: Different roles, different sources and different receptors. *Neurochemistry International*, 38(2):107–125.

Cymbalyuk, G. S. and Calabrese, R. L. (2000). Oscillatory behaviors in pharmacologically isolated heart interneurons from the medicinal leech. *Neurocomputing*, 32:97–104.

da Silva, F. L. (2013). Eeg and meg: Relevance to neuroscience. *Neuron*, 80(5):1112–1128.

Dahan, L., Astier, B., Vautrelle, N., Urbain, N., Kocsis, B., and Chouvet, G. (2007). Prominent burst firing of dopaminergic neurons in the ventral tegmental area during paradoxical sleep. *Neuropsychopharmacology*, 32(6):1232–1241.

Das, A., Chaffey, T., and Sepulchre, R. (2022). Oscillations in mixed-feedback systems. *Systems & Control Letters*, 166:105289.

Davis, G. W. (2006). Homeostatic control of neural activity: From phenomenology to molecular design. *Annual Review of Neuroscience*, 29(1):307–323.

Davis, G. W. (2013). Homeostatic signaling and the stabilization of neural function. *Neuron*, 80(3):718–728.

Davis, G. W. and Bezprozvanny, I. (2001). Maintaining the stability of neural function: A homeostatic hypothesis. *Annual Review of Physiology*, 63(1):847–869.

DeAngelis, D. L., Post, W. M., and Travis, C. C. (2012). *Positive feedback in natural systems*, volume 15. Springer Science & Business Media.

DeFelipe, J. (1999). Chandelier cells and epilepsy. *Brain*, 122(10):1807–1822.

Desai, N. S. (2003). Homeostatic plasticity in the cns: Synaptic and intrinsic forms. *Journal of Physiology*, 97(4-6):391–402.

Desoer, C. and Lin, C.-A. (1985). Tracking and disturbance rejection of mimo nonlinear systems with pi controller. *IEEE Transactions on Automatic Control*, 30(9):861–867.

Desroches, M., Rinzel, J., and Rodrigues, S. (2022). Classification of bursting patterns: A tale of two ducks. *PLoS Computational Biology*, 18(2):e1009752.

Destexhe, A., Contreras, D., and Steriade, M. (1998). Mechanisms underlying the synchronizing action of corticothalamic feedback through inhibition of thalamic relay cells. *Journal of Neurophysiology*, 79(2):999–1016.

Destexhe, A. and Marder, E. (2004). Plasticity in single neuron and circuit computations. *Nature*, 431(7010):789–795.

Dethier, J., Drion, G., Franci, A., and Sepulchre, R. (2015). A positive feedback at the cellular level promotes robustness and modulation at the circuit level. *Journal of Neurophysiology*, 114(4):2472–2484.

DeWitt, C. R. and Waksman, J. C. (2004). Pharmacology, pathophysiology and management of calcium channel blocker and β-blocker toxicity. *Toxicological Reviews*, 23:223–238.

Di Resta, C. and Becchetti, A. (2010). Introduction to ion channels. *Integrins and Ion Channels: Molecular Complexes and Signaling*, pages 9–21.

Dicks, L. M. (2022). Gut bacteria and neurotransmitters. *Microorganisms*, 10(9):1838.

Dipalo, M., Amin, H., Lovato, L., Moia, F., Caprettini, V., Messina, G. C., Tantussi, F., Berdondini, L., and De Angelis, F. (2017). Intracellular and extracellular recording of

spontaneous action potentials in mammalian neurons and cardiac cells with 3d plasmonic nanoelectrodes. *Nano Letters*, 17(6):3932–3939.

Doloc-Mihu, A. and Calabrese, R. L. (2011). A database of computational models of a half-center oscillator for analyzing how neuronal parameters influence network activity. *Journal of Biological Physics*, 37:263–283.

Dora, S. and Kasabov, N. (2021). Spiking neural networks for computational intelligence: An overview. *Big Data and Cognitive Computing*, 5(4):67.

Dossi, E., Blauwblomme, T., Nabbout, R., Huberfeld, G., and Rouach, N. (2014). Multi-electrode array recordings of human epileptic postoperative cortical tissue. *Journal of Visualized Experiments*, 92:e51870.

Drion, G., Franci, A., Dethier, J., and Sepulchre, R. (2015a). Dynamic input conductances shape neuronal spiking. *eNeuro*, 2(1).

Drion, G., Franci, A., and Sepulchre, R. (2019). Cellular switches orchestrate rhythmic circuits. *Biological Cybernetics*, 113:71–82.

Drion, G., Franci, A., Seutin, V., and Sepulchre, R. (2012). A novel phase portrait for neuronal excitability. *PloS one*.

Drion, G., Massotte, L., Sepulchre, R., and Seutin, V. (2011). How modeling can reconcile apparently discrepant experimental results: The case of pacemaking in dopaminergic neurons. *PLoS Computational Biology*, 7(5):e1002050.

Drion, G., O'Leary, T., Dethier, J., Franci, A., and Sepulchre, R. (2015b). Neuronal behaviors: A control perspective. In *2015 54th IEEE Conference on Decision and Control*, pages 1923–1944. IEEE.

Drion, G., O'Leary, T., and Marder, E. (2015c). Ion channel degeneracy enables robust and tunable neuronal firing rates. *Proceedings of the National Academy of Sciences*, 112(38):E5361–E5370.

Driscoll, L. N., Pettit, N. L., Minderer, M., Chettih, S. N., and Harvey, C. D. (2017). Dynamic reorganization of neuronal activity patterns in parietal cortex. *Cell*, 170(5):986–999.

Duff, G. F. D. (1953). Limit-cycles and rotated vector fields. *Annals of Mathematics*, pages 15–31.

Dunlop, J., Bowlby, M., Peri, R., Tawa, G., LaRocque, J., Soloveva, V., and Morin, J. (2008). Ion channel screening. *Combinatorial Chemistry & High Throughput Screening*, 11(7):514–522.

Dutta, S., Parihar, A., Khanna, A., Gomez, J., Chakraborty, W., Jerry, M., Grisafe, B., Raychowdhury, A., and Datta, S. (2019). Programmable coupled oscillators for synchronized locomotion. *Nature Communications*, 10(1):3299.

Duvernoy, H. (2005). Brain anatomy. *Magnetic Resonance in Epilepsy: Neuroimaging Techniques*, pages 29–97.

Edelman, G. M. and Gally, J. A. (2001). Degeneracy and complexity in biological systems. *Proceedings of the National Academy of Sciences*, 98(24):13763–13768.

Eitelberg, E. (1987). A regulating and tracking pi (d) controller. *International Journal of Control*, 45(1):91–95.

Embick, D., Marantz, A., Miyashita, Y., O'Neil, W., and Sakai, K. L. (2000). A syntactic specialization for broca's area. *Proceedings of the National Academy of Sciences*, 97(11):6150–6154.

Engel, A. G. (2008). The neuromuscular junction. *Handbook of Clinical Neurology*, 91:103–148.

Engel, A. G. (2018). Genetic basis and phenotypic features of congenital myasthenic syndromes. In Geschwind, D. H., Paulson, H. L., and Klein, C., editors, *Neurogenetics, Part II*, volume 148 of *Handbook of Clinical Neurology*, pages 565–589. Elsevier.

Enyedi, P. and Czirják, G. (2010). Molecular background of leak k+ currents: Two-pore domain potassium channels. *Physiological Reviews*.

Ergin, B., Saglam, B., Taskiran, E. Z., Bastug, T., and Purali, N. (2022). De novo cloning and functional characterization of potassium channel genes and proteins in the crayfish astacus leptodactylus. *Journal of Crustacean Biology*, 42(1):ruac018.

Ermentrout, B. (1994). Reduction of conductance-based models with slow synapses to neural nets. *Neural Computation*, 6(4):679–695.

Esser, S. K., Hill, S., and Tononi, G. (2009). Breakdown of effective connectivity during slow wave sleep: Investigating the mechanism underlying a cortical gate using large-scale modeling. *Journal of Neurophysiology*, 102(4):2096–2111.

Farmer, T. W., Buchthal, F., and Rosenfalck, P. (1960). Refractory period of human muscle after the passage of a propagated action potential. *Electroencephalography and Clinical Neurophysiology*, 12(2):455–466.

Feldman, D. E. (2012). The spike-timing dependence of plasticity. *Neuron*, 75(4):556–571.

Fenichel, N. (1979). Geometric singular perturbation theory for ordinary differential equations. *Journal of Differential Equations*, 31(1):53–98.

Fernandez Lorden, C. et al. (2023). *Neuromorphic control of embodied central pattern generators*. PhD thesis, Université de Liège, Liège, Belgique.

Fields, C. and Levin, M. (2022). Competency in navigating arbitrary spaces as an invariant for analyzing cognition in diverse embodiments. *Entropy*, 24(6):819.

Filo, M., Chang, C.-H., and Khammash, M. (2023). Biomolecular feedback controllers: From theory to applications. *Current Opinion in Biotechnology*, 79:102882.

Finger, S. (2001). *Origins of neuroscience: A history of explorations into brain function*. Oxford University Press.

Finkbeiner, S. and Greenberg, M. E. (1998). Ca2+ channel-regulated neuronal gene expression. *Journal of Neurobiology*, 37(1):171–189.

Flamm, R. E. and Harris-Warrick, R. M. (1986). Aminergic modulation in lobster stomatogastric ganglion. ii. target neurons of dopamine, octopamine, and serotonin within the pyloric circuit. *Journal of Neurophysiology*, 55(5):866–881.

Franci, A., Drion, G., and Sepulchre, R. (2014). Modeling the modulation of neuronal bursting: A singularity theory approach. *SIAM Journal on Applied Dynamical Systems*, 13(2):798–829.

Franci, A., Drion, G., and Sepulchre, R. (2018). Robust and tunable bursting requires slow positive feedback. *Journal of Neurophysiology*, 119(3):1222–1234.

Franci, A., Drion, G., and Sepulchre, R. (2019). The sensitivity function of excitable feedback systems. In *2019 IEEE 58th Conference on Decision and Control*, pages 4723–4728. IEEE.

Franci, A., Drion, G., Seutin, V., and Sepulchre, R. (2013). A balance equation determines a switch in neuronal excitability. *PLoS Computational Biology*, 9(5):e1003040.

Franci, A., O'Leary, T., and Golowasch, J. (2020). Positive dynamical networks in neuronal regulation: How tunable variability coexists with robustness. *IEEE Control Systems Letters*, 4(4):946–951.

Frei, T., Chang, C.-H., Filo, M., Arampatzis, A., and Khammash, M. (2022). A genetic mammalian proportional–integral feedback control circuit for robust and precise gene regulation. *Proceedings of the National Academy of Sciences*, 119(00):e2122132119.

Fuentealba, P., Klausberger, T., Karayannis, T., Suen, W. Y., Huck, J., Tomioka, R., Rockland, K., Capogna, M., Studer, M., Morales, M., et al. (2010). Expression of coup-tfii nuclear receptor in restricted gabaergic neuronal populations in the adult rat hippocampus. *Journal of Neuroscience*, 30(5):1595–1609.

Fusi, S. and Abbott, L. (2007). Limits on the memory storage capacity of bounded synapses. *Nature Neuroscience*, 10(4):485–493.

Fyon, A. (2024). Dimensionality reduction of neuronal degeneracy reveals two interfering physiological mechanisms, corr_2024. 10.5281/zenodo.10842029.

Fyon, A. and Drion, G. (2021). Apparent neuromodulation-dependent correlation levels in neuron ion channel expression result from a competition between passive and active membrane properties. In *Society for Neuroscience annual meeting 2021*.

Fyon, A. and Drion, G. (2023). Neuromodulation and homeostasis: Complementary mechanisms in ion channel expression adaptation for robust neural function. In *Bernstein Conference 2023*.

Fyon, A. and Drion, G. (2024a). An adaptive controller of reliable neuromodulation on mixed feedback systems. In *43rd Benelux Meeting on Systems and Control*.

Fyon, A. and Drion, G. (2024b). Neuromodulation and homeostasis: Complementary mechanisms for robust neural function. *arXiv preprint arXiv:2412.04172*.

Fyon, A. and Drion, G. (2024c). Neuromodulation robustly tunes rhythmic patterns in a fixed connectome: Application to gait control. In *FENS Forum 2024*.

Fyon, A., Franci, A., Sacré, P., and Drion, G. (2024). Dimensionality reduction of neuronal degeneracy reveals two interfering physiological mechanisms. *PNAS Nexus*, 3(10):pgae415.

Fyon, A., Sacré, P., Franci, A., and Drion, G. (2023). Reliable neuromodulation from adaptive control of ion channel expression. *IFAC-PapersOnLine*, 56(2):458–463.

Gangopadhyay, A., Aono, K., Mehta, D., and Chakrabartty, S. (2018). A coupled network of growth transform neurons for spike-encoded auditory feature extraction. *bioRxiv*, page 303453.

Gautrais, J. and Thorpe, S. (1998). Rate coding versus temporal order coding: A theoretical approach. *Biosystems*, 48(1-3):57–65.

Gazzaniga, M. S. (1989). Organization of the human brain. *Science*, 245(4921):947–952.

Gerstner, W., Kistler, W. M., Naud, R., and Paninski, L. (2014). *Neuronal dynamics: From single neurons to networks and models of cognition*. Cambridge University Press.

Ghosh-Dastidar, S. and Adeli, H. (2009). Spiking neural networks. *International Journal of Neural Systems*, 19(04):295–308.

Gilbert, C. D. (1983). Microcircuitry of the visual cortex. *Annual Review of Neuroscience*, 6(1):217–247.

Gjorgjieva, J., Drion, G., and Marder, E. (2016). Computational implications of biophysical diversity and multiple timescales in neurons and synapses for circuit performance. *Current Opinion in Neurobiology*, 37:44–52.

Goaillard, J.-M. and Dufour, M. A. (2014). The pros and cons of degeneracy. *eLife*, 3:e02615.

Goaillard, J.-M. and Marder, E. (2021). Ion channel degeneracy, variability, and covariation in neuron and circuit resilience. *Annual Review of Neuroscience*, 44:335–357.

Goaillard, J.-M., Taylor, A. L., Schulz, D. J., and Marder, E. (2009). Functional consequences of animal-to-animal variation in circuit parameters. *Nature Neuroscience*, 12(11):1424–1430.

Goldman, M. S., Golowasch, J., Marder, E., and Abbott, L. (2001). Global structure, robustness, and modulation of neuronal models. *Journal of Neuroscience*, 21(14):5229–5238.

Golomb, D. and Rinzel, J. (1994). Clustering in globally coupled inhibitory neurons. *Physica D: Nonlinear Phenomena*, 72(3):259–282.

Golomb, D., Yue, C., and Yaari, Y. (2006). Contribution of persistent na+ current and m-type k+ current to somatic bursting in ca1 pyramidal cells: Combined experimental and modeling study. *Journal of Neurophysiology*, 96(4):1912–1926.

Golub, G. H. and Van Loan, C. F. (2013). *Matrix computations*. JHU press.

Gonçalves, P. J., Lueckmann, J.-M., Deistler, M., Nonnenmacher, M., Öcal, K., Bassetto, G., Chintaluri, C., Podlaski, W. F., Haddad, S. A., Vogels, T. P., et al. (2020). Training deep neural density estimators to identify mechanistic models of neural dynamics. *eLife*, 9:e56261.

González, O. C., Sokolov, Y., Krishnan, G. P., Delanois, J. E., and Bazhenov, M. (2020). Can sleep protect memories from catastrophic forgetting? *eLife*, 9:e51005.

Goodenough, D. and Paul, D. (2009). Gap junctions. *Cold Spring Harb Perspect Biol*, 1(1):a002576.

Grant, A., Starmer, C., and Strauss, H. (1984). Antiarrhythmic drug action. blockade of the inward sodium current. *Circulation Research*, 55(4):427–439.

Grashow, R., Brookings, T., and Marder, E. (2009). Reliable neuromodulation from circuits with variable underlying structure. *Proceedings of the National Academy of Sciences*, 106(28):11742–11746.

Graubard, K., Raper, J. A., and Hartline, D. K. (1983). Graded synaptic transmission between identified spiking neurons. *Journal of Neurophysiology*, 50(2):508–521.

Gray, C. M. and McCormick, D. A. (1996). Chattering cells: Superficial pyramidal neurons contributing to the generation of synchronous oscillations in the visual cortex. *Science*, 274(5284):109–113.

Grienberger, C. and Konnerth, A. (2012). Imaging calcium in neurons. *Neuron*, 73(5):862–885.

Grudt, T. and Perl, E. (2002). Correlations between neuronal morphology and electrophysiological features in the rodent superficial dorsal horn. *The Journal of Physiology*, 540(1):189–207.

Gruhn, M., Guckenheimer, J., Land, B., and Harris-Warrick, R. M. (2005). Dopamine modulation of two delayed rectifier potassium currents in a small neural network. *Journal of Neurophysiology*, 94(4):2888–2900.

Gu, Q. (2002). Neuromodulatory transmitter systems in the cortex and their role in cortical plasticity. *Neuroscience*, 111(4):815–835.

Guertin, P. A. (2009). The mammalian central pattern generator for locomotion. *Brain Research Reviews*, 62(1):45–56.

Guo, W., Fouda, M. E., Eltawil, A. M., and Salama, K. N. (2021). Neural coding in spiking neural networks: A comparative study for robust neuromorphic systems. *Frontiers in Neuroscience*, 15:638474.

Gutierrez, G. J., O'Leary, T., and Marder, E. (2013). Multiple mechanisms switch an electrically coupled, synaptically inhibited neuron between competing rhythmic oscillators. *Neuron*, 77(5):845–858.

Guzman, J. N., Sánchez-Padilla, J., Chan, C. S., and Surmeier, D. J. (2009). Robust pacemaking in substantia nigra dopaminergic neurons. *Journal of Neuroscience*, 29(35):11011–11019.

Haley, J. A., Hampton, D., and Marder, E. (2018). Two central pattern generators from the crab, cancer borealis, respond robustly and differentially to extreme extracellular pH. *eLife*, 7:e41877.

Hall, Z. W. and Sanes, J. R. (1993). Synaptic structure and development: The neuromuscular junction. *Cell*, 72:99–121.

Halnes, G., Augustinaite, S., Heggelund, P., Einevoll, G. T., and Migliore, M. (2011). A multi-compartment model for interneurons in the dorsal lateral geniculate nucleus. *PLoS Computational Biology*, 7(9):e1002160.

Hamam, B. N., Amaral, D. G., and Alonso, A. A. (2002). Morphological and electrophysiological characteristics of layer v neurons of the rat lateral entorhinal cortex. *Journal of Comparative Neurology*, 451(1):45–61.

Hamood, A. W. and Marder, E. (2015). Consequences of acute and long-term removal of neuromodulatory input on the episodic gastric rhythm of the crab cancer borealis. *Journal of Neurophysiology*, 114(3):1677–1692.

Harris-Warrick, R. M., Coniglio, L. M., Barazangi, N., Guckenheimer, J., and Gueron, S. (1995a). Dopamine modulation of transient potassium current evokes phase shifts in a central pattern generator network. *Journal of Neuroscience*, 15(1):342–358.

Harris-Warrick, R. M., Coniglio, L. M., Levini, R. M., Gueron, S., and Guckenheimer, J. (1995b). Dopamine modulation of two subthreshold currents produces phase shifts in activity of an identified motoneuron. *Journal of Neurophysiology*, 74(4):1404–1420.

Harris-Warrick, R. M. and Flamm, R. E. (1987). Multiple mechanisms of bursting in a conditional bursting neuron. *Journal of Neuroscience*, 7(7):2113–2128.

Harris-Warrick, R. M., Johnson, B. R., Peck, J. H., Kloppenburg, P., Ayali, A., and Skarbinski, J. (1998). Distributed effects of dopamine modulation in the crustacean pyloric network. *Annals of the New York Academy of Sciences*, 860(1):155–167.

Heeger, D. J. and Ress, D. (2002). What does fmri tell us about neuronal activity? *Nature Reviews Neuroscience*, 3(2):142–151.

Heiss, W.-D. (2009). The potential of pet/mr for brain imaging. *European Journal of Nuclear Medicine and Molecular Imaging*, 36:105–112.

Herculano-Houzel, S. (2009). The human brain in numbers: A linearly scaled-up primate brain. *Frontiers in Human Neuroscience*, page 31.

Herting, M. M. and Chu, X. (2017). Exercise, cognition, and the adolescent brain. *Birth Defects Research*, 109(20):1672–1679.

Heuschkel, M. O., Fejtl, M., Raggenbass, M., Bertrand, D., and Renaud, P. (2002). A three-dimensional multi-electrode array for multi-site stimulation and recording in acute brain slices. *Journal of Neuroscience Methods*, 114(2):135–148.

Hill, C. L. and Stephens, G. J. (2021). An introduction to patch clamp recording. *Methods in Molecular Biology*, 2188:1–19.

Hille, B. (2008). Ion channels. *Scholarpedia*, 3(10):6051. Revision #91389.

Hille, B. and Catterall, W. A. (2012). Electrical excitability and ion channels. In *Basic neurochemistry*, pages 63–80. Elsevier.

Hirano, T. (2018). Purkinje neurons: Development, morphology, and function. *The Cerebellum*, 17(6):699–700.

Hobson, J. A. (2005). Sleep is of the brain, by the brain and for the brain. *Nature*, 437(7063):1254–1256.

Hodgkin, A. L. (1948). The local electric changes associated with repetitive action in a non-medullated axon. *The Journal of Physiology*, 107(2):165.

Hodgkin, A. L. and Huxley, A. F. (1952a). The components of membrane conductance in the giant axon of loligo. *The Journal of Physiology*, 116(4):473.

Hodgkin, A. L. and Huxley, A. F. (1952b). A quantitative description of membrane current and its application to conduction and excitation in nerve. *The Journal of Physiology*, 117(4):500.

Hodgkin, A. L. and Katz, B. (1949). The effect of sodium ions on the electrical activity of the giant axon of the squid. *The Journal of Physiology*, 108(1):37.

Hodgkin, A. L. and Keynes, R. (1955). The potassium permeability of a giant nerve fibre. *The Journal of Physiology*, 128(1):61.

Hökfelt, T., Björklund, A., and Bloom, F. E. (1998). *The primate nervous system, part II*. Elsevier.

Hooper, S. L. and Marder, E. (1984). Modulation of a central pattern generator by two neuropeptides, proctolin and fmrfamide. *Brain Research*, 305(1):186–191.

Hooper, S. L. and Marder, E. (1987). Modulation of the lobster pyloric rhythm by the peptide proctolin. *Journal of Neuroscience*, 7(7):2097–2112.

Hopkins, M. J. (2004). Anatomy of the brain. https://www.hopkinsmedicine.org/health/conditions-and-diseases/anatomy-of-the-brain. Accessed 2024.

Hossain, A., Islam, M. S., Ullah, H., and Ullah, M. A. (2014). Analysis of membrane potential and ion concentration of axon cell. In *2014 International Conference on Informatics, Electronics & Vision (ICIEV)*, pages 1–6. IEEE.

Hudson, A. E. and Prinz, A. A. (2010). Conductance ratios and cellular identity. *PLoS Computational Biology*, 6(7):e1000838.

Hunter, P., Robbins, P., and Noble, D. (2002). The iups human physiome project. *Pflügers Archiv*, 445:1–9.

Huxley, S. A. (2000). Sir alan lloyd hodgkin, om, kbe 5 february 1914—20 december 1998: Elected frs 1948.

Iacobas, D. A., Iacobas, S., Lee, P. R., Cohen, J. E., and Fields, R. D. (2019). Coordinated activity of transcriptional networks responding to the pattern of action potential firing in neurons. *Genes*, 10(10):754.

Imbrici, P., Nicolotti, O., Leonetti, F., Conte, D., and Liantonio, A. (2018). Ion channels in drug discovery and safety pharmacology. *Computational Toxicology: Methods and Protocols*, pages 313–326.

Izhikevich, E. M. (2000). Neural excitability, spiking and bursting. *International Journal of Bifurcation and Chaos*, 10(06):1171–1266.

Izhikevich, E. M. (2001). Resonate-and-fire neurons. *Neural Networks*, 14(6-7):883–894.

Izhikevich, E. M. (2006). Bursting. *Scholarpedia*, 1(3):1300.

Izhikevich, E. M. (2007). *Dynamical systems in neuroscience*. MIT press.

Izhikevich, E. M. and Hoppensteadt, F. (2004). Classification of bursting mappings. *International Journal of Bifurcation and Chaos*, 14(11):3847–3854.

Jacquerie, K. (2023). *Modeling brain-state dependent memory consolidation*. PhD thesis, ULiège-Université de Liège [Applied Sciences], Liege, Belgium.

Jacquerie, K. and Drion, G. (2021). Robust switches in thalamic network activity require a timescale separation between sodium and t-type calcium channel activations. *PLoS Computational Biology*, 17(5):e1008997.

Jaeger, D. and Bower, J. M. (1999). Synaptic control of spiking in cerebellar purkinje cells: Dynamic current clamp based on model conductances. *Journal of Neuroscience*, 19(14):6090–6101.

James, Z. M., Borst, A. J., Haitin, Y., Frenz, B., DiMaio, F., Zagotta, W. N., and Veesler, D. (2017). Cryoem structure of a prokaryotic cyclic nucleotide-gated ion channel. *Proceedings of the National Academy of Sciences*, 114(17):4430–4435.

Jaquier, A., Tuncel, A., Van Geit, W., Alonso, L. M., and Marder, E. (2023). Currentscape (1.0.12). Zenodo.

Jawabri, K. and Sharma, S. (2023). Physiology, cerebral cortex functions. *StatPearls [Internet]*. [Updated 2023 Apr 24]. Available from: https://www.ncbi.nlm.nih.gov/books/NBK538496/.

Jayakar, S., Shim, J., Jo, S., Bean, B. P., Singeç, I., and Woolf, C. J. (2021). Developing nociceptor-selective treatments for acute and chronic pain. *Science Translational Medicine*, 13(619):eabj9837.

Jehasse, K., Massotte, L., Hartmann, S., Vitello, R., Ringlet, S., Vitello, M., Chua, H. C., Pless, S. A., Engel, D., Liégeois, J.-F., et al. (2021). The gating pore blocker 1-(2, 4-xylyl) guanidinium selectively inhibits pacemaking of midbrain dopaminergic neurons. *Neuropharmacology*, 197:108722.

Jenerick, H. (1963). Phase plane trajectories of the muscle spike potential. *Biophysical Journal*, 3(5):363–377.

Jessen, K. R. (2004). Glial cells. *The International Journal of Biochemistry & Cell Biology*, 36(10):1861–1867.

Jian, Z., Xing, J., Yang, G., and Hu, S. (2004). A novel bursting mechanism of type a neurons in injured dorsal root ganglia. *Neurosignals*, 13(3):150–156.

Johnson, M. G. and Chartier, S. (2017). Spike neural models, part i: The hodgkin-huxley model. *The Quantitative Methods for Psychology*, 13(2):105–19.

Johnston, J. (2021). Pharmacology of a-type k+ channels. In *Pharmacology of Potassium Channels*, pages 167–183. Springer.

Jones, S. W. (1989). On the resting potential of isolated frog sympathetic neurons. *Neuron*, 3(2):153–161.

Juarez-Alvarez, O. and Franci, A. (2023). Circadian rhythmogenesis from neuromodulator-and molecular clock-mediated network mixed feedback. *IFAC-PapersOnLine*, 56(2):482–487.

Katori, Y., Lang, E. J., Onizuka, M., Kawato, M., and Aihara, K. (2010). Quantitative modeling of spatio-temporal dynamics of inferior olive neurons with a simple conductance-based model. *International Journal of Bifurcation and Chaos*, 20(03):583–603.

Kawaguchi, Y. (1995). Physiological subgroups of nonpyramidal cells with specific morphological characteristics in layer ii/iii of rat frontal cortex. *Journal of Neuroscience*, 15(4):2638–2655.

Keck, T., Toyoizumi, T., Chen, L., Doiron, B., Feldman, D. E., Fox, K., Gerstner, W., Haydon, P. G., Hübener, M., Lee, H.-K., et al. (2017). Integrating hebbian and homeostatic plasticity: The current state of the field and future research directions. *Philosophical Transactions of the Royal Society: Biological Sciences*, 372(1715):20160158.

Kepler, T. B., Abbott, L., and Marder, E. (1992). Reduction of conductance-based neuron models. *Biological Cybernetics*, 66(5):381–387.

Khooban, M. H., Naghash-Almasi, O., Niknam, T., and Sha-Sadeghi, M. (2016). Intelligent robust pi adaptive control strategy for speed control of ev(s). *IET Science, Measurement & Technology*, 10(5):433–441.

Khorkova, O. and Golowasch, J. (2007). Neuromodulators, not activity, control coordinated expression of ionic currents. *Journal of Neuroscience*, 27(32):8709–8718.

Kim, J., Kim, Y., Nakajima, R., Shin, A., Jeong, M., Park, A. H., Jeong, Y., Jo, S., Yang, S., Park, H., et al. (2017). Inhibitory basal ganglia inputs induce excitatory motor signals in the thalamus. *Neuron*, 95(5):1181–1196.

Kirchhoff, S. (1845). Ueber den durchgang eines elektrischen stromes durch eine ebene, insbesondere durch eine kreisförmige. *Annalen der Physik*, 140(4):497–514.

Kleppinger, S. (2021). *Comparison of traditional optimal control methodologies to reinforcement learning agents in quadcopter attitude control applications*. PhD thesis, University of Illinois, Urbana-Champaign.

Kloppenburg, P., Levini, R. M., and Harris-Warrick, R. M. (1999). Dopamine modulates two potassium currents and inhibits the intrinsic firing properties of an identified motor neuron in a central pattern generator network. *Journal of Neurophysiology*, 81(1):29–38.

Knospe, C. (2006). Pid control. *IEEE Control Systems Magazine*, 26(1):30–31.

Kodama, T., Gittis, A. H., Shin, M., Kelleher, K., Kolkman, K. E., McElvain, L., Lam, M., and Du Lac, S. (2020). Graded coexpression of ion channel, neurofilament, and synaptic genes in fast-spiking vestibular nucleus neurons. *Journal of Neuroscience*, 40(3):496–508.

Kole, M. H., Ilschner, S. U., Kampa, B. M., Williams, S. R., Ruben, P. C., and Stuart, G. J. (2008). Action potential generation requires a high sodium channel density in the axon initial segment. *Nature Neuroscience*, 11(2):178–186.

Komendantov, A. O., Venkadesh, S., Rees, C. L., Wheeler, D. W., Hamilton, D. J., and Ascoli, G. A. (2019). Quantitative firing pattern phenotyping of hippocampal neuron types. *Scientific Reports*, 9(1):17915.

Krahe, R. and Gabbiani, F. (2004). Burst firing in sensory systems. *Nature Reviews Neuroscience*, 5(1):13–23.

Kramer, R. H. and Levitan, I. B. (1990). Activity-dependent neuromodulation in aplysia neuron r15: Intracellular calcium antagonizes neurotransmitter responses mediated by camp. *Journal of Neurophysiology*, 63(5):1075–1088.

Krebs, J. (1998). The role of calcium in apoptosis. *Biometals*, 11:375–382.

Krishnamurthy, V. and Chung, S.-H. (2003). Adaptive learning algorithms for nernst potential and iv curves in nerve cell membrane ion channels modeled as hidden markov models. *IEEE Transactions on Nanobioscience*, 2(4):266–278.

Krishnan, G. P., Chauvette, S., Shamie, I., Soltani, S., Timofeev, I., Cash, S. S., Halgren, E., and Bazhenov, M. (2016). Cellular and neurochemical basis of sleep stages in the thalamocortical network. *eLife*, 5:e18607.

LeMasson, G., Marder, E., and Abbott, L. (1993). Activity-dependent regulation of conductances in model neurons. *Science*, 259(5103):1915–1917.

Lempka, S. F., Johnson, M. D., Moffitt, M. A., Otto, K. J., Kipke, D. R., and McIntyre, C. C. (2011). Theoretical analysis of intracortical microelectrode recordings. *Journal of Neural Engineering*, 8(4):045006.

Levin, M. (2021). Bioelectric signaling: Reprogrammable circuits underlying embryogenesis, regeneration, and cancer. *Cell*, 184(8):1971–1989.

Liss, B., Franz, O., Sewing, S., Bruns, R., Neuhoff, H., and Roeper, J. (2001). Tuning pacemaker frequency of individual dopaminergic neurons by Kv4.3L and KChip3.1 transcription. *The EMBO Journal*, 20(20):5715–5724.

Liu, C., Wang, J., Li, H., Xue, Z., Deng, B., and Wei, X. (2014). Model-based iterative learning control of parkinsonian state in thalamic relay neuron. *Communications in Nonlinear Science and Numerical Simulation*, 19(9):3255–3266.

Liu, S., Liu, Q., Tabuchi, M., and Wu, M. N. (2016). Sleep drive is encoded by neural plastic changes in a dedicated circuit. *Cell*, 165(6):1347–1360.

Liu, Y., Tao, G., and Joshi, S. M. (2010). Modeling and model reference adaptive control of aircraft with asymmetric damage. *Journal of Guidance, Control, and Dynamics*, 33(5):1500–1517.

Liu, Z., Golowasch, J., Marder, E., and Abbott, L. (1998). A model neuron with activity-dependent conductances regulated by multiple calcium sensors. *Journal of Neuroscience*, 18(7):2309–2320.

Lu, Y., Xin, X., and Rinzel, J. (2023). Bistability at the onset of neuronal oscillations. *Biological Cybernetics*, 117(1):61–79.

Lubke, J., Frotscher, M., and Spruston, N. (1998). Specialized electrophysiological properties of anatomically identified neurons in the hilar region of the rat fascia dentata. *Journal of Neurophysiology*, 79(3):1518–1534.

Magee, J. C. and Grienberger, C. (2020). Synaptic plasticity forms and functions. *Annual Review of Neuroscience*, 43:95–117.

Mairet, F. (2018). A biomolecular proportional integral controller based on feedback regulations of protein level and activity. *Royal Society Open Science*, 5(2):171966.

Manninen, T., Hituri, K., Kotaleski, J. H., Blackwell, K. T., and Linne, M.-L. (2010). Postsynaptic signal transduction models for long-term potentiation and depression. *Frontiers in Computational Neuroscience*, 4:152.

Marcus, D. J. and Bruchas, M. R. (2023). Optical approaches for investigating neuromodulation and g protein–coupled receptor signaling. *Pharmacological Reviews*, 75(6):1119–1139.

Marder, E. (2003). Plateau properties in pain pathways. *Nature Neuroscience*, 6(3):210–212.

Marder, E. (2011). Variability, compensation, and modulation in neurons and circuits. *Proceedings of the National Academy of Sciences*, 108(supplement_3):15542–15548.

Marder, E. (2012). Neuromodulation of neuronal circuits: Back to the future. *Neuron*, 76(1):1–11.

Marder, E. and Bucher, D. (2001). Central pattern generators and the control of rhythmic movements. *Current Biology*, 11(23):R986–R996.

Marder, E. and Bucher, D. (2005). Robustness in neuronal systems: The balance between homeostasis, plasticity, and modulation. In *Robust design: A repertoire of biological, ecological and engineering case studies*. Oxford University Press Oxford.

Marder, E. and Bucher, D. (2007). Understanding circuit dynamics using the stomatogastric nervous system of lobsters and crabs. *Annual Review of Physiology*, 69:291–316.

Marder, E. and Calabrese, R. L. (1996). Principles of rhythmic motor pattern generation. *Physiological Reviews*, 76(3):687–717.

Marder, E. and Eisen, J. S. (1984). Electrically coupled pacemaker neurons respond differently to same physiological inputs and neurotransmitters. *Journal of Neurophysiology*, 51(6):1362–1374.

Marder, E. and Goaillard, J.-M. (2006). Variability, compensation and homeostasis in neuron and network function. *Nature Reviews Neuroscience*, 7(7):563–574.

Marder, E., O'Leary, T., and Shruti, S. (2014). Neuromodulation of circuits with variable parameters: Single neurons and small circuits reveal principles of state-dependent and robust neuromodulation. *Annual Review of Neuroscience*, 37:329–346.

Marder, E. and Paupardin-Tritsch, D. (1978). The pharmacological properties of some crustacean neuronal acetylcholine, gamma-aminobutyric acid, and l-glutamate responses. *The Journal of Physiology*, 280(1):213–236.

Marder, E. and Prinz, A. A. (2002). Modeling stability in neuron and network function: The role of activity in homeostasis. *Bioessays*, 24(12):1145–1154.

Marder, E. and Weimann, J. M. (1992). Modulatory control of multiple task processing in the stomatogastric nervous system. In *Neurobiology of Motor Programme Selection*, pages 3–19. Elsevier.

Markram, H., Muller, E., Ramaswamy, S., Reimann, M. W., Abdellah, M., Sanchez, C. A., Ailamaki, A., Alonso-Nanclares, L., Antille, N., Arsever, S., et al. (2015). Reconstruction and simulation of neocortical microcircuitry. *Cell*, 163(2):456–492.

Markram, H., Toledo-Rodriguez, M., Wang, Y., Gupta, A., Silberberg, G., and Wu, C. (2004). Interneurons of the neocortical inhibitory system. *Nature Reviews Neuroscience*, 5(10):793–807.

Marom, S. and Marder, E. (2023). A biophysical perspective on the resilience of neuronal excitability across timescales. *Nature Reviews Neuroscience*, 24(10):640–652.

Mathieson, W. B. and Maler, L. (1988). Morphological and electrophysiological properties of a novel in vitro preparation: The electrosensory lateral line lobe brain slice. *Journal of Comparative Physiology*, 163:489–506.

Matlab, S. (2012). Matlab. *The MathWorks, Natick, MA*, 9.

Maynard, D. and Dando, M. (1974). The structure of the stomatogastric neuromuscular system in callinectes sapidus, homarus americanus and panulirus argus (decapoda crustacea). *Philosophical Transactions of the Royal Society of London, Biological Sciences*, 268(892):161–220.

McCormick, D. A. and Bal, T. (1997). Sleep and arousal: Thalamocortical mechanisms. *Annual Review of Neuroscience*, 20(1):185–215.

McCormick, D. A., Nestvogel, D. B., and He, B. J. (2020). Neuromodulation of brain state and behavior. *Annual Review of Neuroscience*, 43:391–415.

Mead, C. (1990). Neuromorphic electronic systems. *Proceedings of the IEEE*, 78(10):1629–1636.

Megwa, O. F., Pascual, L. M., Günay, C., Pulver, S. R., and Prinz, A. A. (2023). Temporal dynamics of na/k pump mediated memory traces: Insights from conductance-based models of drosophila neurons. *Frontiers in Neuroscience*, 17:1154549.

Mendolia, L., Franci, A., and Redouté, J.-M. (2023). Networks of low-power cmos neuromorphic neurons with robust neuromodulation capabilities for intelligent and adaptable neuromorphic systems. In *SCIoI & ISAB Summer School 2023:"Embodied Intelligence–Perception and Learning in Nature and Robotics"*.

Mercer, A., Botcher, N. A., Eastlake, K., and Thomson, A. M. (2012). Sp–sr interneurones: A novel class of neurones of the ca2 region of the hippocampus. *Hippocampus*, 22(8):1758–1769.

Mermelstein, P. G., Bito, H., Deisseroth, K., and Tsien, R. W. (2000). Critical dependence of camp response element-binding protein phosphorylation on l-type calcium channels supports a selective response to epsps in preference to action potentials. *Journal of Neuroscience*, 20(1):266–273.

Meyrand, P., Simmers, J., and Moulins, M. (1994). Dynamic construction of a neural network from multiple pattern generators in the lobster stomatogastric nervous system. *Journal of Neuroscience*, 14(2):630–644.

Mihalas, A. B., Araki, Y., Huganir, R. L., and Meffert, M. K. (2013). Opposing action of nuclear factor κb and polo-like kinases determines a homeostatic end point for excitatory synaptic adaptation. *Journal of Neuroscience*, 33(42):16490–16501.

Minniti, M. V., Grandia, R., Fäh, K., Farshidian, F., and Hutter, M. (2021). Model predictive robot-environment interaction control for mobile manipulation tasks. In *2021 IEEE International Conference on Robotics and Automation (ICRA)*, pages 1651–1657. IEEE.

Mitrophanov, A. Y. and Groisman, E. A. (2008). Positive feedback in cellular control systems. *Bioessays*, 30(6):542–555.

Mitterdorfer, J. and Bean, B. P. (2002). Potassium currents during the action potential of hippocampal ca3 neurons. *Journal of Neuroscience*, 22(23):10106–10115.

Mohammad-Zadeh, L., Moses, L., and Gwaltney-Brant, S. (2008). Serotonin: A review. *Journal of Veterinary Pharmacology and Therapeutics*, 31(3):187–199.

Morrison, A., Diesmann, M., and Gerstner, W. (2008). Phenomenological models of synaptic plasticity based on spike timing. *Biological Cybernetics*, 98:459–478.

Mukunda, C. L. and Narayanan, R. (2017). Degeneracy in the regulation of short-term plasticity and synaptic filtering by presynaptic mechanisms. *The Journal of Physiology*, 595(8):2611–2637.

Müller, H. and Villegas, N. (2013). Runtime evolution of highly dynamic software. In *Evolving Software Systems*, pages 229–264. Springer.

Muzur, A., Pace-Schott, E. F., and Hobson, J. A. (2002). The prefrontal cortex in sleep. *Trends in Cognitive Sciences*, 6(11):475–481.

Nadim, F. and Bucher, D. (2014). Neuromodulation of neurons and synapses. *Current Opinion in Neurobiology*, 29:48–56.

Nadim, F., Manor, Y., Nusbaum, M. P., and Marder, E. (1998). Frequency regulation of a slow rhythm by a fast periodic input. *Journal of Neuroscience*, 18(13):5053–5067.

Nagel, S. (2019). *Towards a home-use BCI: Fast asynchronous control and robust non-control state detection*. PhD thesis, Universität Tübingen.

Narahashi, T. (2001). Pharmacology of tetrodotoxin. *Journal of Toxicology: Toxin Reviews*, 20(1):67–84.

Nassim, C. (2018). *Lessons from the lobster: Eve Marder's work in neuroscience*. MIT press.

Nataraj, K., Le Roux, N., Nahmani, M., Lefort, S., and Turrigiano, G. (2010). Visual deprivation suppresses l5 pyramidal neuron excitability by preventing the induction of intrinsic plasticity. *Neuron*, 68(4):750–762.

Neftci, E., Binas, J., Rutishauser, U., Chicca, E., Indiveri, G., and Douglas, R. J. (2013). Synthesizing cognition in neuromorphic electronic systems. *Proceedings of the National Academy of Sciences*, 110(37):E3468–E3476.

Neher, E. and Sakmann, B. (1992). The patch clamp technique. *Scientific American*, 266(3):44–51.

Nelson, M. and Rinzel, J. (1995). The hodgkin-huxley model. *The Book of Genesis*, 2.

Nguyen, N., Krishnakumar, K., Kaneshige, J., and Nespeca, P. (2008). Flight dynamics and hybrid adaptive control of damaged aircraft. *Journal of Guidance, Control, and Dynamics*, 31(3):751–764.

Nomura, H., Shimizume, R., and Ikegaya, Y. (2021). Histamine: A key neuromodulator of memory consolidation and retrieval. *The Functional Roles of Histamine Receptors*, pages 329–353.

Noudoost, B. and Moore, T. (2011). Control of visual cortical signals by prefrontal dopamine. *Nature*, 474(7351):372–375.

Nusbaum, M. P. and Marder, E. (1988). A neuronal role for a crustacean red pigment concentrating hormone-like peptide: Neuromodulation of the pyloric rhythm in the crab, cancer borealis. *Journal of Experimental Biology*, 135(1):165–181.

O'Leary, T., Williams, A. H., Caplan, J. S., and Marder, E. (2013). Correlations in ion channel expression emerge from homeostatic tuning rules. *Proceedings of the National Academy of Sciences*, 110(28):E2645–E2654.

Olshausen, B. A. and Field, D. J. (2005). How close are we to understanding v1? *Neural Computation*, 17(8):1665–1699.

Onasch, S. and Gjorgjieva, J. (2020). Circuit stability to perturbations reveals hidden variability in the balance of intrinsic and synaptic conductances. *Journal of Neuroscience*, 40(16):3186–3202.

Orrenius, S., Zhivotovsky, B., and Nicotera, P. (2003). Regulation of cell death: The calcium–apoptosis link. *Nature Reviews Molecular Cell Biology*, 4(7):552–565.

Otsuka, T., Abe, T., Tsukagawa, T., and Song, W.-J. (2004). Conductance-based model of the voltage-dependent generation of a plateau potential in subthalamic neurons. *Journal of Neurophysiology*, 92(1):255–264.

O'Leary, T. (2018). Homeostasis, failure of homeostasis and degenerate ion channel regulation. *Current Opinion in Physiology*, 2:129–138.

O'Leary, T., van Rossum, M. C., and Wyllie, D. J. (2010). Homeostasis of intrinsic excitability in hippocampal neurones: Dynamics and mechanism of the response to chronic depolarization. *The Journal of Physiology*, 588(1):157–170.

O'Leary, T., Williams, A. H., Franci, A., and Marder, E. (2014). Cell types, network homeostasis, and pathological compensation from a biologically plausible ion channel expression model. *Neuron*, 82(4):809–821.

O'Leary, T. and Wyllie, D. J. (2011). Neuronal homeostasis: Time for a change? *The Journal of Physiology*, 589(20):4811–4826.

Park, H.-L., Lee, Y., Kim, N., Seo, D.-G., Go, G.-T., and Lee, T.-W. (2020a). Flexible neuromorphic electronics for computing, soft robotics, and neuroprosthetics. *Advanced Materials*, 32(15):1903558.

Park, S., Kim, S., Na, B., and Yoon, S. (2020b). T2fsnn: Deep spiking neural networks with time-to-first-spike coding. In *2020 57th ACM/IEEE Design Automation Conference (DAC)*, pages 1–6. IEEE.

Paul, M. and Limaiem, F. (2022). Histology, purkinje cells. *StatPearls [Internet]*. [Updated 2022 Nov 14]. Available from: https://www.ncbi.nlm.nih.gov/books/NBK545154/.

Pawelzik, H., Hughes, D. I., and Thomson, A. M. (2002). Physiological and morphological diversity of immunocytochemically defined parvalbumin-and cholecystokinin-positive interneurones in ca1 of the adult rat hippocampus. *Journal of Comparative Neurology*, 443(4):346–367.

Pfeiffer-Linn, C. L. and Lasater, E. M. (1998). Multiple second-messenger system modulation of voltage-activated calcium currents in teleost retinal horizontal cells. *Journal of Neurophysiology*, 80(1):377–388.

Picciotto, M. R., Higley, M. J., and Mineur, Y. S. (2012). Acetylcholine as a neuromodulator: Cholinergic signaling shapes nervous system function and behavior. *Neuron*, 76(1):116–129.

Pierri, J. N., Chaudry, A. S., Woo, T.-U. W., and Lewis, D. A. (1999). Alterations in chandelier neuron axon terminals in the prefrontal cortex of schizophrenic subjects. *American Journal of Psychiatry*, 156(11):1709–1719.

Pintelon, R., Guillaume, P., Rolain, Y., Schoukens, J., and Van Hamme, H. (1994). Parametric identification of transfer functions in the frequency domain-a survey. *IEEE Transactions on Automatic Control*, 39(11):2245–2260.

Plant, R. and Kim, M. (1976). Mathematical description of a bursting pacemaker neuron by a modification of the hodgkin-huxley equations. *Biophysical Journal*, 16(3):227–244.

Plant, R. E. (1981). Bifurcation and resonance in a model for bursting nerve cells. *Journal of Mathematical Biology*, 11:15–32.

Podda, M. V. and Grassi, C. (2014). New perspectives in cyclic nucleotide-mediated functions in the cns: The emerging role of cyclic nucleotide-gated (cng) channels. *Pflügers Archiv-European Journal of Physiology*, 466:1241–1257.

Poirazi, P. and Papoutsi, A. (2020). Illuminating dendritic function with computational models. *Nature Reviews Neuroscience*, 21(6):303–321.

Pop, M. G., Crivii, C., and Opincariu, I. (2018). Anatomy and function of the hypothalamus. In *Hypothalamus in health and diseases*. IntechOpen.

Pratt, K. G. and Aizenman, C. D. (2007). Homeostatic regulation of intrinsic excitability and synaptic transmission in a developing visual circuit. *Journal of Neuroscience*, 27(31):8268–8277.

Prescott, S. A. (2014). Excitability: Types i, ii, and iii.

Prinz, A. A. (2017). Degeneracy rules! *The Journal of Physiology*, 595(8):2409.

Prinz, A. A., Bucher, D., and Marder, E. (2004). Similar network activity from disparate circuit parameters. *Nature Neuroscience*, 7(12):1345–1352.

Qaswal, A. B. (2020). Quantum electrochemical equilibrium: Quantum version of the goldman–hodgkin–katz equation. *Quantum Reports*, 2(2):266–277.

Qi, Y., Watts, A., Kim, J.-W., and Robinson, P. A. (2013). Firing patterns in a conductance-based neuron model: Bifurcation, phase diagram, and chaos. *Biological Cybernetics*, 107:15–24.

Qian, K., Yu, N., Tucker, K. R., Levitan, E. S., and Canavier, C. C. (2014). Mathematical analysis of depolarization block mediated by slow inactivation of fast sodium channels in midbrain dopamine neurons. *Journal of Neurophysiology*, 112(11):2779–2790.

Rabinovich, M., Huerta, R., and Laurent, G. (2008). Transient dynamics for neural processing. *Science*, 321(5885):48–50.

Rall, W., Burke, R. E., Holmes, W. R., Jack, J. J., Redman, S. J., and Segev, I. (1992). Matching dendritic neuron models to experimental data. *Physiological Reviews*, 72(suppl_4):S159–S186.

Ramirez, J.-M. (2011). The human pre-bötzinger complex identified. *Brain*, 134(1):8–10.

Raper, J. A. (1979). Nonimpulse-mediated synaptic transmission during the generation of a cyclic motor program. *Science*, 205(4403):304–306.

Rasmussen, R., Jensen, M. H., and Heltberg, M. L. (2017). Chaotic dynamics mediate brain state transitions, driven by changes in extracellular ion concentrations. *Cell Systems*, 5(6):591–603.

Rathour, R. K. and Narayanan, R. (2019). Degeneracy in hippocampal physiology and plasticity. *Hippocampus*, 29(10):980–1022.

Ratliff, J., Franci, A., Marder, E., and O'Leary, T. (2021). Neuronal oscillator robustness to multiple global perturbations. *Biophysical Journal*, 120(8):1454–1468.

Raymond, J. L., Baxter, D. A., Buonomano, D. V., and Byrne, J. H. (1992). A learning rule based on empirically-derived activity-dependent neuromodulation supports operant conditioning in a small network. *Neural Networks*, 5(5):789–803.

Ribar, L. and Sepulchre, R. (2019). Neuromodulation of neuromorphic circuits. *IEEE Transactions on Circuits and Systems I: Regular Papers*, 66(8):3028–3040.

Ribar, L. and Sepulchre, R. (2021). Neuromorphic control: Designing multiscale mixed-feedback systems. *IEEE Control Systems Magazine*, 41(6):34–63.

Richardson, M. J. (2004). Effects of synaptic conductance on the voltage distribution and firing rate of spiking neurons. *Physical Review E*, 69(5):051918.

Rinberg, A., Taylor, A. L., and Marder, E. (2013). The effects of temperature on the stability of a neuronal oscillator. *PLoS Computational Biology*, 9(1):e1002857.

Robinson, D. A. (1989). Integrating with neurons. *Annual Review of Neuroscience*, 12(1):33–45.

Roy, S. B., Bhasin, S., and Kar, I. N. (2017). Combined mrac for unknown mimo lti systems with parameter convergence. *IEEE Transactions on Automatic Control*, 63(1):283–290.

Rucci, M., Ahissar, E., and Burr, D. (2018). Temporal coding of visual space. *Trends in Cognitive Sciences*, 22(10):883–895.

Sancataldo, G., Silvestri, L., Mascaro, A. L. A., Sacconi, L., and Pavone, F. S. (2019). Advanced fluorescence microscopy for in vivo imaging of neuronal activity. *Optica*, 6(6):758–765.

Santi, C. M., Ferreira, G., Yang, B., Gazula, V.-R., Butler, A., Wei, A., Kaczmarek, L. K., and Salkoff, L. (2006). Opposite regulation of slick and slack k+ channels by neuromodulators. *Journal of Neuroscience*, 26(19):5059–5068.

Santin, J. M. and Schulz, D. J. (2019). Membrane voltage is a direct feedback signal that influences correlated ion channel expression in neurons. *Current Biology*, 29(10):1683–1688.

Sarma, G. P., Lee, C. W., Portegys, T., Ghayoomie, V., Jacobs, T., Alicea, B., Cantarelli, M., Currie, M., Gerkin, R. C., Gingell, S., et al. (2018). Openworm: Overview and recent advances in integrative biological simulation of caenorhabditis elegans. *Philosophical Transactions of the Royal Society*, 373(1758):20170382.

Savic, N., Pedarzani, P., and Sciancalepore, M. (2001). Medium afterhyperpolarization and firing pattern modulation in interneurons of stratum radiatum in the ca3 hippocampal region. *Journal of Neurophysiology*, 85(5):1986–1997.

Scharfman, H. and Schwartzkroin, P. (1990). Responses of cells of the rat fascia dentata to prolonged stimulation of the perforant path: Sensitivity of hilar cells and changes in granule cell excitability. *Neuroscience*, 35(3):491–504.

Scheler, G. (2004). Regulation of neuromodulator receptor efficacy—implications for whole-neuron and synaptic plasticity. *Progress in Neurobiology*, 72(6):399–415.

Schmetterling, R., Burghi, T. B., and Sepulchre, R. (2022). Adaptive conductance control. *Annual Reviews in Control*, 54:352–362.

Schmetterling, R., Forni, F., Franci, A., and Sepulchre, R. (2024). Neuromorphic control of a pendulum. *arXiv preprint arXiv:2404.05339*.

Schultz, W. (2007). Multiple dopamine functions at different time courses. *Annual Review of Neuroscience*, 30:259–288.

Schulz, D. J., Baines, R. A., Hempel, C. M., Li, L., Liss, B., and Misonou, H. (2006a). Cellular excitability and the regulation of functional neuronal identity: From gene expression to neuromodulation. *Journal of Neuroscience*, 26(41):10362–10367.

Schulz, D. J., Goaillard, J.-M., and Marder, E. (2006b). Variable channel expression in identified single and electrically coupled neurons in different animals. *Nature Neuroscience*, 9(3):356–362.

Schulz, D. J., Goaillard, J.-M., and Marder, E. E. (2007). Quantitative expression profiling of identified neurons reveals cell-specific constraints on highly variable levels of gene expression. *Proceedings of the National Academy of Sciences*, 104(32):13187–13191.

Schutter, E. D. (2010). *Computational modeling methods for neuroscientists*. MIT Press.

Sciamanna, G. and Wilson, C. J. (2011). The ionic mechanism of gamma resonance in rat striatal fast-spiking neurons. *Journal of Neurophysiology*, 106(6):2936–2949.

Seeburg, D. P. and Sheng, M. (2008). Activity-induced polo-like kinase 2 is required for homeostatic plasticity of hippocampal neurons during epileptiform activity. *Journal of Neuroscience*, 28(26):6583–6591.

Seki, S., Tanaka, S., Yamada, S., Tsuji, T., Enomoto, A., Ono, Y., Chandler, S. H., and Kogo, M. (2020). Neuropeptide y modulates membrane excitability in neonatal rat mesencephalic v neurons. *Journal of Neuroscience Research*, 98(5):921–935.

Selverston, A., Szücs, A., Huerta, R., Pinto, R. D., and Reyes, M. B. (2009). Neural mechanisms underlying the generation of the lobster gastric mill motor pattern. *Frontiers in Neural Circuits*, 3:608.

Selverston, A. I. (1976). Neuronal mechanisms for rhythmic motor pattern generation in a simple system. *Neural Control of Locomotion*, pages 377–399.

Selverston, A. I. (2010). Invertebrate central pattern generator circuits. *Philosophical Transactions of the Royal Society: Biological Sciences*, 365(1551):2329–2345.

Selverston, A. I. and Moulins, M. (2012). *The crustacean stomatogastric system: A model for the study of central nervous systems*. Springer Science & Business Media.

Sepulchre, R., Chaffey, T., and Forni, F. (2022). On the incremental form of dissipativity. *IFAC-PapersOnLine*, 55(30):290–294.

Sepulchre, R., Drion, G., and Franci, A. (2018). Excitable behaviors. *Emerging Applications of Control and Systems Theory: A Festschrift in Honor of Mathukumalli Vidyasagar*, pages 269–280.

Sepulchre, R., Drion, G., and Franci, A. (2019). Control across scales by positive and negative feedback. *Annual Review of Control, Robotics, and Autonomous Systems*, 2:89–113.

Shafi, M. M., Vernet, M., Klooster, D., Chu, C. J., Boric, K., Barnard, M. E., Romatoski, K., Westover, M. B., Christodoulou, J. A., Gabrieli, J. D., et al. (2015). Physiological consequences of abnormal connectivity in a developmental epilepsy. *Annals of Neurology*, 77(3):487–503.

Shaout, A. and Jarrah, M. A. (1997). Cruise control technology review. *Computers & Electrical Engineering*, 23(4):259–271.

Sharp, A. A., O'Neil, M. B., Abbott, L. F., and Marder, E. (1993). Dynamic clamp: Computer-generated conductances in real neurons. *Journal of Neurophysiology*, 69(3):992–995.

Sherman, S. M. (2001). Tonic and burst firing: Dual modes of thalamocortical relay. *Trends in Neurosciences*, 24(2):122–126.

Sherman, S. M. and Guillery, R. W. (2006). *Exploring the thalamus and its role in cortical function*. MIT press.

Shine, J. M., Müller, E. J., Munn, B., Cabral, J., Moran, R. J., and Breakspear, M. (2021). Computational models link cellular mechanisms of neuromodulation to large-scale neural dynamics. *Nature Neuroscience*, 24(6):765–776.

Shouval, H. Z. (2007). Models of synaptic plasticity. *Scholarpedia*, 2(7):1605.

Shvartsman, S. Y., Hagan, M. P., Yacoub, A., Dent, P., Wiley, H., and Lauffenburger, D. A. (2002). Autocrine loops with positive feedback enable context-dependent cell signaling. *American Journal of Physiology-Cell Physiology*, 282(3):C545–C559.

Sieling, F. H. and Butera, R. (2011). Aplysia r15 neuron. *Scholarpedia*, 6(10):4181.

Sjöström, J., Gerstner, W., et al. (2010). Spike-timing dependent plasticity. *Spike-Timing Dependent Plasticity*, 35(0):0–0.

Skinner, F. K. (2006). Conductance-based models. *Scholarpedia*, 1(11):1408.

Skou, J. C. and Esmann, M. (1992). The na, k-atpase. *Journal of Bioenergetics and Biomembranes*, 24:249–261.

Smith, S. M. (2004). Overview of fmri analysis. *The British Journal of Radiology*, 77(suppl_2):S167–S175.

Sobie, E. A. (2009). Parameter sensitivity analysis in electrophysiological models using multivariable regression. *Biophysical Journal*, 96(4):1264–1274.

Sotelo, C. and Rossi, F. (2021). Purkinje cell migration and differentiation. In *Handbook of the cerebellum and cerebellar disorders*, pages 173–205. Springer.

Spangler, S. M. and Bruchas, M. R. (2017). Optogenetic approaches for dissecting neuromodulation and gpcr signaling in neural circuits. *Current Opinion in Pharmacology*, 32:56–70.

Sperry, R. W. (1975). Left-brain, right-brain. *Saturday Review*, 2(23):30–32.

Spruston, N. (2008). Pyramidal neurons: Dendritic structure and synaptic integration. *Nature Reviews Neuroscience*, 9(3):206–221.

Starmer, C. F., Lastra, A. A., Nesterenko, V. V., and Grant, A. O. (1991). Proarrhythmic response to sodium channel blockade. theoretical model and numerical experiments. *Circulation*, 84(3):1364–1377.

Steriade, M. and Contreras, D. (1995). Relations between cortical and thalamic cellular events during transition from sleep patterns to paroxysmal activity. *Journal of Neuroscience*, 15(1):623–642.

Stevens, C. F. (1979). The neuron. *Scientific American*, 241(3):54–65.

Still, S., Hepp, K., and Douglas, R. J. (2006). Neuromorphic walking gait control. *IEEE Transactions on Neural Networks*, 17(2):496–508.

Styr, B. and Slutsky, I. (2018). Imbalance between firing homeostasis and synaptic plasticity drives early-phase alzheimer's disease. *Nature Neuroscience*, 21(4):463–473.

Sweadner, K. J. and Goldin, S. M. (1980). Active transport of sodium and potassium ions: Mechanism, function, and regulation. *New England Journal of Medicine*, 302(14):777–783.

Swensen, A. M. and Bean, B. P. (2005). Robustness of burst firing in dissociated purkinje neurons with acute or long-term reductions in sodium conductance. *Journal of Neuroscience*, 25(14):3509–3520.

Swensen, A. M., Golowasch, J., Christie, A. E., Coleman, M. J., Nusbaum, M. P., and Marder, E. (2000). Gaba and responses to gaba in the stomatogastric ganglion of the crab cancer borealis. *Journal of Experimental Biology*, 203(14):2075–2092.

Swensen, A. M. and Marder, E. (2000). Multiple peptides converge to activate the same voltage-dependent current in a central pattern-generating circuit. *Journal of Neuroscience*, 20(18):6752–6759.

Szücs, A. and Selverston, A. I. (2006). Consistent dynamics suggests tight regulation of biophysical parameters in a small network of bursting neurons. *Journal of Neurobiology*, 66(14):1584–1601.

Tabak, J., Tomaiuolo, M., Gonzalez-Iglesias, A. E., Milescu, L. S., and Bertram, R. (2011). Fast-activating voltage-and calcium-dependent potassium (bk) conductance promotes bursting in pituitary cells: A dynamic clamp study. *Journal of Neuroscience*, 31(46):16855–16863.

Takahashi, K., Lin, J.-S., and Sakai, K. (2006). Neuronal activity of histaminergic tuberomammillary neurons during wake–sleep states in the mouse. *Journal of Neuroscience*, 26(40):10292–10298.

Tang, L. S., Taylor, A. L., Rinberg, A., and Marder, E. (2012). Robustness of a rhythmic circuit to short-and long-term temperature changes. *Journal of Neuroscience*, 32(29):10075–10085.

Tapia, M., Baudot, P., Formisano-Tréziny, C., Dufour, M. A., Temporal, S., Lasserre, M., Marquèze-Pouey, B., Gabert, J., Kobayashi, K., and Goaillard, J.-M. (2018). Neurotransmitter identity and electrophysiological phenotype are genetically coupled in midbrain dopaminergic neurons. *Scientific Reports*, 8(1):13637.

Tateno, T., Harsch, A., and Robinson, H. (2004). Threshold firing frequency–current relationships of neurons in rat somatosensory cortex: Type 1 and type 2 dynamics. *Journal of Neurophysiology*, 92(4):2283–2294.

Tatsuki, F., Sunagawa, G. A., Shi, S., Susaki, E. A., Yukinaga, H., Perrin, D., Sumiyama, K., Ukai-Tadenuma, M., Fujishima, H., Ohno, R.-i., et al. (2016). Involvement of ca2+-dependent hyperpolarization in sleep duration in mammals. *Neuron*, 90(1):70–85.

Tatti, R., Haley, M. S., Swanson, O. K., Tselha, T., and Maffei, A. (2017). Neurophysiology and regulation of the balance between excitation and inhibition in neocortical circuits. *Biological Psychiatry*, 81(10):821–831.

Tavanaei, A., Ghodrati, M., Kheradpisheh, S. R., Masquelier, T., and Maida, A. (2019). Deep learning in spiking neural networks. *Neural Networks*, 111:47–63.

Taylor, A. L., Goaillard, J.-M., and Marder, E. (2009). How multiple conductances determine electrophysiological properties in a multicompartment model. *Journal of Neuroscience*, 29(17):5573–5586.

Taylor, B. (1717). *Methodus incrementorum directa & inversa*. Inny.

Tellam, D. J., Mohammad, Y. N., and Lovejoy, D. A. (2000). Molecular integration of hypothalamo-pituitary-adrenal axis-related neurohormones on the gnrh neuron. *Biochemistry and Cell Biology*, 78(3):205–216.

Temporal, S., Desai, M., Khorkova, O., Varghese, G., Dai, A., Schulz, D. J., and Golowasch, J. (2012). Neuromodulation independently determines correlated channel expression and conductance levels in motor neurons of the stomatogastric ganglion. *Journal of Neurophysiology*, 107(2):718–727.

Terman, D. H. and Izhikevich, E. M. (2008). State space. *Scholarpedia*, 3(3):1924.

Thau, L., Reddy, V., and Singh, P. (2022). Anatomy, central nervous system. *StatPearls [Internet]*. [Updated 2022 Oct 10]. Available from: https://www.ncbi.nlm.nih.gov/books/NBK542179/.

Tikidji-Hamburyan, R. A. and Colonnese, M. T. (2021). Polynomial, piecewise-linear, step: A simple, scalable, and efficient framework for modeling neurons. *Frontiers in Neuroinformatics*, 15:642933.

Tkačik, G., Prentice, J. S., Balasubramanian, V., and Schneidman, E. (2010). Optimal population coding by noisy spiking neurons. *Proceedings of the National Academy of Sciences*, 107(32):14419–14424.

Tobey, R. G. (1971). Symbolic mathematical computation—introduction and overview. In *Proceedings of the second ACM symposium on Symbolic and algebraic manipulation*, pages 1–16.

Tobin, A.-E., Cruz-Bermúdez, N. D., Marder, E., and Schulz, D. J. (2009). Correlations in ion channel mrna in rhythmically active neurons. *PLoS one*, 4(8):e6742.

Toledo-Rodriguez, M., Blumenfeld, B., Wu, C., Luo, J., Attali, B., Goodman, P., and Markram, H. (2004). Correlation maps allow neuronal electrical properties to be predicted from single-cell gene expression profiles in rat neocortex. *Cerebral Cortex*, 14(12):1310–1327.

Turrigiano, G. (2012). Homeostatic synaptic plasticity: Local and global mechanisms for stabilizing neuronal function. *Cold Spring Harbor Perspectives in Biology*, 4(1):a005736.

Turrigiano, G. G. (1999). Homeostatic plasticity in neuronal networks: The more things change, the more they stay the same. *Trends in Neurosciences*, 22(5):221–227.

Turrigiano, G. G. and Nelson, S. B. (2004). Homeostatic plasticity in the developing nervous system. *Nature Reviews Neuroscience*, 5(2):97–107.

Tyree, S. M. and De Lecea, L. (2017). Optogenetic investigation of arousal circuits. *International Journal of Molecular Sciences*, 18(8):1773.

V-Ghaffari, B., Kouhnavard, M., and Kitajima, T. (2016). Biophysical properties of subthreshold resonance oscillations and subthreshold membrane oscillations in neurons. *Journal of Biological Systems*, 24(4):561–575.

Van den Brand, R., Heutschi, J., Barraud, Q., DiGiovanna, J., Bartholdi, K., Huerlimann, M., Friedli, L., Vollenweider, I., Moraud, E. M., Duis, S., et al. (2012). Restoring voluntary control of locomotion after paralyzing spinal cord injury. *Science*, 336(6085):1182–1185.

Van Essen, D. C., Anderson, C. H., and Felleman, D. J. (1992). Information processing in the primate visual system: An integrated systems perspective. *Science*, 255(5043):419–423.

Van Ooyen, A., Van Pelt, J., and Corner, M. (1995). Implications of activity dependent neurite outgrowth for neuronal morphology and network development. *Journal of Theoretical Biology*, 172(1):63–82.

Van Pottelbergh, T., Drion, G., and Sepulchre, R. (2018). Robust modulation of integrate-and-fire models. *Neural Computation*, 30(4):987–1011.

van Welie, I., van Hooft, J. A., and Wadman, W. J. (2004). Homeostatic scaling of neuronal excitability by synaptic modulation of somatic hyperpolarization-activated i h channels. *Proceedings of the National Academy of Sciences*, 101(14):5123–5128.

Vida, I., Degro, C. E., and Booker, S. A. (2018). Morphology of hippocampal neurons. *Hippocampal Microcircuits: A Computational Modeler's Resource Book*, pages 29–90.

Vida, I., Halasy, K., Szinyei, C., Somogyi, P., and Buhl, E. H. (1998). Unitary ipsps evoked by interneurons at the stratum radiatum-stratum lacunosum-moleculare border in the ca1 area of the rat hippocampus in vitro. *The Journal of Physiology*, 506(3):755–773.

Von Bartheld, C. S., Bahney, J., and Herculano-Houzel, S. (2016). The search for true numbers of neurons and glial cells in the human brain: A review of 150 years of cell counting. *Journal of Comparative Neurology*, 524(18):3865–3895.

Walters, E. T. and Byrne, J. H. (1984). Activity-dependent neuromodulation: A mechanism for associative plasticity. *Neuronal Growth and Plasticity*, 6:219.

Wang, X.-J. (2010). Neurophysiological and computational principles of cortical rhythms in cognition. *Physiological Reviews*, 90(3):1195–1268.

Wang, Y., Zhao, K., Lu, X.-Y., Song, Y.-B., and Bennett, G. J. (2019). Bio-inspired aerodynamic noise control: A bibliographic review. *Applied Sciences*, 9(11):2224.

Wechselberger, M., Wright, C. L., Bishop, G. A., and Boulant, J. A. (2006). Ionic channels and conductance-based models for hypothalamic neuronal thermosensitivity. *American Journal of Physiology-Regulatory, Integrative and Comparative Physiology*, 291(3):R518–R529.

Wei, Y., Krishnan, G. P., and Bazhenov, M. (2016). Synaptic mechanisms of memory consolidation during sleep slow oscillations. *Journal of Neuroscience*, 36(15):4231–4247.

Weimann, J. M., Meyrand, P., and Marder, E. (1991). Neurons that form multiple pattern generators: Identification and multiple activity patterns of gastric/pyloric neurons in the crab stomatogastric system. *Journal of Neurophysiology*, 65(1):111–122.

Weller, A. S. (2005). Body temperature and its regulation. *Anaesthesia & Intensive Care Medicine*, 6(6):206–209.

Werner, G. and Mitterauer, B. J. (2014). The dynamics of neuromodulation. *Criticality in Neural Systems*, pages 525–538.

Whitacre, J. and Bender, A. (2010). Degeneracy: A design principle for achieving robustness and evolvability. *Journal of Theoretical Biology*, 263(1):143–153.

Whitacre, J. M. (2010). Degeneracy: A link between evolvability, robustness and complexity in biological systems. *Theoretical Biology and Medical Modelling*, 7:1–17.

Whitaker, S. and Pigford, R. (1960). An approach to numerical differentiation of experimental data. *Industrial & Engineering Chemistry*, 52(2):185–187.

Wierenga, C. J., Walsh, M. F., and Turrigiano, G. G. (2006). Temporal regulation of the expression locus of homeostatic plasticity. *Journal of Neurophysiology*, 96(4):2127–2133.

Wilkerson, D. (2016). Modern control system ekt 308 steady-state and stability. *SlidePlayer [Internet]*. [Updated 2016]. Available from: https://slideplayer.com/slide/9281492/.

Wise, R. A. and Rompre, P.-P. (1989). Brain dopamine and reward. *Annual Review of Psychology*, 40(1):191–225.

X Cubeddu, L. (2016). Drug-induced inhibition and trafficking disruption of ion channels: Pathogenesis of qt abnormalities and drug-induced fatal arrhythmias. *Current Cardiology Reviews*, 12(2):141–154.

Xia, Z. and Storm, D. R. (1997). Calmodulin-regulated adenylyl cyclases and neuromodulation. *Current Opinion in Neurobiology*, 7(3):391–396.

Yamada, W. M., Koch, C., and Adams, P. R. (1989). Multiple channels and calcium dynamics. *Methods in Neuronal Modeling*, 1989:137–170.

Yamapi, R. et al. (2022). Birhythmic oscillations and global stability analysis of a conductance-based neuronal model under ion channel fluctuations. *Chaos, Solitons & Fractals*, 159:112126.

Yamazaki, K., Vo-Ho, V.-K., Bulsara, D., and Le, N. (2022). Spiking neural networks and their applications: A review. *Brain Sciences*, 12(7):863.

Yaru, L. and Shenquan, L. (2021). Characterizing mixed-mode oscillations shaped by canard and bifurcation structure in a three-dimensional cardiac cell model. *Nonlinear Dynamics*, 103:2881–2902.

Yèagle, P. L. (1989). Lipid regulation of cell membrane structure and function. *The FASEB Journal*, 3(7):1833–1842.

Yelnik, J., Francis, C., Percheron, G., and Tandéa, D. (1991). Morphological taxonomy of the neurons of the primate striatum. *Journal of Comparative Neurology*, 313(2):273–294.

Yi, G.-S., Wang, J., Deng, B., and Wei, X.-L. (2017). Morphology controls how hippocampal ca1 pyramidal neuron responds to uniform electric fields: A biophysical modeling study. *Scientific Reports*, 7(1):3210.

Yoo, J. and Shoaran, M. (2021). Neural interface systems with on-device computing: Machine learning and neuromorphic architectures. *Current Opinion in Biotechnology*, 72:95–101.

Yu, H.-b., Li, M., Wang, W.-p., and Wang, X.-l. (2016). High throughput screening technologies for ion channels. *Acta Pharmacologica Sinica*, 37(1):34–43.

Yuste, R., MacLean, J. N., Smith, J., and Lansner, A. (2005). The cortex as a central pattern generator. *Nature Reviews Neuroscience*, 6(6):477–483.

Zagha, E. and McCormick, D. A. (2014). Neural control of brain state. *Current Opinion in Neurobiology*, 29:178–186.

Zang, Y. and Marder, E. (2023). Neuronal morphology enhances robustness to perturbations of channel densities. *Proceedings of the National Academy of Sciences*, 120(8):e2219049120.

Zeng, Y., Li, J., Yang, S. X., and Ren, E. (2018). A bio-inspired control strategy for locomotion of a quadruped robot. *Applied Sciences*, 8(1):56.

Zenke, F., Gerstner, W., and Ganguli, S. (2017). The temporal paradox of hebbian learning and homeostatic plasticity. *Current Opinion in Neurobiology*, 43:166–176.

Zhou, H.-X. and McCammon, J. A. (2010). The gates of ion channels and enzymes. *Trends in Biochemical Sciences*, 35(3):179–185.

Zomorrodi, R., Kröger, H., and Timofeev, I. (2008). Modeling thalamocortical cell: Impact of ca2+ channel distribution and cell geometry on firing pattern. *Frontiers in Computational Neuroscience*, 2:306.

Appendix

A Side project

A1 SOCN Graduate School project

During my PhD, I participated in the Graduate School in Systems, Optimization, Control, and Networks (SOCN) 2023, which brought together Belgian research teams. The program was organized by Rodolphe Sepulchre from KUL and Thomas Chaffey from Cambridge, with a focus on mixed feedback systems. At the conclusion of the courses, we were tasked with a project involving half-center oscillators (HCOs) constructed with mixed feedback neurons. The project, which centers on frequency tuning of HCOs, is presented below and was completed in collaboration with Christian Fernandez Lorden, a PhD student from the Neuromorphic Engineering Laboratory at the University of Liège.

A1.1 Introduction

Mixed feedback system theory provides a straightforward approach to studying and designing spiking and bursting neuron models without requiring an enormous number of Ordinary Differential Equations (ODEs) and associated parameters, as seen in conductance-based models. With two timescales, spiking can be achieved through a fast positive feedback and a slow negative feedback. Bursting, on the other hand, requires an ultraslow timescale due to its more complex nature, and this can be achieved by adding another fast/negative feedback pair in the slow/ultraslow timescale.

A significant application of bursting neurons is to use them in networks to study biological rhythms, such as the pyloric or gastric mill rhythms in the crab nervous system. The simplest rhythm can be achieved by a combination of two interconnected inhibitory bursting neurons, which can be modeled using mixed feedback systems. This network constitutes a Half Center Oscillator (HCO) and results in periodic alternating bursts between the two neurons. When one neuron is bursting, the other one is silent, and vice versa. Such a rhythm has been proven to be ubiquitous in locomotion rhythms.

In this brief report, we will be interested in adapting the HCO rhythm by tuning its internal parameters using an emergent simple linear rule.

A1.2 Model

For this report, we will use a model based on the work of Ribar and Sepulchre (2019). A block diagram of the neuron is shown in figure A1.1. This model incorporates 3 timescales to allow bursting behavior.

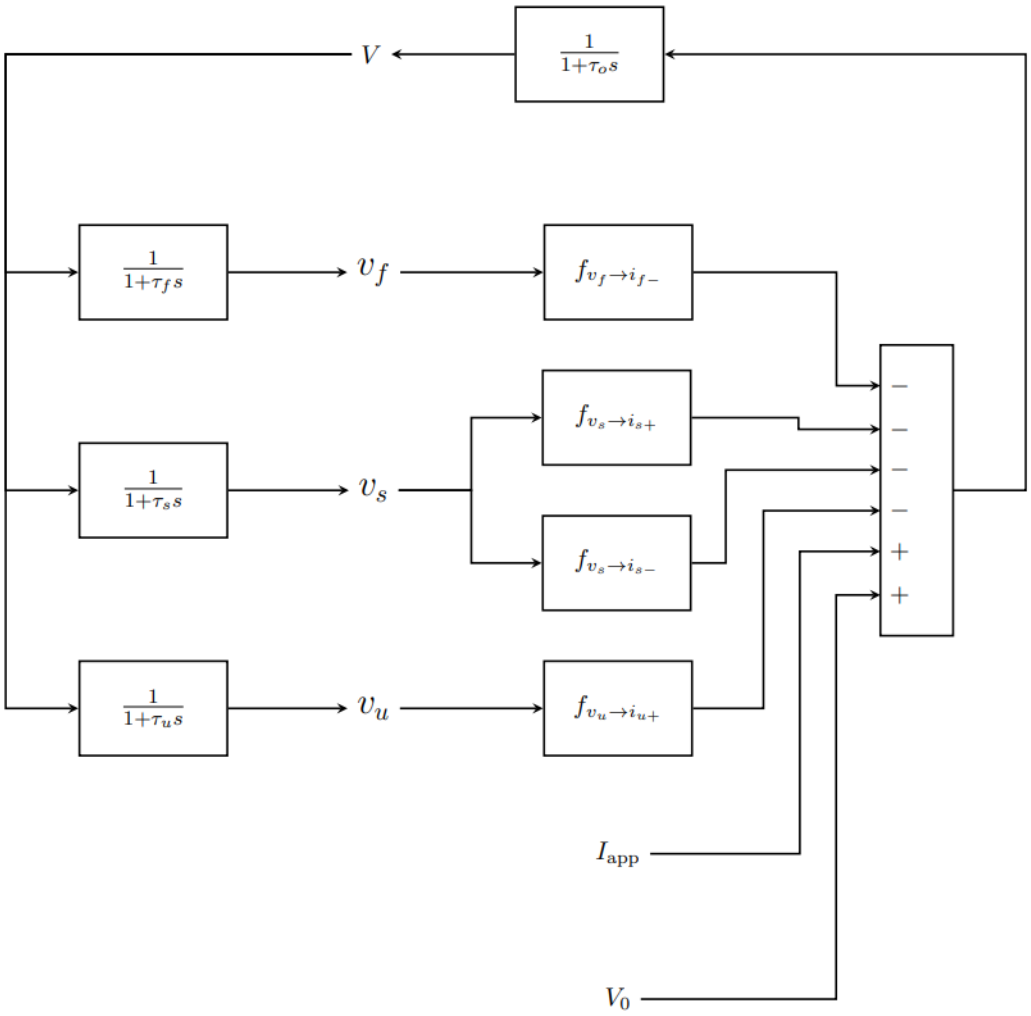

Figure A1.1: Diagram of the Neuron Model. The output of the neuron is V and the input is I_{app}.

Specifically, we can write the equations governing the neuron as an ODE system.

$$\tau_o \frac{\partial V}{\partial t} = V_0 + I_{\text{app}} - i_{f-} - i_{s+} - i_{s-} - i_{u+} - V \tag{A.1}$$

$$i_{f-} = g_{f-} \left(\tanh\left(v_f - d_{f-}\right) - \tanh\left(V_0 - d_{f-}\right)\right) \tag{A.2}$$

$$i_{s+} = g_{s+} \left(\tanh\left(v_s - d_{s+}\right) - \tanh\left(V_0 - d_{s+}\right)\right) \tag{A.3}$$

$$i_{s-} = g_{s-} \left(\tanh\left(v_s - d_{s-}\right) - \tanh\left(V_0 - d_{s-}\right)\right) \tag{A.4}$$

$$i_{u+} = g_{u+} \left(\tanh\left(v_u - d_{u+}\right) - \tanh\left(V_0 - d_{u+}\right)\right) \tag{A.5}$$

$$\tau_f \frac{\partial v_f}{\partial t} = V - v_f \tag{A.6}$$

$$\tau_s \frac{\partial v_s}{\partial t} = V - v_s \tag{A.7}$$

$$\tau_u \frac{\partial v_u}{\partial t} = V - v_u \tag{A.8}$$

with g_{f-}, $g_{s-} < 0$, g_{s+}, $g_{u+} > 0$ and d_{f-}, d_{s+}, d_{s-}, $d_{u+} \in \mathbb{R}$.

This alone only amounts to a single neuron. To create an HCO, we need synapses to connect the

neurons. Such a model can be seen in figure A1.2. It is similar in construction to an internal feedback of the neuron model, only depending on the voltage of another neuron and using a sigmoid instead of a hyperbolic tangent saturation.

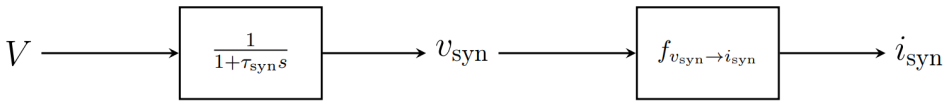

Figure A1.2: Diagram of a synapse between neurons.

More formally, this synapse model can be written as a simple ODE.

$$\tau_{\text{syn}} \frac{\partial v_{\text{syn}}}{\partial t} = V - v_{\text{syn}} \tag{A.9}$$

$$i_{\text{out}} = g_{\text{syn}} \sigma \left(4 \left(v_{\text{syn}} - d_{\text{syn}}\right)\right) \tag{A.10}$$

with $g_{\text{syn}}, d_{\text{syn}} \in \mathbb{R}$ and $\sigma(.)$ the sigmoid function. Depending on the sign of g_{syn} the synapse can be either inhibitory or excitatory.

Interconnecting the neuron model with inhibitory synapses will create a HCO. Figure A1.3 shows an example of the output of such a construction. We can clearly see the classical HCO pattern of the two neurons bursting alternating.

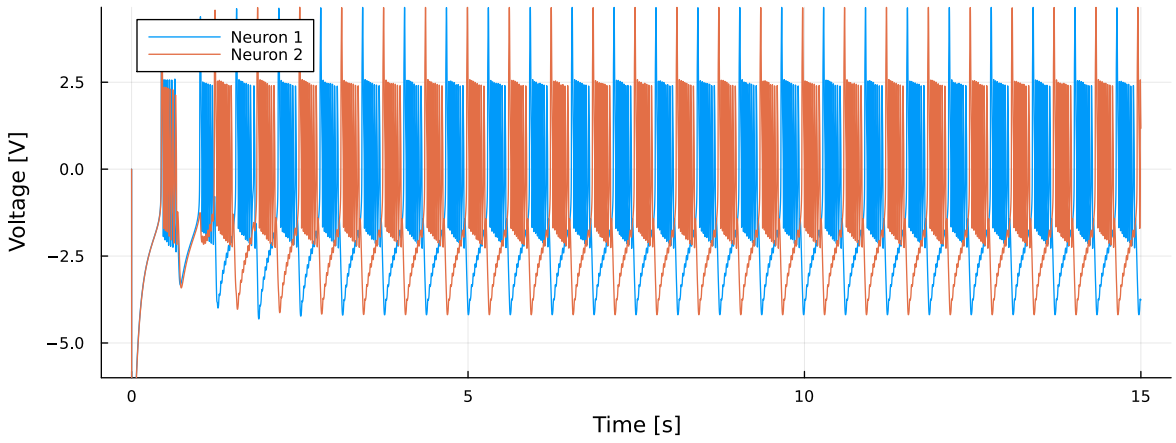

Figure A1.3: Simulation of an HCO.

For the rest of this document, if not specified otherwise, we will use the following values for the neurons and synapses.

g_{f-}	$-2.0\,\text{S}$	g_{s+}	$6\,\text{S}$	g_{s-}	$-4\,\text{S}$	g_{u+}	$5\,\text{S}$
d_{f-}	$0.0\,\text{V}$	d_{s+}	$0.5\,\text{V}$	d_{s-}	$-0.5\,\text{V}$	d_{u+}	$-0.5\,\text{V}$
τ_o	$0.25\,\text{ms}$	τ_f	$1\,\text{ms}$	τ_s	$40\,\text{ms}$	τ_u	$800\,\text{ms}$
V_0	$-0.85\,\text{V}$	I_{app}	$-1.4\,\text{A}$				
g_{syn}	$-1\,\text{S}$	d_{syn}	$0.5\,\text{V}$	τ_{syn}	$40\,\text{ms}$		

A1.3 Burstiness analysis

Before going into frequency control, understanding the model is key. For this purpose, an analysis of burstiness was performed on the HCO.

The burstiness measure chosen can be expressed as

$$\text{burstiness} = f_{\text{burst}} \cdot f_{\text{spike}} \cdot \#_{\text{spike}} \approx f_{\text{burst}} \cdot l_{\text{burst}} \cdot (f_{\text{spike}})^2 \tag{A.11}$$

This measure has the advantage of remaining roughly constant under the same duty cycle if we assume a constant spiking frequency. This approximation can be made since $\#_{\text{spike}} \approx f_{\text{spike}} \cdot l_{\text{burst}}$.

An exploration of that measure over changing conductance can be seen in figure A1.4.

This figure indicates that g_{u+} is instrumental in the existence of bursting because lower values indicate a smaller area of bursting. However, interestingly, the burstiness of the neuron seems mostly unchanged by g_{u+}. Instead, it is dictated by the values of g_{s-} and g_{s+}.

To explore the existence of the steep gradient of burstiness that appears on the grid, we explore the change in the response of the HCO when changing g_{s+}. This exploration can be seen in figure A1.5.

The figure sheds light on the boundary because it shows that when g_{s+} is low, the bursting starts with a plateau of depolarization. Thus, this reduces the burstiness by lowering the number of spikes in the burst. Them being replaced by a region of silent depolarization.

All of this indicates g_{u+} as a good candidate parameter to modulate frequency because it does not seem to perturb the bursting behavior. Thus, if g_{u+} influence the bursting frequency, it can be used effectively to control the HCO.

A1.4 Frequency control

HCOs are ubiquitous in the nervous systems of many living beings. Indeed, they can produce robust, reliable, and resilient rhythmic patterns. Yet simple, their oscillatory pattern can be integrated into more complex systems to produce more intricate rhythmic patterns, such as central pattern generation in the field of locomotion. Moreover, HCOs rhythm shapes can be modulated (through neuromodulation or any other mechanism) so that they become adaptable. Indeed, tuning the interburst frequency (or equivalently their burstiness) of HCO neurons can accelerate or decelerate their pattern to adapt to their environment and fulfill their task adequately.

In this brief project, our focus lies in the modulation of HCOs by adjusting their conductance. While various methods exist for modulation, our interest lies specifically in modifying the interburst frequency, and consequently the burstiness, of HCO neurons by tuning the ultraslow conductance. To achieve this, we employ adaptive control on the mixed feedback system modeling the neuron, enabling the tuning of its ultraslow feedback through the ultraslow conductance. This approach allows users to input their desired interburst frequency into the adaptive control system, leading to the computation of an appropriate value for the ultraslow conductance. Consequently, the HCO behaves according to the specified requirements. Notably, the ultraslow

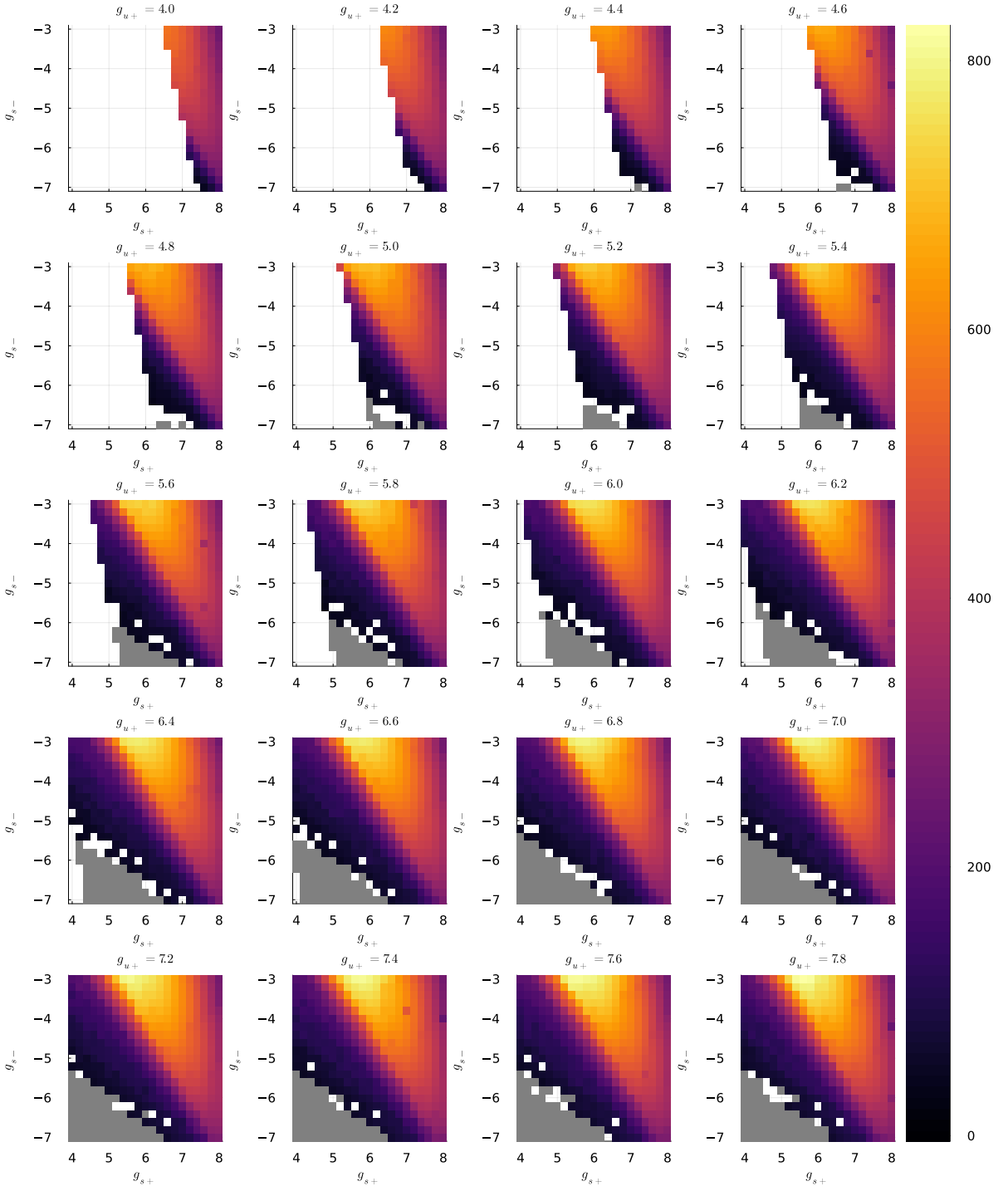

Figure A1.4: Average burstiness value of HCO neurons as a function of slow and ultraslow conductances. The gray areas represent the regions of spiking in the HCO neurons.

conductance transforms from a fixed parameter into a variable that uniquely depends on the inputted interburst frequency.

Indeed, we observed that the relationship between the interburst frequency and the ultraslow conductance is nearly linear (Fig. A1.6). Employing least square regression on this correlation, we obtained

$$f_{\text{inter}} \approx a_0 + a_1 \cdot g_{u+} \iff g_{u+} \approx (f_{\text{inter}} - a_0)/a_1 \tag{A.12}$$

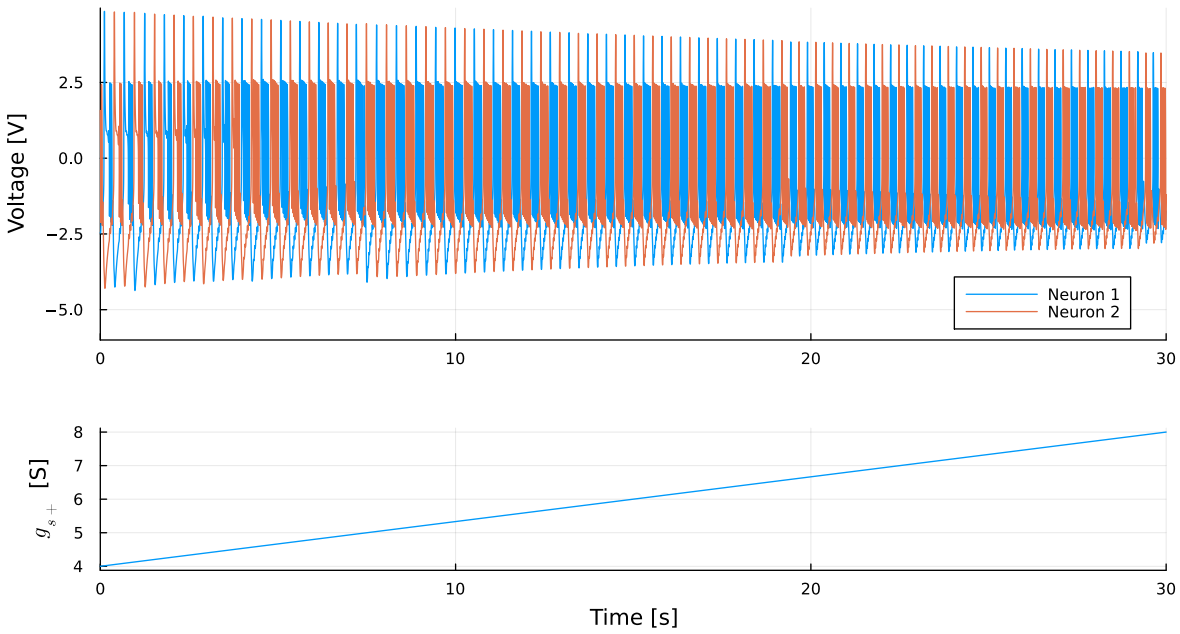

Figure A1.5: Simulation of the HCO with changing g_{s+} for $g_{s-} = -3.5$ and $g_{u+} = 7.0$.

with $a_0 = -0.18$ and $a_1 = 0.26$.

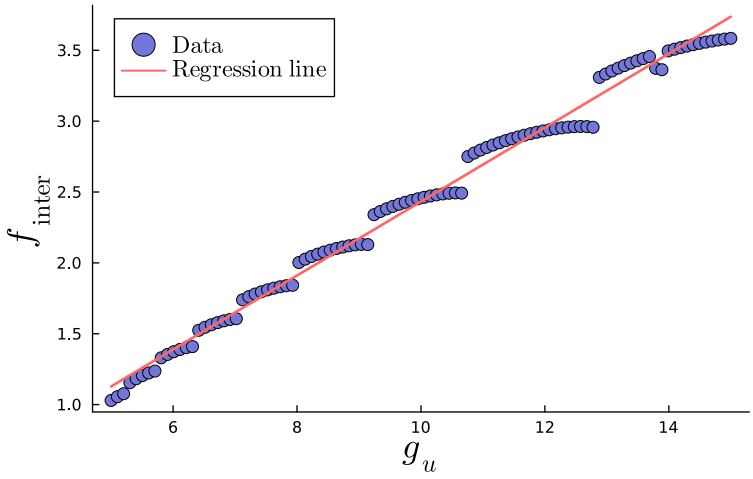

Figure A1.6: Relationship between the interburst frequency and the ultraslow conductance, along with its linear regression.

Utilizing this linear regression as the relationship to connect the desired interburst frequency to the ultraslow conductance, Fig. A1.7 illustrates a toy simulation with a triangular-shaped input interburst frequency. As observed, the adaptive control functions as expected, and the HCO rhythm accelerates when the interburst frequency increases and vice versa. Such a simple control mechanism can be employed to dynamically adapt the HCO rhythm in response to, for instance, its environment. In this manner, another network could compute, based on its environment, the interburst frequency the HCO needs to reach, making the system completely autonomous and usable in locomotion, for example, for transitions between walking and running.

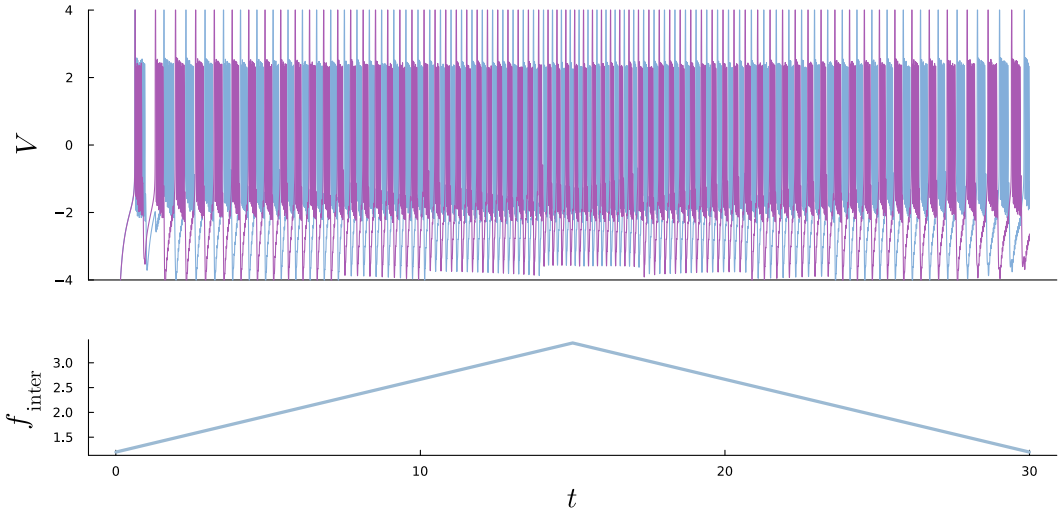

Figure A1.7: Toy simulation of the adaptive control system with a triangular shaped input interburst frequency.

A1.5 Conclusion and limitations

This brief report introduces a straightforward approach to introduce adaptive control in mixed feedback systems interconnected to form an HCO. This method can be applied broadly when studying the relationship between a phenotype characteristic and a model parameter and approximating it adequately. Once this approximation is established, the user can input the desired phenotype characteristic, and the resulting parameter can be computed using this approximated relationship to achieve the desired behavior. However, two main limitations can arise:

1. The regression parameters (a_0 and a_1) depend on the other parameter values of the system. If the slow conductances are modified, the subsequent regression parameters will change. To make this adaptive control more flexible to parameter variation and degeneracy, one should use a higher level of learning that includes other parameters. In this way, the controlled parameter (here the ultraslow conductance) would not only depend on the phenotype characteristic (here the interburst frequency) but also on the other parameter values, making the adaptive control more resilient to parameter variations.

2. In the case of ultraslow conductance control, this conductance (and hence the desired interburst frequency) cannot go outside the ranges shown in Fig. A1.6. In the considered mixed feedback model, a too large or too small value of the ultraslow conductance leads to complete silence in the neuron. Hence, saturation can be added to the adaptive control so that the ultraslow conductance control cannot lead to silence by a too large/small desired value of the interburst frequency, except when required.

B Supplemental equations for the model used in this thesis

B1 Stomatogastric neuron

The STG conductance-based model consists of the following ODE system:

$$
\begin{aligned}
C\dot{V} =& -\bar{g}_{\mathrm{Na}} m_{\mathrm{Na}}^3 h_{\mathrm{Na}} (V - E_{\mathrm{Na}}) - \bar{g}_{\mathrm{CaT}} m_{\mathrm{CaT}}^3 h_{\mathrm{CaT}} (V - E_{\mathrm{Ca}}) - \bar{g}_{\mathrm{CaS}} m_{\mathrm{CaS}}^3 h_{\mathrm{CaS}} (V - E_{\mathrm{Ca}}) \\
& - \bar{g}_{\mathrm{A}} m_{\mathrm{A}}^3 h_{\mathrm{A}} (V - E_{\mathrm{K}}) - \bar{g}_{\mathrm{KCa}} m_{\mathrm{KCa}}^4 (V - E_{\mathrm{K}}) - \bar{g}_{\mathrm{Kd}} m_{\mathrm{Kd}}^4 (V - E_{\mathrm{K}}) \\
& - \bar{g}_{\mathrm{H}} m_{\mathrm{H}} (V - E_{\mathrm{H}}) - g_{\mathrm{leak}} (V - E_{\mathrm{leak}}) + I_{\mathrm{app}}; \\
\tau_{m,\mathrm{Na}}(V) \dot{m}_{\mathrm{Na}} =& m_{\mathrm{Na},\infty}(V) - m_{\mathrm{Na}}; \\
\tau_{h,\mathrm{Na}}(V) \dot{h}_{\mathrm{Na}} =& h_{\mathrm{Na},\infty}(V) - h_{\mathrm{Na}}; \\
\tau_{m,\mathrm{CaT}}(V) \dot{m}_{\mathrm{CaT}} =& m_{\mathrm{CaT},\infty}(V) - m_{\mathrm{CaT}}; \\
\tau_{h,\mathrm{CaT}}(V) \dot{h}_{\mathrm{CaT}} =& h_{\mathrm{CaT},\infty}(V) - h_{\mathrm{CaT}}; \\
\tau_{m,\mathrm{CaS}}(V) \dot{m}_{\mathrm{CaS}} =& m_{\mathrm{CaS},\infty}(V) - m_{\mathrm{CaS}}; \\
\tau_{h,\mathrm{CaS}}(V) \dot{h}_{\mathrm{CaS}} =& h_{\mathrm{CaS},\infty}(V) - h_{\mathrm{CaS}}; \\
\tau_{m,\mathrm{A}}(V) \dot{m}_{\mathrm{A}} =& m_{\mathrm{A},\infty}(V) - m_{\mathrm{A}}; \\
\tau_{h,\mathrm{A}}(V) \dot{h}_{\mathrm{A}} =& h_{\mathrm{A},\infty}(V) - h_{\mathrm{A}}; \\
\tau_{m,\mathrm{KCa}}(V) \dot{m}_{\mathrm{KCa}} =& m_{\mathrm{KCa},\infty}(V, [\mathrm{Ca}^{+2}]) - m_{\mathrm{KCa}}; \\
\tau_{m,\mathrm{Kd}}(V) \dot{m}_{\mathrm{Kd}} =& m_{\mathrm{Kd},\infty}(V) - m_{\mathrm{Kd}}; \\
\tau_{m,\mathrm{H}}(V) \dot{m}_{\mathrm{H}} =& m_{\mathrm{H},\infty}(V) - m_{\mathrm{H}}; \\
20 \cdot \dot{[\mathrm{Ca}^{+2}]} =& -0.94 \left[\bar{g}_{\mathrm{CaT}} m_{\mathrm{CaT}}^3 h_{\mathrm{CaT}} (V - E_{\mathrm{Ca}}) + \bar{g}_{\mathrm{CaS}} m_{\mathrm{CaS}}^3 h_{\mathrm{CaS}} (V - E_{\mathrm{Ca}}) \right] - [\mathrm{Ca}^{+2}] + 0.05,
\end{aligned}
$$

where the different parameters can be found in Table B1.1.

Model parameters	
C	$1\,\mu\mathrm{F/cm}^2$
E_{Na}	$50\,\mathrm{mV}$
E_{K}	$-80\,\mathrm{mV}$
E_{Ca}	$80\,\mathrm{mV}$
E_{H}	$-20\,\mathrm{mV}$
E_{leak}	$-50\,\mathrm{mV}$

Table B1.1: In the STG conductance-based model, parameters include C for membrane capacitance and E_{ion} representing the Nernst reversal potential of the considered ion. These parameters remained constant throughout this thesis.

The steady-state functions of gating variables consist of the following equations:

$$m_{\mathrm{Na},\infty}(V) = \frac{1}{1+e^{(V+25.5)/-5.29}}, \qquad h_{\mathrm{Na},\infty}(V) = \frac{1}{1+e^{(V+48.9)/5.18}};$$
$$m_{\mathrm{CaT},\infty}(V) = \frac{1}{1+e^{(V+27.1)/-7.2}}, \qquad h_{\mathrm{CaT},\infty}(V) = \frac{1}{1+e^{(V+32.1)/5.5}};$$
$$m_{\mathrm{CaS},\infty}(V) = \frac{1}{1+e^{(V+33)/-8.1}}, \qquad h_{\mathrm{CaS},\infty}(V) = \frac{1}{1+e^{(V+60)/6.2}};$$
$$m_{\mathrm{A},\infty}(V) = \frac{1}{1+e^{(V+27.2)/-8.7}}, \qquad h_{\mathrm{A},\infty}(V) = \frac{1}{1+e^{(V+56.9)/4.9}};$$
$$m_{\mathrm{KCa},\infty}(V,[\mathrm{Ca}^{+2}]) = \frac{[\mathrm{Ca}^{+2}]}{[\mathrm{Ca}^{+2}]+3}\cdot\frac{1}{1+e^{(V+28.3)/-12.6}};$$
$$m_{\mathrm{Kd},\infty}(V) = \frac{1}{1+e^{(V+12.3)/-11.8}};$$
$$m_{\mathrm{H},\infty}(V) = \frac{1}{1+e^{(V+70)/6}}.$$

The time constant functions of gating variables consist of the following equations:

$$\tau_{m,\mathrm{Na}}(V) = 1.32 - \frac{1.26}{1+e^{(V+120)/-25}}, \qquad \tau_{h,\mathrm{Na}}(V) = \frac{0.67}{1+e^{(V+62.9)/-10}}\cdot\left(1.5+\frac{1}{1+e^{(V+34.9)/3.6}}\right);$$
$$\tau_{m,\mathrm{CaT}}(V) = 21.7 - \frac{21.3}{1+e^{(V+68.1)/-20.5}}, \qquad \tau_{h,\mathrm{CaT}}(V) = 105 - \frac{89.8}{1+e^{(V+55)/-16.9}};$$
$$\tau_{m,\mathrm{CaS}}(V) = 1.4 + \frac{7}{e^{(V+27)/10}+e^{(V+70)/-13}}, \qquad \tau_{h,\mathrm{CaS}}(V) = 60 + \frac{150}{e^{(V+55)/9}+e^{(V+65)/-16}};$$
$$\tau_{m,\mathrm{A}}(V) = 11.6 - \frac{10.4}{1+e^{(V+32.9)/-15.2}}, \qquad \tau_{h,\mathrm{A}}(V) = 38.6 - \frac{29.2}{1+e^{(V+38.9)/-26.5}};$$
$$\tau_{m,\mathrm{KCa}}(V) = 90.3 - \frac{75.1}{1+e^{(V+46)/-22.7}};$$
$$\tau_{m,\mathrm{Kd}}(V) = 7.2 - \frac{6.4}{1+e^{(V+28.3)/-19.2}};$$
$$\tau_{m,\mathrm{H}}(V) = 272 - \frac{-1499}{1+e^{(V+42.2)/-8.73}}.$$

B2 Dopaminergic neuron

The DA conductance-based model consists of the following ODE system:

$$\begin{aligned}
C\dot{V} =& -\bar{g}_{\mathrm{Na}} m_{\mathrm{Na}}^3 h_{\mathrm{Na}} (V - E_{\mathrm{Na}}) - \bar{g}_{\mathrm{Kd}} m_{\mathrm{Kd}}^3 (V - E_{\mathrm{K}}) - \bar{g}_{\mathrm{CaL}} m_{\mathrm{CaL}}^2 (V - E_{\mathrm{Ca}}) \\
& - \bar{g}_{\mathrm{CaN}} m_{\mathrm{CaN}} (V - E_{\mathrm{Ca}}) - \bar{g}_{\mathrm{ERG}} m_{\mathrm{ERG}} (V - E_{\mathrm{K}}) - g_{\mathrm{leak}} (V - E_{\mathrm{leak}}) \\
& - \bar{g}_{\mathrm{NMDA}} \frac{(V - E_{\mathrm{NMDA}})}{1 + Mg \cdot exp(-0.08V)/10} + I_{\mathrm{app}}; \\
\tau_{m,\mathrm{Na}}(V)\dot{m}_{\mathrm{Na}} =& m_{\mathrm{Na},\infty}(V) - m_{\mathrm{Na}}; \\
\tau_{h,\mathrm{Na}}(V)\dot{h}_{\mathrm{Na}} =& h_{\mathrm{Na},\infty}(V) - h_{\mathrm{Na}}; \\
\tau_{m,\mathrm{Kd}}(V)\dot{m}_{\mathrm{Kd}} =& m_{\mathrm{Kd},\infty}(V) - m_{\mathrm{Kd}}; \\
\tau_{m,\mathrm{CaL}}(V)\dot{m}_{\mathrm{CaL}} =& m_{\mathrm{CaL},\infty}(V) - m_{\mathrm{CaL}}; \\
\tau_{m,\mathrm{CaN}}(V)\dot{m}_{\mathrm{CaN}} =& m_{\mathrm{CaN},\infty}(V) - m_{\mathrm{CaN}}; \\
\dot{m}_{\mathrm{ERG}} =& a_{\mathrm{ERG},0}(V)(1 - m_{\mathrm{ERG}} - i_{\mathrm{ERG}}) + b_{\mathrm{ERG},i}(V) i_{\mathrm{ERG}} - m_{\mathrm{ERG}}(a_{\mathrm{ERG},i}(V) + b_{\mathrm{ERG},0}(V)); \\
\dot{i}_{\mathrm{ERG}} =& a_{\mathrm{ERG},i}(V) m_{\mathrm{ERG}} - b_{\mathrm{ERG},i}(V) i_{\mathrm{ERG}},
\end{aligned}$$

where the different parameters can be found in Table B2.1.

Model parameters	
C	$1\,\mu\mathrm{F/cm^2}$
E_{Na}	$60\,\mathrm{mV}$
E_{K}	$-85\,\mathrm{mV}$
E_{Ca}	$60\,\mathrm{mV}$
E_{NMDA}	$0\,\mathrm{mV}$
E_{leak}	$-50\,\mathrm{mV}$
Mg	1.4

Table B2.1: In the DA conductance-based model, parameters include C for membrane capacitance, E_{ion} representing the Nernst reversal potential of the considered ion and Mg for the magnesium ion concentration. These parameters remained constant throughout this thesis.

The steady-state functions of gating variables consist of the following equations:

$$m_{\mathrm{Na},\infty}(V) = \frac{1}{1+e^{(V+30.0907)/-9.7264}}, \quad h_{\mathrm{Na},\infty}(V) = \frac{1}{1+e^{(V+54.0289)/10.7665}};$$
$$m_{\mathrm{Kd},\infty}(V) = \frac{1}{1+e^{(V+25)/-12}};$$
$$m_{\mathrm{CaL},\infty}(V) = \frac{1}{1+e^{(V+50)/-2}};$$
$$m_{\mathrm{CaN},\infty}(V) = \frac{1}{1+e^{(V+30)/-7}};$$
$$a_{\mathrm{ERG},0}(V) = 0.0036e^{0.0759V}, \qquad b_{\mathrm{ERG},0}(V) = 1.2523 \cdot 10^{-5} \cdot e^{-0.0671V};$$
$$a_{\mathrm{ERG},i}(V) = 0.1e^{0.1189V}, \qquad b_{\mathrm{ERG},i}(V) = 0.003e^{-0.0733V}.$$

The time constant functions of gating variables consist of the following equations:

$$\tau_{m,\mathrm{Na}}(V) = 0.01 + \frac{1}{(15.6504 + 0.4043V)/(1 - e^{-19.565-0.5052V}) + 3.0212e^{-0.007463V}};$$
$$\tau_{h,\mathrm{Na}}(V) = 0.4 + \frac{1}{0.00050754e^{-0.063213V} + 9.7529e^{0.13442V}};$$
$$\tau_{m,\mathrm{Kd}}(V) = 20 - \frac{18}{1+e^{(V+38)/-10}};$$
$$\tau_{m,\mathrm{CaL}}(V) = 30 - \frac{28}{1+e^{(V+45)/-3}};$$
$$\tau_{m,\mathrm{CaN}}(V) = 30 - \frac{25}{1+e^{(V+55)/-6}}.$$

B3 Aplysia neuron

The Aplysia conductance-based model consists of the following ODE system:

$$\begin{aligned}
C\dot{V} =& -\bar{g}_{\mathrm{Na}} m_{\mathrm{Na},\infty}(V)^3 h_{\mathrm{Na}}(V - E_{\mathrm{Na}}) - \bar{g}_{\mathrm{Kd}} m_{\mathrm{Kd}}^4 (V - E_{\mathrm{K}}) - \bar{g}_{\mathrm{TTX}} m_{\mathrm{TTX}}(V - E_{\mathrm{Na}}) \\
& - \bar{g}_{\mathrm{KCa}} \frac{[\mathrm{Ca}^{+2}]}{0.5 + [\mathrm{Ca}^{+2}]}(V - E_{\mathrm{K}}) - g_{\mathrm{leak}}(V - E_{\mathrm{leak}}) + I_{\mathrm{app}}; \\
\tau_{h,\mathrm{Na}}(V)\dot{h}_{\mathrm{Na}} =& h_{\mathrm{Na},\infty}(V) - h_{\mathrm{Na}}; \\
\tau_{m,\mathrm{Kd}}(V)\dot{m}_{\mathrm{Kd}} =& m_{\mathrm{Kd},\infty}(V) - m_{\mathrm{Kd}}; \\
\tau_{m,\mathrm{TTX}}(V)\dot{m}_{\mathrm{TTX}} =& m_{\mathrm{TTX},\infty}(V) - m_{\mathrm{TTX}}; \\
3333 \cdot \dot{[\mathrm{Ca}^{+2}]} =& -0.0085\,[\bar{g}_{\mathrm{TTX}} m_{\mathrm{TTX}}(V - E_{\mathrm{Ca}})] - [\mathrm{Ca}^{+2}],
\end{aligned}$$

where the different parameters can be found in Table B3.1.

Model parameters	
C	$1\,\mu\mathrm{F/cm}^2$
E_{Na}	$30\,\mathrm{mV}$
E_{K}	$-75\,\mathrm{mV}$
E_{Ca}	$140\,\mathrm{mV}$
E_{leak}	$-40\,\mathrm{mV}$
Mg	1.4

Table B3.1: In the Aplysia conductance-based model, parameters include C for membrane capacitance and E_{ion} representing the Nernst reversal potential of the considered ion. These parameters remained constant throughout this thesis.

The steady-state functions of gating variables consist of the following equations with $Vs(V) = \frac{127V+8265}{105}$ (the voltage dependency of Vs is dropped for clarity reasons):

$$\begin{aligned}
\alpha_{m\,\mathrm{Na}}(V) &= 0.1\frac{50 - Vs}{e^{(50-Vs)/10} - 1}, & \alpha_{h\,\mathrm{Na}}(V) &= 0.07e^{(25-Vs)/20}; \\
\beta_{m\,\mathrm{Na}}(V) &= 4e^{(25-Vs)/18}, & \beta_{h\,\mathrm{Na}}(V) &= \frac{1}{e^{(55-Vs)/10} + 1}; \\
m_{\mathrm{Na},\infty}(V) &= \frac{\alpha_{m\,\mathrm{Na}}(V)}{\alpha_{m\,\mathrm{Na}}(V) + \beta m\,\mathrm{Na}(V)}, & h_{\mathrm{Na},\infty}(V) &= \frac{\alpha_{h\,\mathrm{Na}}(V)}{\alpha_{h\,\mathrm{Na}}(V) + \beta h\,\mathrm{Na}(V)}; \\
\alpha_{m\,\mathrm{Kd}}(V) &= 0.01\frac{55 - Vs}{e^{(55-Vs)/10} - 1}; \\
\beta_{m\,\mathrm{Kd}}(V) &= 0.125e^{(45-Vs)/80}; \\
m_{\mathrm{Kd},\infty}(V) &= \frac{\alpha_{m\,\mathrm{Kd}}(V)}{\alpha_{m\,\mathrm{Kd}}(V) + \beta m\,\mathrm{Kd}(V)}; \\
m_{\mathrm{TTX},\infty}(V) &= \frac{1}{e^{-0.15(V+50)} + 1}.
\end{aligned}$$

The time constant functions of gating variables consist of the following equations:

$$\begin{aligned}
\tau_{h,\mathrm{Na}}(V) &= \frac{12.5}{\alpha_{h\,\mathrm{Na}}(V) + \beta h\,\mathrm{Na}(V)};\\
\tau_{m,\mathrm{Kd}}(V) &= \frac{12.5}{\alpha_{m\,\mathrm{Kd}}(V) + \beta m\,\mathrm{Kd}(V)};\\
\tau_{m,\mathrm{TTX}}(V) &= 235.
\end{aligned}$$

C Codes used for NmodController examples

C1 Stomatogastric neuron

C1.1 Initializing the model

The STG model is composed of 7 voltage-gated ionic currents, one of which is calcium-dependent (Liu et al., 1998):

1. Transient sodium current I_{Na} (2 gating variables);
2. T-type calcium current I_{CaT} (2 gating variables);
3. Slow calcium current I_{CaS} (2 gating variables);
4. A-type potassium current I_{A} (2 gating variables);
5. Calcium controlled potassium current I_{KCa} (1 gating variable calcium dependent);
6. Delayed rectified potassium current I_{Kd} (1 gating variable);
7. H current I_{H} (1 gating variable).

The voltage equation is expressed as:

$$\begin{aligned} C\dot{V} = &- \bar{g}_{\mathrm{Na}} m_{\mathrm{Na}}^3 h_{\mathrm{Na}} (V - E_{\mathrm{Na}}) - \bar{g}_{\mathrm{CaT}} m_{\mathrm{CaT}}^3 h_{\mathrm{CaT}} (V - E_{\mathrm{Ca}}) - \bar{g}_{\mathrm{CaS}} m_{\mathrm{CaS}}^3 h_{\mathrm{CaS}} (V - E_{\mathrm{Ca}}) \\ &- \bar{g}_{\mathrm{A}} m_{\mathrm{A}}^3 h_{\mathrm{A}} (V - E_{\mathrm{K}}) - \bar{g}_{\mathrm{KCa}} m_{\mathrm{KCa}}^4 (V - E_{\mathrm{K}}) - \bar{g}_{\mathrm{Kd}} m_{\mathrm{Kd}}^4 (V - E_{\mathrm{K}}) \\ &- \bar{g}_{\mathrm{H}} m_{\mathrm{H}} (V - E_{\mathrm{H}}) - g_{\mathrm{leak}} (V - E_{\mathrm{leak}}) + I_{ext}, \end{aligned}$$

and the intracellular calcium dynamics are described by:

$$\tau_{Ca} \cdot [\dot{Ca}] = -0.94 \cdot I_{CaT} - 0.94 \cdot I_{CaS} - [Ca] + Ca_{\mathrm{eq}},$$

with $\tau_{Ca} = 20$ and $Ca_{\mathrm{eq}} = 0.05$.

The next few lines of code show how to initialize such a model using *NmodController.jl*.

```
### Kinetics and parameters for the STG model
# STG gating Functions
STG_boltz(V, A, B) = 1 / (1 + exp((V+A) / B))
tauX(V, A, B, D, E) = A - B / (1 + exp((V+D) / E))

# Initializing Nernst reversal potentials
STG_ENa = 50. # Sodium reversal potential
STG_EK = -80. # Potassium reversal potential
STG_ECa = 80. # Calcium reversal potential
STG_EH = -20. # Reversal potential for the H-current (permeable to both sodium and potassium ions)
STG_Eleak = -50. # Reversal potential of leak channels
```

```
# Na current
STG_mNa_inf(V) = STG_boltz(V, 25.5, -5.29)
STG_tau_mNa(V) = tauX(V, 1.32, 1.26, 120., -25.)
STG_hNa_inf(V) = STG_boltz(V, 48.9, 5.18)
STG_tau_hNa(V) = (0.67 / (1 + exp((V+62.9)/-10.0))) * (1.5 + 1 / (1+exp((V+34.9)/3.6)))

# Kd current
STG_mKd_inf(V) = STG_boltz(V, 12.3, -11.8)
STG_tau_mKd(V) = tauX(V, 7.2, 6.4, 28.3, -19.2)

# KCa current
STG_mKCa_inf(V, Ca) = (Ca / (Ca+3)) * (1 / (1+exp((V+28.3)/-12.6)))
STG_tau_mKCa(V) = tauX(V, 90.3, 75.1, 46., -22.7)

# CaT current
STG_mCaT_inf(V) = STG_boltz(V, 27.1, -7.2)
STG_tau_mCaT(V) = tauX(V, 21.7, 21.3, 68.1, -20.5)
STG_hCaT_inf(V) = STG_boltz(V, 32.1, 5.5)
STG_tau_hCaT(V) = tauX(V, 105., 89.8, 55., -16.9)

# CaS current
STG_mCaS_inf(V) = STG_boltz(V, 33., -8.1)
STG_tau_mCaS(V) = 1.4 + (7 / ((exp((V+27)/10)) + (exp((V+70)/-13))))
STG_hCaS_inf(V) = STG_boltz(V, 60., 6.2)
STG_tau_hCaS(V) = 60 + (150 / ((exp((V+55)/9)) + (exp((V+65)/-16))))

# A current
STG_mA_inf(V) = STG_boltz(V, 27.2, -8.7)
STG_tau_mA(V) = tauX(V, 11.6, 10.4, 32.9, -15.2)
STG_hA_inf(V) = STG_boltz(V, 56.9, 4.9)
STG_tau_hA(V) = tauX(V, 38.6, 29.2, 38.9, -26.5)

# H current
STG_mH_inf(V) = STG_boltz(V, 70., 6.)
STG_tau_mH(V) = tauX(V, 272., -1499., 42.2, -8.73)

using NmodController

# Building Na current
STG_NaCurrent = initializeCurrent("Na", STG_ENa, numberOfGatings=2, exponents=[3, 1],
    activationSteadyStateGating=STG_mNa_inf, activationTimeConstant=STG_tau_mNa,
    inactivationSteadyStateGating=STG_hNa_inf, inactivationTimeConstant=STG_tau_hNa)
```

```
# Building Kd current
STG_KdCurrent = initializeCurrent("Kd", STG_EK, exponents=4,
    activationSteadyStateGating=STG_mKd_inf, activationTimeConstant=STG_tau_mKd)

# Building KCa current
STG_KCaCurrent = initializeCurrent("KCa", STG_EK, exponents=4,
    activationSteadyStateGating=STG_mKCa_inf, activationTimeConstant=STG_tau_mKCa,
    calciumDependency=true)

# Building CaT current
STG_CaTCurrent = initializeCurrent("CaT", STG_ECa, numberOfGatings=2, exponents=[3, 1],
    activationSteadyStateGating=STG_mCaT_inf, activationTimeConstant=STG_tau_mCaT,
    inactivationSteadyStateGating=STG_hCaT_inf, inactivationTimeConstant=STG_tau_hCaT)

# Building CaS current
STG_CaSCurrent = initializeCurrent("CaS", STG_ECa, numberOfGatings=2, exponents=[3, 1],
    activationSteadyStateGating=STG_mCaS_inf, activationTimeConstant=STG_tau_mCaS,
    inactivationSteadyStateGating=STG_hCaS_inf, inactivationTimeConstant=STG_tau_hCaS)

# Building A current
STG_ACurrent = initializeCurrent("A", STG_EK, numberOfGatings=2, exponents=[3, 1],
    activationSteadyStateGating=STG_mA_inf, activationTimeConstant=STG_tau_mA,
    inactivationSteadyStateGating=STG_hA_inf, inactivationTimeConstant=STG_tau_hA)

# Building H current
STG_HCurrent = initializeCurrent("H", STG_EH, exponents=1,
    activationSteadyStateGating=STG_mH_inf, activationTimeConstant=STG_tau_mH)

# Building calcium dynamics
CaDyn = initializeCalciumDynamics(["CaT", "CaS"], [-0.94, -0.94], 0.05, 20)

# Wrapping all currents in a vector
STG_ionCurrents = [STG_NaCurrent, STG_CaTCurrent, STG_CaSCurrent, STG_ACurrent,
    STG_KCaCurrent, STG_KdCurrent, STG_HCurrent]
STG_gvec = [800., 3., 3., 80., 60., 90., 0.1]

# Initializing the STG model
STG = initializeNeuronModel(STG_ionCurrents, C=0.1, calciumDynamics=CaDyn,
    leakageConductance=0.01, reversalLeakagePotential=STG_Eleak, maximumConductances=STG_gvec)
```

C1.2 Computing the DICs

The next few lines of code show how to compute and plot the DICs, sensitivity matrix, and threshold voltage of the spiking STG model using *NmodController.jl*.

```
# Defining some timescales
STG_tauFast = STG_tau_mNa
STG_tauSlow = STG_tau_mKd
STG_tauUltraslow = STG_tau_mH

# Computing DICs for the spiking model
STG_gf_spiking, STG_gs_spiking, STG_gu_spiking = computeDICs(STG_spiking, STG_tauFast,
    STG_tauSlow, STG_tauUltraslow, tauCa=500000.)

# Computing the sensitivity matrix (which is a voltage function that can be called by STG_S_spiking(
STG_S_spiking = computeDICs(STG_spiking, STG_tauFast,
    STG_tauSlow, STG_tauUltraslow, tauCa=500000., onlyS=true)

# Computing the threshold voltage
STG_Vth = computeThresholdVoltage(STG_gf_spiking, STG_gs_spiking, STG_gu_spiking)

# Plotting
V = -80 : 0.1 : 40.
Vzoom = -53. : 0.01 : -48.
p1 = plot(V, STG_gf_spiking.(V), linewidth=1.5, legend=false, size=(600, 200), color=:gray30)
vline!([Vzoom[1]], linewidth=1.5, color=:black, linestyle=:dash)
vline!([Vzoom[end]], linewidth=1.5, color=:black, linestyle=:dash)
ylabel!("g_f")
p1zoom = plot(Vzoom, STG_gf_spiking.(Vzoom), linewidth=1.5, legend=false,
    size=(300, 200), color=:gray30)
vline!([STG_Vth], linewidth=1.5, color=:firebrick1, linestyle=:dashdot)
p2 = plot(V, STG_gs_spiking.(V), linewidth=1.5, legend=false, size=(600, 200), color=:gray30)
vline!([Vzoom[1]], linewidth=1.5, color=:black, linestyle=:dash)
vline!([Vzoom[end]], linewidth=1.5, color=:black, linestyle=:dash)
ylabel!("g_s")
p2zoom = plot(Vzoom, STG_gs_spiking.(Vzoom), linewidth=1.5,
    size=(300, 200), color=:gray30, label="")
vline!([STG_Vth], linewidth=1.5, color=:firebrick1, linestyle=:dashdot, label="V_th")
p3 = plot(V, STG_gu_spiking.(V), linewidth=1.5, legend=false, size=(600, 200), color=:gray30)
vline!([Vzoom[1]], linewidth=1.5, color=:black, linestyle=:dash)
vline!([Vzoom[end]], linewidth=1.5, color=:black, linestyle=:dash)
xlabel!("V")
ylabel!("g_u")
p3zoom = plot(Vzoom, STG_gu_spiking.(Vzoom), linewidth=1.5, legend=false,
```

```
    size=(300, 200), color=:gray30)
vline!([STG_Vth], linewidth=1.5, color=:firebrick1, linestyle=:dashdot)
xlabel!("V")
CC = plot(p1, p1zoom, p2, p2zoom, p3, p3zoom, layout=(3, 2),
    size=(900, 600), margins=10px, dpi=500)
```

The next few lines of code show how to compute and plot the DICs, sensitivity matrix, and threshold voltage of the bursting STG model using *NmodController.jl*.

```
# Defining some timescales
STG_tauFast = STG_tau_mNa
STG_tauSlow = STG_tau_mKd
STG_tauUltraslow = STG_tau_mH

# Computing DICs for the bursting model
STG_gf_bursting, STG_gs_bursting, STG_gu_bursting = computeDICs(STG_bursting, STG_tauFast,
    STG_tauSlow, STG_tauUltraslow, tauCa=500000.)

# Plotting
V = -80 : 0.1 : 40.
Vzoom = -53. : 0.01 : -48.
p1 = plot(V, STG_gf_bursting.(V), linewidth=1.5, legend=false, size=(600, 200), color=:gray30)
vline!([Vzoom[1]], linewidth=1.5, color=:black, linestyle=:dash)
vline!([Vzoom[end]], linewidth=1.5, color=:black, linestyle=:dash)
ylabel!("g_f")
p1zoom = plot(Vzoom, STG_gf_bursting.(Vzoom), linewidth=1.5, legend=false,
    size=(300, 200), color=:gray30)
vline!([STG_Vth], linewidth=1.5, color=:firebrick1, linestyle=:dashdot)
p2 = plot(V, STG_gs_bursting.(V), linewidth=1.5, legend=false, size=(600, 200), color=:gray30)
vline!([Vzoom[1]], linewidth=1.5, color=:black, linestyle=:dash)
vline!([Vzoom[end]], linewidth=1.5, color=:black, linestyle=:dash)
ylabel!("g_s")
p2zoom = plot(Vzoom, STG_gs_bursting.(Vzoom), linewidth=1.5,
    size=(300, 200), color=:gray30, label="")
vline!([STG_Vth], linewidth=1.5, color=:firebrick1, linestyle=:dashdot, label="V_th")
p3 = plot(V, STG_gu_bursting.(V), linewidth=1.5, legend=false, size=(600, 200), color=:gray30)
vline!([Vzoom[1]], linewidth=1.5, color=:black, linestyle=:dash)
vline!([Vzoom[end]], linewidth=1.5, color=:black, linestyle=:dash)
xlabel!("V")
ylabel!("g_u")
p3zoom = plot(Vzoom, STG_gu_bursting.(Vzoom), linewidth=1.5, legend=false,
    size=(300, 200), color=:gray30)
vline!([STG_Vth], linewidth=1.5, color=:firebrick1, linestyle=:dashdot)
xlabel!("V")
```

```
CC = plot(p1, p1zoom, p2, p2zoom, p3, p3zoom, layout=(3, 2),
    size=(900, 600), margins=10px, dpi=500)
```

C1.3 Simulating the model

The next few lines of code show how to simulate the spiking STG model using *NmodController.jl*.

```
# First writing uncontrolled ODE function file
writeUncontrolledODEs(STG_spiking, filename="STG_ODE.jl")

# Including the newly written file
include("STG_ODE.jl")

# Definition of simulation time (in ms)
Tfinal = 2000
tspan  = (0., Tfinal)

# Definition of membrane capacitance and maximal conductance values
gNa   = 4000. # Sodium current maximal conductance
gCaT  = 3. # T-type calcium current maximal conductance
gCaS  = 4. # Slow calcium current maximal conductance
gA    = 175. # A-type potassium current maximal conductance
gKCa  = 110. # Calcium-activated potassium current maximal conductance
gKd   = 137. # Delayed-rectifier potassium current maximal conductance
gH    = 0.3 # H-current maximal conductance
gleak = 0.01 # Leak current maximal conductance
C = 1. # Membrane capacitance

# Input current definition (always a function of time)
Iapp(t) = 0.

# Parameter vector for simulations
p = (Iapp, gNa, gCaT, gCaS, gA, gKCa, gKd, gH, gleak, C)

# Initial conditions
V0  = -70.
Ca0 = 0.5
x0  = [V0, STG_mNa_inf(V0), STG_hNa_inf(V0), STG_mCaT_inf(V0), STG_hCaT_inf(V0),
    STG_mCaS_inf(V0), STG_hCaS_inf(V0), STG_mA_inf(V0), STG_hA_inf(V0),
    STG_mKCa_inf(V0, Ca0), STG_mKd_inf(V0), STG_mH_inf(V0), Ca0]

# Simulation
prob = ODEProblem(STG_ODE, x0, tspan, p) # Describing the problem
sol  = solve(prob) # Solving the problem
```

```
# Retrieving variables
tt        = 0. : 0.2 : Tfinal
x         = sol(tt)
V_plot   = x[1, :]

# Plot
p = plot(tt/1e3, V_plot, xlims=(0, 2), xticks=[0, 2], ylims=(-100, 60), yticks=[-100, 60],
    linewidth=1.5, legend=false, size=(600, 200), color=:gray30,
    margins=20px, dpi=500)
ylabel!("V (mV)")
xlabel!("t (s)")
```

With `STG_ODE.jl` containing the following code.

```
#=
    This file contains differential equations describing the CB model of interest
=#

# Function that outputs values of variables derivatives
function STG_ODE(dx, x, p, t)
        # Parameters
        Iapp = p[1](t) # Time dependent applied current
        gNa = p[2] # Maximum conductance of current Na
        gCaT = p[3] # Maximum conductance of current CaT
        gCaS = p[4] # Maximum conductance of current CaS
        gA = p[5] # Maximum conductance of current A
        gKCa = p[6] # Maximum conductance of current KCa
        gKd = p[7] # Maximum conductance of current Kd
        gH = p[8] # Maximum conductance of current H
        gleak = p[9] # Leakage conductance
        C = p[10] # Membrane capacitance

        # Variables
        V = x[1] # Membrane voltage
        mNa = x[2] # Activation gating variable of current Na
        hNa = x[3] # Inactivation gating variable of current Na
        mCaT = x[4] # Activation gating variable of current CaT
        hCaT = x[5] # Inactivation gating variable of current CaT
        mCaS = x[6] # Activation gating variable of current CaS
        hCaS = x[7] # Inactivation gating variable of current CaS
        mA = x[8] # Activation gating variable of current A
        hA = x[9] # Inactivation gating variable of current A
        mKCa = x[10] # Activation gating variable of current KCa
```

```
        mKd = x[11] # Activation gating variable of current Kd
        mH = x[12] # Activation gating variable of current H
        Ca = x[13] # Ca concentration

        # ODEs
        dx[1] = (1/C) * (- gNa*mNa^3*hNa^1*(V - 50.0) -
                                        gCaT*mCaT^3*hCaT^1*(V - 80.0) -
                                        gCaS*mCaS^3*hCaS^1*(V - 80.0) -
                                        gA*mA^3*hA^1*(V - -80.0) -
                                        gKCa*mKCa^4*(V - -80.0) -
                                        gKd*mKd^4*(V - -80.0) -
                                        gH*mH^1*(V - -20.0) -
                                        gleak*(V - -50.0) + Iapp)
        dx[2] = (1/STG_tau_mNa(V)) * (STG_mNa_inf(V) - mNa)
        dx[3] = (1/STG_tau_hNa(V)) * (STG_hNa_inf(V) - hNa)
        dx[4] = (1/STG_tau_mCaT(V)) * (STG_mCaT_inf(V) - mCaT)
        dx[5] = (1/STG_tau_hCaT(V)) * (STG_hCaT_inf(V) - hCaT)
        dx[6] = (1/STG_tau_mCaS(V)) * (STG_mCaS_inf(V) - mCaS)
        dx[7] = (1/STG_tau_hCaS(V)) * (STG_hCaS_inf(V) - hCaS)
        dx[8] = (1/STG_tau_mA(V)) * (STG_mA_inf(V) - mA)
        dx[9] = (1/STG_tau_hA(V)) * (STG_hA_inf(V) - hA)
        dx[10] = (1/STG_tau_mKCa(V)) * (STG_mKCa_inf(V, Ca) - mKCa)
        dx[11] = (1/STG_tau_mKd(V)) * (STG_mKd_inf(V) - mKd)
        dx[12] = (1/STG_tau_mH(V)) * (STG_mH_inf(V) - mH)
        dx[13] = (-0.94*gCaT*mCaT^3*hCaT^1*(V - 80.0) +
            -0.94*gCaS*mCaS^3*hCaS^1*(V - 80.0) + -Ca + 0.05) / 20.0
end
```

Note that a small adaptation of `STG_ODE.jl` has been made to ensure that the names of the gating functions match the actual ones.

The next few lines of code show how to simulate the neuromodulated spiking STG model using *NmodController.jl*.

```
# First writing controlled ODE function file
writeControlledODEs(STG_spiking, ["CaS", "A"], ["s", "u"], filename="ControlledSTG_ODE.jl")

# Including the newly written file
include("ControlledSTG_ODE.jl")

# Definition of simulation time (in ms)
Tfinal = 5000
tspan  = (0., Tfinal)
```

```
# Definition of membrane capacitance and maximal conductance values
gNa   = 4000. # Sodium current maximal conductance
gCaT  = 3. # T-type calcium current maximal conductance
gCaS  = 4. # Slow calcium current maximal conductance
gA    = 175. # A-type potassium current maximal conductance
gKCa  = 110. # Calcium-activated potassium current maximal conductance
gKd   = 137. # Delayed-rectifier potassium current maximal conductance
gH    = 0.3 # H-current maximal conductance
gleak = 0.01 # Leak current maximal conductance
C = 1. # Membrane capacitance

# Input current definition (always a function of time)
Iapp(t) = 0.

# Definition of controller parameters
alpha = 5e-3 # Rate of transfer between intracellular and membrane
beta = 5e-3 # Rate of degradation of intracellular proteins
Kp = 3e-4 # Proprtional gain
Ki = 5e-6 # Integral gain
gsth(t) = 5. - 13 * (t > 500) # Reference gs(Vth)
guth(t) = 4. # Reference gu(Vth)

# Parameter vector for simulations
p = (Iapp, gNa, gCaT, gKCa, gKd, gH, gleak, C, alpha, beta, Kp, Ki,
    STG_S_spiking(STG_Vth), gsth, guth)

# Initial conditions
V0  = -70.
Ca0 = 0.5
x0  = [V0, STG_mNa_inf(V0), STG_hNa_inf(V0), STG_mCaT_inf(V0), STG_hCaT_inf(V0),
    STG_mCaS_inf(V0), STG_hCaS_inf(V0), STG_mA_inf(V0), STG_hA_inf(V0),
    STG_mKCa_inf(V0, Ca0), STG_mKd_inf(V0), STG_mH_inf(V0), Ca0, gCaS, gCaS, 0, gA, gA, 0]

# Simulation
prob = ODEProblem(ControlledSTG_ODE, x0, tspan, p) # Describing the problem
sol  = solve(prob) # Solving the problem

# Retrieving variables
tt        = 0. : 0.2 : Tfinal
x         = sol(tt)
V_plot    = x[1, :]
gCaS_plot = x[15, :]
gA_plot   = x[18, :]
```

```
# Plot
p1 = plot(tt/1e3, V_plot, xlims=(0, 5), xticks=[0, 5], ylims=(-100, 60), yticks=[-100, 60],
    linewidth=1.5, legend=false, size=(600, 200), color=:gray30)
ylabel!("V (mV)")
p2 = plot(tt/1e3, gCaS_plot, xlims=(0, 5), xticks=[0, 5], ylims=(0, 20), yticks=[0, 20],
    linewidth=1.5, legend=false, size=(600, 200), color=:gray30)
ylabel!("gCaS")
p3 = plot(tt/1e3, gA_plot, xlims=(0, 5), xticks=[0, 5], ylims=(0, 200), yticks=[0, 200],
    linewidth=1.5, legend=false, size=(600, 200), color=:gray30)
ylabel!("gA")
xlabel!("t (s)")
CC = plot(p1, p2, p3, layout=(3, 1), size=(900, 600), margins=10px, dpi=500)
```

With `ControlledSTG_ODE.jl` containing the following code.

```
#=
        This file contains differential equations describing the controlled CB model of interest
=#

# Function that outputs values of variables derivatives
function ControlledSTG_ODE(dx, x, p, t)
        # Parameters
        Iapp = p[1](t) # Time dependent applied current
        gNa = p[2] # Maximum conductance of current Na
        gCaT = p[3] # Maximum conductance of current CaT
        gKCa = p[4] # Maximum conductance of current KCa
        gKd = p[5] # Maximum conductance of current Kd
        gH = p[6] # Maximum conductance of current H
        gleak = p[7] # Leakage conductance
        C = p[8] # Membrane capacitance
        alpha = p[9] # Rate of transfer between intracellular and membrane
        beta = p[10] # Rate of degradation of intracellular proteins
        Kp = p[11] # Proportional gain
        Ki = p[12] # Integral gain
        SVth = p[13] # Sensitivity matrix at threshold voltage
        gsth = p[14](t) # Reference gs(Vth)
        guth = p[15](t) # Reference gu(Vth)

        # Variables
        V = x[1] # Membrane voltage
        mNa = x[2] # Activation gating variable of current Na
        hNa = x[3] # Inactivation gating variable of current Na
        mCaT = x[4] # Activation gating variable of current CaT
```

```
        hCaT = x[5] # Inactivation gating variable of current CaT
        mCaS = x[6] # Activation gating variable of current CaS
        hCaS = x[7] # Inactivation gating variable of current CaS
        mA = x[8] # Activation gating variable of current A
        hA = x[9] # Inactivation gating variable of current A
        mKCa = x[10] # Activation gating variable of current KCa
        mKd = x[11] # Activation gating variable of current Kd
        mH = x[12] # Activation gating variable of current H
        Ca = x[13] # Ca concentration
        gCaSi = x[14] # Intracellular maximum conductance of current CaS
        gCaS = x[15] # Maximum conductance of current CaS
        zCaS = x[16] # Integral variable of current CaS
        gAi = x[17] # Intracellular maximum conductance of current A
        gA = x[18] # Maximum conductance of current A
        zA = x[19] # Integral variable of current A

        # ODEs
        dx[1] = (1/C) * (- gNa*mNa^3*hNa^1*(V - 50.0) -
                                        gCaT*mCaT^3*hCaT^1*(V - 80.0) -
                                        gCaS*mCaS^3*hCaS^1*(V - 80.0) -
                                        gA*mA^3*hA^1*(V - -80.0) -
                                        gKCa*mKCa^4*(V - -80.0) -
                                        gKd*mKd^4*(V - -80.0) -
                                        gH*mH^1*(V - -20.0) -
                                        gleak*(V - -50.0) + Iapp)
        dx[2] = (1/STG_tau_mNa(V)) * (STG_mNa_inf(V) - mNa)
        dx[3] = (1/STG_tau_hNa(V)) * (STG_hNa_inf(V) - hNa)
        dx[4] = (1/STG_tau_mCaT(V)) * (STG_mCaT_inf(V) - mCaT)
        dx[5] = (1/STG_tau_hCaT(V)) * (STG_hCaT_inf(V) - hCaT)
        dx[6] = (1/STG_tau_mCaS(V)) * (STG_mCaS_inf(V) - mCaS)
        dx[7] = (1/STG_tau_hCaS(V)) * (STG_hCaS_inf(V) - hCaS)
        dx[8] = (1/STG_tau_mA(V)) * (STG_mA_inf(V) - mA)
        dx[9] = (1/STG_tau_hA(V)) * (STG_hA_inf(V) - hA)
        dx[10] = (1/STG_tau_mKCa(V)) * (STG_mKCa_inf(V, Ca) - mKCa)
        dx[11] = (1/STG_tau_mKd(V)) * (STG_mKd_inf(V) - mKd)
        dx[12] = (1/STG_tau_mH(V)) * (STG_mH_inf(V) - mH)
        dx[13] = (-0.94*gCaT*mCaT^3*hCaT^1*(V - 80.0)
            + -0.94*gCaS*mCaS^3*hCaS^1*(V - 80.0) + -Ca + 0.05) / 20.0

        # Retrieving which line of the sensitivity matrix matter
        timescales = [2, 3]

        # Retrieving which column of the sensitivity matrix belong to unmodulated conductances
```

```
        unmodulated = [1, 2, 5, 6, 7]

        # Retrieving which column of the sensitivity matrix belong to modulated conductances
        modulated = [3, 4]

        # Computing the right hand side of the linear system
        gDICr = [gsth, guth]
        gDICr = gDICr - SVth[timescales, unmodulated] * collect(p[2:6])

        # Computing the left hand side of the linear system
        Smod = SVth[timescales, modulated]

        # Computing the solution of the linear system
        g_r = \(Smod, gDICr)

        # Error signals and control inputs
        eCaS = g_r[1] - gCaS
        uCaS = Kp * eCaS + Ki * zCaS
        eA = g_r[2] - gA
        uA = Kp * eA + Ki * zA

        # ODEs of the controller
        dx[14] = alpha * gCaS - alpha * gCaSi - beta * gCaSi + uCaS
        dx[15] = alpha * gCaSi - alpha * gCaS
        dx[16] = eCaS
        dx[17] = alpha * gA - alpha * gAi - beta * gAi + uA
        dx[18] = alpha * gAi - alpha * gA
        dx[19] = eA
end
```

Note that a small adaptation of `ControlledSTG_ODE.jl` has been made to ensure that the names of the gating functions match the actual ones.

C2 Dopaminergic neuron

C2.1 Initializing the model

The DA model is composed of 6 voltage-gated ionic currents, one of which is magnesium-dependent (Qian et al., 2014):

1. Transient sodium current I_{Na} (2 gating variables);
2. Delayed rectified potassium current I_{Kd} (1 gating variable);
3. L-type calcium current I_{CaL} (1 gating variable);
4. N-type calcium current I_{CaN} (1 gating variable);
5. ERG potassium current I_{ERG} (1 gating variable);
6. NMDA current I_{NMDA} (1 gating variable magnesium dependent).

The voltage equation is expressed as:

$$\begin{aligned} C\dot{V} = &- \bar{g}_{\mathrm{Na}} m_{\mathrm{Na}}^3 h_{\mathrm{Na}} (V - E_{\mathrm{Na}}) - \bar{g}_{\mathrm{Kd}} m_{\mathrm{Kd}}^3 (V - E_{\mathrm{K}}) - \bar{g}_{\mathrm{CaL}} m_{\mathrm{CaL}}^2 (V - E_{\mathrm{Ca}}) \\ &- \bar{g}_{\mathrm{CaN}} m_{\mathrm{CaN}} (V - E_{\mathrm{Ca}}) - \bar{g}_{\mathrm{ERG}} m_{\mathrm{ERG}} (V - E_{\mathrm{K}}) - \bar{g}_{\mathrm{NMDA}} m_{\mathrm{NMDA}} (V - E_{\mathrm{NMDA}}) \\ &- g_{\mathrm{leak}} (V - E_{\mathrm{leak}}) + I_{ext}. \end{aligned}$$

The next few lines of code show how to initialize such a model using *NmodController.jl*.

```
### Kinetics and parameters for the DA model
# DA gating Functions
DA_boltz(V, A, B) = 1 / (1 + exp(-(V-A) / B))

# Initializing Nernst reversalPotential
DA_ENa = 60. # Sodium reversal potential
DA_EK = -85. # Potassium reversal potential
DA_ECa = 60. # Calcium reversal potential
DA_ENMDA = 0. # NMDA reversal potential
DA_Eleak = -50. # Reversal potential of leak channels

# Na current
DA_mNa_inf(V) = DA_boltz(V, -30.0907, 9.7264)
DA_tau_mNa(V) = 0.01 + 1.0 / ((-(15.6504 + 0.4043*V)/(exp(-19.565 -0.5052*V)-1.0))
    + 3.0212*exp(-7.4630e-3*V))
DA_hNa_inf(V) = DA_boltz(V, -54.0289, -10.7665)
DA_tau_hNa(V) = 0.4 + 1.0 / ((5.0754e-4*exp(-6.3213e-2*V)) + 9.7529*exp(0.13442*V))

# Kd current
DA_mKd_inf(V) = DA_boltz(V, -25., 12.)
DA_tau_mKd(V) = tauX(V, 20., 18., 38., -10.)
```

```
# CaL current
DA_mCaL_inf(V) = DA_boltz(V, -50., 2.)
DA_tau_mCaL(V) = tauX(V, 30., 28., 45., -3.)

# CaN current
DA_mCaN_inf(V) = DA_boltz(V, -30., 7.)
DA_tau_mCaN(V) = tauX(V, 30., 25., 55., -6.)

# ERG current (this current is a bit special and its gating dynamic is modified to fit
# in the generalized form described earlier)
a0ERG(V) = 0.0036 * exp(0.0759*V)
b0ERG(V) = 1.2523e-5 * exp(-0.0671*V)
aiERG(V) = 0.1 * exp(0.1189*V)
biERG(V) = 0.003 * exp(-0.0733*V)
DA_o_inf(V) = a0ERG(V)*biERG(V) / (a0ERG(V)*(aiERG(V)+biERG(V)) + b0ERG(V)*biERG(V))
# Due to this generalization, we do not have any time constant. However, this current
# is ultraslow anyway, so putting an extremely large time constant is the good way to do
DA_tau_o(V) = 100000.

# NMDA current
DA_NMDA_inf(V, Mg) = 1 / (1 + Mg*exp(-0.08*V)/10.)
# This gating variable is instantaneous, however,
# putting a null time constant is not supported yet
DA_tau_NMDA(V) = 1e-10

using NmodController

# Building Na current
DA_NaCurrent = initializeCurrent("Na", DA_ENa, numberOfGatings=2, exponents=[3, 1],
    activationSteadyStateGating=DA_mNa_inf, activationTimeConstant=DA_tau_mNa,
    inactivationSteadyStateGating=DA_hNa_inf, inactivationTimeConstant=DA_tau_hNa)

# Building Kd current
DA_KdCurrent = initializeCurrent("Kd", DA_EK, exponents=3,
    activationSteadyStateGating=DA_mKd_inf, activationTimeConstant=DA_tau_mKd)

# Building CaL current
DA_CaLCurrent = initializeCurrent("CaL", DA_ECa, exponents=2,
    activationSteadyStateGating=DA_mCaL_inf, activationTimeConstant=DA_tau_mCaL)

# Building CaN current
DA_CaSCurrent = initializeCurrent("CaN", DA_ECa, exponents=1,
```

```
    activationSteadyStateGating=DA_mCaN_inf, activationTimeConstant=DA_tau_mCaN)

# Building ERG current
DA_ERGCurrent = initializeCurrent("ERG", DA_EK, exponents=1,
    activationSteadyStateGating=DA_o_inf, activationTimeConstant=DA_tau_o)

# Building NMDA current
DA_NMDACurrent = initializeCurrent("NMDA", DA_ENMDA, exponents=1,
    activationSteadyStateGating=DA_NMDA_inf, activationTimeConstant=DA_tau_NMDA,
    MgDependency=true)

# Building a more complex model with calcium
DA_ionCurrents = [DA_NaCurrent, DA_KdCurrent, DA_CaLCurrent,
    DA_CaSCurrent, DA_ERGCurrent, DA_NMDACurrent]
DA = initializeNeuronModel(DA_ionCurrents)
```

Note that in this case, we do not specify any membrane capacitance, leakage parameters, or maximum ion channel conductances. As a result, default values will be used: $C = 1$, $g_{\text{leak}} = 1$ and $E_{\text{leak}} = -50$. Not specifying maximum ion channel conductances means that the `maximumConductances` field in the `NeuronCB` data structure will be filled with `NaN`, indicating that no maximum ion channel conductances are set for this model.

C2.2 Computing the DICs

The next few lines of code show how to compute and plot the DICs, sensitivity matrix, and threshold voltage of the spiking DA model using *NmodController.jl*.

```
# Defining some timescales
DA_tauFast = DA_tau_mNa
DA_tauSlow = DA_tau_mKd
DA_tauUltraslow(V) = 100.

# Computing DICs for the spiking model
DA_gf_spiking, DA_gs_spiking, DA_gu_spiking = computeDICs(DA_spiking, DA_tauFast,
    DA_tauSlow, DA_tauUltraslow, Mg=1.4)

# Computing the sensitivity matrix (which is a voltage function that can be called by DA_S_spiking(V
DA_S_spiking = computeDICs(DA_spiking, DA_tauFast,
    DA_tauSlow, DA_tauUltraslow, onlyS=true, Mg=1.4)

# Computing the threshold voltage
DA_Vth = -55. # Here, the algorithm is not able to find any threshold voltage

# Plotting
```

```
V = -80 : 0.1 : 40.
Vzoom = -58. : 0.01 : -53.
p1 = plot(V, DA_gf_spiking.(V), linewidth=1.5, legend=false, size=(600, 200), color=:gray30)
vline!([Vzoom[1]], linewidth=1.5, color=:black, linestyle=:dash)
vline!([Vzoom[end]], linewidth=1.5, color=:black, linestyle=:dash)
ylabel!("g_f")
p1zoom = plot(Vzoom, DA_gf_spiking.(Vzoom), linewidth=1.5, legend=false,
    size=(300, 200), color=:gray30)
vline!([DA_Vth], linewidth=1.5, color=:firebrick1, linestyle=:dashdot)
p2 = plot(V, DA_gs_spiking.(V), linewidth=1.5, legend=false, size=(600, 200), color=:gray30)
vline!([Vzoom[1]], linewidth=1.5, color=:black, linestyle=:dash)
vline!([Vzoom[end]], linewidth=1.5, color=:black, linestyle=:dash)
ylabel!("g_s")
p2zoom = plot(Vzoom, DA_gs_spiking.(Vzoom), linewidth=1.5,
    size=(300, 200), color=:gray30, label="")
vline!([DA_Vth], linewidth=1.5, color=:firebrick1, linestyle=:dashdot, label="V_th")
p3 = plot(V, DA_gu_spiking.(V), linewidth=1.5, legend=false,
    size=(600, 200), color=:gray30)
vline!([Vzoom[1]], linewidth=1.5, color=:black, linestyle=:dash)
vline!([Vzoom[end]], linewidth=1.5, color=:black, linestyle=:dash)
xlabel!("V")
ylabel!("g_u")
p3zoom = plot(Vzoom, DA_gu_spiking.(Vzoom), linewidth=1.5, legend=false,
    size=(300, 200), color=:gray30)
vline!([DA_Vth], linewidth=1.5, color=:firebrick1, linestyle=:dashdot)
xlabel!("V")
CC = plot(p1, p1zoom, p2, p2zoom, p3, p3zoom, layout=(3, 2),
    size=(900, 600), margins=10px, dpi=500)
```

The next few lines of code show how to compute and plot the DICs, sensitivity matrix, and threshold voltage of the bursting DA model using *NmodController.jl*.

```
# Defining some timescales
DA_tauFast = DA_tau_mNa
DA_tauSlow = DA_tau_mKd
DA_tauUltraslow(V) = 100.

# Computing DICs for the bursting model
DA_gf_bursting, DA_gs_bursting, DA_gu_bursting = computeDICs(DA_bursting, DA_tauFast,
    DA_tauSlow, DA_tauUltraslow, Mg=1.4)

# Plotting
V = -80 : 0.1 : 40.
Vzoom = -58. : 0.01 : -53.
```

```
p1 = plot(V, DA_gf_bursting.(V), linewidth=1.5, legend=false, size=(600, 200), color=:gray30)
vline!([Vzoom[1]], linewidth=1.5, color=:black, linestyle=:dash)
vline!([Vzoom[end]], linewidth=1.5, color=:black, linestyle=:dash)
ylabel!("g_f")
p1zoom = plot(Vzoom, DA_gf_bursting.(Vzoom), linewidth=1.5, legend=false,
    size=(300, 200), color=:gray30)
vline!([DA_Vth], linewidth=1.5, color=:firebrick1, linestyle=:dashdot)
p2 = plot(V, DA_gs_bursting.(V), linewidth=1.5, legend=false, size=(600, 200), color=:gray30)
vline!([Vzoom[1]], linewidth=1.5, color=:black, linestyle=:dash)
vline!([Vzoom[end]], linewidth=1.5, color=:black, linestyle=:dash)
ylabel!("g_s")
p2zoom = plot(Vzoom, DA_gs_bursting.(Vzoom), linewidth=1.5,
    size=(300, 200), color=:gray30, label="")
vline!([DA_Vth], linewidth=1.5, color=:firebrick1, linestyle=:dashdot, label="V_th")
p3 = plot(V, DA_gu_bursting.(V), linewidth=1.5, legend=false, size=(600, 200), color=:gray30)
vline!([Vzoom[1]], linewidth=1.5, color=:black, linestyle=:dash)
vline!([Vzoom[end]], linewidth=1.5, color=:black, linestyle=:dash)
xlabel!("V")
ylabel!("g_u")
p3zoom = plot(Vzoom, DA_gu_bursting.(Vzoom), linewidth=1.5, legend=false,
    size=(300, 200), color=:gray30)
vline!([DA_Vth], linewidth=1.5, color=:firebrick1, linestyle=:dashdot)
xlabel!("V")
CC = plot(p1, p1zoom, p2, p2zoom, p3, p3zoom, layout=(3, 2),
    size=(900, 600), margins=10px, dpi=500)
```

C2.3 Simulating the model

The next few lines of code show how to simulate the spiking DA model using *NmodController.jl*.

```
# First writing uncontrolled ODE function file
writeUncontrolledODEs(DA_spiking, filename="DA_ODE.jl")

# Including the newly written file
include("DA_ODE.jl")

# Definition of simulation time (in ms)
Tfinal = 5000
tspan  = (0., Tfinal)

# Definition of membrane capacitance and maximal conductance values
gNa   = 30. # Sodium current maximal conductance
gKd   = 5. # Delayed-rectifier potassium current maximal conductance
gCaL  = 0.03 # L-type calcium current maximal conductance
```

```
gCaN  = 0.03 # N-type calcium current maximal conductance
gERG  = 0.12 # ERG current maximal conductance
gNMDA  = 0.1 # NMDA current maximal conductance
gleak = 0.01 # Leak current maximal conductance
C = 1. # Membrane capacitance
Mg = 1.4 # Magnesium concentration

# Input current definition (always a function of time)
Iapp(t) = 0.

# Parameter vector for simulations
p = (Iapp, gNa, gKd, gCaL, gCaN, gERG, gNMDA, gleak, C, Mg)

# Initial conditions
V0 = -90.
x0  = [V0, DA_mNa_inf(V0), DA_hNa_inf(V0),
    DA_mKd_inf(V0), DA_mCaL_inf(V0), DA_mCaN_inf(V0), 0., 0.]

# Simulation
prob = ODEProblem(DA_ODE, x0, tspan, p) # Describing the problem
sol  = solve(prob) # Solving the problem

# Retrieving variables
tt        = 0. : 0.2 : Tfinal
x         = sol(tt)
V_plot   = x[1, :]

# Plot
p = plot(tt/1e3, V_plot, xlims=(0, 5), xticks=[0, 5], ylims=(-100, 60), yticks=[-100, 60],
    linewidth=1.5, legend=false, size=(600, 200), color=:gray30, margins=20px, dpi=500)
ylabel!("V (mV)")
xlabel!("t (s)")
```

With `DA_ODE.jl` containing the following code.

```
#=
        This file contains differential equations describing the CB model of interest
=#

# Function that outputs values of variables derivatives
function DA_ODE(dx, x, p, t)
        # Parameters
        Iapp = p[1](t) # Time dependent applied current
        gNa = p[2] # Maximum conductance of current Na
```

```
        gKd = p[3] # Maximum conductance of current Kd
        gCaL = p[4] # Maximum conductance of current CaL
        gCaN = p[5] # Maximum conductance of current CaN
        gERG = p[6] # Maximum conductance of current ERG
        gNMDA = p[7] # Maximum conductance of current NMDA
        gleak = p[8] # Leakage conductance
        C = p[9] # Membrane capacitance
        Mg = p[10] # Mg concentration

        # Variables
        V = x[1] # Membrane voltage
        mNa = x[2] # Activation gating variable of current Na
        hNa = x[3] # Inactivation gating variable of current Na
        mKd = x[4] # Activation gating variable of current Kd
        mCaL = x[5] # Activation gating variable of current CaL
        mCaN = x[6] # Activation gating variable of current CaN
        oERG = x[7] # ERG potassium current activation
        iERG = x[8] # ERG current intermediate

        # ODEs
        dx[1] = (1/C) * (- gNa*mNa^3*hNa^1*(V - 60.0) -
                                            gKd*mKd^3*(V - -85.0) -
                                            gCaL*mCaL^2*(V - 60.0) -
                                            gCaN*mCaN^1*(V - 60.0) -
                                            gERG*oERG^1*(V - -85.0) -
                                            gNMDA*DA_NMDA_inf(V, Mg)^1*(V - 0.0) -
                                            gleak*(V - -50.0) + Iapp)
        dx[2] = (1/DA_tau_mNa(V)) * (DA_mNa_inf(V) - mNa)
        dx[3] = (1/DA_tau_hNa(V)) * (DA_hNa_inf(V) - hNa)
        dx[4] = (1/DA_tau_mKd(V)) * (DA_mKd_inf(V) - mKd)
        dx[5] = (1/DA_tau_mCaL(V)) * (DA_mCaL_inf(V) - mCaL)
        dx[6] = (1/DA_tau_mCaN(V)) * (DA_mCaN_inf(V) - mCaN)
        dx[7] = a0ERG(V) * (1-oERG-iERG) + biERG(V) * iERG - oERG * (aiERG(V)+b0ERG(V))
        dx[8] = aiERG(V) * oERG - biERG(V) * iERG
end
```

Note that a small adaptation of `DA_ODE.jl` has been made to ensure that the names of the gating functions match their actual names. Additionally, the NMDA current has been modified to be instantaneous, meaning it no longer has a gating variable dynamic. Furthermore, the gating variable dynamics for the ERG current were corrected, as its dynamic is non-standard.

The next few lines of code show how to simulate the neuromodulated spiking DA model using *NmodController.jl*.

```
# First writing controlled ODE function file
writeControlledODEs(DA_spiking, ["CaL", "CaN"], ["s", "u"], filename="ControlledDA_ODE.jl")

# Including the newly written file
include("ControlledDA_ODE.jl")

# Definition of simulation time (in ms)
Tfinal = 10000
tspan  = (0., Tfinal)

# Definition of membrane capacitance and maximal conductance values
gNa   = 30. # Sodium current maximal conductance
gKd   = 5. # Delayed-rectifier potassium current maximal conductance
gCaL  = 0.03 # L-type calcium current maximal conductance
gCaN  = 0.03 # N-type calcium current maximal conductance
gERG  = 0.12 # ERG current maximal conductance
gNMDA  = 0.1 # NMDA current maximal conductance
gleak = 0.01 # Leak current maximal conductance
C = 1. # Membrane capacitance

# Input current definition (always a function of time)
Iapp(t) = 0.

# Definition of controller parameters
alpha = 5e-3 # Rate of transfer between intracellular and membrane
beta = 5e-3 # Rate of degradation of intracellular proteins
Kp = 3e-4 # Proprtional gain
Ki = 5e-6 # Integral gain
gsth(t) = 0.5 - 4.5 * (t > 2000) # Reference gs(Vth)
guth(t) = 5. # Reference gu(Vth)

# Parameter vector for simulations
p = (Iapp, gNa, gKd, gERG, gNMDA, gleak, C, Mg, alpha, beta,
    Kp, Ki, DA_S_spiking(DA_Vth), gsth, guth)

# Initial conditions
V0 = -90.
x0  = [V0, DA_mNa_inf(V0), DA_hNa_inf(V0), DA_mKd_inf(V0), DA_mCaL_inf(V0), DA_mCaN_inf(V0),
    0., 0., gCaL, gCaL, 0, gCaN, gCaN, 0]

# Simulation
prob = ODEProblem(ControlledDA_ODE, x0, tspan, p) # Describing the problem
sol  = solve(prob) # Solving the problem
```

```
# Retrieving variables
tt        = 0. : 0.2 : Tfinal
x         = sol(tt)
V_plot    = x[1, :]
gCaL_plot = x[10, :]
gCaN_plot   = x[13, :]

# Plot
p1 = plot(tt/1e3, V_plot, xlims=(0, 10), xticks=[0, 10], ylims=(-100, 60), yticks=[-100, 60],
    linewidth=1.5, legend=false, size=(600, 200), color=:gray30)
ylabel!("V (mV)")
p2 = plot(tt/1e3, gCaL_plot, xlims=(0, 10), xticks=[0, 10], ylims=(0, 0.06), yticks=[0, 0.06],
    linewidth=1.5, legend=false, size=(600, 200), color=:gray30)
ylabel!("gCaL")
p3 = plot(tt/1e3, gCaN_plot, xlims=(0, 10), xticks=[0, 10], ylims=(0, 0.2), yticks=[0, 0.2],
    linewidth=1.5, legend=false, size=(600, 200), color=:gray30)
ylabel!("gCaN")
xlabel!("t (s)")
CC = plot(p1, p2, p3, layout=(3, 1), size=(900, 600), margins=10px, dpi=500)
```

With `ControlledDA_ODE.jl` containing the following code.

```
#=
        This file contains differential equations describing the controlled CB model of interest
=#

# Function that outputs values of variables derivatives
function ControlledDA_ODE(dx, x, p, t)
        # Parameters
        Iapp = p[1](t) # Time dependent applied current
        gNa = p[2] # Maximum conductance of current Na
        gKd = p[3] # Maximum conductance of current Kd
        gERG = p[4] # Maximum conductance of current ERG
        gNMDA = p[5] # Maximum conductance of current NMDA
        gleak = p[6] # Leakage conductance
        C = p[7] # Membrane capacitance
        Mg = p[8] # Mg concentration
        alpha = p[9] # Rate of transfer between intracellular and membrane
        beta = p[10] # Rate of degradation of intracellular proteins
        Kp = p[11] # Proportional gain
        Ki = p[12] # Integral gain
        SVth = p[13] # Sensitivity matrix at threshold voltage
        gsth = p[14](t) # Reference gs(Vth)
```

```
guth = p[15](t) # Reference gu(Vth)

# Variables
V = x[1] # Membrane voltage
mNa = x[2] # Activation gating variable of current Na
hNa = x[3] # Inactivation gating variable of current Na
mKd = x[4] # Activation gating variable of current Kd
mCaL = x[5] # Activation gating variable of current CaL
mCaN = x[6] # Activation gating variable of current CaN
oERG = x[7] # ERG potassium current activation
iERG = x[8] # ERG current intermediate
gCaLi = x[9] # Intracellular maximum conductance of current CaL
gCaL = x[10] # Maximum conductance of current CaL
zCaL = x[11] # Integral variable of current CaL
gCaNi = x[12] # Intracellular maximum conductance of current CaN
gCaN = x[13] # Maximum conductance of current CaN
zCaN = x[14] # Integral variable of current CaN

# ODEs
dx[1] = (1/C) * (- gNa*mNa^3*hNa^1*(V - 60.0) -
                                    gKd*mKd^3*(V - -85.0) -
                                    gCaL*mCaL^2*(V - 60.0) -
                                    gCaN*mCaN^1*(V - 60.0) -
                                    gERG*oERG^1*(V - -85.0) -
                                    gNMDA*DA_NMDA_inf(V, Mg)^1*(V - 0.0) -
                                    gleak*(V - -50.0) + Iapp)
dx[2] = (1/DA_tau_mNa(V)) * (DA_mNa_inf(V) - mNa)
dx[3] = (1/DA_tau_hNa(V)) * (DA_hNa_inf(V) - hNa)
dx[4] = (1/DA_tau_mKd(V)) * (DA_mKd_inf(V) - mKd)
dx[5] = (1/DA_tau_mCaL(V)) * (DA_mCaL_inf(V) - mCaL)
dx[6] = (1/DA_tau_mCaN(V)) * (DA_mCaN_inf(V) - mCaN)
dx[7] = a0ERG(V) * (1-oERG-iERG) + biERG(V) * iERG - oERG * (aiERG(V)+b0ERG(V))
dx[8] = aiERG(V) * oERG - biERG(V) * iERG

# Retrieving which line of the sensitivity matrix matter
timescales = [2, 3]

# Retrieving which column of the sensitivity matrix belong to unmodulated conductances
unmodulated = [1, 2, 5, 6]

# Retrieving which column of the sensitivity matrix belong to modulated conductances
modulated = [3, 4]
```

```
        # Computing the right hand side of the linear system
        gDICr = [gsth, guth]
        gDICr = gDICr - SVth[timescales, unmodulated] * collect(p[2:5])

        # Computing the left hand side of the linear system
        Smod = SVth[timescales, modulated]

        # Computing the solution of the linear system
        g_r = \(Smod, gDICr)

        # Error signals and control inputs
        eCaL = g_r[1] - gCaL
        uCaL = Kp * eCaL + Ki * zCaL
        eCaN = g_r[2] - gCaN
        uCaN = Kp * eCaN + Ki * zCaN

        # ODEs of the controller
        dx[9] = alpha * gCaL - alpha * gCaLi - beta * gCaLi + uCaL
        dx[10] = alpha * gCaLi - alpha * gCaL
        dx[11] = eCaL
        dx[12] = alpha * gCaN - alpha * gCaNi - beta * gCaNi + uCaN
        dx[13] = alpha * gCaNi - alpha * gCaN
        dx[14] = eCaN
end
```

Note that a small adaptation of `ControlledDA_ODE.jl` has been made to ensure that the names of the gating functions match their actual names. Additionally, the NMDA current has been modified to be instantaneous, meaning it no longer has a gating variable dynamic. Furthermore, the gating variable dynamics for the ERG current were corrected, as its dynamic is non-standard.